CRANFIELD INSTITUTE OF TECHNOLOGY

School of Industrial Science

PhD Thesis

S. A. IMPEY

THE MECHANISM OF DROSS FORMATION ON ALUMINIUM AND ALUMINIUM-MAGNESIUM ALLOYS

Supervisors:

Dr. D. J. Stephenson
Dr. J. R. Nicholls

December 1989

ABSTRACT

Metal loss is an unavoidable consequence of the large scale melting of aluminium and its alloys. The objective of such processing must be to minimise losses, both from an economic viewpoint and to ensure optimum quality of cast and wrought products. Aluminium losses during melting and casting are primarily due to the formation of dross, a mixture of oxide and melt. Many of the commercially important aluminium alloys contain appreciable levels of magnesium (up to 5%) which can result in enhanced oxidation rates that give rise to particular problems in recycling.

Results are presented from a study aimed at reducing melt loss through a knowledge of the mechanism by which dross is formed. Work has centred on an understanding of the early stages in oxide scale growth, a study of growth kinetics and subsequent breakdown of these initial scales to form dross.

In humid atmospheres, the 'amorphous' oxide covering both aluminium and aluminium-magnesium at 750°C provides a highly effective barrier protecting the molten metal. In the absence of water vapour, oxide crystal development in aluminium-magnesium alloys is dominated by magnesium, and is extremely rapid in comparison with pure aluminium. Despite the different oxides formed, the manner of crystal formation at the 'amorphous' oxide-melt interface at 750°C on both aluminium and aluminium-magnesium is comparable.

Nucleation and growth of crystals in the 'amorphous' film generates high stresses which result in failure of the surface oxide. Scanning electron microscopy has shown that the localised failure of this protective oxide film results in exudations forming on the melt surface, the size and number of which increase with exposure time. These exudations would appear to be the onset of dross formation.

Parallel studies of the wetting characteristics of aluminium to alumina have shown that the reported non-wetting is due to the presence of the thin alumina film on the melt surface. Once broken, wetting of the alumina takes place and accounts for the exudation of molten metal through the surface oxide and hence dross formation.

LIST OF CONTENTS

LIST OF TABLES

9.8 ° Densities of aluminium and magnesium metal and oxide [273].

9.9 ° Mechanical properties of 'amorphous' anodic γ -Al_2O_3 films tested at atmospheric pressure and in vacuo [275].

9.10° Summary of the effect of trace elements on aluminium and aluminium-magnesium alloy.

° in text

LIST OF FIGURES

6.3 The effect of surface finish on the oxidation of aluminium in dry air at 750°C.

6.4 The influence of humidity on the oxidation rate of aluminium at 750°C.

6.5 Oxidation of aluminium in gettered argon at 750°C.

6.6 Oxidation of aluminium in humid argon at 750°C.

6.7 Oxidation of polished aluminium (1μm) at 750°C.

6.8 Oxidation of electropolished aluminium at 750°C.

6.9 Oxidation of aluminium in dry air and gettered argon at 750°C.

6.10 Sequence of rate equations followed during the oxidation of aluminium in air and argon at 750°C.

6.11 Oxidation of aluminium at 750°C in air in the presence of fluoride (KBF_4).

6.12 Oxide growth (x40K) of alumina in dry air at 750°C on skimmed aluminium melts at a) 5 min, b) 1h, C) 5h and on unskimmed aluminium melts at d) 5 min e) 5h

6.13 TEM micrograph of γ -Al_2O_3 crystals at the oxide-melt interface formed on unskimmed aluminium at 750°C in dry air after 150 hours exposure

6.14 Growth (x40K) of γ -Al_2O_3 on skimmed aluminium melts after 1h a) at 650°C in dry air and b) at 750°C in humid air

6.15 SEM of oxide-gas interfaces oxidised at 750°C in humid air for 15h on a) unskimmed aluminium b) skimmed aluminium c) unskimmed aluminium

6.16 Microtome sections through oxide and metal of aluminium oxidised at 750°C in dry air for (a,b) 1h and for c) 5h

6.17 TEM of γ and α -alumina formed at 750°C on aluminium in gettered argon after (a) 5h and (b) 15h with (c) SEM of metal-oxide interface at 15h with excess metal removed.

6.18 Aluminium surfaces after 5h oxidation at 750°C in (a) humid air and (b) in dry air and (d) through the specimen centre and (c,e) through the specimen edge (f) aluminium oxidised in humid air for 70h.

6.19 Oxidation of aluminium at 750°C in dry air for 24h showing oxide growths on (a) top surface, with (b) corresponding section and (c,d) reverse surface.

7.7 Surface of skimmed Al-1%Mg melt at 750°C after (a) 5h showing oxide growth and (b) 15h.

7.8 Sections through oxide-melt interface showing development of nodular growths, illustrated in (e) after 20h in humid air covering surface and (f) after 5h in gettered argon at isolated area.

7.9 Oxidation of 5005 NGR alloy in air and argon atmospheres at 750°C.

7.10 Influence of specimen position to gas flow on the oxidation of polished (1μm) 5005 GR alloy in gettered argon at 750°C.

7.11 Oxidation of machined and polished 5005 GR and NGR alloy at 750°C in gettered argon (plotted per unit surface area).

7.12 Oxidation of machined and polished 5005 GR and NGR alloy at 750°C in gettered argon (plotted per unit weight).

7.13 Hole in oxide on Al-1%Mg (a) low and (b,c) high magnification of surface layers and melt after 5h in fluoride containing atmospheres at 750°C.

7.14 Micrographs of (b,f) skimmed 'amorphous' oxide and (a,e) unskimmed magnesia on 5182 melts after 5 mins in humid air at the oxide gas surface and (c,d) in transverse section.

7.15 Sections through oxide-melt interface on 5182 oxidised at 750°C (a) showing primary MgO crystals after 5 mins and (b) smaller secondary magnesia crystallites after 1h. Oxide crystal dispersion is seen (d) at the oxide melt interface and (c) the thickening oxide surface (e) after 80 mins oxidation.

7.16 Element distribution (by electron microprobe) on a 5182 alloy section oxidised for 1h. Showing (b) magnesium (c) oxygen enrichment of the oxide and (d) remaining aluminium metal.

7.17 (a,b,e) sections through growths on heavily oxidised 5182 alloy 20h at 750°C in gettered argon on the (c,d) oxide surface.

7.18 Oxidation of machined 5182 in dry air at 750°C.

7.19 Oxidation of machined 5182 in air and argon atmospheres at 750°C.

7.20 Oxidation of polished (600μm) 5182 in flowing and still gettered argon.

7.21 Oxidation of polished (1μm) 5182 in air and argon at 750°C.

7.22 The influence of surface finish on oxidation of 5182 in gettered argon at 750°C.

7.23 Oxidation of machined and polished 5182 in humid air at 750°C.

7.24 Vertical section through magnesia on a 5182 alloy oxidised at 550°C in gettered argon. (b-e) shows the development of growths on (a) on oxide surface.

7.25 a) Section of the reverse surface of 5182 oxidised in gettered argon at 550°C showing increased growth at (c,e) the centre to (b,d) the outer edge.

7.26 Oxide growths protruding through glass coat on a 5182 alloy after 15h oxidation at 550°C in gettered argon.

7.27 Micrographs of oxide surface after 5182 oxidation in gettered argon at (a) 450°C; c) 650°C and (d,e) in section (f) 850°C.

7.28 The effect of temperature from 450 to 850°C on the oxidation rates of polished 5182 alloy in gettered argon.

7.29 Effect of preconditioning in humid air at 550°C over 0-15h, on the oxidation rate of 5182 in gettered argon at 750°C.

7.30 Effect of preconditioning in humid air at 750°C over 0-15h, on the oxidation rate of 5182 in gettered argon at 750°C.

7.31 Effect of preconditioning in humid air at 550 to 850°C for 5h, on the oxidation rate of 5182 in gettered argon at 750°C.

7.32 The oxide surface on 5182 after preconditioning in humid air for 15h showing detrimental cracking with exposure to gettered argon after (a) 2h, and (b) 5h. With magnification (c) the surface and (d) the growth.

7.33 The (a,b) oxide surface and (c) oxide section of 5182 after 5h at 550°C and 15h oxidation at 750°C.

7.34 Oxide growth on 5182 in fluoride for 5h at (a) 550°C and (f) 750°C with (b) in section and (d) chloride (5h at 750°C).

7.35 Development of BeO crystallites on skimmed 5182 alloy melts containing 50ppm addition after 5 mins oxidation in air at 750°C, with c) transparent MgO and BeO surface film, after 15h oxidation in gettered argon at 750°C.

* figure in text.

NOTATION

B	Gradient	
f	Force required (to withdraw slide from melt)	N
F_1	Force at point (b) - force measured prior to fracture of surface oxide	N
F_2	Force at point (c) - force measured during insertion of probe	N
F_3	Force at point (d) - force measured during probe removal	N
g	Acceleration due to gravity	ms^{-2}
h_e	Height of aluminium exudation	m
k	Equilibrium rate constant	
k_l	Linear rate constant	$g/cm^2/s$
k_p	Parabolic rate constant	$g^2/cm^4/s$
L	Thickness of electron surface layer	m
Δ_m	Change in specimen weight due to oxidation	kg
P_{O2}	Partial pressure of oxygen	KPa
r	Radius of probe	m
r_e	Radius of aluminium exudation	m
r_p	Radius of pore	m
S^{γ}	Excess interfacial entropy	KJ/(Kg/mol k)
Tcs	Critical temperature for spreading Temperature at which θ approahces zero	°C
t	Oxide thickness	m
t'	time	s
ν	Radial velocity of growth	ms^{-2}
W_a	Weight of 'amorphous' oxide	Kg
W_c	Weight of crystalline oxide per unit area	Kg
W_t	Total weight of oxide	Kg
X_{Mg}	Molecular fraction of magnesium in alloy	
x	Penetration depth of probe into melt	m

$\gamma_{Al_2O_3(s)\text{-air}}$	Surface energy of alumina-air interface	Nm^{-1}
$\gamma_{Al(l)\text{-}Al_2O_3(s)}$	Surface energy of aluminium-alumina interface	Nm^{-1}
$\gamma_{Al(l)\text{-air}}$	Surface energy of interface between unoxidised molten aluminium and air	Nm^{-1}
$\gamma_{Al(+Al_2O_3)\text{-air}}$	Surface energy of interface between molten aluminium covered with thin oxide film (oxide modified aluminium)	Nm^{-1}
Γ_i	Number of species i, in unit area of surface phase ($\Gamma i = NiD/A$)	
γ_{Fowler}	cited [177]	
γ_i	Surface energy to initiate fracture	Nm^{-1}
γ_{lv}	Surface tension of liquid-gas interface	Nm^{-1}
γ_o	Surface free energy (ideal thermodynamic determination)	Nm^{-1}
γ_p	Surface energy from plastic deformation	Nm^{-1}
γ_{sl}	Surface tension of solid-liquid interface	Nm^{-1}
γ_{sv}	Surface tension of solid-gas interface	Nm^{-1}
$\gamma\mu$	Unquantifiable surface energy factor	Nm^{-1}
η	Factor due to a non planar surface	
θ	Contact angle made between melt of liquid and solid	
δ	Thickness of γ-Al_2O_3 crystals	
μ_i	Chemical potential of component i	
ρ_{Al}	Density of aluminium	$Kg\ m^{-3}$
$\rho_o, \rho_{indirect}$	Contributions to density from volume dependent terms	$Kg\ m^{-3}$
ρ_{ox}	Density of γ-Al_2O_3 crystals	$Kg\ m^{-3}$
σ_f, σ_{oxide}	Fracture stress of oxide	Pa
σ_{lv}	Specific surface energies at liquid-gas interface	Jm^{-2}

σ_{sl}	Surface energy at solid-liquid interface	Jm^{-2}
σ_{sv}	Surface energy at solid-gas interface	Jm^{-2}
Ω	Nucleation density	

INTRODUCTION

The economic incentive to recycle aluminium alloys has resulted in a considerable expansion of the secondary aluminium industry [4]. Scrap for recycling takes many forms but often has a large surface area to volume ratio (e.g. swarf, turnings, lacquered scrap). This geometry, together with the high reactivity of the aluminium alloys, is responsible for the oxidation problems encountered during melting. Metal loss due to oxidation can be considerable, especially with aluminium-magnesium alloys, due to the formation of dross, a mixture of oxide and entrapped liquid metal [153]. The magnitude of the problem depends on the alloy composition, physical form of the charge and exposure time in a given environment [24]. For aluminium alloys a metal loss value of 2% is typical for good foundry practice whereas for certain Al-Mg alloys losses may be higher than 10%. Although engineering solutions are being investigated [277] and developed to reduce melt losses, little is understood with regard to the mechanisms of melt incorporation within oxide envelopes and hence dross formation.

To address this problem, fundamental information on the interaction between the melt and furnace environment is required. In particular, the influence of contaminants such as water vapour and the effect of fluorides derived from the use of fluxes require investigation. To this end, a programme to study the oxidation behaviour of commercial purity liquid aluminium and a number of aluminium-magnesium alloys has been carried out to identify the mechanism of dross formation on these metals.

CHAPTER 1 INDUSTRIAL IMPORTANCE OF ALUMINIUM ALLOYS

Aluminium is one of the most diverse and versatile metals. One of its many attractions is the high strength to weight advantage and where weight reduction is important aluminium finds many applications. Alloy development enhances the useful properties of aluminium and after steel, aluminium has become the most widely used metal. Since the discovery 100 years ago of an economical process for producing aluminium from its oxide, annual production has grown to over 16 million tonnes [1,2,3]. These figures are displayed in Table 1.1.

Until recently, there has been a high growth rate demand for aluminium. World consumption of primary aluminium to 1973 had an annual growth rate of 10% [5] with a growth rate of 1.6% per annum thereafter. Some of the growth was supplied from recycled material [4] however this reduction in demand seems to have arisen due to other inter-related factors such as different market demands combined with a world economic recession.

The aluminium industry, along with those of steel and copper, is under competition from developing nations. In 1970 the six largest primary producing companies (Alcan, Alcoa, Kaiser, Reynolds, Pechiney and Alusuisse) held over 70% of the world market share [5]. This currently stands at 33% and is expected to fall to 25% in the next few years [4]. Competition has become necessary to meet increased demands for bauxite. For example, 7.1 million tonnes of bauxite was worked in 1950, the demand in 1987 however was over 93 million tonnes [4,5]. Some of the largest producers of alumina and primary aluminium, the USA, USSR and Japan are heavily dependent on imported bauxite. As a result, major shifts in smelter location have occurred causing the industry great difficulties. Planned increases in capacity in Australia, Brazil and Canada will accelerate the shift of primary aluminium production that has been taking place over the last decade away from industrialised countries in the Northern hemisphere towards those in which major bauxite mines are located [4].

The consumption of primary and secondary aluminium by end use is illustrated in Figure 1.1. More than 50% of aluminium is produced as rolled products ranging from foil, sheet and flat strip, having wide application in building, transport, domestic appliances and containers, to plates used by aircraft manufacturers. Significantly thicker plates (50mm) are required for many items of industrial plant, storage tanks and ships [6]. Some 15% of all aluminium is sold in the form of extruded section and tube which is in demand for building construction, transport, and as wire and cable where, since 1964, aluminium has had a price advantage over copper as the conducting material for electrical transmission [1,7].

Figure 1.1 demonstrates a dramatic change in consumption in the UK, over a ten year period, from 1976 to 1986. The relatively low melting point of aluminium alloys (in comparison with other metals), makes it particularly suitable for die casting. Aluminium alloys have been standard for cylinder heads and gear boxes for a long time [1]. However, while production of semi manufactured forms has been maintained, the home demand for foundry ingot and hence for castings has gone down sharply. This is a direct result of the reduced production of motor vehicles in the UK,since transport applications count for 65% of all aluminium castings [8].

Comparison of aluminium consumption in the UK in 1976 in Figure 1.1, shows similarities with the consumption in developing countries in 1986 where current demand is principally for basic materials particularly for construction and for improved communications. Although there is still a significant domestic market for basic materials the emphasis, and growing market reflected in UK and world consumption in 1986 is in speciality materials [4]. Trends reflect a variety of maturity and innovation, such as expansion in rolled products in engineering from specialised lithographic sheet. Change in investment from new commercial, industrial and residential projects to renovation, including double glazing, secondary and replacement windows has benefitted building applications. Containers for frozen and take away foods have provided a strong growth market for foil.

Aluminium penetration in the beverage can market area is illustrated by the dramatic growth in packaging. This includes more permanent packaging such as beer barrels and high pressure gas cylinders [6].

World consumption of primary aluminium, given in Table 1.2, has been checked by economic recessions. Prior to the OPEC oil crisis in 1973, the rate of growth was over 10% per annum. From 1973 to 1986, although the total world consumption of primary and secondary aluminium has grown at a rate of 2.5% per annum, the contribution from primary metal has decreased annually to 1.6% over the same period [4]. This represents considerable growth and dependence on recovering aluminium scrap.

1.1 THE INCENTIVE FOR RECYCLING AND DEVELOPMENT OF THE SECONDARY INDUSTRY

The statistics in Table 1.1 emphasise the major role the secondary industry plays in ingot production and thus the importance of recycling. The rate of growth in the production and consumption of secondary aluminium derived from obsolete and scrap articles rose 5% per annum from 1973 to 1986 [4], more than twice that of primary aluminium over the same period. In 1986, secondary metal consumption was over 5 million tonnes. In addition, a considerable tonnage of aluminium scrap is recycled within the primary industry as in-house scrap and is not recorded in statistics. In 1985, over one quarter of the total ingot production in Europe was produced from secondary material whilst in the UK one third of all ingots was produced from secondary metal. This larger proportion is due to the fact that the UK is an extensive exporter of secondary ingot into Europe, USA and the Far East. The UK secondary industry has countered the reduced home demand for foundry ingot by increasing its exports. For example, in 1984 the UK exported 42000 tonnes of secondary ingot from a world export tonnage total of 94000 tonnes [8]. The data further show (Table 1.3) that secondary recovery is expected to represent an increasing fraction of the total aluminium comsumption throughout the next decade [2].

The secondary aluminium industry has developed out of necessity for several inter-related reasons. Firstly, in the present economic situation there is a requirement to reduce energy consumption. Typically primary production of aluminium requires 58 GJ of electric energy per tonne of metal [8,9]. Other sources estimate from 86 to 288 GJ/tonne [7,10,11,12] for the production of molten aluminium and 1100 GJ/tonne [13] for the entire production process from bauxite extraction to molten aluminium. Since the start of the energy crisis the UK aluminium industry has put considerable effort into reducing the energy consumed during primary production [6]. Data collected by the E.E.A. Energy Committee show that in the last ten years energy consumption in the primary smelting process has fallen from 63.4 to 57.6 GJ/tonne. This level is still high when compared with some other competitive metals. For example, the energy required to produce one tonne of primary aluminium is five times higher than that required for one tonne of copper or zinc and eleven times higher than for one tonne of cast iron [8].

Estimates from various sources for the energy required to produce one tonne of secondary aluminium vary from 3 GJ/tonne [12] to 14-21 GJ/tonne [10,7] for the entire melting process. This is a considerable energy saving representing approximately 5% of that required to produce the same mass of primary ingot. Thus over twenty tonnes of recycled aluminium can be produced with the energy required to produce one tonne of primary metal. Claims of energy savings of 95% using recycled material [14] can often be misleading for in practice, material is blended to make up charges. For example, beverage cans are made from a blend of primary material such as ordinary commercial forms of primary ingot, either pure or alloyed to dilute the melt, and the remainder scrap. At present cans are not manufactured from 100% secondary aluminium [14].

There is also a need to conserve available metal to limit the drain on bauxite reserves, particularly in countries without domestic supplies. Further, there is considerable pressure from environmentalists to use obsolete components and scrap to reduce the

demand on dumps and unsightly litter such as beverage cans. While consumption of primary aluminium has increased threefold in the last twenty years, this is not yet fully reflected in the supply of scrap available for recycling. It is probable that present mine dumps, scrap yards and even municiple tips may be looked upon in future as man made mines for minerals and metals if waste recycling operates at a lower cost than mining natural deposits [15].

In addition to the above, the industry recycles aluminium in an attempt to maintain its competitive position in many markets and so aid primary metal production. Energy costs in secondary metal tend to be more manageable and often controllable within the industry itself unlike primary metal production, which has considerable dependancy on current fuel and energy costs. A dependence on high cost fossil fuel has been reduced in favour of low cost fossil fuel (such as flare gas or brown coal) and hydroelectricity. The availability of hydroelectricity however, as a secure source of cheap power for smelters is under threat in many locations [4]. Access to cheap and available power has become the most important factor that determines the world competitive position of a primary aluminium producer [16]. Some of the newer producers have their power costs subsidised by the government which tends to distort the true economic situation [5].

Aluminium faces much competition with other materials such as steel, glass, copper, polymers, and composites in very different markets. Product prices are essentially governed in the market place. As the sale value of all aluminium products is dictated by competitive pressures from other materials in specific product and market areas; the availability of secondary metal is important to producers to protect their profitability. By increasing the share of secondary metal used to 33% by 1990 [4] the industry is well maintained to increase the use of recycled material further in case power for the primary plants is not competitively priced. This approach has limitations in that it is possible to reduce smelting below maximum production but once cold,

the smelters can take between 6 months to a year to return to full production [27]. Thus it is important to ensure that in future a favourable balance is maintained between primary and secondary consumption to help the aluminium industry remain competitive.

1.2 THE FUTURE

The aluminium markets are just approaching maturity, and there is time to develop new technologies and expand into new markets.

Utilisation of the material property of superplasticity in fabricating sheet metal components is viewed as a technological breakthrough. The need for superplastic aluminium alloys in the aircraft industry has been well documented [18,19] eliminating expensive manufacturing steps when complex components can be fabricated to the desired configuration from a single sheet. Some superplastic alloys, notably SUPRAL, have found wide application in diverse markets such as medicine, communication, architecture, transport, electronics, and even the leisure industry [27].

There is a growing awareness of aluminium as a potential powder metallurgy base metal. Powder metallurgy offers many advantages over conventional ingot manufacture, particularly in the area of alloy strengthening mechanisms. A significant increase in strength can be achieved by incorporating a dispersion of fine intermetallic or non metallic particles. Such dispersoid phases can be produced by mechanical alloying [1] and rapid solidification [20]. Non metallic additions are found in metal matrix composites for which aluminium and its alloys are considered among some of the best candidates for the matrix [27]. Successful development of these technologies is necessary to preserve the competitive position of aluminium.

In specific markets, aluminium has great potential, particularly in packaging and in the transport industry. Containers and packaging is the single largest market for aluminium in the USA and has almost reached the saturation limit at around 95% of the beverage can market; 98% of the market is forecast for 1990 [4]. Outside the USA, as effective recycling schemes are introduced improved recovery is anticipated. Aluminium food cans make up only 5% of the market at present. Thus introduction of new can designs, easy open convenience cans and a liquid nitrogen packaging process could initiate growth in this area [4]. Although there is considerable competition from other forms of food packaging, especially plastics and paper based cartons, the outlook for aluminium packaged convenience foods is favourable.

All sectors of the transportation industry have generally recovered from the period of recession in the early 1980's. Moves towards improved fuel economy means that low density materials are increasingly adopted. If new Al-Li alloys, improved aluminium alloys and aluminium matrix composites are successful in holding off severe competition from carbon fibre reinforced composites and titanium alloys, aluminium will continue to remain the predominant material for use in aircraft (70-80% of the structural weight [20]). In addition, ongoing research and development of an all aluminium car body [27] and aluminium-air batteries to power electric vehicles [27] will ensure aluminium remains highly competitive in the transport industry.

It is anticipated that greater capacity will be required to meet the increased consumption forecast for the year 2000 (as shown in Table 1.3) and a programme of new smelter constructions is in operation [4]. Meanwhile it is necessary to look to ways of gaining the capital for expansion as there is no guarantee of the price of aluminium remaining firm [5]. Alternative processes for converting alumina to primary aluminium that consume less energy are sought. Currently no commercial alternative to the conventional Hall-Heroult aluminium reduction cell exists and is not anticipated before the

year 2000 [4]. Thus in the interim the most likely area to gain capital is in energy reduction. Here improved foundry practice; good housekeeping and scheduling operations, better scrap control and improved melting procedure offer possible solutions. The most underestimated area is that of metal loss.

The quantity of metal lost in any form (i.e. 'metal oxidised or otherwise lost in melting') is considered by The Department of Industry and Energy to be equivalent to an energy loss of 32 GJ/tonne [7]. This is similar to that used in the extraction of aluminium and is a substantial amount of energy. The Department estimates that a potential saving of £4.2 million is possible from minimising these losses. Other sources estimate the cost of metal losses in the UK as £6 million [24]. At an assumed metal price of £1000/tonne every 1% reduction that can be made is considerable for an industry remelting over 5 million tonnes of aluminium per annum.

Losses are difficult to define but metal can be lost in three forms. Metal is lost as scrap, as items that are not recovered at the end of their service life. Secondly, metal is oxidised during exposure to an oxidising atmosphere during melting. Thirdly metal is lost as finely divided and trapped melt within oxide envelopes in dross. The following sections will examine in detail the loss of metal in the secondary industry, as oxide and as dross. The next chapter considers the secondary industry, scrap reclamation, present foundry melting procedures and parameters attributing to such metal loss.

CHAPTER 2 THE SECONDARY ALUMINIUM INDUSTRY

The importance of the secondary industry has been emphasised in the previous chapter. This section aims to review it in more detail.

The secondary industry has developed using aluminium scrap as its raw materials. A simplified idea of the passage of aluminium material is illustrated in the flow chart of Figure 2.1. However the distinction between a primary and secondary source has become blurred as nearly all primary producers are now involved in large scale reclamation [17]. A number of secondary smelters (ten in the UK, five of these linked with major primary producers) produce metal to primary specifications [18].

2.1 SCRAP RECLAMATION

There are typically three distinct stages in the use of aluminium:

1. Transformation of primary metal into semi-manufactured forms.

2. Further processing of these semi-manufactured forms into servicable articles.

3. Use and final discarding of these articles.

Each stage produces scrap, which is recycled to an extent determined at any time by its economic viability. Sources of secondary aluminium are process scrap from the fabrication of semi-manufactured products, scrap from its conversion into manufactured products (new scrap) and from obsolete or old scrap.

Process scrap is generated within the primary industry and remelted in-house, thus little of it enters the secondary industry and may or may not be included in statistics. New scrap may be fed

back and treated as process scrap if produced in large quantities at one location of known composition, relatively free from contamination.

New scrap originating from product manufacture (such as cuttings, swarf turnings and process waste) is usually produced in separate establishments remote from the smelters. The material consists of a complex mixture of alloys of different composition. The ease of recovering new scrap is highlighted by its recycling rate, almost 100%, the only losses being a small amount of metal lost in low grade drosses [8].

Old scrap, discarded aluminium items, is derived from a variety of end users each with a different level of contamination. Sources range from scrapped aircraft to milk bottle tops. End users are widely scattered, most with no direct incentive to see that the metal they scrap is returned for re-use, hence the collection industry has become established by selling aluminium to secondary smelters.

This collection industry may be divided into four different levels:

1. The charity collector.

2. The small scale professional operation which sells products to metal dealers.

3. Metal dealers with their own yards. Scrap sorted by type may be processed in simple melting equipment on site or sold to the scrap merchant.

4. The scrap merchant may have large yards, but the metal may be sold by the merchant to the secondary smelter and directly transported.

Efforts are now being made to increase the efficiency of this collection system. In 1970 the input to the secondary smelter was made up of three parts new scrap to one part old scrap, suggesting that over 70% of all products manufactured are never recovered [8]. Now with increased effort expended in collecting all nature of discarded aluminium items, the average recycling rate of old scrap in Europe is approximately 35% [8]. This is higher than that in the USA if the beverage can market is excluded, as Table 1.1 shows. The potential of old scrap as a source of aluminium is still very large and will become an important metal supply source in the future.

The life cycle of aluminium articles varies from an extremely short period as in the case of beverage cans (9 weeks), to 40 years in electrical transmission and in building applications. Transport has a life cycle closer to 10 years thus a weighted average life of an article in use is approximately 20 years [13]. It is suggested that for articles with a service life of several years a much higher fraction for recovery is achieved, possibly 40% [27]

No useful data seems to exist whereby actual recovery rates for each end user category can be determined. Efforts have been made to predict regions where old scrap is currently not reclaimed, with the aim of seeking out opportunities for scrap recycling and energy savings [23].

2.2. THE VALUE OF SCRAP

The recovery of scrap must be economically viable, a limitiation recognised for example, in recovering low density scrap. The cost of the material plus the cost of treatment cannot exceed the value of the final product. Scrap value of aluminium on a weight basis is currently seven times that of ferrous metals [28]. The value of various types and grades of aluminium scrap depends on the physical form, composition, metallic recovery and purity.

Higher purity scrap is used in the manufacture of the more expensive alloys. They command a premium price over less pure, less desirable grades. Grades of primary aluminium and commercial grades of scrap that can be obtained are illustrated in Figure 2.2. Skim generated in melting aluminium is worth about 25% (per unit of aluminium) of the value of standard primary metal, whilst extremely pure aluminium (99.99%) is worth 100 times the standard primary aluminium price. On average the value of aluminium is degraded only 6% for each doubling of impurity content. The steepness of the middle portion of the curve of Figure 2.2 is affected by supply and demand for the metal [28].

The potential for scrap recovery in the United States is due principally to increased recycling efforts primarily in aluminium beverage cans and secondly, the impending increased aluminium recovery from scrap cars. These two markets have little in common except for the high rate of recycling which accounts for most of the recycled metal in the USA. The next section looks closer at these developing areas.

2.3 THE ALUMINIUM BEVERAGE CONTAINER

Aluminium is extremely popular as a beverage container due to such favourable properties as corrosion resistance, thermal conductivity, low density and good formability. Further, cans are a good source of secondary aluminium as, other than the ink used to identify the manufacturers name and logo, the cans contain only aluminium alloy.

The all aluminium can has replaced the original convenience package of a steel can with an easy open aluminium lid because it offered better taste preservation and thus longer shelf life. Continued use and growth of this all aluminium container usage is a result of three distinct efforts. Firstly a recycling drive (1970) arising from public concern of litter from discarded cans, saw the

founding of recycling centres and collection points. The image presented by good marketing of the aluminium can as a valuable resource and not as litter scrap increased can sales six fold, along with continued growth of the recycling industry. Secondly, at a 25% recycling rate the aluminium can is more energy efficient than the bimetallic can and with 60% recovery it becomes competitive with the returnable glass bottle [12]. Thus as can recycling increases the total energy required to maintain a beverage can system decreases rapidly [21]. Thirdly, aluminium cans in 1987 are around 50% lighter than those in the mid 1960's. Use of thinner gauge aluminium and shape modifications requires less material [4].

In the USA in 1986 95% of the beverage can market was aluminium, in comparison with 40% of the UK market (5×10^9 cans); The remaining 60% is tinplate [4]. Aluminium cans have not captured as large a share of the beverage container market as the USA mainly due to government intervention [4]. In July 1987 however, the European Aluminium Association launched a campaign to promote aluminium beverage cans throughout Europe and to help companies establish essential recycling programmes. The European beer market is also a target for aluminium can makers [4]. This should ensure a good source of aluminium is present in future scrap bins.

A certain amount of pure metal is required for dilution to bring the elements present in can scrap into compositional limits. The aluminium can itself is two piece and there is an almost universal use of AA3004 alloy (1% Mg) for body stock and AA5182 alloy (4.5% Mg) for end stock [27]. On remelting, the resulting theoretical magnesium level is approximately 2.0%. Prior alloy separation of body and end stock avoids the requirement for large quantities of pure aluminium for diluting the melt. For example, thermomechanical separation [22] yields two metal streams which are remelted separately resulting in usable 5182 alloy in addition to 3004 alloy.

As the volume of new metal required decreases, compositional requirements get tighter hence contamination levels must be lower, and dirt and contaminants need to be removed before melting. Hence, a limit of recyclability is determined by the amount of iron and silicon contamination (the level increases with the number of cycles) which becomes the controlling factor as the body and lid alloys become more compatible with respect to magnesium and manganese [23]. Thus the continued success of the can depends increasingly on the success of recycling and developing melting technology.

2.4 ALUMINIUM IN CARS

The sharp increase in oil prices of 1973/4 and 1979 resulted in a trend to lighter (and in the USA, smaller), more economical cars [4]. Significant weight savings are possible by replacing the traditional mild steel and cast iron components with aluminium. Other advantages are improved fuel economy and performance due to the lighter weight, plus corrosion resistance and beneficial thermal properties for some applications. Currently, the major uses of wrought aluminium alloys in cars are in radiators, suspension components, bumpers and body pannelling [25]. Major weight reductions and greater power to weight ratios are achieved from cast aluminium alloy cylinder blocks and heads. Other applications are gear boxes, castings, wheels, pistons, driveshafts, exhaust manifolds and aluminium chassis [4].

Substantially higher quantities of aluminium are now designed into cars. In 1965, 2% of 1723kg American vehicle was aluminium. By 1987, even with a 33% overall weight reduction, the aluminium content increased to 5% [4]. British cars tend to be smaller than the American counterparts but show a similar trend of increased aluminium usage (4% in 1987) [4].

A number of car manufacturers in cooperation with aluminium producers are actively involved in research and development of an all aluminium car body, using both new and conventional fabrication techniques and designs [4,27]. At present production is restricted to specialist sport cars, providing a structure with significant scrap value at the end of its lifetime. Thus with projected increases of aluminium alloys in car manufacture, aluminium could become the material with the highest aggregate value [14].

Car scrap will be available whether the UK retains a viable motor vehicle industry, as countries exporting cars such as Japan must always be prepared to buy in more raw materials, such as aluminium, since their cars are scrapped out of the country. From a recycling point of view cars are an important source of both wrought and cast aluminium. Over 30% of wrought and 80% cast aluminium used in cars is recovered [26]. Recycling of cast aluminium has been at this level for many years as it is more easily identified, heavier and can be removed before shredding. The level of recovery of cast aluminium may even be higher as castings in good order are cleaned and often offered for sale as reconditioned parts [8]. It is forseen that methods and practices in the auto salvage industry will develop to recover more of the growing potential supply of aluminium.

2.5 PREPARATION OF SCRAP FOR THE SMELTER

Aluminium may be hand picked from scrap, but is generally removed by other means. The ferrous material can be extracted from shredded scrap fragments by electromagnetic separators, magnets, air classifiers, heavy media separators (based on density [28]), and by differences in friction coefficients. Such methods are not suitable when dissimilar metals are mechanically joined, welded, soldered or plated to one another.

Other methods for separating involve melting material in a sloping hearth or rotary furnace. An Alcoa process takes advantage of difference in melting ranges for the two alloys in beverage containers, since 5182 alloy melts approximately 90°C below 3004 alloy. The process also depends on the specific way in which melting in the 5182 alloy is highly localised at grain boundaries. When several of the grain boundaries are melted, the ends become weak and gentle tumbling is enough to cause fragmentation. As the body components remain unaltered, both alloys are then separated by size [22].

Investigations have been carried out into selective melting techniques with fused salt and controlled atmospheres [26]. The aluminium rich fractions extracted (at 590-633°C and 800°C) may be of variable composition, usually 80-85% aluminium [28].

2.6 THE SECONDARY SMELTER

The secondary smelter essentially converts lower value contaminated and obsolete scrap forms into foundry ingots and castings for general engineering purposes according to the British Standards specification BS 1490.

On reaching the secondary smelter, scrap is examined to ensure it meets the description under which it was sold. A classification system exists to describe scrap, although the United States and European systems differ. Scrap is then assigned to a particular intake group or if mixed scrap, will be separated into types and grades. As many as 150 codes of scrap materials may be received [30].

The average composition of mixed scrap will change, differing from suitable foundry casting alloy compositions as wrought alloy applications in goods increase. The probable alloy components expected in future scrap stocks can be estimated by considering

predominant alloys usually used in production, particularly sheet metal alloys which are currently the highest tonnage of aluminium semi manufactured material produced.

The principle commercial wrought alloys are based on additions of five main elements (Zn, Mg, Cu, Mn, Si). These are used in various combinations for age hardening, casting and work hardening. Al-Mn and Al-Mg are work hardening alloys of two basic types. Al-Mn alloys obtain a modest increase in strength from forming a fine dispersion of intermetallic phase particles. In Al-Mg based alloys the magnesium remains in solid solution and is considerably more effective than manganese as a hardener (0.08%Mg = 1.25% Mn). In addition, manganese has a limit of effectiveness at 1.5% [31]. All alloying elements will increase work hardening, but these two systems are extensively used as they both remain stable during processing.

Both classes of alloy are used as sheet metal in transport, chemical storage tanks and equipment, and for appliances in domestic and industrial use. Al-Mn alloys find applications in building and construction as corregated sheeting, residential siding and mobile homes, where moderate strength and good corrosion resistance is required. Al-Mg alloys possess good welding characteristics and so are used for high strength welded structures such as pressure vessels. They show excellent corrosion resistance especially to marine conditions and are widely used for drilling rigs, stressed marine craft fittings, launches and lifeboats. Combinations of Al-Mg-Mn are sucessfully used in aluminium alloy beverage containers where additional requirements for good ductility exist [32].

Scrap of known composition will become more commonplace with the increased returns of beverage cans. Standard body (3004) and end (5182) sheet alloys for beverage containers have been recorded in Table 2.1. Furthermore, a future food can alloy is likely to be compatible with present can alloys, based on systems that contain magnesium and manganese as the principle alloying elements [22].

Estimates of two future car scrap alloys [21] and sheet aluminium alloys used in transport for panels, trim and structural members [25] have been tabulated in Table 2.1, along with alloy mixes used in fabricating plants [33]. It is difficult to envisage the content of scrap bins when using mainly estimates of binary alloys, but it is likely that the mixture of elements (as shown in Table 2.1) will predominantly vary in magnesium content (0.5-4.5%) with or without (less likely) manganese (1.0%) plus a nominal quantity of iron and silicon (1.0%) which increases with recycling. This is for short life time, high recovery material. Alloys used in aerospace possess high copper and zinc additions but have long product life times and hence make up only a small proportion of the total aluminium used in all industries.

A major alloy making considerable impact in the aerospace industry is aluminium-lithium (Al-Li). The addition of lithium to aluminium dramatically decreases the density and increases the elastic modulus, thus Al-Li alloys are of benefit in applications where weight savings are of major importance. Indeed, a broad objective for the aerospace industry is to establish low density Al-Li alloys as the material of choice for all aluminium alloy structures in new designs, where most studies predict an 8-12% reduction in the weight of the affected structure [20]. Further attractions of Al-Li alloys concern their ability to undergo superplastic forming [19]. In possessing mechanical properties similar to current alloys widely used, designers do not have to rethink their design approach. The amount of material generally purchased is 2-10 times that used in the final aerospace structure hence Al-Li scrap costs may be significantly reduced by recycling [40,34]. For these reasons production and development of Al-Li alloys is currently under intense activity [35].

Clearly, scrap aluminium arises in many different forms. Typical scrap arisings in the aluminium industry can be categorised as old castings, sheet cuttings both pure and alloyed, turnings, millings, swarf and foundry dross and sweepings. The form of the

charge, in particular the surface area to volume ratio, is of concern. In secondary melting the scrap often has a high surface area to volume ratio, as with foil, swarf and turnings. Small fragments are not easily charged in a furnace and so are usually baled for efficient transport and melting. Sheet scrap can be dealt with in the same manner [13].

The scrap is not only coated with a surface oxide which thickens when heated but also with surface contaminants such as oil, grease, paint, lacquer, paper and moisture. This is particularly prevelant thin materials such as foil and beverage cans. There is a need to consider the level of contamination. Swarf and turnings are heavily contaminated with cutting fluids and oil. Debris from the cutting tools themselves may also contain paper, oily rags and other litter. Cutting fluids and oils may be recovered by centrifuging the small metal chips and reused. Dirt, heavy oxide and embedded sand can be removed by abrasive blasting. The metal is passed through a swarf drier where it is pulverised before being fed into a rotating kiln, or separate furnace, to be heated to around 450°C under a controlled air flow to drive off oil and moisture. Environmental legal requirements limit treating some forms of coated scrap because of fumes [30].

Thus the scrap is graded according to composition, cleaned, dried and baled, the next step being to allocate the scrap to a heat of the desired composition. Alcan [27] recommends that the amount of scrap allocated to each charge should be such that each charge or heat contains approximately the same proportion of scrap. The ratio of scrap to new ingot (primary metal) depends to some extent on the quality requirements, such as aircraft alloys, and on the control facilities for reprocessing. Thus the furnace charge may be made up of direct scrap returns, pigs of known compositions from a secondary smelter (typically 85-90% aluminium), molten metal if available and perhaps primary metal with alloying elements [28,33]. This procedure is carefully supervised and the task may be assisted greatly by micro computers [27].

2.7 PRODUCTS OF THE SECONDARY INDUSTRY

At present most of the output of secondary smelting goes to the foundry industry, whose processes and products can best tolerate the higher levels of impurity inherent in bulk recycling and which finds remelting of ingots of controlled composition very convenient. 97% of the saleable output of the secondary aluminium industry in the UK goes into foundry castings alloys [3], and may be sold either in ingot form or as liquid metal transported in insulated containers.

Foundry casting alloys are produced to compostions listed in BS 1490, this specification covers 20 different alloys but 80% of the tonnage is accounted for by some 6 or 7 [3]. Table 2.2 has been included to illustrate the most common types of alloys produced (particularly LM2 and LM24). In the USA the main alloys produced by the secondary smelter fall into groups defined for the UK. The most widely used alloy of the general purpose casting alloys is type 380 with the composition listed. The remaining 3% goes into deoxidants for the steel industry [1].

Having reviewed the procedures for preparing scrap metal for remelting and charging into a furnace, the next section outlines and compares the types of furnace available for use with aluminium and aluminium alloys.

2.8 FURNACES FOR MELTING ALUMINIUM AND ALUMINIUM ALLOYS [36].

Furnaces for melting aluminium and aluminium alloys in the foundry may be broadly classified into three types; direct fuel-fired,indirect fuel-fired and electrically heated furnaces.

2.81 Direct heating furnaces [24,37]

The direct fuel-fired furnace is exemplified by the reverberatory furnace. There are two fundamental designs, wet and dry hearth. In the latter the charge is on a sloping hearth above the level of molten metal. Melt drains from the hearth into a holding basin leaving higher melting material, such as iron, on the hearth.

Electric reverberatory furnaces have heating elements in the furnace roof directly above the melt. Gas or oil fired reverberatory furnaces may have burners that can use either fuel to take advantage of changes in availability and cost of fuel. In these fuel fired furnaces, combustion products are in direct contact with the melt surface and heat transfer is by a combination of convection and radiation.

In recent years, new developments have concentrated on lowering the running costs for continuously melting and holding large amounts of aluminium.

2.811 Indirect heating furnaces

In an indirect heating furnace, a barrier of some sort prevents contact of the hot combustion gases with the metal to be melted. Thus, only at the very top of the crucible is the charge exposed to the products of combustion. Crucible or pot furnaces are typical of the indirect fuel fired furnaces and may be stationary, made to lift or tilt. They are used in aluminium foundries for melting and holding because of the ease with which melts can be transferred and changed. Electric resistance crucible furnaces have low running costs and are operated most economically for holding rather than melting [40].

Most electric furnace melting of aluminium and aluminium alloys is carried out in medium frequency induction furnaces of the channel (core) and coreless types. The strong alternating magnetic field in induction furnaces produces electric currents in any conducting metal placed in such a field [37]. The flow of current generates sufficient heat to melt the charge and melting is usually rapid and efficient. All induction furnaces produce electromagnetic stirring action or turbulence which promotes uniformity in temperature and composition of molten metal. Dross forms on the melt surface and builds up on a refractory lining due to the double toroidal stirring pattern [37].

Medium frequency furnaces are operated most economically when melting at their maximum rate. They are completely emptied after each melt enabling different grades or different metals to be produced in successive melts, thus melting a wide range of materials. A molten heel is not necessarily required. Hence, induction furnaces are best for melting rather than holding. [38,39]

Due to their initial cost and relatively small capacity, high frequency induction furnaces are limited almost entirely to use in speciality foundries. An advantage of high frequency furnaces is that they can be used to melt metal fines and chips without initially charging with thicker material. The size of charge pieces is affected by frequency and for melting by lower frequency, the initial charge must consist of thicker metal.

2.8iii Comparison of furnaces

The previous section has outlined a general description of furnace types available for melting and holding aluminium. To select a furnace however, requires careful consideration and comparison of many factors highlighted in this section. The choice, for example, between fuel fired and electric furnaces not only depends on economic considerations such as capital investment, fuel

prices, fuel consumption and efficiency, melt rates and melt losses, but on other factors. Local conditions such as availability and transport of fuel, materials and workers may influence the selection procedure. Existing facilities, requirements of performance efficiency, standards of quality, cleanliness and safety regulations may also have a bearing on the choice.

In order to achieve a qualitative comparison, furnace performance figures have been compiled in Table 2.3. This data comes from many sources and may not be directly comparable. For example, in production conditions, the melting rates of new furnaces would not exceed 75% of the figure given by the manufacturer. Old fuel fired furnaces are often under 10% efficient and so their true melting rates can be half the theoretical maximum, due to refractory erosion, poor insulation and inadequate burner maintenance. Draughts around the furnace and covers off or doors open will increase heat losses and reduce melting rates. Additionally these considerations are not independent, e.g. furnace capacity determines power input and thus melting rates and efficiencies. Hence these factors must be taken into account when examining the furnace performance figures.

The last decade (1970 -1980) has seen a phenomenal increase in oil prices which has, in turn, led to a price increase of other energy forms. Table 2.4 gives the relative changes in cost per KJ of heat available for both fossil fuels and electric energy [9].

	1970	1973	1979	1980	1982	Increase over 10yr (%)
COAL	24	32	98	127	-	530
FUEL OIL	21	29	149	221	275	338
NAT. GAS	43	29	129	166	284	1000
ELEC.	186	205	583	657	929	312

Table 2.4: Relative prices of energy per KJ of heat (in pence) [9].

The increases in a decade are staggering and although the cost of electric melting now competes on a cost basis with melting in fuel fired furnaces, the high capital investment required for an electric furnace is a disadvantage and the tendency is to use electric furnaces for specialist applications. Generally, electric powered furnaces have high energy efficiencies [38]. In fuel fired furnaces the energy used is rarely less than four times and can be ten times that theoretically required to melt the metal [7]. Table 2.3 records comparative thermal efficiencies for electric furnaces, derived by estimating an average efficiency of 33% for converting mainly coal and oil into electric energy per KJ.

Table 2.3 shows that induction furnaces have the highest efficiency of any method of melting and the more metal melted over a melting cycle, the higher this becomes [38]. As the charge heats the rate of heating increases, and solid metal is at a high temperature for only a short time before it melts. Thus melting losses are relatively low. With fuel fired furnaces the heating rate is proportional to the temperature difference between fuel and the charge. Hence, solid metal may be at a high temperature for a long period resulting in high melting losses. Coreless induction furnaces are inherently less efficient than channel furnaces, which possess a better natural power factor. Channel furnaces can build up oxide in the melting channel [36], thus where conditions other than energy efficiency prevail coreless induction furnaces are normally installed [11].

One of the major benefits of electric energy is the degree of control which is possible over many important parameters and for melting and holding there is a marked trend away from fuel fired furnaces to electric furnaces. The principle advantage being the perfect control of the furnace atmosphere, arising from the absence of combustion products. The electric furnace atmosphere is free from the hostile gaseous environment experienced in fuel fired furnaces [11]. The rates of oxidation of aluminium alloys are said

to be increased in the presence of these contaminants. Significantly therefore, the highest melt loss percentages reported in Table 2.3 notably arise in fuel fired furnaces.

Only oil and gas are used today in reverberatory furnaces for melting and holding aluminium and its alloys. Heavy 'Bunker C' oil is used primarily for melting,and light oils are used for holding metal. Natural gas and producer gas are also used depending on availibility and/or cost. Natural gas, predominantly methane, has superceeded the previously used town gas. Large users are supplied on an interruptable basis often necessitating the use of dual fuel burners [36]. Table 2.5 shows the composition of these fuels. Burning 'Bunker C' oil generally produces some sulphur dioxide (SO_2) as this fuel contains up to about 3% sulphur. The supply of oxygen to the burners usually comes from air so nitrogen (N_2) is a major component of the furnace atmosphere. Thus complete combustion of most fuels results in the formation of CO_2, SO_2, N_2, and H_2O.

Complete combustion is achieved when the furnace operates with a slight excess of oxygen or air [33]. The presence of CO and hydrogen (H_2), and a lower concentration of CO_2 in the waste gas than the stoichiometric ratio (shown in Figure 2.4) demonstrates incomplete combustion [27]. Apart from excess air fed in at the burner, air enters via open doors or badly fitting doors, covers and bad brickwork. Some furnaces therefore, operate with a hearth level water pressure of 5Pa to prevent this air ingress [41]. Regardless of burner settings, copious quantities of water vapour are always present in the furnace during the melt [33]. Gas cylinders of argon and nitrogen contain traces of water vapour which exert a vapour pressure. This is normally small but as the cylinder becomes nearly exhausted, the vapour pressure of the water becomes a significant fraction of the argon pressure and the ratio of water to argon increases accordingly [42].

PAGINATION ERROR

2.9 MELTING PRACTICE

Direct charging of large scrap forms into a furnace creates a chilling effect which causes alloying elements to precipitate as sludge. Light gauge scrap such as beverage can scrap with low bulk density [44] tends to float on the molten metal surface and heavy oxidation losses result from prolonged exposure to the environment. The preferred way is to submerge scrap rapidly into the molten metal by manual or mechanical plunging into the open well of a furnace, often with long booms attached to fork lift trucks [30]. An air or nitrogen lance placed below the metal surface, creates a fountain of bubbles which draws in the scrap. Devices for mechanical stirring are utilised such as vortex generators [25], shrouded auger melting systems [45] drawing the charge into a circulating pool of molten metal. Similarly, electromagnetic forces in induction furnaces [39] and the linear induction motor [44] generate molten metal movement.

Foundry experience shows that metal losses are greater with metal of high surface area to volume ratios [36]. Figure 2.3 gives values of metal loss on melting from pigs (0.8-2.0%) to large size scrap (1.0-3.0%), baled sheet (1.5-4.0%), and baled foil (2.0-10.0%) [24]. Current melting procedures recognise the importance of high surface area to volume ratios and aim to minimise metal loss from avoidable oxidation. Hence, furnaces are operated with a molten heel of metal to permit submergence of light gauge scrap which is charged first. Finely divided scrap, saw cuttings and foil scrap may be melted by incremental charging, continuously stirred into the molten heel. Finally heavy scrap is placed on the top of the furnace charge, ideally loaded from preheating ovens. After the charge has been loaded, the furnace doors are closed and the burners set at the maximum rate for melting down.

The melting rate and time spent in the furnace has an effect on the amount of oxidation that takes place [33]. This is observed when subjecting solid aluminium and aluminium alloys to thermal treatment. The effect of holding temperature on the oxidation rate

of an Al-Mg alloy is shown in Figure 2.5. [36]. Thus to reduce oxidation rapid melting and minimum holding time is preferable. The oxide is also thickened when heating aluminium billets to temperatures below the melting point for the purpose of hot working (350-540°C), solution heat treatment (400-560°C), annealing (250-400°C), and for ageing and/or tempering (100-200°C). Indeed any thermal treatment to which material may be subject to appreciably thickens the oxide film [36].

When the charge has become molten the temperature is moderated by keeping the furnace temperature just slightly above the solidification point of the metal. Some foundries keep the furnace temperature at 650 to 680'C over weekends. This practice may cause sludge to form, but the sludge can be dissolved by heating to just below 800°C for a couple of hours before normal operation is resumed.

Oxides of aluminium and aluminium alloys form quickly on the surface of a molten bath, making a tenacious skin that reduces further oxidation provided the surface is not disturbed. If the surface is interrupted or broken the metal loss will increase. Such behaviour is exhibited when melting contaminated stock.

The presence of volatile matter such as cutting oils, rolling lubricants and paints was found to increase the melting loss to a level far in excess of the weight of the contaminant [29]. In tests comparing submerged and exposed melting of bare and coated scrap, the highest metal loss due to oxidation results from submerged melting of coated scrap. It is thought that when melting submerged coated stock volatiles released from coatings below the melt surface percolate the metal generating large quantities of wet dross exposing new melt for oxidation. When coatings were removed prior to melting or voltatiles burn off above the molten metal, the scrap remelts with the same ease as bare scrap [29,33].

Ideally therefore, coatings should be removed from scrap prior to charging. Developments have been made in the form of preheating areas for removing such residues. New types of melting furnaces incorporate washing equipment for oily alumimium and preheat material in the exhaust system, thus utilising waste heat. The shaft furnace preheats and decoats material in the shaft allowing molten aluminium to run down a sloping hearth into the main bath. Preheating also shortens actual melting time in comparison to a cold start. If a preheat or decoating cycle is impractical to operate, the coated scrap should be charged last and placed on top of the scrap pile to allow the coatings to burn off prior to melting. This is not ideal as in tests an 8.2% melt loss was recorded for bare scrap melted in exposed conditions in comparison with bare scrap submerge melted (4.2%) [39].

After melt down has been completed the molten pool is stirred at the appropriate temperature, Alcan use 700-710°C or 720-730°C depending on the main alloy composition [27]. Dross is worked up to the surface by stirring. Stirring is also necessary to aid melting large solids to prevent a steep temperature gradient developing and to prevent segregation in alloys because of the density of some alloying components. However, to minimise oxidation excessive stirring must be avoided. Any disruption of the surface film from turbulence during pouring molten metal or charging the furnace will lead to a continuous build up of further oxide formation. Even oxide sticking to a pouring ladle returned to the melt may act as a centre for nucleation.

An indication of melt losses involved in foundry practice are given in an example of sources of melt losses in an ingot foundry using oil fired pot furnaces [46].

Melting and pouring pot cleanings	0.36%
Splashings	0.47%
Metallic dross (furnace skimmings)	0.30%

Ladle skimmings	0.57%
Unexplained oxidation losses	0.5 - 1.7%
Metal loss owing to pot failures	0.28%

Total	3.68%

Precautions can be taken to avoid excessive turbulence and contamination when transferring metal by withdrawing or charging below the melt surface using a furnace side well instead of the main bath, minimising the disturbance in order to reduce oxide formation.

Melting units are often accompanied by holding units. Fuel is conserved by transferring metal from a high heat input melter to a low heat input holding furnace where homogenisation, final composition and temperature adjustment for casting (pure aluminium 700-750°C) and where further treatment (such as degassing or fluxing) may be carried out. Such holding furnaces may be reverberatory or low and medium frequency induction furnaces. Alternatively one furnace may provide both melting and holding functions.

A recent study [24] confirmed that electric induction furnaces, often used for melting scrap in the secondary industry, give the lowest melt losses over the complete range of materials for all furnace types. The results illustrated in Figure 2.3 are consistent with observations of oxidation minimised by a combination of rapid melting in an environment free from hostile gases and a uniform molten bath temperature as found in induction furnaces but not, to the same extent, in fuel fired furnaces. The savings in metal loss by using induction furnaces rather than fuel fired equivalents (2 to 3% [24]) is considered sufficient to compensate for the higher capital investment and running costs required. However electric furnaces are not economically competitive at present for melting ingots or heavy scrap, heavily contaminated scrap where release of volatiles disturb the surface, and very large volumes of light gauge scrap which are difficult to submerge rapidly [47]. In these cases

melt losses are equivalent to those of fuel fired furnaces and in such marginal cases significant savings are difficult to predict with any certainty.

Popular fuel fired furnaces used for melting scrap are reverberatory furnaces with an internal circulation system. Rotary salt flux furnaces are used for heavily contaminated or light gauge material, although the removal of dross and spent flux can be a problem. Dry hearth and sloping hearth furnaces are found most efficient for sows and for high density contaminated scrap. Moisture and other volatiles are slowly discharged avoiding problems associated with submerged melting, and higher melting contaminants remain on the hearth [44]. The best gas and oil fired competitor of electric furnaces at present is the shaft furnace [29].

2.10 CLEANING THE MELT

This next section looks at impurities and various methods for achieving a clean melt.

The principle contaminants of aluminium and aluminium alloys are oxides, hydrogen and iron. Oxide enters the molten bath from a number of sources. Apart from oxide formation on the melt surface, oxide enters the melt on the surface of charged material. The scrap may be anodised and oxide may enter the melt from stirring tools.

Hydrogen is the only gas that dissolves to any significant extent in molten aluminium alloys [31]. This is usually insignificant in the solid but the amount dissolved increases sharply as the metal temperature increases above the melting point as Figure 2.6 shows. Atomic hydrogen enters liquid aluminium rapidly by a surface reaction with water vapour and only leaves very slowly by release as molecular hydrogen into the atmosphere [48] hence considerable porosity can occur in cast metal. Submerged alumina films may act as nucleation sites.

Molten aluminium dissolves iron from crucibles [36], other contaminants may arise from stirring rods, skimmers and ladles although these are only in contact with the melt for a short time. The melt thus contains non metallic impurities and inclusions such as oxides, carbides, nitrides and sulphides.

Much research has been carried out into ways of removing such impurities and common methods of cleansing the melt are fluxing, degassing and filtration. Fluxing and degassing are methods used extensively, combined degassing and fluxing systems are now available and additional in line systems incorporating filtration devices are becoming more common.

2.10a Filtration

Filtration systems which are used in foundry applications are processes in which filtration is accomplished by passing molten aluminium through various media such as steel wool, perforated plate, woven fibreglass [49], a packed bed of refractory particles such as tubular alumina balls and flakes coated with flux [50] and foamed ceramics [49,51,52]. Foamed ceramics are found to be the most effective in removing both oxide films and intermetallics. The open pore structure gives rise to very little restriction of flow and they appear to operate by retaining the inclusions by surface tension on the pore walls rather than mechanical sieving. Levels of dissolved hydrogen may remain unaffected, but from analysis the foam filters reduce the metallic aluminium content of dross from 51% with conventional treatment to 29% [53].

2.10b Fluxing

Historically chlorine compounds have been used extensively for fluxing and degassing. However with the industry turning away from such materials for reasons of environmental control, conventional powder fluxes are often used [53]. Various types of fluxes are available for aluminium and aluminium alloys and can be classified

according to the purpose for which they are used. Reductions in metal loss arising from oxidation can be achieved partly by covering up the melt with a mixture of alkali chlorides and protecting it from the oxidising environment of the furnace (passive fluxes). Alternatively active fluxes such as the more reactive fluorides (NaF, CaF_2 or cryolite Na_3AlF_6) can be added to molten metal which refine the melt by dissolving and removing oxide suspensions either chemically or mechanically bringing them into dross by enveloping the particles. Thin flux films have been observed to penetrate oxide-metal boundaries [24].

The apparent effect of fluoride is to accelerate the transformation of eta alumina to a highly crystalline film of corundum [48]. Stephenson [48] attributes this rapid transformation to the increase in localised temperature from the strongly exothermic process of adding fluoride to a transition alumina. The presence of fluorides was believed to increase the flux-metal interfacial energy encouraging better separation of metal from the flux [24]. The oxides and flux separate from the metal to form a dry, powdery floating dross that can be skimmed. Al-Mg alloys are especially liable to oxidation, consequently fluxes are normally mixtures of various fluorides and chlorides (mainly anhydrous $MgCl_2$) but free of sodium as this has an embrittling effect [36].

2.10c Degassing

Despite the availability of a large number of suitable fluxes, a clean melt may not be obtained. Some fluxes are hygroscopic and introduce hydrogen to the melt. Removal of hydrogen by degassing is a mechanical action. Hydrogen does not combine with degassing agents which include chlorine gas, nitrogen-chlorine mixtures and hexachloroethane [36].

Attempts to improve melt quality and reduce the lengthy, labour intensive and haphazard process of fluxing and degassing has resulted in many technical developments of automatically controlled processes [42]. Metal treatment processes which are fumeless and can be applied in a continuous manner outside the holding furnace have considerable and environmental advantages and are of great importance. Of the possible processes meeting such criteria, the Alcoa 469 and FILD processes are particularly prevelant [41a]. The Alcoa 469 process is fumeless in-line chlorination method for removing hydrogen, inclusions and trace elements such as sodium. The FILD process from the British Aluminium Company is described as a fumeless in-line degassing and cleaning process involving treatment of metal with nitrogen under a salt flux cover followed by passage through a bed of flux coated alumina balls. Both processes give comparable technical results and are standard molten metal treatments. In the most recent flux injection process development nitrogen gas (15 litres N_2/min) acts as a carrier for the flux [42]. The flux-gas mixture is injected below the molten metal surface through a lance combining fluxing and degassing in a single operation [54]. It is claimed that not only is the melt of a consistently better quality thereby reducing scrap rates, but the casting properties are improved, treatment costs and melt losses are lower as a result. The metallic aluminium content of dross is 35% after treatment in comparison with 70% from conventional operations and 95% with no treatment at all [34].

In current foundry practice the molten metal is stirred and sampled for laboratory analysis. Final adjustments to alloying elements are performed at the end of the operation. These processes depend very much on proper sampling and good, rapid analysis of the components of the metal. Flux is added, the dross taken off allowing excess liquid metal to drain back into the furnace and the metal degassed. The metal is maintained at the correct temperature until laboratory release is obtained, when the metal may be cast into ingots, pigs (15-25Kg) or sows (450-550Kg) or delivered directly as molten metal [35].

CHAPTER 3 - FORMATION AND STRUCTURE OF ALUMINIUM OXIDE

In the previous chapters the relative ease with which oxide forms on any heat treated, but in particular, molten aluminium alloy has been highlighted. This chapter aims to review the current knowledge of the formation and growth of this surface oxide.

The presence of a thin surface film of γ-Al_2O_3 during the initial stages of oxide development protects the metal from further extensive oxidation over a wide range of conditions and provides a barrier between the metal substrate and the environment [55]. This initial oxidation process i.e., formation of an 'amorphous' layer and subsequent crystal nucleation is considered in the opening sections of this Chapter 3.1. The second section (3.2.) expands on the alternative crystal structures which may form such as gamma or eta alumina. The oxide structure is related to the levels of hydration in the crystal lattice and is thus reflected in the alumina properties. This aspect is reinforced by an appreciation of the Al_2O_3-water system. Finally, literature pertaining to the formation of oxide on aluminium at temperatures above and below the melting point is reviewed, and the behaviour compared with binary aluminium alloys containing manganese (Mn) or magnesium (Mg).

3.1 CHARACTERISTICS OF 'AMORPHOUS' AND CRYSTALLINE ALUMINA

At low temperatures and during the initial stages of oxidation, aluminium and certain aluminium alloys develop a thin protective oxide film described as an 'amorphous' layer.

Strictly speaking the term 'amorphous' means without structure. Although the structure is not well known [56,57,58] the existence of some structure is inferred from diffraction patterns where four strong but diffuse lines are exhibited corresponding to the cubic spinel γ-Al_2O_3. [59,60] Pryor [60] reports observing a short range ordered oxide with an estimated density of about $3 g.cm^{-3}$.

Similarities have been established between the characteristically duplex surface films which develop on aluminium and aluminium alloys at high temperatures, consisting of both crystalline and 'amorphous' oxides. In-situ studies have emphasised the importance of the 'amorphous' film in its control of the early stages of crystalline oxide formation at high temperatures [61,62]. The purpose of this section is to review the level of understanding related to the development of the 'amorphous' oxide layer and hence arrive at the structure.

3.1.1. The 'amorphous' oxide film on aluminium

The challenge of using alumina in novel engineering applications and new technology has refined ultra-high vacuum techniques and instrumentation thus advancing studies of clean aluminium surfaces. Such techniques have established that oxygen is dissociatively absorbed on aluminium with a reported energy gain of 482KJ.Mol^{-1} (5eV) [63]. Interaction of oxygen with the aluminium (III) crystal face proceeds via a multistage process according to Cocke et al [56]. Oxygen atoms chemisorb from an oxygen precursor into threefold surface sites, as shown in the general scheme of Figure 3.1. Following initial oxygen absorption, dissociation and immediate incorporation occur at defect sites. The atomic precursor state $[O]_{(p)}$ migrates to adsorption sites. These adsorption sites $[O]_{(ad)}$ are in equilibrium with the incorporated states $[O]_{(inc)}$. $[O_2]_{(p)}$ and $[O]_{(p)}$ are physisorbed states. The dashed arrow in Figure 3.1, represents possible reaction directly from physisorbed oxygen to the 'amorphous' oxide, with higher exposures, higher temperatures and other crystal planes.

It is suggested that a disordered chemisorbed phase forms on aluminium (110) face whilst an 'amorphous' oxide forms immediately on the aluminium (100) face [56]. Crowell et al [64] report that alumina begins to form when a critical number of oxygen atoms cluster

together after prolonged oxygen exposure or temperature increase. Formation of oxide islands following initial oxygen exposure of the aluminium (111) face has been indicated by ellipsometry, XPS, EELS and LEED measurements [55,63,65]. Thus, although the exact 'amorphous' structure is not yet established, some type of chemisorbed state such as an ordered oxygen overlayer with (1 x 1) symmetry up to approximate monolayer coverage is likely to exist on all the simple faces [56,63].

Further growth follows non linear rate laws [55,66] forming a continuous 'amorphous' oxide layer of terminal thickness (2-4nm from room temperature to 350°C [57,59,67]) according to the modified Caberra-Mott theory [68] for low temperature oxidation. This modified theory allows simultaneous cation and anion migration. The driving force behind this is the space charge resulting from cation excess and anion deficit at the metal-oxide interface and anion excess and cation deficit at the oxide-air interface [68]. Other researchers have reported a metal rich region near the metal-oxide interface extending into the oxide [68,69,72].

Structural possibilities have been considered for the defect structure of 'amorphous' alumina. Greenberg and Wright [68] favour an F' centre structure; a deficiency of oxygen ions with two electrons trapped in the vicinity of each oxygen ion vacancy. Pryor [60] compared the high dielectric constant of crystalline γ-Al_2O_3 developed on pure aluminium with reduced values found in crystalline γ -Al_2O_3 formed on Al-Cu alloys. This behaviour was explained in terms of a cation vacancy reduction by copper and leads Pryor to favour the 'amorphous' alumina structure with an excess of aluminium ions contained in otherwise vacant cation sites. Electrical neutrality is maintained by three electrons trapped in the vicinity of each excess aluminium ion. A small number of aluminium ions captured on anion sites leads to the poor long range order of these thin films [60].

Like Pryor, other researchers are of the opinion that the structure of 'amorphous' alumina may be obtained from closer study of its crystalline form. For example, El-Mashri and Forty [58] propose a model of Al_4O_6 molecular units arranged in sheets, which when stacked give a mixture of octahedral and tetrahedral sites occupied by Al^{3+} ions. The 'amorphous' state is said to be a result of distortions of the Al-O bonds with accompanying distortions of the sheet structure.

Recent findings indicate that the 'amorphous' to crystalline transition involves a substantial movement of Al^{3+} ions from tetrahedral (92%) to octahedral sites, either directly or by re-organisation of the oxide ions [56,71]. It has been suggested [71] that the transition involves an intermediate modification (γ'), a regular face-centred cubic oxygen lattice containing interstitial Al^{3+} ions statistically distributed on 30% tetrahedral, 70% octahedral sites. Partial re-arrangement of the cations in (γ') produces the defect spinel structure characterising γ -Al_2O_3 [56].

Little is known of the electronic or geometric structure of defects or of how such defects influence catalytic reactivity. The defect structures act as potential binding sites for active species thus dominating the surface properties of these transition aluminas [56,57,72]. Research work carried out on catalytic behaviour of aluminas infers that during the 'amorphous' to crystalline transformation removal of vacancy type defects is observed [56,57,71]. 'Amorphous' alumina exhibits a higher concentration of various chemical defects than crystalline alumina and whilst gamma and eta are predominant forms of alumina used in heterogeneous catalysis, α -Al_2O_3 is catalytically inert [56,57,71].

In this work, 'amorphous' alumina is shown to be stablised by water vapour (section 9.1.4 and 9.2.3b). Hydroxyl ions are also a necessary component of the defect structure of crystalline gamma and eta alumina [72] (sections 3.1.2 and 3.2). Indeed the number of hydroxyl ions is said to be equal to the number of cation vacancies [73].

In summary, this review has emphasised the lack of fundamental understanding of the nature of this commonly occuring thin 'amorphous' oxide film. At present it is the authors opinion that the 'amorphous' film may be best thought of as an 'excess metal' type structure with some short range order.

3.1.2. The nature of crystalline gamma and eta alumina

The crystalline form nucleated within the 'amorphous' oxide during the oxidation of aluminium has been identified as one of two different transition aluminas, gamma alumina [61,74,75,76] or eta alumina [77,78,79]. The prefix η is often designated γ , hence some confusion often occurs. These transition aluminas possess a cubic close-packed oxygen lattice with essentially the same defect spinel structure. The spinel unit cell consists of 32 oxygen atoms with 21 aluminium atoms and 2 vacant sites (instead of 24 metal atoms) distributed among the positions of fourfold and sixfold oxygen co-ordination. The spinel structure is tetragonally deformed with hydroxyl ions occupying octahedral sites. Transition aluminas differ mainly in the degree of random distribution of aluminium ions between octahedral and tetrahedral sites. John et al. [80], using solid state nuclear magnetic resonance, found 35 ± 4% of the aluminium ions in eta on tetrahedral sites, but 25 ± 4% occupied in gamma, rather than the 8 of 24 available. Thus gamma and eta alumina differ mainly in their structural disorder [57]. However both gamma and eta alumina have similar X-ray diffraction patterns and consequently are difficult to distinguish.

Maciver et al [72] looked at the surface chemistry of eta and gamma alumina. Some differences were observed, although not all eta or all gamma aluminas are necessarily the same in all respects. The basic surface chemistry of alumina is, to a significant degree, a function of the structure of the alumina [81]. For example, gamma alumina retains a great deal more molecular water on its surface at room temperature than eta alumina [72]. This may be directly related

to the distribution of surface hydroxide groups. The strength of binding between two surface hydroxyl groups may be critically dependent on the average distance between them. The place of these transition aluminas in the Al_2O_3-H_2O system will now be considered.

3.2. The Al_2O_3-H_2O System

The nomenclature is frequently confusing in connection with the vast numbers of possible aluminas that can be identified. The Alcoa system of nomenclature (as described by Wefers [57]) is used here to describe the Al_2O_3-H_2O system. This system is composed of aluminium trihydroxides, aluminium oxide-hydroxides and aluminium oxides. The nomenclature is illustrated in Table 3.1.

The structure of a specific alumina depends to a large extent on the state of hydroxylation. Water may be considered as a stabilising factor, removal of which may render the structure unstable and facilitate its transformation into other forms. Thus from these trihydroxide and oxide-hydroxide precursors transition aluminas are formed and ultimately, α-Al_2O_3 (corundum). Figure 3.2 is a representation of phase relations in the Al_2O_3-H_2O system developed by Wefers [57] using data of Neuhaus and Heide and also Kennedy [82,83]

Comprehensive reviews of the Al_2O_3-H_2O system are available [56,57,81]. However, a generalised preparative sequence for the thermal conversion of aluminium trihydroxide to anhydrous aluminium oxide is used here to illustrate the current understanding of alumina characteristics, and of structural and chemical principles common to these forms of aluminium oxide and hydroxides.

3.2.1. Thermal Conversion of Aluminium Trihydroxide to Anhydrous Aluminium Oxide

Aluminium trihydroxides have common crystalline forms of bayerite, gibbsite and nordstrandite. These structures differ only in the stacking sequence of a common structural element, the $(Al_2(OH)_6)$ double layer; a hexagonal close packed hydroxyl lattice with aluminium ions occupying two thirds of the octahedral interstices [57]. Only relatively weak forces operate between layers.

Although rarely found in nature, bayerite has the highest density of the trihydroxides and is the stable hydroxide phase in the alumina-water system. Gibbsite and nordstrandite are naturally occurring trihydroxides however neither can be prepared free of impurities. Several authors [84,85] believe that alkali metal ions are necessary to stabilise the gibbsite structure.

Depending on the chemical and structural composition of the starting material the sequence of thermal decomposition may differ. A general scheme of the decomposition sequence is illustrated in Figure 3.3. [57].

Figure 3.2 shows that when phases are in equilibrium, diaspore and boehmite are produced as the aluminium trihydroxide becomes dehydrated. Bayerite transforms to AlO(OH) at approximately 100°C. At low temperatures (below 300-320°C) and low pressures boehmite is kinetically favoured [82]. Preparation of diaspore requires more extreme conditions, such as above 300°C and 2×10^7 Pa pressure. Diaspore is found to be the only stable oxide-hydroxide modification [83], boehmite is considered metastable [82]. With further dehydration conversion to the stable condensed oxide phase α-Al_2O_3 corundum takes place.

In the course of thermal transformation to anhydrous α-aluminium oxide a number of distinct structural forms are identified; partially hydrated aluminium oxides known as transition aluminas. Under non-equilibrium conditions at least seven transition aluminas may be encountered. Forms of transition aluminas have been assigned Greek letters as they have been discovered; namely chi, delta, eta, gamma, iota, kappa and theta. Two of the forms, gamma and eta, have been discussed earlier in this chapter (Section 3.1.2).

The literature however, is frequently confusing. Wefers [57] acknowledges that a number of modifications appear that are generally summarised as the gamma form. It should be emphasised that although individual forms may be recognised, the transition aluminas are but transitional stages in a continuous solid state reordering process. Generally the structures can be grouped into low and high temperature types:

a. Low temperature forms such as chi, eta and gamma occur at temperatures between 250 and 800°C. Diffusion rates are low despite pores which may be 5-20 oxygen ions in diameter. Structural reordering is short range and favours the spinel type of structure. Rho may be included in this group as a low temperature form, although the structure is amorphous. [57]

b. High temperature transition aluminas are formed above 800°C. Significant sintering occurs producing a very low level of hydration with long range reordering. Delta, kappa, and theta represent varying degrees of structural transition from the spinel type to a hexagonal close packed lattice.

The series of transformations are summarised in Figure 3.3.

During the conversion of gibbsite to corundum by heating, the trihydroxide undergoes a series of structural changes although the original crystal habit is retained [86]. The loss of water and increase in density (2.42 to 3.98cm^{-3}) of the heated trihydroxide is presented graphically in Figure 3.4.

The loss of hydroxyl ions at temperatures of around 300°C coincides with the opening of cracks and fissures (less than 2nm wide) in the heated gibbsite. The network of submicroscopic cracks and crevices creates a large internal surface area. As the temperature increases (above 400°C) the fissures develop into major partings (1µm at 800°C). Above 700°C, three dimensional sintering takes place, lamellae increase in thickness by fusion. A coarsening of crystals and pores (100-200nm) is found [57,86].

The rate of heating, atmospheric water vapour pressure, purity (the influence of impurities or additives) and particle size of the starting material are all parameters which affect transition temperatures and rates of growth. For example, measurements of the boehmite to γ-Al_2O_3 transition temperature vary between 280°C to 470°C according to the degree of crystallinity [57]. Alwitt [87] suggested that boehmite with poor crystallinity would decompose at a correspondingly lower temperature such as 350°C than if highly crystalline (450°C), hence the importance of the degree of crystallinity of these films should be acknowledged.

Alkali metal ions can increase the temperatures of transition considerably [82,85]. The presence of alkali and alkaline earth fluorides and chlorides in the vapour state are observed to increase the rate of crystal growth of γ-alumina [88], of α-alumina [57] and facilitates the conversion of γ- to α-alumina. A few fluorides react exothermically with aluminium increasing thermal activity and rates of reaction. Thus the presence of fluorine catalyses crystalline growth due to an increased surface temperature. The mineralising effect of fluorine or chlorine has not yet been explained.

Noda and Isihara [88] obtained hexagonal platelets rather than granular polyhedrons when γ -Al_2O_3 was heated with sodium or potassium chloride and fluoride, or calcium and magnesium fluoride. Wefers also reports that the presence of fluorine in the furnace atmosphere encourages the appearance of randomly oriented hexagonal platelets [57].

The terminal product from dehydration of any form of alumina above 1200°C is α-Al_2O_3, the only thermodynamically stable oxide of aluminium. Corundum is the most well defined crystalline oxide modification crystallising in the hexagonal rhombohedral system. Hexagonal tabular and prismatic crystal habits are most common. Oxygen ions are hexagonally close-packed, with two-thirds of the octahedral interstices (between oxygen layers) occupied by the smaller Al^{3+} ions.

This corundum structure is maintained up to the melting point at 2050°C [57,86,89]. At high temperatures Al_2O_2, Al_2O, AlO_2 and AlO have been spectroscopically identified. Only Al_2O (1100-1500°C) and AlO (1500-1600°C) species have been confirmed as suboxides from vapour pressure studies [90] and high temperature X-ray identification [89].

In reviewing the formation of α-alumina by dehydroxylation of hydrated aluminium oxide precursors, the importance of structural order and how this is manifested in oxide properties has been highlighted. The overall structure however, may differ greatly from that of the surface. Those properties arising from atomic and electronic arrangement of the surface and the mechanical performance of these oxides will be considered in Chapter 4. Firstly however, oxide formation by direct oxidation of the metal will be considered, below and above the melting point. Finally, the behaviour of aluminium is compared with that of aluminium binary alloys of manganese and later, magnesium in small and large concentrations.

3.3 OXIDATION OF ALUMINIUM

3.3.1. Oxidation of solid aluminium

It is well established that overall kinetics for the oxidation of pure aluminium in dry oxygen are temperature-dependent [66,76,77, 78,91]. A review of data from various investigators reveals that rates of reaction may be generally divided into temperature regimes: At low temperatures (to 300°C) inverse logarithmic kinetics are followed [92], above this (300°C-425°C), logarithmic [93,94] and parabolic [91,95] kinetics are reported. At high temperatures (above 425°C) oxidation rates become more complex and less reproducible [77,78,95] as Figure 3.5 shows. A general trend shown by weight change-time curves in this region is for paralinear kinetics (initially parabolic changing to linear) which develop to non-linear rates with time [59,66,97], schematically shown in Figure 3.6.

The observed reaction rates have been given varied interpretations in terms of growth mechanisms. The initial behaviour is consistent with the formation and continued growth of 'amorphous' alumina on the metal surface. The 'amorphous' surface layer thickens with increasing temperature 350-400°C [56,66,74] following inverse logarithmic, logarithmic and parabolic kinetics. The general concensus is that when temperatures exceed 425°C [57,60,66] transition from the parabolic (or logarithmic) to a linear time function coincides with the formation of a crystalline transition alumina, gamma or eta form.

Observations by Bianconi et al [98] and Wefers [84] support a recrystallisation mechanism. However, Doherty and Davis [99] used electron microscopy of stripped oxide films to show that crystals nucleate at the metal-oxide interface and penetrate down into the metal, as illustrated schematically in Figure 3.6. Other researchers suggest that gamma (γ) or eta (η) alumina [77,78,79] crystals nucleate as a new phase beneath the continuous 'amorphous' oxide film [61,66,71,99].

TEM examinations by Timsit et al [100] reveal a sharp metal-oxide interface. Step heights were not greater than two interplanar spacings and no evidence of a transition zone or suboxide was found.

The nucleation sites of crystalline γ-Al_2O_3 have not been identified although attempts have been made [74,76]. Hart and Maurin [55] conclude from observation on pure aluminium at 440°C in steam (41 MPa) that growth of hexagonal-shaped oxide crystallites and platelets is encouraged by conditions of considerable compression or tension in the substrate. Platelets appeared concentrated near physical defects in the surfaces such as pits, gas blisters and grain boundaries. These features were observed on stripped, randomly oriented polycrystalline films [55].

Thin aluminium films, prepared by evaporation, have been oxidised at 350-500°C in oxygen (1×10^{-3}Pa) in an electron microscope [74]. 'Amorphous' and crystalline oxides form simultaneously within the grains. Growth of hexagonal plates is favoured at higher temperatures in comparison with needle-like crystals. Grain boundaries were not considered to be active nucleation centres [74].

From studies of the orientation of γ-alumina formation Czanderna [101] concluded that oxide growth on polycrystalline aluminium substrate occurred in an apparently random fashion with no strong orientation relationship to the substrate. The same author however, showed that single crystal substrate yielded oxides highly oriented with respect to the substrate. Doherty and Davis [99] found that the (111) plane and [110] direction of new crystals of γ-Al_2O_3 was coincident with the corresponding plane and direction of the aluminium substrate. Table 3.2. shows the similar relationships identified by Hart and Maurin [79] and Scamans and Butler [61].

TABLE 3.2

OBSERVED ORIENTATION RELATIONSHIPS BETWEEN ALUMINIUM AND CRYSTALLINE γ-Al_2O_3

Plane	Hart & Maurin [79]	Scamans & Butler [61]
$(1\bar{1}0)_{Al}$	$(110)[1\bar{1}0]_{Al} \parallel (110)[1\bar{1}0]_{Ox}$	$(110)[1\bar{1}0]_{Al} \parallel (110)[1\bar{1}0]_{Ox}$
$(001)_{Al}$	$(110)[100]_{Al} \parallel (100)[100]_{Ox}$	$(110)[100]_{Al} \parallel (100)[100]_{Ox}$
(110) or $(111)_{Al}$		$(111)[110]_{Al} \parallel (110)[110]_{Ox}$

Shinohara [103] has correlated the rate of aluminium oxidation with orientation by the sequence [111] > [100] >{100} > {112}.

Pryor [60] suggests that crystals grow rapidly into the metal to a fixed and temperature-dependent depth, as schematically illustrated in Figure 3.7. Radial growth occurs at a constant rate until the crystals coalese [60,99]. Crystal expansion or partial recrystallisation and formation of interfaces within the 'amorphous' oxide generates flaws or channels penetrating through the 'amorphous' oxide to the surface [79], as Figure 3.6 shows. Growth of these interfacial crystallites is thought to be controlled by oxygen, supplied from the atmosphere, transported via flaws and pathways through the 'amorphous' layer to the metal-oxide interface. In support, Pryor [60] reports that on removal of oxygen (10^{-4} Pa) crystal lateral growth ceases. Similarly, Dignam and Fawcett [104] find that in the absence of oxygen or aluminium metal oxide crystal growth does not occur until temperatures exceed 1000°C.

The observed linear growth rates are consistent with a phase boundary reaction between oxygen and metal. Lateral growth of transition alumina crystallites eventually results in a continuous layer of thick crystalline oxide which limits oxygen transport to grain boundary diffusion or lattice diffusion only. Being diffusion controlled both these processes follow non-linear rate laws.

While this model can explain paralinear behaviour, weight gain curves published by other investigators [66,76,77,79,99,104] for long exposure times above 450°C are described roughly as sigmodal in shape. That is, the oxidation period is low initially, with time, the reaction rate rapidly rises until sharply decreasing.

Beck at al [76] recognised the importance of the duplex nature of oxide films in the observation of these sigmoidal kinetics. Formation rates of both 'amorphous' and crystalline oxide were considered as mutually independent processes occurring simultaneously [66,76,104]. An electron opacity technique [76] was used to measure the 'amorphous' film thickness. Parabolic kinetics with a high degree of conformity were found, the weight of 'amorphous' oxide (Wa) given by:

$$W_a = (k_1 t + C) \qquad 3.1$$

The crystal growth of γ -Al_2O_3 $_{(Wc)}$ was mathematically expressed in the form of expanding cylinders which grew laterally at a constant rate until impingement, accordingly a sigmoidal function was derived:

$$W_c = \rho\delta[1 - \exp(-\pi v^2 \Omega t^2)] \qquad 3.2$$

and therefore, assuming nucleation occurs immediately, the total weight gain (W_t) is given by a combination of equations 3.1 and 3.2:

$$W_t = W_c + W_a = \rho\delta[1 - \exp(-\pi v^2 t^2)] + (K_1 t + C) \qquad 3.3$$

It is clear from a review of the available literature that the solid state oxidation behaviour of aluminium is extremely sensitive to experimental conditions. Data are often conflicting due to differing surface treatments, degree of exposure, different pressures and environments.

3.3.1.(a) Effects of Surface Finish

Cochran and Sleppy [77] compared the average weight gain at the maximum oxidation rate of mechanically polished samples (30-40 $g.cm^{-2}$) [78,91,95] with those chemically polished (3-5 $g.cm^{-2}$ of figure 3.5) [77,79,96]. The higher mass gain of oxide on mechanically polished samples was attributed to greater surface roughness.

Gulbransen and Wysong [95], also Aziz and Goddard [105] report that unpolished aluminium surfaces gained much less weight than mechanically polished surfaces. Lewis and Plumb [106] were among the first to consider the effects of surface preparation on the surface roughness of aluminium. After special polishing procedures a roughness as high as 25 times the geometric area was determined. Cochran and Sleppy [77] compared the results of Blackburn and Gulbransen [96] (chemically polished specimens) with Smeltzer [91] and calculated the machined specimens of Smeltzer to have a surface roughness of 8-10. Figure 3.8 shows that as the relative surface roughness decreases the gain in oxide weight decreases [77].

No mention is made of other effects of surface preparation on the oxidation behaviour of aluminium. For example, the oxide film formed on chemically polished samples may become saturated with contaminants from the polishing solutions. This may cause large variations and non-reproducible oxidation rates [102].

3.3.1.(b) Effect of Contamination

In a study of the oxidation behaviour of binary Al-Cu and Al-Zn alloys Brock and Pryor [107] found that increasing the copper (0.1-4%) or zinc (0.1-1.0%) content causes a reduction in crystal nucleation density and an increase in the radial growth rate, at temperatures between 475-575°C. The behaviour is attributed to the number of defects in the resulting oxide. However, varying the concentration of zinc has no effect on the rate of formation of 'amorphous' oxide between the crystals, unlike the effect of copper which shows increased oxidation at this stage [107]. The reason for this difference is not known.

The influence of water vapour on the oxidation behaviour of aluminium has been considered by several workers. The kinetics of aluminium oxidised in the presence of moisture were unaltered by additions of oxygen and hydrogen [96], or nitrogen [77]. The rate of oxidation in moist oxygen was similar to that in dry oxygen [91]. At temperatures below 550°C, Hunter and Fowle [79] found oxidation rates decreased due to water vapour. Other investigators however, report that the presence of water vapour during oxidation (above 550°C) results in increased rates for both single and polycrystalline aluminium [77,96].

Although the kinetic data may be conflicting, an observation consistently reported is the appearance and formation of hydrogen blisters on aluminium oxidised in the presence of water vapour. These small cavities and large blisters are found predominantly on grain boundaries or lines parallel to the rolling direction but are absent on samples oxidised in dry oxygen [96]. It is reported that a small quantity of fluoride vapour in the air inhibits high temperature blistering of solid aluminium and is effective above 527°C [108]. Oxidation studies have been concerned with the mechanism of blister formation [77,96] rather than the surface film itself which may control the transport of hydrogen to the metal substrate [68].

It is postulated [109] that hydrogen (as protons) from the surface reaction is transported under the potential and proton-concentration gradient to the oxide-metal interface. Protons then re-combine either at the oxide-metal interface or at cathodic sites such as inclusions and pores. The latter process is more applicable to high-temperature reactions where diffusion rates of hydrogen in the metal are rapid. Increased oxidation weight gains due to hydrogen permeation would only be expected if fresh surfaces were exposed by the blistering reaction. Formation and permeation of hydrogen is thought to be dependent on the type of oxide formed. Winter and Gruhl [110] correlated enhanced permeation of hydrogen into pure aluminium with transformation of AlO(OH) to γ-Al_2O_3. Stephenson [48] has shown that the hydrogen content of liquid aluminium reaches a maximum peak after 10-20 minutes before falling. Overall, during oxidation, there is a continuous decline in hydrogen content from its initial value. Thus when interpreting the kinetics and mechanism of hydrogen entry the degree of hydration of the lattice structure should be taken into account. This is reviewed in more detail in Section 3.2.

In summary, the mechanism of oxidation of high purity aluminium varies considerably with temperature. From room temperature to around 300-350°C the oxidation behaviour is best described in terms of an logarithmic law [94]. From 350 to 425°C the oxide film thickens according to a parabolic law [91,95]. The oxidation product is a thin, uniform 'amorphous' oxide, which may be considered as γ-Al_2O_3 with very poorly developed long range order [60]. Above 425°C the oxidation product is duplex in nature consisting of both 'amorphous' and crystalline γ or η-Al_2O_3. The crystals of γ or η-Al_2O_3 nucleate randomly and grow roughly cylindrically to a constant thickness at a given temperature. The crystals grow into the metal from the 'amorphous' oxide-metal interface by inward diffusion of oxygen through the overlying amorphous film. The 'amorphous' oxide film existing between the crystals of γ or η-Al_2O_3 grows with parabolic kinetics throughout the temperature range. The crystals grow laterally until they touch and form an essentially

complete layer over the metal surface [60,76]. The 'amorphous' oxide existing above the crystalline phase grows at a lower rate because of the additional resistance to cation diffusion conferred by the underlying crystalline phase [60]. As a result, at temperatures upto the melting point the kinetics become more complex. Thus, although trends have been established, the influence of parameters such as surface roughness [77,106] the presence of water vapour [77,79,91] and fluorine on the onset of rapid oxidation is, at best, only estimated. The mechanism of aluminium oxidation or more significantly the means of its control is unclear.

3.3.2. Oxidation of Molten Aluminium

As a result of the higher temperatures involved considerably more oxidation is expected to form on molten aluminium than develops on the solid metal. Despite this however, very little work has been carried out on the oxidation of molten aluminium. Further difficulty arises from poor records of oxidising atmospheres and metal purity.

Thiele [111] records that oxidation of molten aluminium at 800°C is greater than at 700°C however, the kinetics are hard to describe by a single equation. Thiele [111] carried out his work on a low sensitivity (±0.1mg) balance and long time periods (8-170h) were followed. Consequently no details of the initial oxidation behaviour was determined.

From studies of molten aluminium oxidation in dry oxygen, Sleppy [112] postulated that as the temperature increases a change in oxidation mechanism results, associated with the transition from logarithmic rates (660-700°C) to parabolic kinetics (750°C). Aluminium preoxidised for 1h at 600°C was found to exhibit parabolic behaviour at all temperatures.

Plewa and Kolny [97] investigated the oxidation kinetics of molten aluminium foil at 800-1200°C. Sudden changes of increasing and decreasing oxidation rates were interpreted in terms of periodic breaking of the oxide film, preceded by steady periods of diffusion controlled scale build up.

In contrast with the solid, literature on the oxidation of liquid aluminium describes rapid almost immediate development of γ-Al_2O_3 crystals, between temperatures of 650 to 720°C [59,113, 114]. Sleppy [112] identified η-alumina at 660-690°C.

Richards and Meussner [115] observed the growth of α-Al_2O_3 colonies on the γ-Al_2O_3 surface film of an aluminium melt in air. These α-Al_2O_3 colonies nucleated and grew after "a short period at 880°C". It was also observed that the nucleation and rate of growth of the α-Al_2O_3 colonies were very temperature dependent. Thiele [111] obtained data for the time at which α-Al_2O_3 first appeared on the melt surface, as the temperature increases from 700°C (24 hrs) and 800°C (8hrs) to 1000°C (15 mins).

The process of α-Al_2O_3 crystal growth occurs by nucleation at the metal-oxide phase boundary according to Sturm and Winterhager [116] and not by recrystallisation of bulk oxides as suggested by Thiele [111]. Onset of α-Al_2O_3 nucleation is attributed to the incubation period preceeding rapid oxidation. Thiele [111] maintains that above 800°C the oxide on molten aluminium (all α-alumina) is non protective. The layer of α-alumina crystals is said to be less effective in inhibiting reaction than γ-alumina resulting in faster oxidation rates [117]. Derbyshire and Cooper [118] support this view.

3.3.2(a) Influence of contamination

The effect of various elements on the oxidation of aluminium was investigated by several researchers. Results are described below and illustrated for Thiele [111] in Figures 3.9 and 3.10, and for Ginsberg and Data [120] in Figure 3.11.

The scatter in results from three grades of pure aluminium was attributed by Thiele [111] to the presence of (0.0013%-0.24%) sodium, increasing oxidation at 700° and 800°C. Similarly, Sharova [119] obtained a 4-5 fold increase over 30 mins oxidation at 750°C with additions of 0.02-0.057% sodium.

Lithium and calcium are other elements known to increase oxidation of molten aluminium trace additions. Ginsberg and Datta [120] found that 0.2% lithium in aluminium at 690°C resulted in the formation of $Li_2O.Al_2O_3$ and some α-Al_2O_3 after 5hrs in air. Calcium additions of 0.05-1.48% increased oxidation over the temperature range 700-800°C, $3CaO.Al_2O_3$ was identified [111,119]. However, Ginsberg and Datta found that upto 2.65% calcium in aluminium did not increase the oxidation of agitated metal at 690°C in air. The skim consisted of $5CaO.3Al_2O_3$ and α-Al_2O_3. Additions of iron, silicon, (1.5-12.5%) [119,120] copper (1-7%) [11,120] and zinc (1-7%) [111,120] had little effect on molten aluminium oxidation. Above 900°C, aluminium oxidation increased with zinc additions due to disturbance of the alumina film by zinc vapour [117]. Thiele observed that 0.33% beryllium decreased aluminium oxidation at 800°C. The surface was found to consist entirely of beryllia.

The effect on molten aluminium by manganese and magnesium additions are described in Sections 3.4 and 3.5 respectively.

The oxidation rate of pure aluminium is substantially increased in environments containing low levels of sulphur dioxide [77]. This has been attributed to stabilisation of γ-Al_2O_3 crystals and formation of hydrogen disulphide which disrupts the surface oxide film.

It is generally reported in the literature that beyond the effect of fluorine the composition of the atmosphere does not greatly influence oxidation. In direct contrast to the findings of solid aluminium oxidation, Thiele [111] observed that aluminium oxidised more rapidly in dry air, or in dry oxygen than in humid air. Investigations carried out by Talbot and Stephenson [121] support the trend of increased oxidation with decreasing humidity. A hazy explanation provided by Thiele concerned an interaction between steam and sodium impurity (0.0013%) in the aluminium metal.

The formation of hydrogen blisters during molten aluminium oxidation has been discussed earlier, linked particularly with water vapour. Of particular interest however, is work by Talbot [122] on liquid aluminium in humid atmospheres concerning the appearance of oxide growths on the lower oxide surface of the oxide-metal interface. Talbot suggests the oxide morphology is influenced by water vapour. It should be noted that such oxide growths are distinct from hydrogen blisters although it is often difficult to distinguish between such oxide growths and areas thickened by metal which remain following partial removal of aluminium with bromine/ methanol solution.

In summary, the oxide nature is described by rapid development of γ or η -Al_2O_3 crystals in an amorphous film [59,112]. As the temperature increases nucleation and growth of α -alumina increases. A non protective scale results, influenced by impurities and water vapour [121], which encourage new oxide such as beryllia or which influence the alumina scale properties.

Much work is needed to present a coherent theory. The concept of a diffusion controlled oxidation mechanism at high temperatures has stringent limitations as no account is taken of variations in the crystalline structure of the oxide film. Similarities are found in the oxidation behaviour of pure aluminium to some alloy systems such as Al-Zn and Al-Cu [107]. The influence of alloy additions of manganese and magnesium on the oxidation behaviour of aluminium will further aid the understanding of oxidation behaviour of pure aluminium.

3.4 OXIDATION OF ALUMINIUM-MANGANESE ALLOYS

Manganese is used to enhance the beneficial properties of aluminium. This aspect is reviewed in the discussion of secondary smelter operations (section 2.6). In view of the anticipated increase in manganese in scrap stocks the oxidation behaviour of this

element should be examined. Although little is known in connection with oxidation of these alloys, dramatic effects of enhanced oxidation due to manganese additions are not anticipated.

According to available literature, Thiele [111] observed that at 700°C in air, addition of 2% manganese to pure aluminium had little effect on oxidation. Figure 3.10 however, shows increased oxidation occurred after ten hours at 800°C. Additions of 0.5 - 4% manganese at 750°C [119] and 1 - 7% manganese at 690°C [120] to molten aluminium did not increase oxidation over a 5-6 hour period.

3.5 OXIDATION OF ALUMINIUM-MAGNESIUM ALLOYS

Widespread application of aluminium-magnesium (Al-Mg) alloys as a structural material for storage vessels, industrial and domestic appliances is common place. More attention to the diversity of applications and properties of the material is given in section 2.6 on secondary smelter operations. Although additions of magnesium to aluminium are beneficial from the aspect of structure and mechanical properties, oxidation resistance in both liquid and solid state material is significantly reduced. This is manifested clearly in all stages of alloy production, fabrication and recovery.

Rapid oxidation of these alloys is characterised by the formation of dark surface films composed of magnesium oxide [59,123] and severe metal blistering in humid environments [124]. The problem is particularly acute with Al-Mg alloy melts where removal of these surface films before further processing results in significant loss of expensive metal.

The need to control the excessive surface reactivity of Al-Mg alloys in processing is illustrated by the many investigations of high temperature oxidation carried out over the past fifty years. Despite this, negligible work has been carried out characterising oxidation mechanisms of molten Al-Mg alloy.

The authors own work has revealed that the oxidation behaviour of molten Al-Mg alloy is strongly influenced by oxide development on the solid metal. Hence, in order to better understand the mechanisms of Al-Mg oxidation available literature is used in the following sections to characterise the kinetics and morphology of both solid and molten Al-Mg alloys.

3.5.1. OXIDATION OF SOLID ALUMINIUM-MAGNESIUM

3.5.1(a) Kinetics Of Solid Aluminium-Magnesium Alloy Oxidation

Smeltzer [125] observed accelerated oxidation rates of metallographically polished Al-3% Mg alloy in dry oxygen as a function of temperature. The oxidation rates above 350°C, as shown in Figure 3.12, approximated to parabolic followed by linear kinetics (known as paralinear [126]. Faster oxidation rates and higher weight gains were achieved than with high purity aluminium [91].

Cochran and Sleppy [77] found that the rate of oxidation of chemically polished Al-2.35% Mg at temperatures of 450-640°C in dry oxygen and moist air did not conform to any recognised oxidation law, but was more parabolic than linear. In comparison with Smeltzer's work, Cochran and Sleppy found weight gains were reduced 10 fold at 550°C. The difference was attributed to surface roughness. It was estimated that Smeltzer's metallographically polished specimens possessed surface areas 8-10 times greater than the chemically polished surfaces used by Cochran and Sleppy [77]. Cochran and Sleppy attribute the smaller differences in weight gains at lower temperatures to variations in alloy composition. No specific mention however, is made of variations in the magnesium concentration between these materials [77,125].

Field [102] observed that electropolished Al-4.2% Mg alloy rapidly oxidised at 400-575°C in dry 20% oxygen/argon. The overall oxidation kinetics are a strong function of temperature. At 400°C, logarithmic type kinetics are found, linear at 480°C, paralinear at 520°C and pseudo-parabolic at 575°C. Despite low surface roughness levels however, weight gains obtained by Field are substantially greater than those obtained by Cochran and Sleppy [77]. The major factor between the results of these authors is thought to be the variation in magnesium concentration, 4.2% and 2.35% respectively. Associated weight gains are shown in Figure 3.13.

Magnesium levels of 0.03% lead to a degree of passivation, inhibiting oxidation [61,127]. At high magnesium concentrations (10-20%) in the initial oxidation period there is combustion of magnesium and a resultant increase in specimen temperature [59,124].

Smeltzer [125] measured oxidation weight gains and vacuum evaporation losses of an Al-3% Mg alloy and pure magnesium. A comparison of the oxidation rates of magnesium and the alloy showed them to be nearly equal. At the same temperature, at high vacuum (10^{-6} torr), the ratio of magnesium evaporation from the metal or alloy was found to be greater than the oxidation weight gains of either pure magnesium or the alloy. It was concluded that the rate limiting step was not magnesium diffusion within the alloy substrate. Thus the surface oxide acts as a 'barrier' to magnesium evaporation [125]. Cochran and Sleppy [77] also observed that samples losing magnesium by evaporation showed less oxidation than ones with no magnesium loss. It was suggested that a trace of water vapour (10-5mm Mg) prevented magnesium evaporation.

Hine and Guminski [123] investigated the oxidation behaviour of machined Al-3.6%Mg specimens in humid and dry environments. At temperatures between 450-530°C a parabolic law is followed. An initial period of negligible weight gain (plateau state) was extended for about 90 hours in undried air (0.5 - 1.5% KPa) in comparison with 2 hours in dry air (<0.001 KPa) before the onset of an increased

oxidation rate which continued to the limit of the experiment. The overall effect was that total oxidation over the first 200 hours was considerably less in undried air than in dry air. No explanation was given however, for why an increased oxidation rate should occur in dry air. Accurate data were not obtained for the first 24 hours, hence no detailed analysis of the initial stages of oxidation can be made. Chemically treated Al-1.8%Mg was used by Lee et al [128] in oxidation studies in wet and dry air at 500-575°C. As with Hine and Guminski, a longer induction period is recorded in wet air. However, once linear oxidation occurred the oxidation rate was faster in wet air than in dry air.

Investigators [77,123] agree that rapid oxidation in humid atmospheres is due to rupture of hydrogen induced surface blisters. Rupture of these blisters exposes new metal, hence the oxidation rate becomes governed by the rate of metal exposure. Cochran and Sleppy [77] found that by reducing the hydrogen level from 2.8ml/100g to 0.8ml/100g after treatment with 1M solution HCl, the same kinetics in humid atmospheres were obtained with dry oxygen. This treatment however would similarly precondition the surface oxide with the aqueous solution or chlorine ions. Cycling specimens in wet and dry air at 525°C resulted in linear oxidation rates and periods of no mass gain respectively leading Lee et al [128] to conclude that oxides formed in wet and dry air differ.

An informative paper by Grauer and Schmoker [129] emphasised the initial reaction stages of Al-Mg alloy oxidation in oxygen at elevated temperatures. Electropolished samples containing 4.6%, 1.55% and 0.15% Mg, were oxidised at temperatures of 300-500°C. As expected, the alloy with the greatest concentration of magnesium oxidised faster forming more oxide for a given temperature. The authors divide the resultant weight-time curves into three regions: an initial logarithmic rise, an adjacent S-shape region and final section of steady weight gain (1.55% Mg) or linear kinetics (4.6%Mg). At elevated temperatures the logarithmic and S-shape region shorten appearing approximately parabolic.

The S-shape characteristic is more clearly marked in air than in pure oxygen, suggesting that oxidation is more rapid in pure oxygen than in air. The authors suggest that the oxidation kinetics depend on the partial pressure of oxygen, the oxidation rate increasing with decreasing oxygen pressure. This aspect was not followed up by Grauer and Schmoker, but is in contrast to findings by Heine and Guminski [123]. From their investigations, Heine and Guminski conclude that despite similar kinetic results of Al-Mg alloy oxidation in dry argon, and dry air or oxygen, the rate is independent of oxygen partial pressure up to level of 30ppm oxygen.

3.5.1b Morphology Of Oxide on Solid Aluminium-Magnesium alloy

Kinetic data alone is not sufficient to obtain a clear picture of the oxidation behaviour of solid Al-Mg alloys; information gathered from morphological investigations is required.

A common observation of aluminium-magnesium (Al-Mg) alloys is that unlike aluminium, oxidised surfaces have a characteristic blackened appearance. Experimental work by Heine and Guminski, [123] and Smeltzer [125] supports the view held by de Brouckere [59] that the dark oxide appearance is due to discrete particles of free metal dispersed in the oxide film. Despite similar kinetic results specimens appear more blackened when oxidised in argon in comparison with air formed films.

At low temperatures, an 'amorphous' oxide film is present on oxidised aluminium-magnesium alloys, the thickness of which is dependent on the temperature [59,102,129]. Analyses show that as Al-Mg alloy oxidation proceeds above 350-400°C magnesium is progressively enriched in the oxide film, usually in the form of MgO [59,123]. The concentration profile of the magnesium enrichment in the oxide film closely follows the oxidation curve [123]. Leighly & Alam [127] mathematically describe the magnesium depletion, equating the magnesium loss from a low magnesium containing alloy, as equivalent to the concentration of magnesium found in the oxide.

Magnesium is known to diffuse from bulk alloy at temperatures above 350°C [59,125]. Above 350°C,Al-8%Mg [59] and Al-2.3%Mg [77] alloys were found to give reflection electron diffraction patterns of magnesia (MgO). In addition to MgO, metallic aluminium and $MgAl_2O_4$ were identified in oxide powders taken from oxidised Al-3%Mg (60 hours at 550°C) [125]. The contrast may be due in part to the techniques used. Reflection electron diffraction is sensitive to the outer specimen surface 1-3nm. Oxide powders taken for X-ray diffraction are possibly less representative of surface material only. However, it is the authors opinion that the detection of magnesium aluminate reflects its development during the long exposure period.

Ritchie et al [130] used TEM to investigate evaporated thin films of Al-1.2%Mg. Oxidation at 350°C in dry oxygen gave a series of reaction products as a function of time. The original 'amorphous' film contained firstly crystalline MgO, then a mixture of MgO and $MgAl_2O_4$. Ultimately only $MgAl_2O_4$ could be detected. This study did not establish whether the experimental observations were typical of bulk alloy oxidation or a thin film artefact due to magnesium depletion. Similar results were observed by Lee et al at 500-575°C with Al-1.8%Mg [128].

Grauer and Schmoker [129] suggest that a critical limit of magnesium content is passed as oxidation proceeds, which accounts for different oxidation products. Hence, a succession of oxidation products may form on an alloy with progressively decreasing magnesium content.

A thermodynamic stability diagram constructed for the Al-Mg-O system by Grauer and Schmoker is shown in Figure 3.14. Three regions can be distinguished:

a. For $X_{Mg} < 10^{-6}$ ($< 10^{-4}$ At%) γ-Al_2O_3 is stable at the metal-oxide interface.

b. In the region $10^{-6} < X_{Mg} < 10^{-2}$ (10^{-2} to 1 At%) the spinel phase is stable.

c. For $X_{Mg} > 10^{-2}$ (>1 At%) MgO is the stable phase at the metal-oxide interface.

Literature available for oxidation products on alloys varying with magnesium concentration tend to support this proposal. In low magnesium containing aluminium alloy [127], (less than 2% Mg) below 350-400°C, formation of MgO is entirely suppressed in favour of crystalline alumina growth hence γ-Al_2O_3 nucleation is enhanced [59,131]. At 580°C, with 500ppm magnesium, $MgAl_2O_4$ is obtained at the oxide/air interface with a trace of MgO below. MgO predominates with more magnesium (1000pmm) [127].

From investigations carried out on the oxidation of low magnesium containing aluminium alloys a picture of an oxidation mechanism starts to emerge. Davies and Treverton [132] discuss the operation of two mechanisms at 400°C. At low magnesium concentrations (30ppm) oxygen diffuses inwards through the oxide to the oxide-metal interface. At higher magnesium levels (100ppm) magnesium diffusion to the oxide surface predominates over oxygen diffusion and magnesium is concentrated at the metal-oxide interface. Scamans and Butler [61] infer that magnesium stimulates increased oxygen diffusion to the metal-oxide interface. Leighly and Alam [127] find that the migration of metal ions from the metal-oxide interface to the oxide leaves a large concentration of vacancies.

Grauer and Schmoker describe the initial development of $MgAl_2O_4$ spinel on low magnesium alloy (0.17%) taking place beneath an 'amorphous' overlayer. Magnesia forms at a later stage giving rise to the film structure shown schematically in Figure 3.15. For Al-Mg alloys containing 4.6% and 1.55% Mg, crystalline MgO grows beneath 'amorphous' γ-Al_2O_4 [129]. Brock and Hine [62] used stripped films of Al-3%Mg to show that MgO crystals form at the metal-oxide interface.

It was suggested [62] that the crystals form as a result of solid state reduction of the 'amorphous' overlayer of γ -Al_2O_3 by magnesium. The aluminium may subsequently reoxidise:

$$3Mg + Al_2O_3 \longrightarrow 3MgO + 2Al \qquad 3.4$$

$$2Al + 3/2\ O_2 \longrightarrow Al_2O_3 \qquad 3.5$$

The possibility of this reaction was first discussed by de Brouckère [59], although she proposed that the most likely mechanism for magnesia formation was by direct oxidation at the oxide-oxygen interface. Grauer and Schmoker [129] supported these ideas although different morphologies for alumina were postulated:

$$Al_2O_3\ (I) + 3Mg + 3/2\ O_2 \longrightarrow Al_2O_3\ (II) + 3MgO \qquad 3.6$$

Where Al_2O_3(I) is 'amorphous' and unstructured and Al_2O_3(II) is secondary reaction product present in granular form.

Other investigators [102,133] describe the formation of primary and secondary magnesia according to equations 3.4 and 3.5. Primary and secondary magnesia crystals have been characterised by electron optics [133]. The primary oxide phase is formed by direct reaction of magnesium and oxygen at the oxide-metal interface. The secondary oxide phase is formed by reduction, transformation or decomposition of an existing alumina oxide film [102].

TEM of back polished surfaces of Al-4.2Mg oxidised in dry 20% O_2/air shows that primary magnesia coarsens as a function of temperature from 50nm in diameter at 400°C to 200nm at 520°C. Finer secondary oxide crystals remain relatively constant at approximately 5nm [133]. Thicker films develop by the repeated nucleation growth of primary MgO [102].

Thus, although a degree of confusion still exists concerning the oxidation products formed, a base is established from which a model of solid Al-Mg alloy oxidation can be developed. Attempts to correlate the oxidation kinetics with morphology have been attempted mainly by Grauer and Schmoker [129], and Field [102], although the models are not always entirely supported by kinetic results.

Grauer and Schmoker [129], propose that the 'amorphous' film thickens following logarithmic kinetics. The second stage of oxidation (S-shape) proceeds with MgO crystal formation (or $MgAl_2O_4$ with 0.17%Mg) beneath this 'amorphous' film. MgO crystal development continues by secondary reduction of Al_2O_3 by magnesium as in equation 3.4 and subsequent re-oxidation of aluminium as in equation 3.5. Continued oxidation takes place with a linear weight gain. At lower magnesium concentrations spinel crystals form below the amorphous oxide. As conditions for spinel formation are present for a short time only, oxide growth continues with MgO formation as above. Investigations however, were not sensitive enough to provide morphological evidence for the observed parabolic kinetics at elevated oxidation temperatures.

In early studies accelerated oxidation rates and rapid oxide thickening were explained in terms of the porous nature of the covering film of MgO [125] or oxide film disruption. Wefers [134] suggests that at moderate temperatures (400-500°C) the change from parabolic to linear kinetics is a reflection of crystal formation at the oxide-metal interface generating cracks and openings in the 'amorphous' layer from the metal to the surface. It is proposed that thick densely packed MgO crystallites form around these pathways.

Work by Field [102] supports the model outlined above for Al-Mg alloy oxidation between 400-575°C. The following description refers to figure 3.16:

a. Mg diffuses into the 'amorphous' γ-Al_2O_3 layer.

b. Nucleation and growth of primary MgO crystals occurs according to logarithmic kinetics until fracture occurs. An overlayer of γ -Al_2O_3 forms over the fracture area.

c. Oxide thickening takes place by the repeated nucleation and growth of primary MgO crystals from the base of the existing oxide.

d. This gives rise to a corregated interface of stacked oxide peaks which develop rapidly during the transformation branch of paralinear kinetics at 520°C. Troughs are depleted of magnesium. The effective surface area for primary nucleation is increased and the oxidation rate accelerates.

3.5.1c Oxidation of Solid Al-Mg alloy in different environments

In the presence of water vapour in the atmosphere hydroxyl ions are thought to stabilise the 'amorphous' overlayer and increase the parabolic oxidation period [102,133]. Heine and Guminski [123] attribute the reduced oxidation in humid air to the incorporation of hydroxyl ions in the MgO lattice thereby favouring formation of a film with an increased volume ratio $Mg(OH)_2$ or a protective layer of boehmite.

Small blisters develop on the Al-Mg surface on grain boundaries in moist air but not in dry air. Blistering disrupts the oxide and exposes fresh metal surface to the atmosphere resulting in faster oxidation [77,123]. This does not account however for rapid oxidation in dry air.

Oxidation of Al-Mg alloy is suppressed in an atmosphere of carbon dioxide at all concentrations [124]. The carbonate ion is thought to be incorporated in the oxide. Thus the very low oxidation rate is the result of compound formation rather than exclusion of oxygen. Use of a nitrogen stream to protect Al-Zn-Mg proved ineffective [131].

3.5.2. Oxidation Of Molten Aluminium-Magnesium

3.5.2a Kinetics of Molten Aluminium-Magnesium Alloy Oxidation

Thiele [111] found that at 700 and 800°C magnesium additions (0.9wt%) to aluminium markedly increased the rate of oxidation as Figures 3.9 and 3.10 illustrate. Due to the insensitivity of the thermogravimetric apparatus used, Thiele was unable to determine the initial oxidation curve and oxidation periods of 8-170 hours were studied. Investigators found that the oxidation rate increases as the concentration of magnesium increases [111,114,115]. This trend is illustrated by Baliki [135] in Figure 3.17,showing Al-Mg alloys oxidation at 700°C over a 60 minute period.

From studies of Al-Mg (1-14%) melts at 600-1100°C Cochran et al. [124] discuss three oxidation stages. Initially the oxidation rate is low, its duration is termed the induction period. A period of rapid breakaway oxidation follows and finally the rate decreases.

Oxidation weight gains-time curves constructed by Haginoya and Fukusako [136] for holding molten Al-Mg (2.12%) alloys in air, fall into two different groups of low (650-750°C) and high oxide weight gains (800-900°C). He attributes this behaviour to the formation of two different oxides MgO and $MgAl_2O_4$ respectively. The two groups of curves are shown in Figure 3.18. It is now appropriate to consider literature pertaining to morphology of oxides formed on Al-Mg melts.

3.5.2b Morphology of oxides of Molten Aluminium-Magnesium alloys

A mixture of MgO and $MgAl_2O_4$ oxides is reported on melt surfaces formed in air at 700°C containing 1% Mg or less [114], and with alloys containing up to 3% Mg [120] after 30 hours oxidation [111]. Under the same conditions films consisting entirely of MgO were found on melts with greater than 1% Mg [59,114]. With longer oxidation

times (30 hours) a mixture of magnesia and spinel is obtained [120] and Belitskus [137] reports that only spinel forms on Al-4%Mg in air at 750°C after 75-100 hours.

As a result of observations by thermogravimetry, X-ray diffractometry and electron probe microanalysis at 650-900°C on Al-Mg (2-12%) melts, Haginoya and Fukusako [136] proposed a two stage reaction:

$$Mg + \tfrac{1}{2}O_2 \dashrightarrow MgO \qquad 3.7$$

$$MgO + 2Al + \tfrac{3}{2}O_2 \dashrightarrow MgAl_2O_4 \qquad 3.8$$

Magnesium is initially selectively oxidised to MgO. The production of magnesia produces pores which introduce air into alloys, thus more MgO forms. During the second stage an amorphous oxide produces crystallites growing inwards from the surface from the oxide-air to metal-oxide interface. Fine $MgAl_2O_4$ particles develop within this layer [136]. In support, Haginoya and Fukusako noted that during oxidation the mass of $MgAl_2O_4$ increased as the quantity of MgO decreased. At temperatures above 775°C this two step reaction occurs in one [136].

Haginoya [138] discussed these oxides as aggregates of minute particles assigning them into typical groups; granular, layer, globular or filmy type. Granular oxide (usually MgO) is found irregularly distributed around pores open to the alloy surface and is dispersed into molten metal (as is filmy oxide). $MgAl_2O_4$ is a mixed layer oxide composed of fine oxide particles and metal. Globular MgO tends to float on the molten metal surface.

Cochran et al [124] correlated observed oxidation kinetics with oxide morphology although no distinction was made between conditions favouring MgO or $MgAl_2O_4$ formation. The initial oxidation rate was kept low by a protective amorphous MgO film on the metal. Parameters found to influence the duration of the protective interval are

summarised in Figure 3.19. The protective interval ends with a sudden increase in oxidation rate, accompanied by crystallisation of MgO and $MgAl_2O_4$ [124].

The onset of breakaway oxidation is increased by slow melting. Cochran et al anticipated that with slow melting the first liquid to form will be richer in magnesium. However, if the solid is homogenised just below the melting range before rapid melting the protective interval is extended. The same authors [124] investigated seeding the melt with MgO or $MgAl_2O_4$ crystals to initiate breakaway oxidation. They noted that the crystals had to break the film and be wet by the melt to promote rapid oxidation shortly after melting. Refractory containers of MgO or $MgAl_2O_4$ did not encourage oxide nucleation.

Cochran et al suggest that breakaway oxidation ceases only when all magnesium has been consumed. Other suggestions are that α -Al_2O_3 may form on melt surface when all magnesium is depleted from the melt. Thus the corresponding decrease in oxidation rate is thought to be due to the formation of complete layers of $MgAl_2O_4$ and α -Al_2O_3 [139].

The oxidation behaviour of 5182 alloy was studied by Wenz [159] in combustion atmospheres ranging from a slight excess of gas to 50% or more excess air. No change in the amount of skim generated was observed. Wenz concluded from the behaviour of the alloy that there is sufficient O_2, CO_2 and/or water vapour present in all air-fuel ratios to produce the same amount of oxidation at a constant temperature. Combustion gas is protective to Al-4%Mg oxidation, but less so than carbon dioxide [117,124]. The protective action of CO_2 is enhanced with a small amount of moisture (0-38° dew point) in comparison with rapid oxidation in very dry CO_2 (-78° dew point) and with very wet CO_2 (88° dew point). However, bubbling carbon dioxide through an Al-Mg melt encourages faster oxidation than under static conditions [117]. Magnesium (0.7%) is oxidised in two stages for both quiescent and bubbling conditions. Firstly CO_2 is reduced to

carbon monoxide at a rate independent of the concentration of reactants, reduction to carbon then occurs. The reaction is first order with respect to the carbon monoxide concentration [117].

In nitrogen the protective oxidation period on Al-2% melts at 750 and 800°C was prolonged. No nitride phases were detected by X-ray diffraction [124]. Argon substitution for CO_2 or nitrogen promoted breakaway oxidation [124].

In comparison with air, rapid oxidation of molten Al-4%Mg alloy is reduced in SO_2-air and H_2S-air atmospheres [137]. Heating for one hour in SO_2 (>10%) provided protection from further heating in air alone. Belitskus [137] suggests that the inhibiting effect of SO_2 (or the more effective H_2S) probably involves oxidation to SO_3 which reacts with the initial amorphous MgO film forming $MgSO_4$. Protection is maintained until MgO crystals form. X-ray diffraction showed MgO and very small amounts of hydrated $MgSO_4$. No supporting evidence is given for the greater effectiveness of hydrogen disulphide.

Drouzy and Richard [131] find that the oxidation of Al-Zn-Mg alloys melts is not greatly influenced by atmospheric composition with the exception of fluoride containing atmospheres. Introducing fluorine to the melt (even in very small amounts) by thermal dissociation of solid fluoride reduces the formation of large oxide growths on Al-Mg-Zn melts at 800°C, leaving a white powder. Zinc is proposed to be responsible for the formation of growths although no explanation is given [131]. Most authors [111, 124,131] record the existence of growths which form on the oxide surface during breakaway oxidation. The growths are filled with metal and contain more MgO on the surface than the surrounding area [124]. The growths tend to be larger in the presence of moist air.

Cochran and Sleppy [77] report difficulty in reproducing results. Their use of machined samples creates an irregular metal surface which may induce irregular oxide growth. It is possible that localised oxide growths form at non-specific favourable sites. Thiele [111] observed that the heat generated by exothermic reaction of oxide growth formation accelerates further oxidation in the area.

In a study of aluminium brazing alloys at temperatures between 555-590°C in vacuum (10^{-3}Pa), materials containing magnesium above a critical level of 0.25%Mg, disrupt their own oxide by a process of alloy exudation [140,141]. As the temperature increases exudations on the surface swell to the point of collapse when molten metal flows over the surface. It is postulated that the driving force for this disruption is vapourisation of magnesium which reduces the alumina above 400°C [102,141]. Magnesium, diffusing into the surface oxide film renders the oxide porous to more magnesium vapour [140]. Loss of magnesium correlates well with measured weight loss and the reduction in moisture level as magnesium getters the environment [142]. According to Winterbottom and Gilmour [143] the now porous film allows liquid metal to travel up to the oxide surface producing a clean wettable layer of molten metal. Another investigator, Anderson [144] acknowledged that magnesium first modified the oxide film, but that rupture of the film permitted exudation of molten metal.

3.5.3. Effect of Trace Additions On Aluminium-Magnesium alloy Oxidation

Al-Mg alloy oxidation is very sensitive to impurities and trace additions [102,145]. Most work has been conducted with higher concentration of elements than used in production. In this latter area literature is deficient.

Beryllium additions (up to 1000ppm) to Al-Mg have been found to be particularly effective in inhibiting oxidation both in the solid state [102,123,145] and on melts [111,135]. Its use is restricted however, due to the extreme toxicity of the metal and its compounds [146]. Minimal levels of beryllium additions are sought. Further, an understanding of the mechanism of the protective role of beryllium is essential for development of a general oxidation mechanism for Al-Mg alloys, and in the search for alternative effective oxidation inhibitors. In this respect, boron [135,137] and calcium additions [102] have been proposed to reduce oxidation. The increased use of

lithium as an alloying element ensures that traces of lithium impurity will be expected in primary and secondary aluminium (from scrap bins). Lithium is known to be particularly detrimental to the oxidation of Al-Mg [102] and most, if not all, aluminium alloys. Available literature will be divided into two sections, elements which inhibit and enhance oxidation.

3.5.3a Oxidation Inhibitors

Beryllium (Be)

The beneficial effect of additions of beryllium in reducing oxidation rates of molten [131,135,146] and solid [123,145] Al-Mg alloys has been known for many years. On melts, Thiele [111] finds that increased magnesium concentrations require increased levels of beryllium additions to provide absolute protection against oxidation. This is illustrated in Table 3.3. Al-10%Mg requires at least 0.004%Be for up to 170 hours protection in air at 700°C. Sharova [119] equated the oxidation of a Al-10%Mg-0.07% Be alloy in air at 750°C to that of 99.7% Al. Whittaker and Heath [145] found that oxidation weight gains increased with increasing beryllium content for Al-10%Mg at 580°C in steam, following a logarithmic law. The authors reported that the inhibiting effect of beryllium was increasingly removed by additions of sodium (up to 0.06%). Balicki [135] found beryllium additions to Al-5%Mg and Al-10Mg at 700°C changed the oxidation kinetics from linear to parabolic.

Protection for upto 200 hours of an Al-3.6Mg-0.001% Be alloy at 500°C is lost once the metal is deformed by hot rolling [123]. However, the protective nature of Al-3%Mg-0.0004% Be at 700°C remains during agitation of the melt by oxygen [120].

Electron microscopy has revealed that levels of 100ppm and 1000ppm beryllium suppresses nucleation and growth of MgO in favour of primary BeO formation [102]. Examples of the oxides determined by

electron diffraction are tabulated below. Observations have been made that BeO crystal coverage is not complete at the suggested optimum level of 100ppm [102,145]. Field [102] proposes that beryllia formation reduces any oxygen diffusion through the 'amorphous' layer.

TABLE 3.3 - Composition of oxide formed on Al-Mg-Be alloys

	Be Content %	Phases Found	Ref
Al-10%Mg	0.0005	MgO	[147]
in steam	0.004	MgO	
at 580°C	0.013	MgO + small amount BeO	
	0.033	MgO + about 25% BeO	
	0.15	MgO + about 45% BeO	
Al-5%Mg	0.005	MgO	[111]
in air	0.05	MgO + BeO	
at 700-800°C	0.5	BeO	
Al-1%Be	1.0	BeO	[111]
in air			
at 700-800°C			

Boron (B)

Cochran [124] reports that dusting boron onto the melt surface of an Al-4.5Mg alloy decreased oxidation. It was suggested that the small atomic size of boron aids its dispersion throughout the oxide, so acting as an effective inhibitor to $MgAl_2O_4$ crystallisation.

Belitskus [137] investigated treating Al-Mg alloys with boron compounds and proposed that in all cases incorporation of B_2O_3 into the MgO surface film provided oxidation inhibition by increasing the volume quotient. BF_3 did not provide inhibition.

Titanium (Ti)

Addition of 0.1%Ti to an Al-10%Mg alloy at 700°C reduced oxidation although not as effectively as with a 0.1%Be addition [135]. This was also observed by Christiakov and Maltsev [148].

Calcium (Ca)

The inhibiting effect of calcium additions (0.05 - 0.5%) to Al-Mg alloy melts is recorded by Muromachi [149] and Christiakov and Maltsev [148]. Calvet and Potemkine [150] found the calcium was required in quantities 200 times greater than beryllium to reduce oxidation of Al-12%Mg at 720°C to the same level as given by beryllium alone.

Field [102] reports that at temperatures in excess of 400°C additions of 100ppm calcium (or berylium) to Al-4.2%Mg reduces the oxdiation weight gain by a factor of 10. The kinetics are more sensitive to the precise level of calcium addition than for berylium. Field suggests a different mechanism operates, in that calcium reduces the size and density of primary magnesia, but does not form its own oxide.

3.5.3b Oxidation Enhancers

Lithium (Li)

Field [102] reports that lithium additions of 3% Al-4.2%Mg alloy give weight gains an order of magnitude greater than shown with the Al-4.2Mg alloy only at 480°C-520°C. A further ten fold increase in weight gain is given in the presence of water vapour.

Indeed Ginsberg and Datta [120] find that additions of 0.25-1.5%Li to Al-3%Mg melts enhance dross formation considerably. Certain behavioural similarities in Al-Li and Al-Li-Mg to Al-Mg are reported. Primary (γ-$LiAlO_2$) and secondary (Li_2O) oxidation products form [102]. Initial surface formation of Li_2O occurs by direct reaction (equation 3.9) or by secondary reduction (equation 3.10) then reacts with water vapour (equation 3.11) to form spinel (equation 3.12) [102].

$$2Li + O_2 \longrightarrow Li_2O \qquad 3.9$$

$$6Li + Al_2O_3 \longrightarrow 3Li_2O + 2Al \qquad 3.10$$

$$Li_2O + H_2O \longrightarrow 2(Li^+ + OH^-) \qquad 3.11$$

$$2(Li^+ + OH^-) + 2H_2O + 2Al \longrightarrow 3H_2 + 2LiAlO_2 \qquad 3.12$$

Field suggests that oxidation enhancement by lithium additions to an Al-4.2Mg alloy occurs by size and density modification of primary MgO.

Zinc (Zn)

Zinc (100 or 1000ppm) is thought to be responsible for appearance of large growths (grey-black) "resembling mushrooms or cauliflowers" on melts after 48 hours at 800°C [137]. This element increases the oxidation of an otherwise slowly oxidising 0.05-0.1%Mg alloy. Ginsberg and Datta [120] support this observation using up to 5% zinc additions to an Al-3%Mg alloy at 700°C in air.

Sodium (Na)

A study by Cochran et al [124] reports that increased concentrations of sodium at 725°C on Al-0.7%Mg alloy oxidised in air reduces rapid oxidation of meltsalthough the total weight gain slightly increases.

Carbon (C)

It has been suggested that surfaces contaminated with carbon show increased oxidation levels [151].

CHAPTER 4 - SURFACE STRUCTURE AND PROPERTIES OF OXIDES

The oxide generated in the dross layer, primarily on molten metal, during melting and casting was briefly considered in Chapter 2. Literature concerning the oxide structures and their rates of formation have been reviewed in Chapter 3. This chapter considers the network structure of oxide which may form with molten metal, ie, the dross layer; its composition, treatment and formation. Further, in an attempt at quantitatively assessing forces existing between oxide and molten metal, the theory of wetting is introduced and reviewed in relation to the strength and structure of the oxide-solid metal and oxide-liquid metal interfaces.

4.1. THE DROSS LAYER

4.1.1. Dross Composition

It was established in Chapter 2 that exposure of aluminium and aluminium alloys to an oxidising atmosphere at elevated temperatures results in high metal losses from oxidation. Closer inspection reveals that the weight of metal converted to oxide during melting is negligible relative to the levels of metal loss experienced. Thus oxidation cannot account for the total metal losses typical of commercial melting practice [24]. It has been noted in section 2.9 that generally the skim formed in the best bulk melting practice amounts to about 1% of metal melted. In general foundry practice, the metal removed is nearer 5%, and is far more variable (5-15%) in the secondary industry, where losses are highly dependent on the type of scrap melted [24].

The key to the discrepancy is that in aluminium dross (or skim) on a molten bath surface, a large amount of metallic aluminium is bound principally by a small amount of aluminium oxide. The implication is, that the volume of metal held may be

dependent on the quantity of oxide present, ie, the natural oxide film on aluminium surfaces and also that generated by process operations which expose metallic aluminium to an oxidising atmosphere.

In normal melting practice, just before the molten metal is removed from the furnace a flux layer of molten salts in added, stirred into the bath and skimmed off. Thereafter, procedure depends largely on the particular foundry. In most cases the excess molten metal is allowed to drain back into the furnace from the skimmed layer. Dross is then spread on the floor and naturally cooled. A light sand cover may be thrown onto the dross to prevent aluminium from continuing to burn. According to published reports the rate of oxidation of molten aluminium in hot dross is about 1% for every minute the material is exposed to the atmosphere [152]. After cooling, large pieces of metal can be picked out by hand from the dross layer.

Aluminium skim has a variable composition consisting of flux salts, metallic aluminium, oxides, carbides and nitrides. Estimates of the amount of metallic aluminium present in dross varies considerably from 9%, for partly demetallised dross [122] through to 75-95% [16,29,153]. The quantity of metal retained is highly dependent on the process treatment encountered and such factors as temperature, treatment time and care taken by the furnace operator. The use of correct fluxing procedures can be used to reduce the metallic content to less than 50% [24,29]. The salt flux remains clear and capable of considerable re-use when uncontaminated by magnesium. However, incorporation of the spinel $MgAl_2O_4$ increases both the viscosity and density of the flux bringing about a significant reduction, down to 60% or less, in recovery efficiency [154].

Chemical analysis also shows that the alumina content of such dross is far higher than in ordinary ores (only 57% alumina is present in bauxite). Thus aluminium dross is a far richer source of aluminium than any known naturally occurring ores [16].

It is of great financial interest to reduce the metal content of the dross layer. Techniques used for metal recovery from aluminium dross include mechanical separation, chemical treatment and remelting. Dross can be mechanically broken down by ball milling and grinding. Screening and pneumatic classification upgrades the material [16]. The most successful methods used in the chemical treatment of partly demetallised dross involve extraction of alumina with sulphuric acid (achieving a total aluminium content of 91%), and treatment with caustic soda in an autoclave at elevated temperatures, a modification of the Bayer process recovering 80–90% aluminium [16].

Modern recovery practice aims at melting aluminium free from the non-metallic network of oxide. Commonly, commercial practice involves scraping hot dross into a crucible with an endothermic flux cover, leaving metal to drain through a hole in the base [30]. The most effective recovery however, is achieved by the use of a salt flux of equal parts of NaCl and KCl with 5% cryolite (Na_3AlF_6) [153]. Solid dross may be charged into a rotary furnace and melted with flux [152]. Systems employing molten salt fluxes however, have disadvantages of the flux cost, corrosive attack on building steel and other components, additional labour requirements and the environmental problems of the flux usage and disposal.

A method combining melting and mechanical recovery uses a heated power driven press. The pressure creates shear forces within the dross causing free aluminium to coalesce and pass through a small opening which restricts the passage of oxide [155].

4.1.2. Structure of the Oxide Network

Dross skimmed from the melt surface characteristically comprises small metal particles trapped by relatively small amounts of enveloping oxide. The metallic content of dross may be over 95%. Apparently therefore, alumina films are capable of retaining

more than twenty times their own weight of molten aluminium. The cellular structure of aluminium dross at temperatures above the melting point is such that fluidity of the molten aluminium contained within it is suppressed.

Impairment of metal drainage is natural, because of the surface tension forces holding a quantity of metal back inside each oxide envelope [156]. If the metal particle size is increased and forces exceed the interfacial tension, metal may drain from a fractured oxide envelope until the interfacial tension forces dominate. Stirring is used to take material beneath the surface where the fractured oxide films allow the contained metal to assimilate with the melt [156]. Oxide films however, may also re-trap metal by bringing particles within close proximity such that either material bridges or sizeable attractive forces are achieved [29]. Qualitative fusion tests on aluminium swarf show that vacuum melted compact briquettes with negligible surface oxide show excellent melting characteristics and therefore have a high recovery potential. However, air melted samples exhibit low recovery potential as thicker oxide films prevent fusion of individual swarf or foil layers [29]. One may anticipate therefore, that a point must be reached at which recovery of very fine material and highly oxidised or anodised scrap becomes uneconomic.

The mechanics of drainage are complicated further when oxidation takes place by reaction with moisture. For example, in fuel fired furnaces in areas surrounding flame impingement on the charge, oxidation produces severe blistering. These blisters grow and burst, exposing new surfaces to combustion products. Recoveries from blistered metal ranged from 47-90% depending on the severity of blistering in comparison to 96% recovery when no blistering occurred [33].

The structure of dross would suggest that a greater attraction exists between alumina molecules than between alumina and aluminium. A measure of this interaction comes from studies of surface wettability and surface energies. Ceramics such as alumina are not readily wetted by liquid metals [157], both have characteristically high surface energies. This is evident, for molten aluminium gathers itself into small globules when in contact with alumina in order to minimise the energy of the system. Thus if wetting can be encouraged then a reduction in metal trapped in dross and easier metal drainage may result. The next section considers therefore the theory and basic principles of wetting in order to rationalise the wetting of alumina by molten aluminium.

4.2. THE THEORY OF WETTING

The surface tension of a liquid is a measurable force existing in all liquid surfaces. The phenomenon is due to a layer not more than a few molecules thick. A surface molecule has unbalanced forces, ie, it is no longer surrounded symmetrically by other molecules, but experiences a net force towards the bulk of the liquid. For both solids and liquids, molecules in the surface layer possess energy by virtue of the work done in forming the surface. Surface free energy (σ) is the term given to the energy necessary for the formation of unit area of new surface. Surface tension (γ) is the work done, or energy required, in creating this unit area of surface (Jm^{-2}). Hence surface tension can be numerically equated to the free energy of its surface per unit area if no marked change in surface structure occurs. Thus with liquids and solids at high temperatures, the surface tension and surface free energy become numerically equivalent [158].

Surface tension may also be viewed as forces acting in the plane of the surface, tending to minimise its area. On this basis the surface tension is expressed as the amount of force exerted in the surface perpendicular to a line of unit length (Nm^{-1}).

Consider now, a liquid drop in contact with a solid or liquid substrate. This drop will take the shape which minimises the free energy of the system. The angle (θ) which a liquid drop assumes on a plane solid surface, shown in Figure 4.1, is the result of a balance of forces between the liquid-vapour, solid-vapour and solid-liquid interfaces.

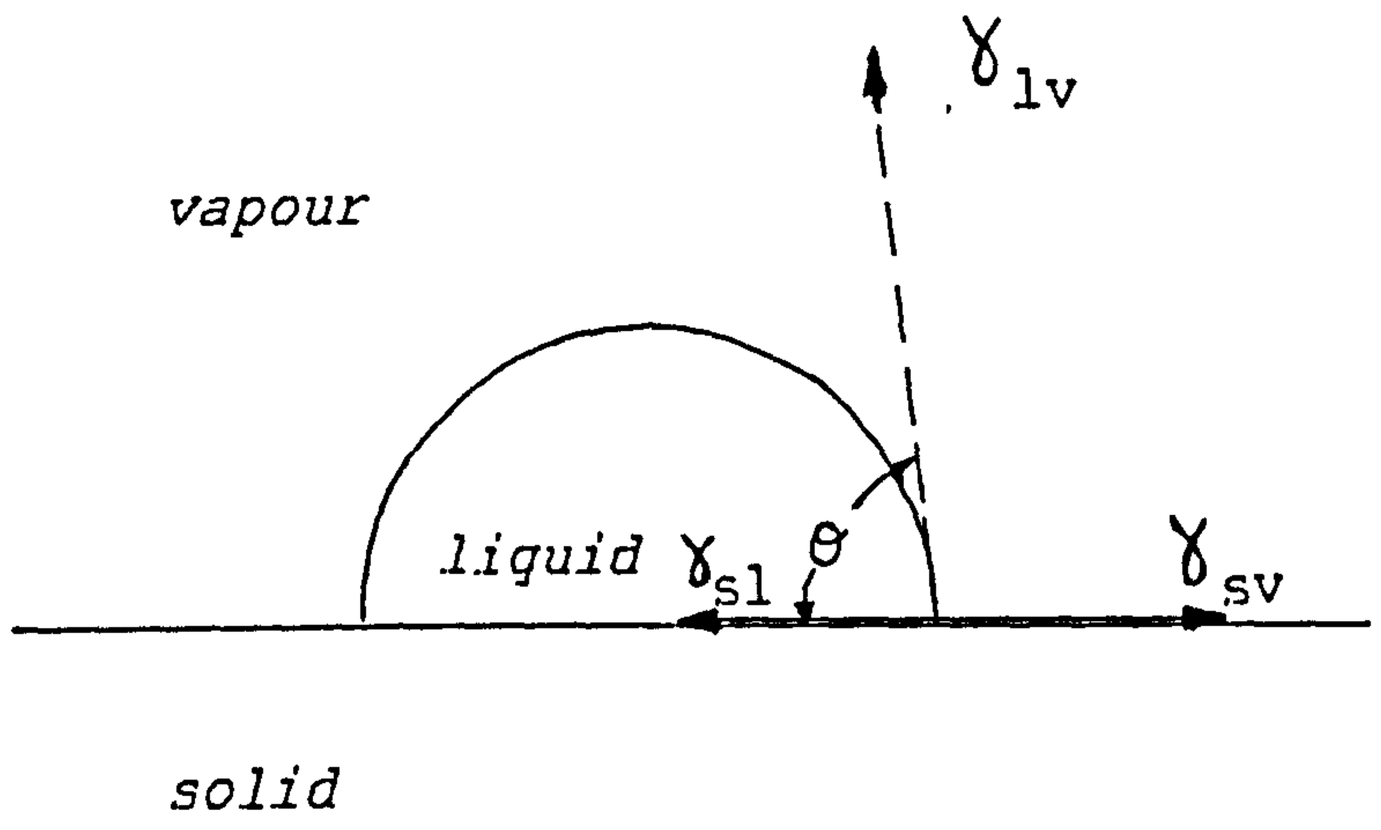

Figure 4.1 : Surface tensions on a liquid drop resting on a solid surface

The relationship of equation 4.1 was expressed by Young [159] in terms of the surface or interfacial energies γ_{lv}, γ_{sv}, and γ_{sl}.

$$\gamma_{sv} = \gamma_{sl} + \gamma_{lv} \cdot \cos\theta \qquad 4.1$$

Thus the contact angle is a useful measure of wettability. If there were no interaction between solid and liquid the interfacial tension γ_{sl}, will be the sum of the two surface tensions ($\gamma_{sv} + \gamma_{lv}$). Hence with a contact angle of 180°, the liquid and solid are said to be non-wetting. As the degree of

interaction between the liquid and solid increases, the liquid spreads, until $\theta = 0^{\circ}$ when the liquid wets the solid completely. Thus the contact angle is also a measure of surface adhesion.

The work of adhesion w_a, is defined as work necessary to separate liquid from a solid. Sixty years after Young's work, Dupre [161] showed that the work of adhesion could be defined in terms of Young's Equation (equation 4.1). Hence if the three-phase system is in equilibrium both before and after separation then, if $\theta <$ 90°, equation 4.2 follows.

$$w_a = \gamma_{lv} (1 + \text{Cos } \theta) \qquad 4.2$$

The main thermodynamic relations of the theory of wetting of solids by liquids are the equations relating the contact angle to surface tensions (or surface energies) and to the work of adhesion (w_a). Although obtained theoretically, use of these fundamental relationships is widespread. Thermodynamic and mechanistic verification of Young's equation has been obtained [161, see 162]. Concern has been expressed over the use and validity of these equations in real situations where non-equilibrium [162,163] and usually heterogeneous surfaces exist [164].

4.2.1. Hysteresis - Wetting In Non-Equilibrium Systems

A fundamental characteristic of wetting is the ability of a liquid drop to have many stable angles on a solid surface. This phenomenon is described as hysteresis. The model so far described is based on classical thermodynamics [165], whereby only one stable contact angle is predicted for a system with a smooth homogeneous, non-deformable solid. Johnson and Dettre [166] extended this model by relaxing these limitations to allow for hysteresis.

The largest (advancing θ_a) and smallest (receding θ_r) contact angles are relatively reproducible. Thus hysteresis can be defined as $\theta_a - \theta_r$. A simple illustration of this is found when a liquid boundary advances over a clean dry surface; θ_a applies. θ_r is observed when the liquid boundary recedes over the previously wetted surface.

Contact angles are also dependent on the relative rate of movement between liquid and solid. Bartell and Bjorklund [167] found that hysteresis was only eliminated with rates of advance or recession as low as 0.02mm min^{-1}.

As any study involving contact angles involves a time factor (particularly if the system requires time to reach equilibrium) then dynamic angles obtained in cases in which the three phase line of contact moves, are probably more reproducible than angles determined with static systems [166]. For systems 'at rest' equilibrium may still not be reached over very long time periods.

Hysteresis has also been interpreted in terms of surface adsorption and surface roughness effects. In wetting, with the emphasis so heavily on the balance of forces at a surface layer the presence of contaminants, impurities or the existence of more than one phase becomes critical. For example, if more than one molecular species exists in a solid or liquid then the surface phase may differ in composition from the bulk. Several authors have drawn attention to the fact that vapour adsorption on a surface is often neglected in deriving equilibrium relations concerning the contact angle [163, see 168]. As vapour is absorbed a monolayer spreads on a solid or liquid surface. The surface free energy will be considerably affected, it is usually decreased [168]. The reduction in surface tension can be defined as a spreading or film pressure π_{sv}, of vapour on a solid, thus

$$\gamma_{sv} = \gamma_s^\circ - \pi_{sv} \qquad 4.3$$

In general π_{sv} is small (nearly zero) for finite contact angles, but becomes significant as θ approaches zero [168].

The importance of surface absorption in wetting can be illustrated by the following example. Zisman classified solid surfaces according to the value of their surface free energies, into low or high energy surfaces [168]. Experiment has shown that a high energy surface is converted by adsorption to that with a lower energy, confirming earlier work by Langmuir [169] that major changes in surface properties of solids occur with adsorption of a monolayer of molecules. For oxide surfaces, alumina in particular, gaseous species once absorbed may result in significant changes in surface energy. A number of authors have shown that a hydroxyl layer exists on the oxide surface, and at low temperatures this is expected to chemically modify the surface [see 170].

Some classification of hysteresis resulted following a study of the effect of macroscopic roughness of a solid surface on the contact angle [171]. Johnson and Dettre [171] modelled the effect of roughness on wetting by using an energy barrier concept. They find that increasing roughness increases θ_a and decreases θ_r. Faber [172] used a ripple model to estimate the roughness of a free liquid metal in thermal equilibrium. For a typical liquid metal the average displacement is not more than 0.3nm. Both surface roughness (substrate topography) and heterogeneity can cause significant contact angle hysteresis. Johnson and Dettre suggest that on optically smooth, non deformable surfaces the major cause of hysteresis is surface heterogeneity. For grossly rough surfaces (asperities >0.5μm) both effects are important [166].

The phenomenon of wettability and adhesion has long been studied in low temperature solid-liquid contact systems. Comprehensive reports have been published by Johnson and Dettre [166], Zisman [168], Fowkes [173] and Good [174]. However, solid body wettability by molten metals at elevated temperatures possesses a number of purely specific features and presents an

independent problem. An example of surface adsorption has already shown that accurate determinations of the degree of wetting in a system is dependent on the level of equilibrium reached. As the apparent contact angle is often controlled by a slow approach to equilibrium, increasing the temperature can increase the rate of equilibrium markedly. Thus for solid-liquid melt systems, which mainly involve elevated temperatures, a knowledge of the effect of temperature on wetting is required.

If a system comes to equilibrium and no chemical reaction occurs at the interface, the cosine of the contact angle of a drop of liquid metal resting on a ceramic substrate increases linearly with increasing temperature [175]:

$$\text{Cos}\,\theta = 1 + B\,(T - T_{cs}) \qquad 4.4$$

If chemical reaction occurs at the solid-melt interface a non-linear relation is followed. Temperature coefficients of the solid-liquid interfacial tension (γ_{sl}) are related to chemical adsorption by classical Gibbs adsorption relations [176]. Hence, the surface energy of a solid may vary discontinuously with respect to temperature because of atomic surface rearrangements or phase transformations. On low energy surfaces contact angles are almost constant with temperature [171].

Values of free surface energies of alumina at different temperatures have been compiled and plotted in Figure 4.2.

4.3. LIQUID METALS

Liquid metals are characterised by high values of surface energy and surface tension. It is useful to consider the structure and properties of liquid metals in order to understand the origin of these values.

Over recent years a number of researchers have developed new approaches to the study of liquid metal surfaces. Informative publications by Faber [172] and Shimoji [177] describe the development of static and dynamic models of a liquid metal. The most notable conclusion of the lattice theory concerns formation of a double layer at the metal-vapour boundary. This is due to depletion of electrons from bulk metal and an excess of electrons in the bulk vapour. Alternative approaches use distribution functions. In this latter approach, liquid metal is considered as a two component system in which conduction of electrons moves under a disordered arrangement of ions. The temperature dependence of surface tension of liquid metals can be predicted in terms of these distribution functions [177].

Understanding of electronic, thermodynamic and kinetic liquid metal properties was substantially aided by the advent of a pseudopotential concept. The effective potentials of the ions are sufficiently weak that the electrons can be described in terms of nearly free electron model. Hence, from this theory ion-ion potentials in metals can be represented to a first approximation by simple pair potentials [177].

The pseudopotential theory of liquid metals describes the total energy in two parts: structure dependent and structure independent energy. Structure dependent energy (arising from effective pair potentials) depends on detailed configurations of respective ions. Structure independent energy is density dependent and depends only on the atomic volume [177]. Calculations show that the main contributions to surface tension come from changes in structure independent energy. The numerical results depend strongly on the magnitude of thickness of the electron surface layer L, a measure of surface thickness [178]. A relationship between surface tension and surface thickness (L) is described by Evans [179]:

$$\gamma \simeq - \tfrac{1}{2} L \rho_o - \tfrac{1}{4} L \rho_{indirect} + \gamma_{fowler} \qquad 4.5$$

These theoretical descriptions of liquid metal surfaces have been supported by experiment. Using simple model theories surface tension values of the order of magnitude predicted for alkali metals have been observed [180]. Pseudopotential theories yield promising results for polyvalent metals [181] however, Wood and Stroud [181] predict larger surface tension values for aluminium than found experimentally. The inaccuracy is thought to be due to inadequate data inputs rather than fundamental shortcomings of the theory [181].

4.3.1. Addition of Elements to Liquid Metals

Some non-metallic elements, due to strong surface active features, markedly lower surface tension values of liquid metals, even if concentrations are extremely small [177].

Kozakevitch and Urbain [182] propose that surface oxides such as FeO consist of an ionic double layer, with 'anions' (the most electronegative atoms) resting on top of metal cations. This gives rise to the formation of a surface compound. The adsorbed surface species is loosely close packed [177]. While formation of a compound may be an extreme situation, certainly surface adsorption of non-metallic impurities in alloys provide a barrier. This barrier inhibits contact between the alloy and substrate, resulting in a poorly wetted system. Low levels of carbon and nitrogen have been observed to segregate in every alloy system studied by Bozack [183]. The existence of surface segregation casts doubt on many previous wetting studies. The use of pure materials and surface analytical techniques is therefore imperative to the study of wetting.

In view of the difficulties encountered in determining the magnitude of the surface tension of pure liquid metals, literature concerning liquid alloy surface tension, although extensive, is of dubious accuracy and provision of a general theory for liquid

alloys is far from complete. In most cases, interfacial tension of pure metal A is taken as a reference and calculations are limited to changes in this value γ_A due to additions of metal B at a given temperature [176]. However, the concentration in the surface layers may be quite different from in the bulk. In general, for substitutional alloys, if $\gamma_B < \gamma_A$ there is a tendency for solute ions (B) to congregate at the surface thereby lowering the free energy. Even when the bulk concentration is very small, if $\gamma_B \ll \gamma_A$, a monolayer covering is still anticipated. The solute atoms can be considered as surface inactive only if $\gamma_B > \gamma_A$. This theory predicts that isothermal curves for surface tension as a function of concentration should be concave downwards [176,177,184]. A number of liquid alloys conform to these predictions in a qualitative fashion, as shown in Figure 4.3.

If component B in a liquid phase is a strong electropositive metal the reduction in interfacial tension, γ_{sl}, may be due to an adsorption plus reaction process rather than pure adsorption [176]. The chemical composition of interfaces [176,185] in multicomponent systems is based on the Gibbs adsorption equation, which at constant temperature has the form:

$$d\ \gamma_{sl} = -\sum_i \Gamma_i\ d\mu_i - S^{\gamma}\ dT \qquad 4.6$$

4.3.2. Additions of Elements to Liquid Aluminium

Studies of fluxless brazing of aluminium in both vacuum and inert gas show that the wetting process is facilitated by the presence of a promoter. The promoter also acts as a gettering agent for oxygen and water. Many metals can act as promoters, with many aluminium alloys magnesium is a good gettering agent [143]. The results of studies of the effect of added elements on the surface tension of aluminium in argon at 700°C - 740°C is illustrated in Figure 4.3. Magnesium and lithium give substantial reductions but manganese has little effect [184].

Although the density of aluminium is only slightly changed by the presence of magnesium [186], the surface tension of liquid aluminium is noticeably modified with magnesium concentrations up to 8% [186]. As the magnesium content [x] increases, the surface tension (γ) of unoxidised (equation 4.7) and oxidised (equation 4.8) aluminium alloy surfaces at 700°C decreases following a logarithmic function [186].

$$\text{Unoxidised} \qquad \gamma = \gamma_{(Al)} - 96.7 \ln (1 + 0.26x) \qquad 4.7$$

$$\text{Oxidised} \qquad \gamma = \gamma_{(Al)} - 71.8 \ln (1 + 0.31x) \qquad 4.8$$

4.4. SOLID - LIQUID METAL INTERACTION

So far this section has reviewed the concept of wetting in characterising relationships, the effect of temperature, and also the state of equilibria of a system. The purpose of this section is to examine the interaction between solid and liquid metal and the resulting interfacial tension.

4.4.1. Solid Metal - Liquid Metal

The solid-liquid interfacial tension γ_{sl}, is a fundamental thermodynamic quantity giving some insight into the structure of the interface. This applies to a solid metal and its own liquid phase during melting, or the interaction between a solid metal and liquid metal of very different materials. At an atomic level, in relation to the former situation, the interfacial structure has a decisive influence on solid growth mechanisms and corresponding morphologies. Aspects of crystal growth such as morphological stability of planar interfaces and dendrite growth from the molten state are clearly influenced by the interfacial tension of the solid metal and its liquid phase. Characteristics of solidification and nucleation from the melt are reviewed by Woodruff [158].

4.4.2. Solid Oxide - Liquid Metal Interaction

To calculate the interfacial energy between a solid and liquid metal of differing compositions it is necessary to consider the nature of molecules making up the surface, i.e, the nature of the interaction.

A theoretical approach was taken by Zisman [168] initially based on Young's equation. Zisman defined a critical surface tension of a solid (γ_c) related to the surface free energy of the solid through the parameter $\phi . \phi$ is a characteristic of a given system and is indicative of the nature of interactions and on the configuration of molecules at the surface (eg, a measure of misfit of molecules of unequal size) [174]. Fowkes [173] extended this concept, initially proposed by Good [174], to include differences in interactions between molecules. He postulated that surface and interfacial tensions can be divided into additive parts associated with various forces between molecules, such as, dispersive forces (d) and hydrogen bonds (h).

$$\gamma_{lv} = \gamma_{lv}^{d} + \gamma_{lv}^{h} \qquad 4.9$$

Miedema and den Broeder [189] studied the physical and chemical contributions to the interfacial energy of solid metal-liquid metal systems. The physical term consists of surface energy contributions; a fraction of the heat of fusion and an entropy term representing atomic disorder of surface layer atoms [189]. These theoretical approaches are useful in showing the importance of some specific contributions. Indeed, experimental observations are approximated by these theories [162,168,173].

Many authors consider that changes in interfacial tension are due to chemical reaction [190,191,192]. Indeed the change in interfacial tension is found to be directly proportional to the corresponding change in chemical potential in the contacting phase [191].

$$\Delta\gamma = M\Delta\mu \qquad 4.10$$

According to this relation as the system tends to equilibrium the value of the interfacial tension decreases while the chemical properties of the contacting phases become increasingly similar. Equation 4.10 applies until stability is reached. When major contributions to the wetting of a solid and liquid metal are chemical reactions and formation of interfacial compounds, other contributions to wetting are hard to isolate.

Stoneham and Tasker [193] argue that many phenomena associated with metal/non-metal interfaces and similar situations with a large dielectric constant mismatch can be understood in terms of image interactions due to changes in the non-metal. The effects are especially significant when no reaction between the phases occur [193].

The idea of an image charge is long established, eg, a lattice of ions adjacent to a boundary generates a lattice of image charges. Image terms influence interfacial energies whenever there is a change in dielectric constant across the boundary. Image interaction charges may be fixed charges or immobile defect charges (ie components of an ionic lattice), defects created by ionic re-organisation or charge transfer and mobile charges [193]. Experimental data by Naidich [191] gives support to this concept. Analysis of data from oxide substrates with non-reacting liquid metals showed that wetting appeared to be determined entirely by the non-metal substrate [191].

Naidich finds wetting occurs when either the ions can readily change valence or when the static dielectric constant exceeds a critical value of about 25 [191]. These conditions correspond to a high degree of non-stoichiometry or disorder. NiO, V_2O_3 and UO_2 are wetted oxides, presumably because the disorder provides a high concentration of defect charges and hence strong image interactions. Such a solid surface is formed by negatively charged

ions with characteristically large anion radii and high polarisability. Further research has established a correlation between the strength of the metal-oxide bond in the solid and wettability by the metal. A liquid metal is not expected to wet an oxide with strong intramolecular oxide bonds [191]. Zisman [168] reached a similar conclusion earlier stating that a high energy surface attracts liquid molecules more strongly than they attract one other, i.e, wettability is high.

The structure and properties of an interface between a metallic phase and alumina was described by McDonald and Eberhart [157]. The basis of the model was the assumption that adsorption of metallic atoms occurs on two types of surface sites on alumina; metal-oxide bonds and Van de Waals forces, as illustrated in Figure 4.4. Sites situated directly over the centre of the hexagonal array of aluminium ions in the second layer are termed A sites (area 1.62nm^2). Metal atoms are assumed to be chemically bonded to the oxide ions on the surface with bond energies comparable to the bulk metal oxide. B sites (area 0.814nm^2) are situated directly over the aluminium ions in the second layer. Metal atoms are attracted to the surface oxide ions of B sites by Van der Waals forces [157].

4.4.3. Alumina - Molten Aluminium Interaction

As far as possible the surface energy and interaction of liquid metals and ceramic phases has been generalised. This work however, is concerned specifically with the wetting behaviour of aluminium or aluminium alloy melts and their corresponding oxides.

The wetting of alumina single crystals and polycrystalline material by molten aluminium has been investigated mainly using methods which require measurements of melting point depression, dihedral angles and sessile drops [176]. From such investigations, contact angles determined between molten aluminium and alumina are

presented as a function of temperature in Figure 4.5. As the temperature increases, the contact angles decrease. A wetting condition is observed at temperatures above 950°C [194] on single [195,196] and polycrystalline alumina [194,196,197]. Although as Figure 4.5 shows, the transition temperature varies considerably with different investigators [198].

At these elevated temperatures, the characteristic sudden decrease in contact angle is suggested to correspond to a change in the molten aluminium structure. However, chemical attack on the alumina surface beneath the molten metal drop is increasingly observed [195]. Reaction rings around the drop perimeter are likely to be controlled by removal of volatile Al_2O [195,196]. Under some experimental conditions, the interface builds by a vapour-liquid-solid mechanism [194]. Thùs, as Figure 4.6 shows, a substantial amount of time is required for an Al-Al_2O_3 system in vacuo to reach equilibrium [197,199].

Inspection of surface tension values collated for pure aluminium in Table 4.4 show considerable scatter with different investigators. The variation is attributed to experimental procedure [194], to different vacuum systems used and to the strong affinity of aluminium for oxygen. Most data are obtained with a vacuum of the order of 10^{-4}Pa with a liquid nitrogen cold trap. This only results in a reduced oxide thickness as removal of oxygen is not complete.

John and Hausner [198] investigated the effect of oxygen on the wetting of alumina by aluminium. When sessile aluminium drops at 700°C were exposed to controlled levels of oxygen the thickness of the oxide layer of the molten aluminium surface was greatly influenced. At oxygen pressures above 10^{-8}Pa, the mechanical strength of the oxide skin is such that formation of an equilibrium molten drop shape is prevented. Below this oxygen level the thin oxide envelope deforms easily and the wetting angle is proportional to the logarithmic value of the oxygen partial pressure [198].

Goumiri and Joud [200] linked the molten aluminium surface tension to the proportion of surface oxide coverage, X as shown in Figure 4.7. It was estimated that the mean value $\gamma_{Al} = 870 \pm 5 mJm^{-2}$ obtained by investigators at melting temperature represents the interaction of aluminium with its substrate in the presence of an oxide film at least a monolayer thick. Wierauch [194] found a linear relationship exists between oxide thickness and contact angle. Linear extrapolation of this plot, Figure 4.8, to zero oxide thickness gives a contact angle value of 55°-78°. Earlier calculations are at the upper end of this range [197,200]. Thus for an atomically clean aluminium surface the surface tension is equal to $1050 mJm^{-2}$ [200]. Similar conclusions were reached by Garcia-Cordovilla et al [186] using a maximum bubble pressure method. A value of $1100 mJm^{-2}$ was obtained for the surface tension of a clean molten aluminium surface, which decreased to $865 mJm^{-2}$ as oxygen entered the system.

Similarly, the degree to which solids are wetted by molten silicon was found to be largely determined by the partial pressure of oxygen in the environment [202]. The formation of alumina under low levels of oxygen can be deduced from studies of the deoxidation of steels using aluminium. Such studies have shown that the alumina morphology is controlled largely by the dissolved oxygen content, which in turn, is determined by the alumina-melt surface energy [203]. High interfacial energy causes agglomeration of small particles [204].

To summarise, literature concerning the wettability of ceramics by molten metal is fairly specific, but lacks reproducibility, since vapour adsorption and segregation of additional elements considerably affects the surface tension of the substrates. Limited availability of modern surface analytical techniques meant progress was slow until fairly recently. Extensive measures are now taken to ensure a high degree of purity and cleanliness during experimentation. However, recent re-evaluation of the surface tension and its contact angle with aluminium

substrates suggest that most measurements represent the interaction of aluminium with its substrate in the presence of an oxide film at least a monolayer thick [200]. For atomically clean aluminium a surface tension value of 1050-1100mJm^{-2} is anticipated [186,194].

Ceramics such as alumina are not readily wetted by liquid metals. It is assumed, but not established that non-wetted interfaces are weak, indeed the implication is to the contrary and Al-Al_2O_3 consistently forms a strong interface [157]. The nature and packing of atoms in the surface of a solid essentially determines the adsorptive properties of the surface and hence surface interactions. Liquid metal contact with the oxide surface is the interaction with the oxygen atom of the oxide [191] on two types of surface sites [157].

The partial pressure of oxygen in molten iron with dissolved aluminium has a strong dependence of alumina morphology by virtue of the effect on the interfacial surface energy [203,204]. It is implied that control of alumina morphology and the quantity of metal trapped within the oxide is possible through influencing the interfacial energy by external means, i.e. adjusting phase compositions and concentrations.

From work on aluminium brazing it is known that an efficient flux removes surface oxides. Molten fluxes penetrate, but do not dissolve oxide films on aluminium. The mechanism by which a salt flux strips the oxide from the metal and holds solids in suspension is not well understood. It has been suggested that a low interfacial tension between the salt and molten aluminium is the primary cause of oxide stripping [205]. Since the salt wets the metal and oxide particles, and aluminium does not wet the oxide at melting temperatures the stripping action is very effective. It is also suggested that the presence of fluorides in the salt lowers the interfacial tension, further enhancing the stripping action. Hence, fluxing salts are commonly made up of chlorides with a small percentage of fluoride [205].

An oxide film may be removed sufficiently for brazing by heating in vacuo [205]. Liquid metal can penetrate the oxide film and lift the oxide by spreading along the oxide-metal interface. Penetration is said to occur by vapour phase diffusion through the oxide. It was noted however, that satisfactory spreading occurs in vacuum if the oxide film is first punctured mechanically [206].

CHAPTER 5 - EXPERIMENTAL

EXPERIMENTAL APPROACH

The requirement for any experimentation is that it reflects current and future industrial practice bearing in mind the constraints of a laboratory environment, and at the same time enables the close control of experimental parameters which is essential if fundamental studies are to be successful. This section introduces the philosophy behind the experimental approach.

In the laboratory the maximum mass of metal used in oxidation studies is limited by the high sensitivity required for the microbalance system to 1g. A high surface area for oxidation is achieved without reducing the metal thickness to a foil by using specimens in the form of thin discs (7mm diameter and 1mm in height). In this way enough molten metal is available to monitor the early stages of oxidation despite the extremely small scale. In comparison with industrial melting furnaces which range from 1-80 tonnes capacity, these small specimens have considerable advantages.

The progress of oxidation from initial adsorption of oxygen to the total consumption of metal may be followed over a 24h period. Data are produced throughout the entire oxidation process giving valuable information for formulating a mechanism of dross formation otherwise unattainable from large melt baths. This is very useful for magnesium containing aluminium alloys where the effect of oxidation by the depletion of magnesium has yielded particularly relevant data on oxide transformations and oxidation of a series of aluminium-magnesium alloys.

A further advantage of these specimen dimensions is that the volume of molten metal is contained within the developing oxide envelope, thus the melt may be supported on plates without requiring walled containers. This also enables the surface area exposed to the atmosphere to be maximised in a controlled manner.

The oxidation trends determined from the thermobalance studies were also compared to those observed using larger volumes of molten metal (10mm by 10mm cylindrical specimens) which were oxidised in autoclave furnaces, held in crucibles of similar dimensions. In addition, small molten baths (20mm in diameter and 10mm in height) were produced on which surface oxide films were developed for morphological studies. While the small specimens size may seem initially to be a limitation, it should be emphasised that large industrial furnaces recovering secondary material such as beverage cans and thin foil, will experience oxide generation at a considerable rate by these same processes applicable to high surface area, and low volume material. Indeed these small specimen dimensions worked particularly well for the purposes required and comparison with industrial beverage can recovery gave highly comparable results (Chapter 10).

All aluminium and aluminium alloys possess a thin surface oxide film, and recovered material carries a considerable assortment of oxide coatings. Current methodology for studying oxide films on molten metal requires the removal of this surface film, appreciably thickened by the high furnace temperatures, prior to any oxide film formation for investigations. Hence the first formed oxide is removed from the melt surface by skimming. This procedure is not reflected in industrial practice before a charge is melted, although skimming the melt surface is standard practice for removing the dross layer prior to casting. In this experimental work therefore, the oxide formed on both skimmed and unskimmed melts (melts with the original surface oxide preserved) is investigated and it is shown that this has a considerable effect on oxidation behaviour and recommended industrial melting practice.

Industrial melting rates and holding times differ considerably depending on the furnaces used and the procedures adhered to. However, in general, the aim is to achieve a molten metal as rapidly and as efficiently as possible. Although large furnaces require

longer melt down times, a melt will usually not be held for over 2 hours. In this experimental work, in order to study the early stages of oxide formation in detail over the first few hours, the small metal specimens were melted very rapidly (5-10mins). To obtain maximum data, the exposure times were extended to 15h and occasionally considerably beyond 24h. From these longer exposure times valuable information was collected which helped in understanding the mechanism of dross formation. In particular this showed that the mechanism of oxidation on aluminium and aluminium-magnesium alloys was very similar, but that the oxidation process was far slower for pure aluminium. Temperatures of 550°C and 750°C were chosen to reflect the industrial temperatures of preheating or decoating and general melting, respectively.

Melting in fuel fired furnaces generates a mixture of combustion gases (air, CO_2, SO_2, N_2, H_2O) which are traditionally viewed as hostile, containing reactive gases. This combustion environment generates considerable dross on a melt. With electric furnaces the opportunities of producing clean, controlled atmospheres has encouraged investigations into the effects of inert or non-reactive, non oxidising atmospheres. In practical terms and from economic considerations the ultimate clean environment, from a industrial point of view, is argon. It has been chosen for melting aluminium-lithium alloys and is classified as a non-reactive atmosphere acceptable in production. From an experimental point of view, the low oxygen content of argon allows comparison of an increase in oxygen content of over two orders of magnitude from argon to air.

As industrial furnaces and foundries vary greatly in humidity, the moisture content of atmospheres should be experimentally controlled. Argon may be dried conveniently by passing the gas over heated titanium chips, a process known as gettering. Moisture can be introduced by bubbling the gas through water. The next section, the experimental method, describes in detail the experimental conditions used in the present study. These were designed with a view to undertaking a fundamental mechanistic study of the oxidation process whilst remaining relevant to current and future industrial practices.

5.0 EXPERIMENTAL METHOD AND MATERIALS

To follow the scale growth process on liquid aluminium, oxidation kinetics have been studied and related to changes in oxide scale morphology, occurring as a function of exposure time. In parallel, the wetting characteristics of liquid aluminium on alumina have been investigated. From these studies, a mechanism for the oxidation of aluminium melts is presented which accounts for the observed changes in oxide morphology and the progressive development of dross. Results from parallel studies carried out with aluminium-magnesium alloys are compared to the behaviour of pure aluminium in order to determine the effect of increased magnesium concentration on the mechanism of dross formation of these alloys. This section describes the experimental techniques and procedure followed to determine the oxidation kinetics, scale morphology and wetting characteristics.

Materials were chosen to monitor the effect of magnesium and manganese additions in aluminium. Materials containing 5% magnesium (5182) and 1% magnesium with and without 1% manganese (3004 and 5005 respectively), also 1% manganese (3003), were compared to commerically pure aluminium. The composition of these five materials, supplied by Alcan is given in Table 5.1. The 5182 alloy was supplied with and without beryllium (10ppm and 50ppm) in order to study the effect of these additions. 5182 alloy was also supplied with and without titanium diboride grain refiner (GR).

5.1. OXIDATION KINETICS

Because of the directness and general convenience, measurements of oxidation rates of aluminium and aluminium alloys are most commonly carried out using thermogravimetric techniques. Thermogravimetry allows continuous determination of specimen weight i.e. oxide formation, with time.

Specimens were machined from 10mm diameter rod to produce discs 1mm high by 7mm diameter and polished to a 1μm finish, or electropolished. If required the specimens were ultrasonically cleaned in a degreasant based on perchloroethylene (gramasol). However specimens were consistently washed in methanol, dried and introduced into the environmental chamber of the microbalance on alumina plates or in alumina crucibles, pre-conditioned at 750°C for 5hrs.

The specimen is held on an alumina plate or crucible, freely suspended by a platinum wire in the centre of a quartz glass tube (with a gas inlet and outlet) within the hot zone of a vertical furnace. Thermocouples monitor the temperature of the furnace and the sample. Progressive displacements of a balance beam (counter-balanced) by a pan of weights) record the weight gain. The beam position relative to a fixed point is monitored in theC.I. electronics system MK2 vacuum balance head by a Robal digital control unit which displays readings of ±1μg on a chart recorder. The microbalance used (shown schematically in Figure 5.1) has a readability of 1μg and stated weighing resolution of ± 10μg/C°. Previous work however, describes difficulties in obtaining a stable base line (± 300μg over a 24hr period) despite extensive modifications to the experimental conditions and procedure [207].

Particular attention therefore was paid in order to ensure that all data were accurate and reproducible.Sources of measuring errors and consequent modifications are described in Appendix A. With room temperature control of ± 1°C the estimated error in the results, after smoothing, is ± 5μg in air at 750°C.

Experiments were performed on solid specimens at 450 and 550°C, in the melting range at 650°C, and on molten metal at 750°C and 850°C. The furnace temperatures were controlled to within ± 1°C and chosen to correspond with those most commonly encountered in industrial practice from annealing and delacquering to melting.

To encourage rapid melting, the thermobalance furnaces were preheated to the required temperature and positioned around the specimens. Thus, for a required temperature of 750°C, aluminium specimens were at temperature within 5 minutes. With no preheating, specimens melted after 13-15 minutes and were at 750°C by 20 minutes in both the furnaces used. The thermal responses from an aluminium specimen and specimen holder are shown in figure 5.2

The specimens were exposed to air or argon, at a flow rate of $20cm^3$/min and controlled humidity for exposure times upto 25 hours. The following atmospheres were chosen to vary the moisture (0.05-3KPa) and oxygen (0.06-21.2KPa) content of the environment.

i. Dry argon (as supplied 0.2 - 0.8KPa was passed through a gettering system containing titanium chips at 725°C to remove any moisture. Theoretically, an equilibrium partial pressure of water vapour of 10^{-24}Pa is possible. However, 0.05-0.3KPa water vapour pressure was determined in the system used.
ii. Humid Argon (about 3KPa water vapour pressure, generated as for humid air(iv)).
iii. Dry air (0.07KPa water vapour pressure) obtained by passing air through magnesium perchlorate [207].
iv. Humid air (3KPa water vapour pressure, typical of a combustion environment [209]) obtained by bubbling air through a series of water-filled Dreschel bottles, maintained at 24.5°C.

Two microbalances systems, F_1 and F_2, were run simultaneously. In one, microbalance F_1, the specimen was placed in a flowing gaseous environment ($20cm^3$/min); with the second F_2, the specimen was exposed to a static gaseous environment.

For comparison, a set of oxidation experiments was undertaken using much larger specimens, cylinders (10mm in diameter and height) having a surface area of $4.75cm^2$. These specimens were machined to fit alumina crucibles (height 20mm and internal diameter from base (10mm) to top (20mm)). In these tests,crucibles of molten metal were

exposed to both dry and humid air in autoclaves. Specimens were weighed before and after various exposure times and the results correlated with the microbalance experiments.

The effect of contaminants such as fluorides and chlorides generated by the decomposition of potassium fluoroborate and sodium chloride respectively was investigated using autoclaves.

5.2. OXIDE MORPHOLOGY STUDIES

To complement the kinetic studies, a parallel series of exposure tests was performed in which oxide samples were removed from melts at exposure times of 5, 60, 300 and 900 mins using a copper loop technique [210]. Retained aluminium was removed in a 3% bromine-methanol solution. Oxide films are generally formed on melts carrying the original surface oxide. Oxide was also generated on melts after the original surface oxide had been removed by skimming the molten metal with a copper loop or an alumina rod. These two types of oxide generation are termed unskimmed and skimmed respectively.

Surface films, formed during the early stages of the oxidation process, were examined by transmission electron microscopy to determine their structure and composition as a function of exposure time. The structure of the oxide-melt interface was also examined in the TEM by taking microtomed sections through solidified melts. The development of 'dross' during the oxidation process was studied by monitoring changes in surface morphology using optical and scanning electron microscopy.

5.2.1. Optical Microscopy

Specimens were coated with a thin layer of gold-palladium prior to immersion in a solution of electroless nickel (Canning Group, Nifoss 3000) at 90°C for 20-30 mins. This nickel coat (4-6μm) helped support the oxide layer whilst specimen cross sections were

polished to 1μm and finished with a silica 0.3μm suspension [27]. Micrographs were taken to illustrate the thickness and structure of the oxide layers.

5.2.2. Electron Microscopy

Techniques such as TEM and SEM provide detailed knowledge of surface oxide morphology and are a necessary prerequisite for interpreting gravimetric data and the results of elemental analyses.

5.2.2a Transmission Electron Microscopy (TEM)

Different techniques are used in preparing thin oxide layers (up to 100nm thick) suitable for the small depth of penetration of the electron beam used by the TEM. Al-Al_2O_3 studies have concentrated on TEM of stripped oxide films [62,129], of in-situ oxidised thin foils [61] or oxidised films attached to thin metal substrates [102], back polished [61] or ion beam thinned. Replica methods are often employed to examine the morphology of thicker oxide films [210].

In this work, early stages of oxide growth were followed by stripping oxide films from metal using chemical attack with a 3% bromine/methanol solution. Although convenient for pure aluminium, oxide development with Al-Mg alloys restricts the use of this method [207]. Such oxide films were cut to 3mm diameter discs and jet electropolished. Electrolyte (25% nitric acid, 75% methanol) at -20°C and 0.1mA was directed from one jet at the metal side of the disc. The specimens were then immediately washed in methanol. Particular features were protected with lacomite, thinned by jet-electropolishing and the lacomite removed with acetone.

Thicker oxide films were microtomed (0.1 - 0.2μm thickness) and collected over water. Disadvantages of this technique [100,211] were the degree of difficulty in obtaining coherent, undamaged specimens. Hence, structural adhesive (Scotch-weld 9323 B/A) was used to aid

retention and identification of a coherent oxide-metal interface during microtoming. Areas of water corrosion were also observed. It is anticipated that galvanic reactions are set up in water between the metal and such particles as $FeAl_3$ and $(Fe,Mn)Al_6$.

Specimens were examined on a Jeol JEM 200B or 2000FX electron microscope to determine crystal size and variations in structure within the oxide film. At selected areas the phases present were identified by electron diffraction [207] and dark field imaging. Corroboratory evidence was obtained from X-ray diffraction of oxide scrapings and direct surface analysis. Energy dispersive X-ray analysis (EDX) including light element analysis revealed the elemental constituents. Using a combination of these analytical techniques and the ASTM index files [212] the material structure and composition was identified.

5.2.2b Scanning Electron Microscopy (SEM)

The large depth of field obtainable makes SEM an ideal technique for the investigation of topographical details of surface oxide films. Oxide layers, on copper grids and specimen surfaces, were attached to stubs with conductive cement for SEM examination and coated with a thin conducting layer of gold-palladium.

The Cambridge S600 and Stereoscan 250MK3 facilities for detecting secondary and back scattered electrons allow the examination of topographical surface detail and the detection of any irregularities such as cracks, blisters and growths. Gas-oxide and oxide-metal interfaces were examined.

5.3. WETTING STUDIES

In contrast to free solid surfaces, for which techniques such as low-energy electron diffraction and auger spectroscopy allow direct structural and chemical surface analysis to be made, the only data on the equilibrium properties of a solid-liquid interface to

date are obtained from interfacial tension measurements γ_{sl}. Solid-liquid interfacial tensions can be divided into two types; that between a solid and its own liquid (or melt) and that between a solid and a different liquid. Two kinds of methods are widely used to determine 'like' solid-liquid interfacial tensions. The Gibbs-Thompson equation [158] is the basis of γ_{sl} measurements in 'homogeneous nucleation' and 'depression of melting point' experiments. A second class of methods involves measurements of dihedral angles formed at the intersections of solid-liquid interfaces with other interfaces. γ_{sl} is calculated from known values of grain boundary tensions. A description of these methods and a compilation of experimental results is presented by Eustathopoulous [176].

The present work however is more concerned with methods for determining the interfacial tensions between unlike solid-liquid systems. Methods of surface tension measurement may be made on surfaces at rest (static) or on moving continually formed fresh surfaces (dynamic). Any difference between static and dynamic results will only occur if there is a time delay in reaching equilibrium.

The methods available are based on one theory. Young and Laplace [213] recognised that the pressure P at a point across a curved interface between two liquids is a consequence of two different radii (R_1 and R_2) of curvature in orthoganol planes at the same point on the surface.

$$\frac{1}{R_1} + \frac{1}{R_2} = \frac{P}{\gamma} \qquad 5.1$$

The derivation of equation 5.1 in terms of liquid surface tension governs the shape of all macroscopic menisci and forms the basis of all methods of measuring surface and interfacial tension. Useful summaries are provided by Padday [214] and Partington [215].

Methods expected to be the most suitable for surface tension determination of molten aluminium and Al_2O_3 systems are the sessile drop, pendant drop and plate-weight methods.

5.3.1. Sessile Drop Method

The surface tension may be derived mainly from direct measurement of a molten drop resting on a horizontal plane surface using the geometry of Dorsey [216]. More accurate but lengthy approaches describe the dimensions of a drop profile in terms of two parameters (β and b) [217] which can then be compared with known tabulated values. The tabulated values of β and b are solutions to equation 5.1 rewritten by Bashforth and Adams [218]. Improved calculation procedures were introduced as computation abilities increased [219,220,221]. More recently, accurate and reproducible drop shape images have been viewed using an image analysis system from which dimensional measurements can be easily made thereby aiding calculation of surface and interfacial tensions [222].

Errors in surface tension measurements by this sessile drop method may be influenced by surface irregularities and the horizontal level of the substrate. At high temperatures however, with aluminium and aluminium alloys on any substrates, the contact angles are controlled to a great extent by volatilisation of components but particularly by the oxide film which envelopes the sessile drops and controls the extent of deformation.

5.3.2. Pendant Drop Method

Determinations of surface and interfacial tensions have been made from observations on pendant drops. An image of the drop hanging from the end of a tube can be projected or photographed so that measurements can be taken. Pendant drop mensici are described by the equations of Bashforth and Adams [218]. Thus from two accurately known parameters of the drop profile it is possible in theory to derive the true surface tension [223]. Difficulties associated with this method arise in forming and maintaining drops over the long periods required for equilibration.

Both methods described use contact angle measurements and thus are highly dependent on the choice of axes and accuracy of reading dimensions since small variations result in large errors. Thus to achieve reproducible results care must be taken with corrections made and the accuracy of the liquid density value used in mathematical calculations. For example, measurements are considered significant only when temperatures are controlled to within ± 0.1°C. However with care, in experimental procedure and calculations, the surface tension of the materials in the experimental system can be measured to within ± 0.05Nm^{-1} [214].

Both the sessile and pendant drop methods are static and therefore suitable for studying ageing effects and for following slow changes in the surface. Indeed, the factor thought responsible for most errors is surface adsorption or contamination. This has been discussed previously in section 4.2.1. and is illustrated by the large number of reproducible but unrepresentative values for the surface tension of oxide-free molten aluminium in Table 9.6.

Aware of the difficulty in restricting the formation of even a thin film of oxide on aluminium melts using available vacuum systems and also the problems in restricting magnesium vaporization in vacuum, it was decided for the purpose of this work to reflect systems encountered in industry, that a third technique would be more practical.

5.3.3. Plate-Weight Method

Gustalla [224] describes a method of determining surface tension using a thin slide (perimeter 1cm) of solid material initially immersed in the melt. The slide is raised slowly through the surface until the external pull f, becomes constant. After a buoyancy correction, this force is:

$$f = \gamma_{lv} \text{Cos}\ \theta \qquad 5.2$$

The work done in withdrawing the slide a little further is now the work of dewetting the slide and is given by the product of γ_{lv} Cos θ and the change in the height of the slide, Δh. The force f, is determined for a slide of material under test and then for a platinium or mica slide roughened to make it completely wetted. This method is a modification of the Wilhelmy plate method [225] which uses a wetted slide only.

Practical application of this principle is demonstrated by the wetting balance test applied to solder systems upto temperatures of 450°C [226]. A similar method was used at higher temperatures (740°C - 800°C) in order to obtain surface tension data relevant to the fluxing of molten aluminium [227].

All three methods for determining surface tensions of molten aluminium may be conducted in the experimental apparatus used in this work, a description can be found in a later section; recommendations for further work. However, the plate-weight method was found most useful for this study and the experimental procedure is set out below.

5.3.4. Surface Tension Balance

A schematic diagram of the surface tension balance is illustrated in figure 5.3. An electronic top-pan balance with a weighing resolution of ±10μg records the resistance from an oxidising melt of pure aluminium or aluminium-magnesium alloy to the immersion and removal of a vertical alumina probe of 2mm diameter. The probe is suspended from the balance by a platinum wire. The melt, held at temperature within an environmental cell, is raised or lowered on a support rod at a constant rate, such that the depth of probe insertion correlates with test duration. The balance is

interfaced to a data storage and processing system (see Appendix B) which enables the variation in force provided by the oxide covered melt to be measured as a function of the penetration depth of the alumina probe. The technique enables the surface tension between the alumina probe and the surface oxide and/or melt to be determined.

CHAPTER 6 - RESULTS OF MOLTEN ALUMINIUM OXIDATION

6.0 INTRODUCTION TO THE RESULTS

The experimental work described in Chapter 5 was designed to investigate dross development on molten aluminium and aluminium-magnesium alloys. Rates of oxide growth were followed using thermogravimetry. Oxide structures and features at particular points during the oxidation process were examined and the oxides identified. The results from these studies are presented in four subsections.

The first section follows oxide growth and its development with time (0-150hrs), temperature (650-850°C), atmospheric water vapour content (0.05-3KPa) and oxygen content (0.06-21.2KPa).

A clean melt surface was achieved by skimming the molten metal surface in controlled oxidation conditions. This practice is reported in the literature and generates much information on the manner of oxide development. Under industrial conditions however, the dross formed on molten aluminium baths initiates on existing oxide films since a thin oxide film is always present on solid aluminium. The second section therefore reviews results from studies carried out on unskimmed melt surfaces. The presence of the existing oxide film prior to melting is found to greatly increase the quantity of oxide formed on the liquid metal. Thus further investigations were carried out to examine the influence of the condition of the oxide formed on solid material at temperatures between 450°C and the melting point. This part of the study also highlights the importance of specimen preparation on oxidation, which is described in the third section.

The final section considers the influence of added elements on aluminium oxidation. Additions may be in the environment, as are fluorides and chlorides, or trace additions in the metal such as grain refiner or beryllium. Such modifications are of particular relevance to industrial practice.

The results are presented firstly for commercial purity aluminium (Chapter 6) and then for a range of commercial aluminium-magnesium alloys containing 1%, 4.5% and 5% magnesium (chapter 7). Oxidation rates and oxide morphologies are evaluated separately. In Chapter 9.1 oxidation rates are correlated with oxide structure. The effect of magnesium additions to aluminium is reviewed in section 9.2 to evaluate the mechanism of dross development on molten aluminium alloys.

6.1. KINETICS OF MOLTEN ALUMINIUM OXIDATION

6.1.1. Thermogravimetric results

Weight gain data recorded from the microbalances directly or after smoothing, were plotted per unit of geometric specimen surface area prior to oxidation as a function of time. A standard spread sheet (LOTUS 1-2-3) and graphics package (GRAPHPAD) was used on an IBM PC for plotting data. To eliminate any offset the data was corrected for Archimedian buoyancy (given in figure 6.1 for the two furnaces F1 and F2 at 750°C) by carrying out blank runs with crucibles containing alumina substituted for the correct weight of metal.

Oxidation kinetics can be described in terms of a number of possible rate equations [126]. Such rate equations alone are insufficient for interpretating oxidation mechanisms, but may be used to classify oxidation behaviour and indicate a group of possible mechanisms. The integral form of the generalised oxidation rate equation for a specimen changing in weight Δ_m with time t is used:

$$\Delta_m^n = kt + c \qquad 6.1$$

Plots of log Δm against log t yield the exponent value n, which can be used to examine any trend in oxidation progress in terms of ideal behaviour. n = 1, 2, 2.72 or 3 corresponding to linear, parabolic, logarithmic and cubic rate equations respectively. For each particular type of specimen several microbalance runs were carried out to establish the overall reproducibility of the resulting oxidation kinetics.

Figure 6.2 shows a narrow range of weight gains exhibited by machined aluminium specimens oxidised at 750°C in dry air, humid and gettered argon. With a variety of surface finishes aluminium specimens oxidised in dry air at 750°C show considerable differences within and between oxidation rates and weight gains, as Figure 6.3 illustrates. This figure also demonstrates the good reproducibility between similar experiments and the importance of surface finish on oxidation behaviour which is discussed in Section 6.1.3. However, the following section examines general kinetic trends.

6.1.2. The rate of aluminium oxidation at 750°C on unskimmed melts

The rates of oxidation of pure aluminium in dry air at 750°C are shown in Figure 6.3. Following a rapid initial increase, the oxidation rate is gradually reduced to a low level. In humid air, this period of minimal oxidation is maintained out to long exposure times (greater than 70hrs). However, in dry air, a period of rapid breakaway oxidation is observed after 5-20hrs. This can be seen in Figure 6.4.

In general higher weight gains are achieved more rapidly in gettered argon (Figure 6.5) in comparison with either dry or humid air (Figure 6.3) and humid argon (Figure 6.6). This environmental influence is illustrated in Figure 6.7 for oxidation at 750°C on polished aluminium (1μm). Weight gains achieved after 20hrs oxidation are extremely varied but initially the oxidation rate is more rapid in gettered argon compared to dry air or humid argon.

High weight gains are illustrated (Figure 6.8) when electropolished aluminium is oxidised in gettered argon at 750°C. This figure reveals that the initial oxidation rate in a 'still' environment (thermobalance system F1) is significantly increased in comparison with the slower, but more constant rate achieved in flowing gettered argon (thermobalance system F2). Breakaway oxidation was also observed (Figure 6.2) initiating in gettered argon only after 12hrs oxidation at 750°C on machined aluminium specimens. The results of individual specimens oxidised from 1 to 100 hours are plotted in Figure 6.9, from this the onset of breakaway oxidation after only a few hours exposure can be clearly observed.

As the oxide layer develops the oxidation mechanism changes, thus the rate law best describing the oxidation behaviour will change with time. From the kinetic data of different types of aluminium surfaces oxidising at 750°C in dry air, humid and gettered argon, values of the rate exponent n, have been calculated. The rate exponent and hence rate law varies considerably depending on the surface finish and oxidising environment, but a trend is followed. The values have been used to build up a sequence of rate laws followed during oxide development on aluminium. A summary is given in Figure 6.10. The rate laws followed initially are logarithmic and cubic (n=2.3,3). As oxidation progresses linear type behaviour (n=1), parabolic and finally linear rate relationships are observed.

Thus specimens oxidised for the same period of time, but under different oxidising conditions, will exhibit behaviour corresponding to different parts of the sequence. The reaction rates observed at 750°C on molten aluminium specimens and duration in each regime are summarised in Table 6.1. Where advanced oxidation is exhibited at short oxidation times it is anticipated that the majority of oxide development occurs prior to melting, during the heating up period.

All the surfaces oxidised in argon show little variation from logarithmic and cubic rate laws, both being characteristic of low temperature oxidation and the formation of a thin oxide film. Detailed kinetic theories are discussed by Kofstad [126].

In air, machined and polished specimens follow similar rate laws, namely linear kinetics tending to parabolic. Linear kinetics are characteristic of oxide growth where the rate of reaction is not restricted by diffusion hence components have unlimited access to the surface and interfacial reactions are rate controlling. Kofstad proposes that linear kinetics apply to the formation of a compact inner layer of constant thickness and simultaneous development of a porous outer layer. Parabolic kinetics however are more applicable to compact scales where diffusion processes determine the rate of reaction.

Electropolished specimens oxidised in air tend to parabolic behaviour faster than coarser specimen surfaces. Rapid linear to parabolic transformation is also observed in stagnant air, where less moisture is available to delay rapid oxidation. The loss of water vapour results in faster oxidation.

In gettered argon, oxidation rates are extremely rapid. Initially linear kinetics are observed but reaction rates are predominately parabolic. Rates are accelerated further in a still environment or on an electropolished surface and linear kinetics predominate and are observed to the end of the oxidation test. Such behaviour may occur if there is unlimited access to the melt through cracks and pathways in the oxide.

6.1.3. The effect of surface finish on molten aluminium oxidation rates

Samples were produced with surface finishes ranging from machined, ground and polished to electropolished surfaces. Rates of oxidation of these polished and machined aluminium specimens, determined at 750°C in dry air, are illustrated in Figure 6.3. In general, the rates of oxidation in air at 750°C of coarsely finished aluminium surfaces follow a sigmodial function such that a short induction period may occur before the rate of oxide formed becomes quantifiable. With electropolished specimens rapid oxidation takes place almost immediately.

The greatest weight gain achieved on aluminium during oxidation in dry air at 750°C (Figure 6.3) is obtained on electropolished surfaces. Conversely the lowest increase in oxide weight occurred on machined specimens. Thus on comparing the weight gain in dry air at 750°C of these different aluminium surfaces it is found that the smoother the starting surface the greater the gain in weight.

These trends observed in air are reflected in gettered argon (Figure 6.5) and humid argon environments (Figure 6.6). Larger weight gains are achieved and attained faster on smoother surfaces of aluminium than on specimens originally having a coarse surface finish.

6.1.4. Oxidation rates of molten aluminium in the presence of fluorine

Figure 6.11 shows that the rate of oxidation of aluminium at 750°C in humid air in the presence of fluoride is initially greater than in dry or humid air alone. After the first five hours however, due to the wide scatter in each determination, two curves

may be plotted, one with increasing oxidation rate, closely following the rate of oxidation for dry air in the absence of fluorine. The second weight change - time curve demonstrates a loss in weight as oxidation progressed.

In summary, rapid breakaway oxidation is observed on pure aluminium unskimmed melts at 750°C. The onset of breakaway oxidation is achieved more quickly with decreasing water vapour content of the atmosphere and in still rather than flowing environments. When similar water vapour pressures are considered weight gains are increased slightly in oxygen containing atmospheres (air) in comparison with 'oxygen free' (argon).

At the same time and temperature greater weight gains are achieved on smooth starting surfaces compared to coarser finished aluminium. The smoother the starting surface the greater the weight gain. This trend is followed in all environments.

From the kinetic data, values of the rate exponent n, have been calculated for aluminium specimens with different surfaces oxidised in air and argon environments at 750°C. Initially logarithmic and cubic rate laws are followed which transform to linear, then parabolic and finally a linear rate relationship. Where paralinear kinetics are observed (at the end of the sequence) considerable oxidation has occurred during the heating up period. The highest oxidation rates are observed for electropolished aluminium oxidised in stagnant gettered argon at 750°C.

6.2. OXIDE MORPHOLOGY OF OXIDISED ALUMINIUM MELTS

6.2.1. Oxide development on skimmed aluminium melts

The oxide films grown on pure aluminium in dry air at temperatures above the melting point show crystals of γ - or η - alumina developing in an 'amorphous' γ -alumina film.

Some difficulty arises in distinguishing between γ and η - transition aluminas. Confusion also exists in the literature because these aluminas differ only slightly in their degree of hydration and in the amount of lattice disorder (Section 3.1.2). According to the ASTM X-ray powder diffraction file [212] one extra line distinguishes η -alumina from the γ -form in their respective X-ray or electron diffraction patterns. In this experimental work, although η -alumina was often identified, the general γ -form will be referred to in the text indicating a transition alumina of γ or η.

At 750°C and in dry air, oxide crystals of γ -alumina are seen to grow to cover the surface of skimmed aluminium melts. A series of micrographs taken at 5 minutes (Figure 6.12a), at one hour (Figure 6.12b) and at 5 hours (Figure 6.12c) illustrate the progress of oxide growth with time. Crystals of γ -alumina nucleate in an 'amorphous' film and are dispersed throughout the film in various stages of growth. The oxide crystals grow laterally until the surface is covered (Figure 6.12b). Further lateral growth is now restricted and the oxide film thickens. Traces of α -alumina are detected by electron and X-ray diffraction after 5 hours oxidation, the level increasing with further exposure time, particularly in dry environments. This coincides with the appearance of rod-like crystals in the oxide film but no correlation has been made between this phase and α-alumina.

After 150 hours oxidation in dry air, at 750°C a microtomed section normal to the oxide surface was produced to illustrate the melt-oxide interface. Due to the thickness and brittle nature of the oxide, not all the oxide film could be retained. However Figure 6.13 shows the considerable length that the oxide crystals have grown to and these were identified by electron diffraction as α -alumina.

The effect of temperature on oxide grown on skimmed aluminium melts after 1 hour is illustrated in Figures 6.14a and 6.12b which show oxide films after exposure to dry air at 650° and 750°C

respectively. At 650°C, Figure 6.14a shows fairly regular crystals of γ-Al_2O_3 dispersed in an 'amorphous' γ-alumina film. At 750°C after the same time period, these γ-alumina crystals cover the surface so that they almost touch. Similarities between the stage of oxide film development shown at 650°C after 1 hours oxidation with that of 5 minutes oxidation at 750°C (Figures 6.14a and 6.12b respectively) demonstrate that the rate of oxidation increases with temperature.

So far only oxide growth on skimmed molten aluminium in dry air has been considered. In humid air, such oxide films are predominantly composed of amorphous alumina or an extremely thin γ-alumina layer containing many small nuclei and crystals. Figures 6.14c and d demonstrate this early crystalline oxide development. Comparison of oxide films formed in dry and humid air for the same exposure time, say 1 hour (Figure 6.12b) show that much slower oxide development takes place in humid air (Figure 6.14b) slower even than in dry air at 750°C for 5 mins (Figure 6.12a) or at 650°C for 1 hour (Figure 6.14a).

SEM examination of the oxide-gas interface on skimmed aluminium after oxidation at 750°C in dry air reveals numerous single nodules, as Figure 6.15b shows. These nodules cluster in rings or crowns around larger outgrowths or protrusions from the surface. More examples of such growths are given in the following section.

6.2.2. Oxide development on unskimmed molten aluminium

At 750°C, oxide development on unskimmed aluminium in dry air follows a similar growth pattern to that found on skimmed aluminium melts. Gamma-alumina crystal nuclei dispersed in an amorphous film grow laterally until contact is made with neighbouring crystals. Oxide films then thicken. The presence of α-alumina, on unskimmed aluminium is detected in trace amounts after 5 minutes exposure. As the quantity of α-alumina increases with time, the number of

increases with time, the number of rod-shaped crystals present in the oxide film increases. Micrographs at 5 minutes and 5 hrs (Figures 6.12d and 6.12e respectively) illustrate this oxide development with time.

Microtomed sections taken normal to the metal surface support this proposal for oxide growth. A crystalline oxide monolayer is observed following oxidation at 750°C after 1 hour. The crystalline oxide dimensions are similar in magnitude to those obtained in the transverse direction. This is illustrated in Figure 6.12b and in the cross-section of Figure 6.16a. Increased magnifications such as Figure 6.16b show that the oxide film is layered. Larger crystals are seen to develop at the melt-oxide interface. After 5hrs exposure, further growth has transformed the oxide monolayer into a thick film, illustrated in Figure 6.16c. In this micrograph a crystalline projection is observed with dimensions the same magnitude as the nodules present on the oxide-gas surface of aluminium melts.

Direct comparison of the oxide films formed in dry air at 750°C for the same period by exposure suggests that oxide development on unskimmed melts is far in advance of that found on skimmed melts. Indications are that on unskimmed films the oxide crystal dimensions are larger with more lateral growth. The crystalline surface coverage is faster and dense, thick oxide films form. In addition, alpha-alumina is detected at an earlier stage in the development of unskimmed films. Also crystalline projections are observed after 5hrs in comparison with 15 hours on skimmed films. This behaviour implies that the majority of oxide development occurs prior to melting during the heating up stage, and that the presence of an existing oxide encourages faster crystal growth.

In addition to this accelerated growth rate, oxide films formed on unskimmed aluminium are composed of a large proportion of elongated or rod-shaped oxide crystals. In comparison, a large number of regular crystals nucleate on skimmed melts(Figures 6.12a and d). Figures 6.12c and e also show these features.

Unskimmed oxide films grown on aluminium melts in argon are similar in appearance to films formed on unskimmed melts in dry air. Figure 6.17a is a micrograph of an oxide developed after five hours in gettered argon. Compared to films formed in dry air under the same conditions, the former film appears more dense, the crystals are more compact and one may conclude that oxide growth is more advanced in gettered argon, than in dry air. Following 15 hours oxidation in gettered argon the elongated and cubic oxide crystals (a mixture of γ and α-Al_2O_3, determined by electron diffraction), characteristic of unskimmed oxide (illustrated in Figures 6.17b, diffraction pattern of b) are consistent with the oxide morphology at the oxide-metal interface shown in Figure 6.17c. With excess metal removed from the oxide-metal interfaces, the presence of large pits 2-4μm in diameter is revealed. The corresponding oxide-gas interface such as Figure 6.15c also shows pits associated with clusters of oxide nodules on the surface. The general surface is covered with these small nodules illustrated in Figure 6.15a. A comparison of the nodule clusters on these surfaces with those oxidised on skimmed aluminium over 15 hours in humid air at 750°C (Figure 6.15b) supports the opinion that a more advanced stage of oxide formation is reached on unskimmed melts in comparison with skimmed melts.

Aluminium films developed in dry air characteristically exhibit many nodule clusters and growths on the oxide surface. Such development is far in advance of equivalent specimens exposed in humid air. Figure 6.18b shows that a considerable oxide development has been achieved after oxidation for 5 hours at 750°C in dry air on unskimmed aluminium unlike in humid air (Figure 6.18a). Thus the presence of water vapour in the atmosphere can delay oxide development for substantial time periods. For example, the oxide growths after 15 hours in humid air (Figure 6.15c) are not as prolific as after 5 hrs in dry air (Figure 6.18b). The influence of water vapour on aluminium oxidation is observed in many situations.

For example, the concentration of oxide growths generated on microbalance specimen surfaces was, in general, lower than that obtained on larger aluminium melts oxidised in an autoclave or an open furnace. This is attributed to the effect of humidity. Microbalance specimens were supported on flat alumina plates, allowing access to a flowing atmosphere (and hence water vapour adsorption) on all specimen surfaces except the base. Large specimens as used in the autoclave and open furnaces, were contained in alumina crucibles in which the melt surface was usually below the top of the container. Thus access to the atmosphere, on all surfaces was severely restricted.

On these restricted surfaces, the melt base or sides (in a crucible), increased oxidation is observed compared with the top surface. This increased oxidation is considered, in this work, to be a consequence of the reduced access of water vapour to the developing oxide surface.

Cross sections taken at 90° to the oxide surface show that the growths are essentially a granular oxide with a minor amount of retained metal. The majority of the melt surface is covered by a thin oxide. Figure 6.18d and e are cross sections taken respectively from the centre and edge of aluminium oxidised for 5 hours in dry air. The oxide is retained by a layer of resin. The cross section of an oxide growth on aluminium after 24hr at 750°C, Figure 6.19b, shows that the thin oxide is still present between the melt and nodule except at one position where the oxide film has failed. It is thought that failure of this film permits aluminium exudation and initiates nodule growth. The oxide failure and aluminium exudation was observed in many of the sections taken through isolated oxide growths on aluminium after 24hr at 750°C.

Figure 6.20 is typical of a section examined in the transmission electron microscope, illustrating an area of remnant oxide at the base of an oxide cluster. This section illustrates a 2μm wide protrusion through the thin surface oxide. The dark field image and corresponding diffraction pattern indicates that the remaining oxide is γ-Al_2O_3.

The stages in the development of each oxide growth support the suggestion of molten aluminium exudation. Figure 6.19c is a micrograph of an isolated growth developed on the underside of the specimen adjacent to an alumina plate. The majority of the growth occurs at the centre of an oxide nodule crown. In general, surfaces adjacent to alumina plates showed increased growth rates over the initial oxidation period. However, once oxide growths have initiated, the plate restricts the height or extent of protrusion from the surface that the oxide clusters and crowns reach. Figure 6.19a shows an unrestricted heavy oxide growth on an upper surface of aluminium after 24 hours oxidation in dry air.

Greater oxidation can be found at specimen edges and sides, compared to the centre. This is illustrated by Figure 6.18f and also in Figures 6.18c and e where large oxide clusters not only predominate at the specimen edge but are larger than those in the centre of the specimen (Figures 6.18b and d). This is attributed to an effect of specimen geometry, or more particularly to areas in which the potential for surface oxide cracking is greatest. Cracks on the oxide surface arise predominantly during solidification. The path of such a crack through an oxide cluster, as in Figure 6.19d, supports the proposal that such growths form on molten metal and do not arise during solidification. Stress induced solidification cracks are illustrated in Figure 6.21 running across the surface generating flakes of surface oxide. Radial cracks surround columns of oxide clusters confined in smooth thin oxide sheaths. The structure of these growths further reinforce the theory that they are formed by liquid metal exudation through the surface oxide.

The SEM differentiates two crystalline oxide morphologies present beneath the thin surface oxide film. Both structures, elongated rod like oxide crystals, and large regular cubic crystals, shown in Figure 6.12, have been distinguished by transmission electron microscopy of unskimmed films.

Elongated crystals are illustrated in Figure 6.22a beneath an oxide film formed in dry air after 20 hours at 750°C. Clusters of such crystals may take on a more granular appearance if spheroidisation takes place as in Figure 6.22b or aggregation occurs (Figure 6.22c). Projections from such granular surfaces shown in Figure 6.22d, resemble single nodules characteristic of later oxide development on the oxide gas surface.

Large regular cubic-like crystals also form under the surface oxide. Figure 6.16b shows such development after oxidation for 1 hour in humid air where two large crystals have formed at the oxide-metal interface.

Large cubic crystals are also revealed inside oxide growths. An example is given in Figure 6.23. Micrographs a and b are of the top and reverse oxide-gas interface of a specimen oxidised for twenty hours in gettered argon at 750°C. The oxide on the reverse of the specimen was developed adjacent to an alumina plate. As with heavily oxidised specimens, often the plate becomes attached. Micrograph 6.23c shows such an alumina plate with a section of the reverse oxide surface still attached. The exposed metal and oxide appear in micrograph 6.23b. On the alumina plate, the outline of a thin oxide covering can be distinguished. This supports cubic crystals quite unlike the round morphology characteristic of the alumina plate. The oxide crystals are arranged as separate entities, approximately 5μm across one crystal structure, each unit containing smaller granules, These dimensions are equivalent to the size of the oxide growths in micrographs 6.23a and b. The exposed oxide surface Figure 6.23b, also illustrates vacant cubic pits with central granular regions (5μ diameter) which exist within the metal substrate.

6.2.3. The influence of surface finish on molten aluminium behaviour

A direct comparison was made of unskimmed aluminium surfaces, prepared by machining, grinding, mechanical polishing or electropolishing following oxidation at 750°C. Considerable variation in oxide morphology was exhibited, particularly in a gettered argon environment, in which the oxidation rate and consequent weight gain is greater than in dry air, humid air or argon.

Specimens were examined on completion of 20 hours oxidation in the microbalance. In general, as the surface roughness of the starting specimen decreases, the degree of oxide nodule development increases. Scanning electron micrographs taken of the uppermost surface of specimens oxidised in gettered argon reveal wide variations in the oxide morphology.

On machined surfaces oxide clusters and nodules characteristic of long term oxidised unskimmed aluminium melts form, as illustrated in Figure 6.24a. On smoother electropolished surfaces, clusters of spheroids emerge (Figure 6.24b). These spheroidal protrusions do not aggregate into clusters typical of the nodular type oxide growths illustrated in Figure 6.24a. In addition, the 'smoother' starting surfaces prepared by mechanical polishing to 1 m produced extremely convoluted and irregular surfaces after oxidation, for example Figure 6.24c.

6.2.4. Oxidation of aluminium in the presence of fluorides

Oxide films grown on molten aluminium in the presence of fluorides are highly crystalline. Rapid growth of many small crystals results in complete surface coverage after short exposure times. TEM sections showing the early stages of oxide film development in the presence of fluorine at 750°C are illustrated in

Figure 6.25. Figure 6.25a is an example of a rapidly formed crystalline γ-alumina film. Rod-like and cubic crystals, form after longer exposure times. These are shown in Figure 6.25c, a section taken normal to the oxide surface oxidation for 1 hour in humid air. Thus, although the oxide morphology and growth is similar to the oxide films formed in air alone, the rate of oxide development when fluorides are present is little affected by the presence of water vapour.

Air formed films on unskimmed aluminium characteristically show a small number of large crystals, for example Figure 6.12e. However oxide films formed in the presence of fluorides consist of numerous fine crystals which are densely packed such as in Figure 6.25a.

Oxide-gas interfaces clearly display these highly crystalline structures. Aluminium exposed to fluorides at 750°C, even for short periods of time, displays a white brittle coating when cooled. Scanning electron microscopy was used to examine the surfaces of such specimens after 5, 15 and 20hrs exposure to fluoride in air at 750°C.

After 5hrs,two or more crystalline layers can be distinguished on the metal, for example Figure 6.26a. The lower layer covers the metal substrate and appears to be composed of whisker-like dendritic crystals, vertically aligned. Figure 6.26b illustrates the morphology more clearly. Spherical mounds appear where crystal tips have combined. Areas adjacent to these sites appear as holes. This crystal layer may have developed initially from finer whisker-like crystals, platelets and rods, the vertical alignment developing as the crystals thicken. Cubic crystals are often embedded in this layer.

The upper layer of oxide shown in 6.26c resembles the lower crystal film in its early stages of growth. Vertically aligned whisker crystals with small diameter stalks give the fine

appearance shown in Figure 6.26c. Platelets are to be found embedded in this layer. The crystals grown at 5h and 15h are identified by X-ray diffraction as α-alumina.

Crystal aggregations may take a more dendritic form resembling a solidification structure. Figure 6.26d and 6.26e show such a morphology indicating that a surface liquid phase may have been present during oxidation.

With time, the tips of the whisker-like crystals aggregate providing a granular surface covering. Clusters of crystals (3μm diameter) protrude from the surface as shown in Figure 6.27a after 15hrs exposure. Over the same oxidation period and temperature other specimens showed an upperlayer similar in appearance to the oxide surface formed in air alone. In comparison with the oxide clusters formed in air (Figures 6.15c and 6.18b), the growths in fluoride containing atmospheres (Figures 6.27b and c) appear smoother and more spherical.

The addition of chlorides to the furnace environment also generates extremely crystalline surface morphologies on alumina at 750°C in air. Chloride additions promote large crystals (Figure 6.25f) which possess more directional character than exhibited by the dendritic alumina structures generated in fluoride atmospheres. A direct comparison of the oxides formed in humid air at 750°C in the presence of fluoride and chloride after 5 hours oxidation is given in Figures 6.25e and f respectively.

6.2.5. Summary of results of molten aluminium oxidation

Results have been presented which show that oxide crystals of γ-Al_2O_3 nucleate and grow in an 'amorphous' oxide film on a molten aluminium surface. The oxide crystals grow laterally until neighbouring crystals touch and the surface is covered. The oxide layer thickens and at longer exposure times α-alumina becomes

incorporated in the γ -Al_2O_3 layer. Growths from the oxide surface appear either as clusters of individual oxide nodules or spheroidal protrusions. These growths which consist of oxide and trapped metal are associated with long exposure times and increase in number and size with time. Large crystals are also associated with these features. The initiation of oxide growths is believed to be the start of dross formation.

Such development seems little affected by the presence or absence of oxygen but increases with time, temperature, decreasing humidity and on aluminium melts subject to a preheating period i.e. unskimmed melts. A large proportion of oxide development occurs prior to melting due to the existing oxide film. The condition of this initial oxide is critical to the onset of rapid oxide growth. In general, the smoother the starting surface the rougher and more convoluted is the oxide formed. Cracks in the oxide and surface irregularities seem to increase the onset of these oxide protrusions.

In the presence of fluorides highly crystalline films develop rapidly, protecting the melt from any significant oxidation. As the concentration of fluoride depletes detrimental oxide growths can develop. Oxide development in fluoride containing atmospheres is less affected by humidity than in air alone.

CHAPTER 7 - OXIDATION OF MOLTEN ALUMINIUM-MAGNESIUM ALLOYS

Oxidation rates and oxide morphologies have been separately examined for aluminium alloys containing 1% magnesium (Alcan 5005 alloy) and for higher magnesium additions of 4.5 and 5% magnesium (Alcan 5182 alloy). Materials were both non-grain refined and grain refined with titanium diboride additions.

It was demonstrated in the preceding chapter, that oxide films formed on unskimmed aluminium melts are more highly developed than films formed on skimmed melts over the same time period. Unlike studies of pure metals, skimming an aluminium-magnesium melt depletes the alloy of any component enriched at the surface. Examples are given to demonstrate the effect of magnesium depletion on the oxidation process. To reflect industrial practice oxidation studies were mainly conducted on unskimmed melts. The results are presented in the first part of this section.

Part two reviews solid state oxidation behaviour. In particular the importance of the first formed oxide. The effect of surface finish and grain refiner on oxide development will be considered. Other influences on the rate of Al-Mg oxidation such as the effect of humidity, fluorides and additions of beryllium are also presented.

7.1. OXIDATION OF AL-1%MG (5005) ALLOY

7.1.1. Oxidation of molten Al-1%Mg alloy

During the early stages of oxidation, the oxide generated on unskimmed molten aluminium - 1% magnesium alloy was identified as primarily magnesia with traces of γ-alumina. Electron diffraction (Figure 7.1e) demonstrates continuous rings with superimposed spots. These oxide films consist of coarse and fine crystals dispersed in a dense 'amorphous' layer. Figure 7.1c illustrates an oxide film formed in humid air on a grain refined 5005 alloy melt after 15 minutes oxidation (10 minutes heating up and 5 mins at 750°C). Even at this early stage the oxide film is fairly dense and uneven. The surface shown in Figure 7.1a illustrates how the oxide has become rough and irregular.

Oxide films developed on skimmed alloy melts for 5 and 15 minutes show considerable crystal depletion (Figure 7.1d). Electron diffraction of these films show continuous rings identified as magnesia and γ-alumina (Figure 7.1f). The surface of this slowly developing oxide (Figure 7.1b) is smoother than the heavily crystalline films of unskimmed melts and with time exhibit a dispersion of nodules ranging in size upto about 4μm. Figure 7.2b shows the initial nodule development on a skimmed melt after 1 hour exposure to gettered argon at 750°C. Further development occurs with time. Thus the original surface becomes a mass of nodules on an irregular oxide surface.

The series of TEM sections in Figures 7.3a and 7.3b show the fine crystallites which make up the oxide layer on unskimmed melts, increasing in number and size with time. Embedded in the magnesia matrix are dense oxide crystals of much larger dimensions identified as spinel (Figure 7.3d). The large spinel crystals are present at the early stages of melting, as shown in Figure 7.3a following 15 minutes exposure, and can sometimes appear to be heavily distributed in the oxide film (Figure 7.3e).

Further oxidation of the first formed overlayer of magnesia and γ-Al_2O_3 results in advanced growth of the coarse magnesia crystals from 200nm to 500nm as shown in Figure 7.3f after 5h oxidation. No further increase in the dimensions of the fine crystallites takes place. The transmission electron diffraction pattern of the matrix, Figure 7.3c, identifies only magnesia and γ-alumina is not detected. The large spots correspond to coarse magnesia grains and the continuous rings correspond to the fine crystallite dispersion in the film.

Scanning electron microscopy reveals the characteristic appearance of the large spinel crystals formed on non grain refined (NGR) unskimmed Al-1%Mg melts. Micrographs are shown of crystals embedded in molten metal (Figure 7.4c) and in the oxide layer (Figure 7.4b). The same oxide film also supports nodules on its oxide-gas interface as illustrated, in Figure 7.4a, an oxide film taken from a 5005 NGR melt at 750°C. Further examination shows that each nodule is closely associated with a single crystal. Thus, even after short oxidation times the growth of a rhombohedral crystal distorts the surrounding amorphous oxide into a nodular form. Indeed, through a broken nodular surface, crystals are seen embedded in metal (Figure 7.5). EDX-analysis of a nodule (Figure 7.6a) and the surrounding surface (Figure 7.6b) is a further illustration of the arrangement of magnesium rich crystals seated directly below the top surface film.

In humid air, at exposure times greater than one hour (Figure 7.2c) the roughness of an oxide surface is increased greatly by large growths distributed over the surface. These large growths (10-25 μm) support nodules on the surface. One such growth, formed on a skimmed 5005 grain refined (GR) melt surface after 5h, and a collection of growths with surface nodules developed on an unskimmed 5005 GR melt in humid air for 15h, at 750°C is illustrated in Figures 7.7a and 7.7b respectively. A series of cross sections, taken normal to the oxide surface at increasing times of oxidation in humid air at 750°C illustrate the development of these large growths. A sequence is given in Figure 7.8a-7.8c.

Examples of two specimen surfaces showing heavy oxidation in an isolated area, and a reverse surface showing smaller growths covering the whole specimen are illustrated in Figures 7.8f and 7.8e on 5005 GR alloy melts after oxidation in humid air at 750°C for 20 and 5 hours respectively.

The results presented so far have demonstrated rapid oxide development of Al-1%Mg alloys, particularly on unskimmed melts, in comparison to pure aluminium. The oxidation rates of 5005 GR and NGR melts at 750°C were quantified by continuous determination of weight-change with time. Oxidation rates and weight gains determined on machined 5005 NGR specimens in air and argon atmospheres at 750°C are illustrated in Figure 7.9. In general, a sigmoidal oxidation curve is followed. An induction period is observed prior to rapid oxidation. With time, the oxidation rate sharply declines and a plateau stage representing slower, almost negligible weight gain is followed to the end of the oxidation period.

Al-1%Mg alloy in humid air and humid argon shows similar oxidation weight change-time curves. It is concluded therefore that the effect of oxygen partial pressure on Al-1%Mg alloy oxidation, as with pure aluminium, is negligible or is masked by the considerable influence of water vapour. The influence of humidity on Al-1%Mg alloy oxidation is also illustrated in Figure 7.9. An crystalline incubation period is observed only on Al-1%Mg specimens oxidised in humid atmospheres. In dry environments rapid oxidation is instantaneous. The onset of rapid breakaway oxidation increases as the humidity decreases.

Figure 7.10 was compiled from an investigation of specimen position in relation to the path of a flowing gas and demonstrates the importance of replenishing the oxide with water vapour from the environment. When the specimen is close to the flow of gas a long induction period occurs before the onset of rapid oxidation. The supply of water vapour in the immediate atmosphere is replenished

by residual water vapour in the flowing gas. When the specimen is positioned away from the gas flow and is therefore in a stagnant environment, the oxide is more difficult to replenish with water vapour and once consumed the oxidation behaviour conforms to that expected in a dry environment.

7.1.2. The influence of specimen surface condition and grain size prior to oxidation of Al-1%Mg alloy

In the first part of this section 7.1.1 the effect of skimmed and unskimmed melt surfaces on oxidation was illustrated. It is concluded from the magnesium-rich oxides that develop that the delay in crystalline oxide development on skimmed melts is a consequence of magnesium depletion from the melt. However, as with pure aluminium ,increased oxidation may be due to solid state oxide development as the specimen heats up. The presence and condition of the initial surface oxide may affect the oxidation behaviour of molten metal.

Data obtained during oxidation of machined and mechanically polished specimens of 5005 GR and NGR alloy at 750°C in gettered argon are illustrated in Figure 7.11. As expected rapid oxidation rates are observed and on both alloys virtually all oxidation takes place over the first 5hrs. After this time further weight gains are negligible. The final weight gains per unit surface area on polished surfaces are reduced in comparison to those achieved with machined specimens. This difference is thought to be a similar effect of surface finish to that observed on pure aluminium. The initial rate of oxidation is higher on smooth surfaces than on rough surfaces.

Oxidation curves are usually plotted in weight gain per unit surface area, however where material has been removed by polishing, less magnesium is available for oxidation. Plotting the weight gain per unit weight of the starting specimen in Figure 7.12 showed

that the mass of oxide attained at the plateau stage after breakaway oxidation was similar for each specimen. This implies that the gain in weight of these Al-1%Mg alloys is almost entirely due to the oxidation of magnesium. This continues until the magnesium is depleted down to a low level.

Figure 7.12 shows that machined specimens of non-grain refined metal show increased oxidation rates compared with the grain refined equivalents. It is further noted that when the non-grain refined alloy is polished the subsequent oxidation rate is reduced. This is thought to be a demonstration of grain refining by polishing.

Thus the results show that the rate of oxidation of molten Al-1%Mg alloys at 750°C is influenced by the oxide first formed on solid metal. There may also be a contribution from impurities or trace additions in or on the alloy such as titanium diboride and polishing lubricants. The next section reviews another means of influencing the oxidation rate by addition of fluoride to the atmosphere.

7.1.3. The influence of fluoride on Al-1%Mg alloy oxidation

The presence of fluoride in the atmosphere changes the appearance of surface films considerably. Fine whisker-like crystals cover the top surface. Analysis shows the top layer to be magnesium rich and magnesium fluoride was identified by electron diffraction Figure 7.13 illustrates such a surface on 5005 NGR alloy after 5hrs at 750°C in humid air. Beneath the fluoride crystals an aggregate of small granular crystals cover the molten metal. Comparison of the oxide surface formed on Al-1%Mg melts at 750°C in gettered argon (Figure 7.8f) or dry air (Figure 7.8c) with that oxidised in fluoride after 5 hours (Figures 7.13) shows that fluoride inhibits the formation of large nodular metal containing growths.

In summary, the oxidation behaviour of molten Al-1%Mg alloys is dominated by magnesium oxidation. Initially, coarse and fine magnesia crystals nucleate in a film of γ-Al_2O_3. The rapid increase in oxidation rate on Al-1%Mg melts appears to be a consequence of the formation of rhombohedral spinel crystals at the oxide-melt interface at 750°C in atmospheres both deprived and rich in oxygen.

Large metal containing growths protrude from the oxide surface after long exposure times. The onset of rapid oxidation at 750°C is reduced in the presence of water vapour and by the presence of fluorine in the atmosphere. The rate of oxidation, once breakaway behaviour has initiated, seems to be a consequence of the condition of the first formed oxide and a reflection of the solid surface and grain size prior to heating. Increased oxidation rates are observed on grain refined or polished material. It may be possible therefore to control the rate and onset of oxidation by external means, for example, by control of the atmosphere or trace impurities present in or on the material.

Further support for these observations is obtained from results of oxidation behaviour of 5182 (Al-4.5%Mg) alloys. Strong similarities are exhibited between the oxidation behaviour of higher magnesium-containing alloys and Al-1%Mg. The results are presented in the following section.

7.2. OXIDATION OF 5182 ALLOYS

7.2.1. Oxidation of molten alloy

Oxide growth and development was examined on melts of three 5182 alloys : Al-4.5%Mg grain refined (GR), Al-4.5%Mg non grain refined (NGR) and Al-5%Mg GR alloys.

The first part of this section examines the progress of oxidation on Al-5%Mg melts. At short oxidation times small and coarse magnesia crystallites nucleate in an 'amorphous' film. After 5 minutes at 750°C (15 minutes total exposure time) a dense, finely crystalline layer develops (Figure 7.14c). Agglomerates of coarse MgO crystals often dense and thick are illustrated in Figure 7.14d. Electron diffraction patterns with superimposed spots on continuous lines (Figure 7.14e) show this oxide to be a mixture of MgO and γ-Al_2O_3.

Oxide films develop thick and thin areas as the oxide folds and distorts. Figure 7.14a illustrates an oxide surface developed in humid air on an unskimmed melt. A layer of very small crystallites is visible on the oxide surface. On a skimmed melt (Figure 7.14b) the oxide surface is much smoother and is mainly 'amorphous' γ-Al_2O_3 (Figure 7.14f) with only a few small crystals. Thus oxide development is considerably delayed on skimmed melts compared with unskimmed melts.

With increased exposure time both TEM and SEM observations show that a mixture of oxides develop. Large rhombohedral crystals 1-3μm and a smaller crystalline dispersion approximately 0.05 - 0.2μm are observed. The rhombohedral crystals resemble those identified as spinel on Al-1%Mg melts (Figure 7.4). However only magnesia is identified from X-ray diffraction of the 5182 surface after oxidation at 750°C. Figure 7.15d shows the appearance of such crystals embedded in molten metal after oxidation in dry air for 1h at 750°C. At the oxide-gas interface (Figure 7.15c) the surface film covering the oxide crystals appears to thicken as oxidation progresses. After 80 minutes in humid air at 750°C the surface has developed a nodular-type surface illustrated in Figure 7.15e. This thickening oxide surface layer is thought responsible for the magnesia identified by X-ray diffraction and observed at short exposure times. Sections through the oxide film demonstrate the fine magnesia crystallites (Figure 7.15a) making up the oxide outer layer. This micrograph also shows one of the coarser MgO

crystals (200nm) embedded in the metal, almost extending beyond the thickness of the surrounding oxide. Figure 7.15b is taken through one of the dense areas of coarse magnesia crystals which are embedded in the metal and develop into crystalline aggregates. Only a trace of magnesium is detected in the adjacent metal substrate, highlighting the selective oxidation of magnesium. Maps of elemental distributions are reproduced in Figure 7.16 from a section of oxidised Al-5%Mg (5182). The metal section shows magnesium enrichment in the outer oxide layer.

With long exposure times in dry environments at 750°C oxide development is considerable. Large growths containing molten metal increase in number and size as oxidation progresses. The appearance of such an oxide surface exposed for 20 hours at 750°C in air is illustrated in Figure 7.17c. The level of the original oxide surface can be seen at the left of the micrograph, with the structure to the right (in focus) showing the side of a massive growth carrying secondary and tertiary oxide growths. The oxide covering these structures is a mass of small crystals (Figure 7.17d) principally magnesia. X-ray diffraction of the powdered oxide film after oxidation (20h) identifies a mixture of magnesium aluminate, aluminium metal and α-alumina. This analysis is characteristic of heavily oxidised surfaces. Sections through these oxidised specimens support the mechanism proposed for developing oxide films.

The first oxide to develop at the oxide-melt interface is clearly defined (Figure 7.17a). A series of growths, predominantly molten metal, protrude above this original oxide layer. Figures 7.17a and 7.17b are cross sections through individual oxide growths. Figure 7.17b shows that oxide growth from the oxide-gas interface has developed towards centre of the structure. The light flecks indicative of molten metal are absent from the area of intense oxidation at the interface between the oxide and a supporting nickel layer. Eventually the remaining trapped metal will become oxide.

A heavily oxidised section of 5182 alloy after oxidation (12h) at 750°C in dry air is shown in Figure 7.17f. This micrograph also shows metal exuding through a large crack in the oxide layer.

Heavy oxidation is not always obtained on 5182 melts however. The simplest way to investigate the influence on oxidation of parameters such as time, oxygen content, humidity and temperature is from microbalance determinations. The rate of oxidation of a machined Al-5%Mg specimen at 750°C in dry air (70Pa saturated water vapour pressure) is illustrated in Figure 7.18. The weight change-time curve follows a sigmoidal function with a point of inflection. Calculations show that the end of the inflection corresponds to the weight gain generated by complete consumption of magnesium in the specimen as magnesia. The final plateau corresponds to consumption of magnesium as magnesium aluminate. This supports the analysis of the oxide structures presented in the early part of this section with magnesia the first formed oxide, transformed to a thick magnesium aluminate layer after long exposure periods during which all magnesium has been consumed.

The oxidation curve shows that an induction period exists before rates of magnesia and magnesium aluminate formation become rapid. The effect of the environment on the rate of oxidation of 5182 alloy at 750°C will now be examined.

A comparison of oxidation rates on machined Al-5%Mg in dry air and dry oxygen shows little effect from the presence or absence of oxygen (Figure 7.19) the overall rates of oxidation are very similar.

The effect of humidity is more spectacular however. In Figure 7.19 three curves are plotted for molten 5182 for oxidation in air; one in still dry air, one in flowing dry air and one in flowing humid air. In flowing humid air, the presence of water vapour is sufficient to prevent rapid oxidation of Al-5%Mg specimens for upto 20 hours at 750°C. It can be seen that with a constant supply of

water vapour to the specimen surface the onset of rapid oxidation is delayed. The differences between this and the onset of rapid oxidation in dry air is attributed to the low quantity of water vapour available at the melt surface over the entire exposure time.

Figure 7.20 further illustrates the effect of flowing and static environments on oxidation. Similar oxidation profiles are produced for specimens polished to 600μm and oxidised at 750°C for 20h in gettered argon. The four curves plotted however, fall into two groups making a band of error (or variation) differentiated by the water vapour content in the immediate vicinity of the melt surface. Thus the onset of breakaway oxidation is delayed in environments containing available water vapour such as in flowing rather than in quiescent atmospheres.

The same effect of humidity as observed on machined specimens (Figure 7.19) is found with polished 5182 alloy surfaces. Figure 7.21 shows that while the onset of rapid oxidation is delayed by humid air, dry air provides a very short protection period. With polished specimens, rapid oxidation occurred almost instantaneously in both wet and dry argon environments. A study carried out to establish the effect of surface finish on the oxidation behaviour of alloy melts containing 1% and 4.5%Mg showed that the starting specimen surface has a considerable influence on the subsequent oxidation rates of molten metal. In general, smooth polished surfaces exhibit a delay before rapid breakaway oxidation behaviour is observed unlike the trend exhibited by the machined specimens of the Al-5%Mg alloy in Figure 7.22. Once breakaway oxidation has initiated the rates of oxidation for each type of specimen are similar.

The influence of surface finish on the rate of oxidation in humid air at 750°C is shown in Figure 7.23. Rough (machined) or smooth (polished to 1μm) specimens are plotted as weight gain per unit weight of specimen against time. This figure shows that over the oxidation period the polished specimens gain more weight in

comparison to the rougher machined specimens. The inference from this is that the progress of oxidation and consequent increase in oxide growth and surface area before breakaway oxidation is greater than on initially rough surfaces. This is the same effect demonstrated by aluminium specimens presented in Section 6.1.3. and discussed in Section 9.1.3.

It is interesting to note that at the start of oxidation in flowing and static humid environments the trend observed is the reverse of that previously recorded for dry environments. Thus in the presence of a greater supply of water vapour, the rate of oxidation in humid atmospheres at 750°C is greater than in static environments. This implies the developing oxide or melt surface has an affinity for water vapour.

The results presented for molten Al-5%Mg alloy have demonstrated that the oxidation behaviour is controlled by oxide envelopes which form prior to melting, in the solid state during heating up. The importance of the oxide condition prior to oxidation (a function of surface finish) has also been illustrated. It is important therefore to look at the oxidation behaviour of Al-5%Mg in the solid state and at temperatures between the solidus and liquidus in order to be able to influence or control the condition of the surface oxide prior to oxidation.

7.2.2. Oxidation of solid 5182 alloy

A temperature of 550°C was chosen for this study of the oxidation behaviour of solid 5182 alloy, as this corresponds to temperatures used in industrial practice, particularly in the secondary aluminium industry for burning off paints, oil and grease from scrap material.

A characteristic feature of these specimens (as with melts) was the dense black oxide surface produced. In the scanning electron microscope the oxide surface was covered with small crystallites, characterised by electron diffraction as magnesia. Figure 7.24a shows such a surface after 5hrs oxidation. Cross sections taken normal to the oxide surface show a thick magnesia dispersion with an uneven oxide-metal interface. A sequence of micrographs (Figures 7.24b-e) shows how this interface may develop on grain refined Al-4.5%Mg alloy in gettered argon after 20h exposure at 550°C.

The solid metal is covered by dark circular magnesium rich regions, the surrounding oxide carries small nodules. Clusters of oxide nodules and columns protrude from these magnesium rich areas (Figure 7.24c, 7.24d) resembling oxide growths formed on liquid metal. The number of growths on the surface increases with time and the structures are gradually covered by small magnesia crystals. Thus a top surface layer of magnesia develops. This is illustrated in Figures 7.24d and 7.24e.

Oxides grown on solid Al-4.5%Mg were influenced by the humidity of the oxidising atmosphere in a similar manner to oxides grown on melts. Thus in dry environments the rate of oxide development is greatly increased. The influence of humidity is illustrated in several ways. Specimens were supported on alumina plates during the oxidation process. At 550°C in flowing gettered argon, the rate of oxide growth was increased on the reverse of the specimen adjacent to the alumina plate, and oxidation preferentially occurred towards the centre of the specimen. The alumina plate acts as a barrier to water vapour and a moisture gradient exists across the specimen resulting in the observed zonal pattern of oxidation. Further, a reduced number of growths is observed on the upper surface which is in direct contact with the atmosphere.

Micrographs of an Al-4.5%Mg specimen at 550°C in gettered argon illustrate the oxidation stages described above. Figure 7.25a is a section of the reverse surface. Growths initiate from the surface and are then covered with fine magnesia crystals. The central surface area (Figure 7.25c) and cross section (Figure 7.25e) shows a far greater number of growths associated with advanced oxidation than at towards the specimen edge (Figure 7.25b, 7.25d).

In addition, Figure 7.25a shows increased oxidation at the extreme specimen edge where a sharp change in geometry occurs. This is thought to be due to the higher stresses generated in the oxide in this region, resulting in a greater incidence of oxide fracture and consequent formation of oxide growths. The question arises therefore, if the oxide is known to be damaged, do oxide growths develop over these ruptured areas? To clarify this behaviour a layer of 7070 borosilicate glass, less than 0.5μm thick, was sputtered onto a clean Al-4.5%Mg surface. This glass coating is known to possess occasional pinholes [231]. The specimens were oxidised for 20h in gettered argon, a dry atmosphere which encourages the appearance of oxide growths at 550°C. This low temperature was chosen in order to allow liquid metal oxidation to occur without seriously deforming the nature of the glass coating. Following oxidation a small number of oxide growths (Figure 7.26) were observed corresponding to the number of pinholes anticipated. The number of oxide growths is considerably reduced in comparison with specimens carrying oxide films only. It is concluded that the protection provided by the surface layer forming on Al-4.5%Mg alloy at 550°C and above, is easily damaged. Once damage occurs, oxide growths form.

The ease of influencing the oxidation protection afforded by the surface oxide will be investigated further in the next section, following a summary of the effect of temperature on 5182 alloys.

7.2.3. The effect of temperature on 5182 alloy oxidation

A summary of the effect of temperature on the oxidation rate of 5182 alloys is presented at this point.

As expected, the oxidation rate of Al-5%Mg (5182) in gettered argon increases with temperature from 450 to 850°C as shown in Figure 7.28. On the solid metal, oxidation rates are low but increase rapidly as the fraction of liquid metal increases.

Illustrations are given of the oxide appearance following oxidation. The thickness of the 'amorphous' or finely crystalline surface layer is increased by exposure at 450°C as shown in Figure 7.27a. At 550°C, the surface layer consists of numerous growths covered with magnesia crystals (Figure 7.24). At slightly higher temperatures very square crystals, identified as magnesia are observed (Figure 7.27b). Sections normal to this oxide surface show the formation of large growths Figure 7.27d and Figure 7.27e illustrates secondary and tertiary growths.

Despite the dissimilar morphologies, the oxides generated upto liquidus temperatures are all associated with magnesia. At higher temperatures and with long exposure times however the resulting oxide layers are often identified as magnesium aluminate. The appearance of the oxide surface at 750 and 850°C is similar (Figures 7.8f and 7.27f respectively). High surface areas are exhibited and the oxide is generated with high oxidation rates. Thus the large difference in weight gains generated at temperatures of 650°C and 750°C seems to be related to the rate of magnesium consumption. At 750 and 850° rapid oxidation continues to the point of total magnesium depletion.

7.2.4 The effect of surface finish grain size and oxide preconditioning on 5182 oxidation

From the results presented so far, it is concluded that increased high temperature oxidation is a consequence of metal containing growths developing on the surface of Al-Mg alloys in dry environments at both 550°C and 750°C. Hence, rapid breakaway oxidation is associated either with a loss of surface protection due to magnesia formation or to breakdown of a magnesia layer. The presence of water vapour is found to delay the onset of breakaway oxidation. To investigate this further, experiments were carried out which consisted of preconditioning the surface oxide in a humid atmosphere to enhance the surface protection period under vigorous oxidising conditions and thus restrict molten metal growth or formation of aluminate.

To precondition, polished 5182 alloy specimens were preheated in humid air for various times upto 15h at temperatures from 550 to 850°C prior to oxidation in gettered argon at 750°C. The results show that exposure for 15h in humid air at 550°C prevents breakaway oxidation for upto 15 hours in gettered argon at 750°C. The rate of rapid oxidation was reduced only slightly with 5h preheating in humid air. These results are illustrated in Figure 7.29 where zero time corresponds to the start of exposure in gettered argon at 750°C after preheating.

When specimens were preconditioned at higher temperatures (750°C), rapid oxidation in gettered argon is delayed for upto 20h by short exposure times in humid air (5h). If a similarly preconditioned oxide is cooled before reheating in gettered argon, all protection is lost. On reheating this damaged oxide surface provides no protection to molten metal exudation. These results are plotted in Figure 7.30.

A summary of these studies on preconditioned oxides in given in Figure 7.31. Specimens exposed to humid air for 5 hours at temperatures from 550-850°C show that the best protection is given by preheating the oxide in humid air at 750°C or over. Slow heating in gettered argon reaching 750°C over 5 hours reduced the subsequent oxidation but was not sufficient to prevent breakaway behaviour altogether.

The appearance of surfaces following such treatments support the view that rapid oxidation is a consequence of surface oxide damage. The surface oxide is unable to prevent cracking and melt exposure. Figure 7.32 shows micrographs of two Al-5%Mg polished samples preconditioned for 15 hours at 550°C. After 2h exposure to gettered argon at 750°C oxide growths are present beneath visible cracks in the surface (Figure 7.32a). Large oxide growths are seen to emerge from within the bulk of the specimen as illustrated in Figure 7.32b after 5h exposure to gettered argon. Higher magnifications are shown of the general surface and of rhombohedral crystals on a large growth. (Figure 7.32c and 7.32d respectively). X-ray diffraction of both specimens indicate the presence of a mixture of MgO, $MgAl_2O_4$ and metallic aluminium.

As a control experiment, specimens were oxidised for 5 hours at 550°C in gettered argon to encourage non protective oxide development. Indeed the Al-Mg surface rapidly becomes non protective and oxidised at this temperature by formation of primary magnesia. The temperature was raised to 750°C and exposed for a further 15h. As the micrographs (Figure 7.33) show, a thick oxide layer develops, predominantly of magnesium aluminate. The oxide surface developed in gettered argon does not provide an effective barrier to further oxidation. Stacks of crystals are observed developing in a manner which suggests an association with easier paths of diffusion around oxide areas of reduced thickness.

It has been shown that the rate of oxidation on molten Al-Mg alloys can be controlled by surface pretreatment during solid state oxidation. The next section looks at the influence of element additions such as fluoride in the atmosphere and beryllium on the oxidation behaviour of molten 5182 alloy.

7.2.5. The influence of fluoride and beryllium on the oxidation of Al-5%Mg (5182) alloys

7.2.5.a The influence of fluoride on Al-5%Mg alloy oxidation

In humid air in the presence of fluorine, Al-5%Mg alloy surfaces oxidised for 5 hours at 550°C and 750°C display a dense layer of fine whisker-like crystals as illustrated in Figures 7.34a and 7.34c respectively. Nodular oxide growths are not observed over this time period.

X-ray diffraction of these surface oxides reveal a combination of MgO and of γ-alumina with traces of MgF_2 at 550°C. These crystals are much smaller and less dense than those obtained at 750°C. At this higher temperature over 5h MgO, γ-alumina and α-alumina are identified. With longer oxidation periods $MgAl_2O_4$ develops in addition to the other oxides. Figure 7.34b is a cross-section taken normal to the surface oxide at 750°C. This demonstrates that a layer of cubic crystals may exist beneath the continuous whisker-like layer, in a similar arrangement to the oxide formed with fluoride on Al-1%Mg melts.

In conclusion, highly dense crystalline films composed of MgO, γ- and α-alumina rapidly develop on Al-5%Mg alloys in the presence of fluoride. In the presence of chloride at 750°C for 5 h the surface is composed of a number of small cubic crystals.

7.2.5.b The influence of beryllium on Al-4.5%Mg alloy oxidation

Al-4.5%Mg GR materials with 10ppm and 50ppm of added beryllium were exposed for 20h in argon and air environments at 750°C. The surface oxides formed on beryllium-containing alloys were examined using electron microscopy at various stages of oxidation. On unskimmed melts with 50ppm beryllium BeO nuclei slowly develop in an 'amorphous' film over the first five minutes exposure and grow across the surface. BeO is identified from electron diffraction (Figures 7.35a and 7.35b).

As oxidation progresses, MgO develops. Figure 7.36b shows an 'amorphous' film containing MgO crystals which protrude to the surface. Figure 7.35c, a TEM of a transparent film covering a gas hole (Figure 7.38a) was identified as MgO with traces of BeO. SEM and TEM sections taken normal to the oxide surface illustrates this mixture of beryllia and magnesia crystalline oxides. Despite the low weight gains considerable oxide crystallinity was observed in sections taken vertically (Figure 7.36c) and also transverse (Figure 7.36a) to the oxide surface. Additionally, beneath the transparent oxide film at the base of gas holes considerable quantities of MgO crystals were observed embedded in the metal (Figure 7.36d).

The rate of oxidation remained extremely low with Al-Mg alloys containing 10ppm or 50ppm beryllium over 20h exposure at 750°C to wet and dry air and argon environments as Figure 7.37 illustrates. With the exception of one of three specimens containing low beryllium concentrations (10ppm), beryllium additions delayed breakaway oxidation. Where rapid oxidation did occur, the rate of conversion of MgO to $MgAl_2O_4$ was much slower in the beryllium containing alloy. Figures 7.39a and 7.39b show the appearance of an Al-4.5%Mg specimen with beryllium (10ppm). Signs of breakaway oxidation are observed after exposure to the more vigorous oxidising conditions of gettered argon. Spherical type growths emerge from a rough surface after 20h exposure. Thermal cycling of

an oxidised specimen by cooling to crack the surface oxide and reheating resulted in a slight weight gain over the oxidation period but no rapid oxidation behaviour.

Figure 7.38 shows that surfaces oxidised in humid air at 750°C characteristically form slightly folded and distorted oxide films with several dark areas supporting oxide nodules. Figure 7.36b is a cross section through the nodule. With time the crystals associated with the surface nodules will develop in size and grow through the surface film (Figure 7.38c, 7.39a and 7.39b). The protective oxide closely resembles oxides developed on Al-4.5Mg surfaces after oxidation at 550°C. These surfaces are shown in Figure 7.24.

In conclusion, Al-4.5%Mg alloys containing 50ppm beryllium prevent breakaway oxidation by the formation of BeO in dry and wet air and argon environments at 750°C. The beryllia restricts or delays growth of MgO and $MgAl_2O_4$.

7.3 SUMMARY OF THE RESULTS OF AL-MG ALLOY OXIDATION

The rate of oxidation of an Al-Mg alloy is increased by increasing temperature. At temperatures of 550°C oxidation with magnesium is much faster than with pure aluminium. Rapid oxide growth produces an initial layer of magnesia. The condition and morphology of this first formed oxide dictates the subsequent behaviour of the alloy under vigorous oxidising conditions.

Rapid oxidation is observed as the fraction of molten metal increases. Breakaway oxidation is characterised by the appearance of growths on the surface. Such growths are believed to arise by exudation of molten metal through the original oxide layer. Cracks and weak points in the magnesia layer provide the means for the rapid breakaway oxidation behaviour characteristic of all molten Al-Mg alloys. New oxide develops at the top of these metal

exudations and the process is repeated. Tall structures thus develop on the surface which continue to grow until the magnesium is totally depleted.

With the exception of Al.4.5%Mg alloys the final oxide weight reached with all Al-Mg alloys is equivalent for the same specimen mass per unit of magnesium. Rapid oxidation takes place with aluminium alloys of 5% and 1% magnesium until all the magnesium is converted to magnesium aluminate. The oxidation rates are illustrated in Figure 7.40 and 7.41. Alloys with 4.5%Mg show a preferred tendency to form magnesia (Figure 7.41). The reason for this is unclear, but is suggested to be a reflection of trace additions in the metal such as sodium.

The rates of oxidation are decreased on machined surfaces of grain refined materials. It is unclear whether this is an effect of the presence of TiB_2 or of grain size. The effect is harder to quantify if polished specimens are used. It is suggested that specimen polishing produces a grain refining effect in the extreme surface layer. This modification accounts for the observed reduction in oxidation rates with polished surfaces of non-grain refined materials (Figure 7.12). Thus the surface finish dictates the rate of oxidation by influencing the condition of surface oxide formed on the solid metal. The protective nature of the first formed oxide and hence the time to breakaway oxidation is influenced by water vapour, fluoride and beryllium additions.

The presence of water vapour provides the early oxide (magnesia) with a degree of protection delaying the onset of breakaway oxidation behaviour. This information was used to precondition the oxide. An Al-5%Mg specimen preheated in humid air for at least 15 hours at 550°C or 5 hours at 750°C prevents breakaway oxidation when gettered argon is introduced at 750°C. Cooling the preconditioned oxide prior to reheating removes this protection.

Fluorine in the atmosphere modifies the surface oxide by producing a dense crystalline film of small crystallites.

Beryllium (50ppm) additions to Al-4.5%Mg delays breakaway oxidation in dry and wet air and argon environments at 750°C by the formation of beryllia.

CHAPTER 8 - RESULTS FROM THE SURFACE TENSION BALANCE

The wetting characteristics of liquid aluminium/alumina and liquid Al-Mg/alumina systems were assessed by measuring the force provided by an oxide covered melt to the insertion and removal of an alumina probe. Results are obtained as a function of penetration depth of the alumina probe. The sequence is described for a pure aluminium melt in Figures 8.1a and 8.1b.

Figure 8.1a illustrates the change in force as a function of the relative position of the probe and melt surface, when the melt pool is raised at a constant rate towards the Al_2O_3 probe. Initially no change in force is recorded (a) until the probe contacts the melt surface. Once this point is reached a linearly increasing compressive force is recorded that increases with probe depth. Finally, fracture of the thin surface alumina scale occurs (b) and the melt surface recovers until the force recorded reflects the energy balance shown at position (c) between:

$$Al_2O_{3(\text{thin surface film})}/Al_2O_{3(\text{probe})}/Al_{(\text{melt})}$$

On removal of the probe, (Figure 8.1b), further recovery of the applied force occurs, until a positive meniscus is achieved which reflects the force due to wetting of the Al_2O_3 probe by the aluminium (d). A linear region (e) then follows which is due to the change in buoyancy as the probe is removed from the melt. This reaches a constant value (f) prior to separation.

When the molten bath contains magnesium, for example Al-5%Mg (5182) alloy, the results are strongly influenced by the exposure time of the molten bath prior to experimentation. Results are illustrated for an Al-5%Mg melt skimmed just prior to the immersion of an alumina probe in Figure 8.2a. The subsequent removal is shown in Figure 8.2b. These results are very similar to that of pure aluminium. Figure 8.3a and b were obtained with an unskimmed molten Al-5%Mg bath exposed for 5 hours. In this case, despite the large force applied to deform the oxide, fracture is not achieved.

A standard set of conditions were used for each experiment, these were that the alumina probe (2.25mm radius) was immersed at a rate of 0.64mm at 2 minute intervals in a molten bath held at 750°C in air.

PAGINATION ERRORS

CHAPTER 9 - DISCUSSION

In this chapter, the oxidation kinetics of both pure aluminium and aluminium-magnesium alloys are correlated with changes in oxide scale morphology as a function of time. From these reviews a general oxidation mechanism is proposed. Examination of the wetting characteristics of the corresponding melt-oxide systems supports the proposed mechanism and accounts for the observed changes in oxide morphology and the progressive development of dross on pure aluminium, aluminium-magnesium and recovered aluminium alloy melts.

9.1 THE OXIDATION OF MOLTEN ALUMINIUM

To study the oxidation mechanism of molten aluminium the first step is to review the main features highlighted by the experimental results presented in Chapter six, for both oxidation rates and oxide structures. By correlating oxidation kinetics with the morphology studies, the mechanism of dross formation is proposed. Hence the following points are emphasised:

i. The initial formation and early development of an oxide film on molten aluminium melts at 750°C proceeds as follows: Oxide crystals of γ-Al_2O_3 nucleate and grow in an 'amorphous' oxide film. The crystals expand radially until no further expansion is possible and a monolayer of oxide crystals covers the entire surface. α-alumina is detected as the oxide film thickens with time.

ii. On unskimmed aluminium melts the rate of oxide development is considerably enhanced by solid state oxidation and is dependent on the surface condition prior to melting.

iii. Rapid breakaway oxidation observed on skimmed or unskimmed aluminium melts at 750°C is associated with the appearance of nodular growths protruding from the oxide surface. These projections are a mixture of oxide and entrapped metal.

iv. The onset of breakaway oxidation and the formation of oxide nodules is little affected by the partial pressure of oxygen but is significantly increased as the atmospheric water vapour content decreases.

v. The addition of fluorides to the furnace environment has a marked effect on the oxide morphology, reducing breakaway oxidation.

It will be shown that the formation of nodular growths accounts for the development of dross and further, that these growths are due to liquid metal exudation through the initial surface oxide film.

9.1.1. Early development of oxide on molten aluminium

On skimmed aluminium melts the development of oxide proceeds by the nucleation of γ-alumina crystals in an 'amorphous' film. These oxide crystals grow radially until the molten metal is covered by a γ-alumina monolayer. As the oxide film thickens, alumina is detected. This manner of crystal growth is consistent with that reported in the literature, reviewed in Section 3.3.1 for solid state oxidation.

The kinetic results show that over the entire oxidation period a combination of rate laws are followed (Figure 6.10). It has also been shown that over 20 hour exposure periods, between 30-75% of the total weight gain is achieved over the first 60 minutes. Such rapid initial rates of molten aluminium oxidation in any one atmosphere make it difficult to isolate the 'amorphous' to crystalline transition.

Generally when growth of 'amorphous' alumina predominates (in humid air and argon environments) logarithmic and cubic kinetics are obtained. This is consistent with an ultra thin oxide film in which the oxidation rates are surface controlled [126]. As the film thickens and crystals develop diffusion controlled mechanisms will start to operate. On examination most oxide films taken from a melt, however rapidly, were found to contain crystalline nuclei. One concludes that the 'amorphous' to crystalline transition on melts is not sharp. Hence this early oxidation period is best described as a combination of the independent formation of both 'amorphous' and crystalline oxide as the duplex oxide film develops. Such behaviour has been mathematically expressed for solid aluminium oxidation [76] and is described in section 3.3.1.

On unskimmed aluminium melts fully developed crystalline γ or η-alumina films are rapidly attained. The nucleation of γ-alumina crystals on such melts is thought to take place prior to melting during the heat up period. Thus points of inflection in the weight change-time curves of molten aluminium observed predominantly between 120-220 minutes in Figure 6.3, correspond to the nucleation of α-alumina. Since the thermogravimetric determinations were carried out on unskimmed aluminium it is pertinent to consider the influence of the existing surface oxide film on further growth.

Mechanism + Fracture.

9.1.2. Development of oxide on unskimmed aluminium melts

Mechanism

It has been established (Section 6.2.3) that the development of an oxide film on molten aluminium more reaches a more advanced stage on a surface exposed to the heating up period prior to melting, than oxide developing on a skimmed aluminium melt. Oxide films formed on unskimmed melts are not only far advanced in crystalline development, but differ morphologically from oxide films developed in the molten state only. The difference is so marked that the oxidation behaviour of skimmed and unskimmed melts

is not comparable. For example, under the same conditions of dry air at 750°C oxide growths appear on an unskimmed aluminium melt more than ten hours before a single oxide growth protrudes from a skimmed surface.

In industrial practice, and indeed in most gravimetric studies, heating aluminium through the solid state is a necessary prerequisite. Care should be exercised therefore when comparing kinetic data from the literature with reported oxide structures, as it is standard practice to skim melts prior to investigations of oxide morphology.

In general, oxide films grown on unskimmed melts at 750°C in humid air are composed of a few large regular oxide grains and unevenly distributed elongated oxide crystals. According to crystal nucleation theory [158] the number and size of γ-alumina grains is qualitatively consistent with slow heating conditions in which a few well ordered crystals nucleate and develop. During rapid heating conditions numerous small nuclei form. Such oxide development is observed on skimmed aluminium melts where the oxide films are a mass of fine, regular γ-alumina crystals. The implication is that the majority of oxide growth takes place on solid aluminium, where slower oxide development results during the low temperatures encountered in the heating up period. Thus the initial oxide developed on solid aluminium differs from that grown on the melt, but more importantly, directly determines the oxidation behaviour of molten aluminium by preconditioning the oxide in the solid state.

Solid specimen surfaces may be contaminated or carry impurities and surface defects. These are all parameters which can influence rates of oxide nucleation growth and morphology in the solid state. It is postulated therefore that these parameters will influence the rates of oxidation on molten aluminium by virtue of the condition of the first formed oxide. This is found experimentally from the significant and reproducible effect that

the type of specimen surface finish has on subsequent molten aluminium oxidation. The effect of specimen preparation and surface finish on aluminium will now be reviewed.

Four types of surface finish were examined. Aluminium specimens were machined, ground, polished and electropolished. Specimens were either degreased with a perchloroethylene solution and treated in an ultrasonic bath for 15 seconds or washed in a strong soap solution with a clean polishing cloth prior to rinsing in isopropanol. Once dried the specimens were kept in a desicator to allow reproducible oxide surface films to develop.

The oxidation rates and weight gains achieved during oxidation in dry and wet air and argon environments at 750°C were enhanced on electropolished specimens compared to the 'rougher' surfaces. Thus reduced oxidation rates were obtained on polished, ground and machined surfaces as illustrated in Figures 6.3, 6.5 and 6.6.

Data concerning the effect of surface finish on molten metal oxidation was not available in the literature for comparison. Data from early studies on solid aluminium oxidation that neglect methodical surface preparations have been difficult to interpret. However, variations in oxidation rates and oxide weights between specimens have been discussed in the literature in terms of surface roughness or surface contamination. To support the proposed explanation of the results obtained in this study, further investigations were conducted and are discussed in terms of surface roughness and contamination.

For specimens of equal geometric dimensions, the surface roughness, and hence true surface area, decreases as the degree of polishing increases. Surface roughness measurements carried out on typical specimens used in this study, using a tallystep, are given in terms of vertical characteristics R_a and R_{tm} in Table 9.1. R_a is the arithmetic mean of the departures of the roughness profile from a mean line and R_{tm} is the mean of all the maximum peak to valley heights of the profile within the assessment length.

TABLE 9.1 - Roughness Measurements of aluminium surfaces used in this study

Type of surface finish	Electropolished	Polished			Machined
		1μm	6μm	600μm	
R_a(nm)	4	12-20	30-50	330-370	1000-1600
R_{tm}(μm)	-	.17	.21-.29	2.15	6.5-8.8
Ratio of increased roughness	1	5	10	100	350

Table 9.1 shows that the surface roughness decreases dramatically with polishing, more so than reported in the literature. Measured and estimated specific surface areas are reported to be increased by factors of 25 by rough abrasion [106], 8-10 from mechanical polishing [96], 3-4 by grinding to 600μm [102] and 2 with chemical polishing. Electropolished surfaces are said to be at unity.

MECH

The general feeling of other investigators concerning specimen surface roughness is that as the surface area available for oxidation increases greater weight gains result. Thus greatest and least oxidation levels will be exhibited by machined and electropolished surfaces respectively. Figure 3.8 supports this statement. This trend however is in complete contradiction to data collected in this study.

Estimates of the starting surface area (50-3500cm^2/g) do not quantitatively or even qualitatively account for the observed rates of oxidation of molten aluminium. From the onset of oxidation the surface area rapidly increases. Considerable variation is expected depending on the number and size of surface growths. Despite such rapidly changing surface areas, the rates of oxidation and weight gains attained when samples with the same surface finish are oxidised at 750°C are extremely reproducible.

Surface areas were determined from BET nitrogen isotherms at 77K for Al-Mg (1% and 5%) alloys oxidised at 750°C for 20 hours in gettered argon and humid air, with and without surface oxide growths respectively. The values given in Table 9.2 are of the same order of magnitude and do not reflect the very different surface areas estimated from examination by electron microscopy.

TABLE 9.2 - Calculation of surface area by BET nitrogen adsorption

Specimen	Oxidising Atmosphere	Appearance	Calculated surface area cm^2/g
Al-5%Mg 5182	Humid air	grey, smooth	260
Al-5%Mg 5182	Gettered argon	black, rough heavily oxidised	312
Al-1%Mg 5005	Gettered argon	black, rough heavily oxidised	227

Mech

It is implied that the only effect of roughening a surface is to increase the surface area. However, the evidence shows that the oxidation rates, quantity of oxide generated and estimated surface area during and after oxidation do not reflect the starting surface area. This simple interpretation of surface roughness ignores other contributions such as the introduction of cold work, considerable deformation and contamination of surface layers by the roughening process.

It is proposed that the oxidation rate is influenced by deformation introduced into aluminium surfaces. Considerable surface distortion arises from the subsequent mechanical polishing and grinding of machined specimens. During polishing the soft aluminium smears and distorts, thus the surface is composed of a pseudo-amorphous layer of distorted metal grains carrying traces of silicon carbide picked up from the polishing wheels. Closely spaced cutting marks on the surface may act as sharp detrimental angular features increasing the oxidation rate.

Electropolishing removes such distortion from the surface layers. However there is some opinion that the film on an electropolished surface is not strictly comparable to the normal air formed film in that the electropolished film contains residual chemical ions such as perchlorate ions [76]. Figure 9.2 gives the results of kinetic oxidation studies at 480°C on Al-4.2%Mg surfaces prepared in four ways using abrasive (600μm grit), chemical (phosbrite solution) and electropolishing techniques. Field [102], concludes that specimens electropolished in perchloric acid - ethanol solution gave the most reproducible starting surface. The worst scatter is found on surfaces electropolished in nitric acid-methanol solutions. The difference is attributed to the incorporation of chemical species from the polishing solutions on the specimen surface and thus incorporated in the air formed film of γ -Al_2O_3. It is possible that chemical doping can create

defects but as polished and ground specimens exhibit individual kinetic responses to oxidation, factors other than purely chemical are thought to influence oxidation rates. This thesis maintains that the manner in which the surface roughness is achieved is more important than the number of oxidation sites initially available.

It is proposed that the degree of oxidation achieved reflects the ability of the first formed oxide film to provide protection from further oxidation. Oxidation rates become rapid if this surface oxide is damaged or exhibits a tendency to crack. Hence on highly polished aluminium rapid oxidation is believed to be a consequence of stressed oxide films which damage and crack easily. The degree of polishing and surface distortion is reflected in the wide scatter in oxidation rates and weight gains obtained with polished specimens as Figure 6.7 illustrates. In contrast, machined specimens, less influenced by surface distortion and damage exhibit high reproducibility during oxidation. Indeed a low protective oxidation period is observed with machined specimens (Figure 6.2).

The 'smooth' electropolished surface is actually granular (Figure 9.1a) a consequence perhaps of preferred areas of polishing. Over -electropolished specimens display large pits. Electropolishing also reveals inherent surface features such as circular iron-intermetallic structures shown in Figure 9.1b. It is suggested that electropolishing exposes most surface irregularities and defects. If crystal nucleation is disrupted by irregularities such areas may be considered to be weak when levels of stress in the oxide increase. Rapid oxidation rates illustrate that the oxide generated on electropolished specimens is stressed and defective. However the features influencing this behaviour are extremely regular, dependent only on the quantity of surface available, results are therefore far more reproducible.

In the literature, other materials exhibit substantially higher oxidation rates for electropolished specimens than abraded and machined surfaces. An example is given in Figure 9.3 for the

oxidation of Fe-26%Cr-0.5%Si alloy in flowing dry oxygen at 1100°C [230]. When active oxidation sites are removed from the specimen by preferential etching or when the oxide is conditioned by chemical doping both abraded and electropolished etched specimens oxidise in a similar fashion. Dignam [66] too reports that mechanical surface preparations give anomolous results for aluminium oxidation. In support of the appearance of electropolished surfaces obvious nodules 0.28μm suggested to be extraneous matter are reported on electropolished aluminium surfaces following oxidation [27].

A possible explanation is offered for the contradictory trends reported in this study with the literature for solid aluminium oxidation. In the solid state, as in Figure 3.8, γ-alumina crystal development on aluminium at 525°C is slow and in humid air the oxide development over a 1h period may indeed reflect oxidation of the true surface area. However, some researchers [91,106] carried out a degassing procedure prior to data collection in which specimens were exposed at high temperatures of 600°C in vacuum (10Pa). Such vacuum levels will be insufficient to reduce surface oxidation and may in fact encourage rapid oxidation by virtue of the dry conditions. Thus it is likely that much information is lost over this initial oxidation period. The data recorded therefore corresponds to slower weight gains with time. An illustration is given in Figure 9.4 using trends seen on molten aluminium oxidation.

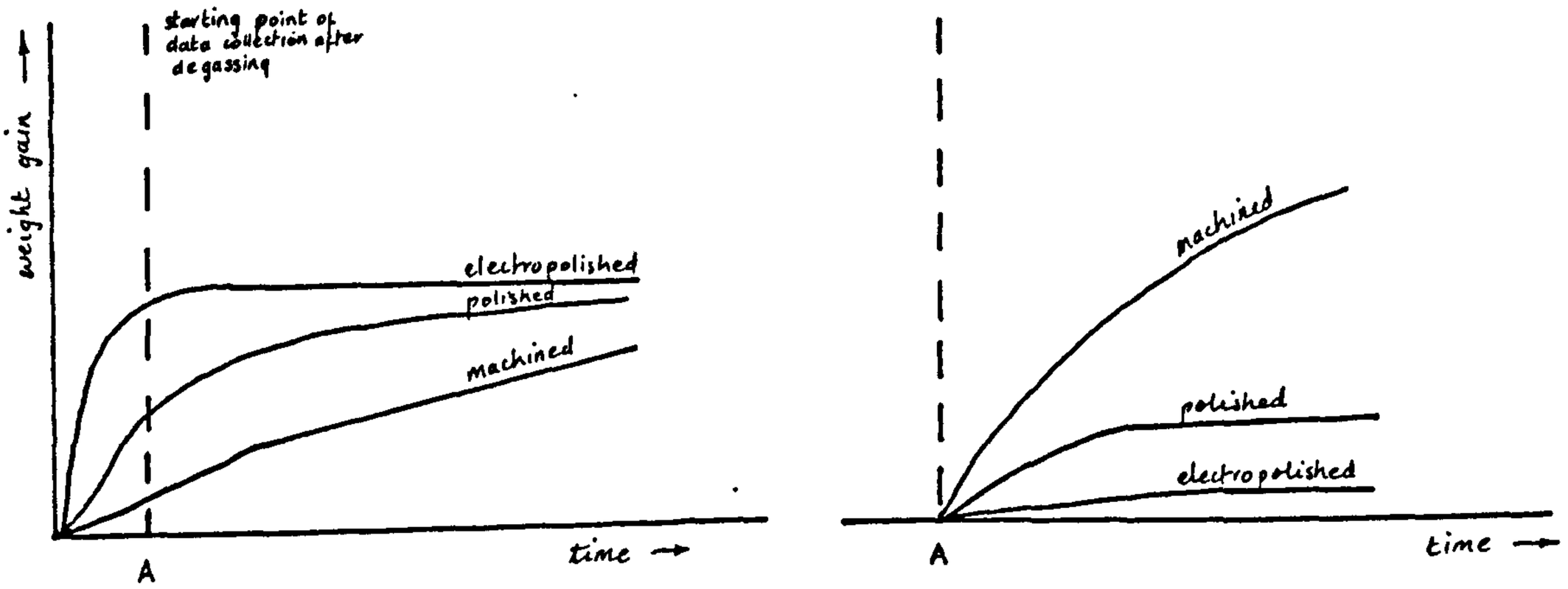

Figure 9.4 Schematic of aluminium oxidation rates reported in the literature showing the possible loss of data

The effect of surface finish on the oxidation rate on molten aluminium has shown that the rate of molten aluminium oxidation is dependent on the oxide formed on the solid metal, but in particular, is dependent on the condition of this first formed oxide. The following section explains why this should be so.

9.1.3. Development of metal containing oxide growths on molten aluminium

Aluminium surfaces oxidised at 750°C exhibit oxide growths. These protrusions, shown in Figures 6.15 and 6.19, develop into clusters of individual nodules with time. Growths are primarily oxide supporting entrapped molten metal (Figure 9.5a and 9.5b).

The morphologies presented in Figure 9.1 illustrate the initial stages in the development of an oxide cluster. Small nodulues emerge from within the oxide scale but are confined to a circular form (Figure 9.1c). Further nodule development is thereafter concentrated within the centre of this nodule ring (Figure 9.1d). TEM sections have been taken through oxide formed on unskimmed molten aluminium at 750°C in dry air after 5 hours. These micrographs, Figure 9.1e and f clearly show oxide rings approximately 2-4μm diameter with regions of thin and thick oxide.

Morphological observations suggest that the development of nodular oxide growths results from the local penetration of the first formed oxide by liquid metal which is exuded through the surface scale. Large crystals are present at these sites and in all cases the width of metal penetration at the point of scale fracture is in the region of 2μm. This process would appear to be related to the γ -Al_2O_3 to α-Al_2O_3 transition where a change in oxide density value (Table 9.8) results in the development of tensile stresses and subsequent localised failure of the scale.

In dry environments and at long exposure times (over 15 hours) at 750°C, when the gamma to alpha alumina transition is abundant, the aluminium specimen and alumina crucible or plate bonded together. Scanning electron microscopy of sections showed that this was due to the penetration of liquid metal into the pores of the alumina substrates as in Figure 6.23c. This clearly supports the proposed mechanism of oxide growth by molten metal exudation.

It has been established that the condition of the first formed oxide determines the rate of oxidation of molten aluminium. If the oxide remains continuous and free from cracks, exudation of molten aluminium, development of growths and hence rapid oxidation behaviour may be prevented. Coatings less than 0.5μm thick of 7070 borosilicate glass known to have occasional pinholes [231] were sputtered onto Al-Mg alloy surfaces. These alloys were used in preference to pure aluminium to encourage liquid metal exudation at temperatures low enough to preserve the integrity of the glass coating. Following 20h oxidation at 550°C in gettered argon occasional growths were observed protruding through the glass coat where pinholes existed, as Figure 7.26 shows. In comparison to the more easily damaged surface oxide film (Figure 7.25) the number of these growths was considerably reduced by the protective glass coat.

The effect of surface finish on the oxidation rates of molten aluminium is a good illustration of the protection offered by the surface oxide film. Greater stress and more defects present in the developing oxide will encourage early breakdown of the protective film, and where mechanical failure results, accelerated oxidation is observed. The aim of the rest of this section is to highlight factors or features which may act as stress raisers, responsible for weak areas arising in the oxide film.

During oxidation, growth stresses are generated as the oxide develops and thickens. The origin of stress in most cases is due to a combination of factors particularly from epitaxial stress, the

volume of oxide produced, oxide scale thickness [232] and oxide morphology. Features of oxide morphology considered to be contributory to stress are local imperfections such as iron intermetallics and ultrasonic pits. Stress raising sites can also arise from specimen geometry and crystal growth. These features will be examined separately.

Circular irregularities present on the metal prior to oxidation are revealed by electropolishing, as shown in Figures 9.1a and b. Analysis shows that these areas contain more iron (Figure 9.6a) than in the surrounding metal (Figure 9.6b) which is consistent with these areas being iron rich intermetallics. The structures are thought to be generated during casting from rapid solidification and are of similar dimensions to the growths on oxide surfaces. It is tempting to suggest that these sites are initiation points for growth formation. However, while there may be contributions, statistically there are not enough intermetallic features to account for all the growth structures observed.

In order to prevent unnecessary damage to the soft aluminium metal, care was taken with polishing and cleaning to minimise the polishing material becoming embedded in the metal surface. It is common practice however to remove adherent polishing fragments or traces of grease or lubricant by ultrasonic cleaning usually in a chlorinated solvent [71, 233]. Comparison of specimens in this work treated either with perchloroethane or isopropanol showed no effect of chemical contamination.

The oxidation behaviour of specimens ultrasonically cleaned was compared with those cleaned using soap solution prior to oxidation. SEM examination of aluminium surfaces subjected to ultrasonic cleaning from 30 seconds to over 5 minutes, exhibited cavities as shown in Figure 9.7 which increase in penetration depth with time. These cavities may arise from gas bubble erosion. A demonstration of the effect of these cavities on oxidation behaviour is illustrated for three aluminium-magnesium 5182 alloys.

Figure 9.8 is plotted from weight-change time curves of grain refined (GR) Al-5%Mg oxidised in gettered argon at 750°C. Oxidation rates of Al-4.5%Mg (GR and NGR) alloys polished in various media are given in Figure 9.9. Both graphs indicate that ultrasonically damaged surfaces lead to increased oxidation rates, and in some cases the onset of this rapid oxidation occurs earlier than specimens not cleaned ultrasonically. Thus the indications are that ultrasonically treating aluminium or aluminium magnesium alloys for long exposure periods may be detrimental to oxide protection and accelerate rapid oxidation behaviour.

Many illustrations have been given which support the idea that high oxidation rates are a consequence of rupture of the surface oxide, and that this mechanical breakdown is due to stresses in the film arising from specimen geometry. In particular the majority of growths occur at specimen edges, areas which are characteristically highly stressed and hence the first to rupture to relieve this stress. The dimensions or spacing of surface troughs and valleys which arise from mechanical cutting can generate geometry stresses. Figure 9.9 shows that rapid oxidation is delayed on surfaces finely polished with alumina (0.3μm) in comparison to a 1μm diamond polish.

At the foot of oxide growths, large crystals are found. Large crystals such as α-alumina generated from the γ to α-alumina transition considerably increase stress in the surrounding oxide and act as stress raisers. In Figures 6.16b and 6.16c, vertical cross sections of aluminium metal and oxide taken after 1h and 5h exposure at 750°C in dry air, large oxide crystals are seen at the oxide-melt interface beneath single oxide projections.

It is common for molten metal to extrude during oxidation into pores of an adjacent alumina substrate or container. Figure 6.23b and 6.23c are micrographs of such a specimen, of the remaining oxide and alumina substrate respectively after separation,

following 20h oxidation at 750°C in gettered argon. Characteristic angular pits are left in the molten metal after oxide growths are removed. At the centre of these structures are smaller granular sites. The original oxide film covering surrounding areas of the specimens is seen on the substrate supporting these crystals. With longer exposure times such as 70 hours, the centre of oxide growths take on a more granular appearance. As the metal exudes the granular oxide covering the metal is carried with it. The cracks in the oxide (Figure 6.21 and Figure 6.19d) show that these extrusions are unlikely to be the product of molten metal solidification. Hence the oxide growth develops before any volume changes occur solidification.

Thus, it is concluded that oxide growths protruding from the surface are a direct result of molten metal exuding through the oxide. The metal column may support nodule clusters. The different oxide morphologies observed on oxidised aluminium melts are summarised and illustrated in Figure 9.10.

This section has reviewed the formation of oxide growths which are believed to be responsible for rapid breakaway oxidation behaviour. It has been seen that breakaway oxidation can be encouraged by mechanical means. This next section 9.1.4. considers how atmospheric control can be used to delay the onset of rapid oxidation with regard to the proposed mechanism for oxide growth development, summarised in Section 9.1.5.

9.1.4 Environmental Interactions of Molten Aluminium

9.1.4a. The influence of oxygen on molten aluminium oxidation

Thermodynamic calculations using an Ellingham diagram show that at 750°C the oxidation of aluminium to alumina occurs if the partial pressure of oxygen is greater than 10^{-43} - 10^{-38}KPa and at

650°C, 10^{-48} - 10^{-43}KPa. Argon passed through a titanium getter at 725°C will contain a residual oxygen partial pressure of 10^{-37} - 10^{-35}KPa if equilibrium is reached. It is unlikely therefore, that in normal experimentation, oxygen levels are reduced beyond a partial pressure of 10^{-38}KPa. Hence there is always sufficient oxygen in the system for the formation of alumina. This situation applies at the oxide-gas interface. Beneath a thin oxide film, at the oxide-melt interface conditions may be very different and reduced oxygen levels are anticipated. Hence a period of time will elapse before the correct conditions are established for the nucleation and growth of γ and α-alumina oxide crystals.

On liquid melts, Hehn and Fromm [234] found that the initial stage of aluminium oxidation varied with oxygen pressure. At 10^{-5} - 10^{-6}KPa, a thick 10nm oxide of relatively large oxide crystals formed. The reaction becomes independent of oxygen partial pressure at higher levels and a dense 1μm film formed following parabolic kinetics.

In general, breakaway oxidation occurred slightly faster for aluminium oxidised in argon atmospheres in comparison with air with the same moisture content. The rate of diffusion of oxygen is dependent on the concentration gradient between the atmosphere and oxide-melt interface and hence dependent on the thickness of oxide. It is proposed that the 'amorphous' oxide film formed in a limited oxygen supply is thinner than that formed in air. Hence the partial pressure of oxygen at the oxide-melt interface increases faster in argon environments than in air and is reflected in the rapid rate of oxide crystal development and short time to breakaway oxidation observed on aluminium in argon environments.

Many authors, concerned with solid state oxidation, emphasise a need for pathways for oxygen transport to the oxide-metal interface. Dignam and Fawcett [104] propose that oxygen diffuses along the phase boundary between the periphery of growing crystallites and the thin 'amorphous' layer next to the melt. Brock

and Pryor [107] consider that a constant rate of crystal growth is achieved due to oxygen transport through regions of stress i.e. stress induced pathways. Thus if a plentiful supply of oxygen reaches the oxide-melt interface the rate determining step is independant of oxygen. This accounts for the similarity of aluminium oxidation rates reported in the literature which remain unaltered by additions of oxygen and hydrogen [96] or by nitrogen [77].

In this work, within the limits of experimental error the oxidation seemed to be unaffected by oxygen levels. However it is more likely that any deviation is masked by the influence of water vapour on the oxidation behaviour. This will now be considered.

9.1.4b The influence of water vapour on molten aluminium oxidation

The oxidation rate of molten aluminium is dominated by the influence of water vapour. The oxidation kinetics of aluminium with different surface preparations at 750°C in wet and dry air and argon environments fall into a sequence of oxide growth represented by different rate relationships.

Initially, the 'amorphous' oxide film develops according to logarithmic or cubic kinetics, characteristic of the formation of thin oxide films. Further oxide film development takes place according to a short linear relationship. This suggests that rate is governed by an interfacial or surface reaction [126]. As the film thickens and the reaction rate is more controlled by the rate of diffusion, parabolic kinetics are observed. Once a critical thickness is reached rupture can occur, the rate of oxidation then becomes dependent on the speed of adsorption on exposed metal surfaces, and a linear relationship dominates [126]. It is suggested that the developing oxide reaches a limit of stress or strain which when reached culminates in oxide rupture.

The presence of water vapour in the atmosphere extends the duration of the linear oxidation regime in the early stages of oxidation. This is illustrated for air in Figure 6.4 and for dry and humid argon in Figures 6.5 and 6.6 respectively. In stagnant atmospheres, humid or dry, a short linear oxidation period is observed. Hence, in comparison with a circulating atmosphere, faster oxidation rates are obtained if the aluminium sits in a static local environment. This effect is a consequence of the presence of absence of water vapour. Water vapour in the local atmosphere surrounding the aluminium is consumed. When the water vapour can be replenished from a circulating atmosphere, the oxidation rate is stabilised. Figure 6.8 and 6.3 illustrate this oxidation behaviour where circulating and stagnant environments are used in microbalances F1 and F2 respectively. Further examples of the influence of water vapour on oxidation can be found in Chapter 7 where the effect with magnesium is more dramatic.

Crystalline oxide development is considerably slower in the presence of water vapour than in dry environments. It is suggested that in the linear regime molecular water is absorbed at the oxide surface. The presence of hydroxyl ions stabilises the 'amorphous' film and nucleation of γ-Al_2O_3 and α-Al_2O_3 at the oxide-melt interface is considerably reduced. The rate of oxide nucleation and therefore oxidation is dependent on either the rate of removal of hydroxyl ions or of hydrogen ions at the oxide-metal interface.

As the number and size of oxide crystals at the oxide-melt interface increases, the rate of reaction becomes more dependant on the rate of diffusion, and the oxidation kinetics tend to parabolic behaviour. Thus, in comparison with air and argon, the appearance of parabolic kinetics at shorter times in gettered argon is consistent with the faster development of a complete crystalline oxide layer in a dry environment. The oxidation sequence is summarised in

Figure 9.11. The results used for this analysis (20h oxidation) do not extend over the long periods which include complete breakaway kinetics. Breakaway oxidation is shown in Figure 6.9 for aluminium at 750°C in gettered argon over a 100h exposure period.

Hence the oxidation data of molten aluminium does not conform precisely to any one theoretical oxidation curve but may be represented by a series of simple rate laws. Despite the good fit of experimental results with the theory, statistical use of these results is difficult to justify. The oxidation relationships are largely empirical due to the assumptions made, in particular that the diffusion coefficient, concentration gradient and surface area remain constant through the oxidation process.

The kinetic trends obtained in this research support work by Thiele [111] and by Stephenson [121] where aluminium oxidation rates at temperatures between 700 and 800°C increase with decreasing humidity. Weight-time curves plotted by Stephenson for the oxidation of pure aluminium at 750°C show larger weight gains in air (1300-3250$\mu g/cm^2$ from 3KPa water vapour pressure) than observed in this work (30 - 100$\mu g/cm^2$). The equipment used by Stephenson was reported to be rather insensitive. Indeed earlier thermogravimetric work [207] of molten aluminium oxidation has been shown in this thesis (Appendix A) to be influenced temperature variations of the equipment.

Thiele's data in Figure 9.12 demonstrates that oxidation levels achieved with pure aluminium are strongly influenced by trace additions present in the metal. The presence of impurities may considerably alter properties and oxidation characteristics making comparisons very difficult. However, the weight gains established in this work fall well within the range Thiele achieved with aluminium specimens of various purity oxidised at 800°C.

Formation of alumina by removal of water is well established. Indeed the sequence of crystalline aluminas, with their transitional nature, results from the most common means of reordering, the statistical removal of hydroxyl groups. Both γ and η -alumina contain hydroxyl ions which can be thought of as a necessary component of the defect spinel structure resulting in the characteristic degree of lattice disorder. 'Amorphous' alumina, as examined in the literature (section 3.3.1) may possess a pseudo spinel γ -Al_2O_3 'structure' with a larger amount of disorder. Hence the number of defect sites is linked to the degree of hydration. This implies that the concentration of hydroxyl ions in 'amorphous' alumina must drop to a critical level before crystalline transformation or nucleation of γ -alumina and subsequently α -alumina is favoured. The sequence terminates in the crystalline oxide modification α -alumina, the only thermodynamically stable aluminium oxide, thus the process of water removal is energetically favourable. The main activity however occurs at the melt-oxide interface. At this interface hydroxyl ion removal can proceed by absorption of hydrogen into the melt. Hence nucleation of crystalline oxide and transition of γ to α -alumina occurs naturally with exposure time due to the presence of the molten metal.

In support, Talbot and Anylebeci [235] find the maximum amount of hydrogen adsorbed in liquid aluminium at 750°C reaches a peak over the critical early stages of oxidation in the first 10-20 minutes and falls thereafter. Also, according to Dignam and Fawcett [104] 'amorphous' alumina does not crystallise in the absence of oxygen or aluminium metal except at temperatures exceeding 1000°C. A suggestion is that, without the aluminium melt to adsorb hydrogen, loss of moisture and thus increased oxide crystal formation is totally dependent on increased diffusion rates at high temperatures.

Thiele [111] observed the γ to α-alumina transformation and concluded that α-alumina is less effective in inhibiting further oxidation than alumina. Derbyshire and Cooper [118] reported corundum nucleating at the metal-oxide phase boundary. This work supports these findings.

Oxide morphology or the particular crystal habit of alumina seems related to the degree of hydration or more particularly to the rate or sequence of hydroxyl ion removal. Thus in order to enhance interfacial activity high surface area morphologies are found during rapid dehydration. It is suggested that the spheroidised alumina structures observed in Figure 6.22b may be attribution to rapid rates of formation.

In summary, the ease of nucleation and crystal oxide growth is enhanced by reducing the water vapour pressure in the environment and results in a more rapid conversion of γ-alumina to corundum. The water vapour therefore acts as a γ-alumina stabiliser and conversely the melt acts as a α-alumina stabiliser.

Apart from water vapour the most dominant addition to the environment in influencing alumina morphology found in this study was fluorine. The effects of fluoride on the oxidation behaviour of aluminium are examined in the next section.

9.1.4c. The influence of fluoride on molten aluminium oxidation

In the presence of fluoride the mode of oxide development closely resembles that of the γ- to α-alumina transition found in air. At the early stages of oxidation complete layers of fine, regular γ-alumina crystals develop. As oxidation progresses, the oxide surfaces exhibit highly crystalline whiskers of α-alumina. Aluminium fluorides are rarely detected at 750°C, but can be found on surfaces oxidised at lower temperatures.

The rate of oxide development however is considerable and perhaps reflected in the morphology and high topography of α-alumina layers. The rate of aluminium oxidation at 750°C in the presence of fluoride is initially faster than in air alone. Two curves are drawn through the scattered data points of Figure 6.11 collected from many specimens following oxidation at 750°C upto 100 hours exposure in humid atmospheres with fluoride. In both cases the maximum rate of oxidation is achieved over the first five hours. The oxide films at this time are highly developed layers of α-alumina whisker-like crystals (Figure 6.26). These develop to equal intensity in both dry and humid environments.

In the literature, Wefers [84] reports that the presence of fluoride (and chloride) in the vapour state increases the rate of crystal growth of γ and α-alumina, and facilitates the transition of γ to α-alumina. The results of this study are in agreement with this statement.

The mineralising effect of fluoride or chloride however has not yet been explained. It is generally accepted that fluoride catalyses crystal growth due to increased surface temperatures from exothermic reaction of aluminium with fluorine [48]. Dissociation of potassium borofluorate occurs around 600 and 700°C [236], and solid potassium fluoride melts at 858°C [237].

$$KBF_{4(s)} \longrightarrow BF_{3(g)} + KF_{(s)} \qquad 9.1$$

$$BF_{3(g)} \longrightarrow BF + F_2 \qquad 9.2$$

It is proposed that fluoride is rapidly adsorbed on to the 'amorphous' γ-alumina surface, occupying all available sites. The adsorbed molecules may be gaseous BF_3 generated from the dissociation of solid potassium tetraborofluorate or other fluoride containing derivatives. Gaseous BF_3 has a planar structure with a

central boron atom in an equilateral triangle of fluorine atoms. The molecule is a strong electron acceptor forming tetrahedrally configured negatively charged compounds:

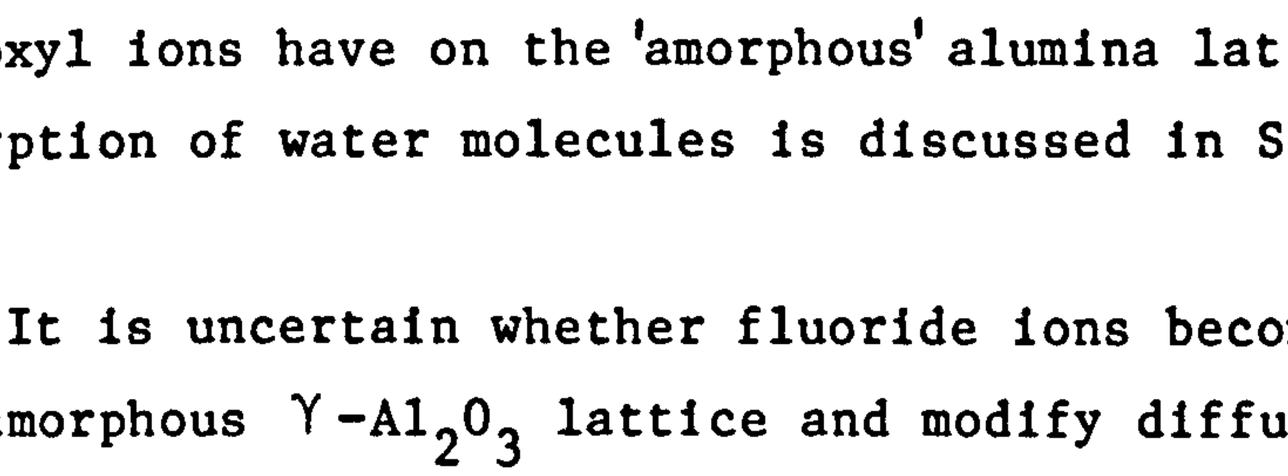

Initially reactive fluorine containing molecules are absorbed onto the surface in preference to water molecules. Thus the nucleation of γ-alumina and transition from γ to α-alumina is extremely rapid and unhindered from any stabilising effect that hydroxyl ions have on the 'amorphous' alumina lattice. Surface adsorption of water molecules is discussed in Section 9.1.4b.

It is uncertain whether fluoride ions become incorporated in the amorphous γ-Al_2O_3 lattice and modify diffusion rates. Certainly evidence is available to show surface adsorption takes place. Fluorine is abundant at the surface layer and aluminium fluorides do form, generally in the heating up stage at lower temperatures of 550°C.

$$Al_2O_3 + 2BF_3 \xrightarrow{450°C} 2AlF_3 + B_2O_3 \qquad 9.3$$

At 750°C oxides become more stable (Figure 9.13). It is uncertain whether the formation of fluorides is favoured as the specimen solidifies. Characteristically surfaces are covered with a white brittle coating, possibly hydrated aluminium fluoride $AlF_3 \cdot 3.5H_2O$. The white, milky appearance of the surface coating and dendritic crystal structures, illustrated in Figures 6.26d and e, suggests a surface liquid phase once existed even at short exposure times. At 750°C molten aluminium and BF_3 or KF may set up a

protective liquid phase on the surface of aluminium in equilibrium with the atmosphere according to Figure 9.14.

Whether the surface phase at 750°C is liquid or a highly crystalline solid, it is important that sufficient fluorine is available. Examination of the surface oxides show multilayer formation. When cracking or spalling occurs and the melt is exposed, if sufficient fluorine is present in the atmosphere new crystals or a liquid phase rapidly develops.

The two curves plotted in Fig. 6.11 for weight changes with time for aluminium oxidised at 750°C with unspecified quantities of solid KBF_4 can be discussed as being extreme examples of oxidation with both an abundant and depleted supply of fluorine.

With high levels of fluorine available, formation of α-alumina films rapidly occurs. Thereafter further crystal growth is restricted to the thickening of the whisker like α-alumina crystals and development of hexagonal platelets. This is well demonstrated by comparing Figure 6.26c at 5hrs exposure with that of 15 hours in Figure 6.27a. The rate of oxidation or of increased weight gain is low over this period. Indeed a weight loss is observed in Figure 6.11 after 10 hours exposure. This may be due to a loss of oxide as the crystalline layer or coat cracks and spalls or alternatively from the removal of volatile material. Indeed the whisker-like morphology of crystalline α-alumina suggests that the oxide growth is influenced by a vapour phase mechanism.

Unstable oxyfluorides can be removed in the vapour phase. BF_3 also reacts with aluminium and hydrogen to form diborane [236].

$$2BF_3 + 3H_2 + 2Al \longrightarrow B_2H_6 + 2AlF_3 \qquad 9.4$$

The removal of gaseous hydrogen fluoride is more likely to occur. As volatile hydrogen fluoride is lost to the atmosphere more source BF_3 is required to maintain an equilibrium. This will continue until BF_3 can no longer be supplied by dissociation of KBF_4.. Protection of the melt surface from further oxidation is lost with depletion of the fluoride. Hence the aluminium surface now oxidises with similar growth formations to that observed in air.

While fluoride ions are present, the manner of oxide growth, porous nature of the α-alumina crystals and the fine crystal dispersion ensures that only a minimal level of stress exists at the melt-oxide interface. No large confined α-alumina crystals form to cause a volume change or allow exposure of the melt in a manner which encourages liquid metal to exude to the surface. As oxidation progresses the level of crystallinity appears to be reduced. The crystals aggregate and a continuous layer resembling a granular surface (Figure 6.27c), rather than a fine crystal dispersion, results. Crystal clusters forming at longer exposure times such as given in Figure 6.27a become spheroidal.

It is anticipated therefore that any dross arising from nodular growths formed on aluminium at 750°C is generated when the concentration of fluoride becomes depleted. Fluxes, mixtures of different fluorine and chlorine sources, are expected to behave by a similar mechanism. Hence providing it is thermodynamically energetically favourable at the temperature of exposure, adsorption of reactive fluorides and chlorides takes place at the surface in preference to the adsorption of water molecules.

The oxide films generated after 5 hours exposure to potassium tetrafluoroborate and solid potassium fluoride show randomly oriented hexagonal platelets dispersed in a film of whisker-like dendritic crystals (Figure 6.27a). With dissociated sodium fluoride, hexagonal plates are predominantly produced [207]. Large directional crystals with no secondary branching develop on molten

aluminium during 5 hours exposure at 750°C with sodium chloride as Figure 6.25f illustrates. Although the oxide morphology differs,in all cases the crystals were identified by X-ray diffraction as dense α-alumina layers. These observations are supported by other workers. Noda and Hasegawa [239] found that α-alumina crystals heated with sodium and potassium fluorides and chlorides in the vapour state formed crystalline hexagonal platelets, randomly oriented [84]. In LiF, needles, columns and other granular polyhedrons were obtained [84]. Salt additions and their relation to crystal size have been examined by Noda and Isihara [88] but no trends or conclusions were proposed.

From this work, it is suggested that the morphology of γ-alumina crystals formed in the presence of mineralisers is a consequence of the oxidation rate or rate of transformation to α-alumina. As conditions become more vigorous, the alumina structure changes from platelet morphology to a coral-like alumina structure with maximum surface area and minimum volume. Exactly why this should occur is uncertain.

To summarise, fluoride ions or fluorine containing species from the vapour phase are adsorbed onto the surface of 'amorphous' alumina. Formation of γ-alumina crystals and transition to α-alumina is rapid. The corresponding oxidation kinetics are initially high and high surface temperatures may be involved. The schematic of Figure 9.15 illustrates that weight gains are similar to those reached in dry environments prior to breakaway oxidation (point A). Further weight gains are low until the fluoride containing species is depleted thereafter breakaway oxidation is observed. Thus a constant, critical level of fluoride is required in the atmosphere to maintain a high level of surface crystallinity or a protective liquid phase on molten aluminium at 750°C. When this level is reached a period of protection from formation of metal containing oxide growths is achieved.

9.1.5. A review of the proposed mechanism for development of oxide growth on molten aluminium

1. Nucleation and growth of γ-alumina (or η alumina) occurs rapidly within the original 'amorphous' alumina film. The crystals grow in size as both temperature and time increase until surface coverage is complete. The crystalline monolayer then thickens with time.

2. Transition of γ to α-alumina crystals occurs at the oxide -melt interface and results in a build up of stress which is relieved by rupturing. The oxide cracks at weak areas exposing the melt.

3. Molten metal exudes via the ruptured oxide path to the surface where the exposed metal instantly combines with oxygen. The protruding structure of metal enveloped in an oxide film is described as an oxide growth.

4. Rapid oxidation ensures that conditions are favourable for repeated transport of molten metal through the newly formed oxide at these active sites. Thus the growth is made up of a network of oxide clusters and metal pathways. The number and size of these growths increases with time.

5. When oxide growths appear, rapid breakaway oxidation kinetics are observed. The time to breakaway and thus the rate of α-alumina formation increases with temperature, with decreasing water vapour pressure and in the presence of fluoride and chloride.

6. Breakaway oxidation increases in the presence of magnesium. The next section 9.2. discusses how the oxidation behaviour of aluminium is modified by additions of magnesium.

7. The growth mechanism is developed further in Section 9.3. From liquid metal wetting studies it is shown that a driving force exists for liquid metal aluminium and aluminium-magnesium alloy exudation.

9.2 THE OXIDATION OF MOLTEN ALUMINIUM WITH MAGNESIUM

9.2.1 Oxide Development on aluminium-magnesium alloy

Results gathered from oxidation studies of molten Al-Mg alloys containing 1 and 5 weight % of magnesium show striking similarities. The oxide film grown on Al-Mg melts supports coarse crystals (200-500nm) but also fine MgO crystallites (20nm). Transmission electron diffraction patterns separate coarse and fine magnesia crystallites with spots superimposed on continuous rings. Both electron diffraction and electron micrographs indicate that these oxides are two distinct and separate phases. This agrees with literature where duplex films of primary and secondary magnesia crystals are identified on Al-Mg alloys oxidised above 400°C [61, 102].

Coarse primary magnesia crystals form at the oxide-metal interface. The smaller secondary oxides exist within the oxide film and originate from the secondary reduction reaction of the amorphous γ-Al_2O_3.

$$3Mg + \gamma\text{-}Al_2O_3 \longrightarrow 3MgO + 2Al$$

This secondary reduction reaction has been observed by several investigators [61, 102, 129]. Field [102] reports that secondary MgO crystallites remain a constant diameter unlike the primary MgO crystals which coarsen with increasing temperature.

Amorphous γ-alumina is reported to have close packed oxygen ions with disordered aluminium ions. Field favours the idea that increased oxygen transport takes place via defects (Schottky or Frenkel) in this lattice, in the following manner. Substituting three divalent Mg^{2+} ions in place of two Al^{3+} ions reduces the number of vacant cation interstitial sites. To keep the concentration of anion and cation vacancy sites in equilibrium the number of anion sites increases. This results in increased oxygen diffusion to the oxide-metal interface. Hence a faster rate of oxide crystal formation occurs in Al-Mg alloys. A critical partial pressure of oxygen at the metal-oxide interface will be reached faster in the presence of magnesium ions. This may account for the fact that the temperature of crystal nucleation in Al-Mg alloys is reported to be around 350°C, lower than the temperature of nucleation in pure aluminium (475°C).

In contrast to Field [102], Brock and Pryor [107] consider that reducing the number of vacant interstitial sites by substituting divalent cations will result in less vacancies available for diffusion. Oxygen transport to the oxide-metal interface is reported to be slower consequently crystal nucleation at the interface is reduced. Growth of the 'amorphous' film is thought to occur by outward diffusion of metal ions thus formation of a crystal barrier at the interface is delayed. Continued cation diffusion increases the thickness and growth of the 'amorphous' film. In Al-Mg alloys the increased weight of this 'amorphous' film and the associated formation of secondary magnesia crystals may be considerable and account for the characteristic rapid weight gains.

It is difficult to comment on the validity of these theories since the rate of primary oxide nucleation in this work was found to be totally dominated by the water vapour content. However, direct comparison of early oxide films formed on unskimmed Al-Mg melts (1-5%) at 750°C in dry air for 5 minutes (Figures 7.1c and

7.14c) show dense 'amorphous' films with reduced number of coarse primary crystals in comparison with films formed on unskimmed aluminium under the same conditions (Figure 6.12d). Thus the latter proposal of Brock and Pryor is favoured.

:

According to the literature [107,129] the depth of penetration of the primary oxide crystals into the metal substrate is constant and dependent on the available oxygen content. The crystals themselves grow into the metal to a thickness where the supply of oxygen is limited. Brock and Pryor [107] consider that the volume change generated by crystal formation raises the level of stress. Regions of high strain develop which allow a constant supply of oxygen ions to reach the perimeters of the growing crystals. Thus due to a plentiful supply of oxygen, lateral crystal growth is rapid and continues at a constant radial rate until adjacent crystals touch and the interface is continuous.

This situation was not observed in this work for Al-Mg alloys oxidised at 750°C. Stressed oxide films were observed but any preferred growth direction of the oxide crystals embedded in the metal substrate, took place vertically towards the oxide-gas interface. The estimated increased volume occupied by the crystals imply that stresses develop in the surrounding 'amorphous' oxide. On solid metal the limited stress relief possible may result in loss of adhesion of the oxide and metal at the interface, allowing oxygen transport. However, on melts, the interface deforms to reduce the stress, frequently resulting in irregular, folded oxide films. It is suggested that oxygen transport to the interface is not encouraged by this mechanism.

A continuous layer of primary oxide crystals was not observed, on melts or on the solid alloy. Regions adjacent to the primary magnesia crystals were depleted in magnesium. The crystals act as sites for further nucleation and MgO stacks were seen to develop at a large number of growth sites, but areas devoid of magnesia crystals existed between these oxide stacks.

So far the oxide crystals have been considered as geometrical structures; cylinders or cubes expanding laterally and vertically. The following discussion proposes a sequence of oxide development constructed from the oxide layers indentified on Al-Mg specimens after oxidation under various conditions.

MECHANISM

An ultra thin film of 'amorphous' γ-alumina forms on Al-Mg surfaces in air at room temperature. As temperatures increase magnesium diffuses from bulk metal into the 'amorphous' film. It combines in the film to form secondary MgO and at the metal-oxide interface primary magnesia crystals nucleate. As previously noted, primary magnesia crystals grow at preferred sites in clusters around a source crystal. These clusters eventually grow through the 'amorphous' film to the surface. Thus an irregular layer of primary oxide crystals exist on the surface of the original oxide. Formation of magnesia continues until the magnesium is consumed or magnesium depletion in the alloy reaches a critical level.

In areas depleted of magnesium continued oxidation occurs. Alumina crystals (gamma or alpha) develop at the oxide-melt interface. This ensures that any magnesium reaching the interface or magnesia in the immediate vicinity will be in a favourable condition for rapid conversion to the spinel form. Magnesium aluminate forms from reaction of alumina with magnesia as shown below:

primary reaction $\quad 2Mg + O_2 \longrightarrow MgO$

$\quad 2Al + 3O_2 \longrightarrow 2Al_2O_3$

secondary reaction $\quad MgO + Al_2O_3 \longrightarrow MgAl_2O_4$

In low magnesium containing alloys and at high temperatures, magnesia forms so rapidly that the two stage reaction appears to take place in one stage. This sequence of oxide development is demonstrated in Figure 7.18 from a kinetic trace of the oxides grown

on an Al-Mg melt at 750°C in dry air. The quantity of magnesium in the sample is estimated and the dotted lines show the increased weight expected for this conversion of magnesium to MgO and as $MgAl_2O_4$. The rate of oxidation decreases as the quantity of magnesium depletes and a period of negligible weight gain exists for some specimens until the conditions become favourable for transformation to magnesium aluminate.

Analyses of the oxide films of heavily oxidised specimens, exposed at 750°C for over 20h show predominantly $MgAl_2O_4$, MgO but also α-Al_2O_3. It is proposed that magnesia forms on molten Al-Mg alloys initially. As the magnesium concentration decreases formation of magnesium aluminate is favoured. With time, and as oxidation continues, γ or α-alumina becomes the most stable phase. These results support the literature reported in Section 3.5.1b. Haginoya and Fukusako [136] distinguished between MgO and $MgAl_2O_4$ and noted (Figure 3.18) that during oxidation the mass of MgO decreases as $MgAl_2O_4$ increases in the stepwise sequence demonstrated above. The proposed sequence of oxide development supports the work of Grauer and Schmoker [129].

In the literature, the magnitude of oxide generated during oxidation of Al-Mg alloys under very similar conditions varies considerably. These variations were attributed to available surface area, a consequence of specimen roughness [77]. It has been shown in this work that the surface finish and manner of specimen preparation influences oxidation rates and may indeed account for the differences observed between investigators particularly on pure aluminium. A far greater influence for Al-Mg alloys particularly at temperatures near the liquidus is the quantity of magnesium readily available in the specimen and the specimen dimensions, as distinct from the percentage of magnesium in the alloy. MECHANISM.

In this work the percentage of magnesium in the alloy material ranged from 1-5%. It has been shown in Figures 7.11, 7.12, 7.40 and 7.41 that the oxide mass generated is dependent only on the mass

of magnesium present. In the literature, kinetic data are usually plotted in units of weight gain per unit area. Assuming no preheating or degassing takes place before data collection started, if the results are replotted in units of weight gain per unit weight or percent of magnesium in the sample far better agreement between the results of different investigators will be observed. For example, compare the ratios of magnesium percentage to oxide weight achieved by Balicki [135] in Figure 3.17.

Direct comparison of specimens with different dimensions presents some difficulty. In this work data was collected from small specimens (1mm x 7mm discs) and hence only small quantities of magnesium are present. Oxidation is encouraged using dry environments, high temperatures and exposure times upto 20 hours thus magnesia is rapidly generated. The magnesium concentration quickly depletes and transformation to magnesium aluminate follows. Thus the weight gains achieved are quite unlike those attained on larger bulk specimens containing more magnesium, such as molten baths where the oxide transformation sequence will not be exhibited. The melt surface will generate only magnesia and the oxidation rate remains constant. Specimen comparison is complicated further since oxide development is influenced by stress generated in the oxide film. Oxide formation will be slower on a thin foil which can deform easily than on a more highly stressed cylindrical specimen. This influence of stress is discussed further in Section 9.2.3a.

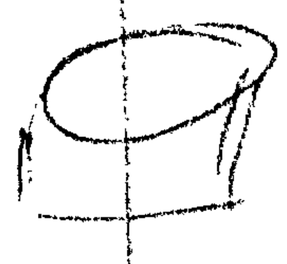

The oxidation rate of Al-Mg alloys is determined by the specimen surface area. Contributions attributable to the specimen shape used in this work were investigated further. Cylinders or discs were machined for use in the microbalances and the end surfaces carefully prepared. It was anticipated that the contribution to oxidation from the machined cylindrical surface would be in keeping with the rest of the specimen surface. Any additional contribution to the oxidation rate would arise from edge effects. However, Figure 9.16 demonstrates that as the height of the specimen is increased from 0.5 to 3mm increased oxidation rates

KINETICS DISCUSS

are observed and the gain in oxide weight per unit surface area increases in gettered argon at 550°C. This behaviour is a consequence of more magnesium available for oxidation in larger specimens. Only when the data is plotted per gram of specimen weight is the magnesium content standarised. Figure 9.17 shows that the cylindrical surface has a uniform response to the total oxidation.

The major contribution to the oxidation rate is found to be a consequence of the method of supporting the specimen during oxidation. The Al-Mg alloy discs are seated on alumina plates in the environmental chamber. The alumina plate shields the oxide surface from the atmosphere and specifically from the water vapour in the atmosphere.

This thesis demonstrates (sections 9.1.4b and 9.2.3b) that the oxidation rate on Al-Mg alloy is increased in dry environments. Hence oxide growth is increased at the surface adjacent to the plate (Figure 7.25) and consequently reflected in the oxidation rate. The increased weight gain due to the alumina plate is quantified in Figure 9.18 for 5182 alloy in gettered argon at 550°C. Data is plotted for samples oxidised with two alumina plates at either end of the specimen, with one support plate, and for a specimen suspended on platinum wire. The greatest oxidation rate is achieved for samples with two plates. Figure 9.19 shows that when the sample weights are standarised and contributions for the plates are subtracted the kinetic traces exhibited are equivalent to the oxide gain for the suspended specimen.

Hence it has been shown that the specimen dimensions used are reproducible quantitatively during oxidation, with the main contribution to oxide weight arising from the method of specimen support. The weight gain-time curves given in this thesis have not been adjusted in this respect and so contain data due to the supporting plate. Suspension is not suitable for specimens at temperatures higher than 550°C as some support is necessary for molten metal specimens. Further, the effect given by the alumina

plate varies with the water vapour of the surrounding atmosphere. The contribution from increased oxidation will be greater in humid environments than in dry air. Consequently quantification is difficult to apply in a practical manner.

:

On oxide films taken from all Al-Mg alloy melts large rhombohedral crystals are observed (Figure 7.4 and 7.15) with transmission and scanning electron microscopy. These crystals are magnesium rich and their presence and considerable size is critical to the rate of dross formation (Section 9.2.3a). However their indentification is uncertain, the crystals being either primary MgO or primary magnesium aluminate. The term 'primary' is used to describe an oxide formed from direct combination of the elements and not from reduction of alumina or magnesia.

Electron diffraction suggests that these rhombohedral crystals are magnesium spinel. However the only magnesium aluminate previously observed is a fine oxide usually dispersed with metal in a thick oxide layer. As these large crystals are only seen on melts it may be argued that spinel formation is encouraged by the ability of the melt to absorb hydrogen. Hence the hydroxyl ion concentration at the melt interface is rapidly reduced, a situation found favourable for the nucleation of alumina spinel structures. The abundance of surrounding alumina in the amorphous film would enable any magnesium to be directly transformed to spinel. The crystals are particularly abundant on low magnesium containing alloys such as Al-1%Mg (5005) alloy, as observed in Figures 7.4 and 7.8. For spinel to form on Al-5% Mg alloys it must be assumed that the magnesium becomes segregated in the alloy in distinct regions of the melt-oxide interface. Indeed, this behaviour is observed and is discussed in the next section (9.2.2). Conversely, it may be argued, by appearance, that these large crystals are extreme examples of coarse primary magnesia. Growth of the magnesia crystals may be encouraged during solid state oxidation in the heating up process at sites of magnesium aggregation.

It is perhaps surprising that no mention is made of these dominant features in the literature. However few investigators have used transmission electron microscopy to study the longer-term oxidation behaviour of Al-Mg melts. Films are often difficult to observe as the surface oxide layer covers most of the important features. Also, despite their abundance, careful work is required to obtain specimens for transmission electron microscopy. When bromine-methanol solution is used to remove excess metal the oxide crystals simply remain in solution. It is suggested that these large rhomobehdral crystals are magnesium spinel, although further work is required to verify this. However, the emphasis in this work is placed on the role of these oxide crystals as geometrical structures, as discussed in next section.

9.2.2. Development of oxide growths on Al-Mg alloys

Despite the different crystals of primary magnesia or magnesium aluminate formed at the oxide-metal interface during high temperature oxidation, the morphology of the oxide-gas interface on Al-Mg alloys is dominated by the appearance of growths protruding from the surface. Large outgrowths at the surface of oxidised pure aluminium were attributed to exudations of molten metal, similarly growths developing on Al-Mg melts and small growths present on solid surfaces Al-4.5%Mg oxidised at 550°C contain considerable quantities of metal.

Closer examination of the oxides surfaces formed at 550°C in dry air (Figures 7.24b and 7.24c) show an oxide surface layer with dark magnesium rich regions. Magnesium diffuses through the bulk alloy and concentrates in regions at the oxide-melt interface. According to the phase diagram for the binary Al-Mg alloy [240] in Figure 9.20, the melting point of the alloy lowers as the content of magnesium increases. With 5% Mg a liquid phase can be present at temperatures down to 580° and with 8%Mg the solidus is at 550°C. Thus where magnesium concentrates in areas at the surface the

melting point is lowered. In addition, the surface temperature is raised due to the intense activity from oxidation. Indeed magnesium can often ignite [27]. Liquid metal forms beneath the surface oxide and the oxidation behaviour reflects this transformation.

:

The combination of a stressed oxide film due to the presence of crystalline oxide at the oxide-metal interface (large rhomobedral crystals are visible) and the solid to liquid metal volume change provides the driving force for metal exudation shown in Figure 7.24c. The molten metal exudation itself rapidly oxidises, hence these structures appear more like oxide clusters wetted with molten metal. As the level of magnesium builds up, MgO crystals cover the oxide surface.

At lower temperatures no liquid phase is possible and the surface is completely devoid of all growths. For example, at 450°C, as oxidation progresses Figure 7.27a shows that the surface layer of Al-5% Mg alloy only thickens. At 550°C the oxide surface and hence the oxidation rate is dominated by oxide growths (10μm diameter). The weight rapidly increases as thick 'amorphous' oxide films rapidly form over the emerging molten metal. Thereafter, growth of magnesia continues in a steady manner. Individual oxide structures are observed at 550°C in Figure 7.25 but when the specimen is totally molten (at 650°C) competition for available surface area for growth development is severe. The whole surface is covered by nodules which appear confined and restricted by their prolific number and diameter (15-100μm) as shown in Figures 7.27c-e. Oxidation rates are steady as magnesia surface films develop. At higher temperatures the growths develop in both diameter and height into large significant structures correspondingly oxidation rates at 750°C and 850°C are very rapid.

Most authors of molten Al-Mg oxidation studies record the existence of growths which form on the oxide surface during breakaway oxidation [111,124,131]. The growths are filled with metal and are said to contain more magnesia on the nodular surfaces than on the surrounding areas [124].

In summary, the percentage of magnesium whether 1% or 5% has little influence on oxidation rates. It is proposed that at temperatures above the melting point, a highly stressed rapidly formed crystalline surface film develops, encouraging an eruption of metal. This is observed on the surface as a metal protrusion enveloped in an oxide coat. The surface temperature is raised by the considerable activity hence magnesium diffusion is rapid. In areas rapidly depleted by magnesium nucleation and growth of magnesium aluminate at the oxide-melt interface is favoured.

This oxidation process continues uninterrupted as these spinel crystals are characteristically large and act as points of stress, encouraging further metal exudation and crystal growth at the new oxide growth-metal interface, also depleted in magnesium. The rapid oxidation rate encourages the formation of widely dispersed, numerous oxide crystals of smaller dimensions. This results in a thick, dense oxide layer. Rapid growth behaviour does not cease until all the available magnesium is consumed.

Oxidation rates or onset of breakaway oxidation is influenced by the surface finish of the specimen, the humidity of the atmosphere, additions of grain refiner, beryllium and fluorides. To understand the mechanism of oxidation further it is necessary to examine these influences, particularly on the first formed oxide films.

9.2.3. Influences on the oxidation rate of Al-Mg alloy

9.2.3a Mechanical Breakdown of the Oxide and the Influence of Surface Finish on Al-Mg Alloy Oxidation

The discussion so far has emphasised the importance of forming a protective coherent oxide on any Al-Mg alloy at the start of oxidation in order to reduce the possibility of cracking at a later stage. Oxide cracking is a direct result of stressing particularly in areas of weakness. Primary origins of stress are expected to arise from extreme concentration gradients, from rapid oxide crystallisation [241] and from crystals growing at the oxide-melt interface acting as stress raisers.

Folded and irregular oxide films form on Al-Mg melts (Figures 7.1a, 7.2c and 7.14a). These confirm that the oxide initially developing on solid metal was stressed but is relieved to some extent by deformation once the metal becomes molten. Thus the condition of the first formed oxide is critical. A measure of the original condition of the oxide film is obtained by monitoring the time to breakaway oxidation and changes in oxidation rates. Factors influencing these parameters are the surface finish, grain size and trace additions of the Al-Mg alloy.

The condition of the first formed oxide is influenced by surface preparation. On Al-Mg specimens in dry environments at 750°C, breakaway oxidation occurs faster on machined specimens than on polished surfaces. With pure aluminium under the same conditions this trend is completely reversed.

With pure aluminium it was proposed that the level of stress accumulates as the amount of surface preparation increases. This influences the subsequent behaviour of the alumina film and the oxide is less likely to remain intact during the oxidation of polished surfaces than for machined specimens. During the polishing process on small Al-Mg alloy specimens surface temperatures may be

raised sufficiently to encourage a build up of magnesium in the outer surface layers. A greater proportion of magnesium at the surface layer would ensure that this region is the first to melt. Stress building up at the oxide-metal interface is relieved in the polished surfaces before machined specimens. Thus the oxidation rates for both polished Al-1%Mg and Al-5%Mg alloys oxidised at 750°C are reduced in comparison with the non stress relieved machined specimens.

Hence the behaviour of the oxide is determined by the rapid diffusion of magnesium to the surface of an Al-Mg alloy and any means of enhancing this magnesium diffusion and hence oxide crystal growth will encourage the onset of breakaway oxidation.

MECHANISM.

Grinding or machining induces cold work in a surface and provides an increased number of short circuit diffusion paths [241]. Polishing can remove this cold worked layer but leaves a surface of deformed and smeared metal thereby reducing the number of diffusion paths. Consequently magnesium diffusion will be faster on cold worked machined surfaces. Hence oxide growth and the onset of breakaway oxidation is enhanced on machined surfaces of Al-Mg alloy than on polished specimens.

Alternatively, during the polishing process surface temperatures are raised and fine recrystallisation grains are produced during the heating up period leading to melting. Polished surfaces will have more grain boundary diffusion paths than machined specimens and the increased diffusion can lead to a faster rate of surface coverage. By rapidly forming an almost continuous layer in the solid state a greater degree of protection is provided for the melt, thereby delaying breakaway oxidation. Indeed grain-refined aluminium alloys with 1% and 4.5% magnesium additions exhibit slower oxidation rates than non-grain refined material. Further, if a machined non grain refined alloy is polished, the resulting oxidation rate is equivalent to that of the grain refined material. Hence, polishing has refined the grains. Oxidation curves for both

polished grain refined and non grain refined Al-Mg alloys fall in a band of reproducibility reflecting the various degree of polishing and consequent grain refinement.

In support of this behaviour, an analogy is drawn from the literature between the preferential oxidation of chromium in steels and magnesium in Al-Mg alloys. The oxidation of chromium containing steels is reported to be dependent on the surface treatment prior to oxidation. For example, as the grain size of these steels decreases a continuous protective, chromium-rich surface layer develops at short exposure times as a consequence of the increased number of diffusion paths [243]. Diffusion of chromium ions is enhanced in fine grained materials produced by cold working [243] and the corresponding rates of oxidation are low in comparison with larger grained electropolished surfaces [242]. It is suggested by the author, but not confirmed, that nucleation and growth of oxide crystals is influenced by the size of metal grains. Constraints at the base of the scale may dictate the grain size of the growing oxide [242]. Formation of a fine-grained oxide provides the surface layer with more strength and more resistance to cracking.

Despite good correlation between the oxidation rates of a fine grained surface and a grain refined material, grain refinement has been achieved by titanium diboride additions. Reduced oxidation rates are reported in the literature for Al-Mg alloys dusted with boron. The small atomic size of this element, incorporated in vacancy sites of the γ-alumina oxide lattice reduces diffusion rates [146] and is reflected by delayed breakaway oxidation. The effect of modifying diffusion rates by doping an oxide lattice or by generating a different surface compound is discussed in section 9.2.3c.

P_{H_2O}/P_{O_2}.

9.2.3b. The Effect of Water Vapour on Al-Mg Oxidation

In a manner similar to that of pure aluminium the onset of breakaway oxidation on Al-Mg alloys is considerably delayed in the presence of water vapour. During this study, many illustrations have been presented of the dramatic influence that water vapour has on the oxidation behaviour of Al-Mg alloys.

For example, increased oxidation occurs on 5182 alloy at 550°C in the centre of a specimen base where atmospheric contact is restricted by an alumina plate (Figure 7.25a). On Al-Mg alloy melts of 1,4.5 and 5% magnesium at 750°C in humid environments of argon or air, rapid breakaway oxidation is delayed as Figures 7.9, 7.19 and 7.21 show. The delay is enhanced on specimens placed in the path of a circulating atmosphere where water vapour reaches the developing oxide surface (Figure 7.20).

In the presence of water vapour, formation of both magnesia and magnesium aluminate is restricted. It is suggested in the literature that vapourisation of magnesium is restricted by a humid atmosphere, and that the atmospheric pressure above the film is not sufficiently reduced. The present study suggests that the water vapour, in particular the hydroxyl ions, stabilise the first formed 'amorphous' γ-alumina film. Thus at high temperatures and in dry environments formation of oxide crystals at the oxide-melt interface, which may then disrupt the existing oxide film, is delayed.

INCREASE P_{H_2O}/P_{O_2}.

It is possible that adsorption of water vapour at the oxide surface encourages the formation of a thin layer of hydroxide. This may act as a protective, coherent surface but is undetected in such quantities by electron or X-ray diffraction.

In the literature, greater oxidation rates have been observed in dry air than humid air for Al-Mg alloys oxidised in the solid-state [123, 128]. It is also reported that once rapid

KINETICS + MECHS

H_2O Increase

oxidation occurred, the oxidation rate was faster and weight gains higher in humid air than in dry air. Investigators reported this trend with temperatures between 500-640°C [124,128,134], temperatures at which liquid metal oxidation may occur at the surface. With the surface film 'protected' in humid air, magnesium will concentrate at the surface over the long induction period. Thus faster oxidation rates may be obtained in humid atmospheres once breakaway oxidation has occurred. These investigators attribute rapid oxidation in a humid atmosphere to the rupture of small blisters which expose the metal. They do not suggest however why rapid oxidation is observed in dry air where such small blisters are absent.

Lee et al [128] found that Al-Mg alloy cycled in wet and dry air at 525°C resulted in fast and slow oxidation rates respectively. Although the rates of oxidation are in contrast with the results in this thesis, on a large thin surface it may be possible to discourage and encourage formation of oxide crystals without rupturing the surface film, hence keeping some degree of control in the system.

Sufficient water vapour is expected to be present in most 'undried' atmospheres to provide a delay in oxide crystal development, provided there is good access to the melt surface. This influence of water vapour was successfully used to precondition the developing oxide. Conditions will vary for particular furnaces but with an atmosphere circulating over an Al-Mg alloy melt at 750°C during a slow melt down period, 5h exposure is sufficient to delay rapid oxidation for upto 20h when the melt is then placed in a dry or static environment (Figure 7.30).

With no preheating in humid air, rapid oxidation was instantaneous (Figure 7.30 and Figure 7.33). Preconditioning the first formed oxide below 750°C requires longer time periods to protect the melt from rapid oxidation. Traces of magnesium hydroxide were identified on only one occasion. Even if the

quantity of hydroxide present is insufficient for detection by electron or X-ray diffraction, it is thought that rates of diffusion are not sufficient to allow complete saturation of the film or complete $Mg(OH)_2$ formation. Preconditioning at shorter time periods and lower temperatures often delayed rapid oxidation but the behaviour was not consistent.

It was found that if preheating in humid air took place below 750°C, periods over 5 hours were necessary to delay oxidation, and 15 hours at 550°C consistently delayed breakaway oxidation.

It may be argued that during the period of preheating in humid air at molten temperatures specimens completely oxidise. Thus when the samples are subsequently exposed to a dry environment the negligible oxidation observed reflects the absence of molten metal. However if a similarly preconditioned oxide is cooled before reheating in gettered argon all protection is lost as a direct consequence of solidification cracks. On reheating, this damaged oxide surface provides no protection to molten metal exudation (Figure 7.30). Hence significantly this latter behaviour illustrates that following preheating the molten metal remains enveloped in a protective oxide film.

If oxide cracking is not encouraged, over long periods of exposure to dry conditions, oxide crystal development takes place beneath the surface film. As oxide clusters increase in size the structures grow through the surface film causing considerable damage. Rapid oxidation behaviour after preconditioning was marked by crystals protruding through large cracks or holes in the outer surface film (Figure 7.32).

9.2.3c Influence of Beryllium and Fluoride additions on Al-Mg Oxidation

The behaviour of Al-4.5%Mg alloy when oxidised in gettered argon varied slightly to that of Al-1%Mg or Al-5%Mg under the same conditions. The Al-4.5%Mg alloy had a strong tendency to delay conversion of MgO to $MgAl_2O_4$. This behaviour may be due to the influence of additional elements in the alloy. For example, calcium and sodium impurities have been reported by Field [102] and by Cochran and Sleppy [112] respectively as reducing the oxidation rate of Al-Mg alloys. The effect element additions have on the oxidation mechanism can be considered in terms of diffusion rates when incorporated in the original 'amorphous' γ-Al_2O_3 layer.

Theories reported in the literature to date concerning the effect of element additions on properties of amorphous γ-alumina do not seem to be totally consistent.

Brock and Pryor [107] studied γ-Al_2O_3 oxide formation at oxide-metal interfaces during oxidation of Al-Cu alloys. It was observed that as the copper content increased the nucleation density and depth of oxide crystal intrusion into the alloy decreased. The suggested mechanism was temperature dependent. At low temperatures below 500°C cupric ions (Cu^{2+}) incorporated in the original 'amorphous' γ-Al_2O_3 film will create interstitial Al^{3+} ions. Three cupric ions (Cu^{2+}) replacing three aluminium ions in the 'amorphous' oxide require one Al^{3+} ion in an interstial position to maintain electrical neutrality. Hence the number of vacant interstial sites is reduced but the number of ionic vacancies remains unchanged. At higher temperatures above 525°C, three cupric ions replacing two aluminium ions, reduce the number of ionic vacancies. Brock & Pryor propose this mechanism accounts for the slow nucleation and minimal vertical growth of primary crystals at the oxide-metal interface of the Al-Cu alloy. They suggest that oxygen diffusion slows as the number of oxygen ion vacancies in the lattice decreases.

In support Brock and Pryor [107] present the results of oxidation studies carried out on high purity binary aluminium alloys each containing 0.2% Si, 0.1% Ti, 0.1% Zn or 0.1% Ag. The results indicate that the larger the ionic radius of the impurity ion in the oxide, the smaller the depth of intrusion of the crystalline oxide into the underlying metal. Large ions in the oxide lattice physically restrain inward diffusion of oxygen. The calculated radius of an Al^{3+} ion is 45-53pm [102, 107]. The ionic radius of a divalent copper ion is reported as 74-92pm [102. 107]. Thus when ions of similar dimensions such as Mg^{2+} (72pm) and Li^{+} (74pm) [102] are incorporated into the 'amorphous' film, it is anticipated that rates of nucleation and the depth of oxide growth into the metal would be reduced in an analogous fashion.

Conversely, investigators of Al-Mg [61, 102] and Al-Li [102] alloys find that the presence of alloying additions in the 'amorphous' γ-alumina film is responsible for increased oxygen transport to the oxide-metal interface. Oxide nucleation and the depth of growth into the metal is reported to be greater in the presence of alloying additions than with pure aluminium. It was proposed that the reduction in vacant cation sites leads to an equivalent increase in the number of vacant anion sites to keep the number of defects in equilibrium. As a result increased oxygen diffusion to the oxide-metal interface takes place. Both these binary oxide systems however are characterised by the formation of magnesium and lithium oxides and not γ-Al_2O_3 crystals.

Beryllium additions to the metal are found to either delay or prevent breakaway oxidation on Al-Mg alloy melts. Beryllium is a small enough ion (Be^{2+} 27pm) to be incorporated interstially in the lattice [102]. In conjunction with Mg^{2+} ions, from morphological and thermogravimetric investigations, the rate of crystal formation and presumably oxygen ingress appears greatly reduced. This is consistent with the mechanism favoured by Brock and Pryor.

If all vacant cation positions available in the 'amorphous' γ-Al_2O_3 film are occupied by beryllium ions then any outward cation diffusion is severely restricted. Oxygen diffusing to the oxide-melt interface is consumed as beryllia. Early films of melt surfaces show the growth and development of BeO crystals. Additions of 10 and 50ppm beryllium are not thought to be sufficient quantity to provide total surface coverage. Reports in the literature suggest that beryllia is detected only in melts with greater than 0.01% Be, 100ppm (Table 3.3).

TEM micrographs show that crystalline growth occurs at the oxide-melt interface. It is tempting to suggest, like Field [102], that BeO has a plate-like morphology growing laterally along the interface rather than vertically through the 'amorphous' oxide. Early micrographs show such development (Figures 7.35a and 7.35b), but cross sections taken normal to the oxide surface do not confirm this type of growth (Figure 7.36c). However, the volume change associated with beryllia formation is suggested to be minimal and the stresses associated with growth of the oxide film are negligible. Hence the growth of BeO on a melt takes place without disturbing the 'amorphous' γ-Al_2O_3 overlayer. At the low levels studied the beryllium oxide is non-disruptive. After long exposure times thicker films are identified as primarily MgO. The appearance resembles an original amorphous γ-Al_2O_3 film with secondary MgO crystals formed by a reduction reaction.

The surface of a Al-4.5%Mg alloy containing 10 or 50ppm beryllium following 20h oxidation in dry or humid air or argon at 750°C strongly resembles that of the Al-4.5%Mg alloy after 20h at 550°C (Figures 7.38b and 7.24b respectively). Both oxide surfaces exhibit crystal nodules emerging from the surface, areas of high magnesium segregation and occasional oxide outgrowths. The oxide appearance therefore certainly suggests that the oxidation mechanism is delayed in the presence of beryllium.

If the 'amorphous' film is damaged the weight gain increases. This was observed on occasional specimens with low (10ppm) beryllium concentrations (Figure 7.37) after long exposure times and when damage was encouraged by thermal cracking from a cool and reheat cycle (Figure 7.39a). In general, the resulting oxide protrusions were small in height but covered wider areas. This implied the molten metal flowed with ease over the surface. Holes often appeared on solidification. At the base of the holes crystals had developed (Figure 7.36d). It is suggestion that diffusion is not restricted within these areas and hence magnesia crystalline development is rapid.

Heine and Guminiski [123] also find that when the 'amorphous' film on Al-Mg-Be alloys is damaged, by hot rolling, increased oxidation behaviour is reported. It is proposed therefore that beryllium dramatically reduces the oxidation rate, and even influences the surface energy, but does not change the mechanism of oxidation. The oxidation process is delayed. Beryllia forms at the oxide-melt interface, is less disruptive than other oxide crystals, and may prevent complete exposure of the melt even when the 'amorphous' film is damaged. With higher concentrations of beryllium, the increased volume of beryllia formed will raise the stress at the oxide-melt interface and disrupt the 'amorphous' film sooner. Such behaviour is reported in the literature for beryllium additions above 0.01% or 100 ppm [102,111].

In the presence of fluoride above Al-4.5%Mg melts at 750°C magnesium rapidly diffuses through the 'amorphous' γ-Al_2O_3 film to form a protective layer of whisker-like magnesium-rich crystals, generally identified by electron diffraction as MgF_2.

Unlike beryllium, fluoride is not thought to be incorporated in the amorphous γ-Al_2O_3 film. The diffusion of magnesium ions in particular seems to be very rapid. Reaction of magnesium and fluoride at the oxide-gas interface will be exothermic and is expected to raise the immediate surface temperature encouraging

further diffusion. Thus irrespective of the percentage of magnesium in an Al-Mg alloy, it is anticipated that provided sufficient quantities of magnesium are present and the temperature is high enough for rapid diffusion, magnesium and fluoride will combine at the surface forming whisker-like crystals. The whisker-like growth morphology may disperse the build up of any stresses arising at the oxide-melt interface. Thus the likelihood of oxide breakdown at the surface is reduced. In fluoride containing atmospheres, crystals are usually whisker-like and a vapour growth mechanism is anticipated. The mechanisms of nucleation and growth of whiskers, blades and other analogous crystal morphologies are still a matter of conjecture. However research strongly suggests that crystal whiskers are not in direct contact with the metal [102].

Indeed, beneath the surface film, at the melt interface (Figure 7.13) primary magnesia crystals develop, favoured by the low saturated water vapour pressure and rapid uptake of hydrogen ions into the melt. It is suggested that oxygen transport to the 'amorphous' oxide-melt surface is restricted by the surface layer of fluoride. The uptake of magnesium as MgF_2 reduces the amount of magnesium incorporated as primary oxide at the melt surface. Fluorides rapidly combine with any exposed melt. Thus if sufficient quantities of fluoride are present in the atmosphere rapid oxidation is delayed.

At lower temperatures of 550°C formation of MgO is more favourable thermodynamically than MgF_2. In addition, magnesium diffusion to the surface is slower at lower temperatures and therefore the crystal surface layer formed is not as dense and therefore not as protective. Oxide crystals, possibly MgO, penetrate the surface (Figure 7.34a) thus rapid oxidation is expected to occur over long exposure times.

9.2.4 Review of the proposed mechanism for the development of oxide growth on molten aluminium-magnesium alloys

A summary of the oxidation behaviour of Al-Mg melts is presented schematically in Figure 9.22, adapted from Figure 3.19 of Cochran et al [124].

9.3 SURFACE ENERGIES OF MOLTEN ALUMINIUM AND ALUMINA

It has been reported in the literature, using a sessile drop technique that aluminium does not wet alumina. The Al-Al_2O_3 interfacial energy is said to be greater than that of the Al-air interface [191]. If this were so, then no exudations of aluminium could occur unless the aluminium were under sufficient pressure to overcome the required increase in surface energy. Measurements of surface energies and contact angles formed between the melt and the ceramic substrate are therefore of prime importance in evaluating the oxidation behaviour of a melt.

Of the methods developed for such determinations the sessile drop and pendant drop methods are most widely used. Despite the simplicity of these methods there are doubts remaining whenever high accuracy and consistency are needed [245]. A third method of surface energy determination based on 'a hanging plate' [225] is used in this study. This is the principle on which the surface tension balance [247] or a meniscograph [226] is designed. In the literature various forms of a wetting test or surface tension balance have been used to study solderability qualitatively [226]. Figure 9.23 is a schematic from the General Electric Company (GEC) of typical traces arising from the immersion of an electronic component in a bath of molten solder [226].

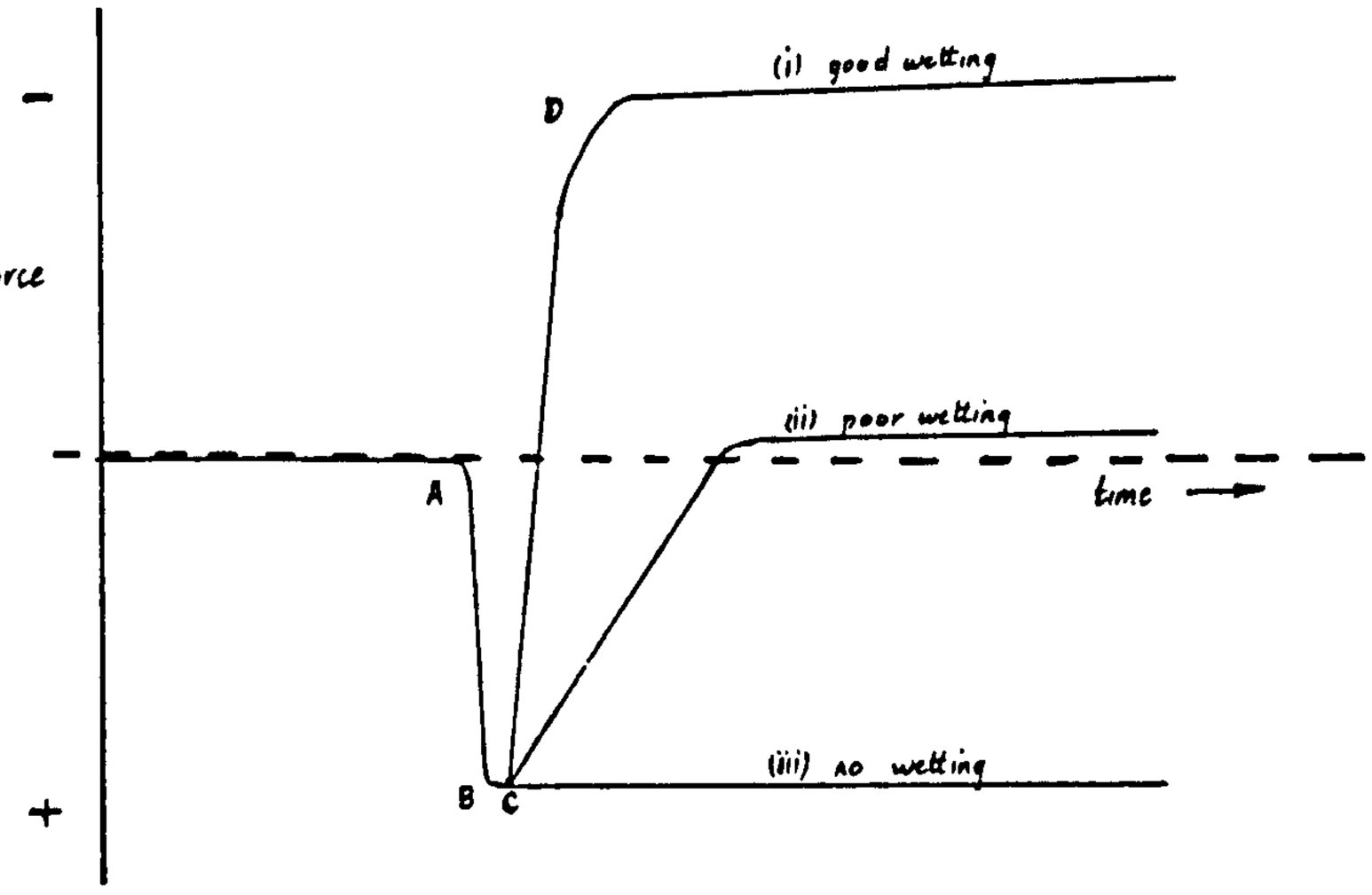

Figure 9.23 Schematic of solderability tests of force with time [226]

The specimen and solder first make contact at A. At B the specimen reaches the required immersion depth and the solder bath stops. Trace (i) demonstrates good wetting, the rapid climb of solder up the specimen surface is reflected by the steep gradient CD. As the gradient CD is reduced poor wetting (trace (ii)) or no wetting (trace (iii)) is demonstrated.

In comparison, alumina immersed in molten aluminium (Figure 8.1a) is qualitatively very similar. The response of the GEC system however seems more dramatic with less noise. This is not unexpected as test conditions differ dramatically.The specimen and solder are brought sharply into contact at speeds of 15-25mm/s at temperatures in the range 280-460°C. The Al/Al_2O_3 system was studied at speeds no greater than 0.65mm every 2 minutes giving an opportunity for equilibration, at a higher temperatures of 750°C. In addition, the presence of the thin oxide film on molten aluminium and the viscosity of the molten metal dampens or slows the wetting response

to the solid probe. For example immersing the same probe in water gives a clear, noise free trace shown in Figure 9.24 which is more comparable to the GEC solder traces. The balance system (Chapter 8) used in this thesis is therefore valid and qualitatively comparable with other meniscographs.

Data from such a surface tension balance has been quantified by Martin-Garin et al [227]. The measured force as the probe encounters resistance from the melt is related to the meniscus profile of the molten surface using a differential form of the Laplace law (equation 5.1). This law describes the equilibrium between surface tension and pressure forces. The authors treatment requires that the probe is an infinitely long and thin blade (edge effects are not considered) and that the melt is contained in a crucible with an infinite radius. Similar methods have been used to study molten aluminium and halide systems [247].

Despite the different test conditions, the force-time responses observed qualitatively agree with those obtained described in the experimental section (Chapter 8) of this study. In this work, a circular alumina rod is inserted into a molten bath of metal covered with a thin oxide film. This oxide film modifies the balance of surface energies between the probe and liquid metal. Thus the probe encounters the oxide layer at first contact. Because a circular probe has been used then the solution of Martin-Garin et al [227] cannot apply. The following mathematical analysis of the system allows evaluation of the surface energies assuming circular symmetry.

In Figure 8.1a, as point (b) is reached the probe indents the melt but does not fracture the surface scale. Just before fracture of the thin surface oxide:

$$F_1 = 2\pi r t \sigma_{oxide} - \rho_{Al} \left[\left(\pi x (x+r)^2 + \frac{2\pi x^3}{3} - \frac{\pi^2 x^2}{2} (x+r) \right] g \right. \qquad 9.5$$

The second term in equation 9.5 relates to a buoyancy effect resulting from the melt displaced by indentation of the surface oxide film.

Analysis of the interfacial tension between the molten metal and its oxide layer depends on a force balance of the form:

$$F = \gamma . \cos\theta \qquad 9.6$$

F is the measured force supporting or depressing the meniscus of molten metal against the solid oxide surface and θ is the angle of contact where the oxide film meets the surface of the solid oxide probe. As the probe is immersed in a bath it is necessary to add to this force a term due to buoyancy, related to the volume of metal displaced, the metal density and the force due to gravity. Following oxide fracture an instantaneous increase in the buoyancy effect results which increases with further probe immersion, such that at point (c) in Figure 8.1a, the force on the alumina probe is given by:

$$F_2 = 2\pi r \left(\gamma_{Al(l)-Al_2O_3(s)} + \gamma_{Al(+Al_2O_3)-air} \cdot Cos\theta - \gamma_{Al_2O_3(s)-air}\right) - \rho_{Al}\pi r^2 . x . g. \qquad 9.7$$

The slope of the region around (c) enables the buoyancy effect to be evaluated. It is also possible to calculate the term theoretically.

In this study a circular probe and small crucible was used. It was observed that as the probe pushes down the meniscus profile tends to a constant degree of curvature. This behaviour supports work by Wakeham and Skau [248]. In addition, as the probe is removed the position of the molten metal meniscus slides down the probe in order to preserve a constant meniscus profile. As the melt is contained in a small crucible the meniscus profile at this

maximised position can be approximated by a circle. On removal of the probe the force at point (d) in Figure 8.1b is given by:

$$F_2 - F_3 = 2\pi r(\gamma_{Al(l)-Al_2O_3(s)} + \gamma_{Al(l)-air}.Cos\theta - \gamma_{Al_2O_3(s)-air}) - \rho_{Al}\pi r^2.x.g \qquad 9.8$$

Measured values of the forces F_1, F_2, F_2-F_3 and depth of probe immersion for the Al/Al_2O_3 system are given in Table 9.3. Using the three equations 9.5, 9.7 and 9.8 the interfacial energies of the melt, surface oxide and oxide substrate can be calculated. Results for the $Al-Mg/Al_2O_3$ system are also included in Table 9.3.

TABLE 9.3 - Summary of measured forces F_1, F_2, F_2-3 and depth of probe immersion

	F_1 (a-b) mN	Probe depth mm	F_2 (b-c) mN	Probe depth mm	F_2-F_3 (a-c) mN	Probe depth mm	Estimated oxide thickness, nm skimmed	unskimmed
Al skimmed 5 mins	23.1	2.2	18.0	2.5	19.9	13.3	10	
	23.4	2.1	19.5	2.8	15.1	9.8		
	25.7	2.2	17.1	2.8	15.7	5.4		
	24.4	2.2	17.7	2.8	15.4	8.2		
5182 skimmed 5 mins	24.0	2.5	21.0	4.1	16.4	9.8	10	
	22.9	2.5	14.3	4.1				
5182 unskimmed 5 hours	114.3	2.2			114.3	2.2.		750

9.3.1. Calculation of fracture stress and oxide thickness

Oxide thickness values for both skimmed and unskimmed aluminium and Al-Mg alloy melts have been estimated from kinetic data and from TEM micrographs of the metal-oxide interface for exposure times upto

5 hours. The oxide thickness at the point of scale fracture was estimated to be 10nm, for both skimmed aluminium and Al-Mg alloys. The density of molten aluminium is only slightly changed by magnesium additions [186]. Therefore all calculations use a value of 2715kg.m^{-3}. Thus the fracture stress of the 10nm surface oxide on aluminium is calculated from equation 9.5 to be between 154-162 MPa. Tensile data for bulk Al_2O_3 (0-2% porosity) is in the range 200-310 MPa [251], hence these thin surface films would appear to have mechanical properties at the lower end of the range measured for bulk ceramics or alternatively, the film thickness tested is somewhat less than the estimated 10nm, nearer 5-8nm.

The oxide formed on the skimmed Al-Mg alloy has a calculated fracture stress of 150-158 MPa. This is very close to the value measured for the oxide formed on skimmed aluminium. A summary of the reported and calculated valves of the fracture stress for aluminium and magnesium oxides is given in Table 9.4.

9.3.2. Evaluation of Surface and Interfacial Energies

At point (c) in Figure 8.1b wetting equilibrim between the alumina probe and an oxide modified melt surface is established. Hence from equation 9.7 using the values of F_2 for pure aluminium and the corresponding probe depths in Table 9.3 one obtains:

$$\gamma_{Al(l)-Al_2O_3(s)} + \gamma_{Al(+Al_2O_3)-air} \cdot \cos\theta - \gamma_{Al_2O_3(s)-air} = -1.230 \pm 0.06 Nm^{-1} \qquad 9.9$$

θ is the contact angle measured for an oxide modified aluminium surface. At this point one must consider what is meant by the term 'oxide modified aluminium surface'. It is not possible to have a molten aluminium surface in contact with air because an instantaneous oxide forms. Hence the oxide modified aluminium surface must have a thin surface alumina layer. If this is the case then:

$$\gamma_{Al(+Al_2O_3)\text{-}air} = \gamma_{Al(l)\text{-}Al_2O_3(s)} + \gamma_{Al_2O_3(s)\text{-}air}. \qquad 9.10$$

Contact angles for aluminium on Al_2O_3 available in the literature are recorded in Table 9.7. The values are found to depend on the relative thickness of any surface oxide formed [194, 200]. When the surface oxide is relatively thick (32nm) a contact angle of 165° has been measured [194]. This value is found empirically to decrease linearly as the surface film thickness decreases, such that by extrapolation the contact angle for a newly formed melt surface is expected to be 78° [194]. Weirauch [194] commented that there is no theoretical reason to expect a linear dependence and his work suggests that a fresh aluminium melt surface could have a contact angle as low as 55°.

Evaluation of the surface energies of the Al-Al_2O_3 system from early work in this study has been published [252] for which a contact angle of 99.5° was estimated for a 10nm γ-Al_2O_3 film. However using Wierach's data, a better estimate of the contact angle is obtained, giving a value of 102° for a 10nm thick oxide. Using equation 9.9, and replacing $\gamma_{Al(+Al2O3)\text{-}air}$ with ($\gamma_{Al(l)\text{-}Al2O3(s)}$ + $_{Al2O3(s)\text{-}air}$) it is only necessary to estimate $\gamma_{Al2O3(s)\text{-}air}$ to calculate the surface energy term $\gamma_{Al(l)\text{-}Al2O3}$, which is the surface energy for molten aluminium wetting alumina.

The surface energy term $\gamma_{Al2O3(s)\text{-}air}$ can also be estimated by extrapolating data collated by Hardie and Petch [253]. Figure 4.2 demonstrates the good agreement between the data presented by Hardie and Petch and published data measured at 1850°C [254] and 1900°C [255]. From this figure, $\gamma_{Al2O3(s)\text{-}air}$ at 750°C is estimated to be 1.510Nm^{-1} (Jm^{-2}). Using these values, $\gamma_{Al(l)\text{-}Al_2O_3}$ is calculated to be 0.748 ± 0.100Nm^{-1}.

Referring to Figure 8.1b, at point (d) a change in force of 0.0154 $\pm$ 0.004N is measured as the probe direction is reversed, moving from probe insertion to probe removal. Using the probe depth corresponding to point (d) for aluminium (Table 9.3), then from equations 9.7 and 9.8 one obtains:

$$F_3 = 2\pi r \left(\gamma_{Al(+Al_2O_3)\text{-air}} \cdot \text{Cos}\,\theta - \gamma_{Al(l)\text{-air}} \cdot \text{Cos}\,\theta' \right) \qquad 9.11$$

Hence on substituting for F_3, r, $\gamma_{Al(+Al_2O_3)}$ and Cos θ, the term $\gamma_{Al(l)\text{-air}} \cdot \text{Cos}\theta'$ is calculated to be 0.624 $\pm$ 0.043Nm^{-1}. If the contact angle for a fresh aluminium surface is assumed to be 55° [194] then $\gamma_{Al(l)\text{-air}}$ is calculated to be 1.088 $\pm$ 0.04Nm^{-1} (Jm^{-2}). This value for surface energy is in excellent agreement with the work of Goumri and Joud [186] and Garcia-Cordovilla et al. [200] who have shown that for an unoxidised aluminium melt the value is expected to be higher than 1.100Nm^{-1} and that with oxidation this value drops to around 0.865Nm^{-1}. Surface energies in the range of 1.050-1.100Nm^{-1} correspond to contact angles of the order of 53-56°.

The interfacial energy of aluminium with a surface oxide film (0.748nm^{-1}) corresponds to a contact angle of 160°. The similarity of this value with the initial results obtained in the literature from the sessile drop technique (Table 9.6) representing the 'interfacial tension of aluminium in air' is emphasised. Further, as stated earlier, a surface oxide of γ-Al_2O_3 rapidly forms on a new melt surface exposed to air. Therefore the term $\gamma_{Al(l)\text{-air}}$ should in fact be ($\gamma_{Al(l)\text{-}Al_2O_3(s)} + \gamma_{Al_2O_3(s)\text{-air}}$). If this is the case then θ' is calculated to be 70.2°, a surface oxide film less than 2.5nm according to the measurements made by Weirauch [194].

Thus the experiments of this study imply that in the sessile drop work, it is the presence of a thin surface alumina scale that accounts for the non wetting of alumina by aluminium. Once this surface film is broken, to allow metal-alumina probe contact, the aluminium wets alumina.

For liquid aluminium with magnesium additions, the molten metal is surrounded by layer of magnesia, or a film of magnesium aluminate if the magnesium alloy content is low. With skimmed Al-Mg alloys the oxide formed over the initial period is alumina. Calculating the surface energies in the same manner as for aluminium, the balance of surface energies in equation 9.9 becomes $-1.248 \pm 0.1 Nm^{-1}$. Hence the interfacial energy between the melt and oxide $\gamma_{Al(l)-Al_2O_3}$ is calculated to be $0.727 Nm^{-1}$. Similarly using equation 9.11, a value for the term $\gamma_{melt/air} \cdot Cos'$ is calculated to be $0.697 \pm 0.03 Nm^{-1}$ for an unoxidised Al-Mg melt.

If it is assumed that magnesium has no influence, then the surface energy of the unoxidised melt is found to be $1.216 \pm 0.05 Nm^{-1}$ if a contact angle of 55° from the work of Weirauch [194] is used. Conversely, if surface energies of aluminium are assumed to be as in the literature ($1.100 Nm^{-1}$) then the corresponding contact angle lies between 49-53°.

Oxidation studies show that a melt surface initially depleted in magnesium will become enriched as oxidation progresses if sufficient quantities of the element are present in the alloy. This will be reflected by a greater proportion of magnesium rich oxide in the surface film and, in addition, a thickened surface film. If the surface oxide is predominantly magnesia or magnesium aluminate then the surface energy of $\gamma_{Al_2O_3-air}$ used in the calculation must be replaced by $\gamma_{MgO-air}$ or $\gamma_{MgAl_2O_4-air}$. Reported values for these ceramic surface energies in the literature are extremely variable. Data are listed for single(s) and polycrystalline material in Table 9.5.

Experimental determination of the ceramic surface energy is generally carried out by monitoring the energy required to fracture the surface. A certain amount of variation is expected, since in real systems other energy absorbing mechanisms such as secondary cracking, heat generation and formation of plastic deformation zones will influence these measurements. The surface energy thus

varies with particular microstructural variables such as grain size. Evans [256] quantified factors (see notation) contributing to the experimental effective surface energy value γ_i, in the equation below:

$$\gamma_i = \eta\gamma_o + \gamma_p + \gamma_\mu \qquad 9.12$$

However, because of the large number of contributing factors some researchers regard the surface energy to fracture as largely empirical [257]. These parameters are not expected to account for the very wide range of values observed in the literature. For example, when $\gamma_{Al_2O_3\text{-air}}$ varies between 0.5 and 2.0, $\gamma_{Al(l)\text{-air}}$ ranges from -2.14 to + 0.77Nm^{-1} (for θ = 55°). Thus, for the surface energy of the unoxidised melt to be equal or lower than that of pure aluminium, the ceramic surface energy needs to be greater than 1.45Nm^{-1}. It is also shown that the surface energy of the melt decreases as the oxide thickens. Using the surface energy value for Al_2O_3 and a contact angle of 102-103° then Wierauch's data corresponds to an oxide thickness of 10nm, as estimated previously.

The above calculations have demonstrated close similarity between the surface energy and oxide thickness formed on pure aluminium and skimmed aluminium-magnesium alloy melts. The oxide forming on an unskimmed Al-5%Mg (5182) melt is calculated to have a fracture stress greater than 800 MPa. Values reported in the literature for MgO are around 140 MPa [257]. No data was found for $MgAl_2O_4$. Such high stress levels for the unskimmed Al-Mg system indicates oxide thicknesses greater than 10nm, typically 60nm. In support the MgO oxide film on unskimmed Al-Mg alloy after 5 hours at 750°C in air is calculated from weight gain measurements to be of the order of 50nm. Under these conditions, the weight of the probe was insufficient to fracture the oxide and thus penetrate the melt.

From these results it is anticipated that the oxide on both aluminium and skimmed Al-Mg melts is 'amorphous' γ-Al_2O_3 of a similar thickness. Hence the oxide formed on the 5182 alloy is considerably depleted in magnesium by skimming. This is in agreement with oxide film development discussed in Section 9.2.1. By depleting the surface of magnesium, the thickness of oxide is significantly reduced primarily from delayed crystalline development.

Results of Al-Mg alloy wetting studies are available in the literature although data are not reliable. Researchers have commonly found difficulty in measuring the Al-Mg-O wetting system. A spinel reaction product is found at the interface between Al-Mg alloys and an Al_2O_3 substrate [258] Oxide formation has also been observed between aluminium and Al-Mg alloy melts and MgO substrates [259], and in this work (Figure 6.23). Such reactions at the interface cause protrusions at the base of the sessile drop and lead to uncertainties in measurements making values of contact angles questionable [201, 259, 260].

In the literature the surface tension of an aluminium-magnesium melt is reported to decrease as the magnesium content increases [184,186,259] Garcia-Cordovilla et al [186] derived the following logarithmic relationships for the surface tension of binary Al-Mg alloys. The surface tension (γ) decreases as the percentage of magnesium (x) increases both for unoxidised (equation 9.13) and oxidised (equation 9.14) melts.

$$\gamma = \gamma_{(Al)} - 96.7 \ln (1 + 0.26 x) \qquad 9.13$$

$$\gamma = \gamma_{(Al)} - 71.8 \ln (1 + 0.31 x) \qquad 9.14$$

These relationships vary less steeply with magnesium content than linear functions produced by Lang [261] and Korol'kov [262] Al-Mg alloy oxidation above 750°C was found to be independent of

the percentage of magnesium in the alloy between 0.87-5%Mg. Diffusion of magnesium through the melt to the surface was extremely rapid. Hence surface enrichment and magnesium vaporisation are felt to be important considerations and differences between these functions are attributed to segregation of magnesium to the surface. However, from the work carried out on the surface tension of aluminium melts, the major factor influencing the surface tension and contact angles is expected to be the development and condition of the oxide formed over the Al-Mg melt.

It has been calculated that the surface tension of skimmed Al-Mg alloy is very similar to that of pure aluminium. Correspondingly contact angles of the 'oxide free' skimmed Al-Mg alloy on alumina are low and comparable to values of 'unoxidised' aluminium on alumina. Wierauch [259] has determined contact angles of 83-93° for an Al-3%Mg alloy on oxide substrates at 800°C. He too correlates these results with those of an 'unoxidised' pure aluminium where contact angles range from 74-90°. Wierauch concludes that the final contact angle of the Al-3%Mg alloy is that of aluminium on an alumina substrate because the magnesium is rapidly lost from the melt by volatilisation. This conclusion of Wierauch's is surprising as his experimental evidence suggests a proportion of the magnesium lost from the Al-Mg melt becomes incorporated in an interfacial layer, mainly of spinel on substrates of Al_2O_3, MgO and $MgAl_2O_4$. The evidence is provided in several ways:

i. Thermodynamic and theoretical considerations of oxide formation.
ii. Observation of an oxide coat
iii. Profilometer traces of surface build up on a substrate.
iv. Consistently lower contact angles are obtained on Al-Mg melts than with pure aluminium melts regardless of the substrate.

Hence the contact angle of the Al-Mg melts is more likely to reflect an interaction at the interface between aluminium and $MgAl_2O_4$ or at the very least to be associated with an interfacial oxide.

From the data generated from Al-Mg alloys with magnesia and spinel substrates, Wierauch [259] obtains a value for the 'true' $\gamma_{Al-Al_2O_3}$ interfacial energy at 800°C of $1.688 Nm^{-1}$ using Youngs equation (equation 4.1). The validity of this relationship for an oxide modified melt is questionable (Section 4.2). But using Young's equation with data obtained in this thesis for an oxide free melt, interfacial surface energies of 0.878 and $0.745 Nm^{-1}$ with contact angles of 45.5° and 51° are obtained respectively for aluminium and skimmed Al-Mg alloy on alumina substrates. It is suggested that magnesium affects the nature of the oxide formed on Al-Mg melts and causes the oxide to be non protective [263], hence the low contact angle values above. At high temperatures where the melt-substrate interface can display capillary penetration through the oxide film the contact angle falls rapidly. Low contact angles have been attained at 800°C by physically rupturing the oxide film [259] or by using sacrificial substrate coatings that react with the oxide [198]. Wall and Milner [206] report that molten aluminium alloys (Al-Cu, Al-Ni, and Al-Fe) will flow over an oxide in vacuum if the film is first mechanically punctured. Thus contrary to accepted theory and normal experience in vacuum, liquid aluminium alloys wet alumina.

In summary, aluminium and aluminium-magnesium alloy melts supporting negligible or very thin 'amorphous' oxide exhibit high surface energies for 'unoxidised' metal ($1.09-1.22 Nm^{-1}$) and low contact angles (55-70°). Both systems are quantitatively similar. With time the oxide film thickens and the surface energy of the melt, initially high, decreases. A surface energy of $0.865 Nm^{-1}$,

reported by a number of reseachers for molten aluminium [195,201], has been correlated with a thin monolayer of oxide [200]. Contact angles of this 'oxide modified melt' in contact with an oxide substrate are reported (Table 9.7) to be above 110° [194,195,198,201].

When the melt surface is rich is magnesium, the oxide develops faster (in comparison with pure aluminium) hence the surface energy of Al-Mg alloys will decrease faster. This may explain reports that magnesium additions decrease the surface energy of aluminium [186, 261,262]. The surface of aluminium and aluminium-magnesium alloy melts do not always decrease with time. Observations in this work have led to the proposal that formation of crystalline oxide produces cracks and pores in the surface oxide through which molten metal is transported. The molten metal wets the oxide and can exude into pores in the solid substrate forming a strong interfacial layer and making contact angles difficult to measure by sessile drop techniques [201,258,259]. As the surface oxide becomes wetted by molten metal, a thin oxide instantly reforms. This thin oxide will demonstrate the high surface energies and low contact angles observed initially.

9.3.3. The formation of exudations on a newly formed aluminium melt

It has been shown that if a path exists through the oxide a liquid metal penetrates its oxide coating. The surface energies are favourable for molten aluminium to wet alumina and this situation is observed in practice [206].

Examination of micrographs of the early stages of exudation in Figures 6.19b, 6.19c and 6.24a show that the oxide growths are typically 5μm in length and 2μm diameter. These obviously result from the oxidation of exuded melt.

From a knowledge of the surface energy it is possible to calculate the size of pore required to support these exudations or oxide and melt envelopes. Figure 9.25 is a schematic diagram of a newly formed oxide exudation and illustrates the forces acting during its growth.

Applying a longitudinal force balance gives:

$$2\pi\gamma_{Al/Al_2O_3} r_p = \rho_{Al}\pi r_e^2 g h_e + 2\pi r_e . t\sigma_{oxide} \qquad 9.15$$

For the radial force balance per unit length one obtains:

$$2\pi\gamma_{Al/Al_2O_3} r_p/\pi r_p^2 . 2r_e = 2\sigma_{oxide} . t \qquad 9.16$$

$$\text{i.e. } 2\gamma_{Al/Al_2O_3} r_e/r_p = \sigma_{oxide} . t \qquad 9.17$$

Solving these equations for r_p and t for both Al and Al-Mg exudations gives:-

r_p = 1.41 - 1.42μm radius and t = 6.65 - 6.67nm

Thus, this approach predicts a pore size in the region of 2.5 - 3μm which is consistent with the maximum width of metal penetration observed at the point of scale failure at the base of oxide nodules.

The vertical force balance, equation 9.15 is insensitive to surface energy. Calculation shows that if the crack in the oxide has a radius of 1.4$_\mu$m or above exudation will occur. If the size of the flaw is less than this value no molten metal will emerge. The limiting factor to the height of the exudation is the radial force acting horizontally. This radial force is sensitive to the surface energy and fracture stress of the oxide. Once a crack larger than 1.4μm appears on the newly formed oxide of the exuding column, secondary branching occurs. The extent of this secondary branching is also limited by the hoop stress. The large growths observed on aluminium and Al-Mg alloy melts develop from multidirectional exudations.

9.3.4. The proposed effect of fluoride and fluxes on the Al-Al_2O_3 wetting system

At this point, it is pertinent to consider the effect that fluxes with fluorides have on the wetting of the Al-Al_2O_3 system. It is generally regarded that a flux cover removes the surface oxide by chemical interaction and the oxide is incorparated into the flux layer. However, particularly at high temperatures, the surface beneath the flux cover will never be completely oxide free since oxygen can diffuse through the flux to react with the liquid aluminium alloy [206]. In this work, it has been observed that even in the presence of fluoride an oxide forms beneath any surface crystals that form (Figure 6.26, 7.13). Indeed the presence of fluoride accelerates oxide formation. Therefore, it is important to consider why, despite the plentiful oxide, large oxide growths do not form on the surface until the fluorine in the atmosphere is considerably reduced (Figures 6.27b and 6.27c).

Calculations with aluminium have shown that the criteria for exudations occurring is the presence of a flaw with a radius greater than 1.4μm. A molten flux or liquid phase can penetrate into any pores developing in the oxide, effectively sealing the cracked areas. Indeed there is evidence to suggest that a liquid phase forms on molten aluminium in the presence of gaseous fluorine or boron trifluoride (Figures 6.26d and 6.26e). On cooling, the aluminium surface is comprised of small, extremely dense γ -alumina crystals. In the fluorinated environment, rapid oxidation and the high crystalline density and small dimensions ensure that pathways as large as 2.8μm are unlikely to develop. Only when the oxide crystals increase in size as the concentration of fluoride decreases, do such pores develop.

The expression for radial force, equation 9.17, states that a change in the interfacial energy will be directly reflected in the fracture stress and thickness of the oxide. The interfacial energy of an AlF_3, sodium free flux is estimated to be above $0.650 Nm^{-1}$

[247,264]. Hence using Youngs's equation (equation 4.1) the interfacial tension between an aluminium melt and such a flux can be calculated. It is estimated that if pores develop in the oxide then secondary branching on exudations will only occur if the contact angle between the flux and aluminium is less than 44°. Above this value exudations will appear as single columnar entities, with diameters exceeding 2.8μm. Such structures are observed on aluminium-magnesium alloys oxidised in the presence of fluoride at 550°C and illustrated in Figure 7.34a. At 550°C the oxide development may be insufficient to provide the completely dense oxide layer which is exhibited at 750°C, hence pores develop. Single, unbranched growths are observed on aluminium melts oxidised in environments depleted of fluoride over 15-20h exposure as Figures 6.27b and 6.27c illustrate.

9.4. A MECHANISM OF ALUMINIUM AND ALUMINIUMN-MAGNESIUM ALLOY OXIDATION AND DROSS FORMATION

In this section, similarities of the oxidation behaviour of aluminium and aluminium-magnesium alloys (discussed in Sections 9.1 and 9.2 respectively) and the wetting characteristics (established in Section 9.3) are used to present one model for the oxidation of the solid and liquid aluminium system. In addition this model will be shown to be applicable to other aluminium alloy systems. Each step or stage is discussed and later summarised.

The first oxide film to form at room temperature in air on pure aluminium and aluminium-magnesium alloy is 'amorphous' γ-alumina. Beneath this film, at the 'amorphous' oxide-metal interface, crystalline oxides develop. It is suggested that a critical concentration or partial pressure of oxygen is required for crystalline nucleation to occur. If the 'amorphous' oxide remains continuous, then the speed at which sufficient oxygen reaches the oxide-metal interface is dependent on the thickness of surface oxide, the rate of diffusion and hence the temperature.

Gamma and alpha alumina are the principal crystalline oxides which develop on aluminium. Gamma alumina develops after a temperature dependent induction period during which the critical oxygen concentration necessary for nucleation to occur is established, this is usually above 475°C. As the temperature increases, the saturated water vapour pressure of the local environment and the surface oxide lowers. This encourages transformation of gamma to alpha alumina on molten metal at the oxide-melt interface.

The threshold temperature for crystalline oxide formation on aluminium-magnesium alloys is thought to be about 350°C. Transport of oxygen to the oxide-metal interface is increased by the presence of magnesium ions in the 'amorphous' γ-Al_2O_3 overlayer. This enhanced diffusion accounts for the absence of a temperature dependent induction period, characteristic of aluminium, with aluminium-magnesium alloys [102]. Crystalline oxide development on aluminium-magnesium alloys takes the form of a two stage reaction. Primary magnesia crystals nucleate and in conditions of severe magnesium depletion $MgAl_2O_4$ develops.

It is proposed, in agreement with current oxidation models for pure aluminium and for Al-4.2wt%Mg alloy [102] that the crystalline oxides formed by direct oxidation at the 'amorphous' oxide-metal interface, penetrate into the metal substrate. The depth of crystalline oxide penetration and therefore the size of developing crystals is dependent on the depth of the oxygen saturated layer throughout the entire oxidation period [60,76].

The original air formed film on aluminium grows to a terminal thickness of 2-4nm at 25°C [57] and rapidly thickens with temperature. At high temperatures, the height of the crystalline oxide can be greater than the thickness of the overlayer. Thus tips of crystals protrude from the surface and are seen as individual nodules. The 'amorphous' overlayer may accommodate the crystal penetration or may result in rupture.

This is not a new phenomenon. It is commonly observed that an oxide may be protective during the initial stages of oxidation but looses its protective properties during the later stages of reaction because of rupture and fragmentation of the oxide scale after it has reached a certain critical thickness. In such situations rupture is a consequence of a stressed metal-oxide interface. Such stress systems are often difficult to define.

During the oxidation of metals and alloys substantial stress develops either in the oxide film or metal substrate. The level of stress accumulates from several origins.

Stress may develop as the composition of either the metal or oxide changes near the interface as a result of oxidation. This is particularly relevant to the oxidation of aluminium-magnesium alloys with rapidly diffusing magnesium but may also occur in the oxidation of pure aluminium if, for example, oxygen diffuses readily into the metal substrate.

Stress can be induced in oxide films as a result of specimen geometry. Sharp points and angles or surface topography often occur after a polishing process for example, by cutting closely spaced valleys and troughs in the surface.

The change in volume of oxide crystals to the metal substrate is estimated from values of density. As Table 9.8 shows, the changes in density between the oxide crystals and metal are considerable and will result in compressive stress in the surrounding metal.

TABLE 9.8 Densities for aluminium and magnesium metal and oxide [273]

Metal	ρ	Oxide	ρ
Aluminium	2.7	γ - alumina	3.5-3.9
		α - alumina	3.97
Magnesium	1.75	magnesia	3.58
		magnesia aluminate	3.6

Internal stresses generated in the oxide can be dissipated by the deformation of thin metal specimens. Oxide stresses with large components or thick metal sections are not relieved in this manner and as a consequence may crack or lack adhesion at the oxide-metal interface.

On unskimmed melts oxide crystals nucleate in the heating up period before the metal becomes molten. The high stress that results is reflected in the rapid rate of oxide rupture exhibited in these surfaces in comparison with oxides developed on molten metal only. On molten materials the build up of stress is relieved by substrate deformation. However, when cylindrical specimens of aluminium and aluminium-magnesium alloys were used the melt is confined within the dimensions of the oxide envelope formed on the solid metal prior to melting. With cylindrical specimens the metal interface retreats from the initial outer oxide surface as oxidation progresses. If the oxide is to remain in contact with the metal substrate appreciable deformation of the scale will be required. If the scale does not have sufficient plasticity to follow the metal interface, porosity and lack of adhesion are reported to occur [274]. These effects of specimen geometry are demonstrated by the loss of protective oxide at the cylindrical specimen edges in this work (Figure 6.18f).

The ruptured oxide exposes a channel from the atmosphere through to the metal surface. In the literature rupture of the surface film has often been postulated as being responsible for rapid breakaway oxidation behaviour. Investigators have attributed oxide rupture to be a consquence of the development of small blisters which expose new metal. Although this condition occurs, blisters have only been reported from oxidation in humid atmospheres. As discussed above, oxide rupture occurs as a direct consequence of the build up of stress from several origins, but predominantly from oxide crystal growth, and is particularly relevant for the cylindrical specimens used in this work. Hence the stress relief takes the form of pinholes or small cracks appearing in the surface film.

In support of this proposal, both Wefers [134] and Field [102] postulate that the oxide film cracks in response to underlying crystal stress. Cochran et al [124] tried to encourage rapid oxidation by seeding a melt with oxide crystals, and breakaway oxidation occurred only when the film had been physically ruptured by the crystal.

The oxide channels allow rapid transport of oxygen to the metal. This is in agreement with theories of solid aluminium [134] and aluminium-magnesium [102] oxidation. For example, during the oxidation of solid aluminium-magnesium alloy regions between the growing 'primary' magnesia crystallites become depleted in magnesium. Further development of magnesia is therefore localised at sites of existing 'primary' oxides. Oyxgen can diffuse via short circuit paths down the primary oxide-metal boundaries and combine with magnesium. Thus magnesia stacks develop from the repeated nucleation and growth of primary crystallites at these specific sites. Complete coverage is achieved when crystals from neighbouring oxide stacks overlap, resulting in a corregated oxide-metal interface.

Field [102] suggests that any Al-Mg alloy substrate surrounded by oxide and depleted of magnesium remains trapped in the oxide film. Previous studies have also reported the presence of elemental aluminium in surface films of magnesia grown on Al-Mg alloys [123, 125]. Thus it is generally held that oxidation of molten aluminium [122] and molten Al-Mg [124] alloy follows the proposed solid-state mechanism but proceeds at a very rapid rate. A greater quantity of oxide is thereby formed and is thought to correlate with the large weight gains observed. This however, does not account for the considerable size of oxide growths that develop and for the high proportion of trapped metal that is observed in dross layers on aluminium and aluminium alloy melts. More than 50% of the oxide layer may consist of trapped metallic aluminium. It is this combination of metal and oxide which is known as dross.

In this study it is shown that liquid metal is transported through cracks in the oxide film. As molten metal emerges from the surface into the atmosphere, an 'amorphous' oxide film instantly covers the exposed metal. This results in the appearance of spherical metal-containing structures protruding from the original oxide overlayer.

For molten metal to exude through the surrounding oxide, liquid aluminium must wet alumina. Such behaviour is in contrast to most early research from studies mainly determined by the sessile drop method, which involves measurements of the profile of a molten aluminium drop under argon or in a vacuum. It has been clearly demonstrated that formation of oxide on molten aluminium in argon and dry environments is not negligible. Thus the wetting system is of molten aluminium modified by a thin oxide film and in carrying out aluminium wetting studies the nature and thickness of the oxide must be taken into consideration.

Using a surface tension balance, the surface tension of 'oxide-free' aluminium is calculated to be $1.088 \pm 0.04 Nm^{-1}$. The corresponding contact angles formed with the melt and alumina are estimated to be 53-56°. These values are in excellent agreement with those of current publications. [186,194,198]. The results imply that the presence of a thin alumina scale accounts for the non-wetting of alumina by molten aluminium. Once this surface film is broken, the aluminium wets alumina.

Calculations show that if this oxide crack has a radius above 1.4μm molten metal exudation will occur. The balance of forces on the exudation limits the height reached. Secondary branching can occur but is sensitive to surface energy and the fracture stress of the oxide. At the new oxide-metal interface of the envelope which instantly forms around the molten metal structure crystallites develop and may be associated with some stress. This is a consequence of rapid oxidation rates and temperatures enhanced by vigorous exothermic surface reactions. Secondary exudations occur where a break or flaw greater than 1.4μm develops in this new oxide film. Thus molten metal exudes through any resultant failure sites. The process is repeated as oxidation progresses hence exudations do not appear as single columnar entities but are highly branched and multidirectional. On molten aluminium metal exudations and surface growths appear as long as failure sites occur in the oxide overlayer. The number and size of these structures increase with exposure time. A scheme of this sequence of oxide development is given in Figure 9.26.

The presence of magnesium greatly increases the rate at which oxidation takes place. If the oxide is thin and mainly 'amorphous', as found on a skimmed Al-Mg melt surface, the surface tension of the melt ($1.1 - 1.2\ Nm^{-1}$) and corresponding contact angles (55-60°) formed between the melt and aluminium are numerically equivalent to that of molten aluminium also modified by a thin 'amorphous' oxide film. Further, in response to the large crystallites which rapidly develop on Al-Mg alloy melts, rupture frequently occurs and the metal containing growths rapidly cover the surface.

As the magnesium content of the alloy decreases, formation of magnesia slows. The metal most severely depleted in magnesium will tend to be trapped in the oxide growths. This condition favours formation of spinel magnesium aluminate, thus the volume of trapped metal in the nodule decreases as the metal is consumed by spinel formation. This continues until all magnesium is in the form of $MgAl_2O_4$.

9.4.1 Modifications to molten metal oxidation behaviour using atmospheric control and alloy additions

The proposed mechanism for dross formation may be used to rationalise why breakaway oxidation is reduced or delayed using atmospheres with water vapour and fluoride or with beryllium additions to the Al-Mg alloy.

It is reported that hydroxyl ions improve the mechanical integrity of 'amorphous' anodic γ -Al_2O_3 films [275] and 'amorphous' films on aluminium-magnesium alloys [102].

Field [102] used mechanical data of anodic γ -Al_2O_3 films generated by Grosskreutz [275] in Table 9.9 to estimate the maximum possible deflection of the 'amorphous' film prior to fracture under dry and humid conditions using the expression below:

$$\delta = \frac{1.5\sigma_f P^2}{E\ d} \qquad 9.18$$

TABLE 9.9 Mechanical properties of 'amorphous' anodic γ-Al_2O_3 films tested at atmospheric pressure and in vacuo [275]

Atmosphere (KPa)	E Youngs Modulus (NMm^{-2})	σ_f Fracture Stress (MPa)
101.3	$5.36 \pm 2.67.10^{10}$	178
1.3×10^{-7}	$2.09 \pm 0.67.10^{11}$	257

For a film thickness d of 10nm, primary oxide crystal diameter P of 100nm and values of the fracture stress σ_f, of 'amorphous' alumina taken from wetting studies, the maximum deflection of oxide prior to fracture δ is calculated from equation 9.18 to be 8.7 ± 0.2nm in humid conditions. In dry conditions only a small oxide displacement of 2.2 ± 0.05nm is possible before fracture occurs. The errors of these figures are likely to be greater than estimated, as the data used is from room temperature measurements with anodic films 300nm thick. Further, equation 9.18 predicts that as the dimensions of the primary oxide decrease the sensitivity of the film to cracking increases, this is in direct contrast to observations from this work. However comparison of the fracture stress of the anodic film in vacuo is well within reported values of the bulk oxide (Table 9.5) and this analysis demonstrates the dramatic effect of water vapour. The 'amorphous' film will tolerate about 4 times more deflection in the presence of water vapour than in conditions of extreme dryness.

This thesis has demonstrated that such behaviour is a reflection of the degree of crystallinity of the oxide film which influences the amount of mechanical deformation possible. In dry environments, the film is predominantly crystalline and exhibits mechanical properties of the bulk crystalline oxide. When the

'amorphous' nature of the oxide film is extended by water vapour and crystallinity is low, the film can deform to a greater degree before fracture occurs. The system is dynamic and a constant supply of water vapour delays the nucleation of disruptive oxide crystals. Tests show that by preheating in humid air some protection is achieved for many hours after the all available water vapour has been consumed. The exact mechanism by which crystal growth is delayed is uncertain.

Hydroxyl ions are readily adsorbed on the surface of developing oxide films, and the migration of protons seems energetically more favourable than the transfer of oxygen ions. Hence transport through the film is slowed considerably by the absorbed hydroxyl layer or by large hydroxyl ions which become incorporated in the film as an integral part of the alumina. In the presence of water vapour longer periods are necessary for favourable conditions to be established at the interface for crystal nucleation to occur. The concentration of hydroxyl ions on surface adsorption sites or incorporated in the surface oxide film is reduced by the absorption of hydrogen ions into the metal. Hence on molten metal, in addition to the raised temperature, the rate of crystalline nucleation is dramatically increased by rapid hydrogen absorption into the melt. Alternatively, hydroxyl ions or protons act as bridges and bonds holding the disordered 'amorphous' material together restricting areas from becoming ordered by crystalline growth.

In the presence of fluorides, preferential adsorption of fluorine or fluoride derivatives at the surface prevents the stabilisation of the 'amorphous' film by hydroxyl ions. Hence oxide nucleation at the oxide-melt interfaces rapidly occurs. Increased surface temperatures arising from the exothermic reaction of fluorides ensure that oxide development is rapid. Thus on molten aluminium transformation of γ-alumina to α-alumina readily occurs and the oxide crystals are characteristically small and dense. Channels through the oxide to the melt above 1.4μm are rarely found.

Where sufficient fluoride (or chloride) is present in the atmosphere, reactive fluoride derivatives are readily available at the surface. If it is thermodynamically favourable, dense crystalline MgF_2 or AlF_3 layers are formed on Al-Mg and aluminium melts. Evidence suggests that fluorine readily combines with aluminium or magnesium ions in a protective liquid phase. Thus any fine cracks and pinholes are sealed as they are generated and the melt is never exposed. Sulphur hexafluoride and boron trifluoride may produce such liquid phase protection on magnesium melts [276].

In the literature, additions of trace elements to otherwise pure aluminium and Al-Mg alloys are reported to be either inhibitors or enhancers of oxidation rates and weight gains. A summary is given in Table 9.10.

TABLE 9.10 Summary of the effect of trace elements on aluminium and Al-Mg alloy

Substrate	Oxidation Inhibitors		Oxidation Enhancers	Details in section
	Surface Additions	Additions to the metal		
Al		Be	Mg, Li, Ca, Na, Zn	3.3.1b 3.3.2a
Al-Mg	B,C	Be Ca Ti Na	Li, Zn	3.5.3

Ions such as Ca, Na, OH^- may become incorporated in the oxide structure by substituting for Al^{3+} ions [60,102]. The result of such a mechanism is unclear but the defect structure of the oxide may be modified by vacancy compensation or from lattice strain. Small ions such as beryllium and boron are easily incorporated in vacant lattice sites and interstitial positions influencing diffusion pathways and rates of oxidation.

The low density of beryllium ensures that any additions will concentrate in the surface layers of an alloy melt, and is readily available to preferentially form beryllia. Flat beryllia plates lie parallel to the alloy substrate [102]. Thus mechanical damage to the 'amorphous' film from growth stresses or other disruptive effects of the crystalline oxide is minimal and does not readily occur during oxidation over 20h in dry environments at 750°C. As the quantity of beryllia increases beyond complete surface coverage, the alumina film may rupture as a result of increased stress. The BeO plates may still restrict diffusion or direct exposure of the melt.

These trace elements additions and atmospheric influences which modify the oxidation behaviour are used in chapter 10 to suggest improvements for reducing the level of dross obtained during industrial melting practice.

9.4.2 The oxidation behaviour of molten aluminium alloy systems

This proposed mechanism of molten metal exudation accounts for the large quantities of metal that are incorporated in the dross layer of melt surfaces while supporting present theories on solid state oxidation. Further, it is proposed that oxide growths will develop where any liquid aluminium phase exists under an 'amorphous' γ-Al_2O_3 layer and oxide discontinuities exceed 1.4μm.

Aluminium alloy systems can be divided into two extreme behavioural types groups according to the rate at which molten metal exudations are displayed on the surface during oxidation: Those that remain protective over long periods of time, for example pure aluminium and Al-Mn alloys and those in which the oxide surface rapidly becomes non protective and is quickly covered by numerous growth structures.

In the literature reports of observations of growths on pure aluminium melts are unobtainable. This is not surprising as the period of exposure required to obtain numerous growths on molten aluminium in combustion environments is beyond that usually encountered in industrial practice.

Alloys of aluminium-manganese behave in a similar manner to pure aluminium under oxidation. Manganese does not form a preferential surface oxide and the phase diagram (Figure 9.27) shows a liquid phase forms only above 660°C. It is anticipated that growths develop only after long exposure times. This behaviour has been confirmed using Al-1%Mn (3003) alloys oxidised at 750°C in gettered argon and is illustrated in Figure 9.28.

Many authors record the existence of metal filled growths forming on the surface of Al-Mg alloy melts during breakaway oxidation [77,111]. Field [102] did not observe any metal filled growth structures on solid Al-Mg surfaces exposed for 5h at 550°C. His specimens were however thin, flat sheets which can deform to relieve stress. It is predicted that growths would develop over longer exposure times.

Rapid diffusion of lithium dominates the oxidation behaviour of aluminium-lithium alloys, in a similar manner to the preferential oxidation of magnesium in aluminium-magnesium alloys. Rapid diffusion of lithium to the alloy surface enhances crystalline oxide development at the oxide-metal interface. The oxide ruptures as a consequence of the high stress and volume change rapidly

experienced at the interface. Surface temperatures are particularly high due to the exothermic nature of the oxidation reaction. The phase diagram (Figure 9.21) shows that where lithium concentrates at the surface, the melting point is lowered. Hence at 580°C, a liquid phase may be expected. Field [102] observes numerous eruptions at the surface of aluminium lithium alloy in the presence of water vapour. The growths increase in size as oxidation proceeds. Field attributes these structures to hydrogen blisters, however it is proposed that the growths are a consequence of molten metal oxidation according to the mechanism proposed in this thesis.

CHAPTER 10 - RECOMMENDATIONS FOR INDUSTRY - METHODS OF REDUCING DROSS FORMATION ON ALUMINIUM AND ALUMINIUM-MAGNESIUM MELTS

The mechanism of dross formation has developed from a study of the oxidation of clean, cylindrical specimens of pure aluminium and aluminium-magnesium alloys under carefully controlled laboratory conditions. The question arises, are these results valid for the very different situations encountered in industrial practice?

Over the melting period, a molten bath with scrap aluminium-magnesium alloy will not reach the limit of magnesium depletion to the extent of spinel formation as experienced with the thin section material used in this work. Thus if the supply of magnesium is effectively unlimited, a high rate of magnesia formation will continue to the end of the exposure period. Specimen geometry and dimensions have an effect on oxidation rates. The cylindrical specimens used produce internal stresses in the oxide which are considerably higher than found in the oxide on thin flat surfaces. Scrap aluminium material however, will undoubtedly carry surface oxides with a history of considerable deformation and damage. Material exposed to high temperatures during charging whilst above the melt and unsubmerged will be vulnerable to further oxidation.

A high proportion of scrap stocks are baled beverage cans [30]. Standard beverage cans are thin walled Al-1%Mg-1%Mn (3004) alloy with thicker ends of Al-5%Mg (5182) alloy, covered with paint, lacquer and drink residue. Analysis shows the presence of significant proportions of iron, silicon and titanium and contributions from trace additions and impurities. The role of trace additions in the development of the first formed oxide overlayer and on transport and diffusion through the film is currently inadequate for estimating oxidation behaviour.

An investigation was carried out using contaminated beverage cans as described, oxidised under the same conditions as the Alcan materials. After 5h at 550 and 750°C weight losses were recorded from oxidation of the thin side walls due to the removal of paint and lacquer. A white titanium rich oxide coat remained. At 750°C the molten metal collected into a small pool, leaving a skeletal structure of this oxide coat. At the lower temperature of 550°C the oxidised surface of the can wall (Figure 10.1a) appears distorted and crumpled, characteristic of stressed oxide films developed in the solid state on Al-1%Mg alloys observed in Figure 7.1a.

The thicker gauge material used for can ends is almost free of the manufacturers painted logo, hence weight gains are achieved with oxidation at 750°C. The oxide surface consists of oxide nodules and large oxide growths composed of nodule clusters demonstrative and characteristic of liquid metal oxidation. The oxidised surfaces of can ends at 750°C are shown in Figures 10.1b and 10.1c. This investigation provides valuable support for the proposed mechanism of dross formation and its direct application in industrial practice.

According to the proposed mechanism the initial stage of dross formation is the appearance of metal containing growths at the oxide surface. To stop these growths forming, the surface film must remain free of cracks and holes. Methods of delaying rapid oxidation should be aimed at encouraging the formation of a low-stressed surface oxide film during the first stages of heating. Conversely, if it is accepted that damage or exposure will take place, then a means of providing an alternative protective coating should be considered. To examine these influences three independent possibilities are considered:

1. Extend the protection period of the 'amorphous' film.

2. Provide a new protective surface.

3. Enhance the protective nature of the 'amorphous' film.

1. Extend the protection period of the 'amorphous' film

The use of trace additions can extend the period of protection by delaying the formation or reducing the size [102] of oxide crystals at the oxide-melt interface. This route is at present not viable from two aspects. In dealing with scrap material, close attention to the individual concentration of one trace element with respect to the others throughout the entire heating and melting process is difficult practically and economically. Also, much research is necessary to develop this work as a viable proposition.

Alternatively, trace additions may be used to encourage preferential oxidation, so that the oxide crystals which nucleate at the oxide-melt interface are replaced by a non disruptive oxide such as beryllia. The protection period of the oxide film is thereby enhanced. Beryllium is well known for its toxicity, and despite its effectiveness its use in foundries is not recommended if alternatives exist.

There are some indications that the crystal size is modified by the rate of heating and the vigour of surface oxidation. The faster the reaction and higher the surface temperature, the smaller the crystal size. Hence less stress is introduced into the surface oxide film and the chances of oxide damage are reduced. For example, this behaviour is observed in atmospheres containing fluorides.

2. Provide a new protective surface over the damaged 'amorphous' film

Fluorides are formed at the surface from the rapid surface adsorption of fluorine and fluoride derivatives. Conditions however need to be thermodynamically favourable and in this respect surface temperatures and quantities of fluoride are critical. There is evidence that a liquid fluoride phase develops at the surface which will penetrate and effectively seal any cracks in the oxide as they develop. With liquid phases breakaway oxidation is restricted, but the use of fluoride fluxes is detrimental to the equipment and working atmosphere of the foundry. Further, although fluorides encourage rapid development of α-alumina, particularly on molten aluminium, this oxide development is of sufficient quantity that the objective of minimalising metal loss will not be met.

There is no evidence to substantiate or disprove the proposal that surface adsorption of water molecules or hydroxyl ions generates an ultra thinlayer of hydroxide. If a coherent protective surface is provided it is of insufficient quantity to be detected by the transmission electron microscope hence this claim remains speculative.

3. Enhance the protective nature of the 'amorphous' film

The simplest, most effective way of delaying breakaway oxidation in this work, was obtained by covering the surface with an atmosphere heavy with water vapour. In tests, it was observed that the water vapour present in most atmospheres is sufficient to delay nucleation of oxide crystals. It is important however, that this atmosphere has access to the melt surface and is not shielded or stagnant.

Exposure of the melt surface to humid atmospheres at high temperature conditions the developing oxide. This treatment is found to be sufficient to delay the onset of breakaway oxidation for a substantial time period once the molten state is reached and the water vapour is consumed.

It is advisable to keep the melt surface tranquil and encourage factors which aid the formation of a continuous, self-healing surface film. However with this approach a dilemma arises in that if scrap material is covered by an oxide film which is difficult to rupture, the removal of molten metal from within the oxide envelope becomes extremely difficult. Since aluminium wets alumina it may be aniticipated that if oxide cracks and fissures are encouraged then, once molten, the melt acts as its own flux penetrating through the cracks in the oxide. The empty oxide envelopes in the melt will then combine together at the surface. In recognition of this predicament the following melting procedure is suggested.

When heat treating any aluminium or aluminium-magnesium components for minimal oxidation it is sufficient to ensure that the metal surface is in the path of a flowing humid atmosphere. Similarly the surface of molten baths should remain tranquil and in direct contact with water vapour. It is suggested that heat from the main furnace and combustion gases are mixed with water vapour and channeled off to preheat scrap in a separate furnace or side well. Thus volatile paint, lacquers and residues are removed without disturbing the melt surface.

Following this preheating stage, it is recommended that the oxide be cracked, prior to charging the melt. This may be achieved by rapidly cooling the oxide. The charge may be externally transferred from the preheating furnace to the melting bath ensuring the temperature of the charge drops. Small volumes will rapidly cool and can be transferred on a continuous line. Alternatively the metal can be preheated in a side well with ultrasound to encourage oxide damage.

Once submerged, the separated oxide can be brought to the surface of the molten bath by the stirring action of electric currents, gentle enough to leave the surface undisturbed. The atmosphere above the melt can be dried so that once the oxide is ruptured, hydrogen absorption is less dramatic. Also if dross rapidly increasesat the surface, it may be more suitable to lightly skim the surface in a dry environment to reduce further trapping of metal.

Currently most furnaces are equipped to accommodate these changes to readily test these suggestions. The simplicity of this approach superceeds requirements for critical attention to trace elements in scrap melts and for stocks of raw materials for additive purposes. The opportunity for removing toxic materials such as beryllium and fluorine from the foundry, thereby increasing lifetime of equipment and cleaning the working atmosphere is particularly encouraging.

CHAPTER 11 - CONCLUSIONS

1. On pure aluminium γ-alumina or η-alumina nucleate at the oxide-metal interface in the first formed 'amorphous' oxide film. Crystals grow laterally until they touch, then the monolayer thickens. At longer exposure times α-alumina develops.

2. The oxidation behaviour of molten aluminium alloys containing 1 to 5%Mg is dominated by the preferential oxidation of magnesium. At 750°C the magnesium oxidises rapidly, irrespective of the percentage in the alloy, greatly increasing the rate of oxidation in comparison with pure aluminium.

   Coarse primary magnesia crystals nucleate at the oxide-metal interface, and fine secondary magnesia crystals develop in the first formed 'amorphous' alumina film. As the magnesium content decreases formation of $MgAl_2O_4$ is favoured. In low-magnesium containing alloys or areas severely depleted in magnesium, rapid conversion through magnesia to spinel ($MgAl_2O_4$) dominates. If oxidation progresses still further α-alumina develops.

3. For both aluminium and aluminium-magnesium alloys, formation of oxide crystals beneath the protective 'amorphous' film is associated with considerable stress, primarily due to volume expansion. The 'amorphous' film deforms to accommodate the growing crystals. As the degree of crystal growth and stress increases the likelihood of oxide fracture increases. Cracks and pathways through the oxide allow oxygen transport to the interface which increases crystal growth at these sites.

4. Oxidation rates of molten metal are increased dramatically by breakaway oxidation behaviour. This is associated with molten metal exudation through cracks (with a radius above 1.4μm) on aluminium and Al-Mg alloy melts. At the surface, protruding metal is trapped in the oxide envelope which subsequently develops. This structure is described as an oxide growth.

5. The thickness and condition of the oxide film modifies the surface energy of the melt. The surface energy of unoxidised liquid aluminium is calculated to be $1.09Nm^{-1}$. The interfacial energy between aluminium and a 10nm thick 'amorphous' alumina film at 750°C is calculated to be $0.748Nm^{-1}$ and when free of surface oxide the molten aluminium wets alumina.

6. The surface energy of unoxidised aluminium-magnesium at 750°C is equivalent to that of unoxidised pure aluminium. The mangesium encourages increased crystallisation and oxide thickening and the resulting reduction in oxide fracture stress dominates any change in surface energy that magnesium has on the melt.

7. The oxide-melt interfacial energy is sensitive to the fracture stress of the oxide. When flaws in the oxide on the protruding structure exceed 2.8μm further exudations take place resulting in secondary and tertiary growths. The resulting structure is a complex network of oxide and trapped metal.

8. The oxide growths increase in number and size with time. Their appearance is believed to be associated with the onset of breakaway oxidation and is the initial stage of dross formation.

9. On solid Al-Mg alloys, sufficient magnesium builds up at the surface to reduce the melting point below that of the homogeneous alloy. In these areas liquid phase oxidation and formation of molten metal exudations are observed.

10. A substantial amount of oxide development takes place on solid metal during the heating up period. The level of oxide development is far advanced on specimens preheated in the solid state to 750°C to those formed on a skimmed melt. Such oxides are not directly comparable. With aluminium-magnesium alloys the effect is more dramatic, since skimming the melt depletes the surface of magnesium and lower oxidation rates result.

11. The condition and morphology of the first formed oxide determines the oxidation rate of the molten metal. Thus the oxidation of molten aluminium and aluminium-magnesium alloys at 750°C is influenced by the surface finish and preparation of the specimen prior to oxidation.

    On pure molten aluminium the onset of rapid oxidation increases as the degree of specimen preparation increases. Breakaway oxidation is delayed on polished and grain-refined aluminium-magnesium surfaces oxidised at 750°C in comparison with machined and non grain-refined specimens.

12. Adsorption of water vapour at the surface stabilises the 'amorphous' film and greatly reduces the rate of oxide crystallisation. Preheating Al-Mg specimens for 5 hours at 750°C in a humid atmosphere sufficiently preconditions the oxide so that on exposure to a dry, oxygen free environment breakaway oxidation is delayed for over 20 hours. Thus dross formation is decreased by melting in the presence of water vapour.

13. Fluorides are adsorbed at the surface in preference to water vapour hence the rate of oxide crystal formation is extremely rapid. On aluminium and Al-Mg surfaces small, densely packed crystals of α-alumina with AlF_3,and magnesia with MgF_2 crystals develop respectively. A liquid phase may provide the surface protection. Thus molten metal exudation and dross formation is reduced in the presence of fluoride.

14. Beryllium preferentially oxidises at Al-Mg melt surfaces forming a beryllia layer which causes minimal disruption to the surface 'amorphous' oxide. As little as 50ppm of beryllium in Al-4.5%Mg prevents breakaway oxidation for 20h in gettered argon at 750°C.

CHAPTER 12 – PROPOSALS FOR FURTHER WORK

1. In view of the significance and importance to oxidation of the 'amorphous' film formed on aluminium and aluminium alloys it is of great benefit to obtain a clear understanding of the nature and 'structure' of this film. To expand the oxidation model further studies are required to understand the mechanism by which additional elements modify the amorphous layer. Oxide films can be generated on melts and pure 'amorphous' or γ-alumina impregnated with the required elements for study. Surface spectroscopy (ESCA), high resolution TEM and resistivity measurements can be used to fully characterise the film. The influence of incorporated elements can be eludicated from comparisons of mechanical properties of the oxidation of such films.

2. To protect the melt from rapid oxidation the surface oxide film must be defect free and possess a high fracture stress. Hence a study of the effect of oxide grain size on mechanical strength will be of industrial significance. This study can be extended to correlate the metal grain size with the growth of the first formed surface film and subsequent oxide grain size reached.

3. The present design of the surface tension balance provides the opportunity to broaden determinations of surface tension by other techniques, namely by sessile and pendant drop methods. A light source of variable intensity at the opposite end of a camera assembly enables shadow images of the specimens to be viewed and recorded throughout the entire experimental procedure. Images monitored over a long interval reveal changes in drop profile with time. The alumina support rod provides an excellent platform to carry out the sessile drop experiments and also acts as a fixture for a compression cage holding an oxide plate which provides a measure of the fracture stress of a thick oxide. An

expression relating the compressibility of a liquid (or an oxide-free melt) to the surface tension is described by Padday [214]. The combination of these techniques will provide considerable data which will lead to increased understanding of the wetting behaviour of oxide free and oxide modified aluminium and aluminium alloy melts.

4. More work is required to be conclusive about the effect of magnesium on wetting. It is felt that further work should be carried out on unskimmed Al-Mg melts. In order to control the growth of the oxide,humid atmospheres and water soaked substrates are recommended. If no precautions to control the oxide are taken the oxide development will be too great.

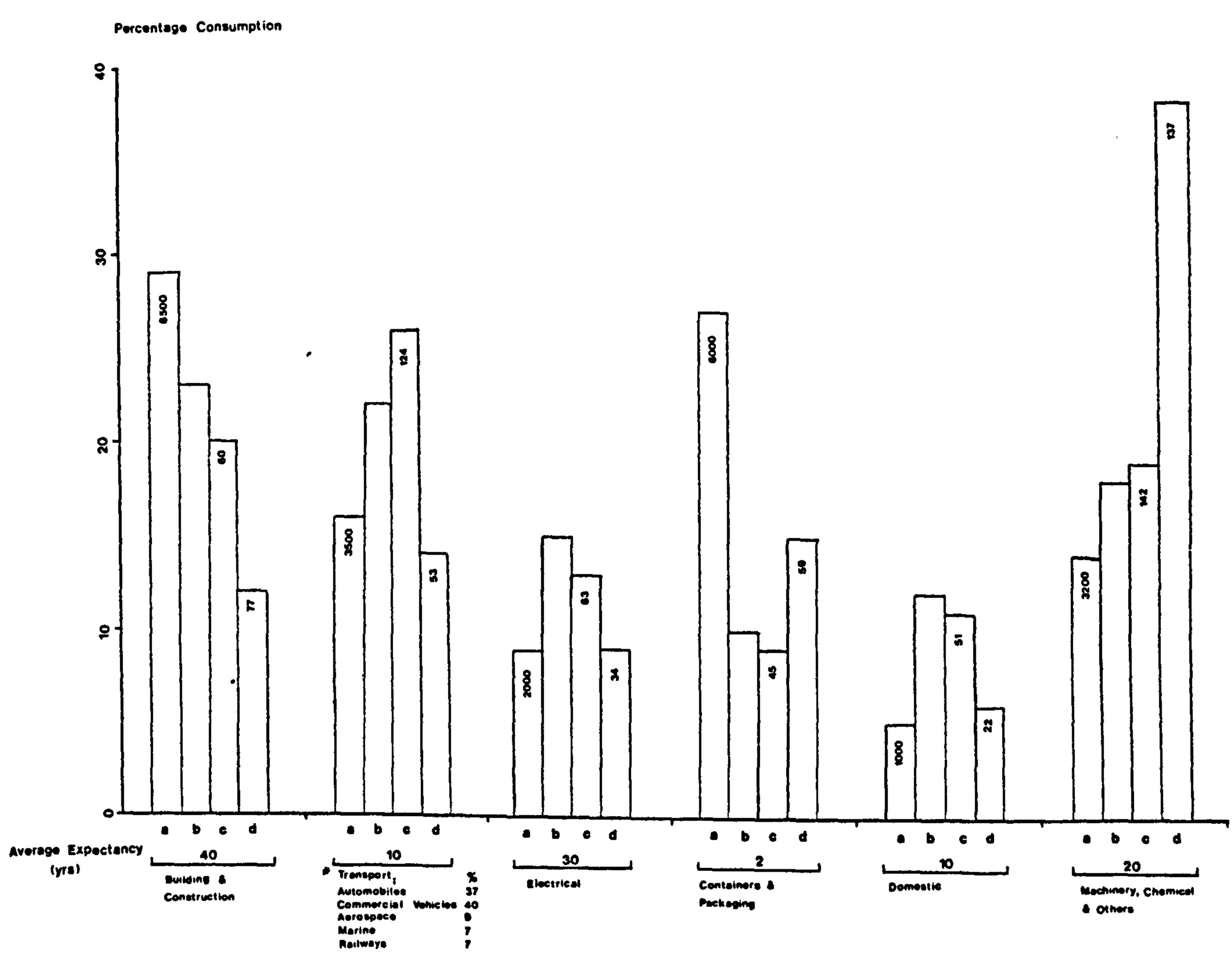

a. World Consumption 1986 (thousand tonnes)

b. Developing Countries 1986

c. U.K. 1976 (thousand tonnes)

d. U.K. 1986 (thousand tonnes).

Figure 1.1 Consumption of primary and secondary aluminium by end use [4]

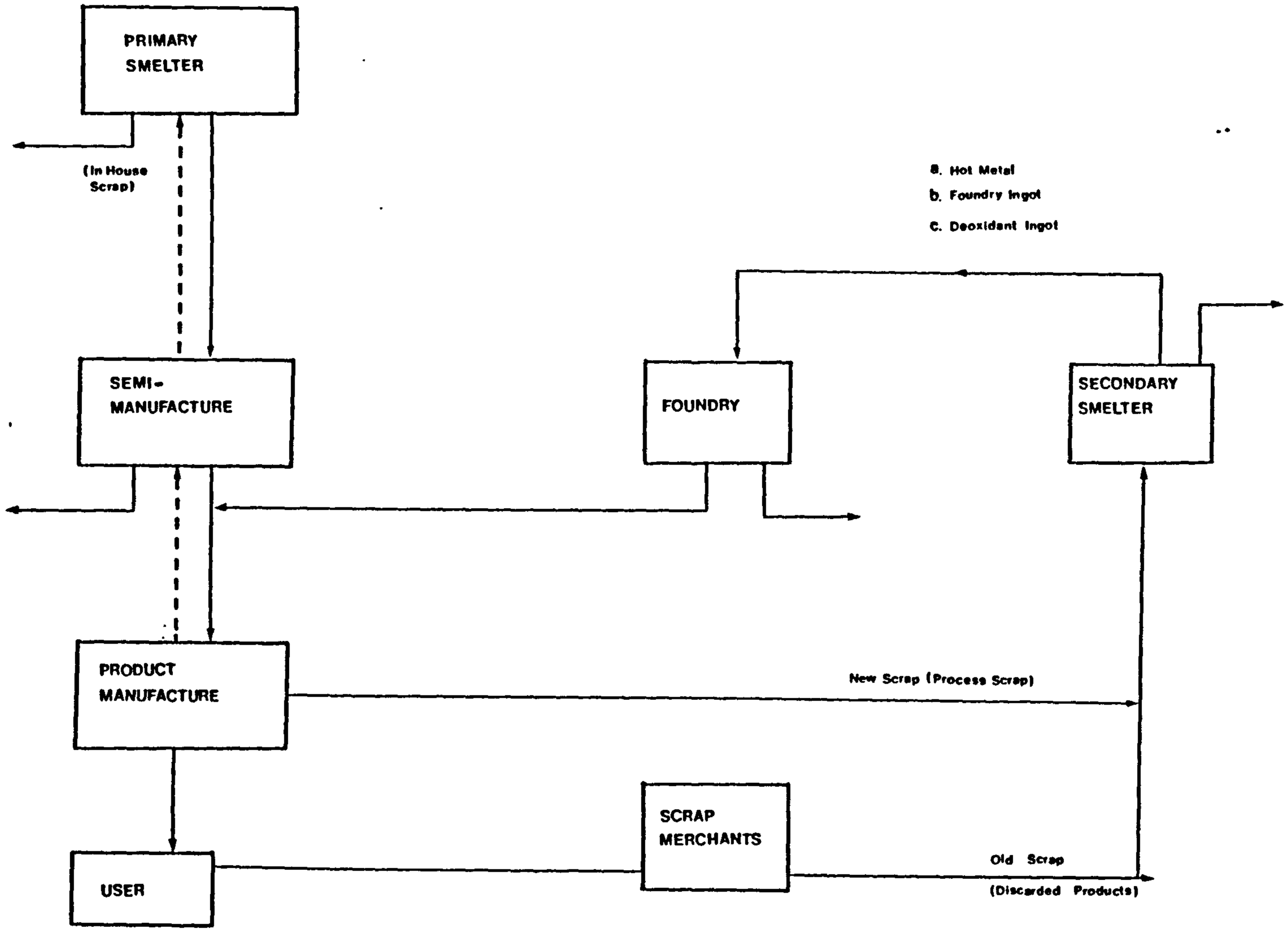

Figure 2.1 The route of aluminium [after 17]

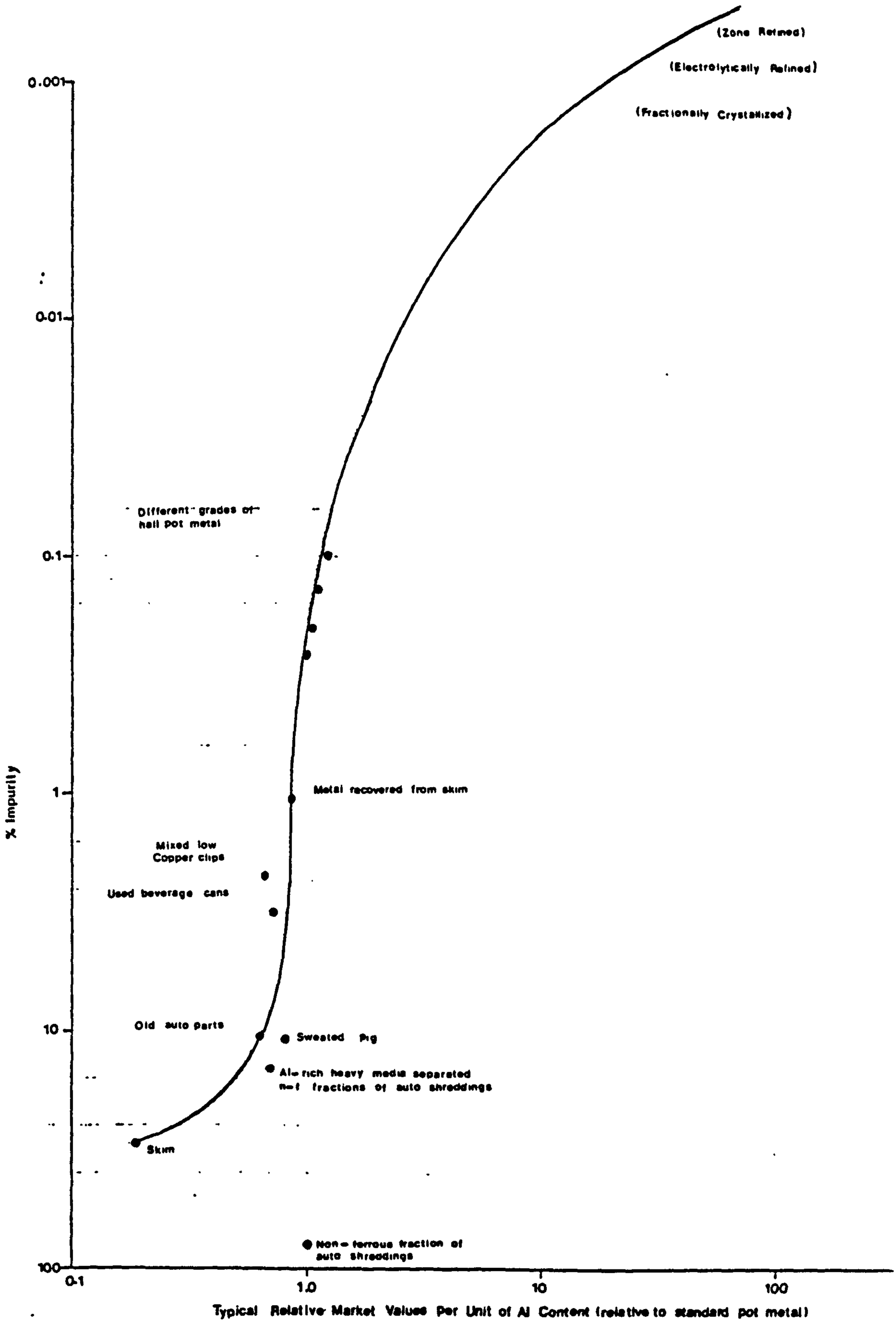

Figure 2.2 Relative market value-impurity relationship for aluminium [28].

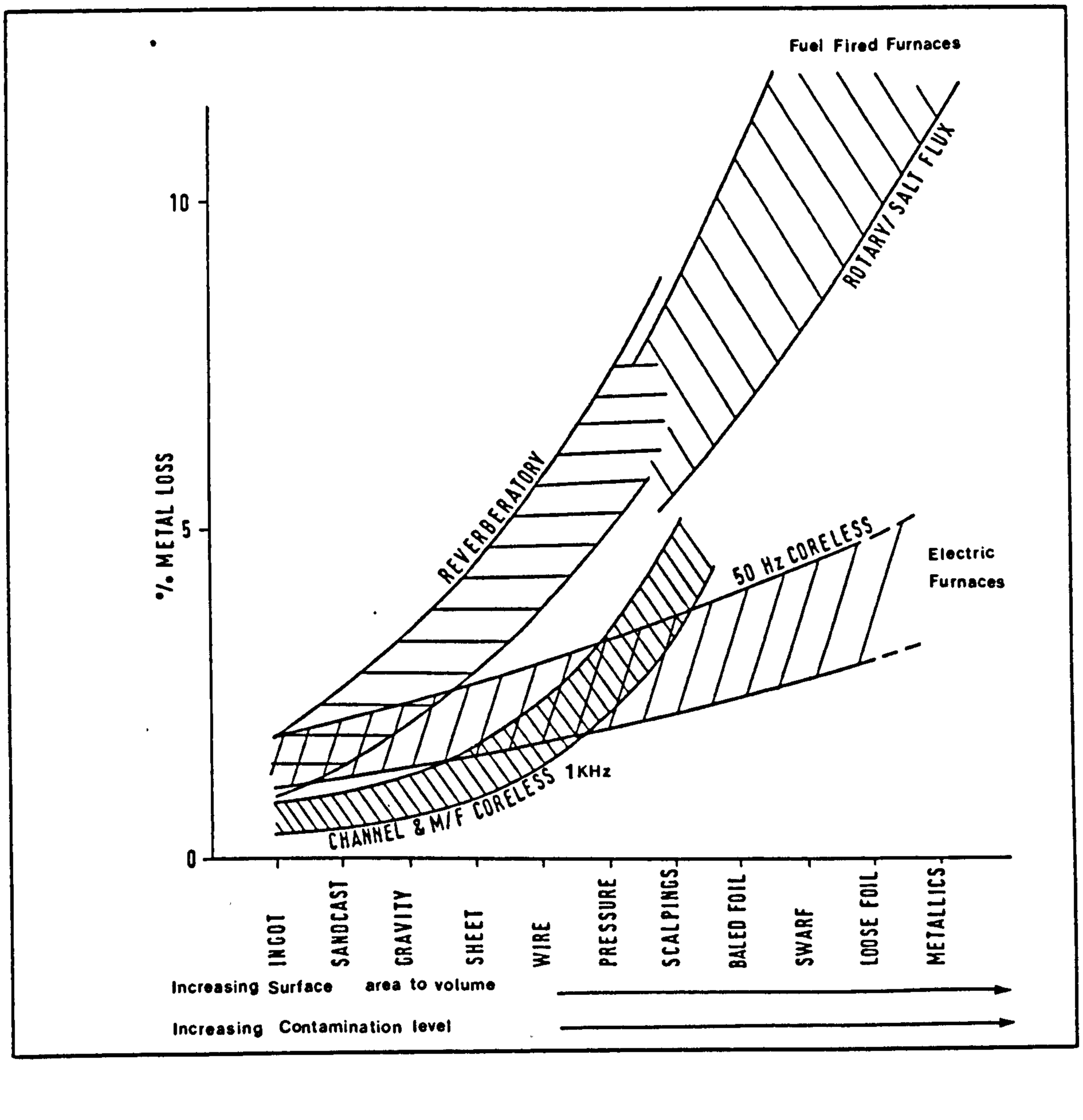

Figure 2.3 Metal loss with scrap form by furnace type [24]

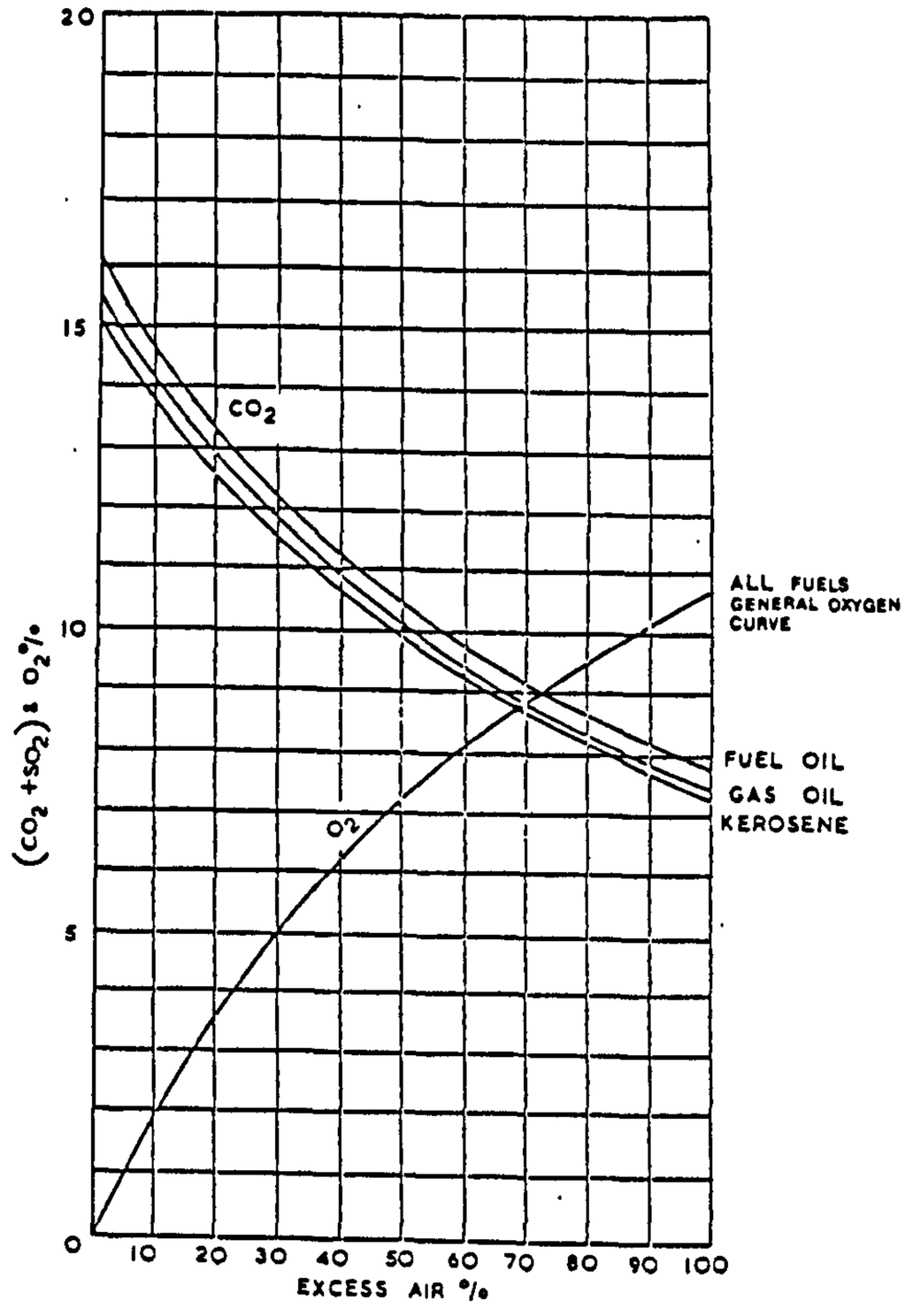

Figure 2.4 Relationship between air and carbon dioxide content in flue gas [27]

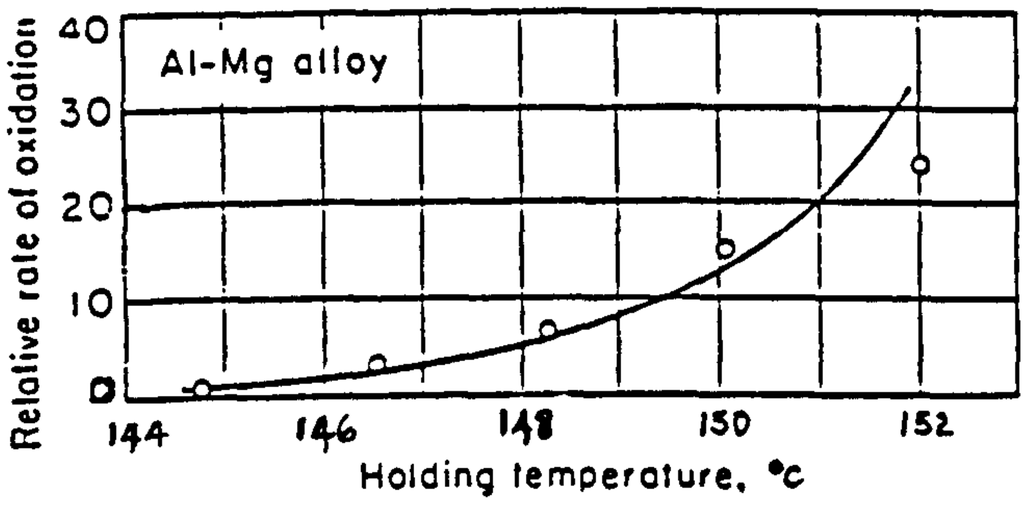

Relative rates of oxidation are based on total weight of oxide generated (insoluble in NaOH), with amount at 144 °C being assigned an arbitrary value of one.

Figure 2.5 Effect on holding temperature on the oxidation rate of molten Al-Mg alloy [36]

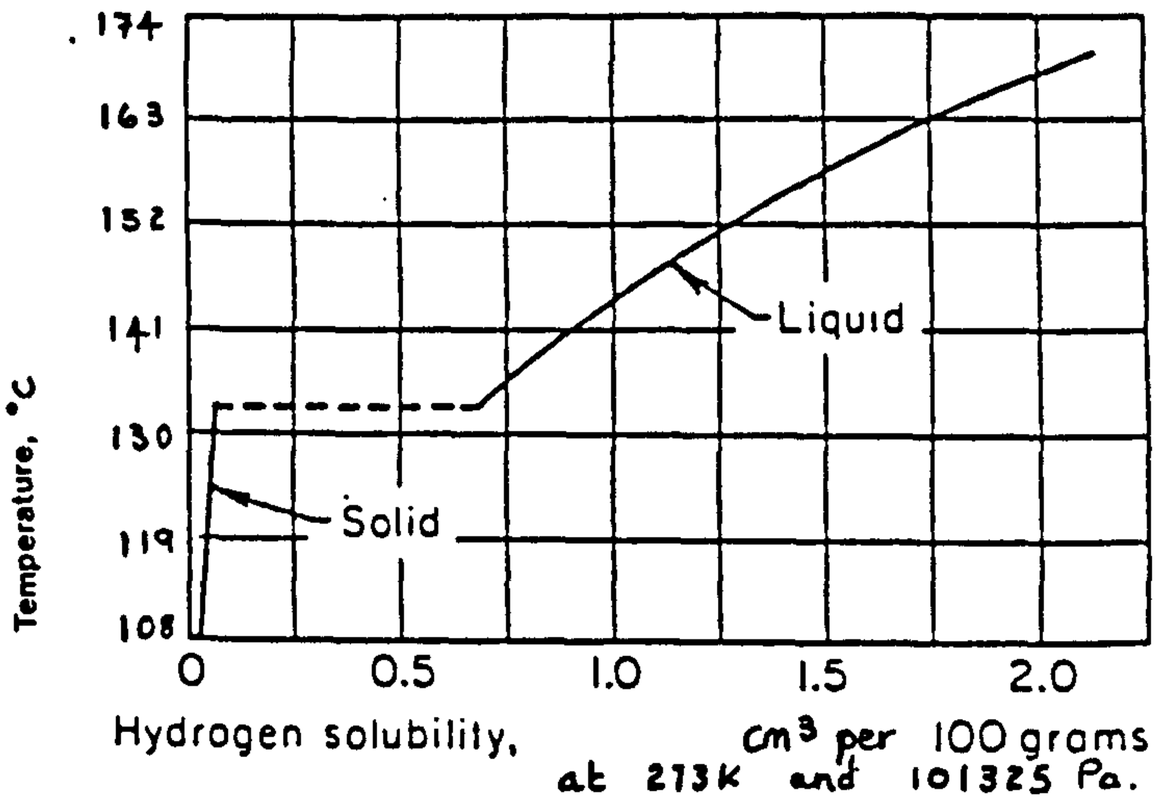

Figure 2.6 Solubility of hydrogen in aluminium [31]

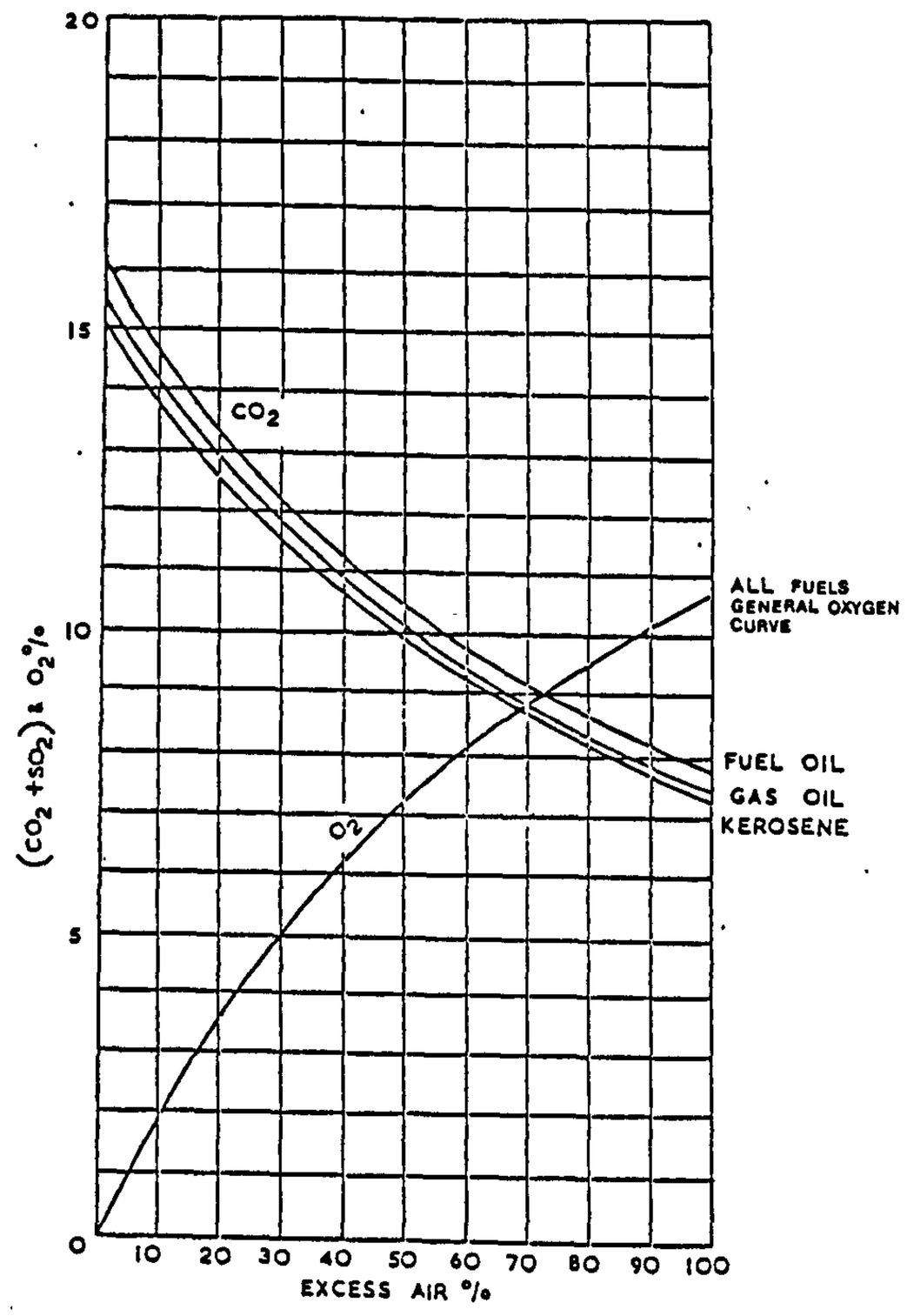

Figure 2.4 Relationship between air and carbon dioxide content in flue gas [27]

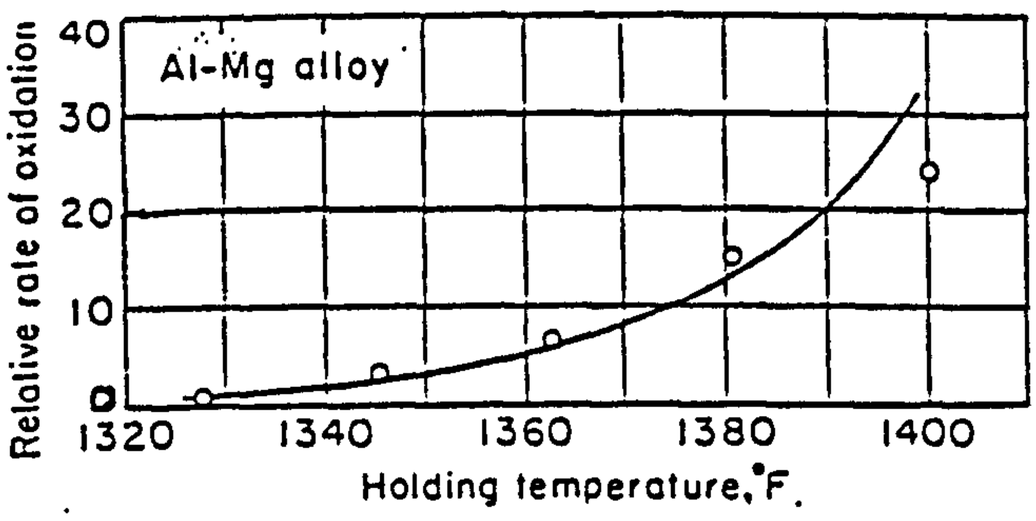

Relative rates of oxidation are based cn total weight of oxide generated (insoluble in NaOH), with amount at 1328 F being assigned an arbitrary value of one.

Figure 2.5 Effect on holding temperature on the oxidation rate of molten Al-Mg alloy]36]

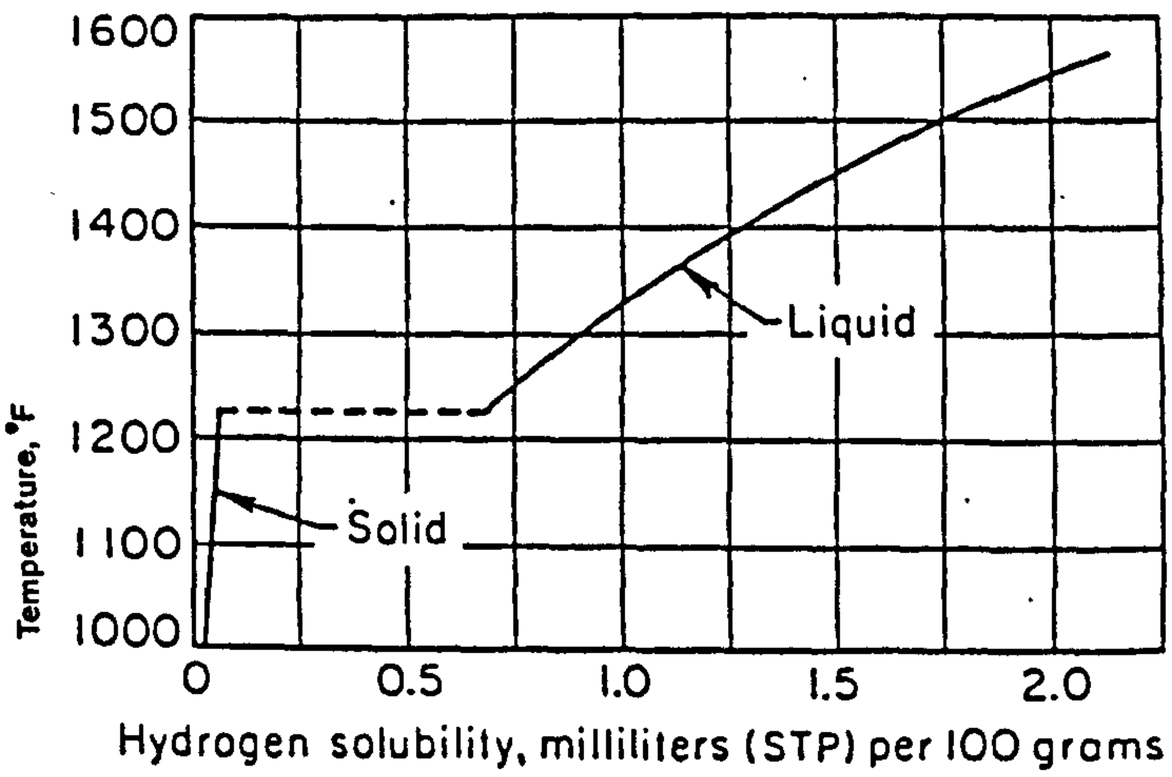

Figure 2.6 Solubility of hydrogen in aluminium [31]

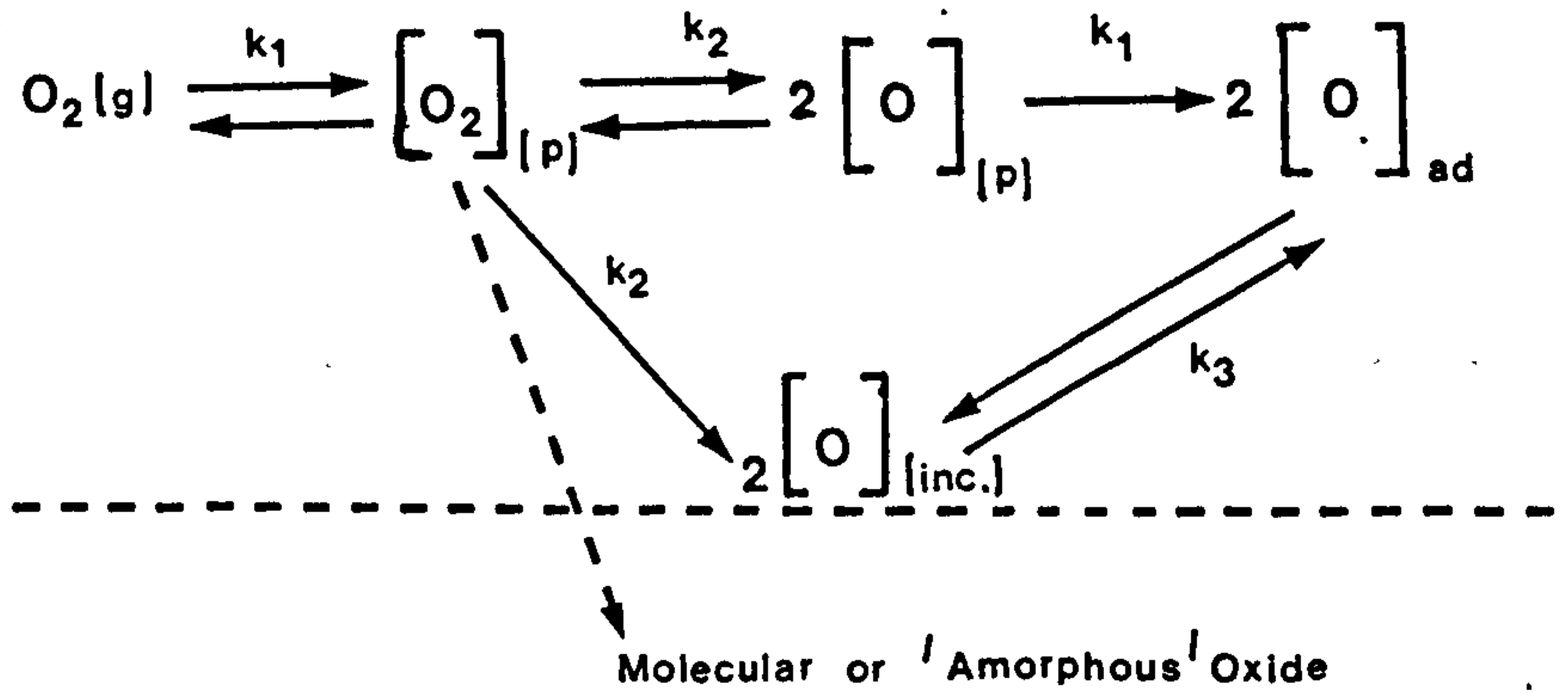

Figure 3.1 Interaction of oxygen with an aluminium (111) crystal Face [56]

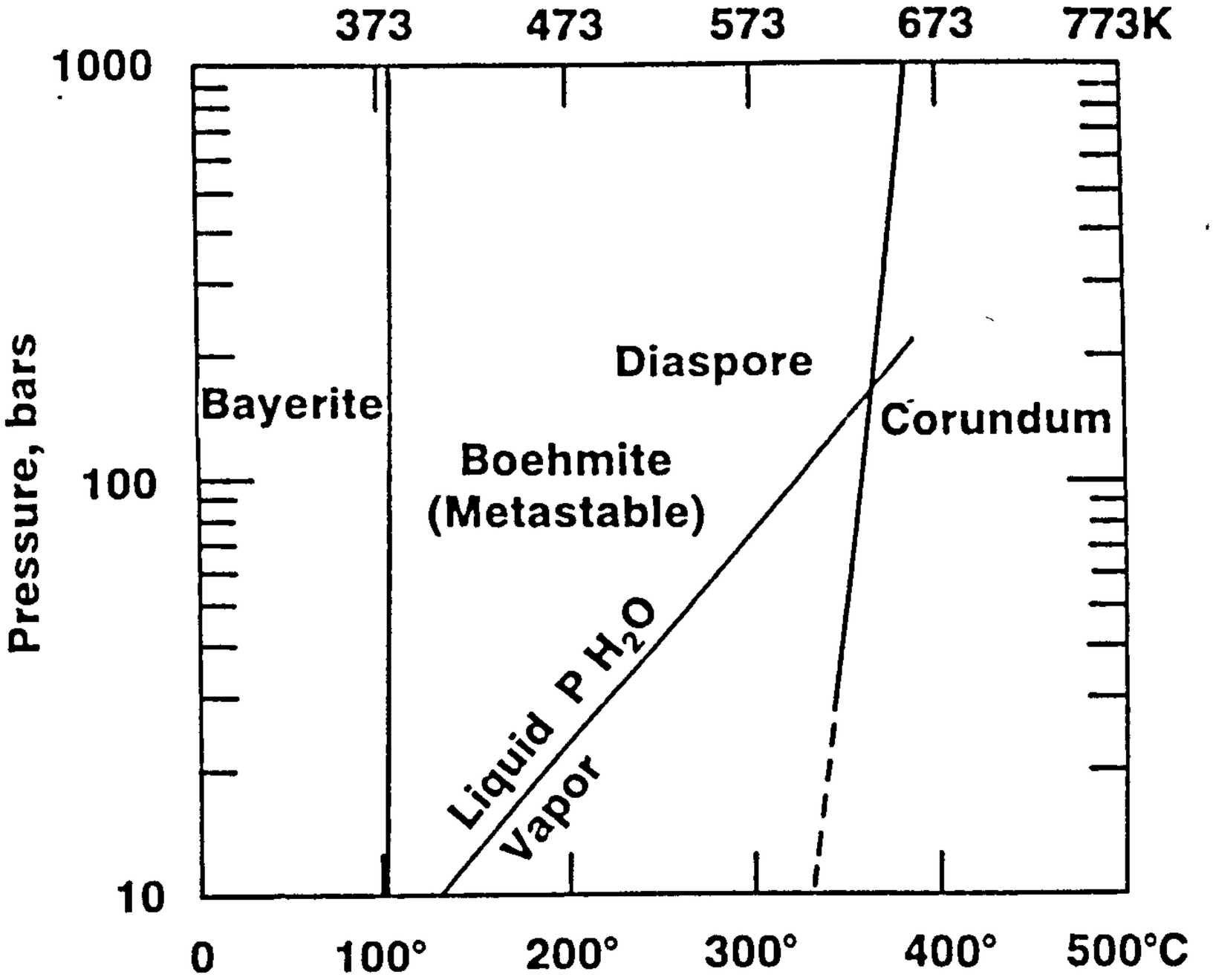

Figure 3.2 Phase relations in the Al_2O_3-H_2O System [57]

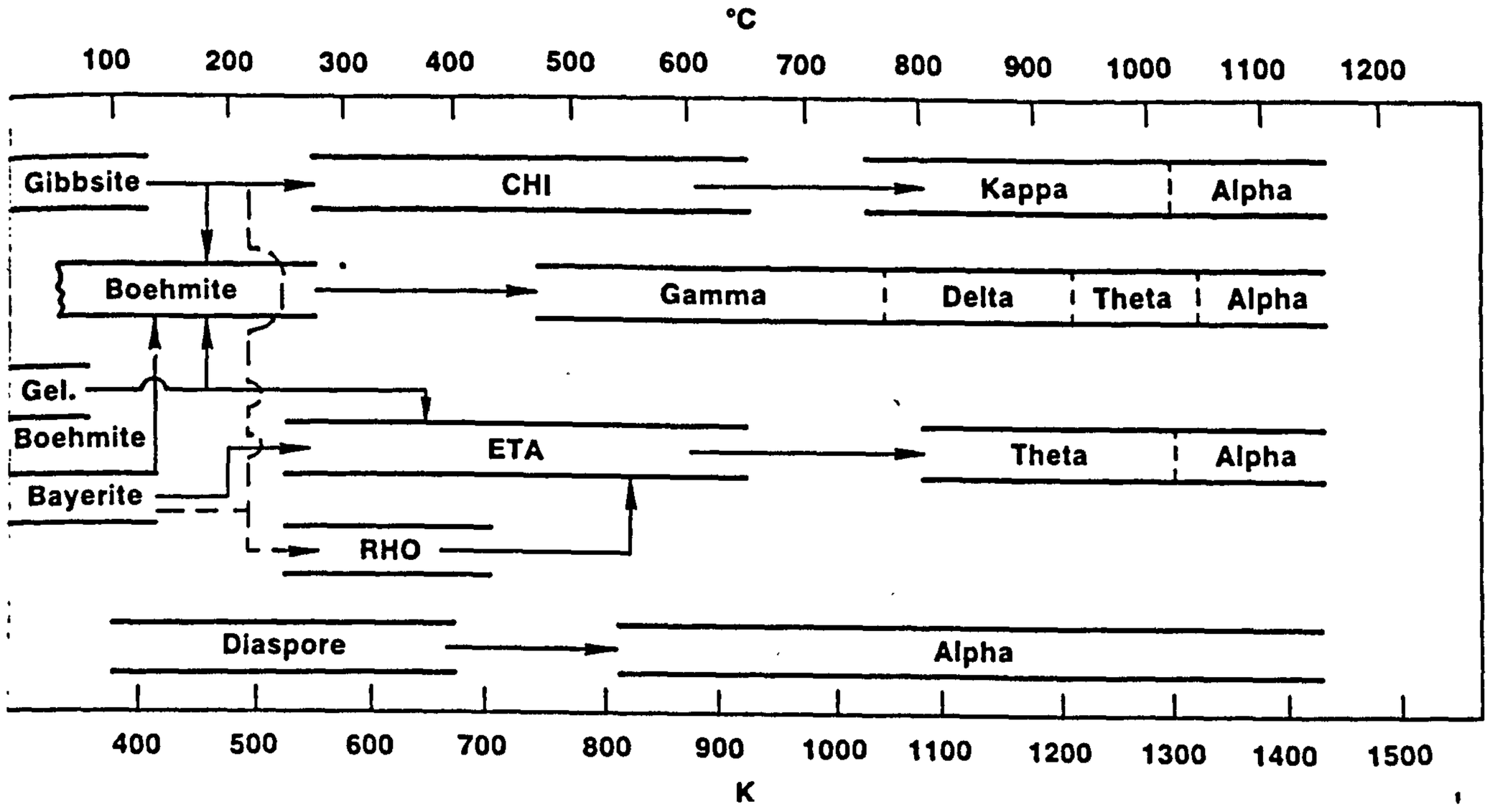

Figure 3.3 The $Al(OH)_3$-- Al_2O_3 transformation sequence [57]

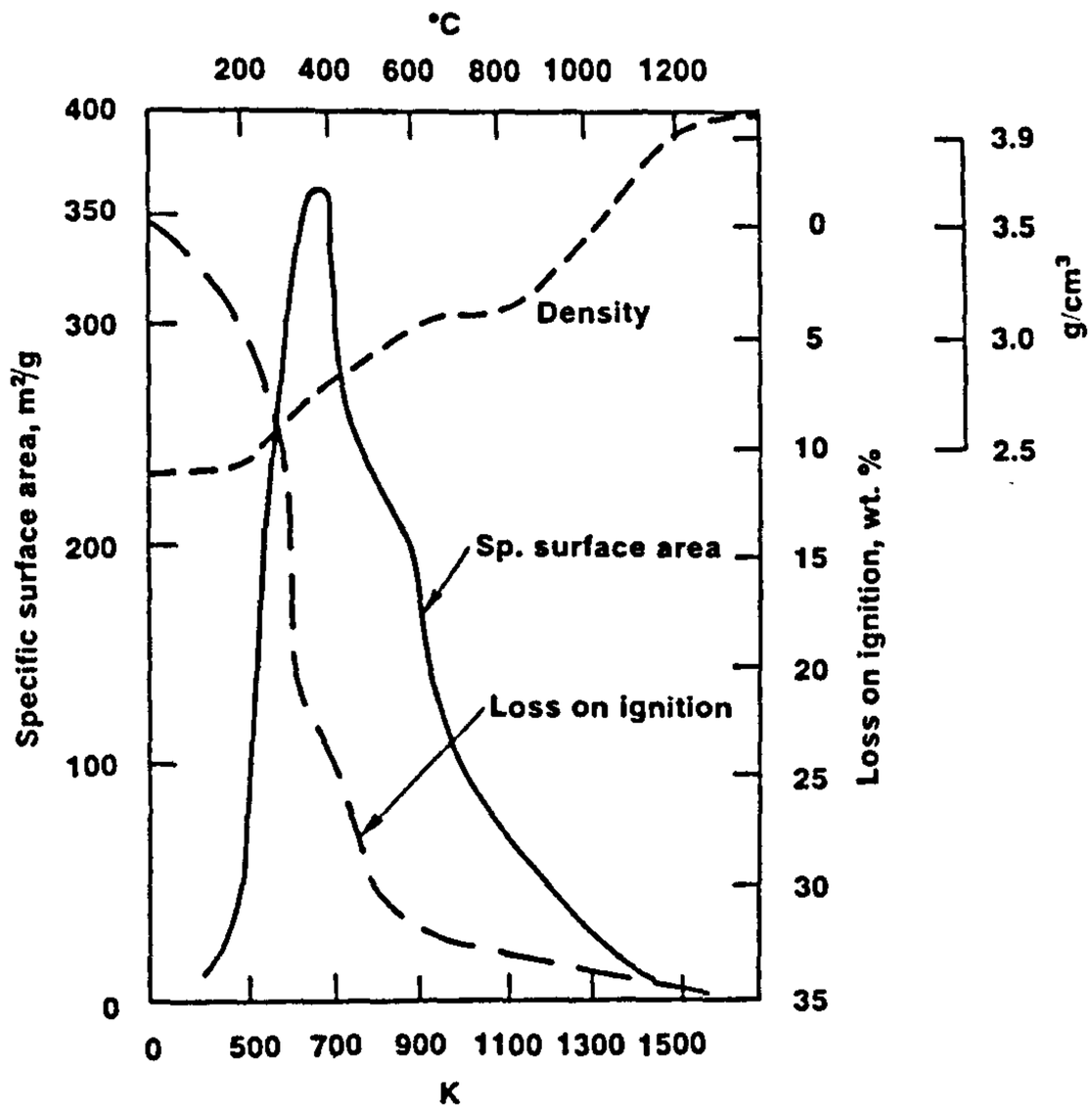

Figure 3.4 Changes in specific surface area, water content and density of heated $Al(OH)_3$ [57]

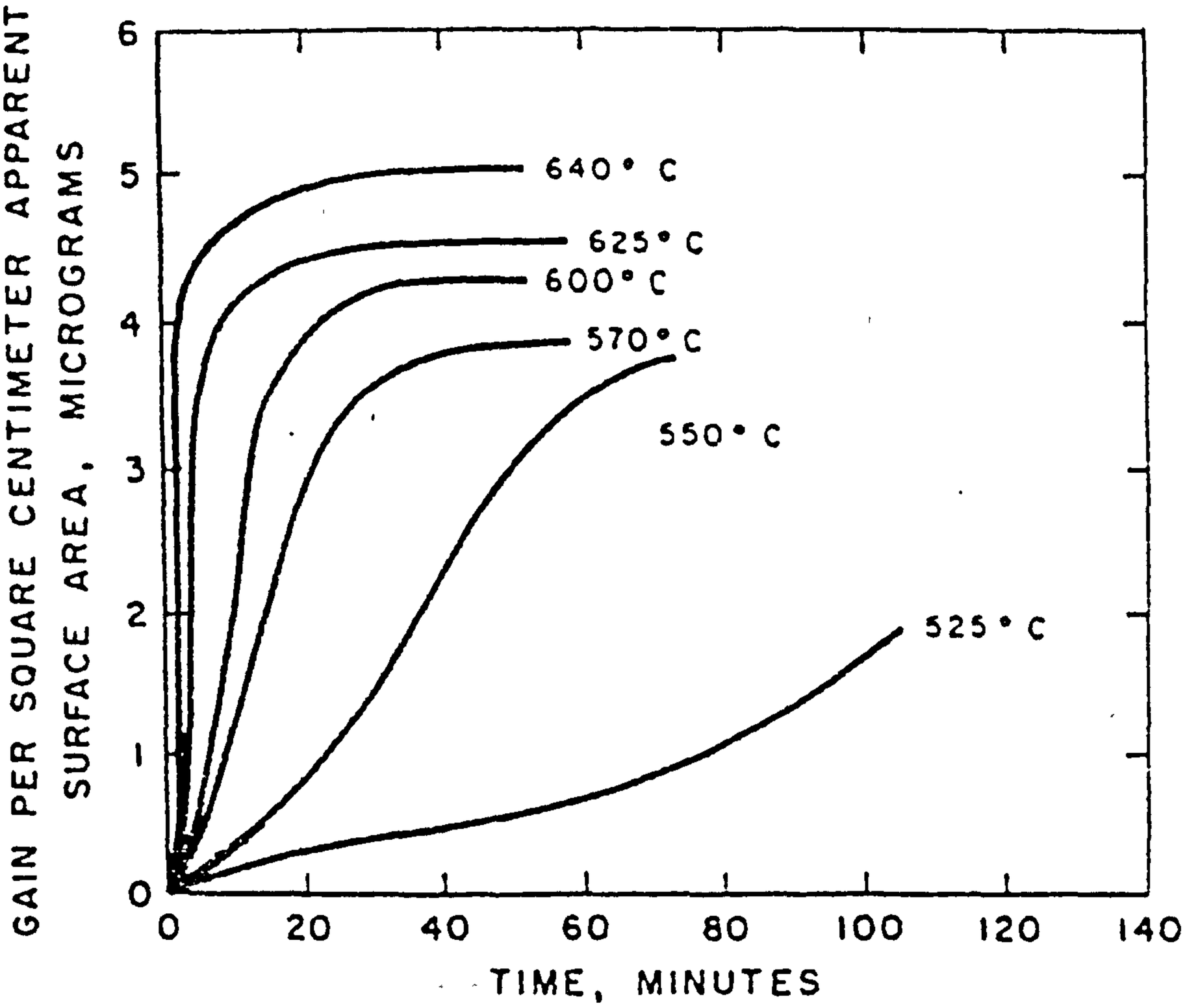

Figure 3.5 Oxidation of high purity aluminium in dry oxygen [77]

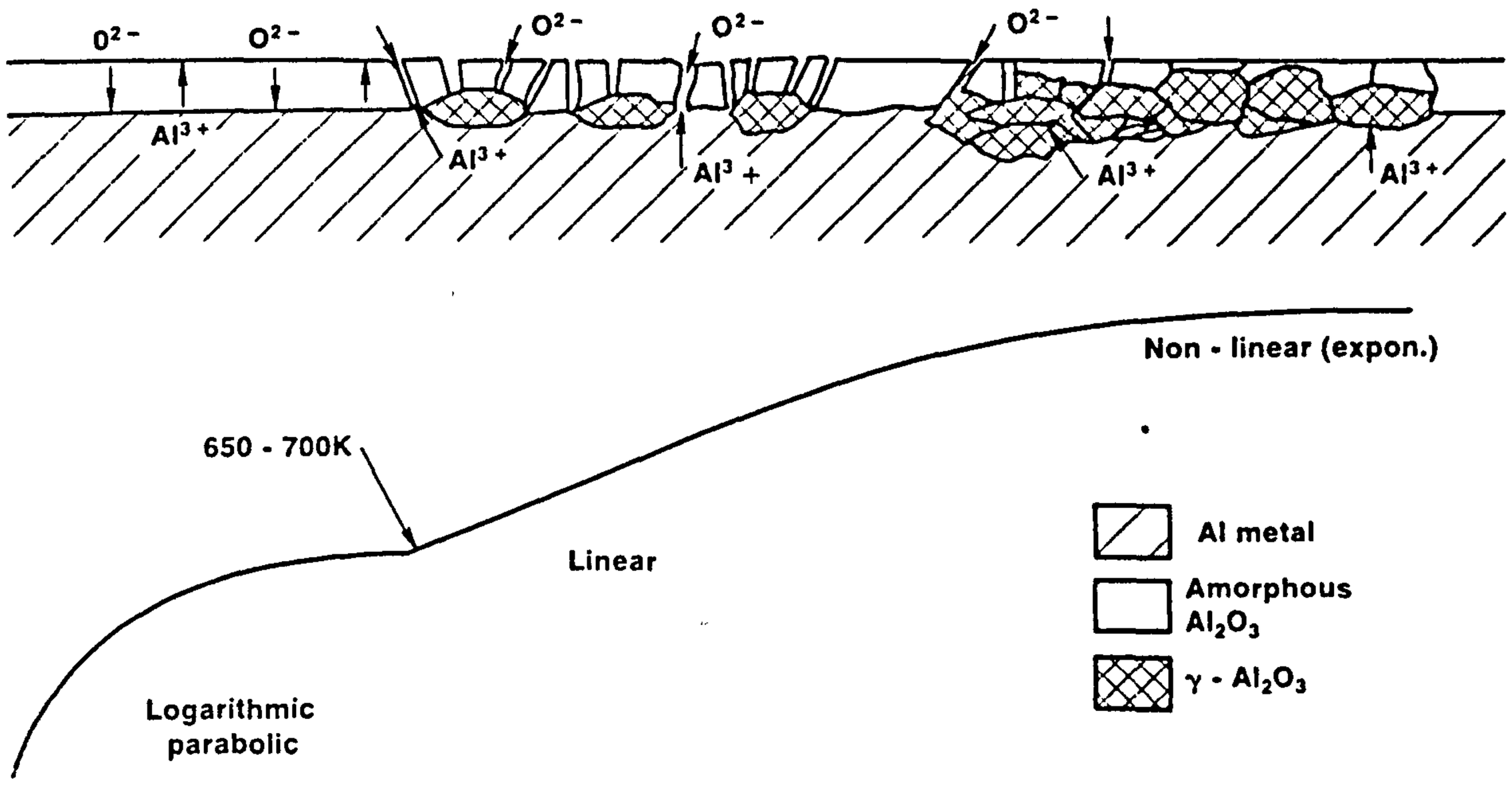

Figure 3.6 Growth and transport mechanisms of thermal oxides, schematic [77]

Fig 3.1

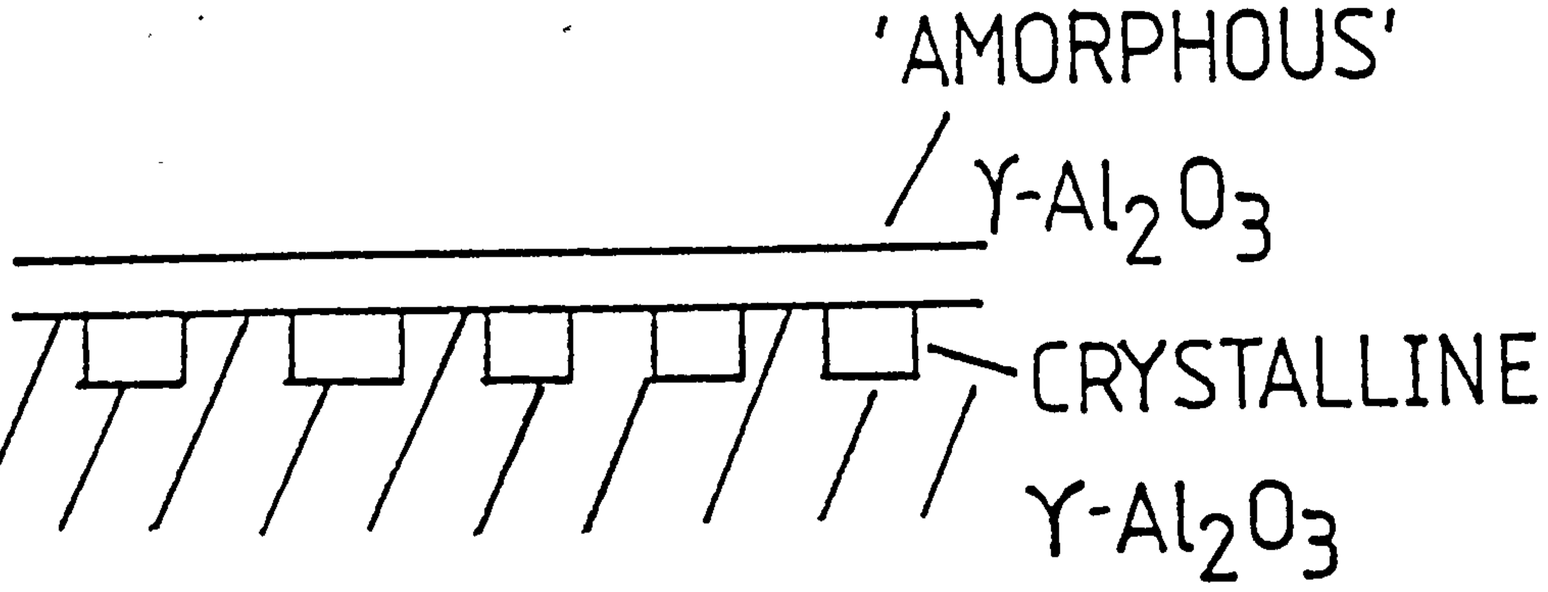

Figure 3.7 Schematic of the oxide film structure of pure aluminium following the nucleation and growth of crystalline γ-Al_2O_3 [102]

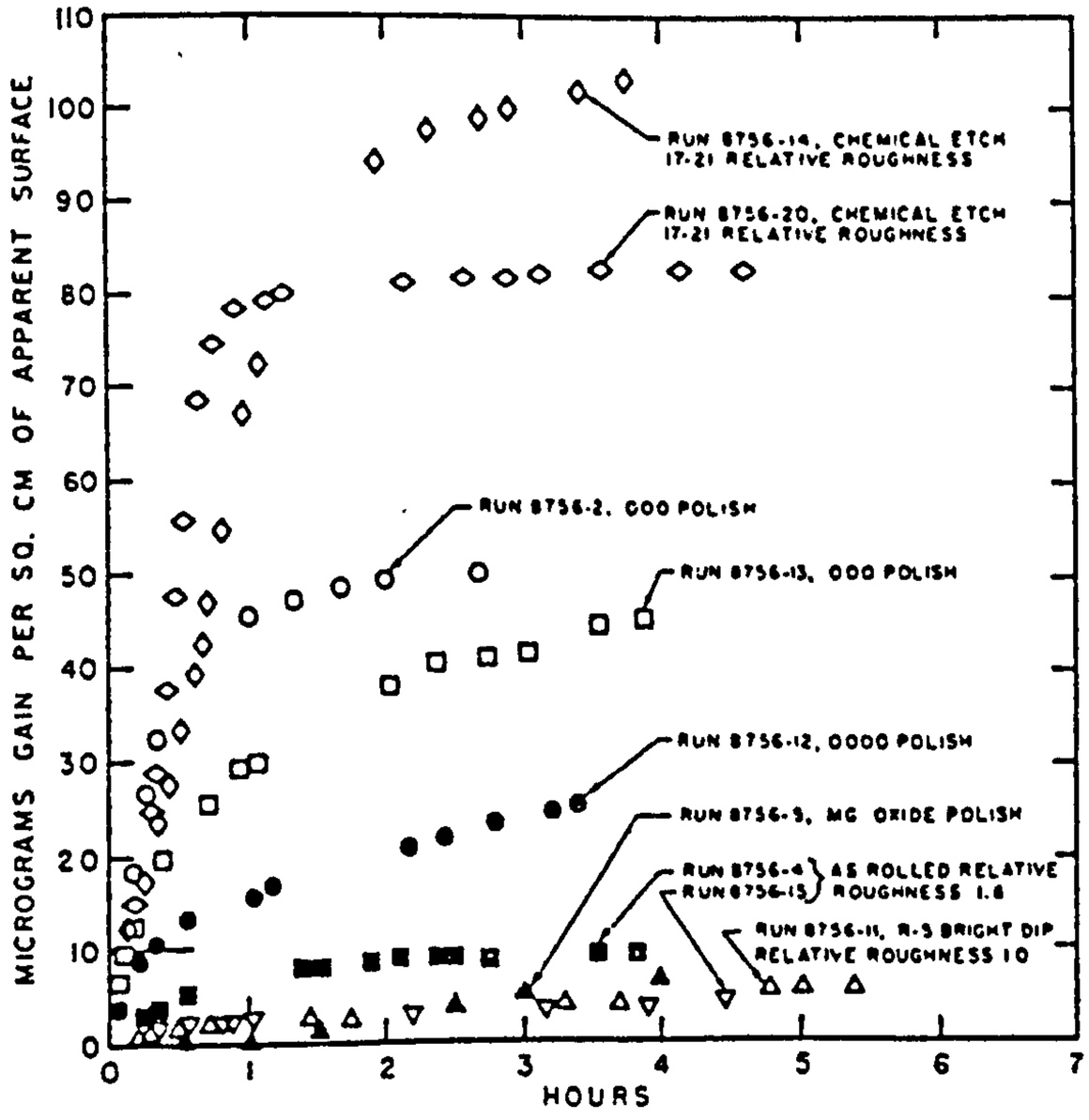

Figure 3.8 Effect of surface roughness on the oxidation of high purity aluminium foil at 525°C in humid air [77]

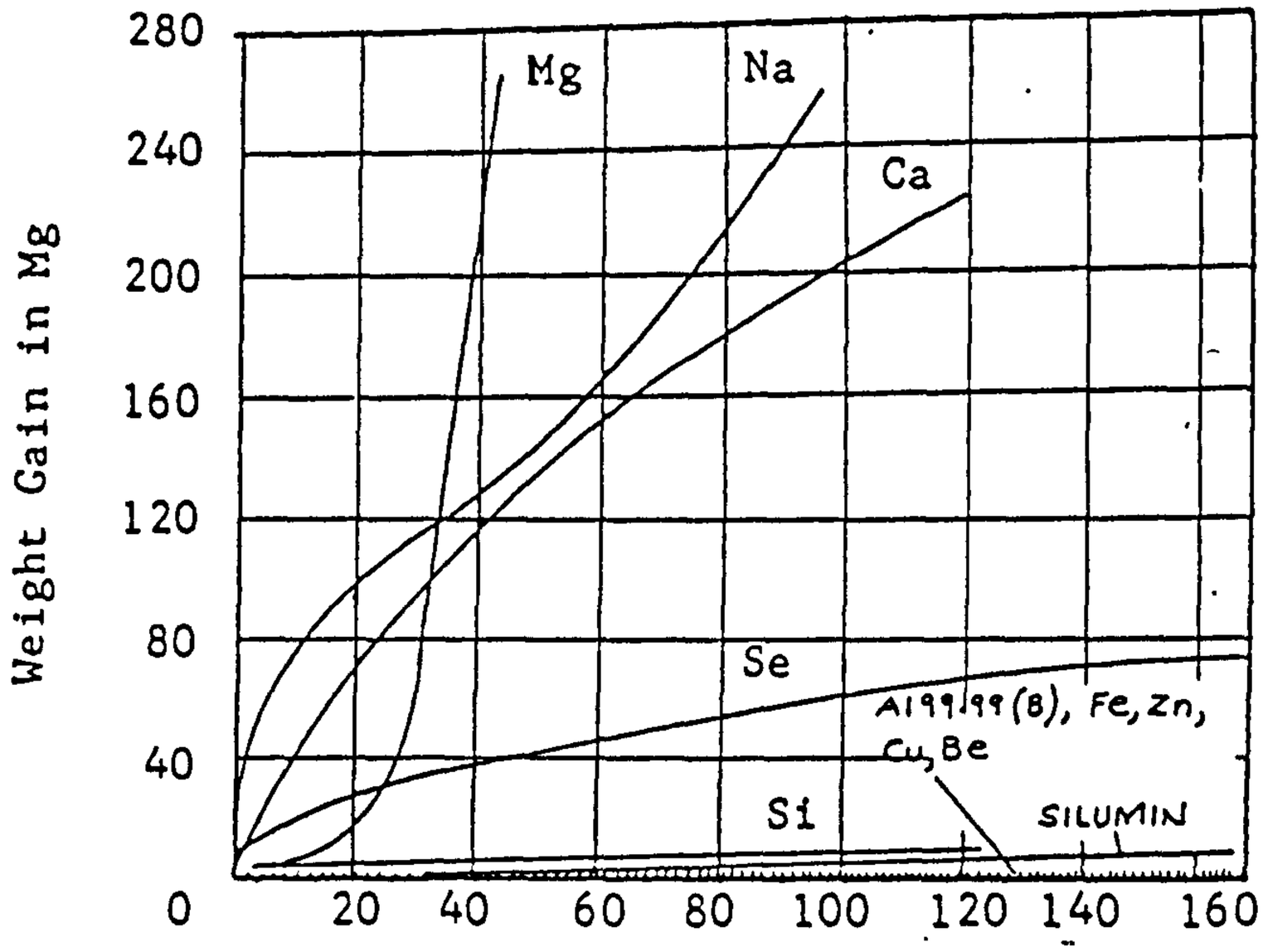

Figure 3.9 The effect of elements on the oxidation of aluminium at 700°C as found by Thiele [111]

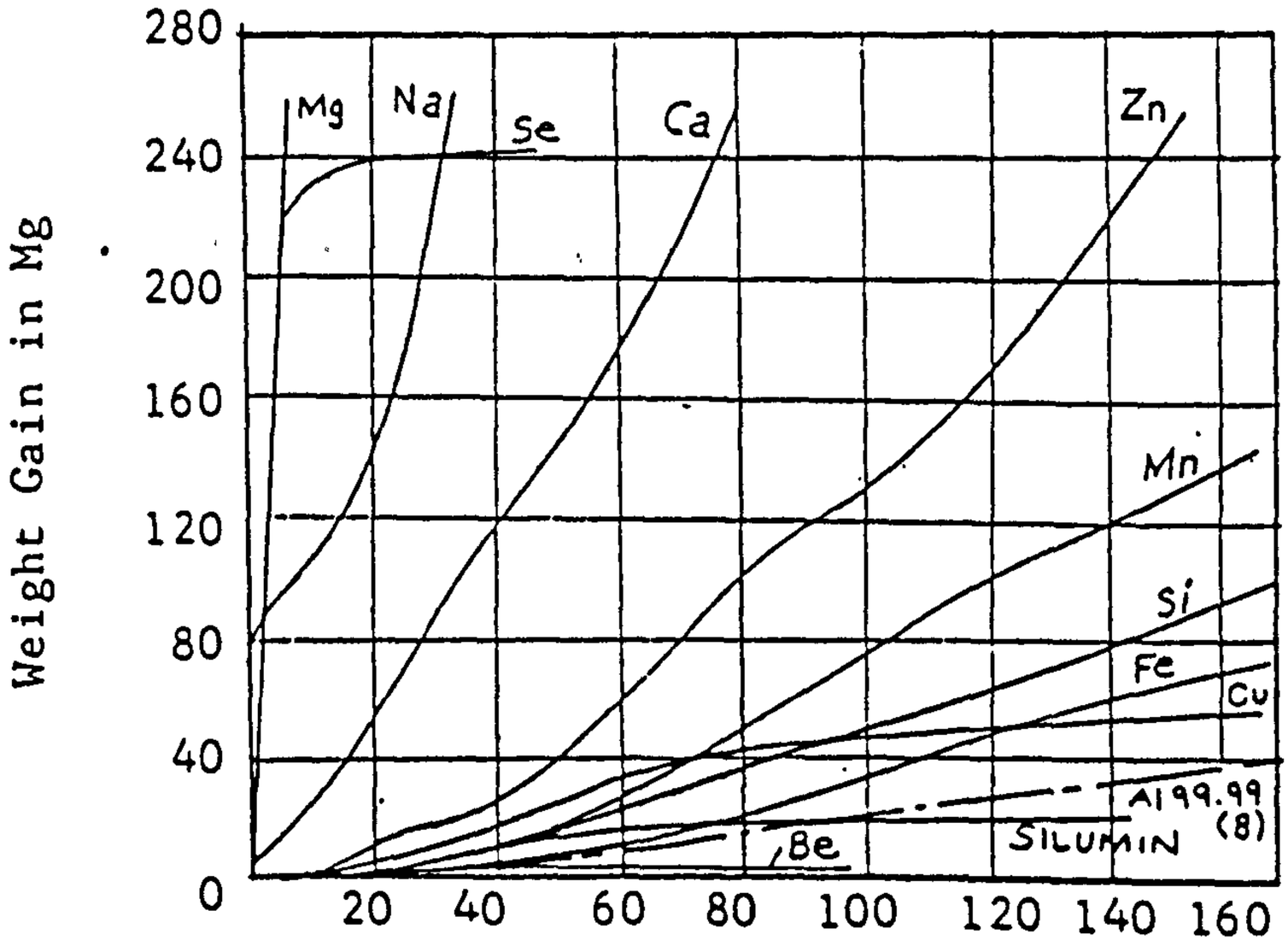

Figure 3.10 The effect of elements on the oxidation of aluminium at 800°C as found by Thiele [111]

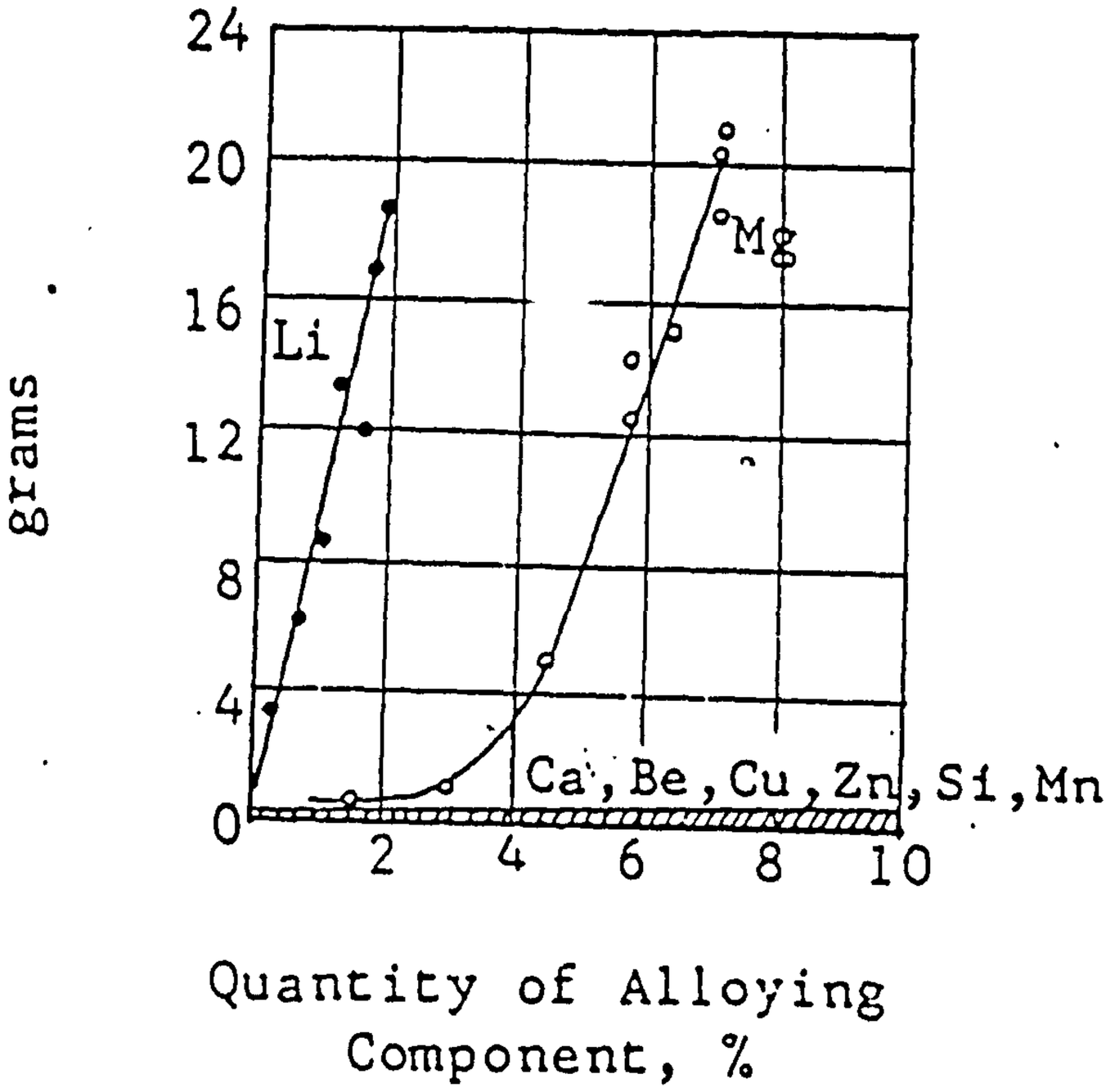

Figure 3.11 The effect of elements on the oxidation of aluminium at 690°C as found by Ginsberg and Datta [120]

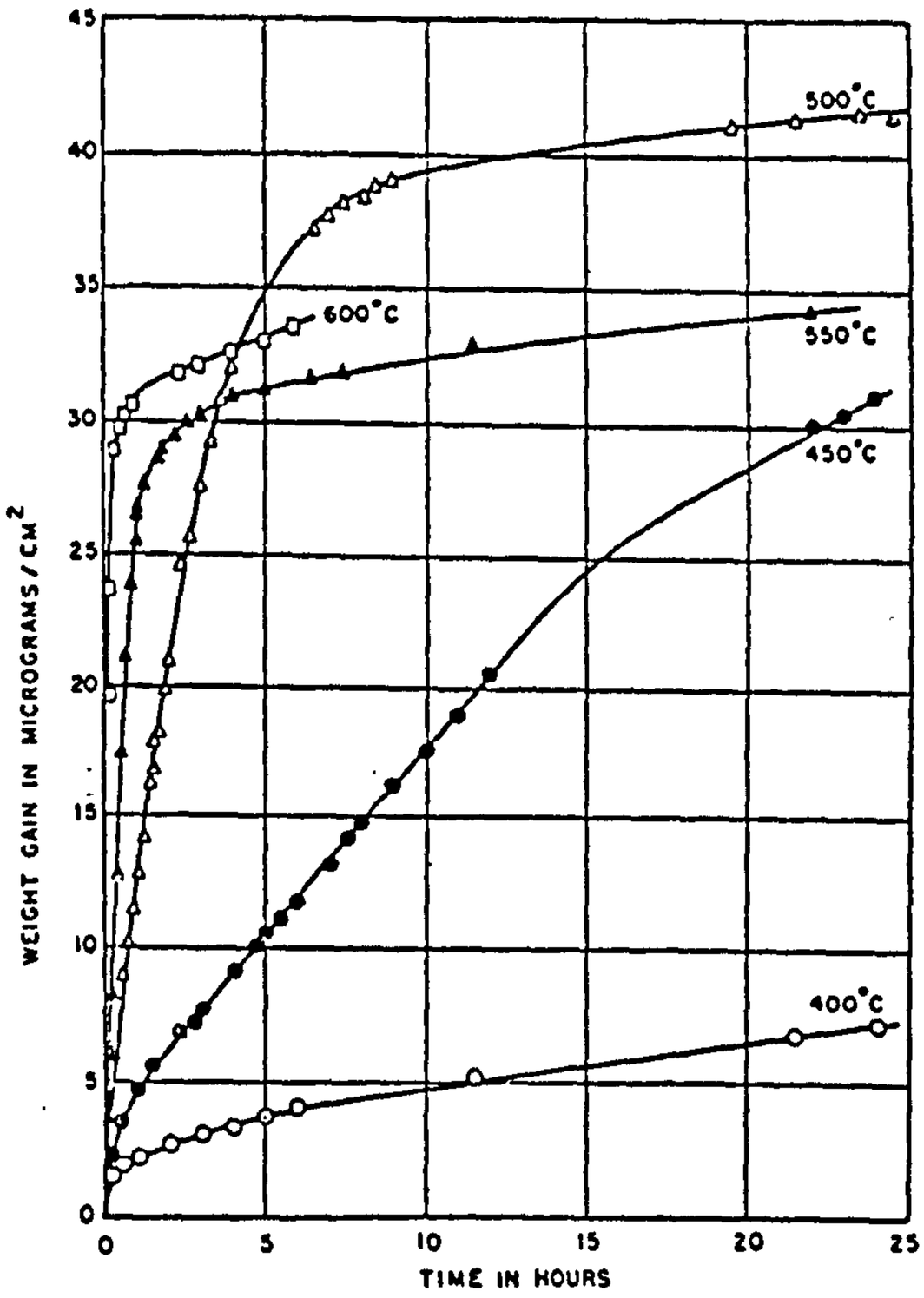

Figure 3.12 Oxidation tests at 400-600°C of metallographically polished specimens of Al-3%Mg [125]

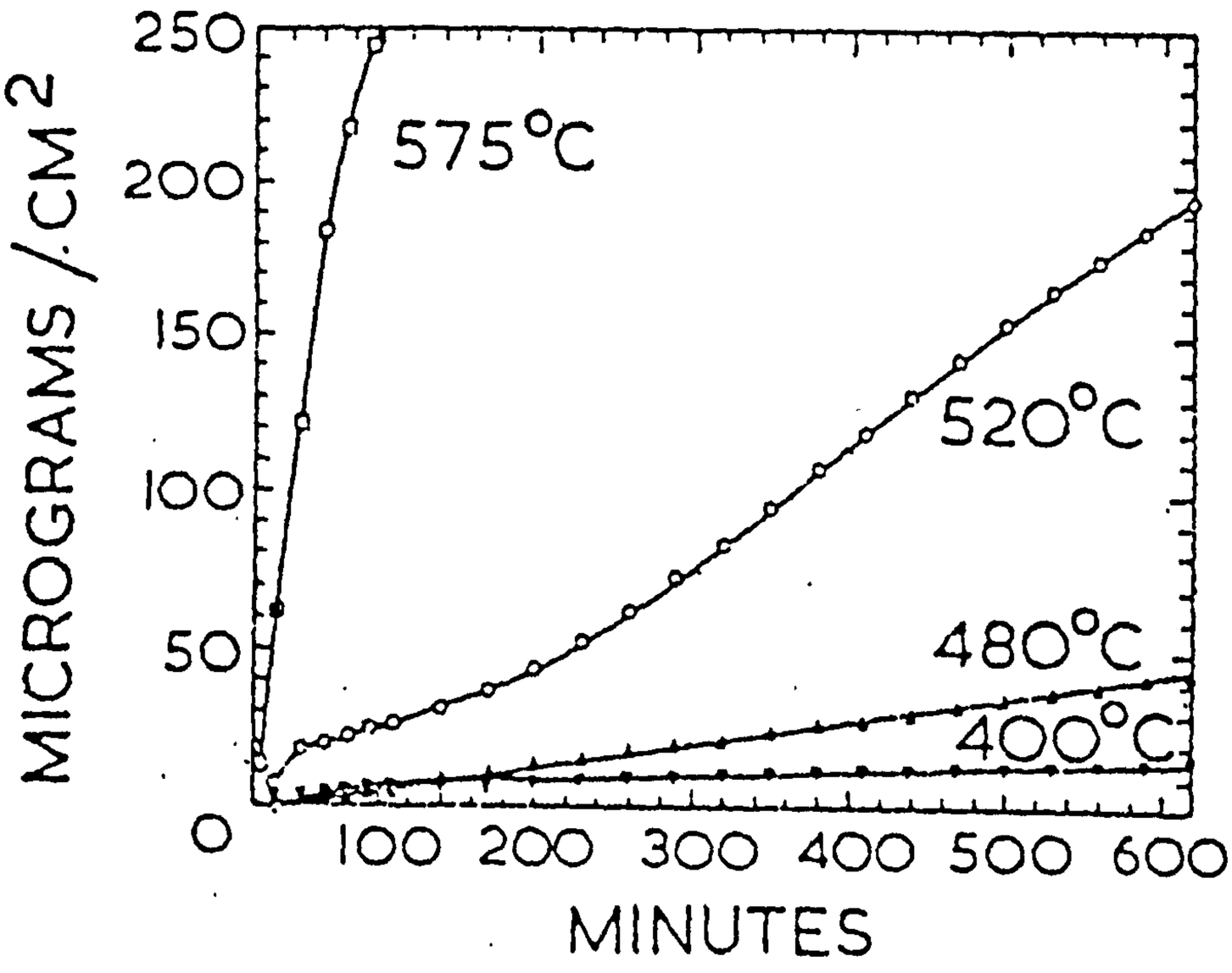

Figure 3.13 Oxidation tests at 400-600°C of electropolished Al-4.2%Mg specimens [102]

fig 3.3

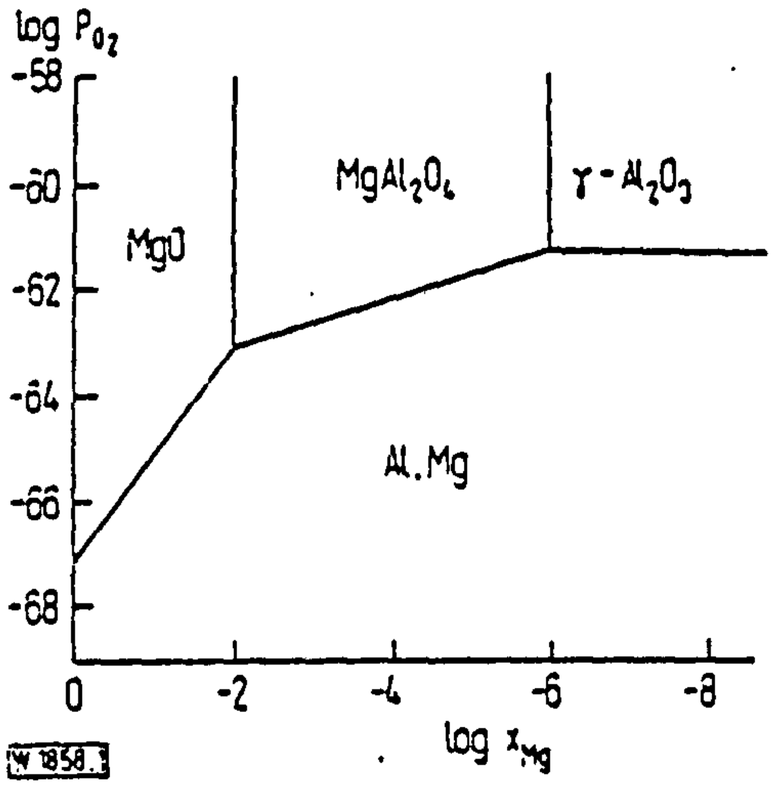

Figure 3.14 Stability diagram for the Al-Mg-O_2 system at 527°C [129]

table 3.2

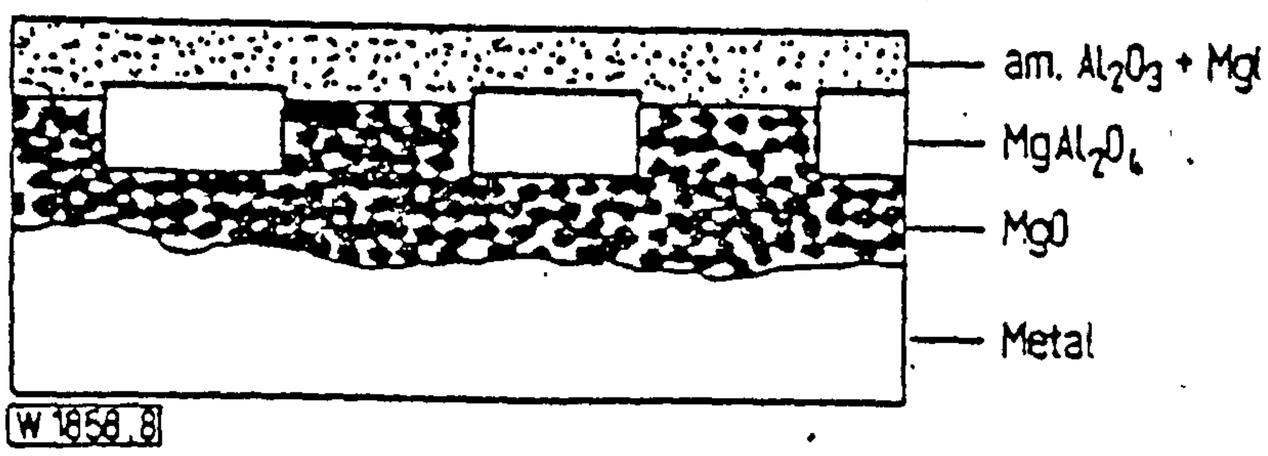

Figure 3.15 Schematic of the oxide film of Al-0.17%Mg [129]

(a)

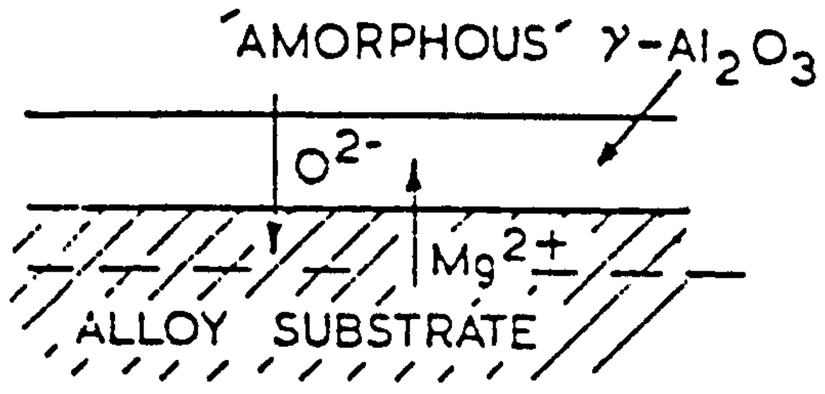

Figure 8a

(b)

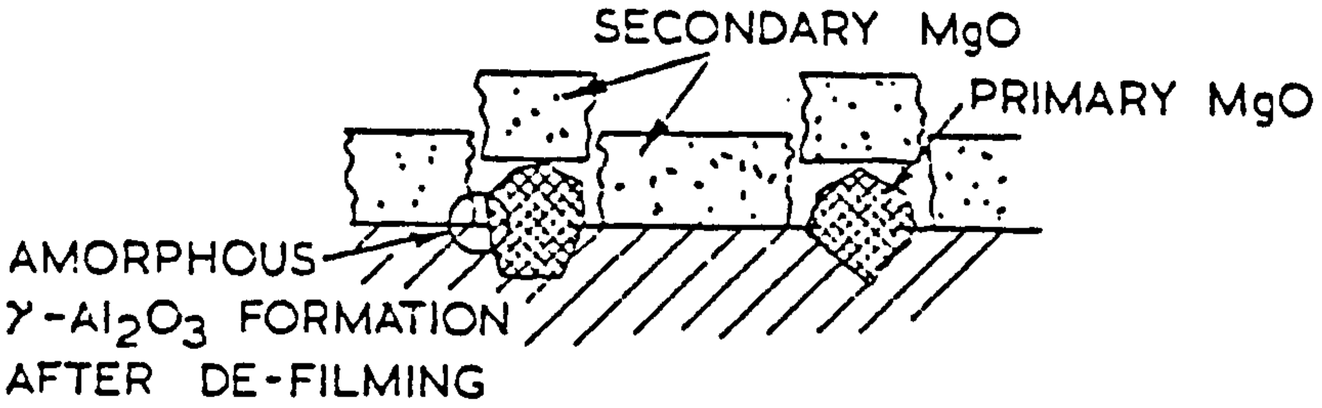

Figure 8b

(c)

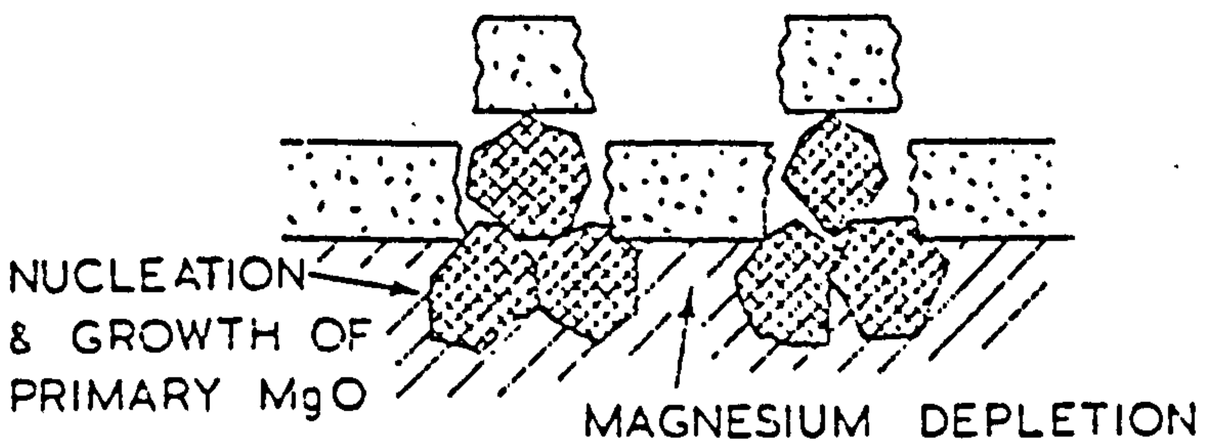

Figure 8c

(d)

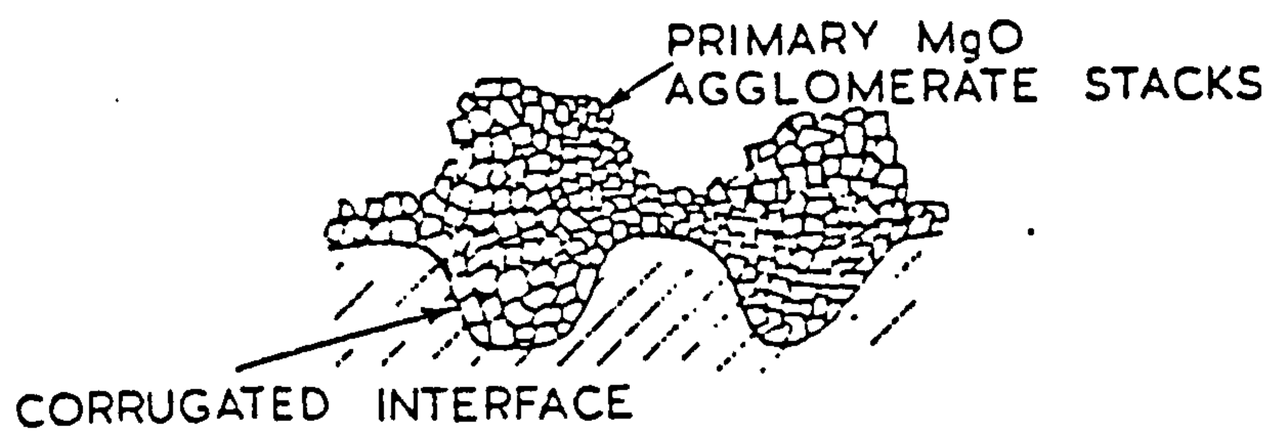

Figure 3.16 Oxidation model for Al-Mg alloy as found by Field [102]

Fig Table 3.4 p65-66 pw contain Impy

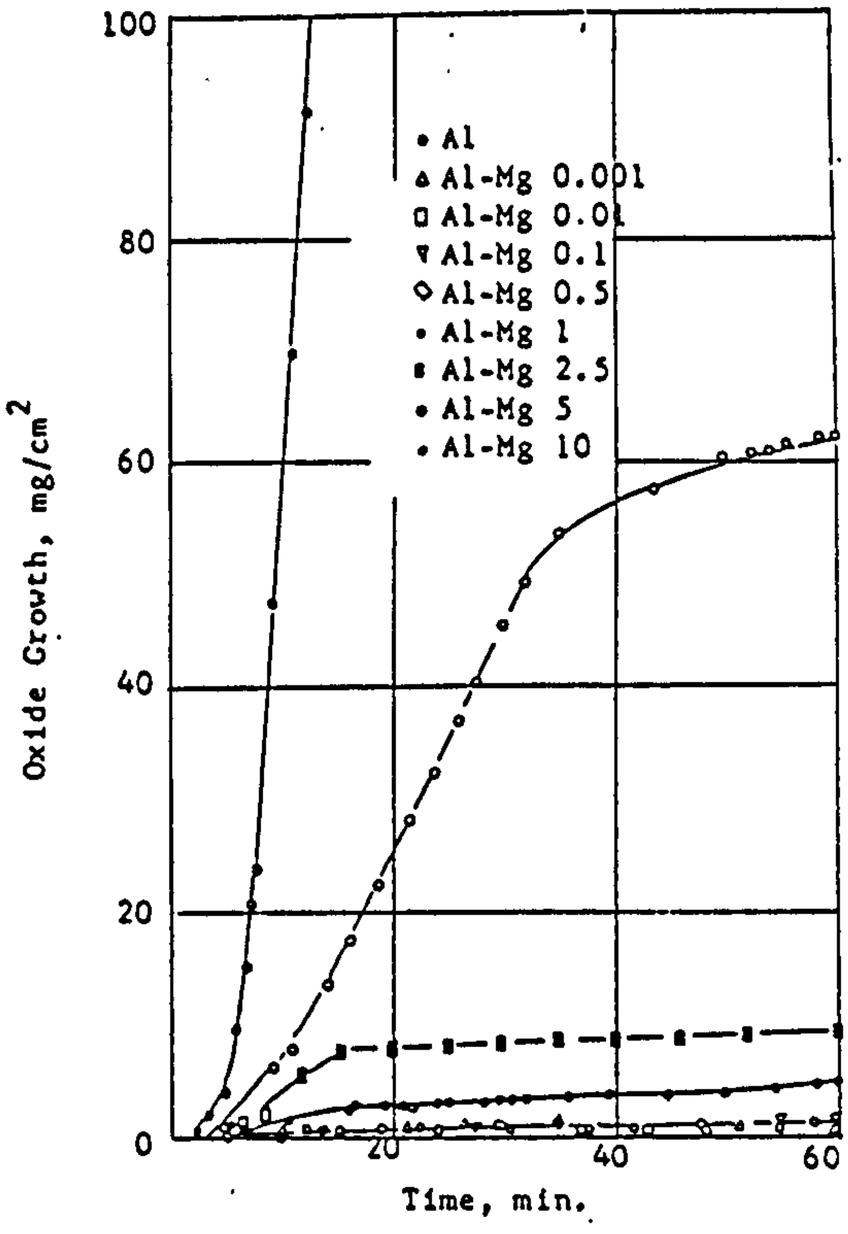

Figure 3.17 The effect of magnesium on the oxidation of aluminium at 700°C [135]

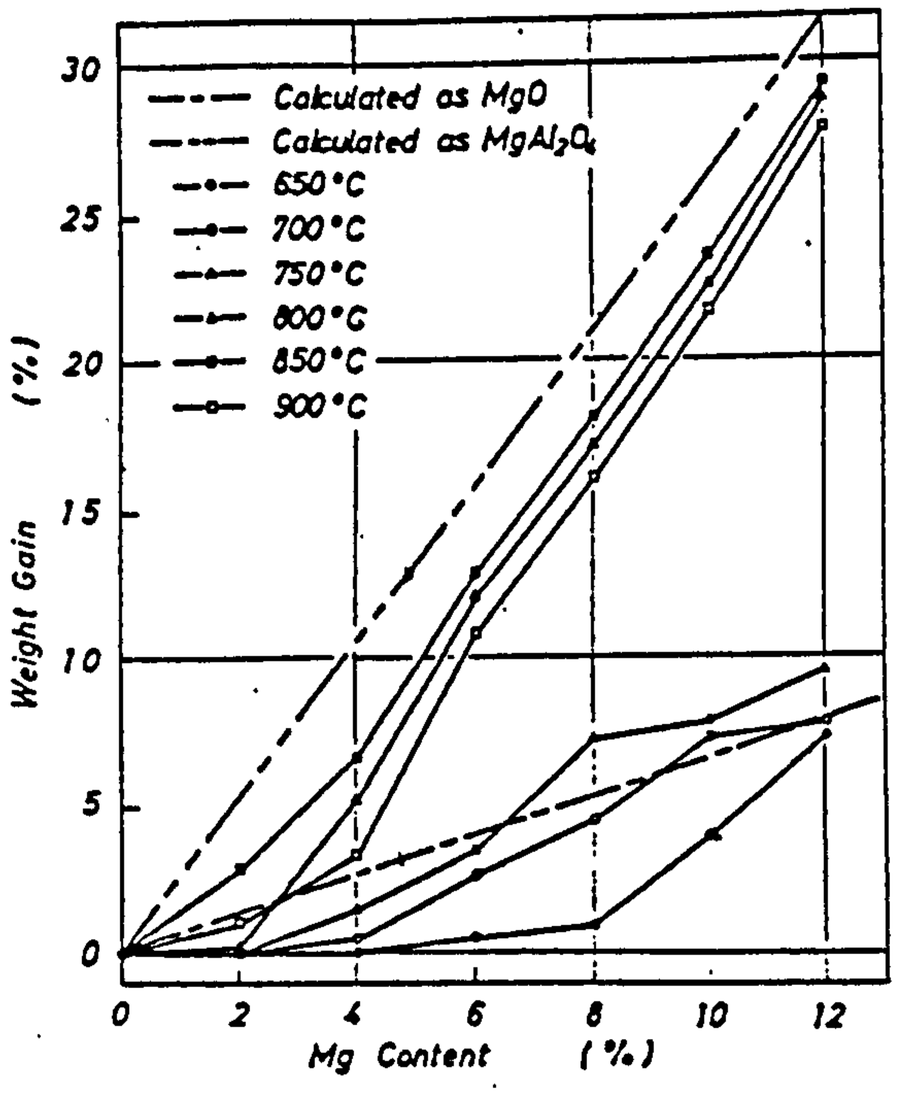

Figure 3.18 The relation between weight gain and magnesium content [136]

Table 3.5.B

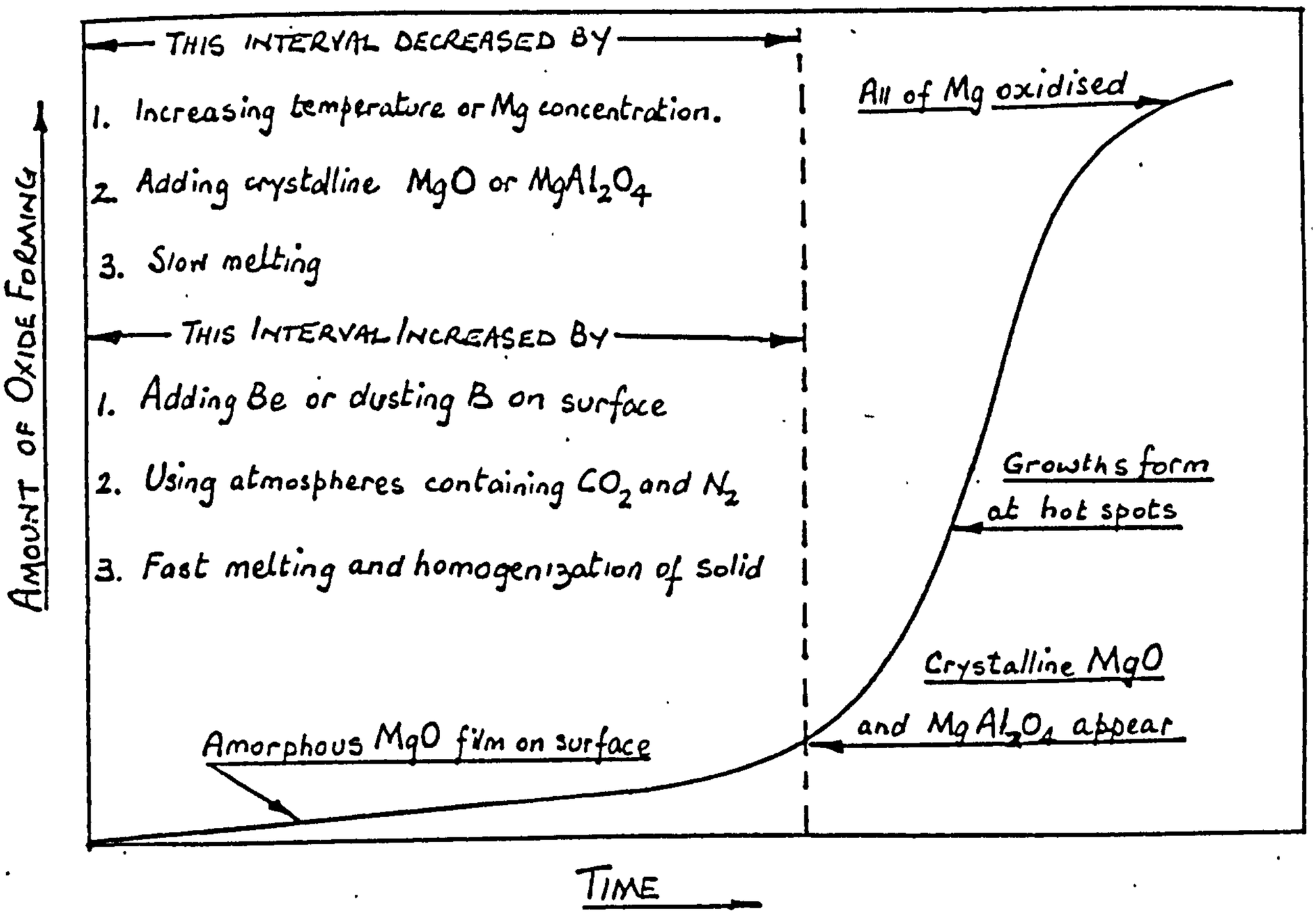

Figure 3.19 General oxidation behaviour of Al-Mg melts [124]

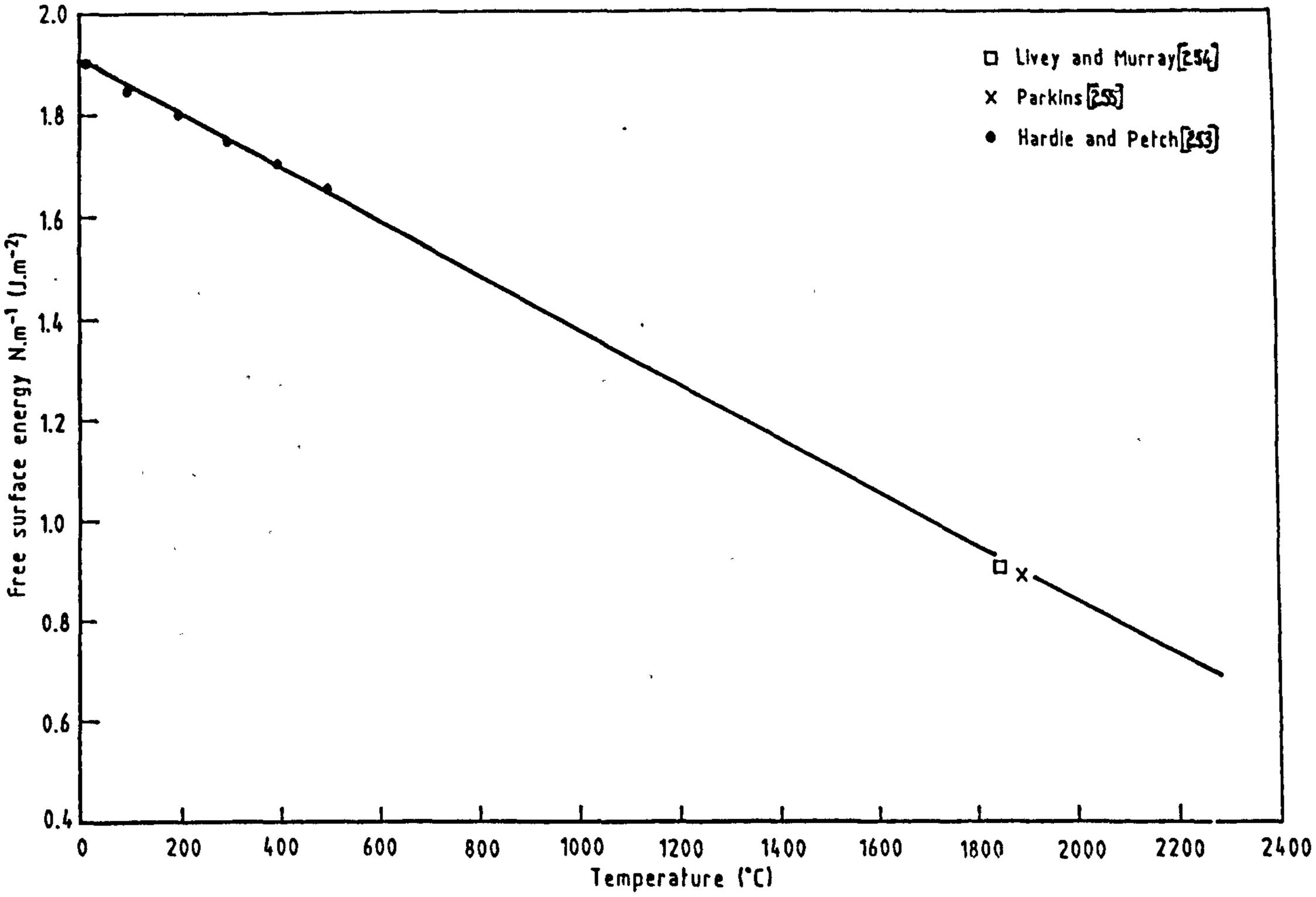

Figure 4.2 Plot of estimated free surface energy values for alumina with temperature

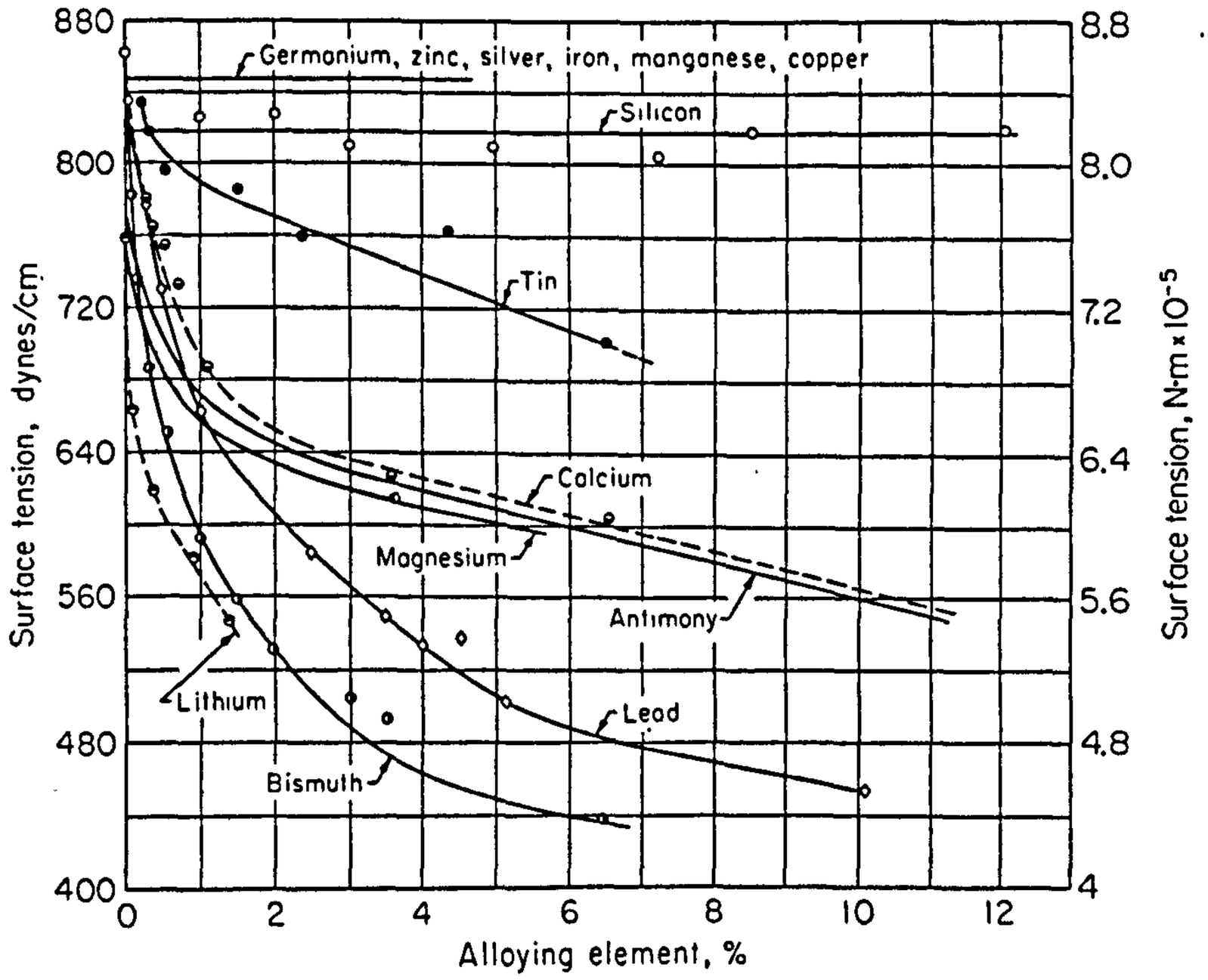

Figure 4.3 Effect of added elements on the surface tension of pure aluminium at 700-740°C in argon [184]

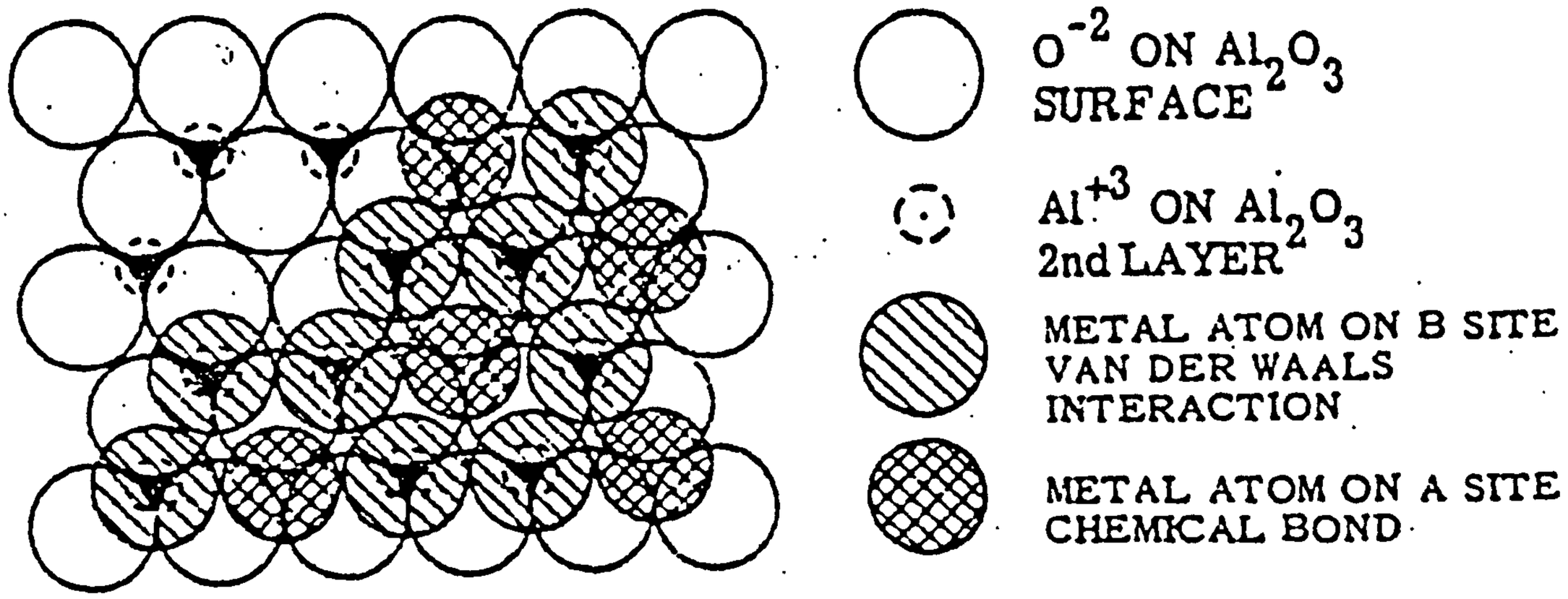

Figure 4.4 Adsorption sites (A and B) for metallic atoms on a <0001> sapphire surface [157]

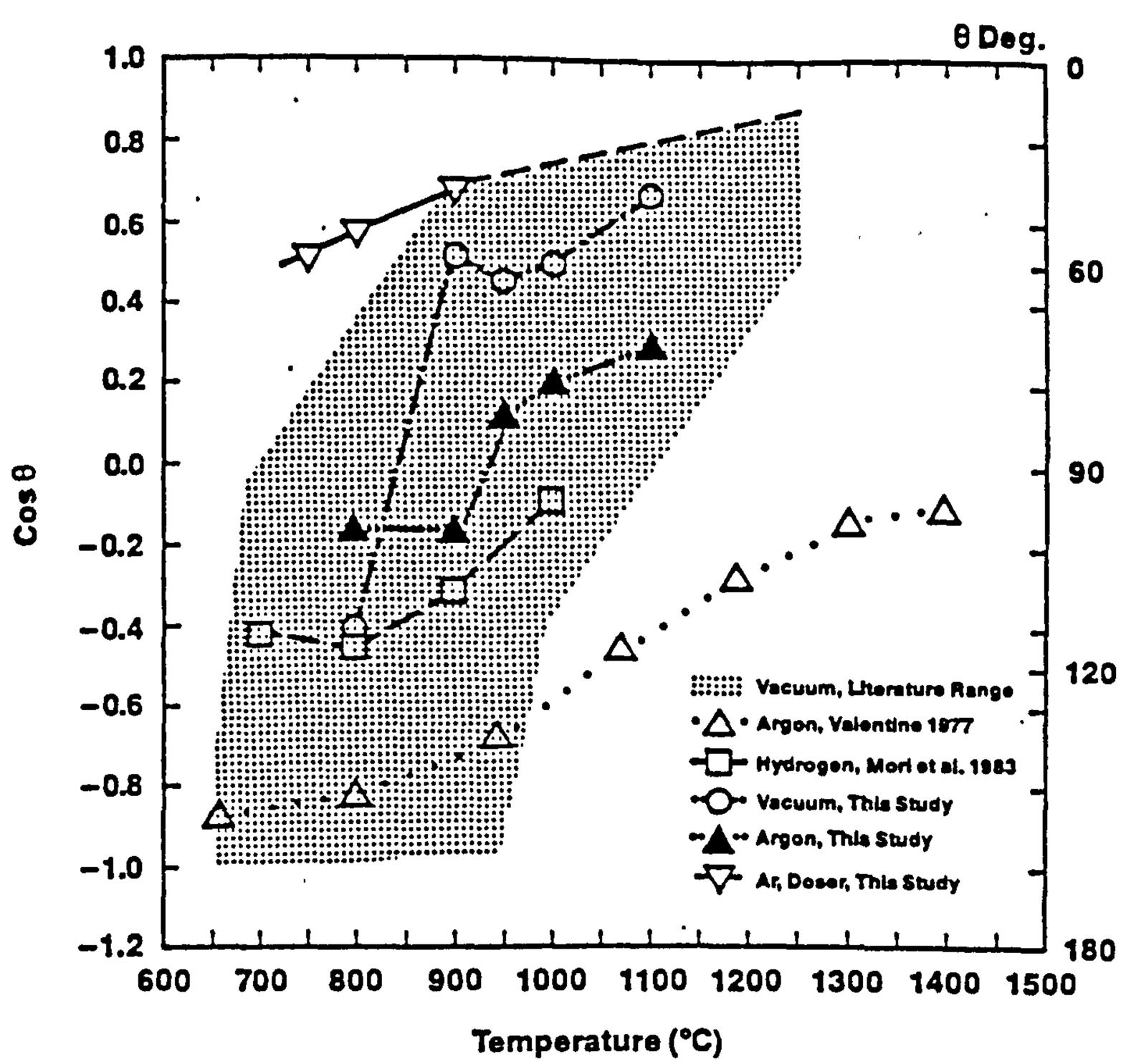

Figure 4.5 Temperature dependence of the equilibrium contact angle for pure aluminium on alumina [194]

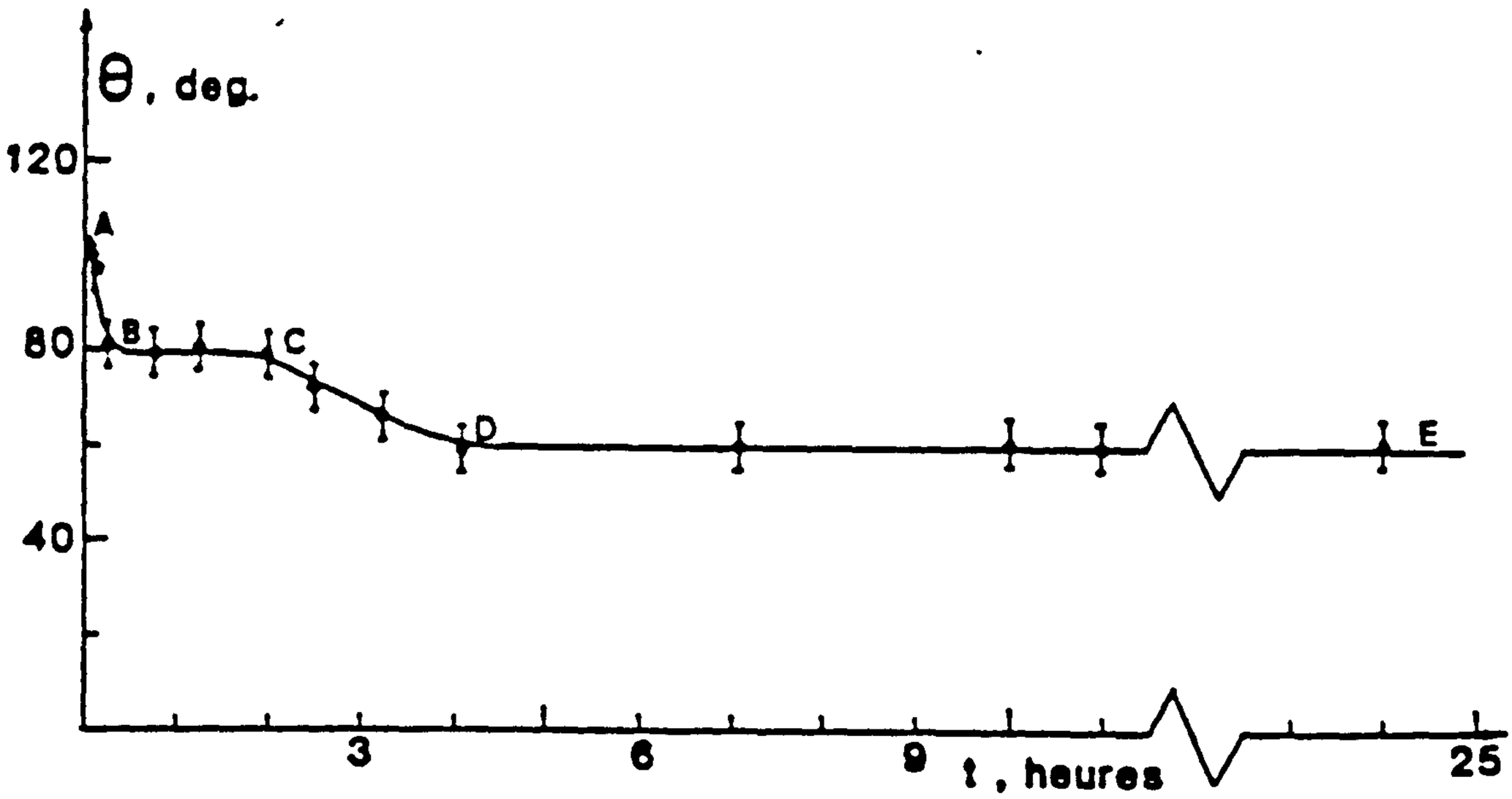

Figure 4.6 Variation with time of the contact angle of the Al/Al_2O_3 system at 1000°C [196]

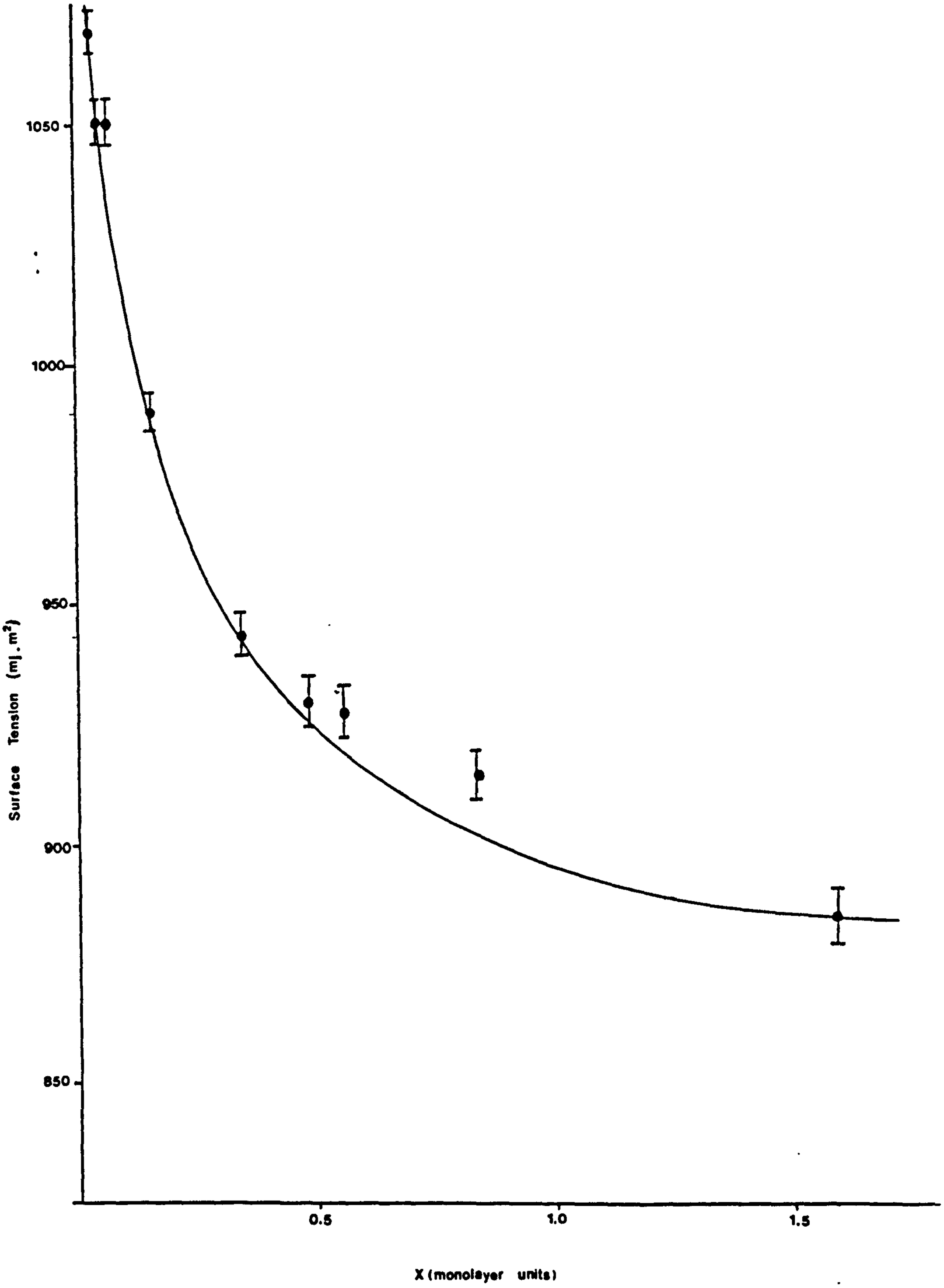

Figure 4.7 Variation in aluminium surface tension with oxide coverage [200].

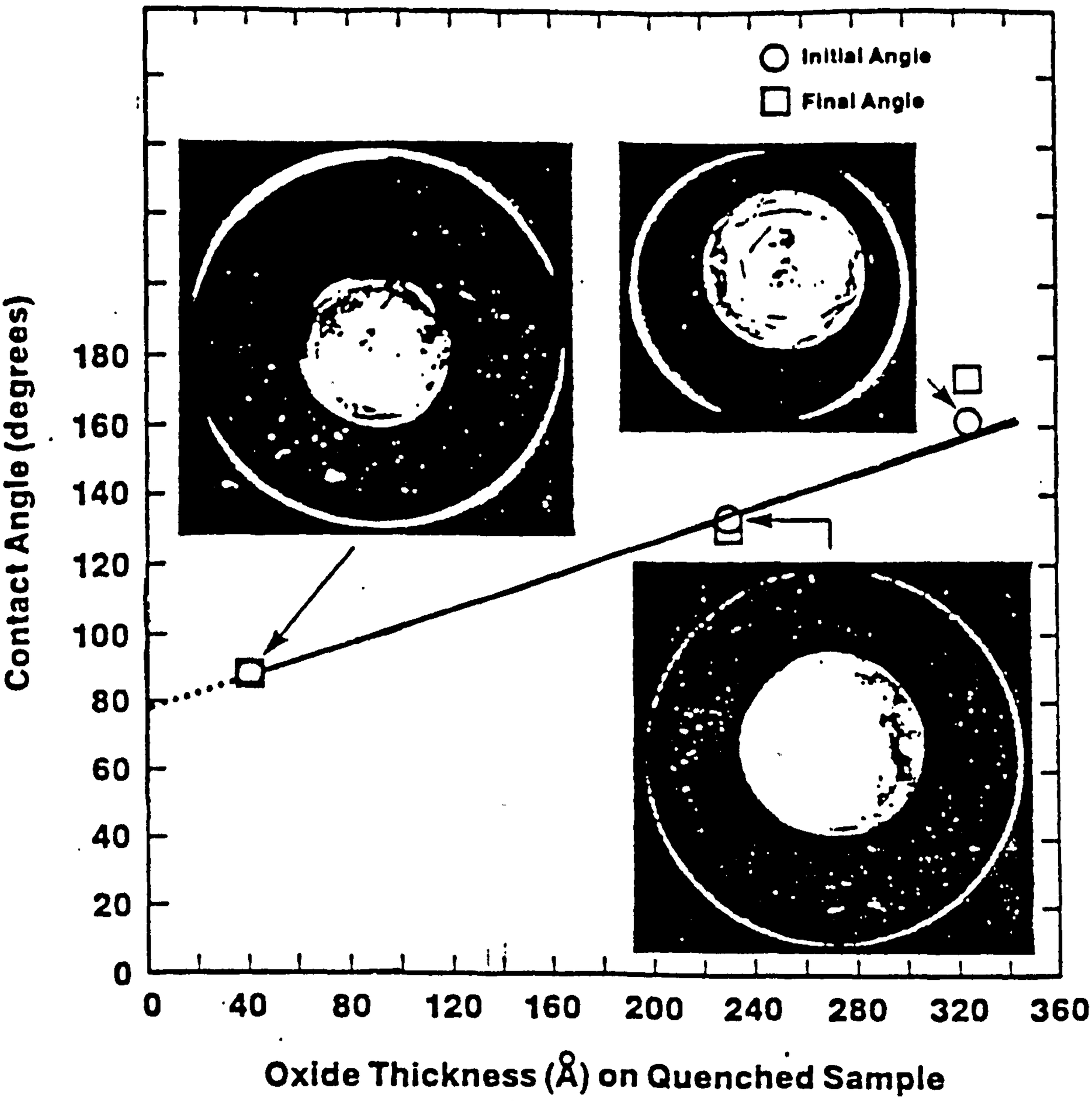

Figure 4.8 Effect of oxide film thickness on the aluminium contact angle at 800°C in vacuum [194]

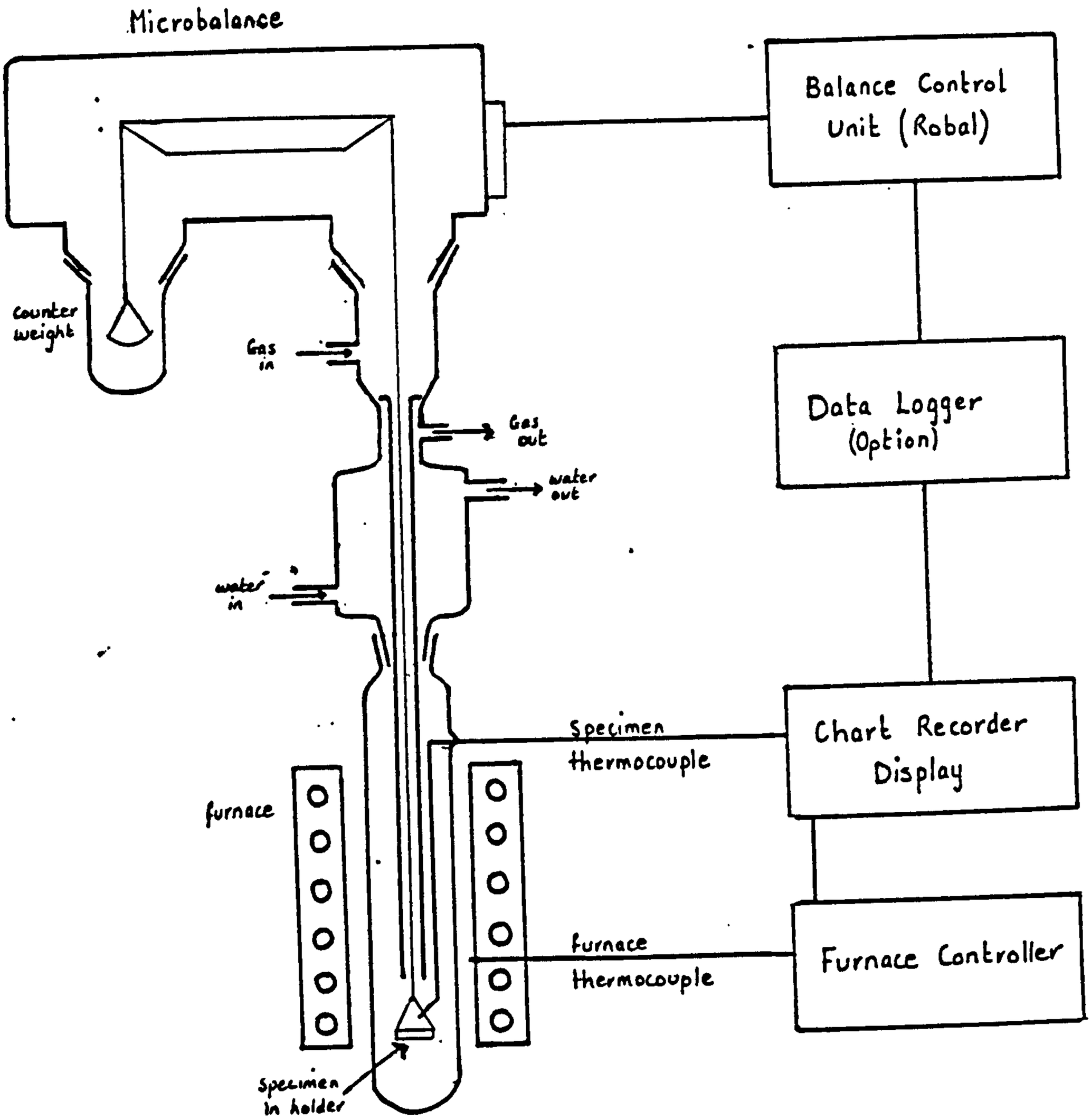

Figure 5.1 Schematic diagram of the microbalance system

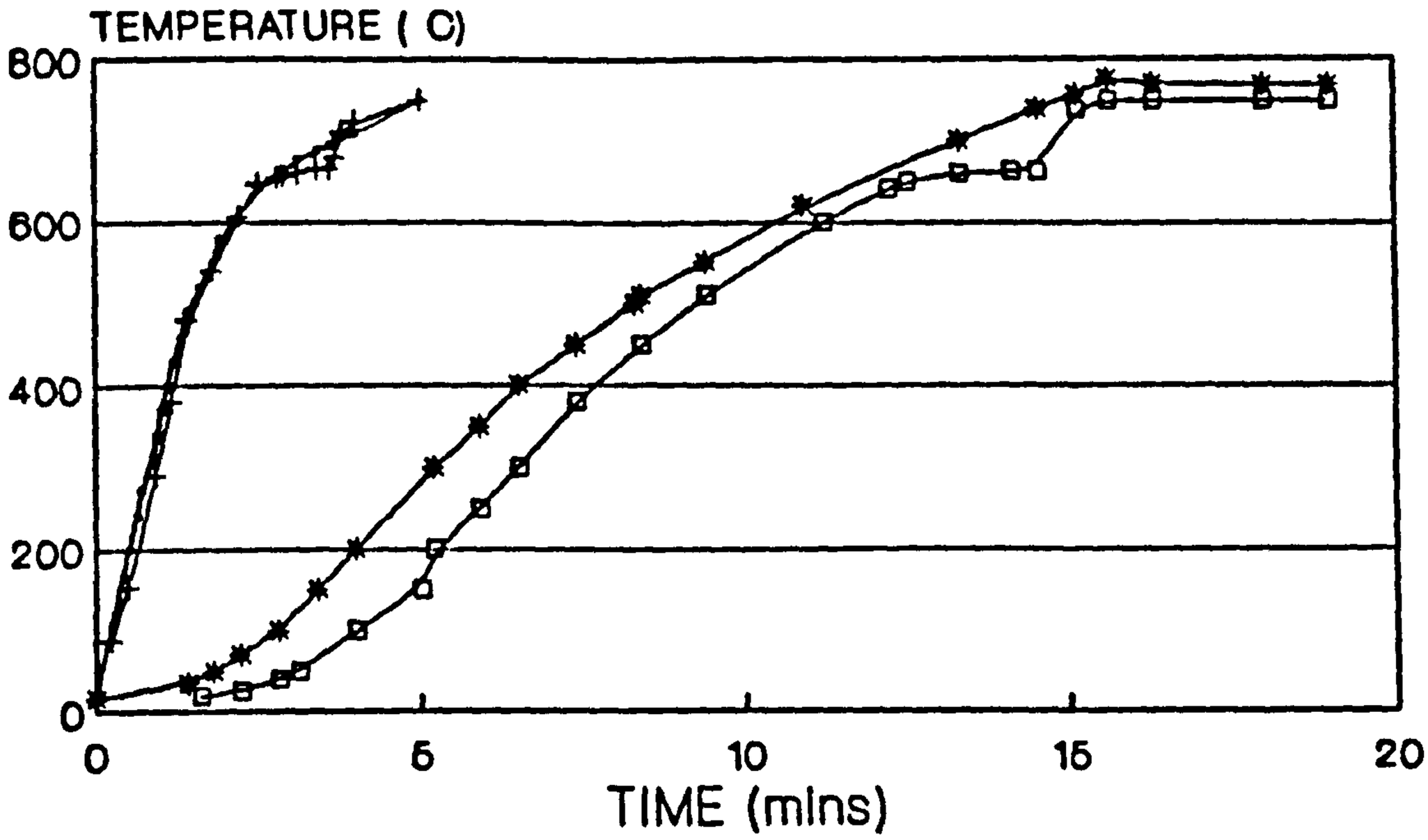

✱ *specimen with furnace raised cold*
□ *specimen holder with furnace raised cold*

\+ *specimen with preheated furnace*
• *specimen holder with preheated furnace*

Figure 5.2 Thermal response of an aluminium specimen and specimen holder to a furnace heated to 750°C and at 750°C (preheated)

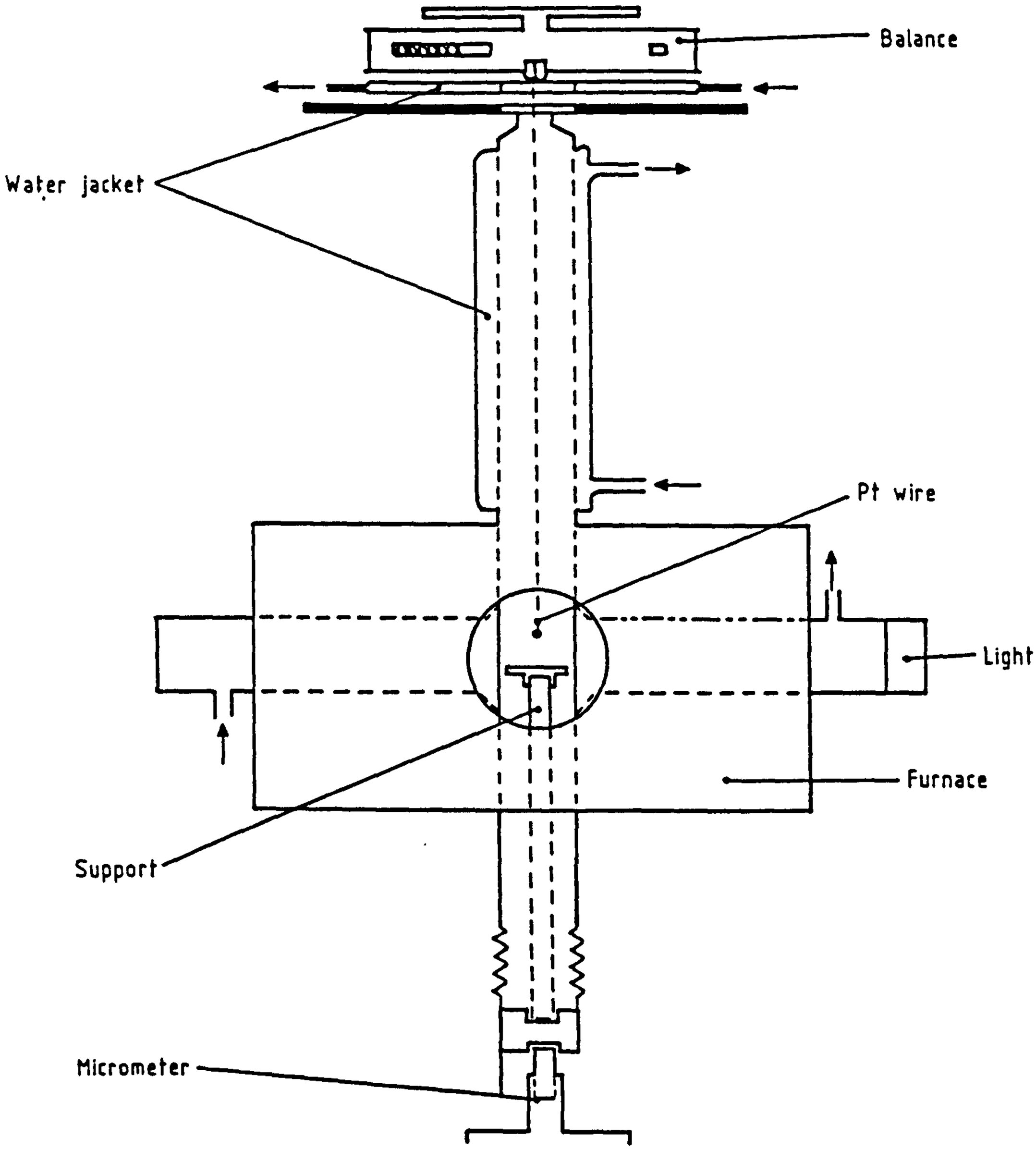

Figure 5.3 Schematic diagram of the surface tension balance. Details of alumina probe and crucible are given in Figure 8.1

(a)

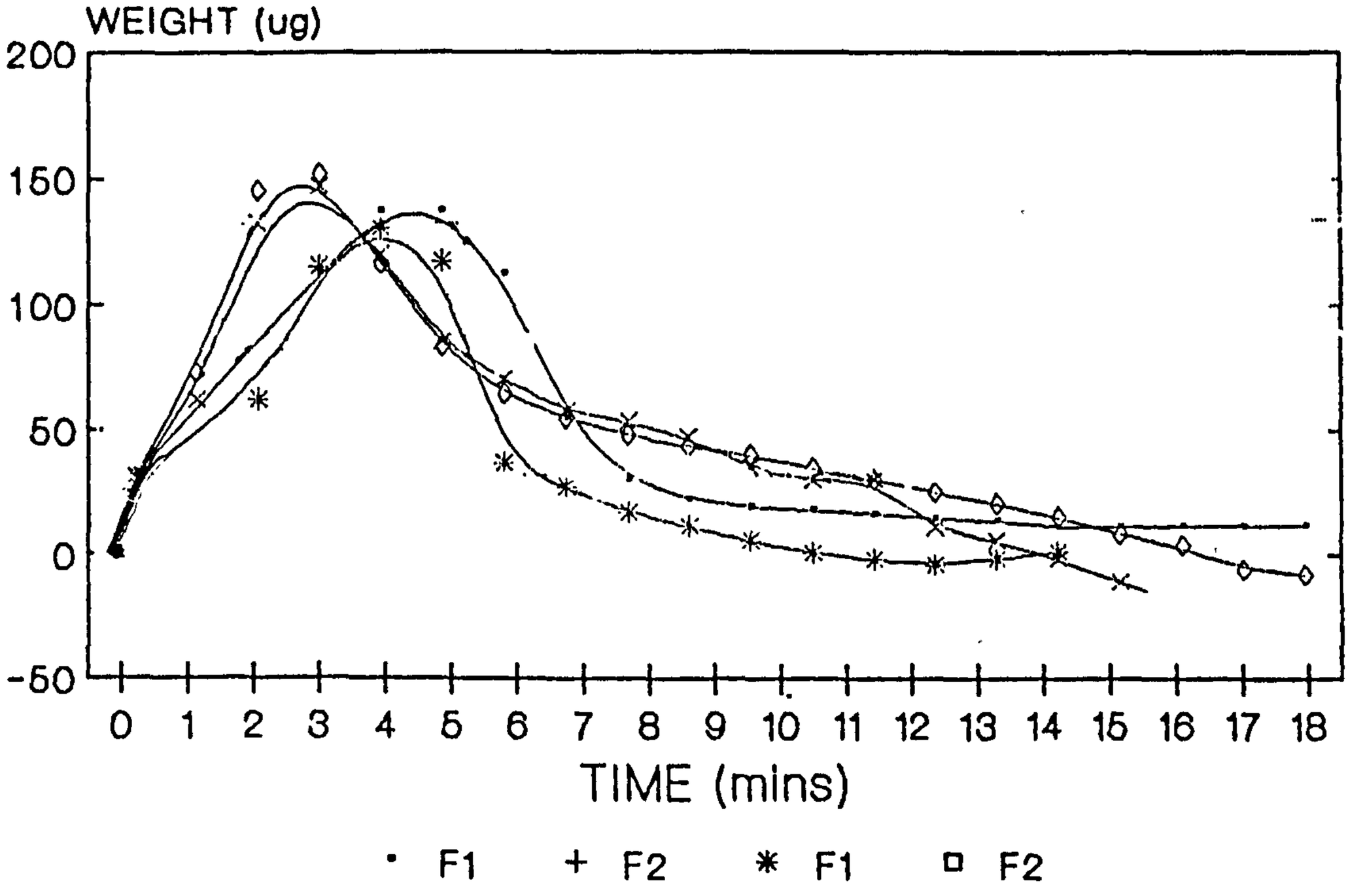

Preheated Furnaces

(b)

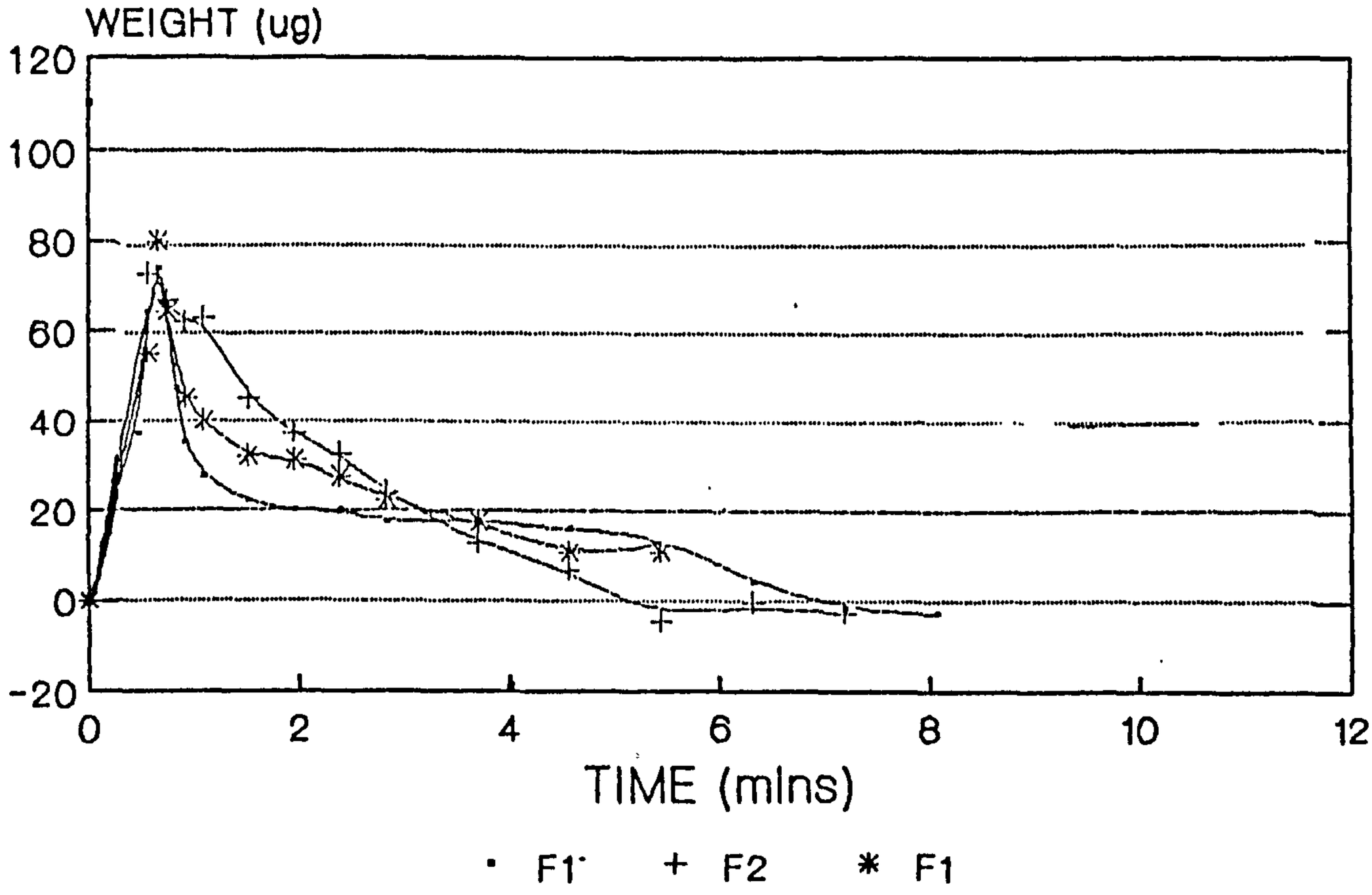

Non-Preheated Furnaces

Figure 6.1 Thermal response of furnaces F1 and F2 at 750°C
(a) with preheating (b) without preheating

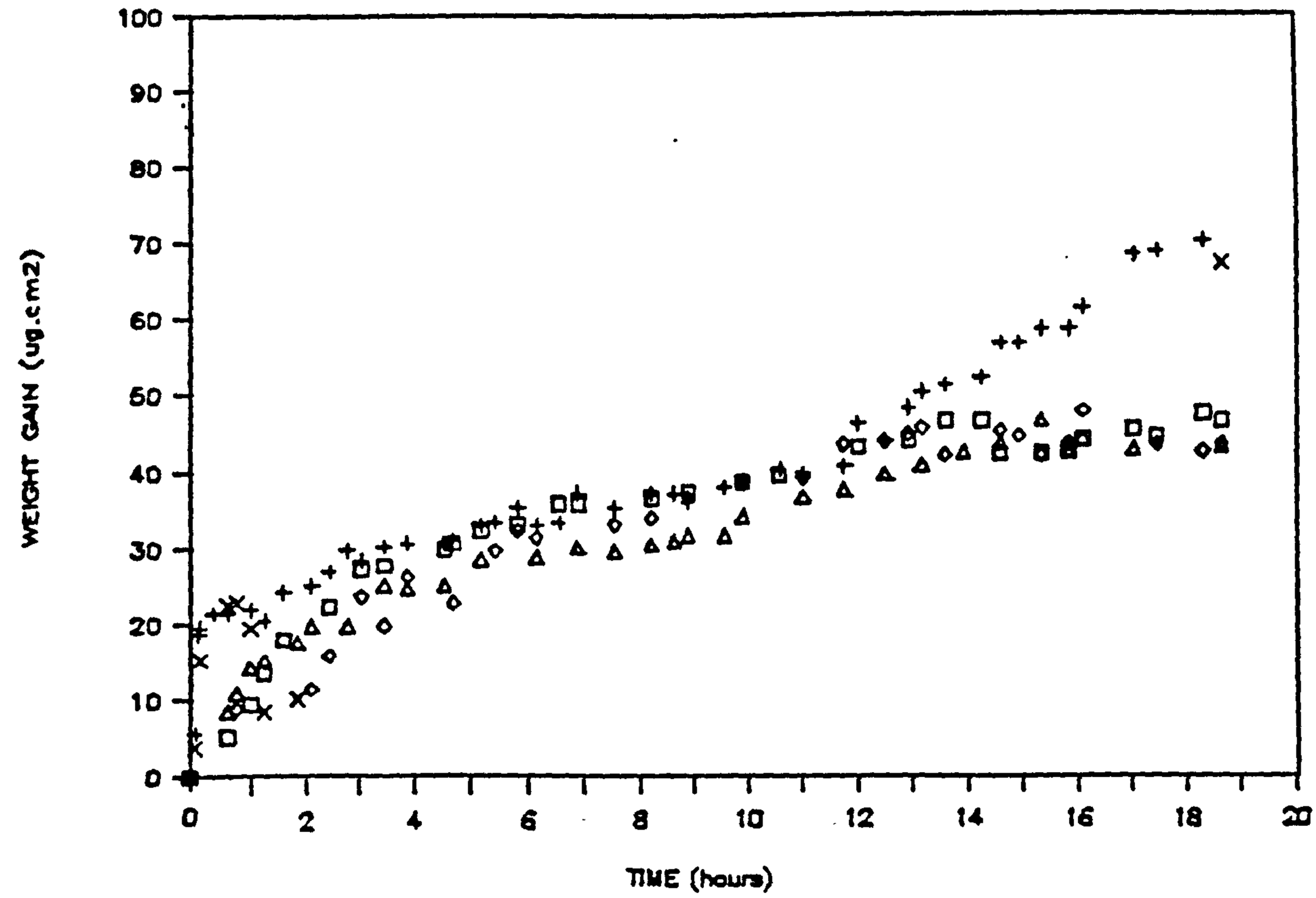

+, □ *flowing gettered argon*

◇ *flowing humid argon*

Δ, X *flowing dry air*

Figure 6.2 Oxidation of machined aluminium in flowing dry air, humid air and gettered argon at 750°C.

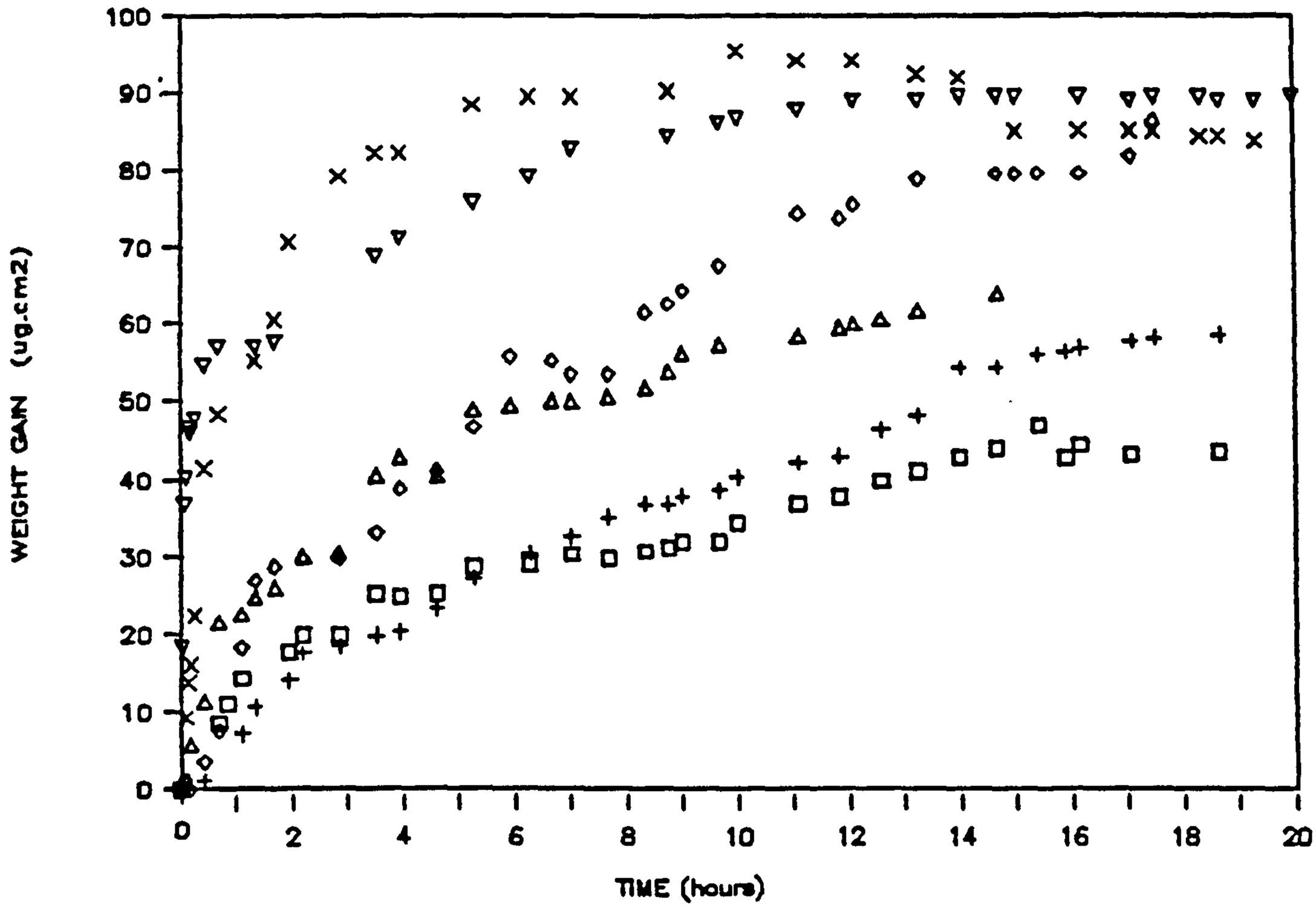

□ *machined surface in flowing dry air*
\+ *machined surface in still dry air*

◇ *polished (1μm) surface in flowing dry air*
△ *polished (1μm) surface in still dry air*

× *electropolished surface in flowing dry air*
▽ *electropolished surface in still dry air*

Figure 6.3 The important effect of surface finish on the oxidation of aluminium showing good reproducibility between flowing and static dry air at 750°C.

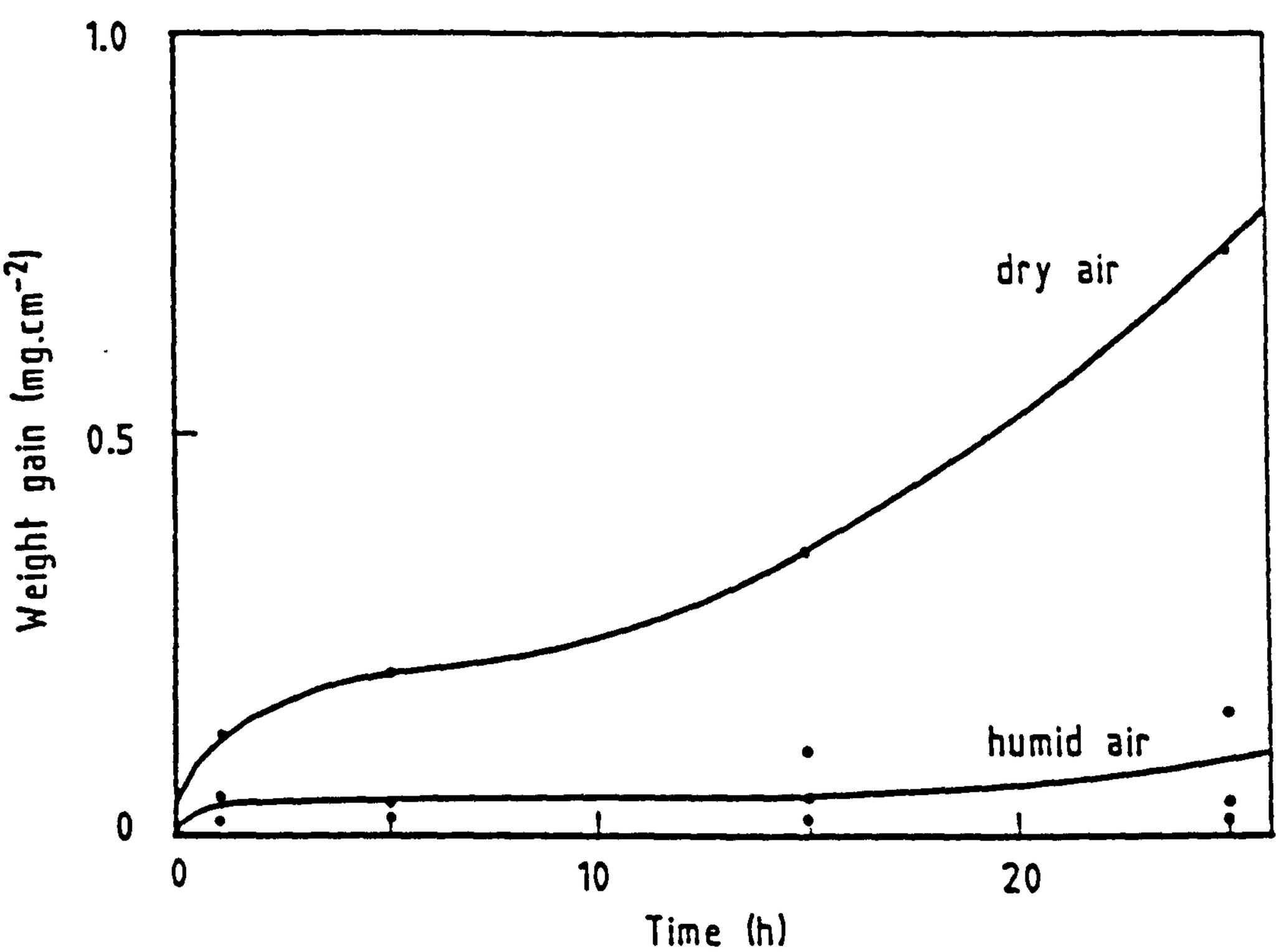

Figure 6.4 The influence of humidity on the oxidation rate of aluminium at 750°C.

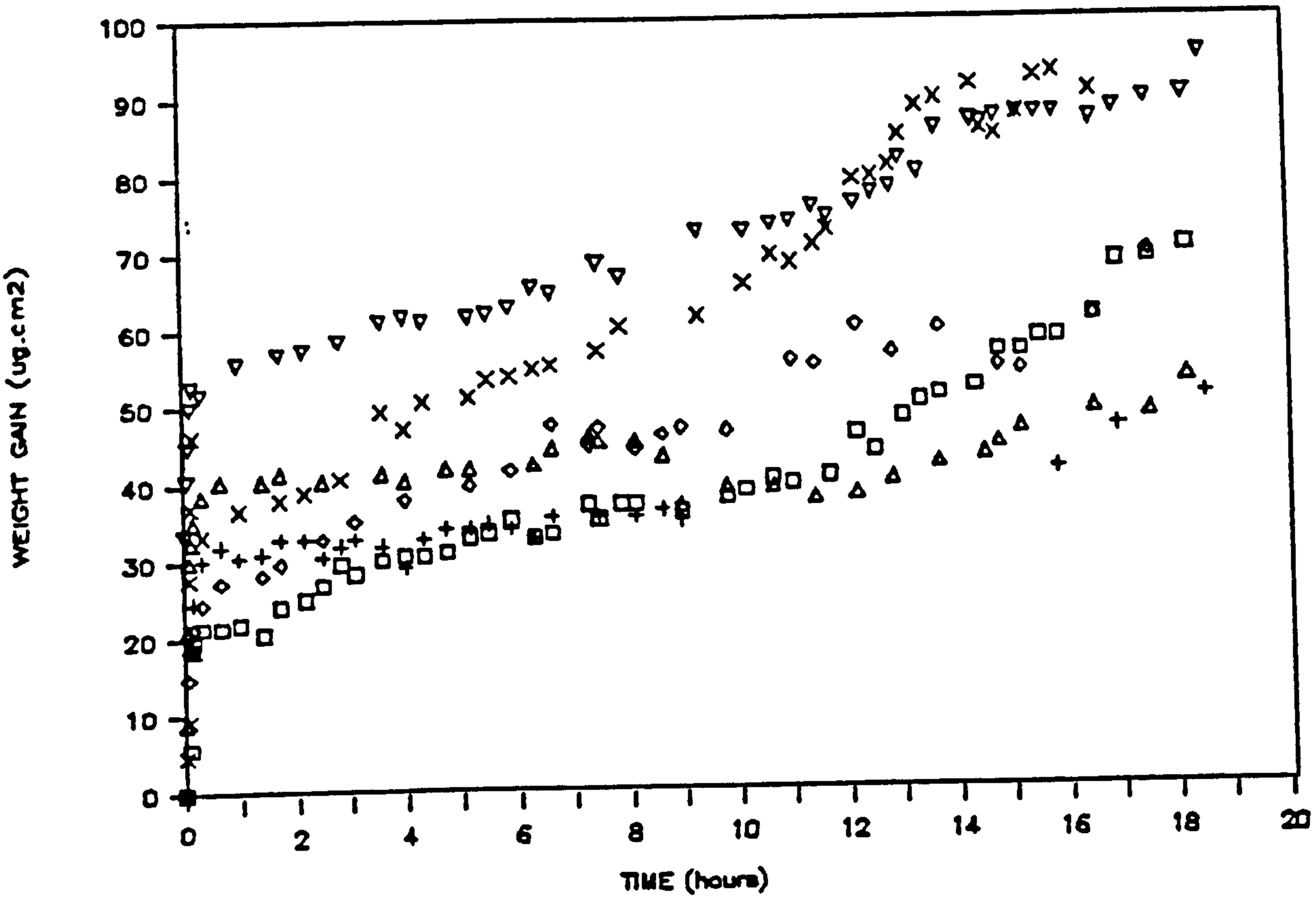

□ *machined surface in flowing gettered argon*
\+ *machined surface in still gettered argon*

◇ *polished (1μm) surface in flowing gettered argon*
△ *polished (1μm) surface in still gettered argon*

× *electropolished surface in flowing gettered argon*
▽ *electropolished surface in still gettered argon*

Figure 6.5 Oxidation of aluminium in flowing and still gettered argon at 750°C.

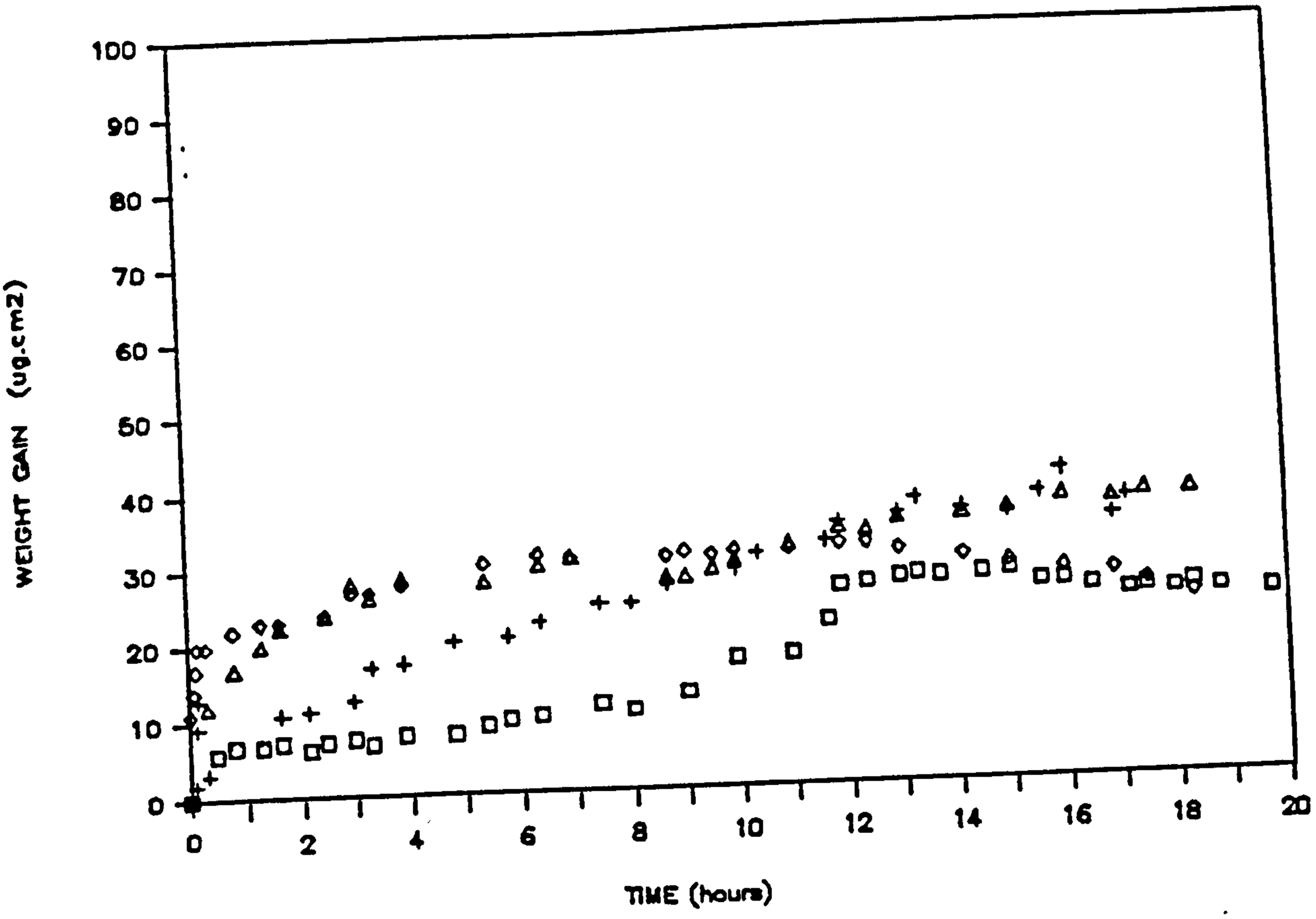

□ *machined surface in flowing humid argon*

\+ *polished (600μm) surface in still humid argon*

△ *polished (1μm) surface in flowing humid argon*

◇ *polished (1μm) surface in still humid argon*

Figure 6.6 Oxidation of aluminium in flowing and still humid argon at 750°C.

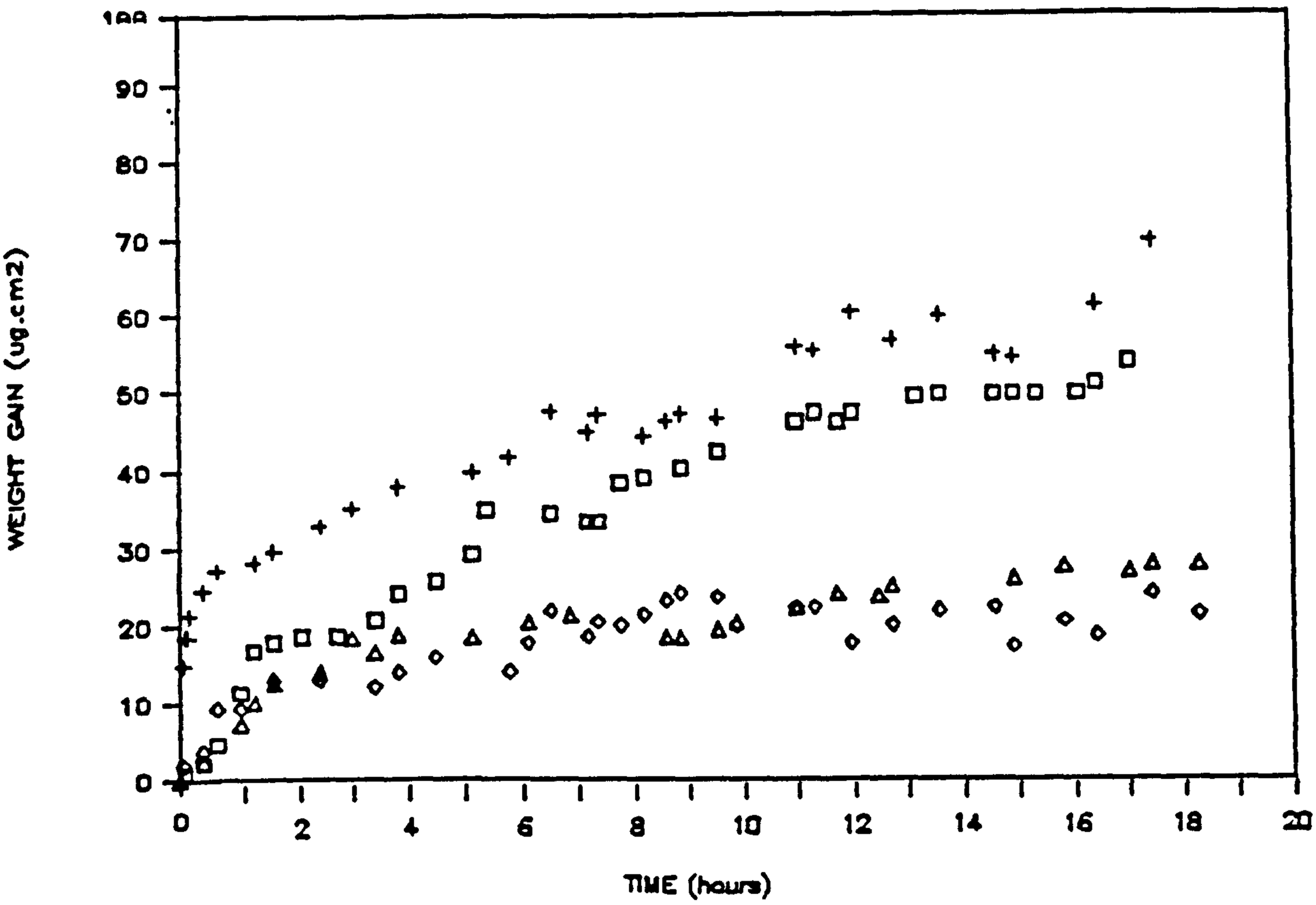

+ *gettered argon*

□ *dry air*

▽ , ◇ *humid argon*

Figure 6.7 Oxidation of polished aluminium (1μm) at 750°C in flowing environments.

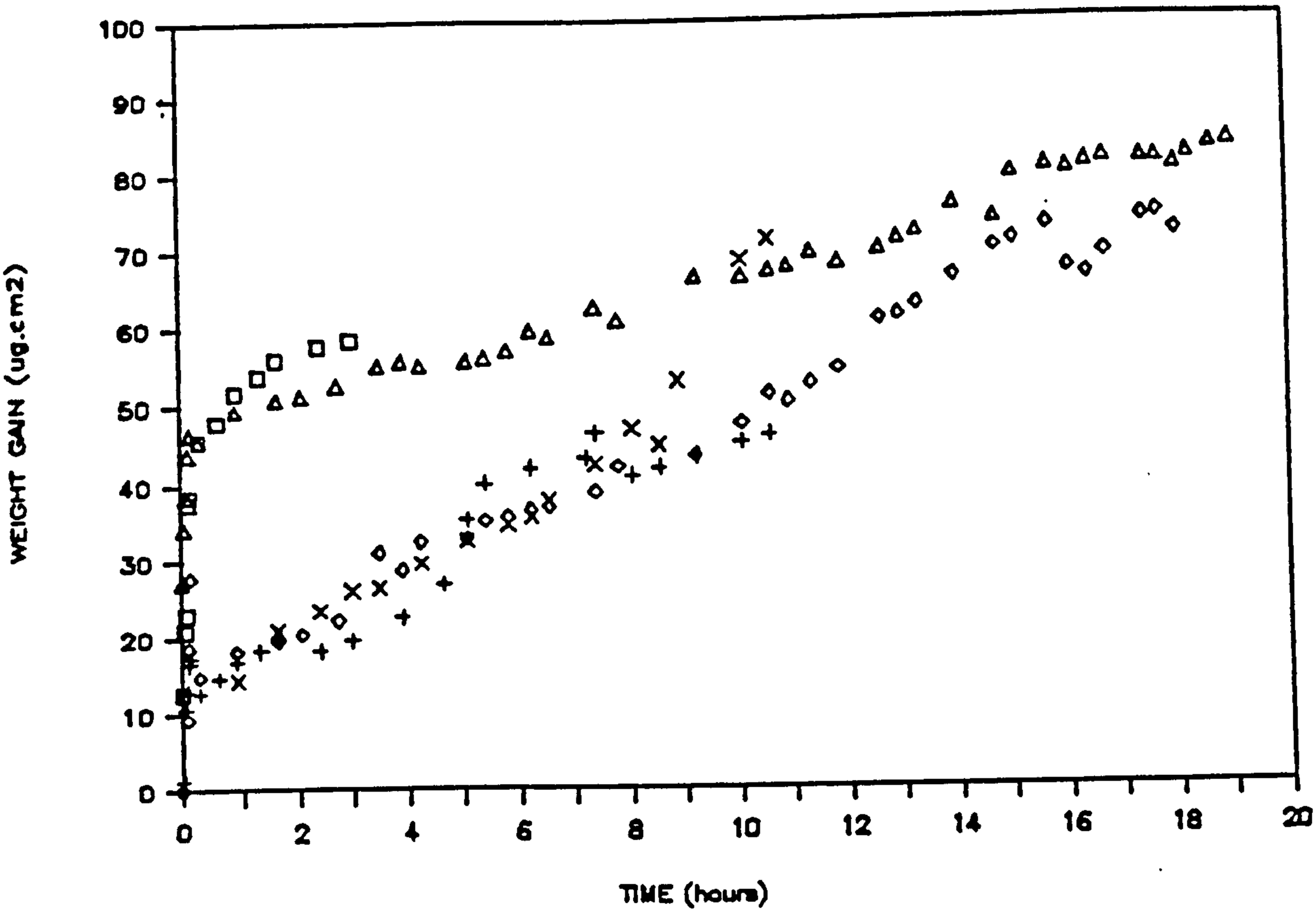

+, ×, ◇ *aluminium in flowing humid air*

△, □ *aluminium in still humid air*

Figure 6.8 Oxidation of electropolished aluminium at 750°C in humid air.

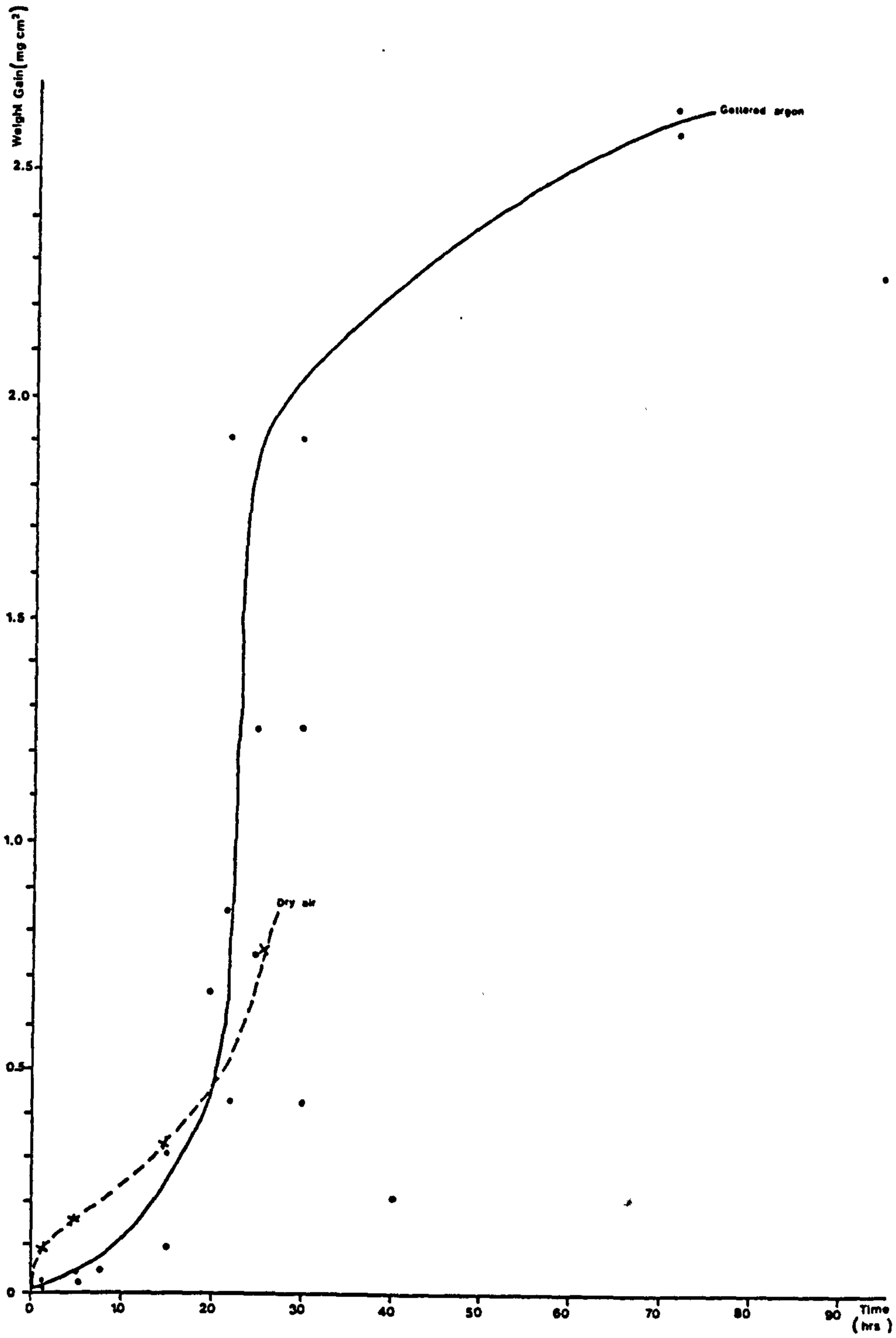

– – – – *dry air*

——— *gettered argon*

Figure 6.9 Oxidation of aluminium in dry air and gettered argon at 750°C.

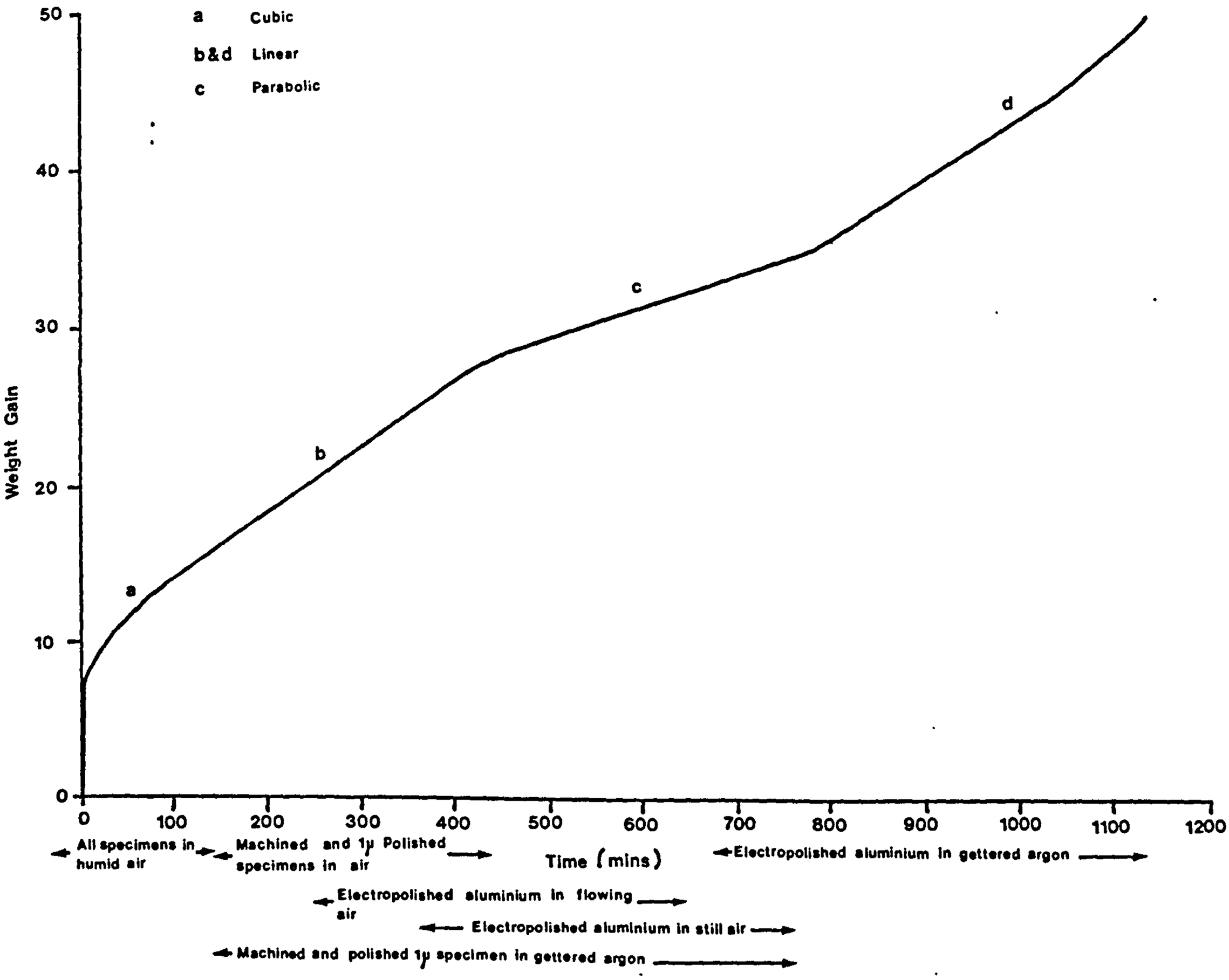

Figure 6.10 Sequence of rate equations followed with different surface finishes during the oxidation of aluminium in flowing and still air and argon environments at 750°C.

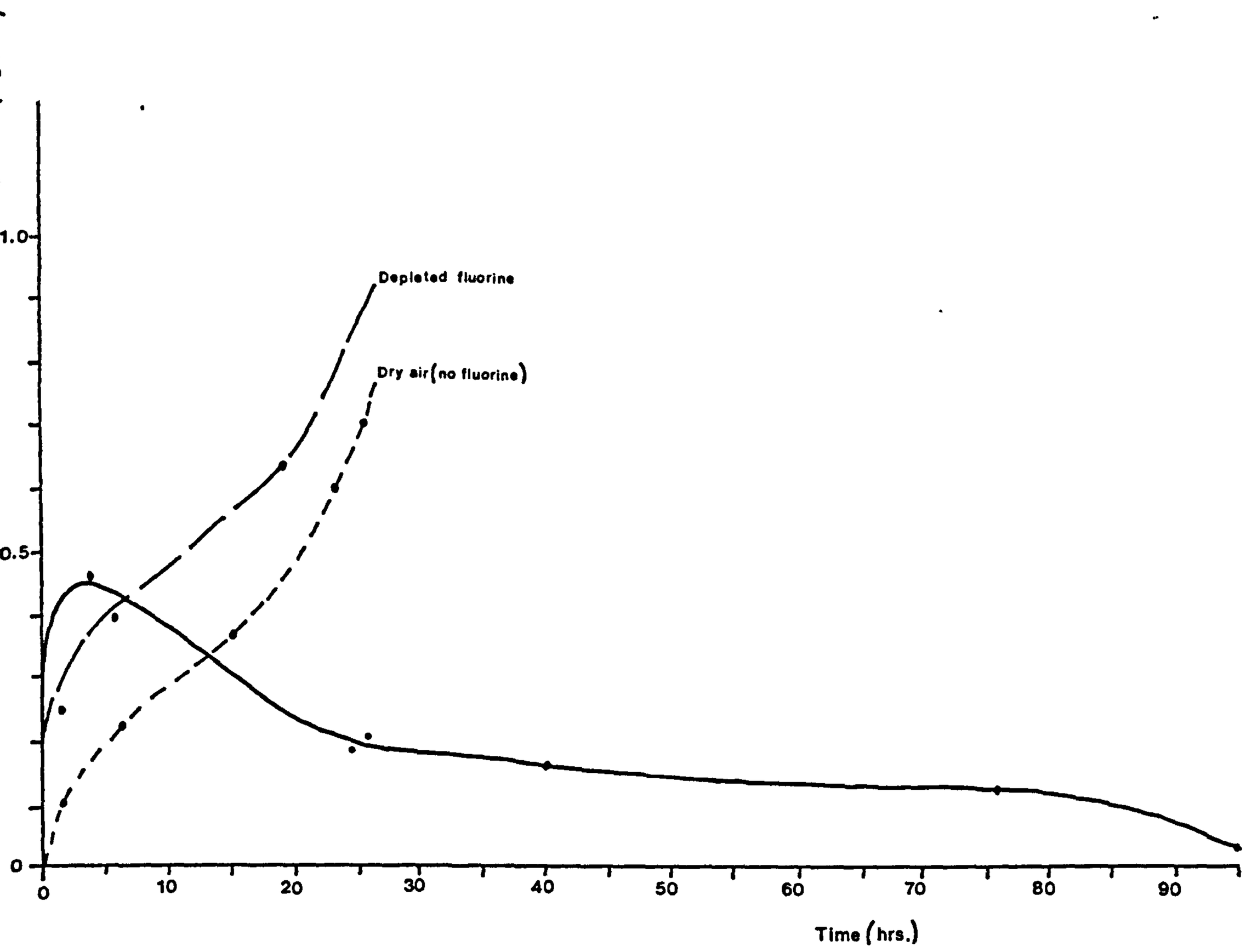

Figure 6.11 Oxidation of aluminium at 750°C in air in the presence of fluoride (KBF_4).

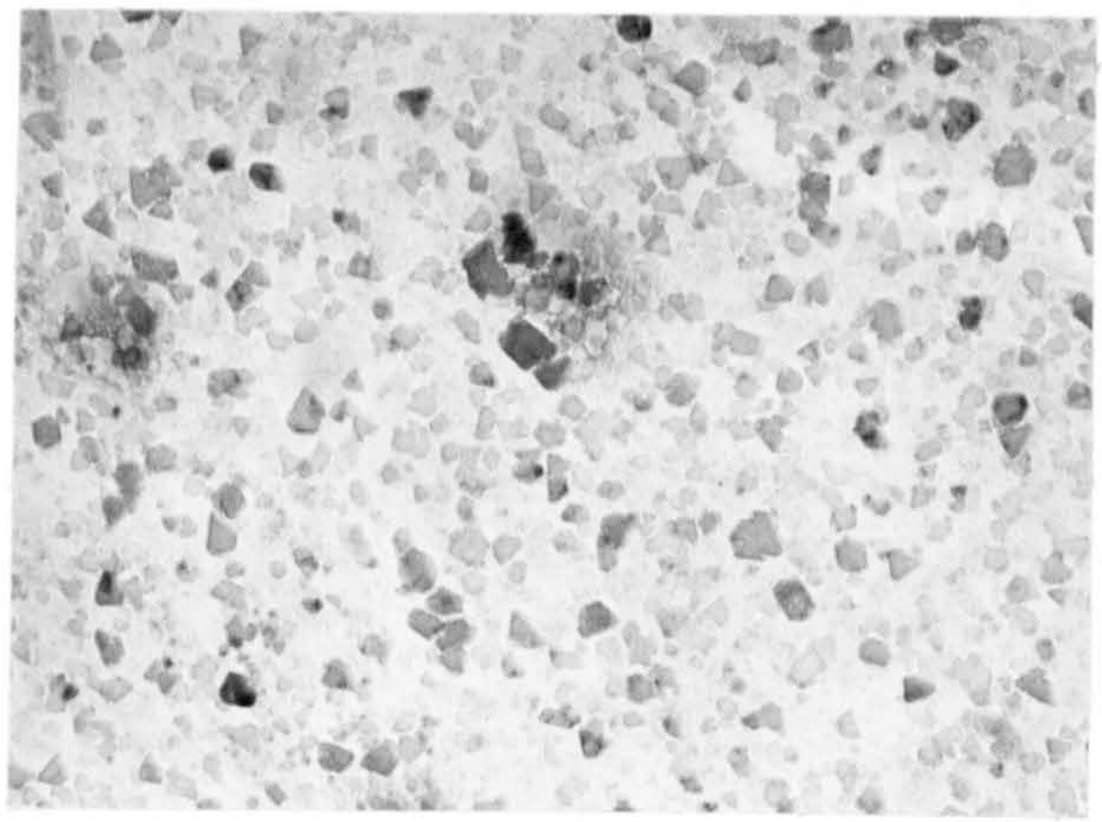

(a)

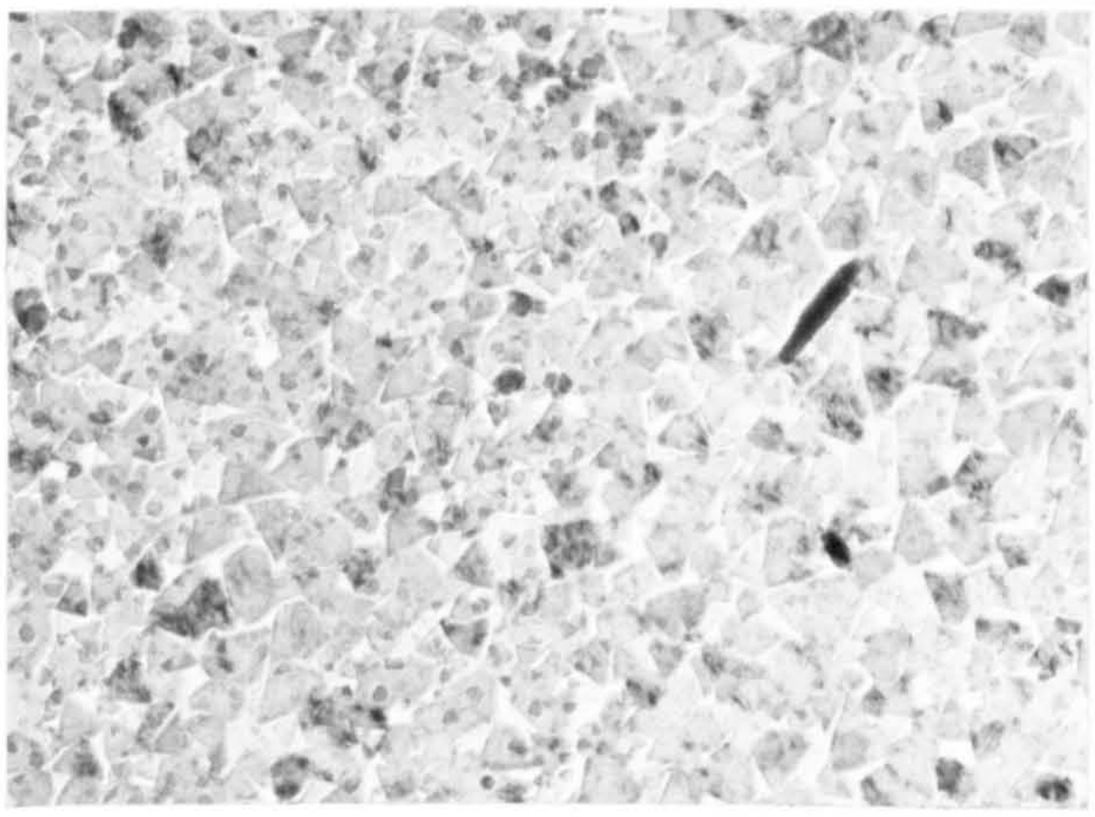

(b)

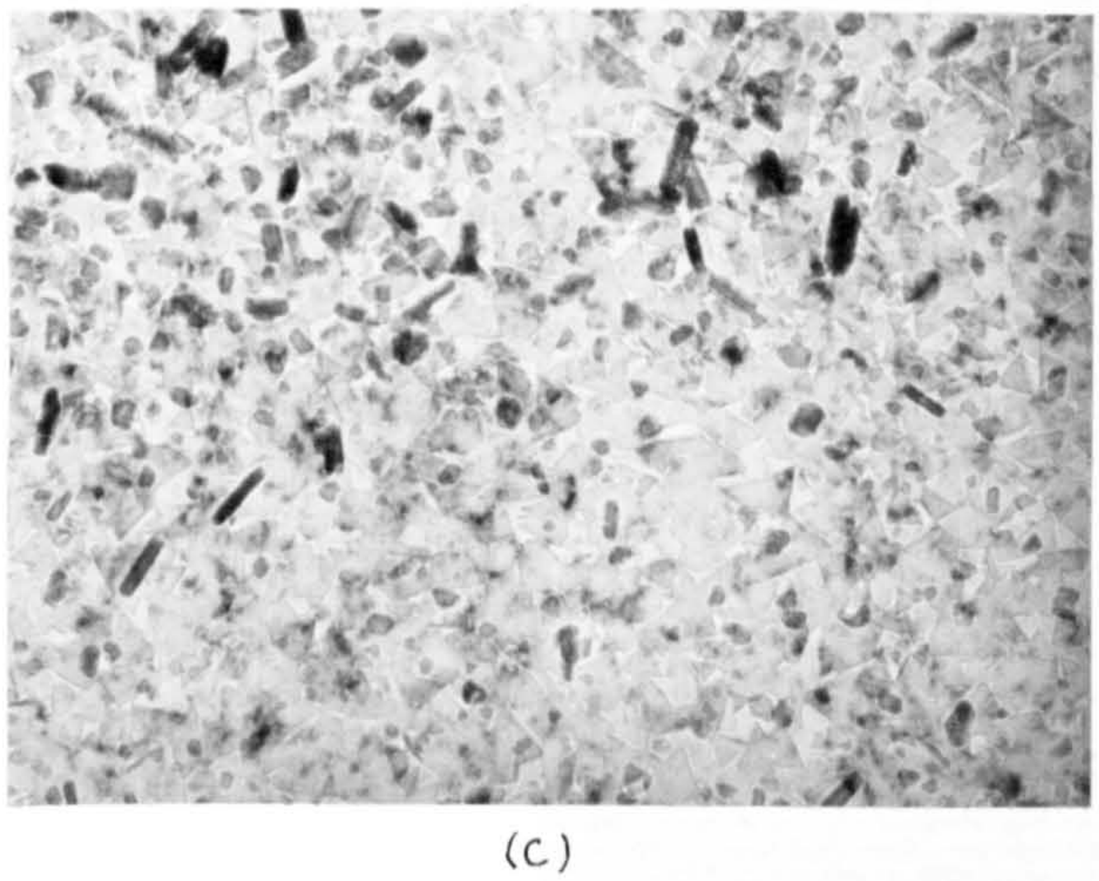

(c)

(d)

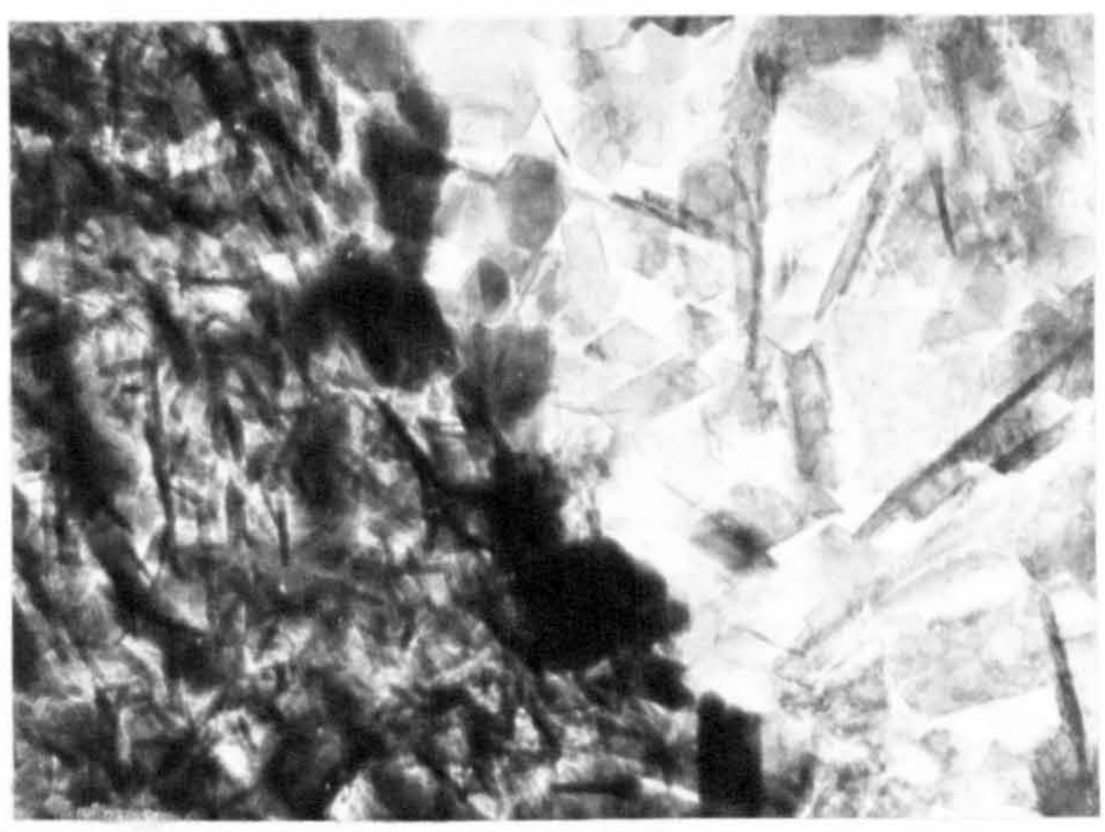

(e)

200nm

Figure 6.12 Oxide growth (x40K) of alumina in dry air at 750°C on skimmed aluminium melts at (a) 5mins (b) 1h (c) 5h and on unskimmed aluminium melts at (d) 5mins (e) 5h

(a)

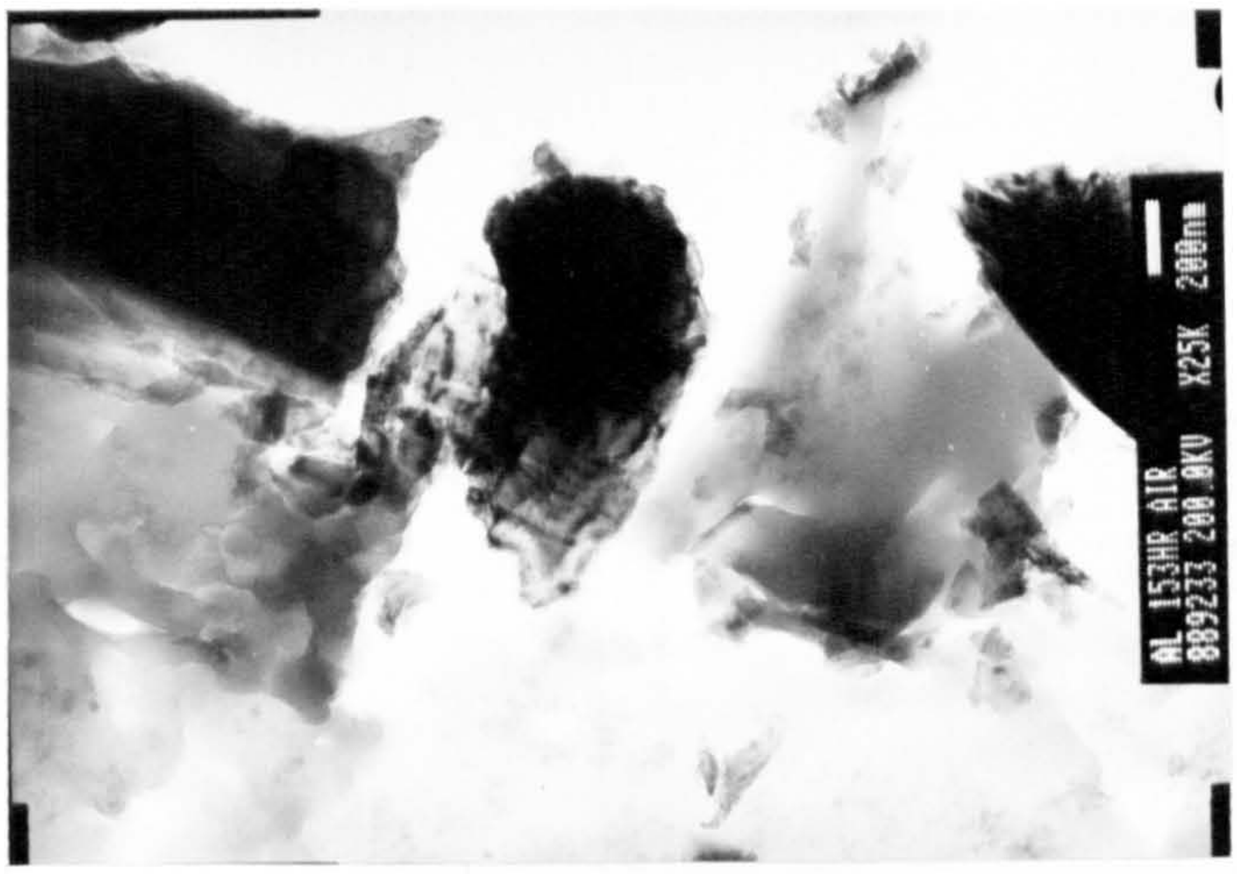

bright field

(b)

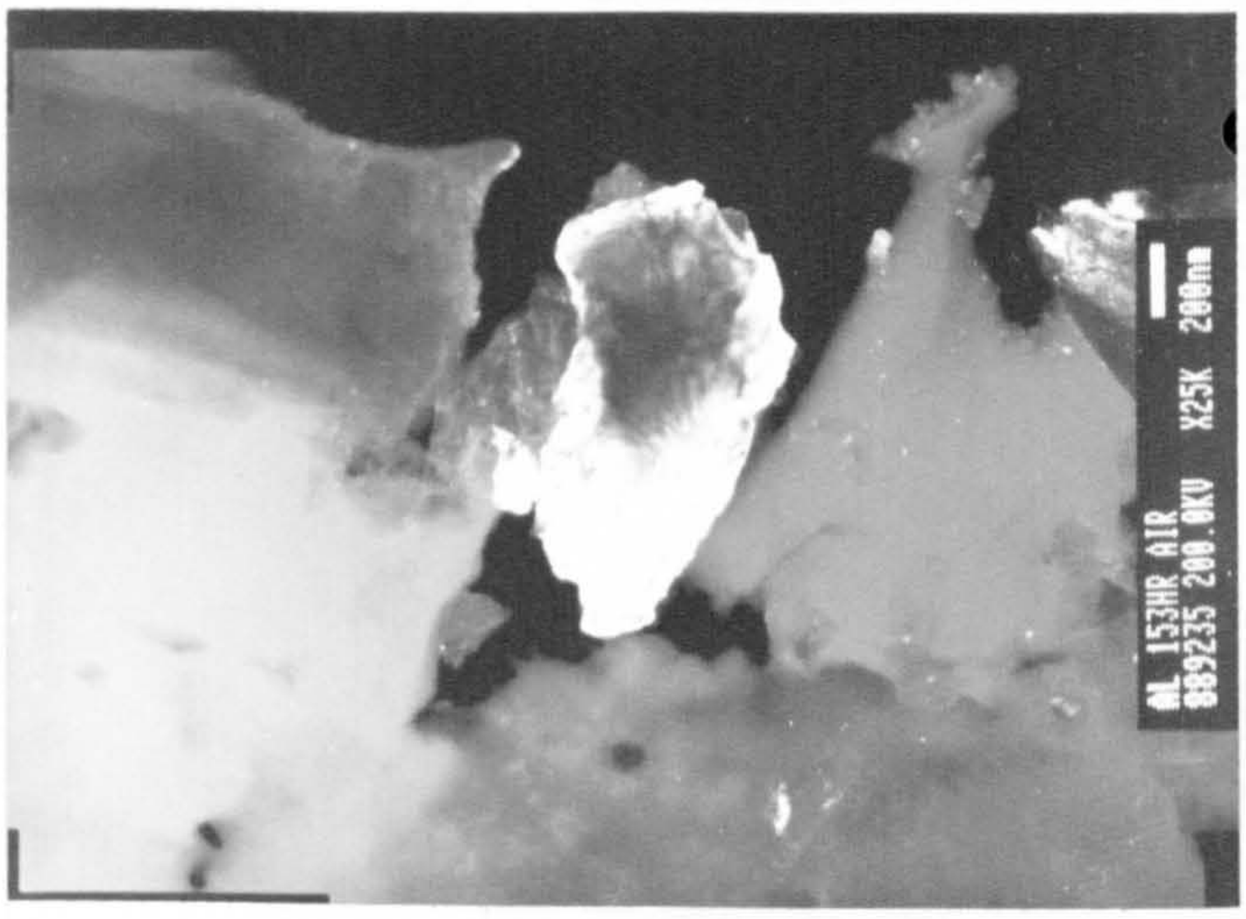

dark field

(c)

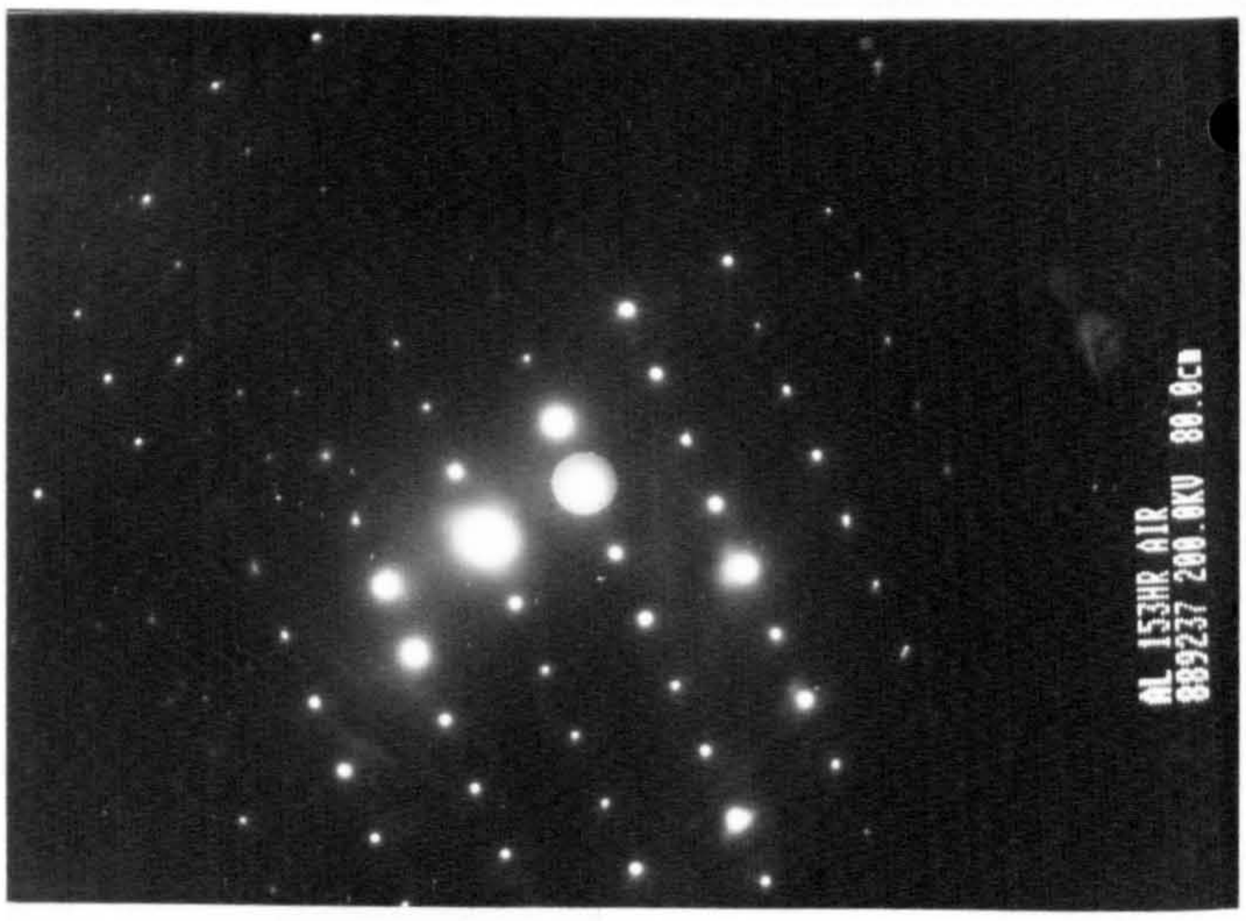

diffraction pattern

Figure 6.13 TEM micrographs of α-Al_2O_3 crystals at the oxide-melt interface formed on unskimmed aluminium at 750°C in dry air after 150h exposure.

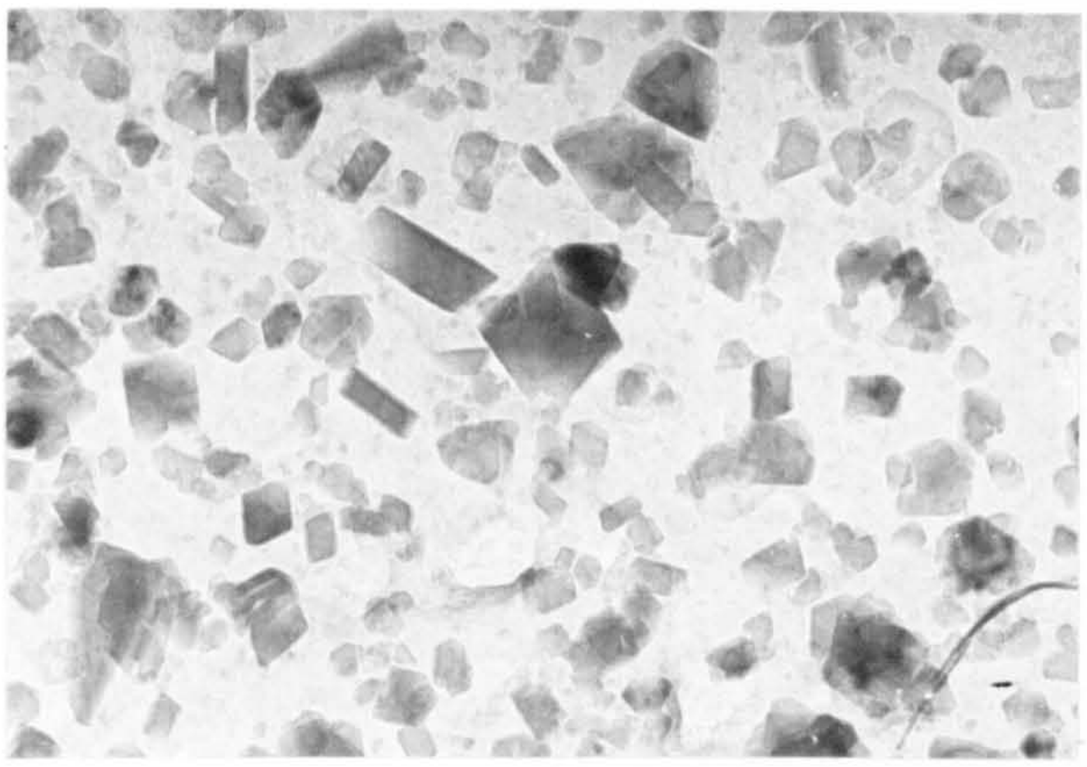

(a)

200 nm

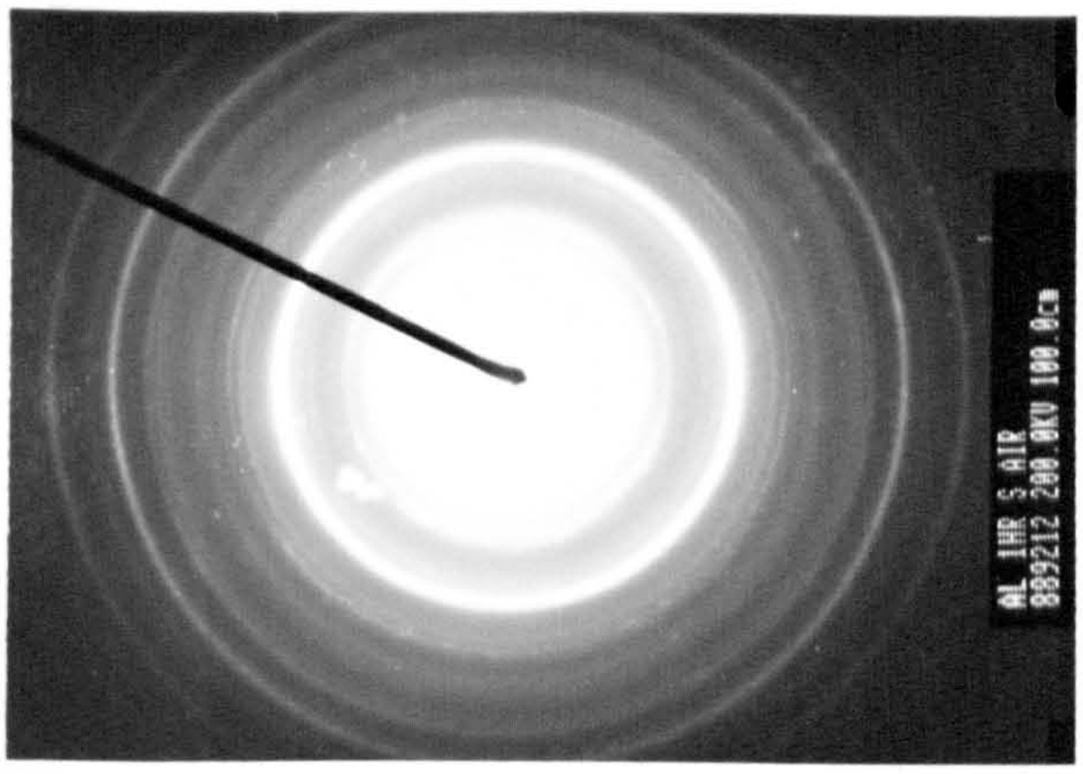

diffraction pattern of (a)

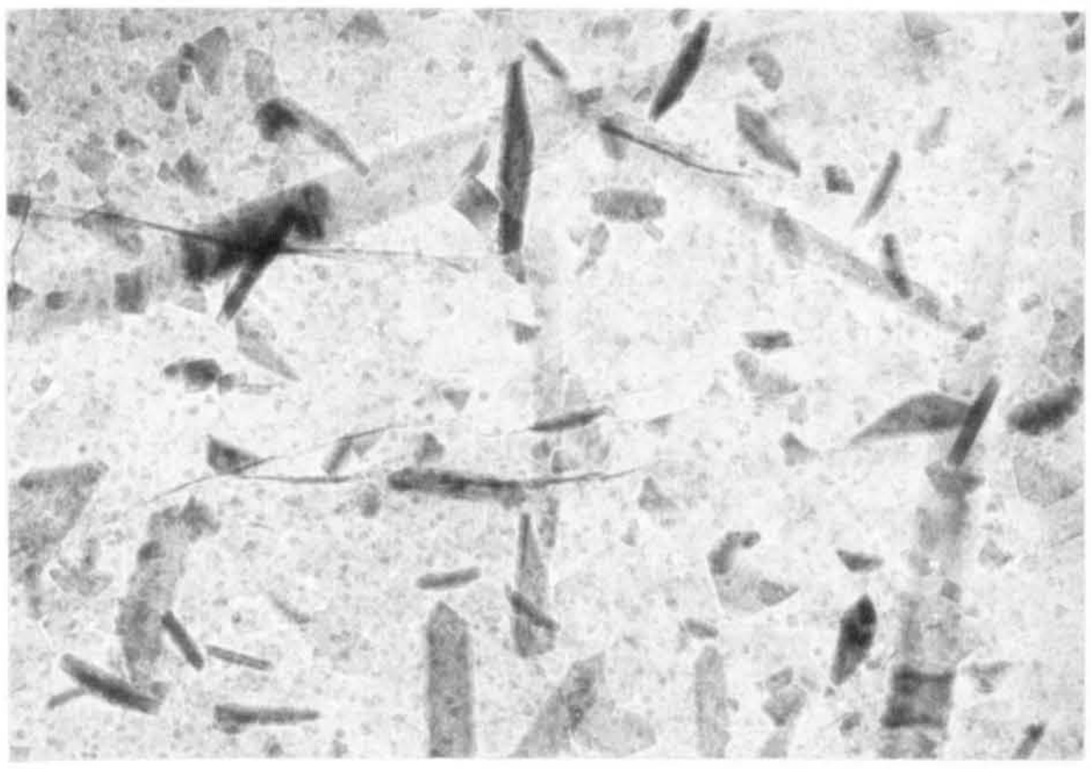

(b)

200 nm

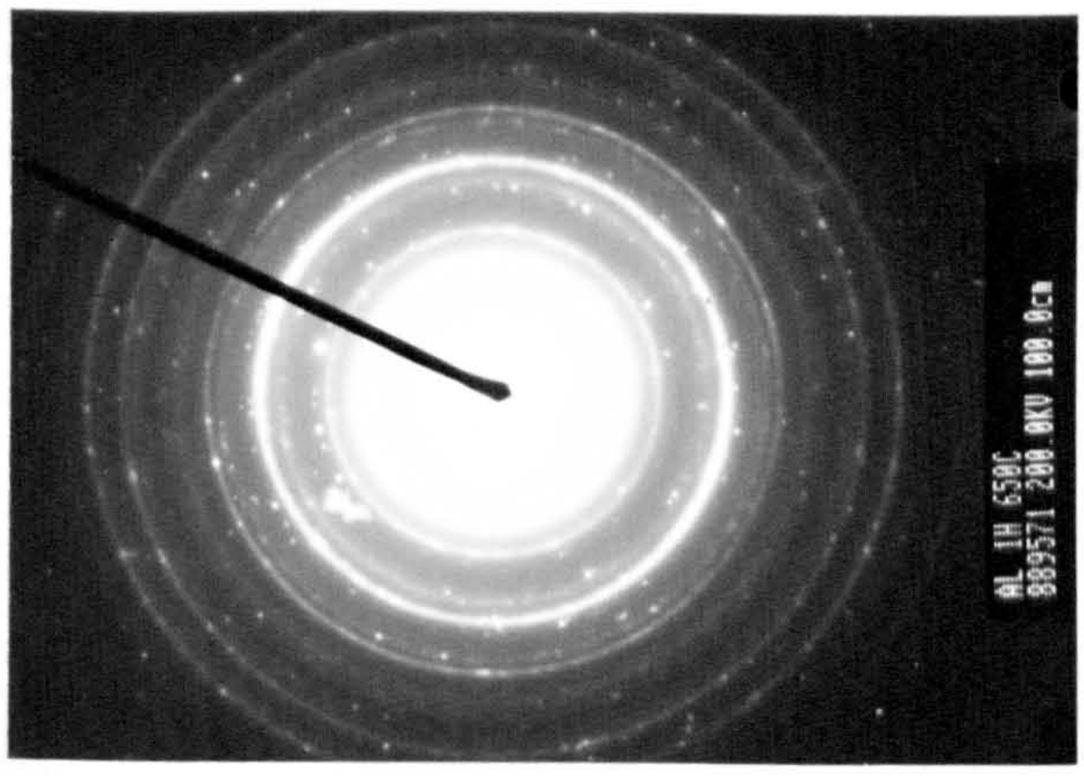

diffraction pattern of (b)

Figure 6.14 Growth (x40K) of γ-Al_2O_3 on skimmed aluminium melts after 1h (a) at 650 C in dry air (b) at 750°C in humid air

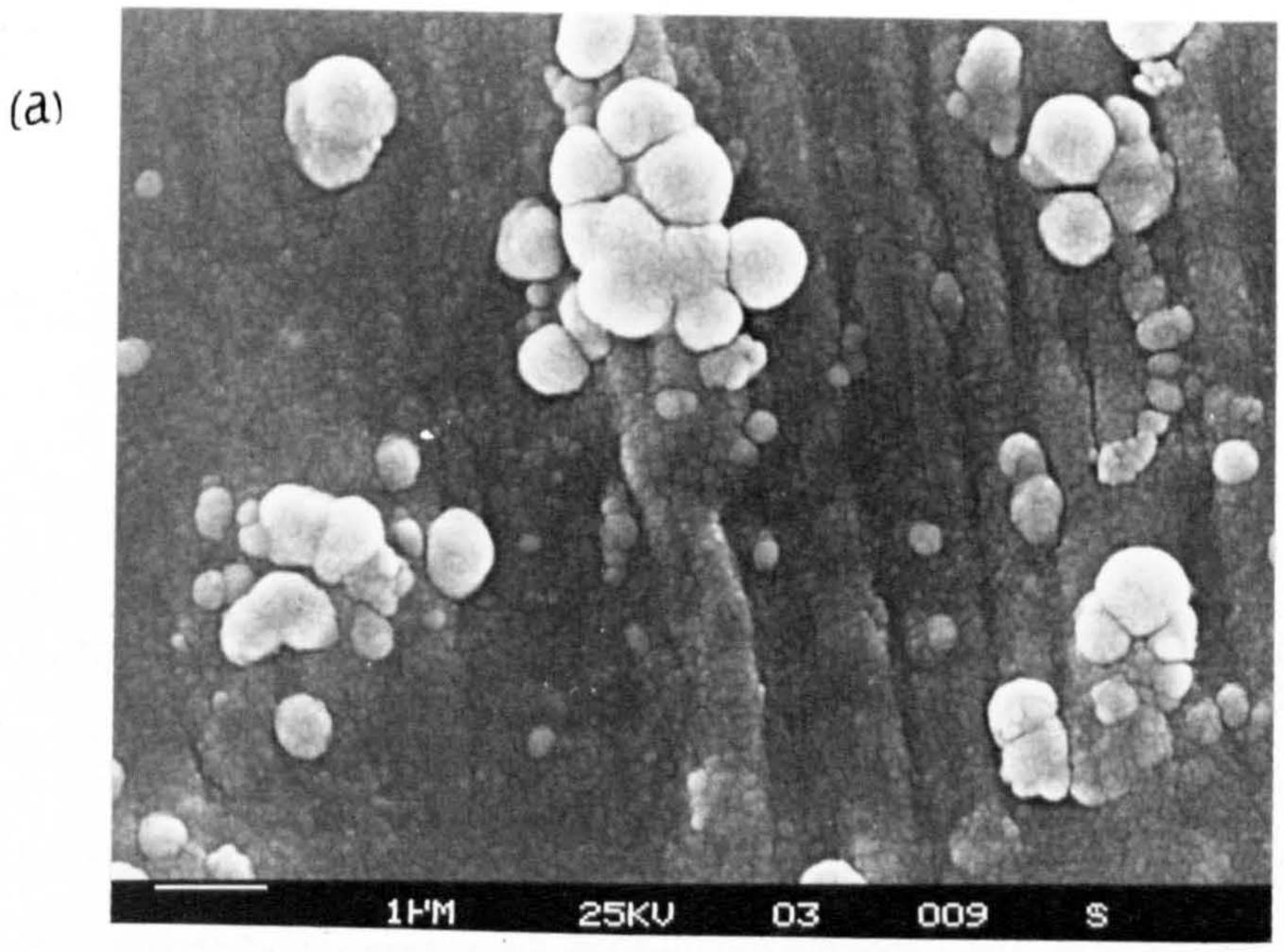

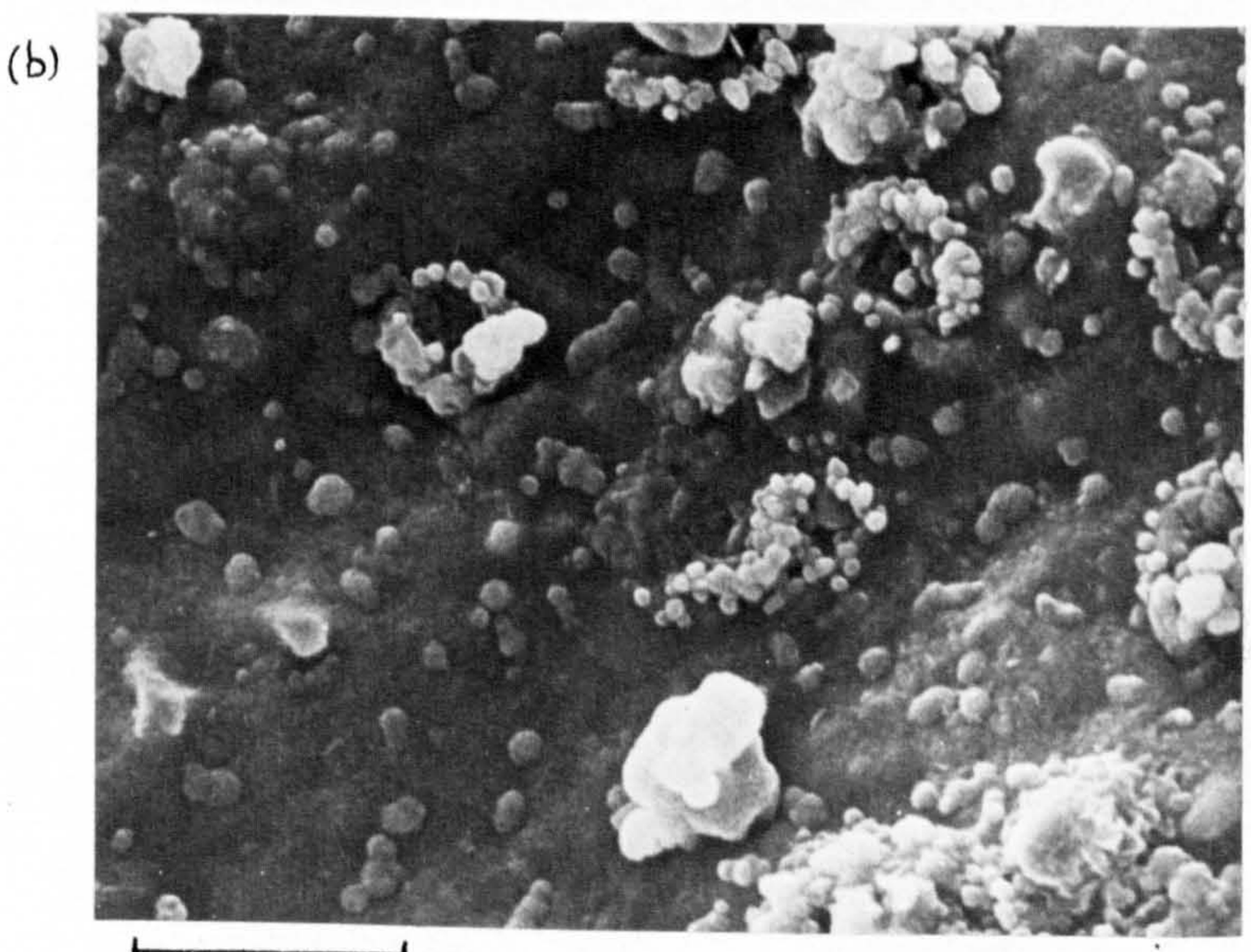

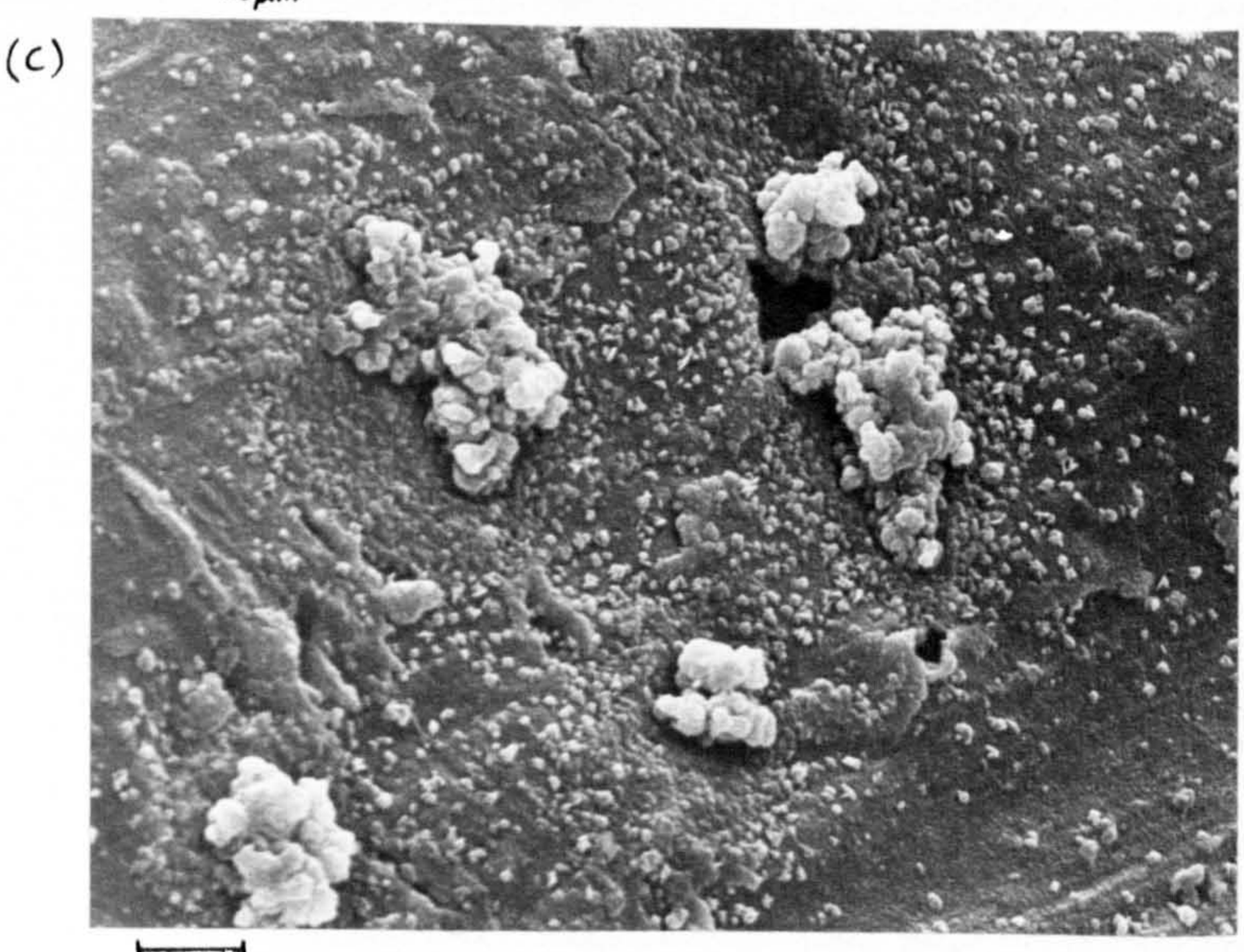

Figure 6.15 SEM of oxide-gas interfaces oxidised at 750°C in humid air for 15h on (a) unskimmed aluminium (b) skimmed aluminium and (c) unskimmed aluminium

(a)

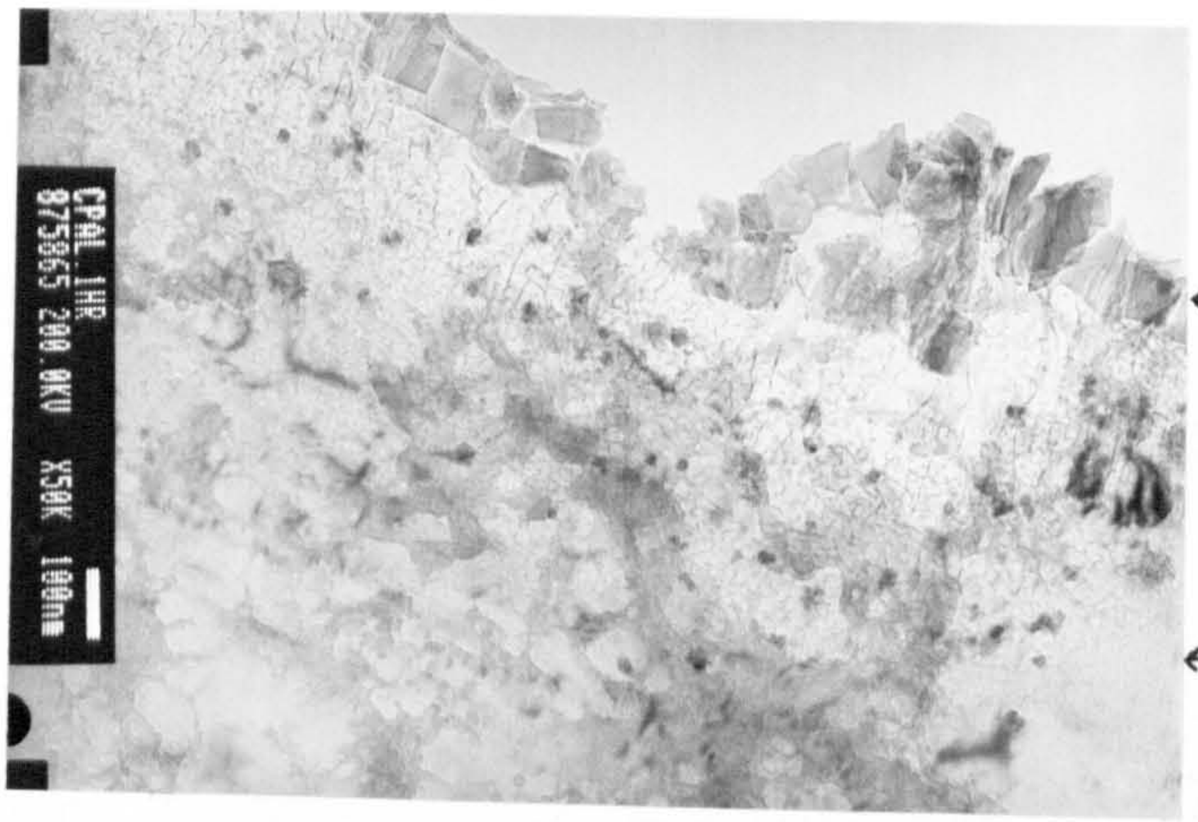

(b)

(c)

Figure 6.16 Microtome sections through oxide and metal of aluminium oxidised at 750°C in dry air for (a,b) 1h and for (c) 5h

(a)

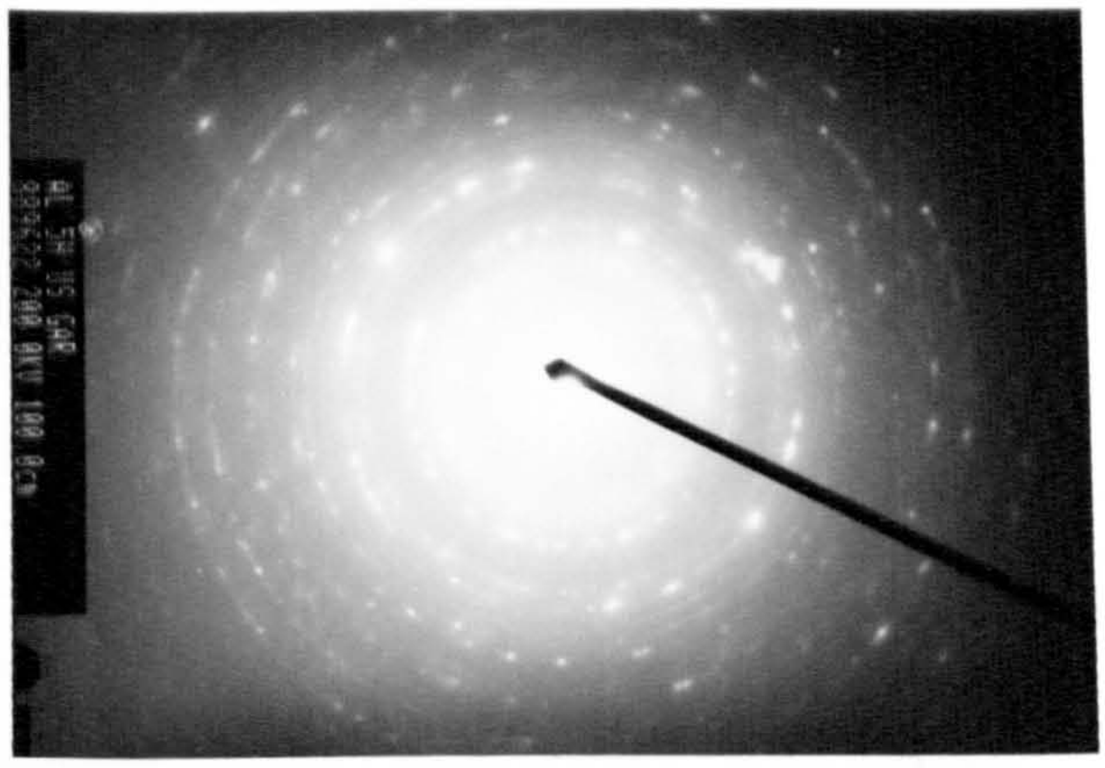

diffraction pattern of (a)

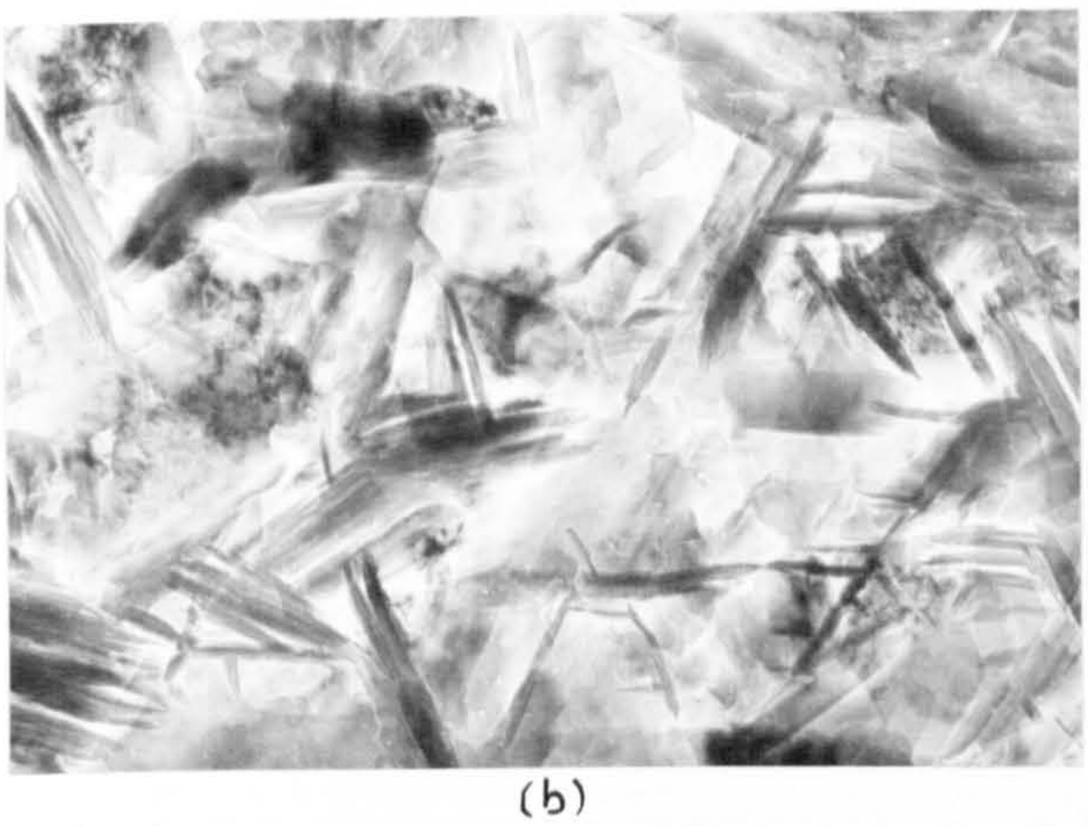

(b)

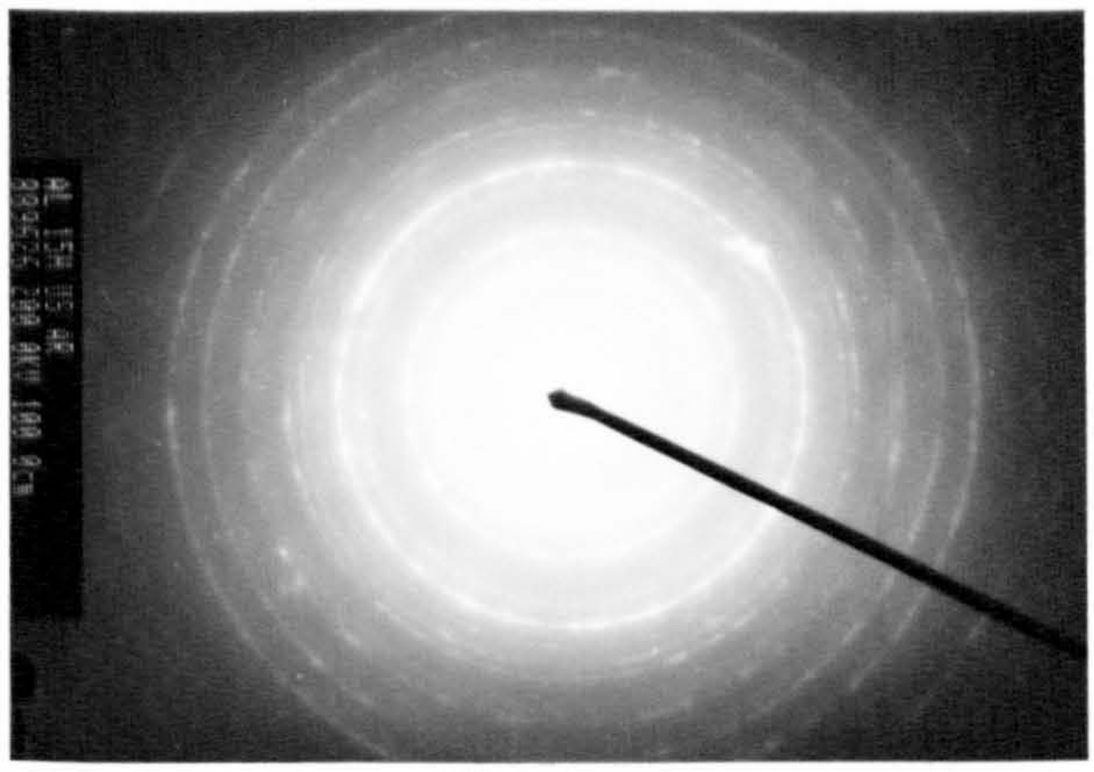

diffraction pattern of (b)

100nm

(c)

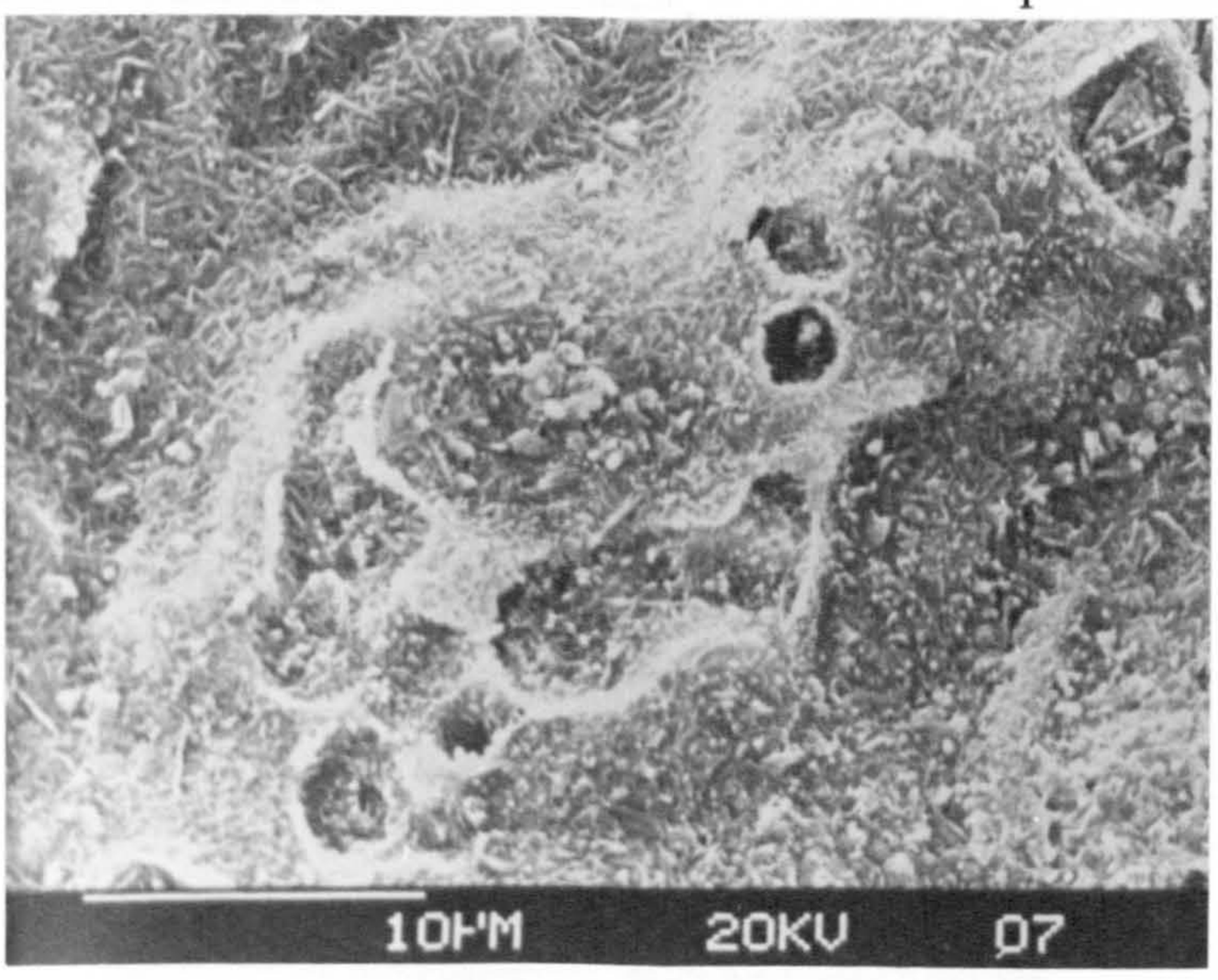

Figure 6.17 TEM of γ and α-alumina formed at 750°C on aluminium in gettered argon after (a) 5h and (b) 15h with (c) SEM of metal-oxide interface at 15h with excess metal removed

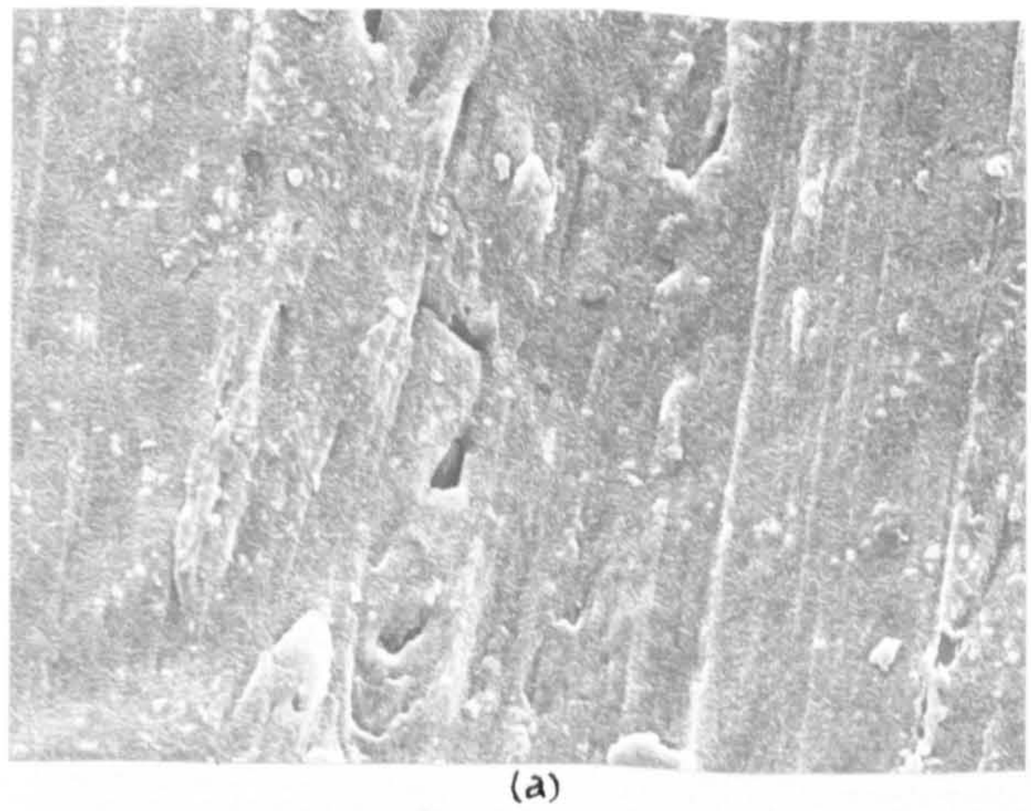

(a)

10μm

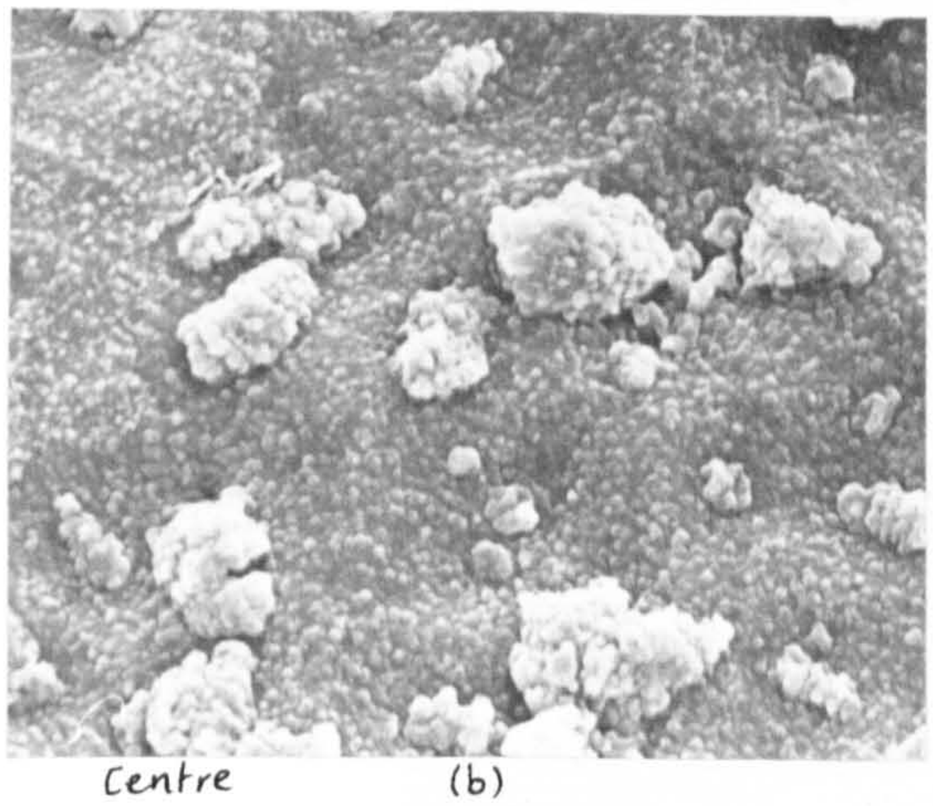

Centre (b)

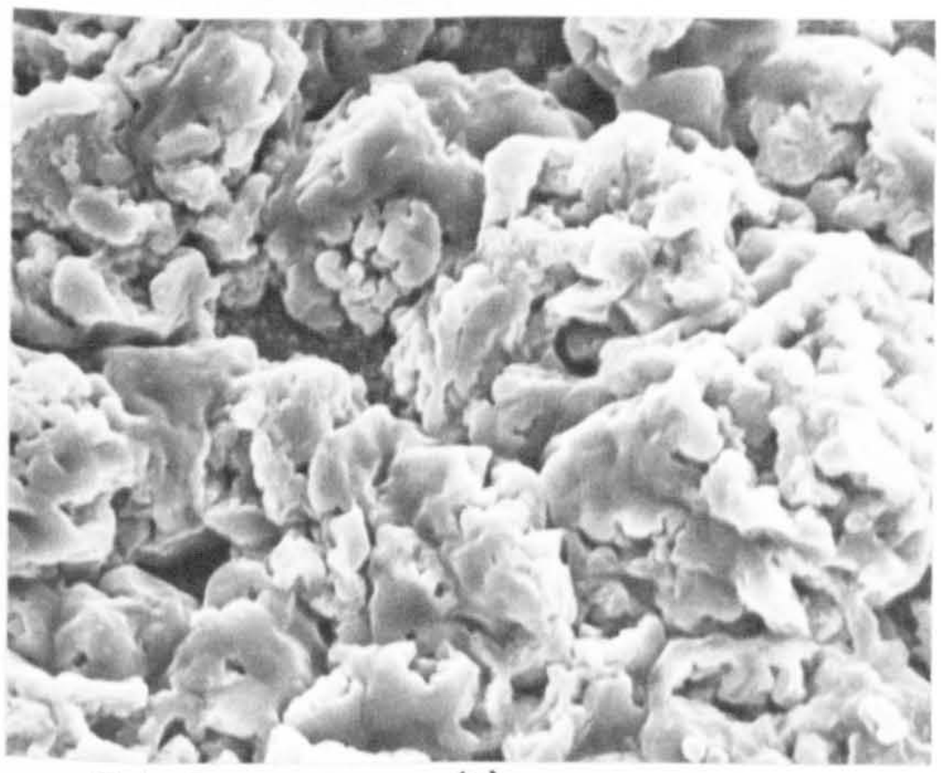

Edge (c)

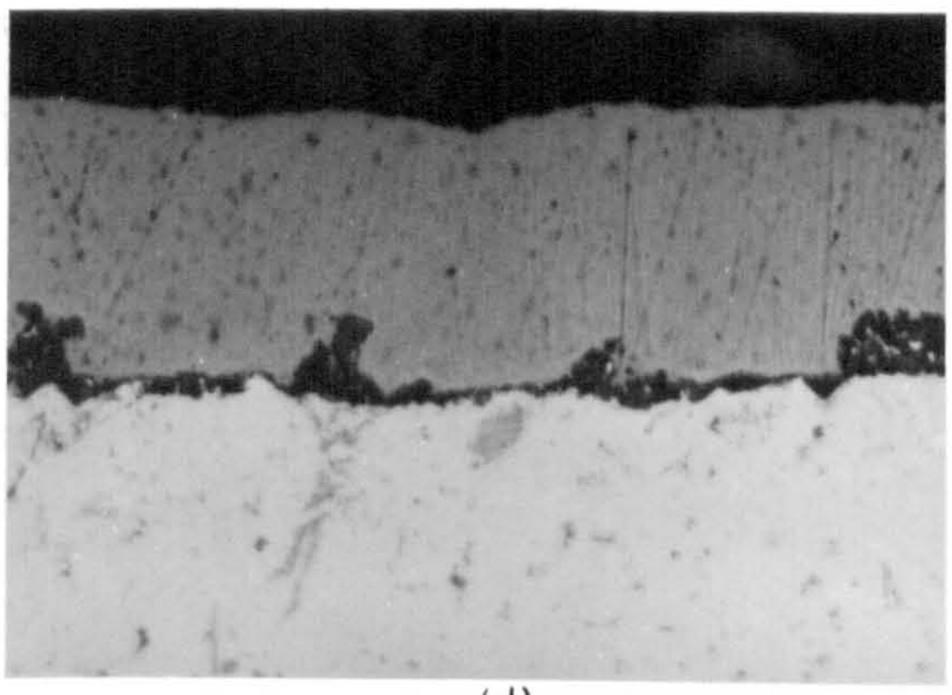

(d)

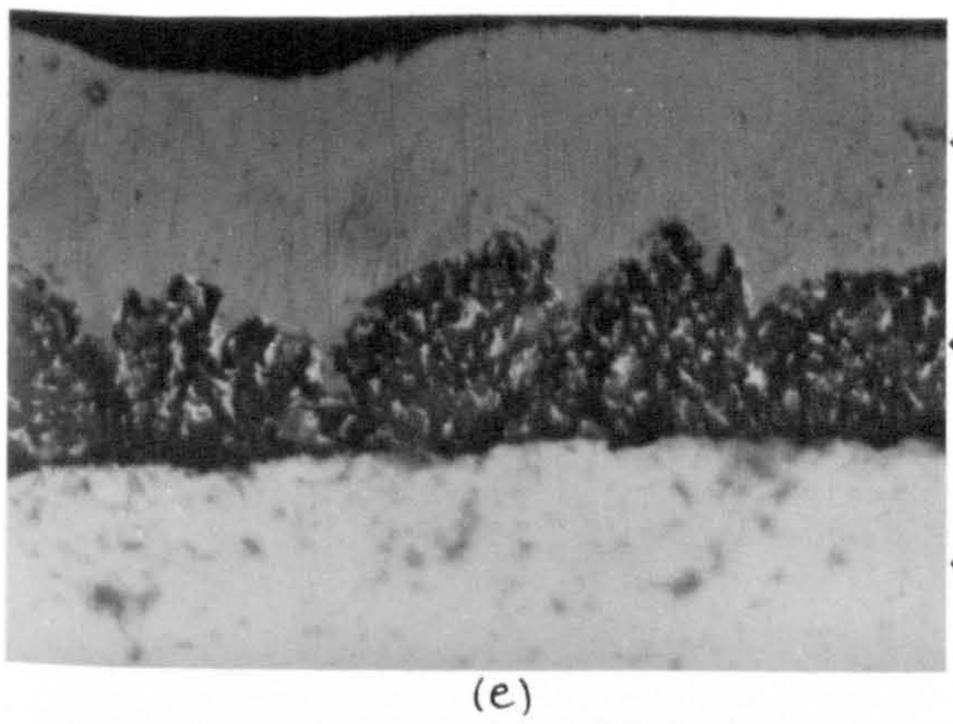

(e)

(f)

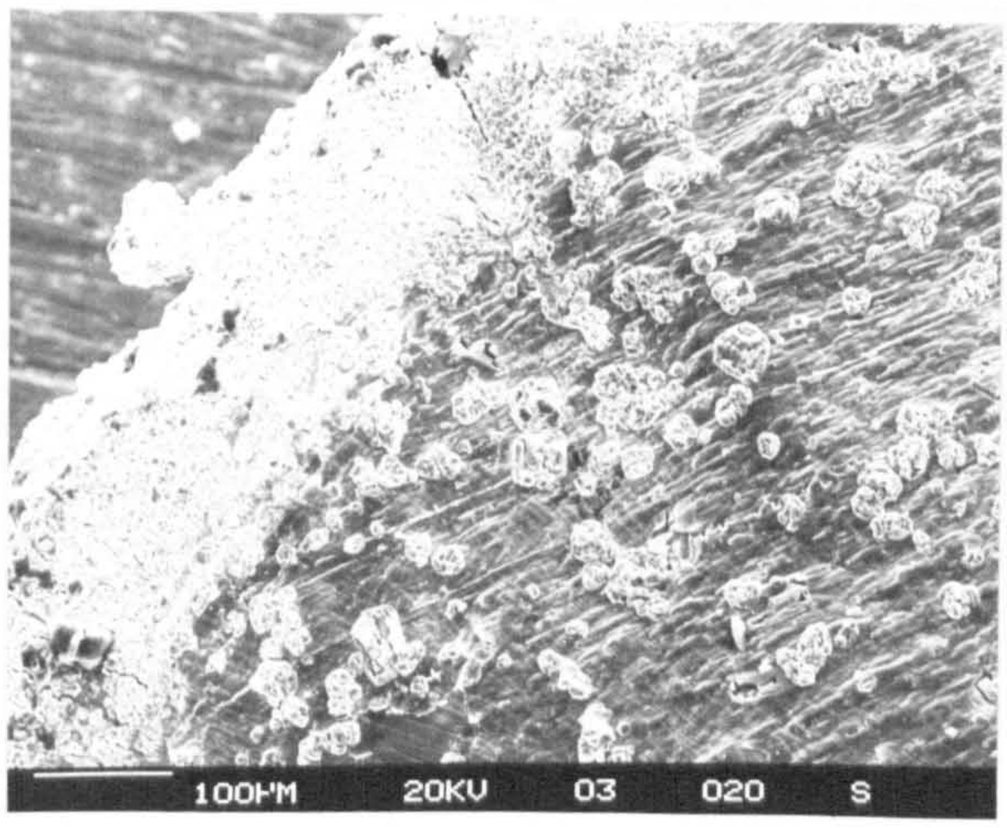

Figure 6.18 Aluminium after 5h oxidation at 750°C in (a) humid air and (b) in dry air and (d) through the specimen centre and (c,e) through the specimen edge. (f) Al oxidised in humid air for 70h

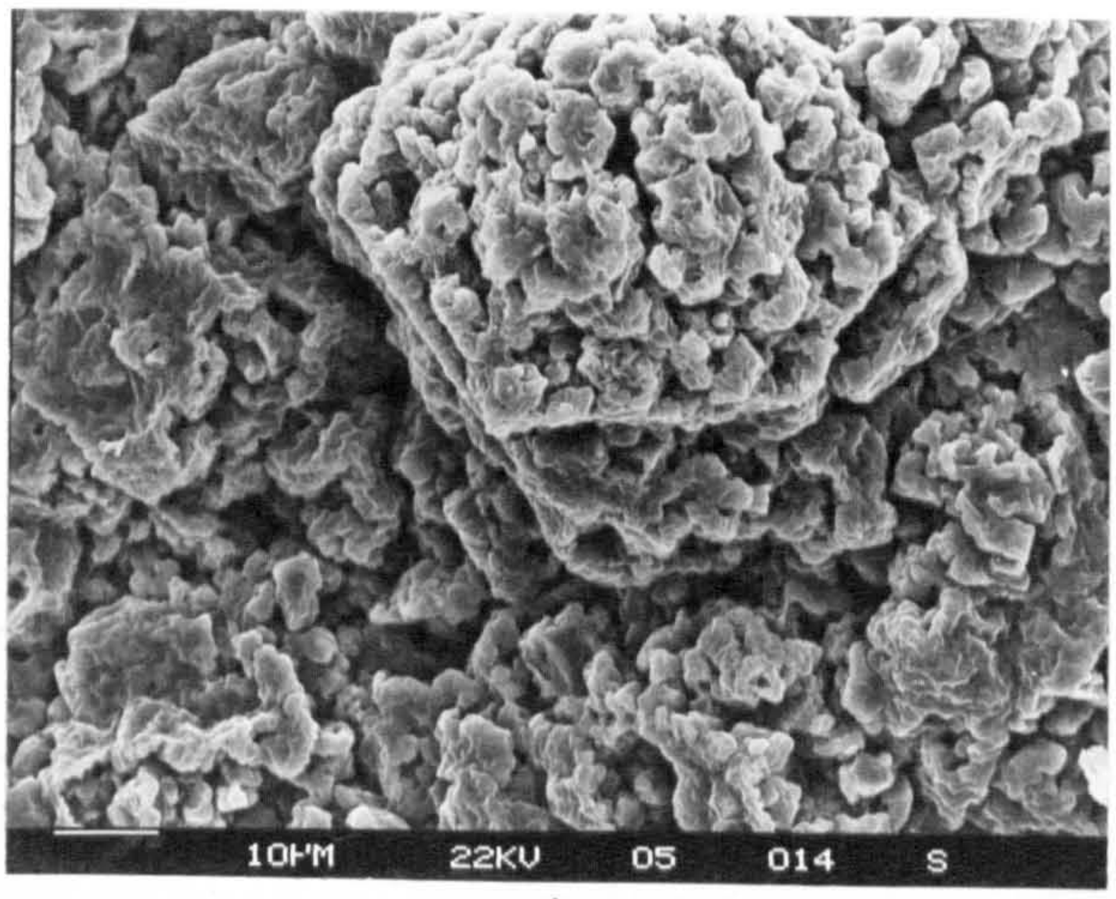

(a)

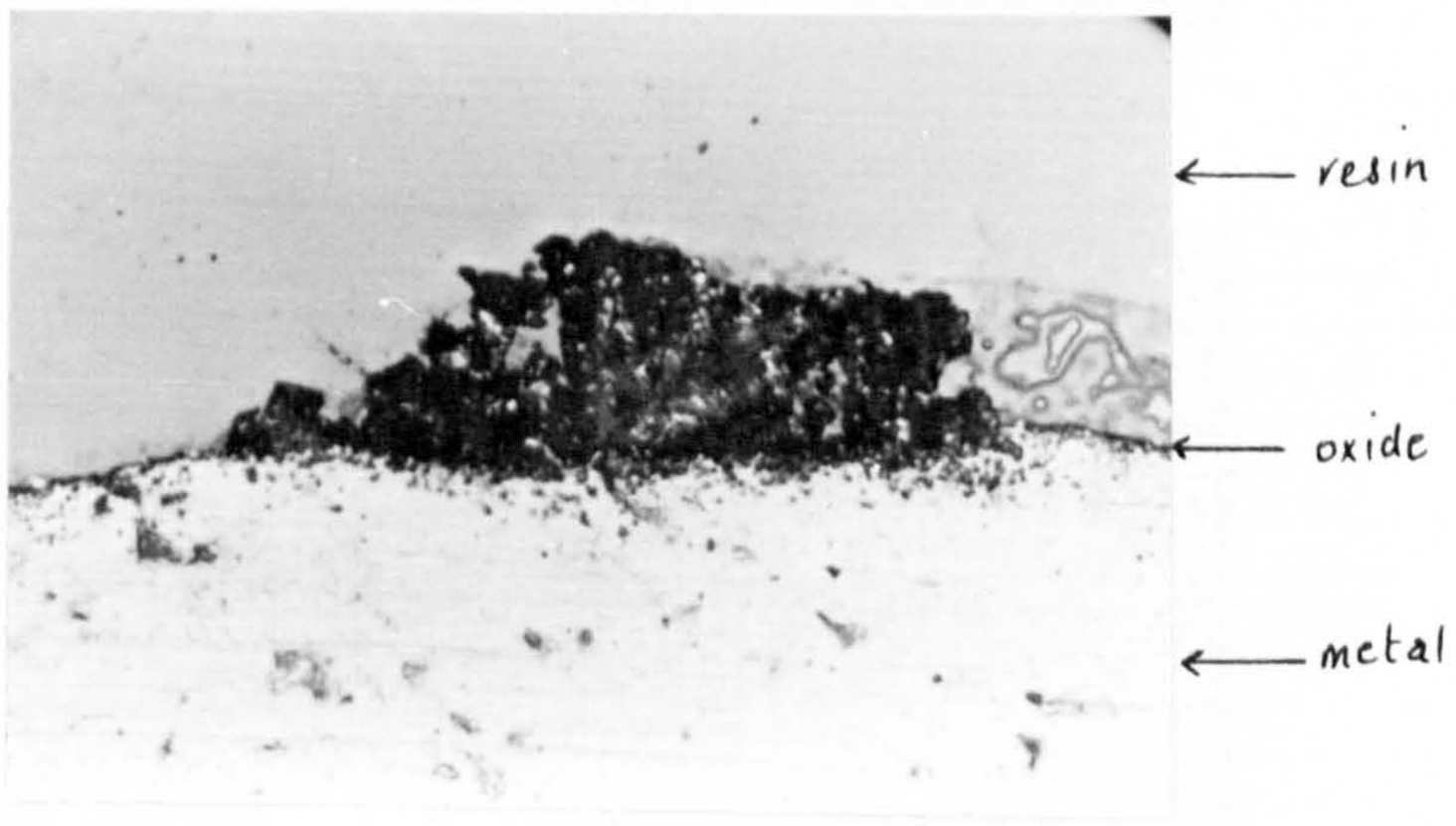

(b)

10µm

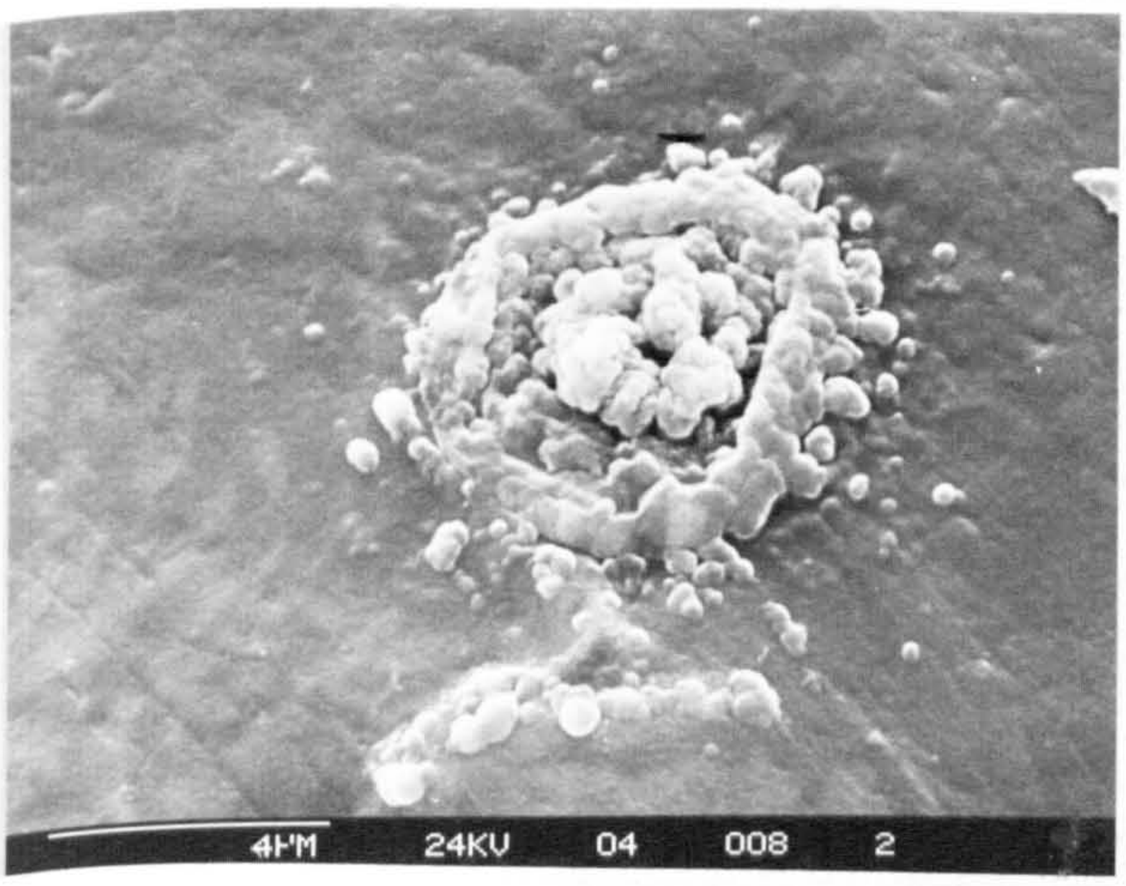

(c)

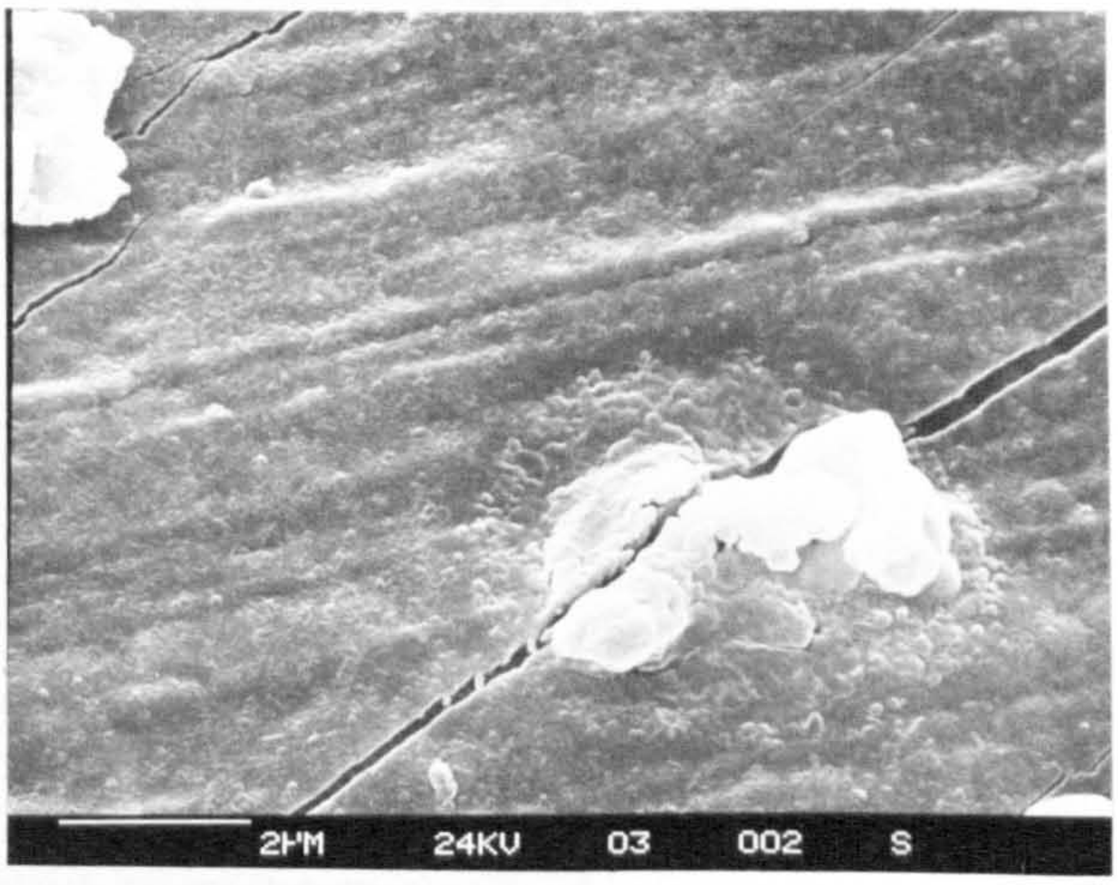

(d)

Figure 6.19 Oxidation of aluminium at 750°C in dry air for 24h showing oxide growths on (a) top surface with (b) section and (c,d) reverse surface

bright field

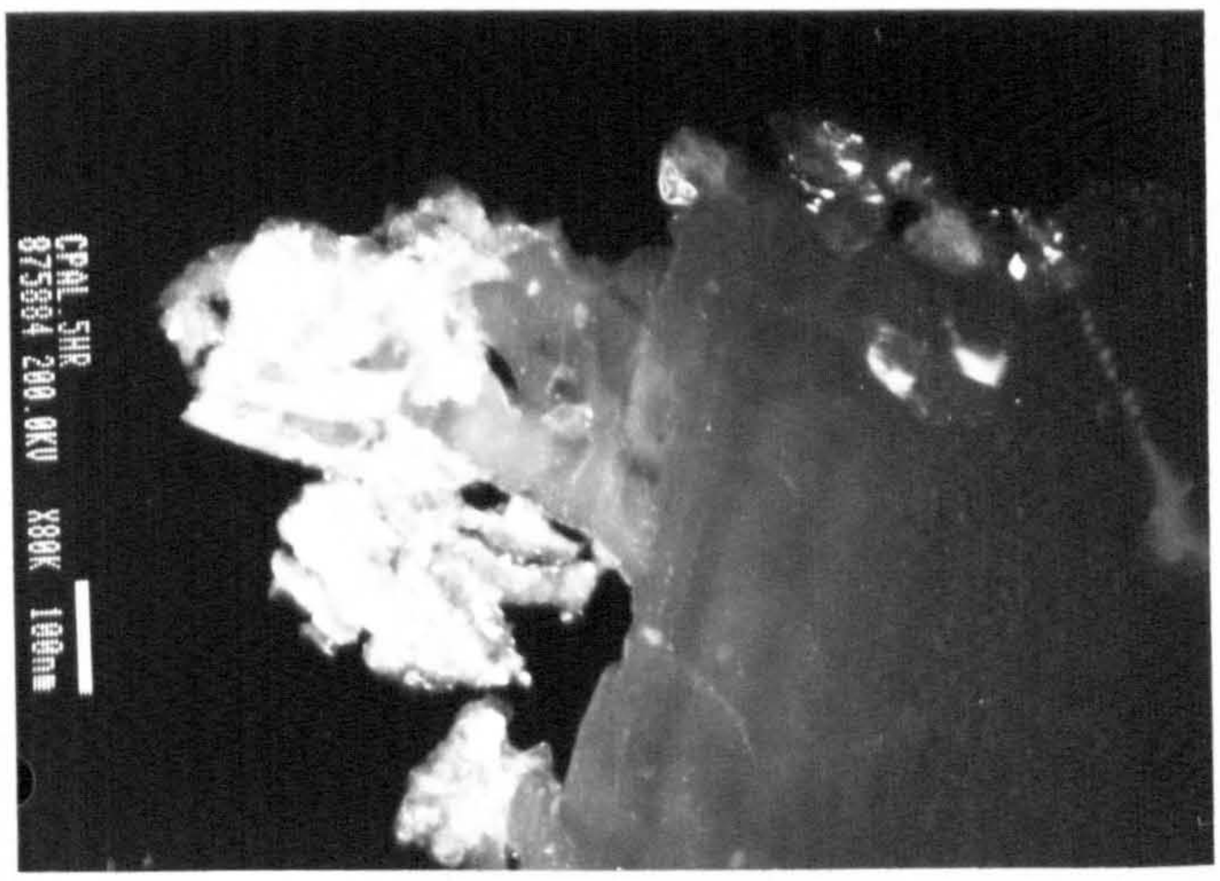

dark field

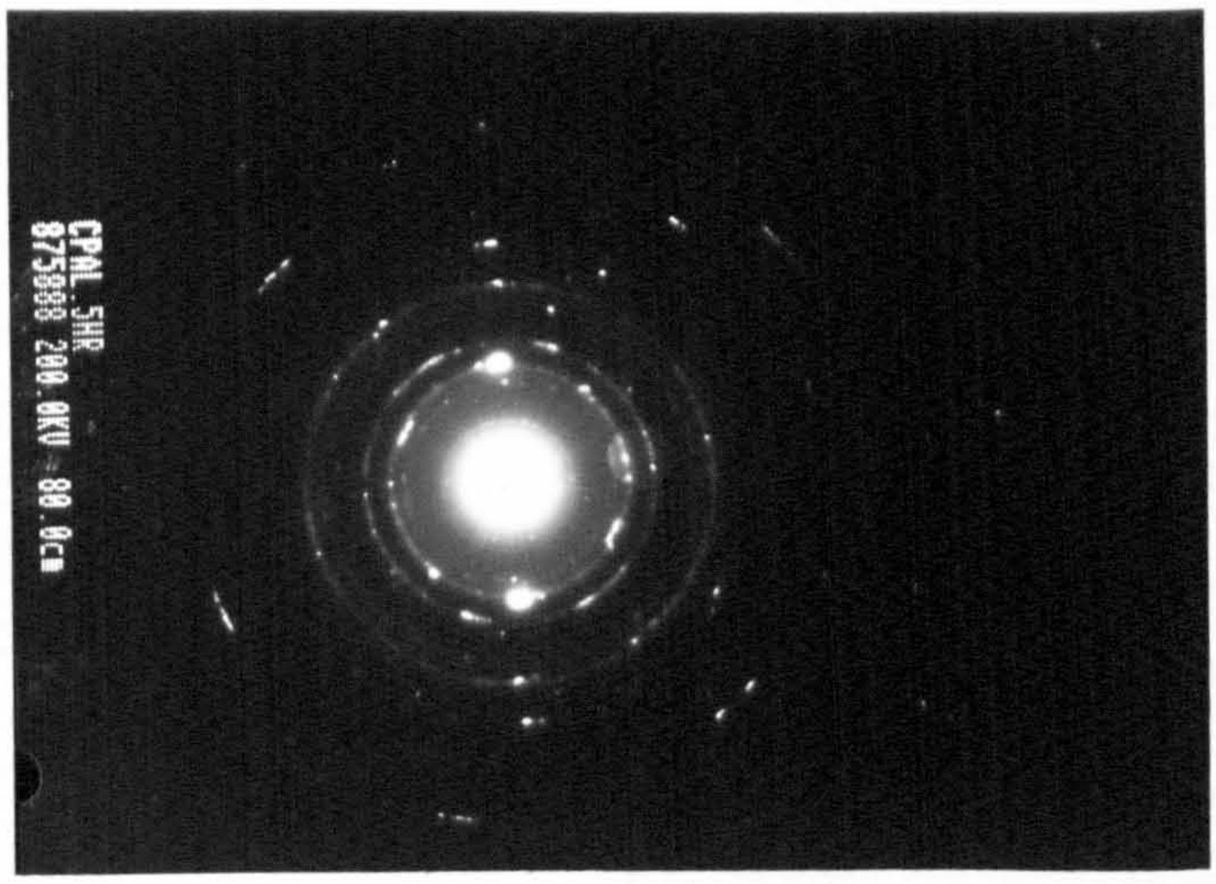

diffraction pattern

Figure 6.20 TEM of microtomed sections of γ -Al_2O_3 and aluminium after 5h oxidation in dry air at 750°C

(a)

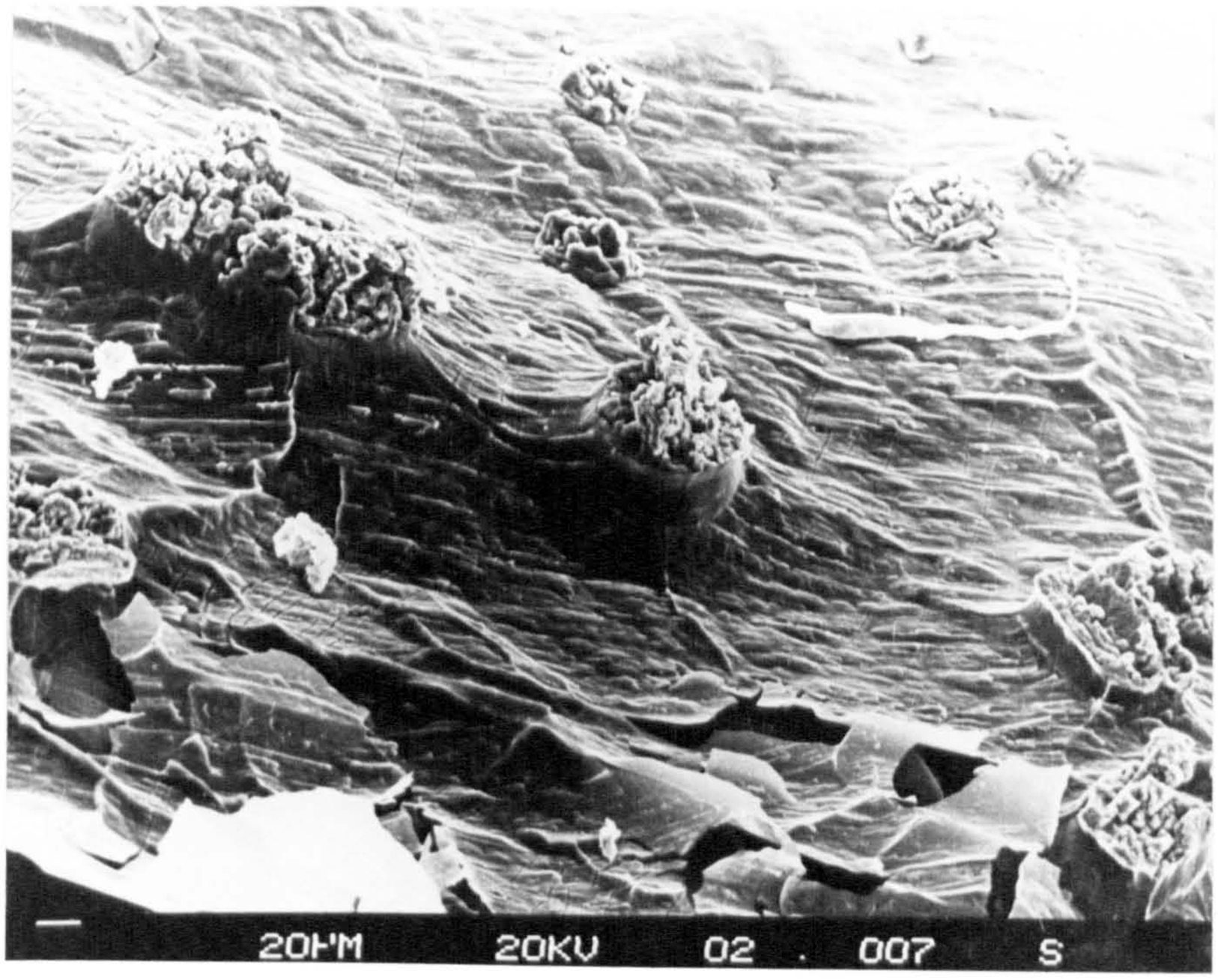

(b)

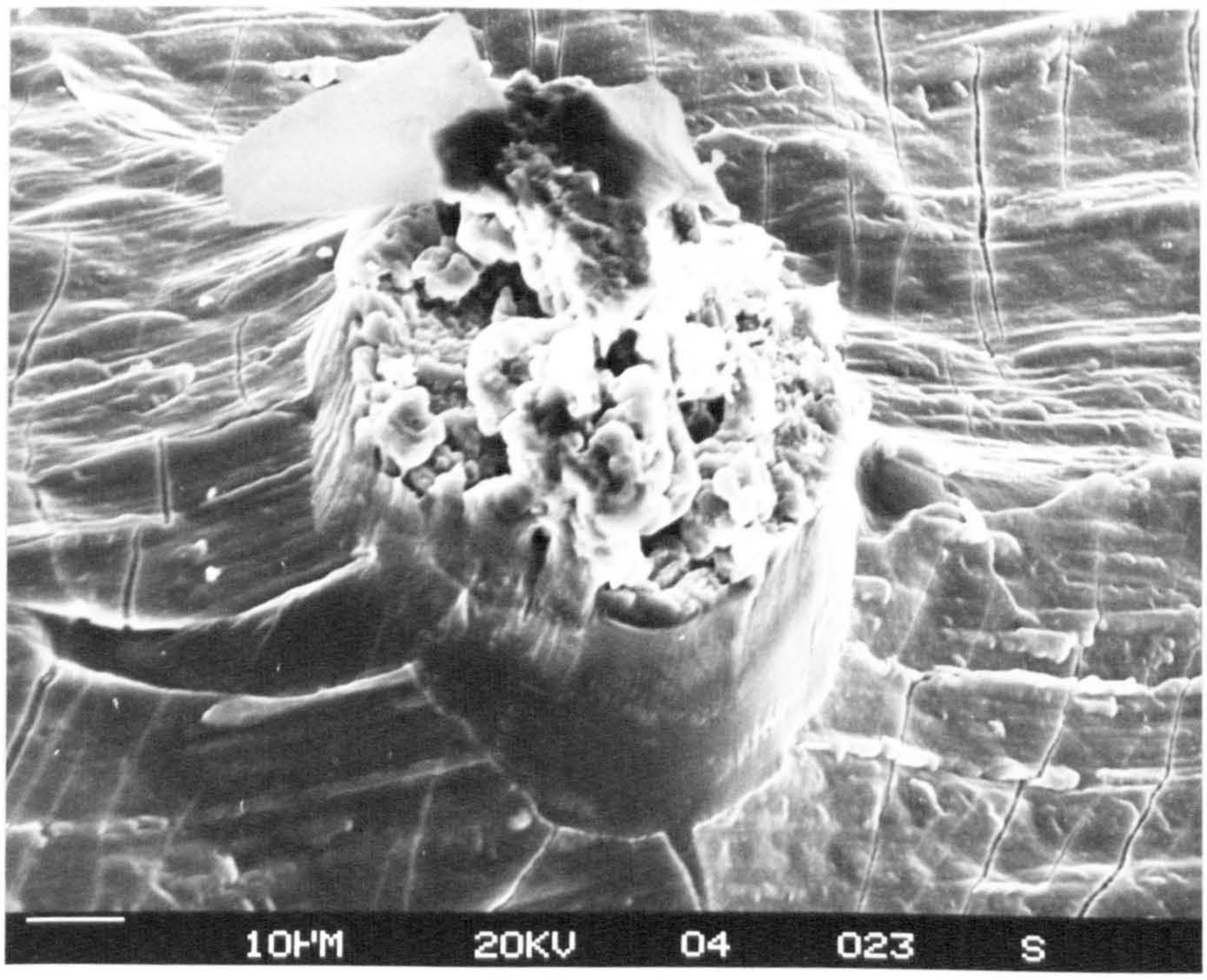

Figure 6.21 Oxide protrusions on aluminium surface after 70h oxidation at 750°C in humid air

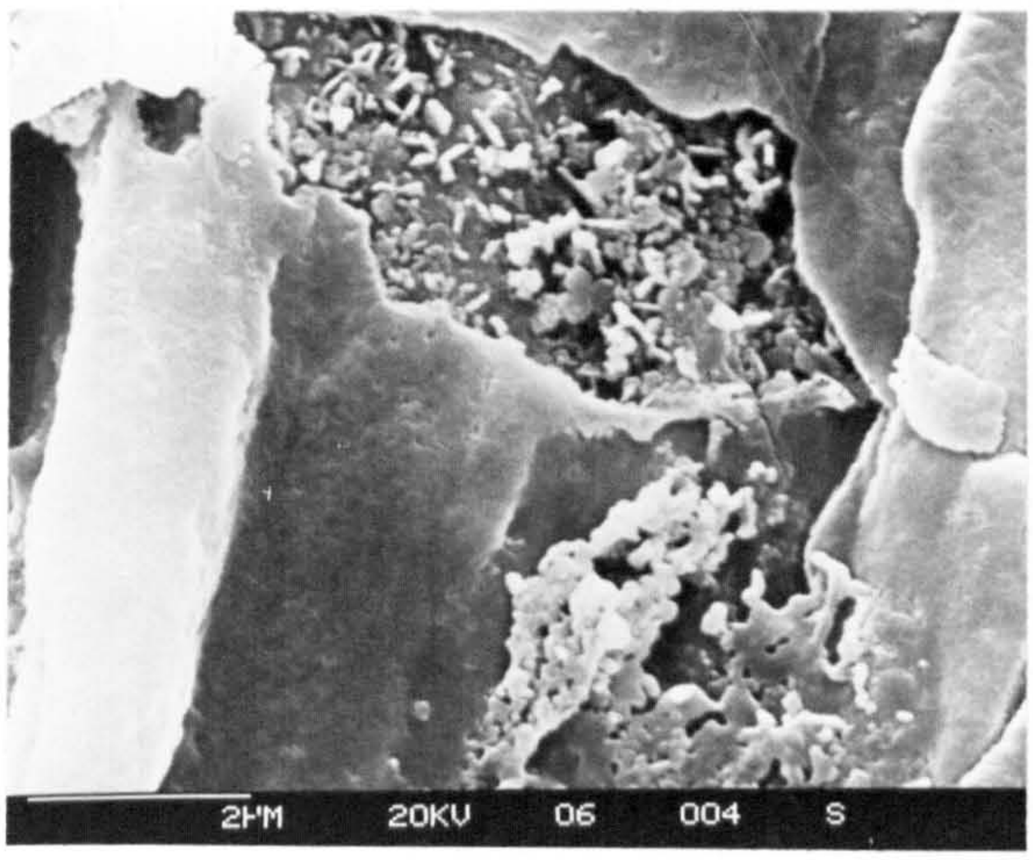

(a)

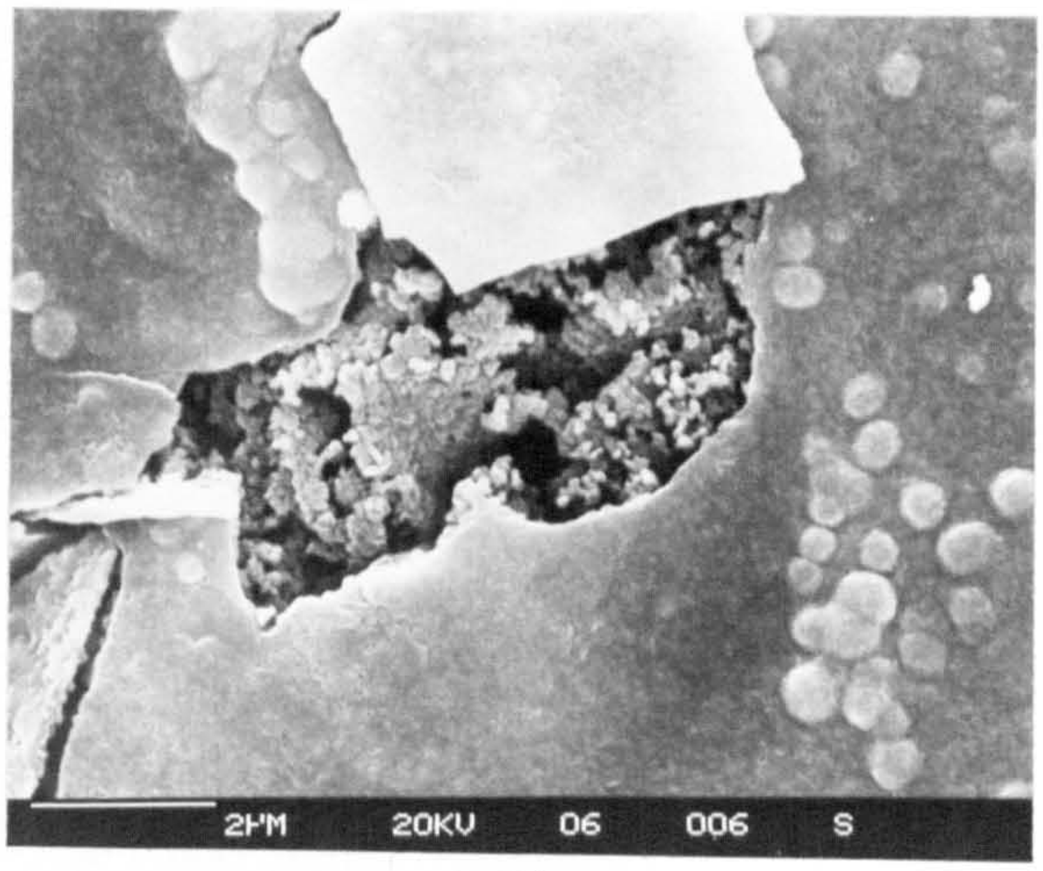

(b)

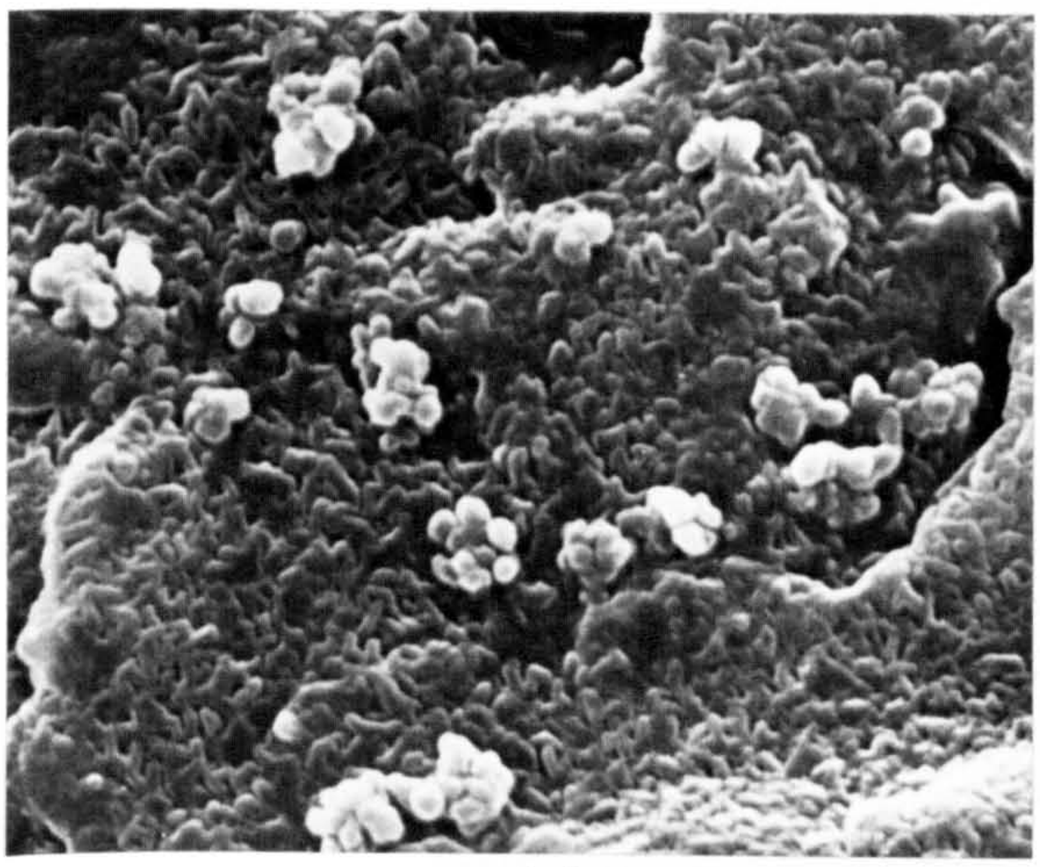

(c)

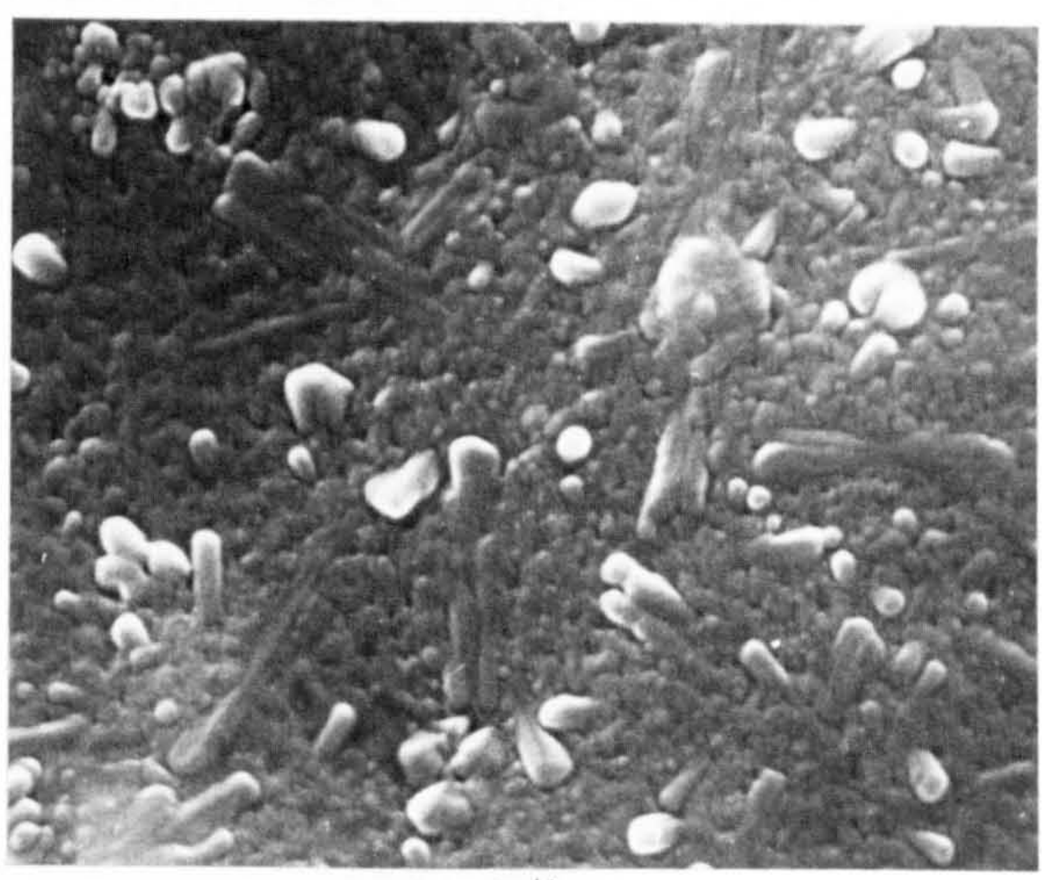

(d)

2μm

Figure 6.22 Oxide morphology on aluminium specimens following 20h oxidation at 750°C in humid air

(a)

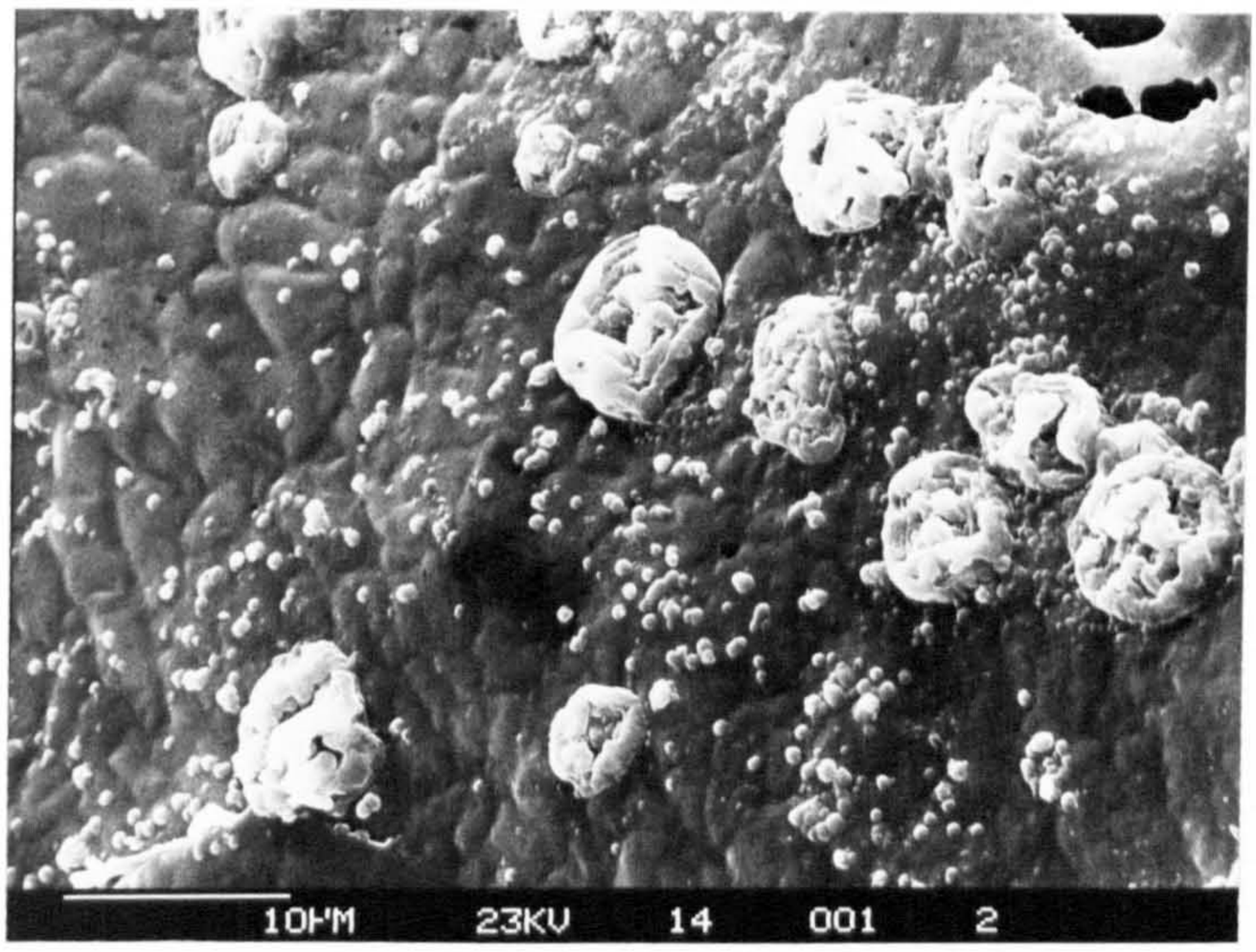

(b)

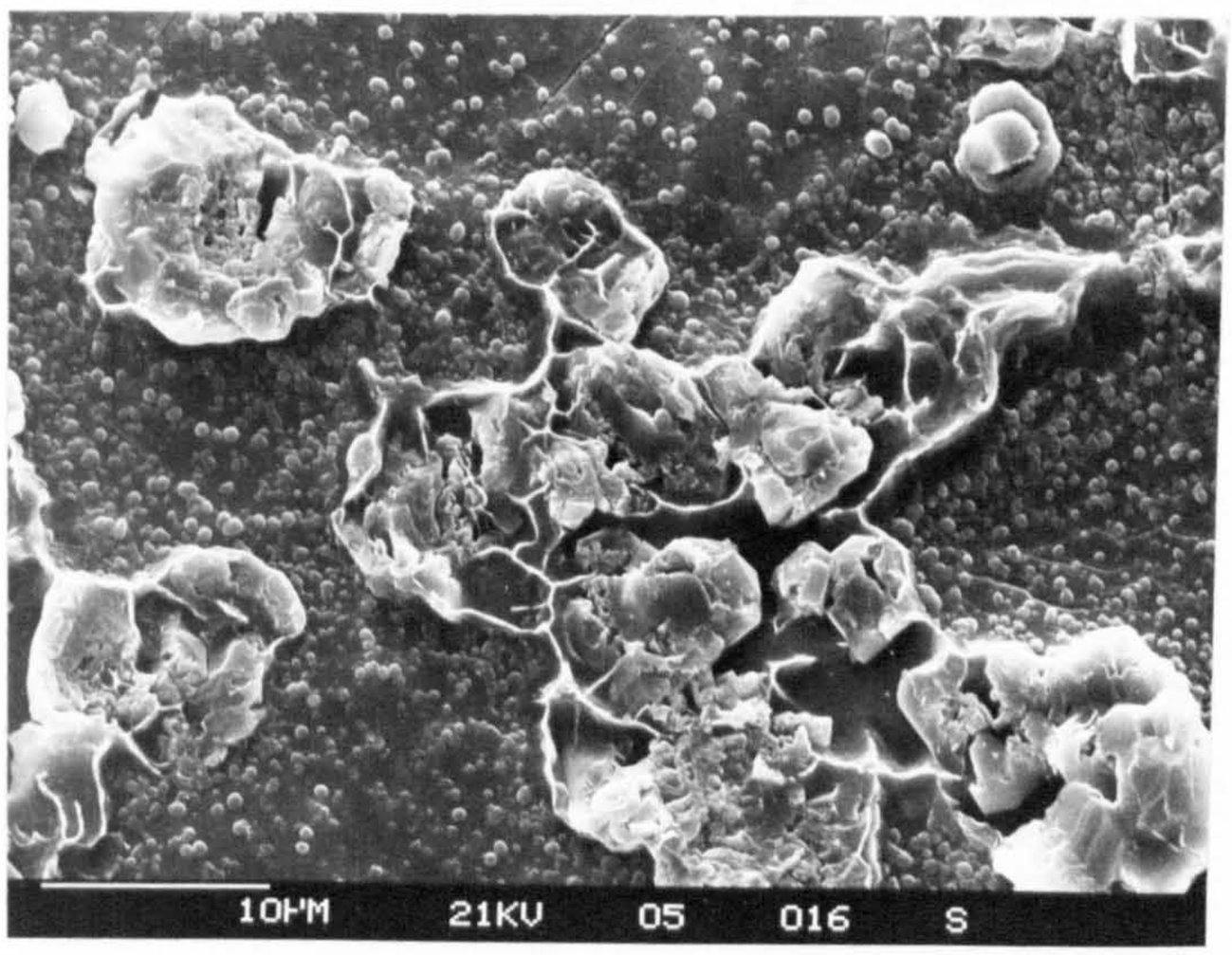

(c)

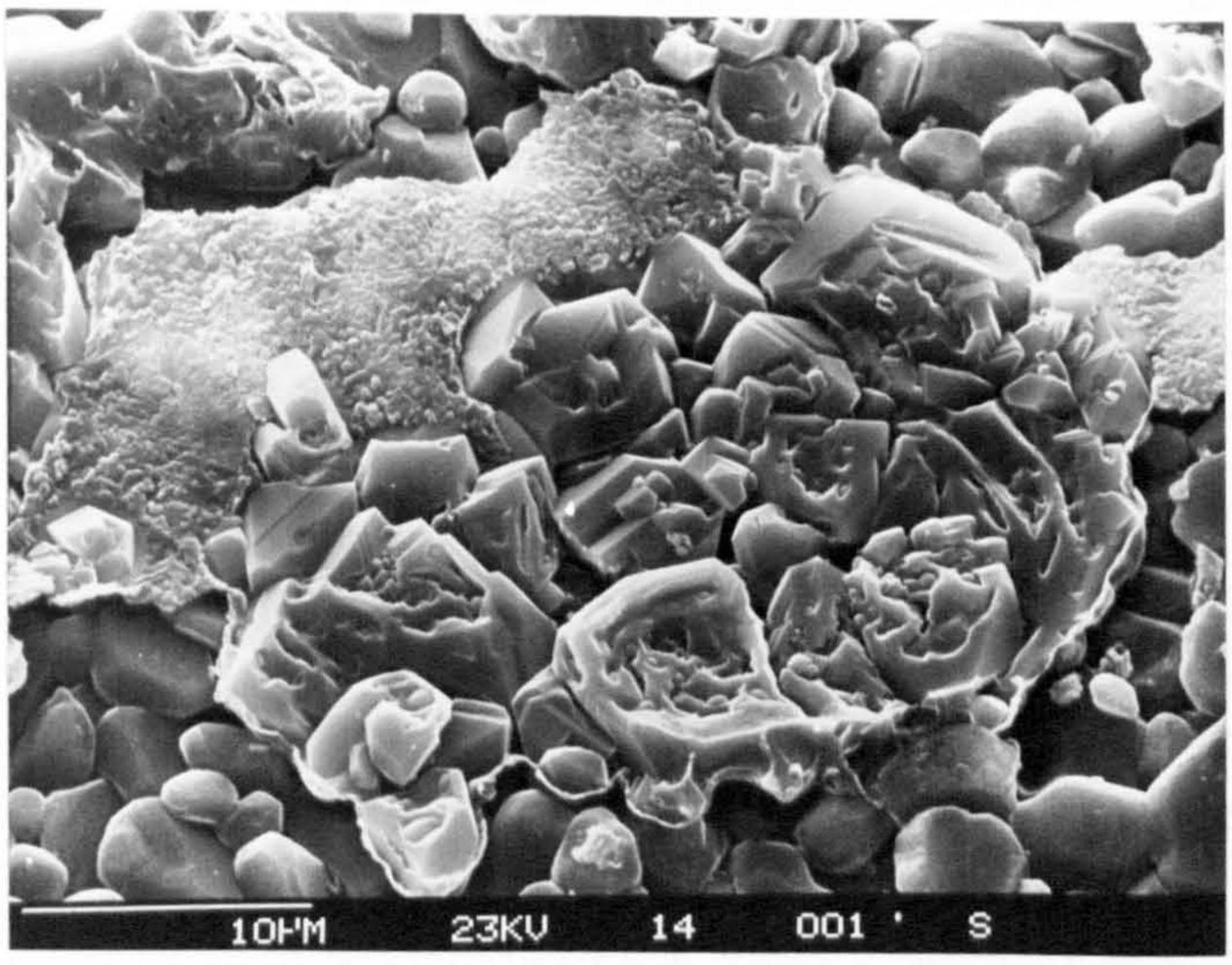

Figure 6.23 Internal structure of oxide growths developed on aluminium after 20h oxidation at 750°C in humid air with (a) top surface (b) fractured reverse surface (c) remains of reverse surface attached to alumina plate

(a)

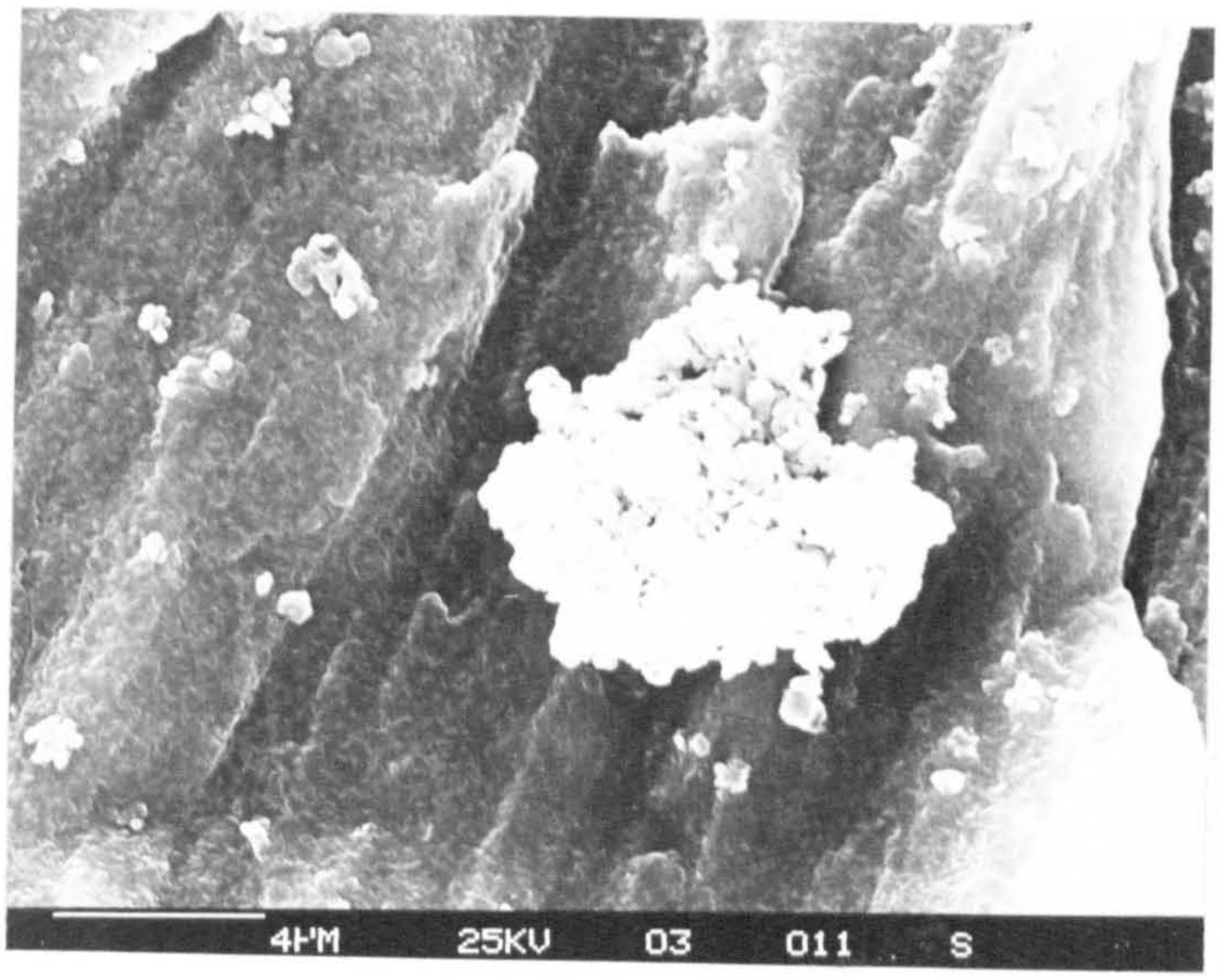

(b)

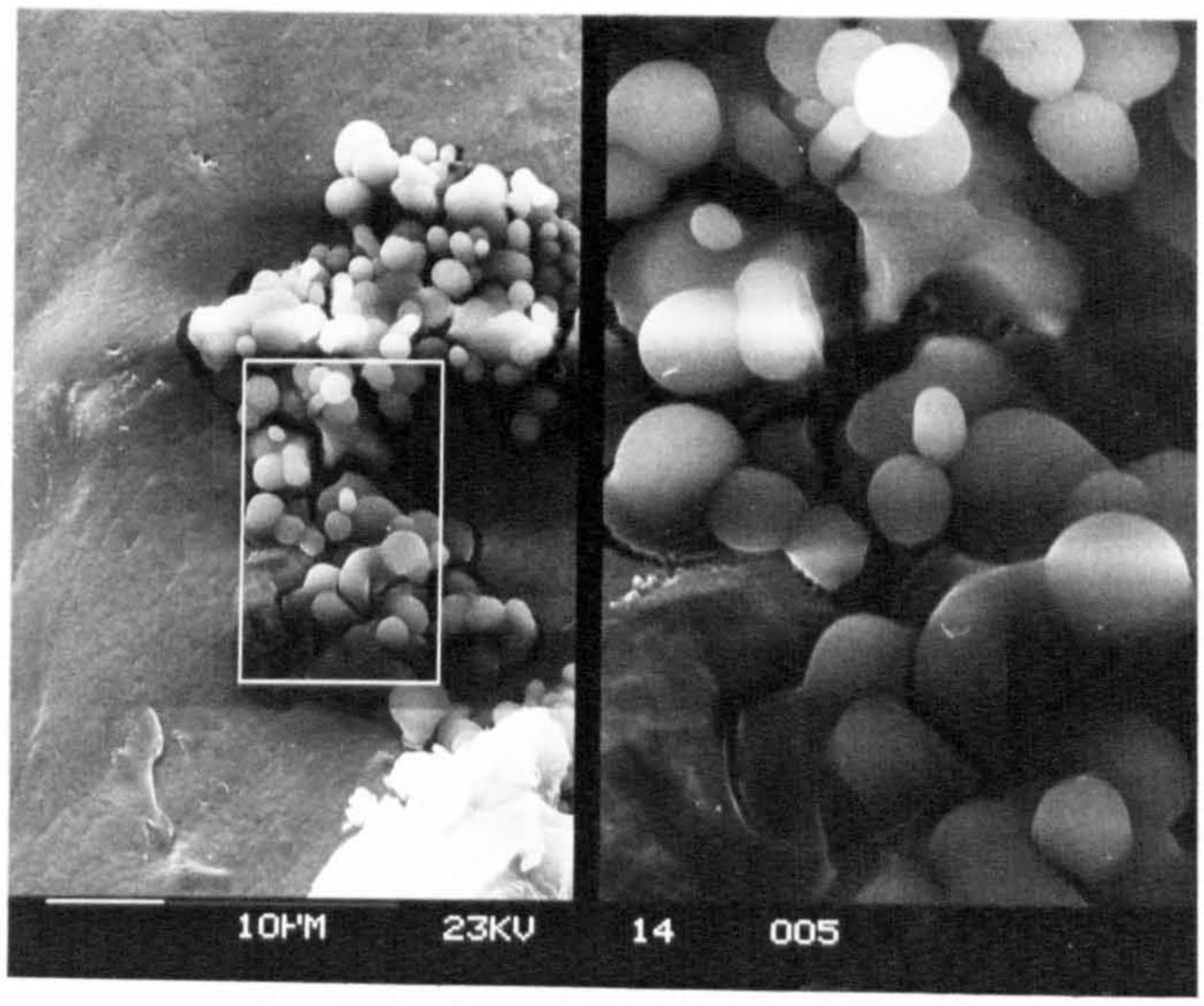

(c)

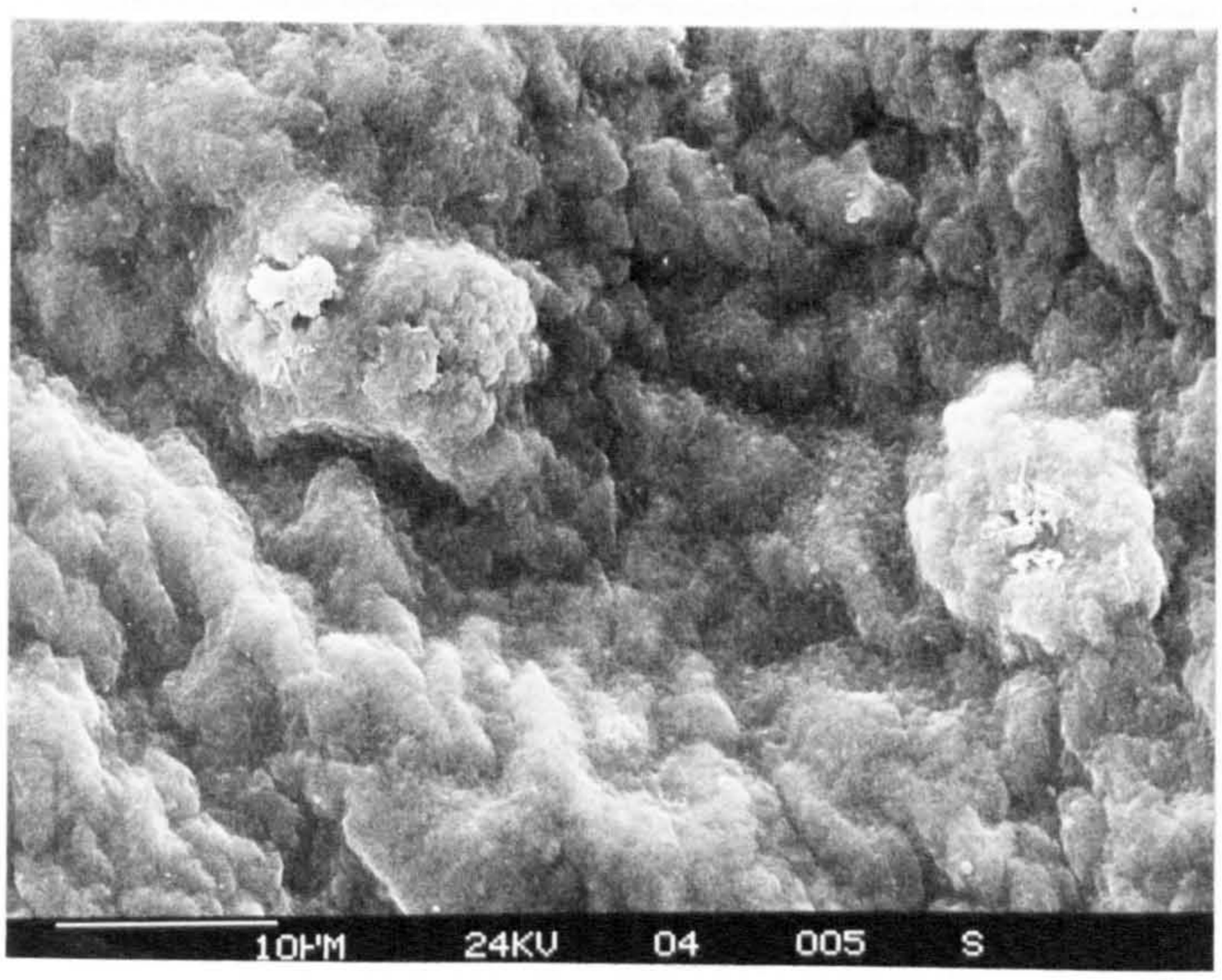

Figure 6.24 Effect of surface finish on aluminium at 750°C in gettered argon on (a) machined (b) electropolished and (c) mechanically polished surfaces

(a)

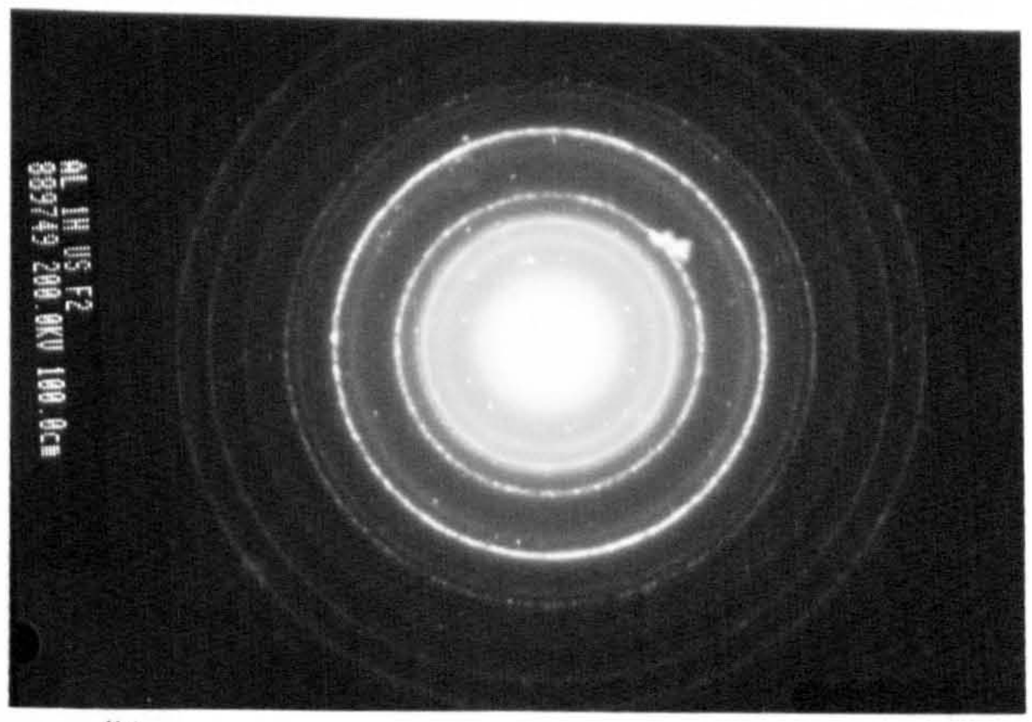

(b) diffraction pattern of (a)

(c)

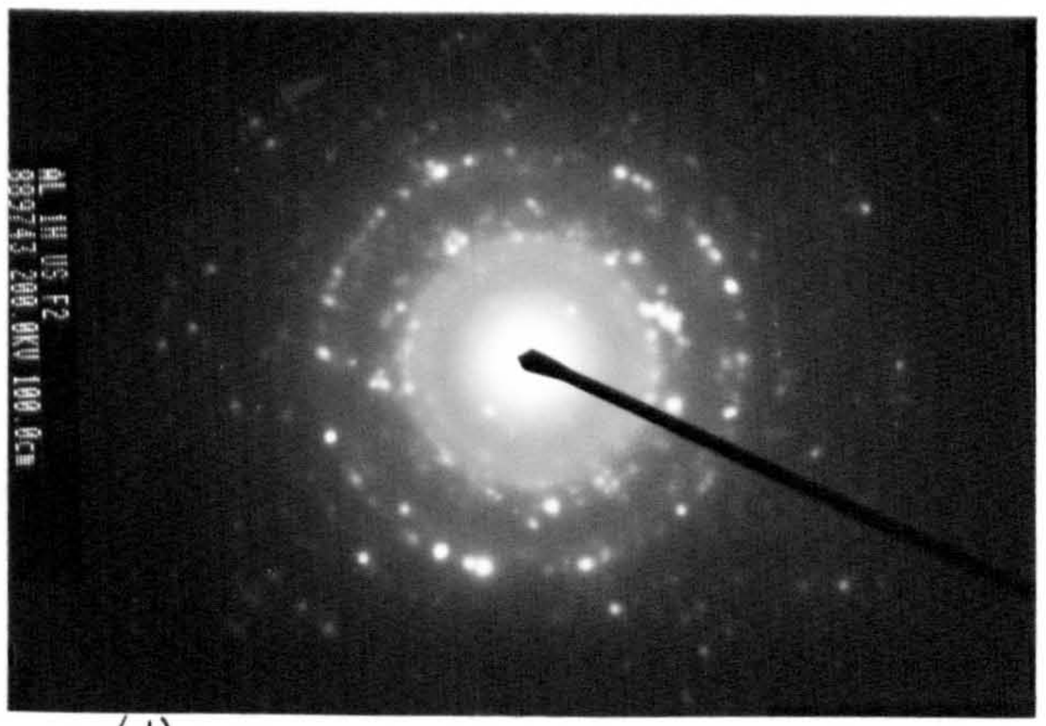

(d) diffraction pattern of (c)

(e)

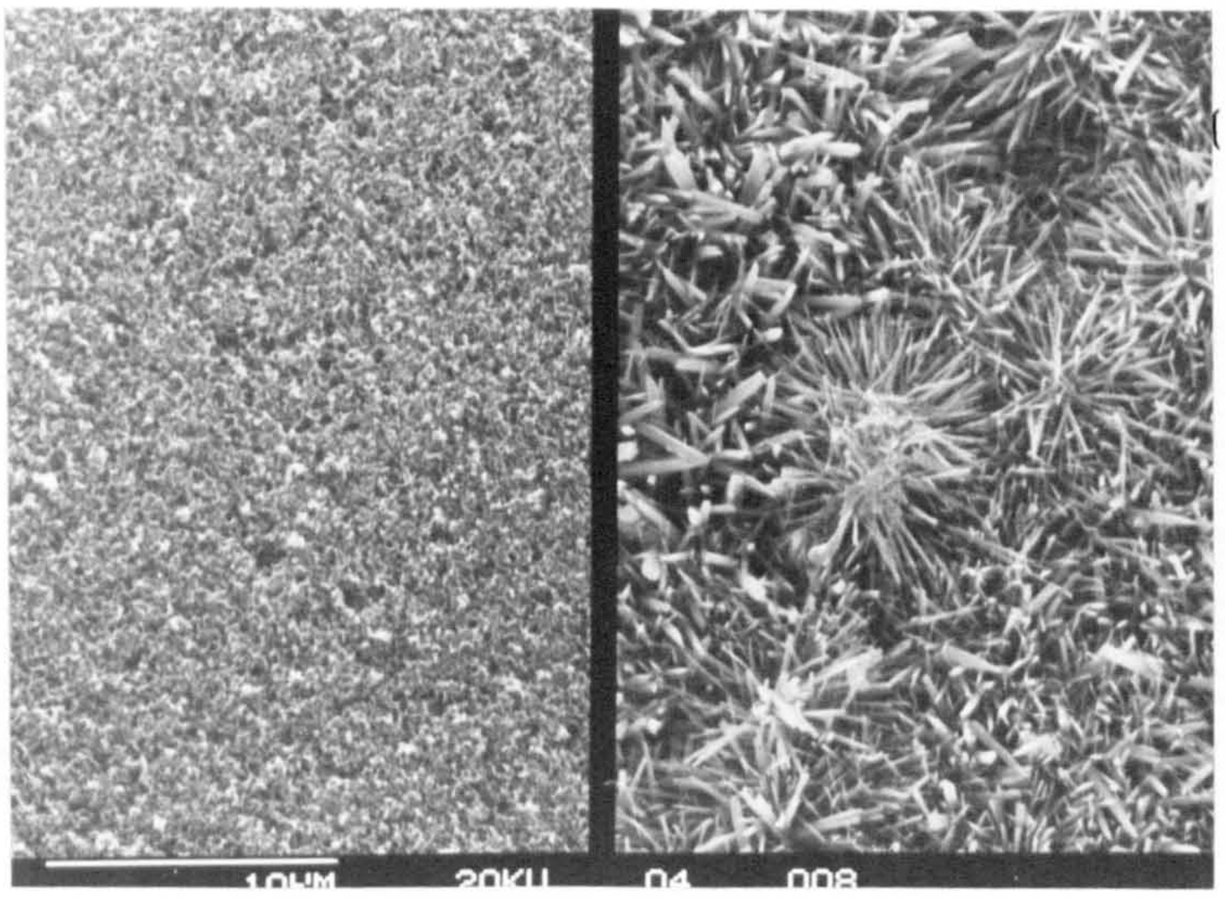

(f)

Figure 6.25 TEM of aluminium oxidised at 750°C (a,b) in presence of fluoride for 1h and (c,d) in section with SEM of 5h exposure with (e) fluoride and (f) chloride

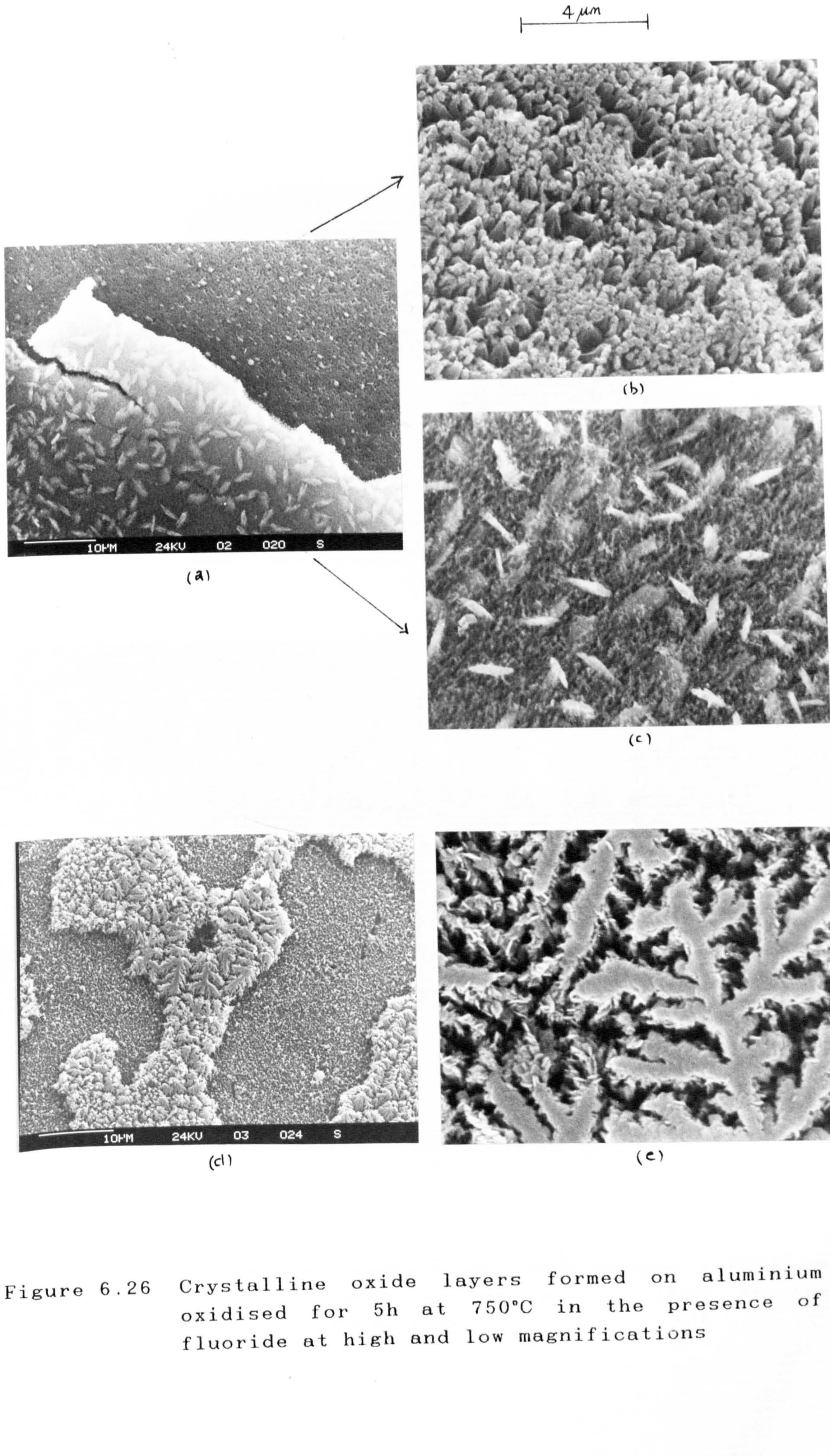

Figure 6.26 Crystalline oxide layers formed on aluminium oxidised for 5h at 750°C in the presence of fluoride at high and low magnifications

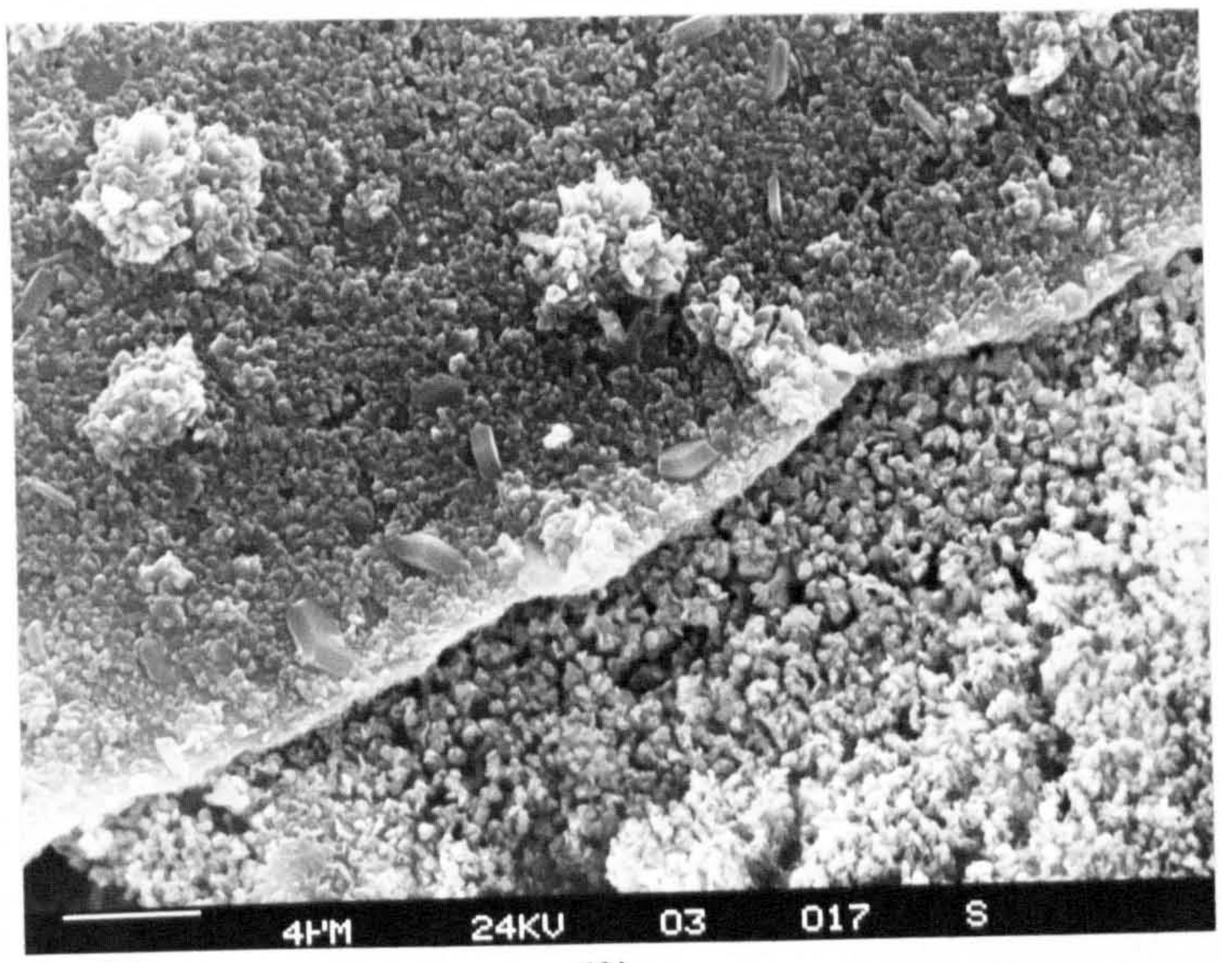

(a)

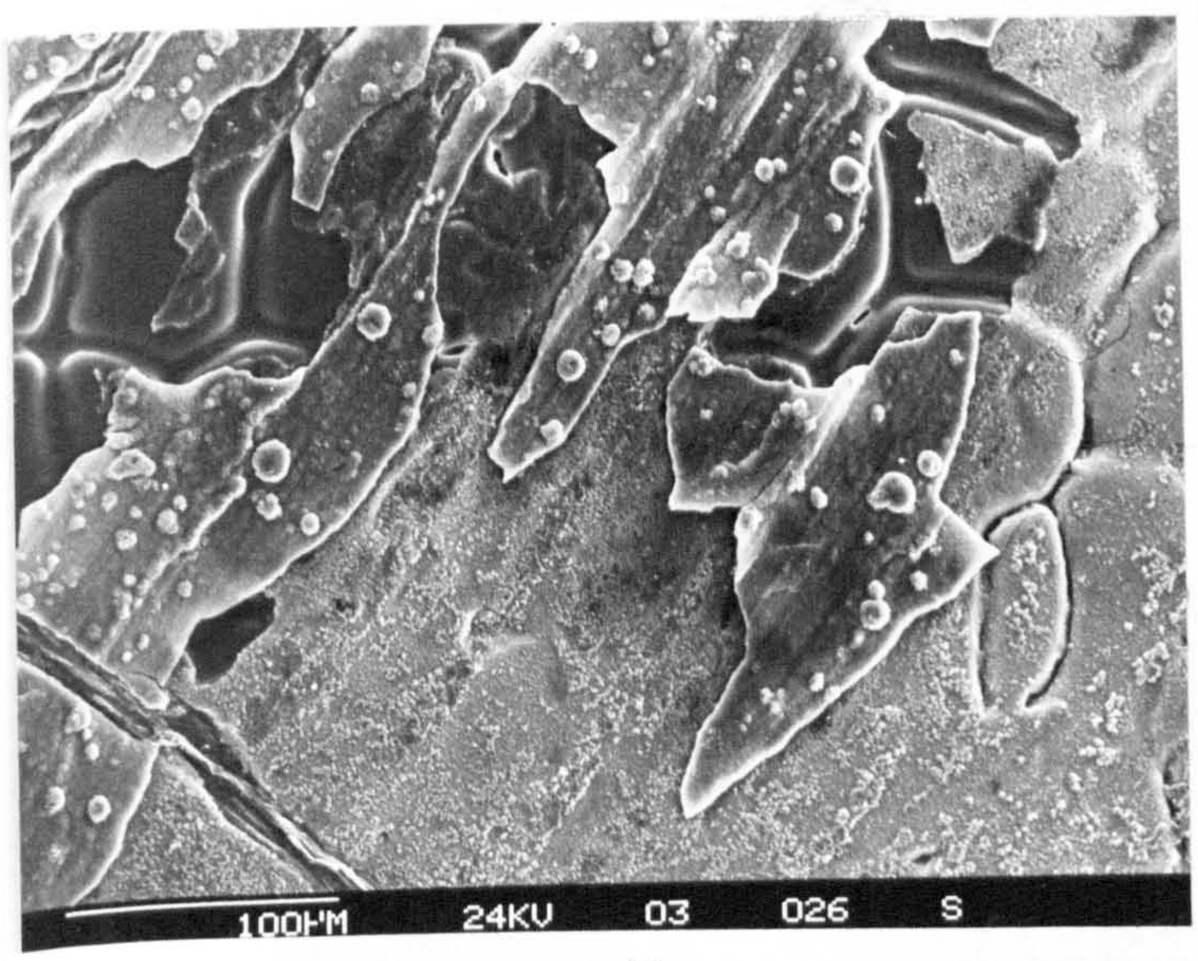

(b)

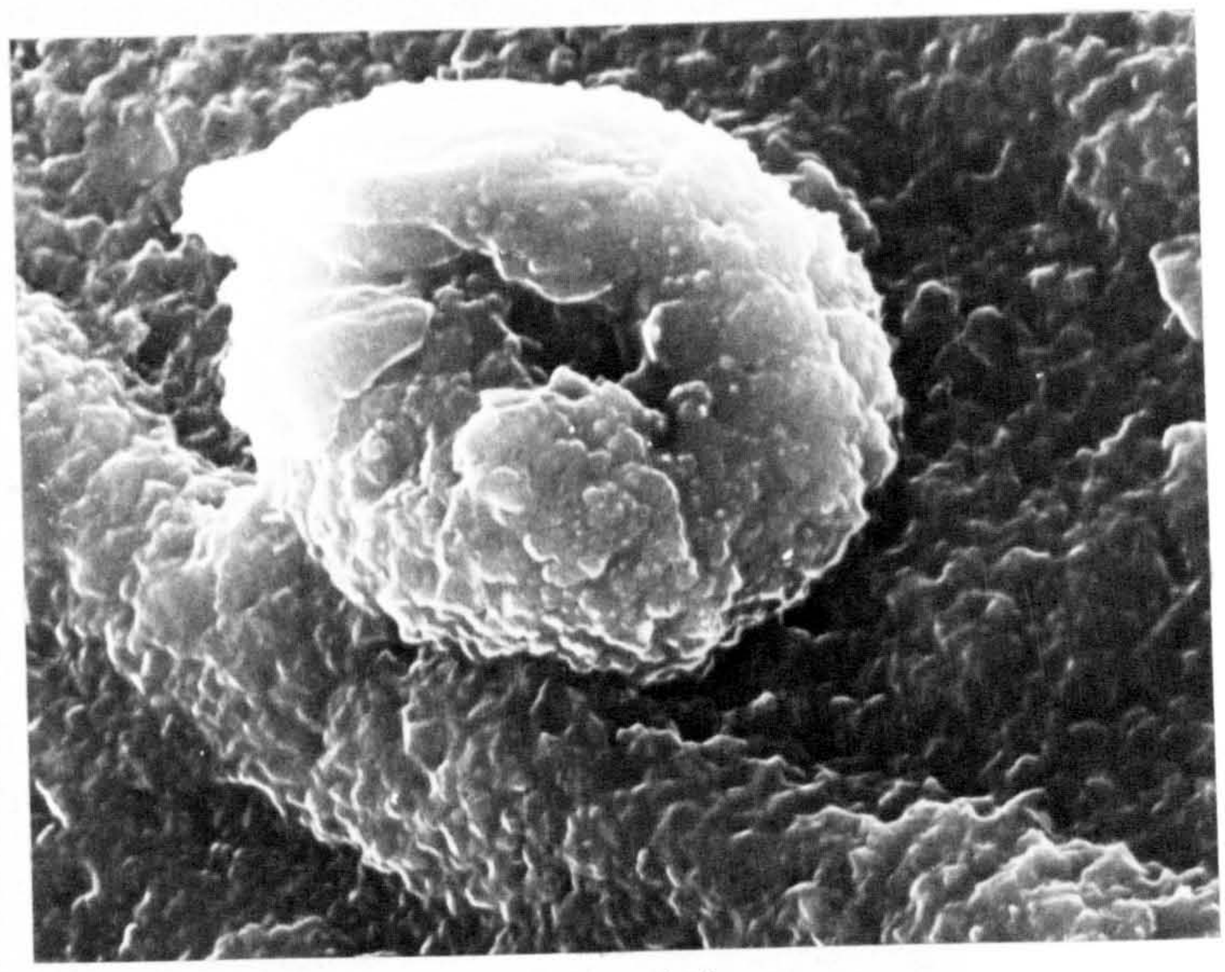

(c)

10μm

Figure 6.27 Thickened crystalline oxide layers formed on aluminium oxidised for 15h at 750°C in the presence of fluoride.

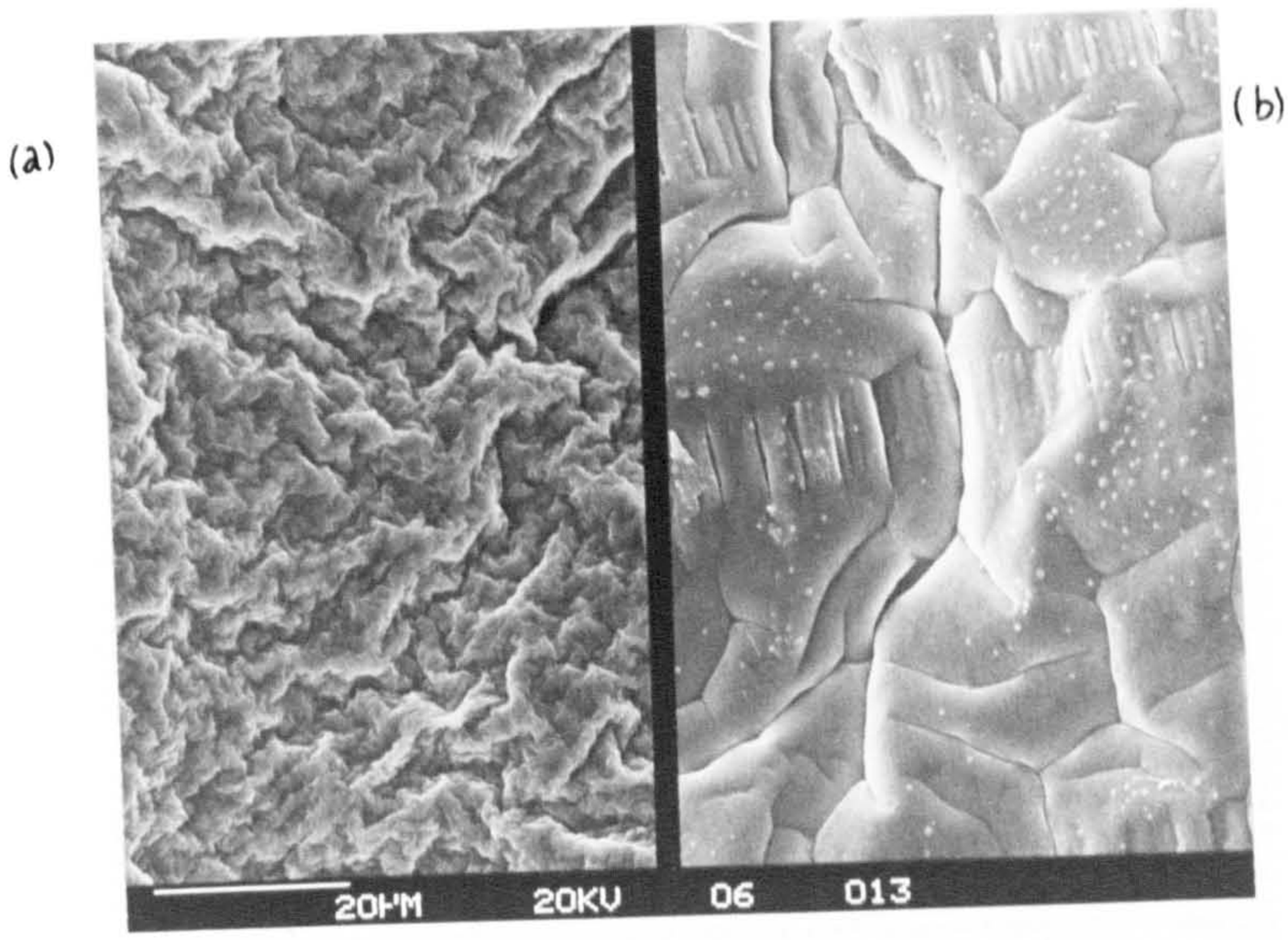

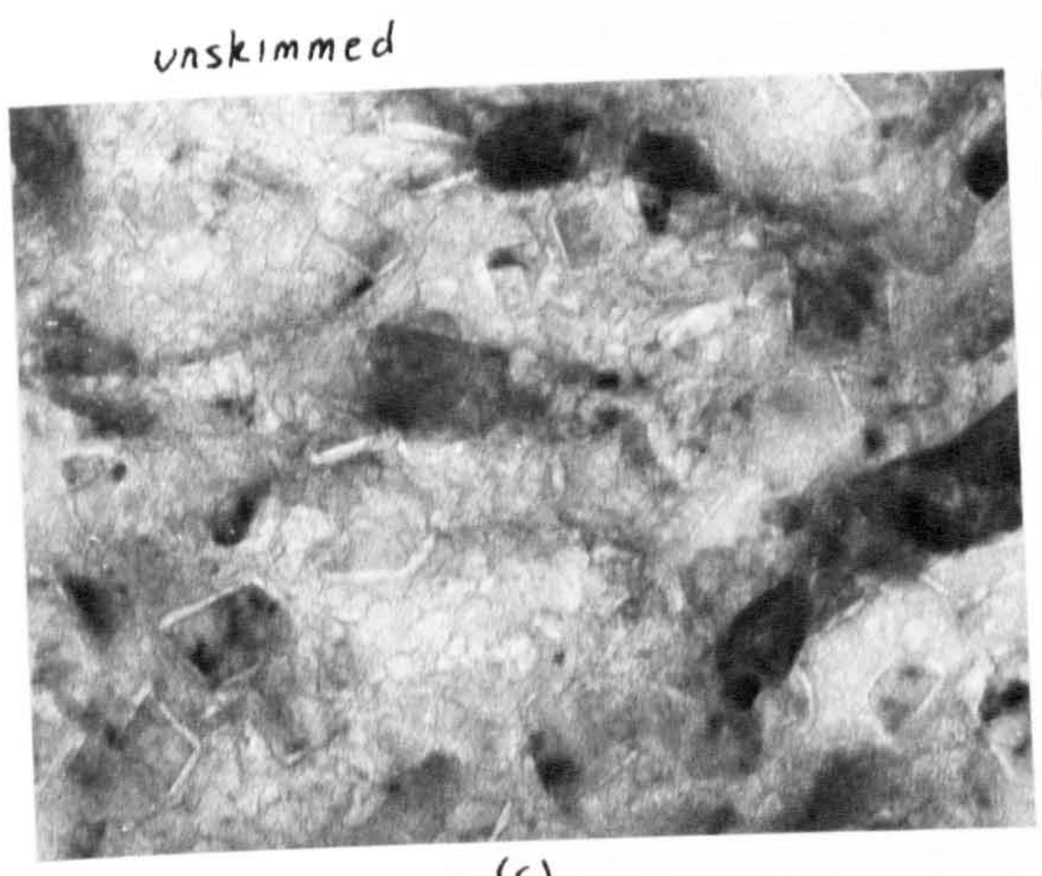

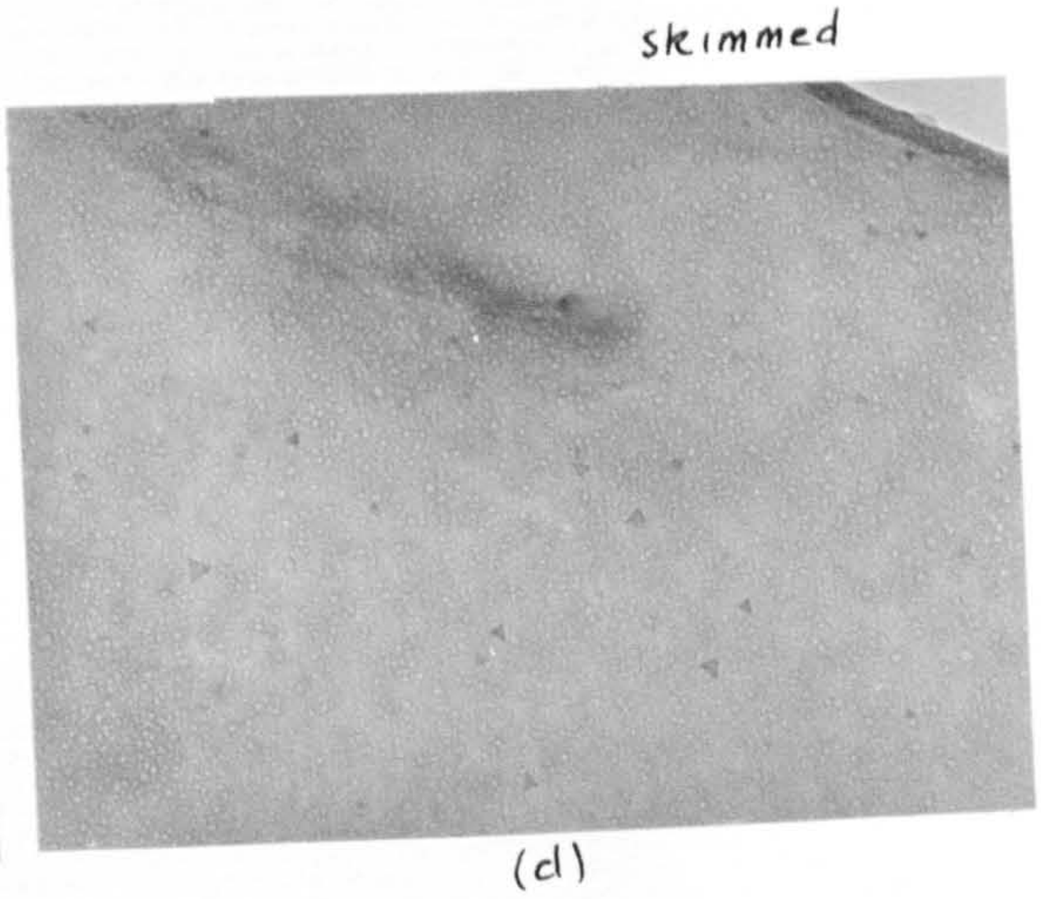

100 nm

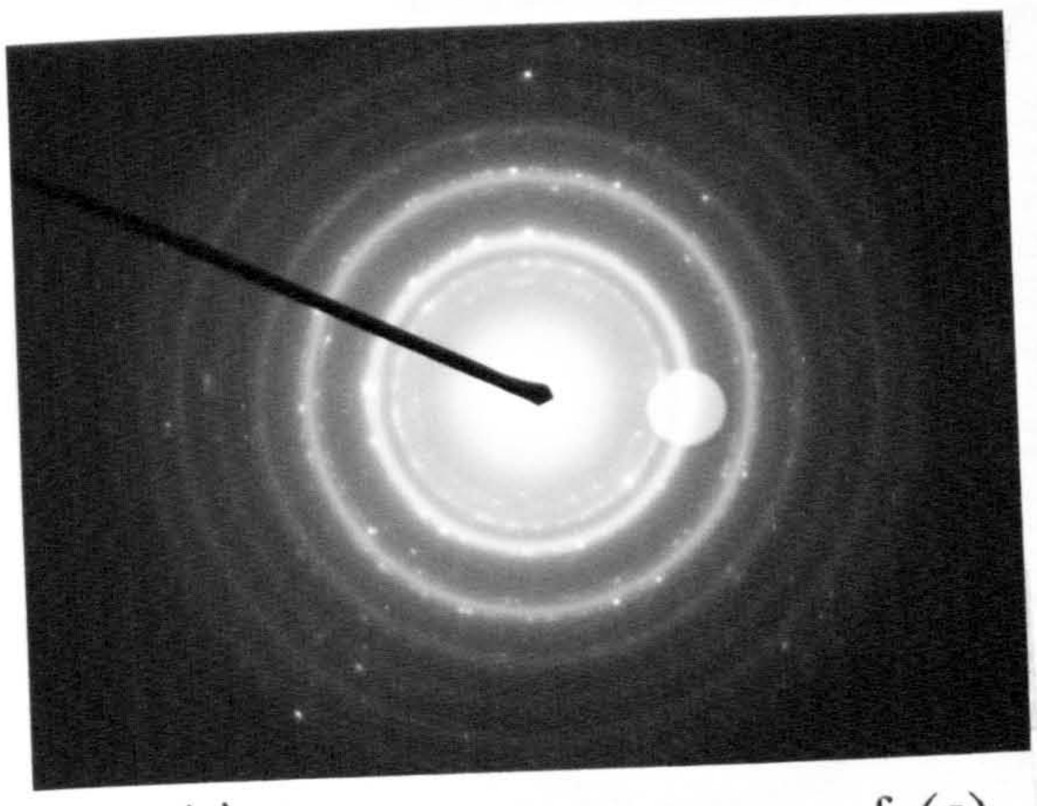

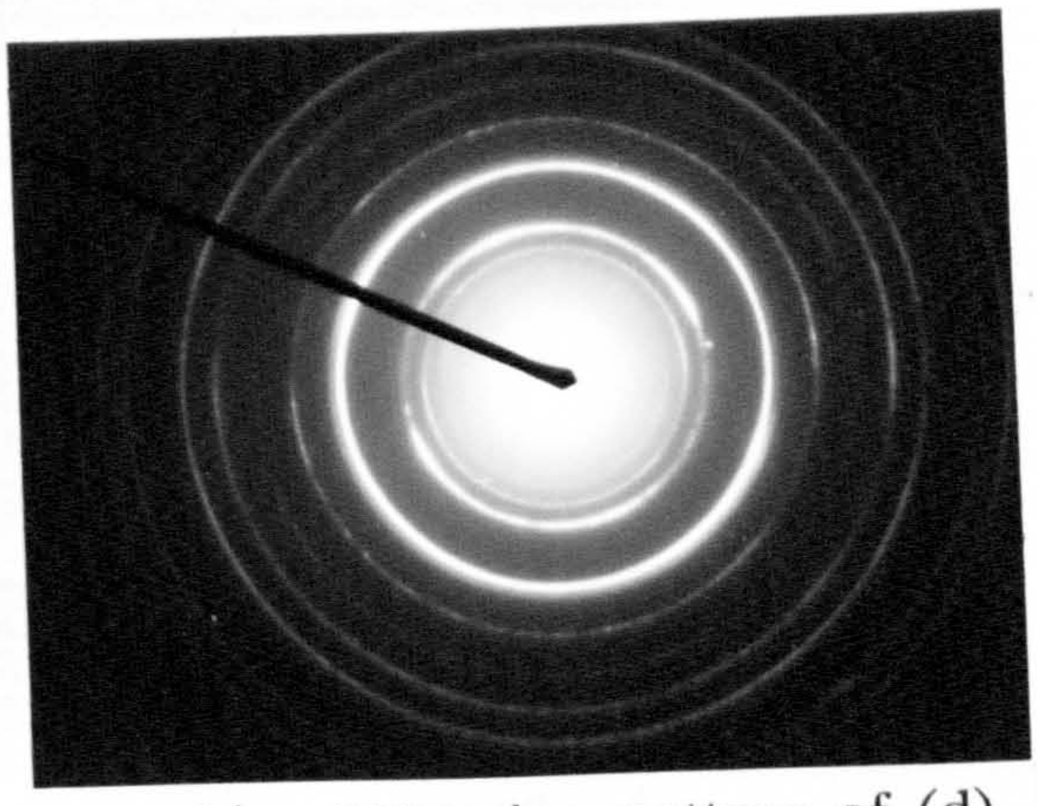

Figure 7.1 Oxidised surfaces (GR) of (a) unskimmed and (c) skimmed Al-1%Mg alloy at 750°C in humid air after 5 min with corresponding TEM of (c,e) of unskimmed and (d,f) skimmed oxide films

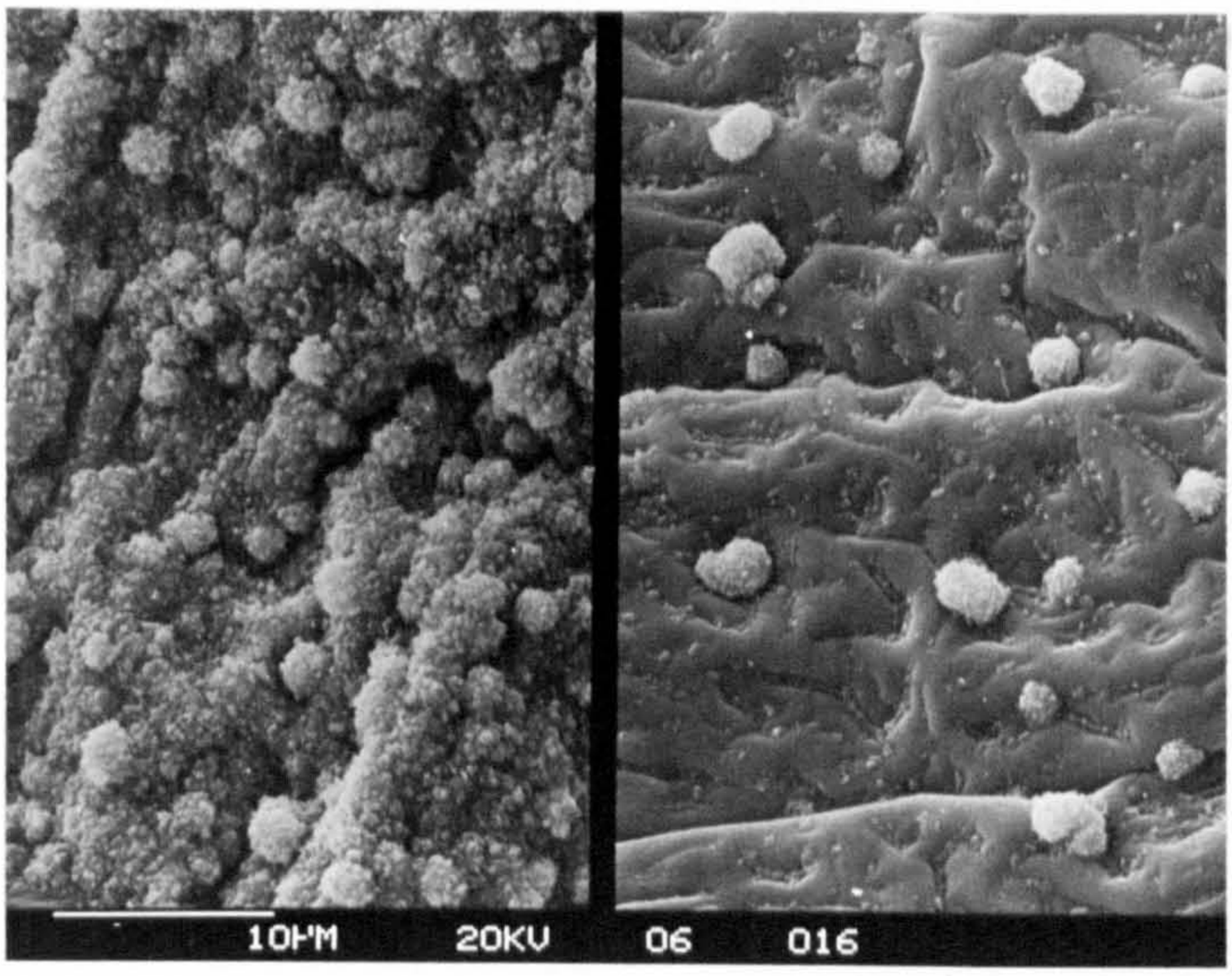

(a) (b)

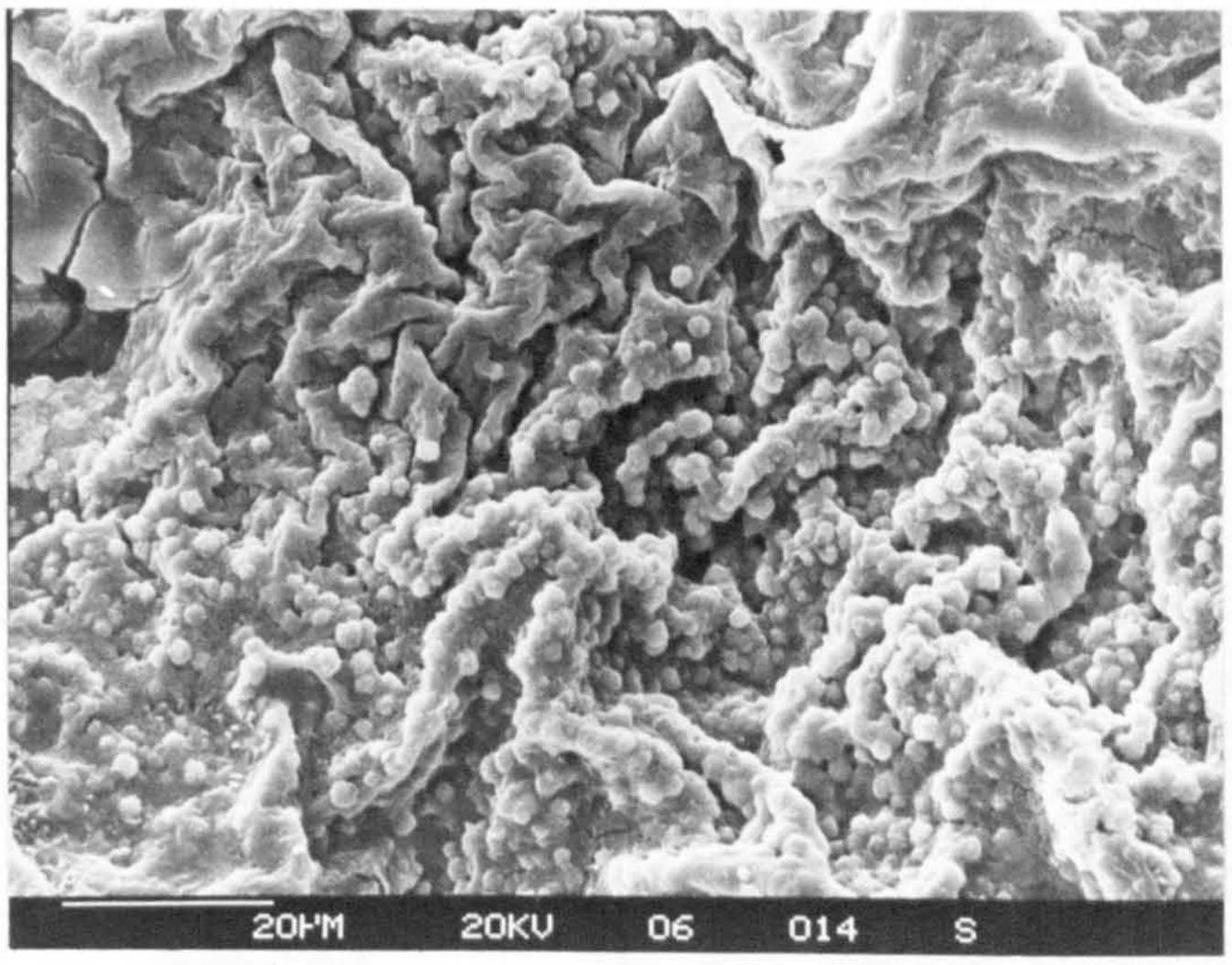

(c)

Figure 7.2 Oxide surfaces of Al-1%Mg GR after 1h oxidation at 750°C in gettered argon of (b) skimmed and (a) unskimmed melts with (c) in humid air

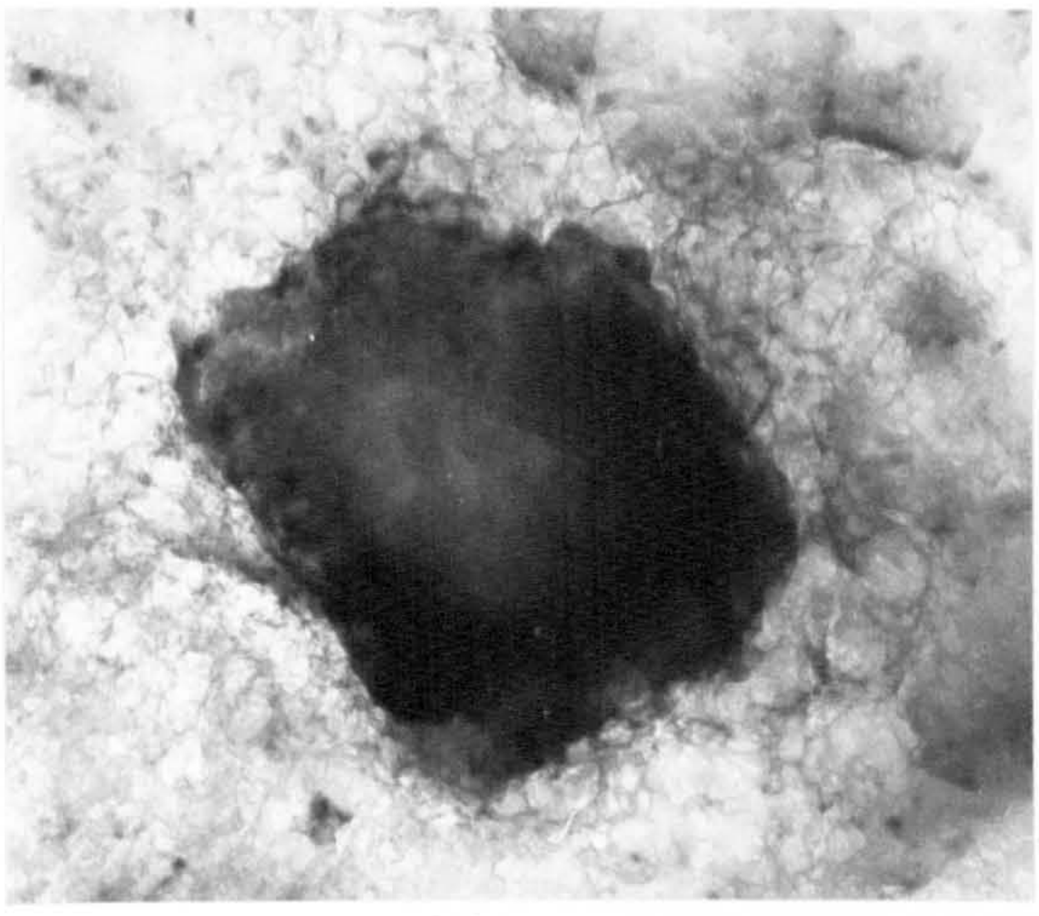

(a)

200nm

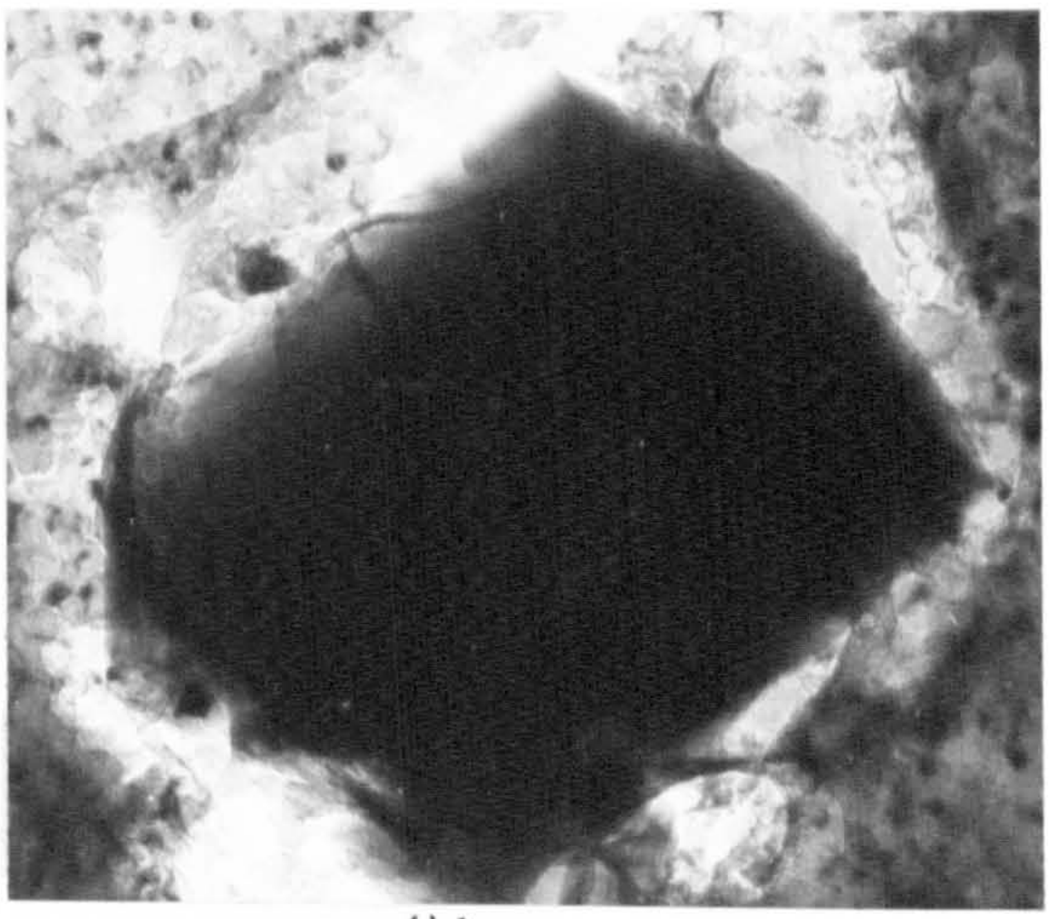

(b)

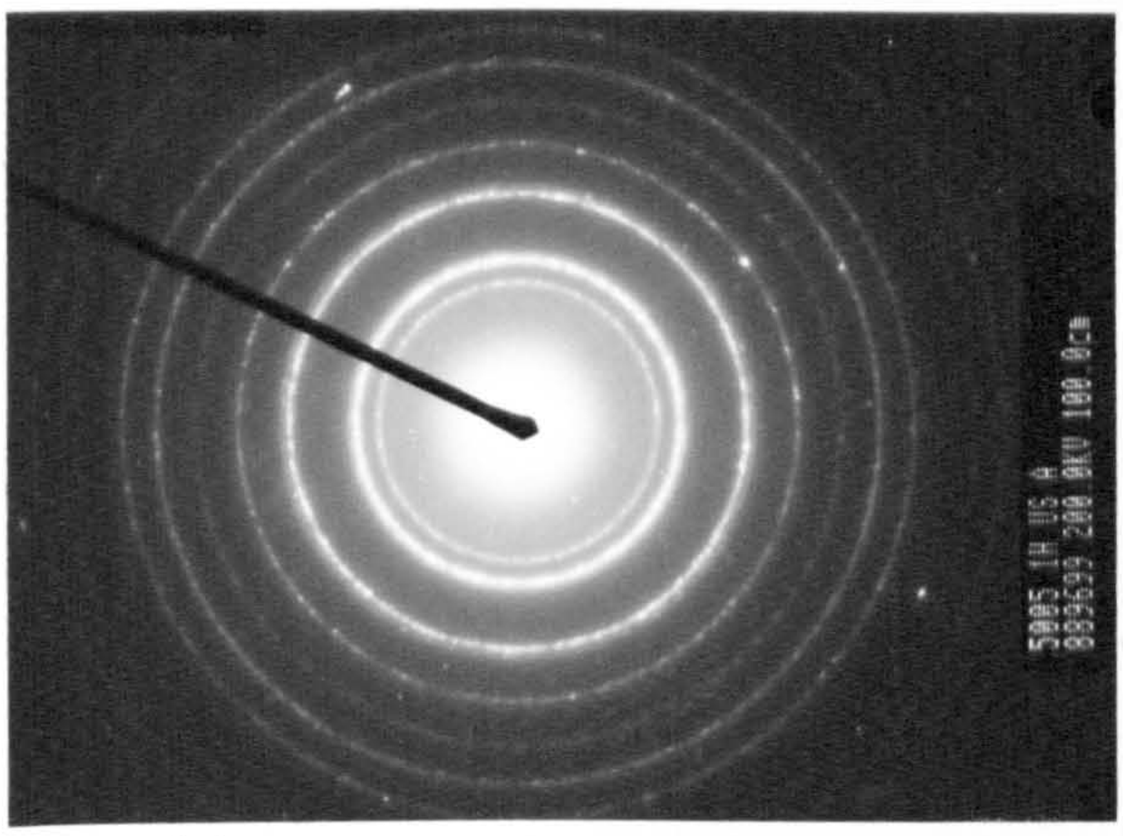

(c) diffraction pattern of matrix

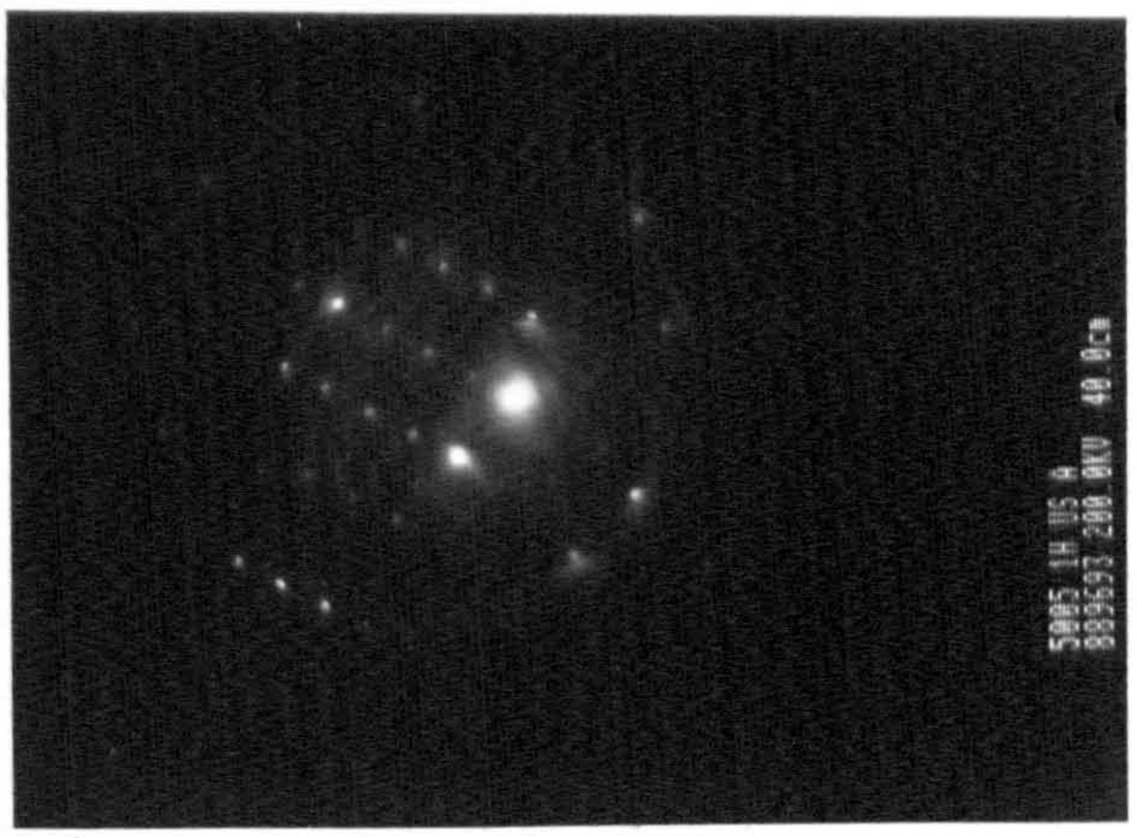

(d) diffraction pattern of large crystal

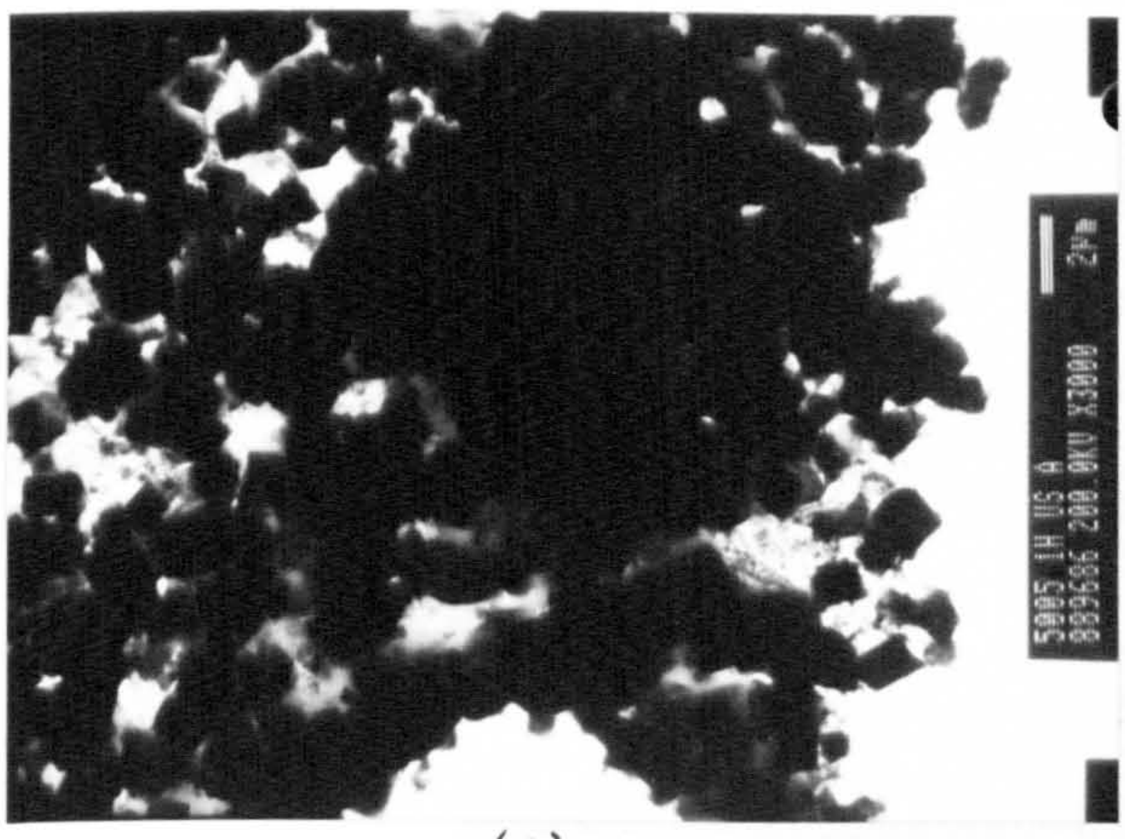

(e)

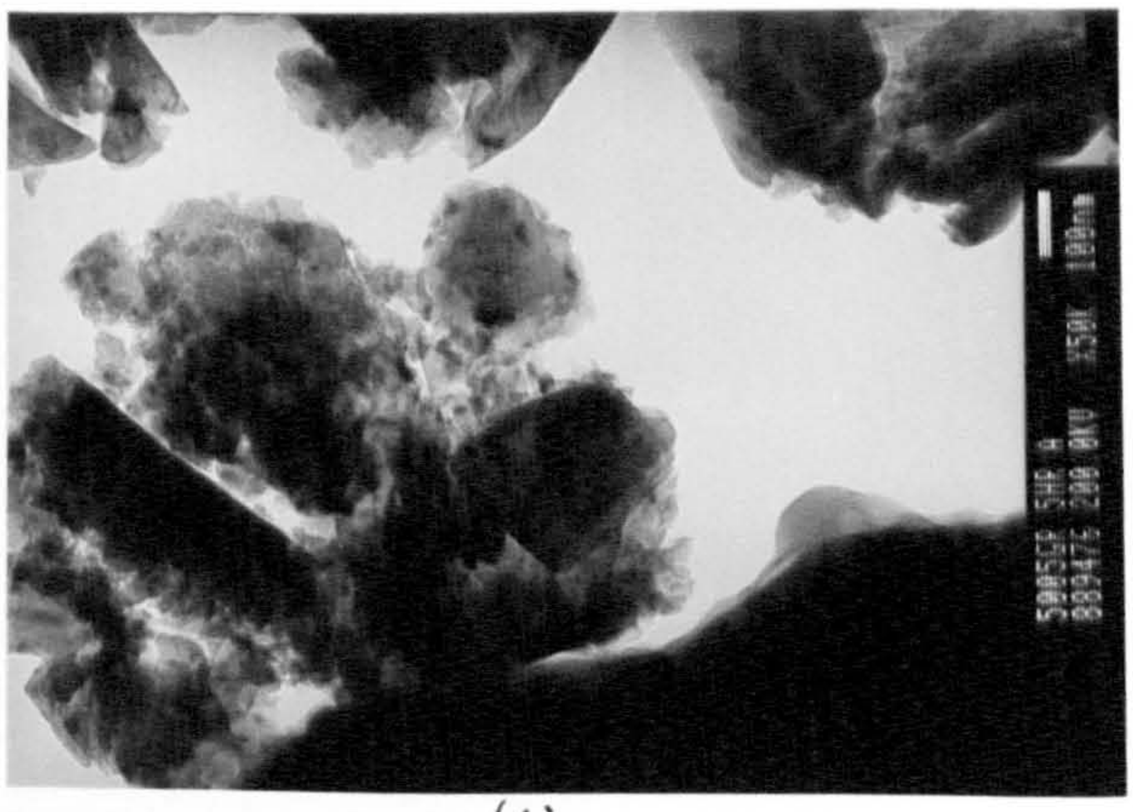

(f)

Figure 7.3 TEM of oxide films formed on unskimmed Al-1%Mg GR melts at 750°C in dry air after (a) 15min (b,e) 1h with diffraction (c) of matrix and (d) large crystal and (f) 5h

(a)

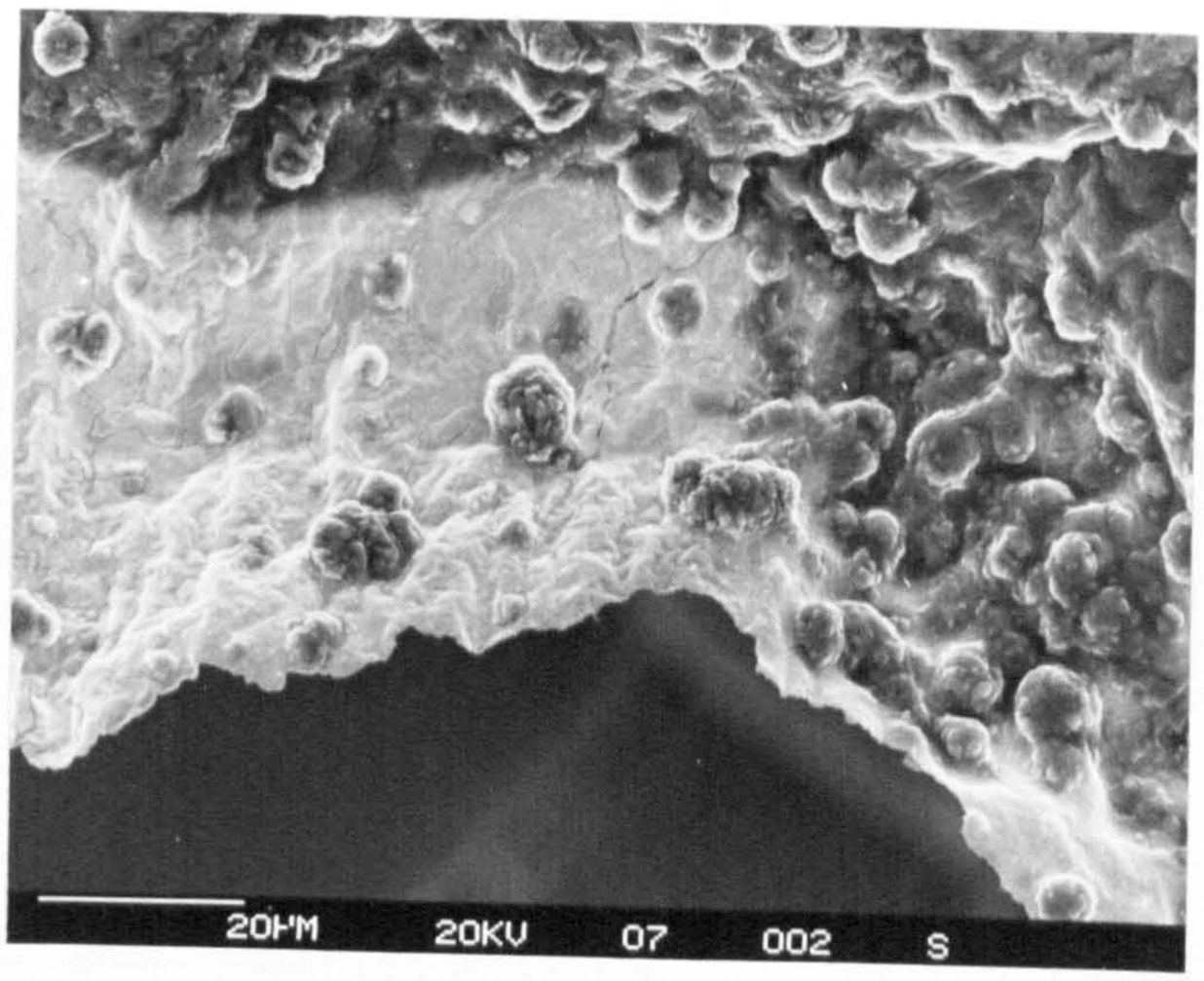

(b)

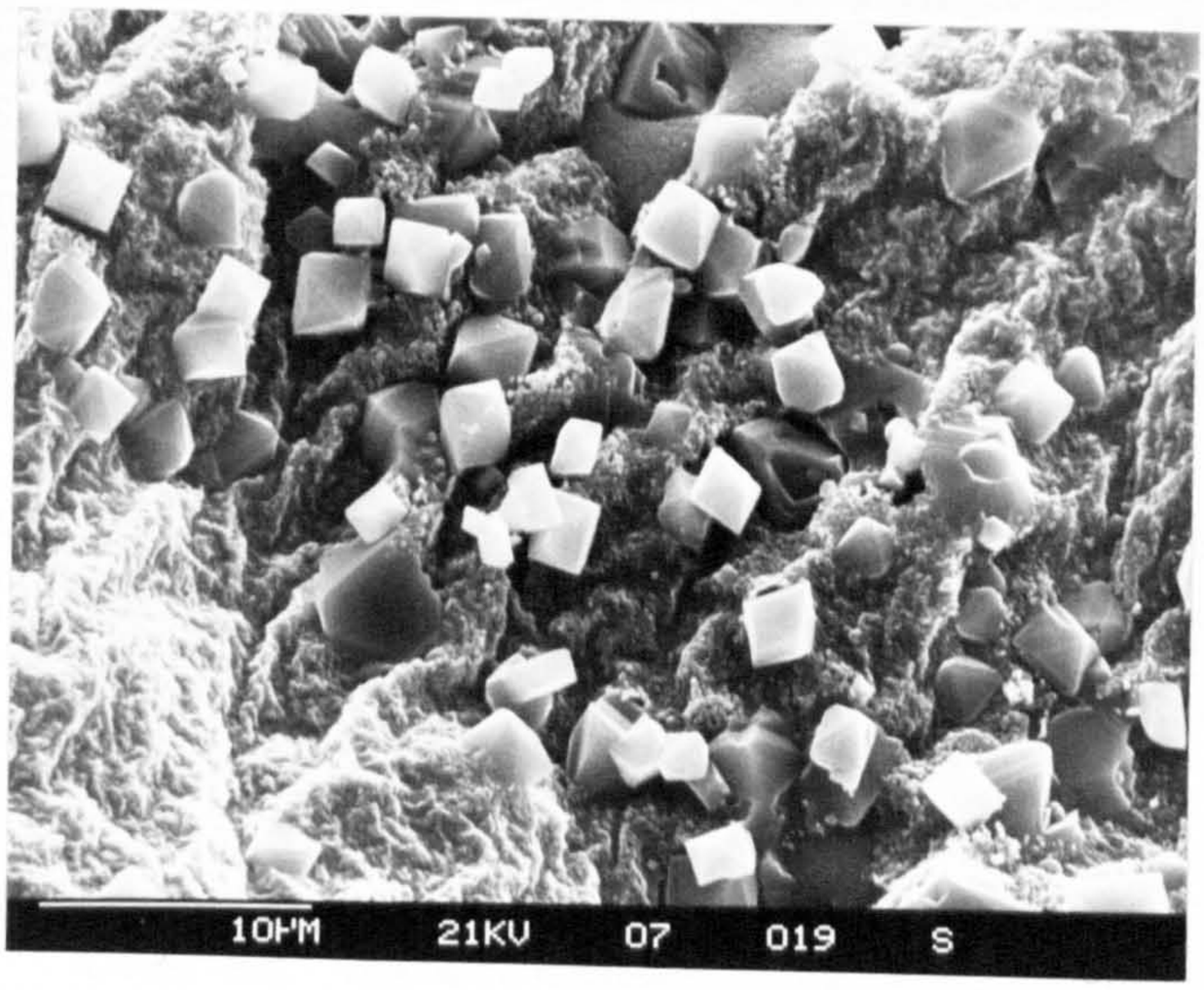

(c)

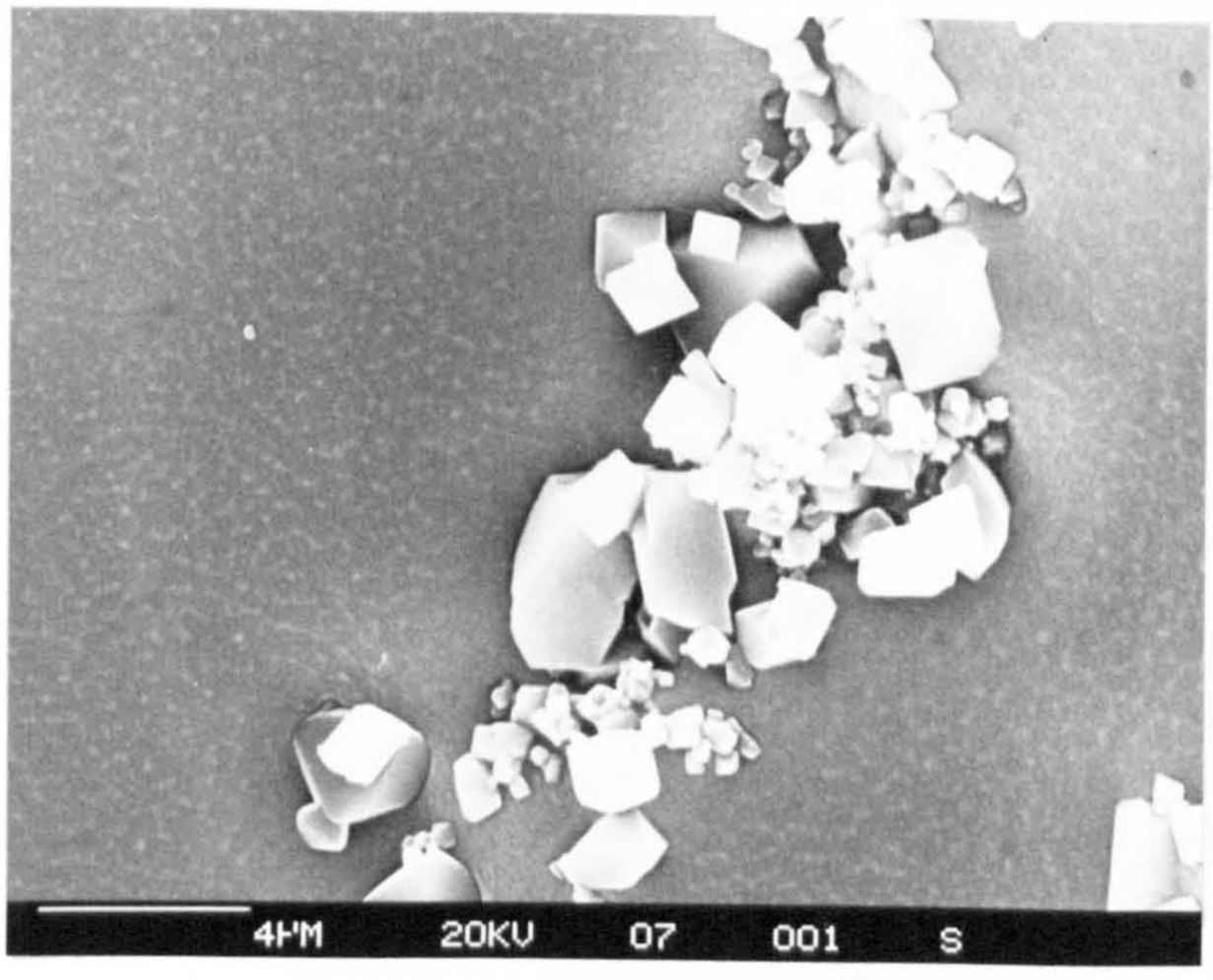

Figure 7.4 Oxide films on Al-1%Mg NGR alloy after 15h in dry air at 750°C showing (a) oxide-gas interface and (b,c) oxide-melt interface (b) oxide side and (c) metal side.

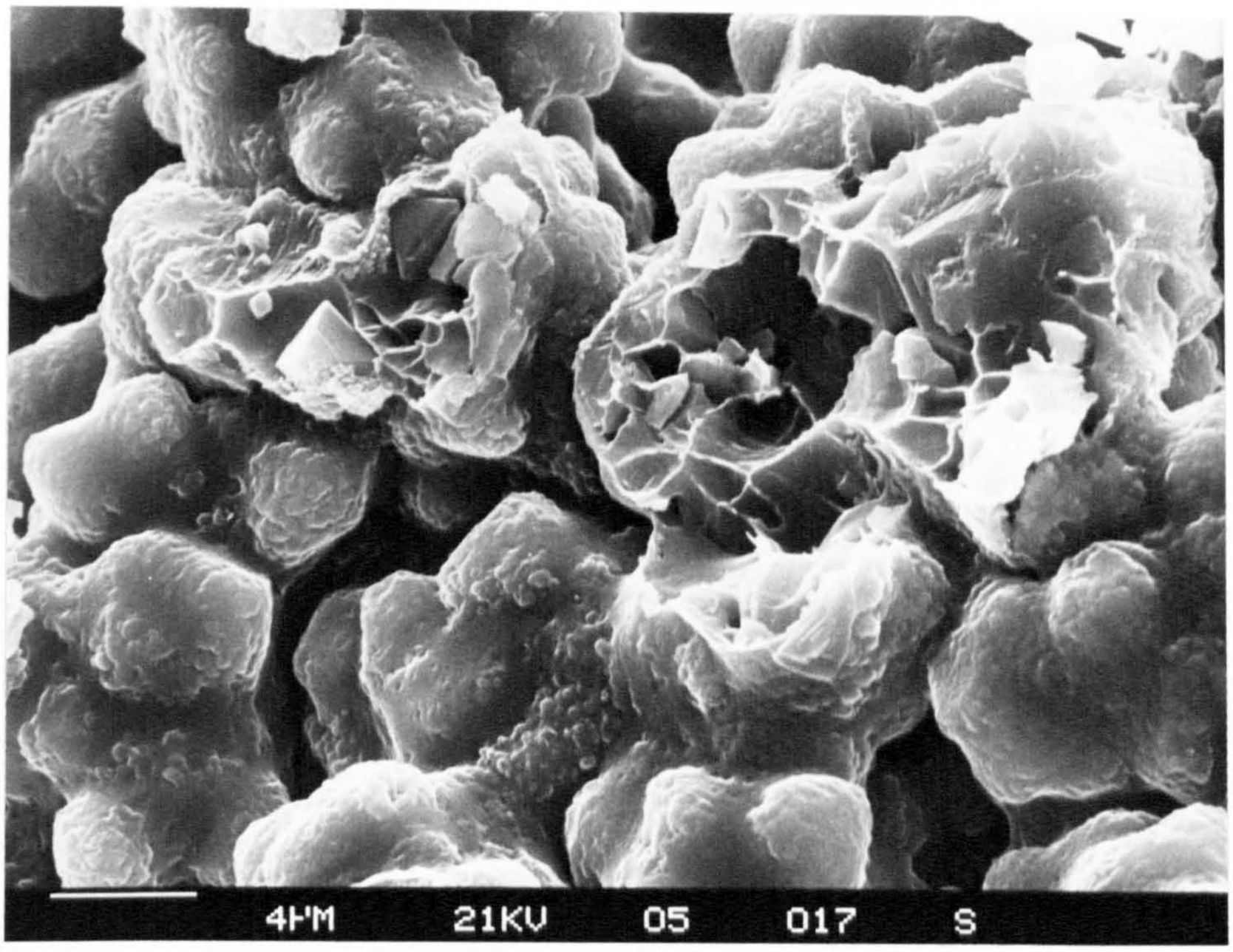

Figure 7.5 Oxide film formed on molten Al-1%Mg at 750°C after 15h in humid air showing exposed nodules

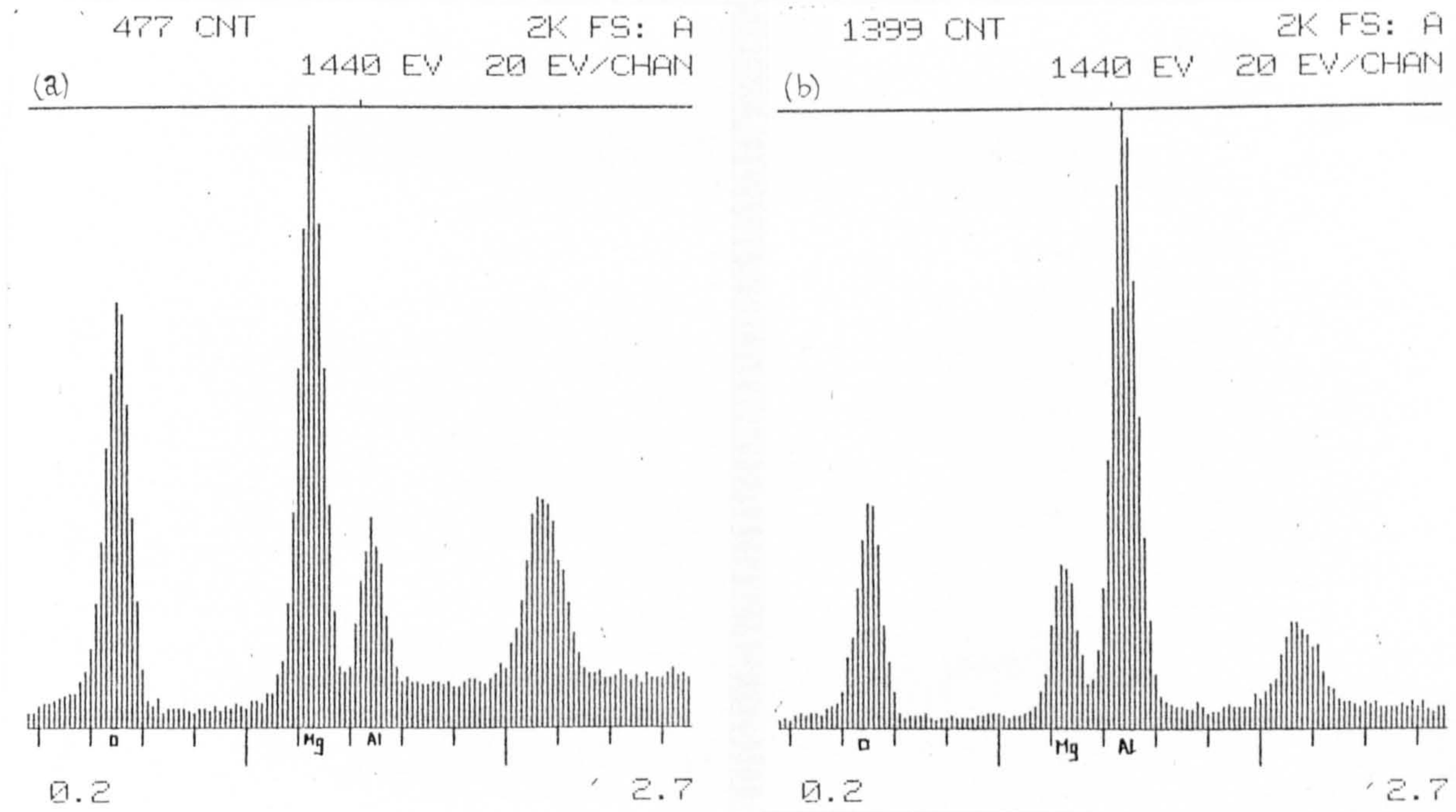

Figure 7.6 Analysis of oxide film on molten Al-1%Mg at 750°C after 15h oxidation (a) on nodule and (b) the surrounding surface

(a)

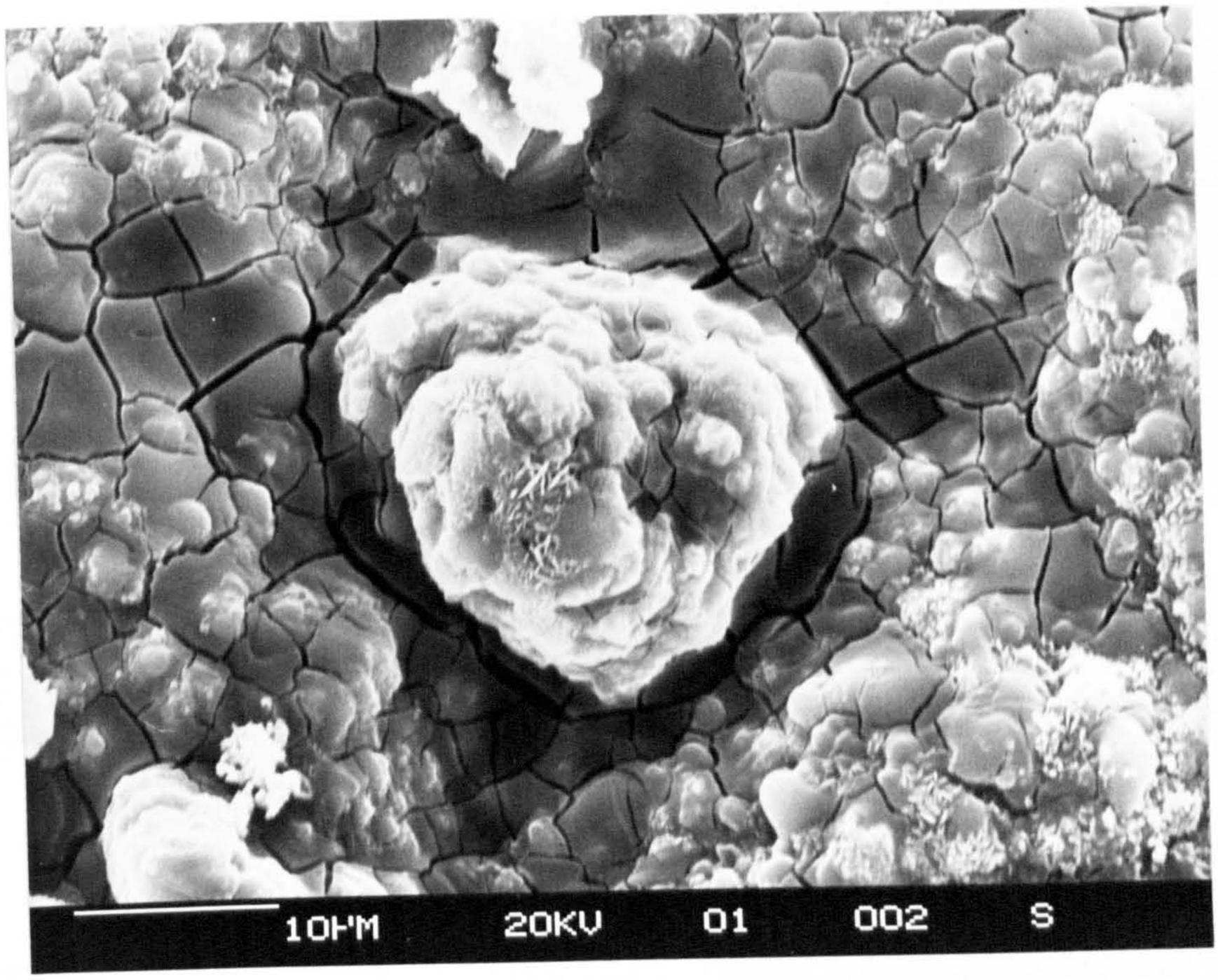

(b)

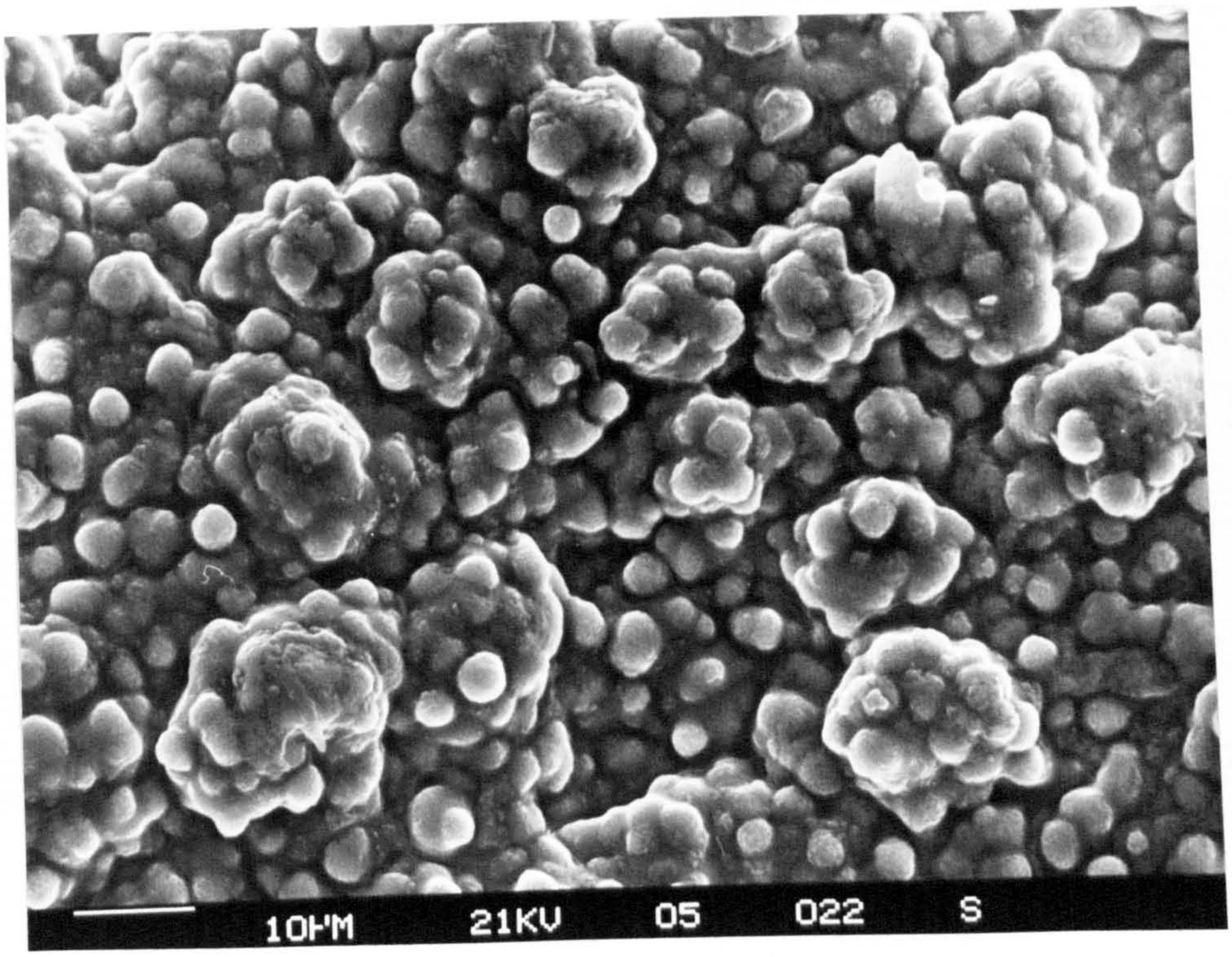

Figure 7.7 Surface of skimmed Al-1%Mg melt at 750°C after (a) 5h showing oxide growth and (b) 15h

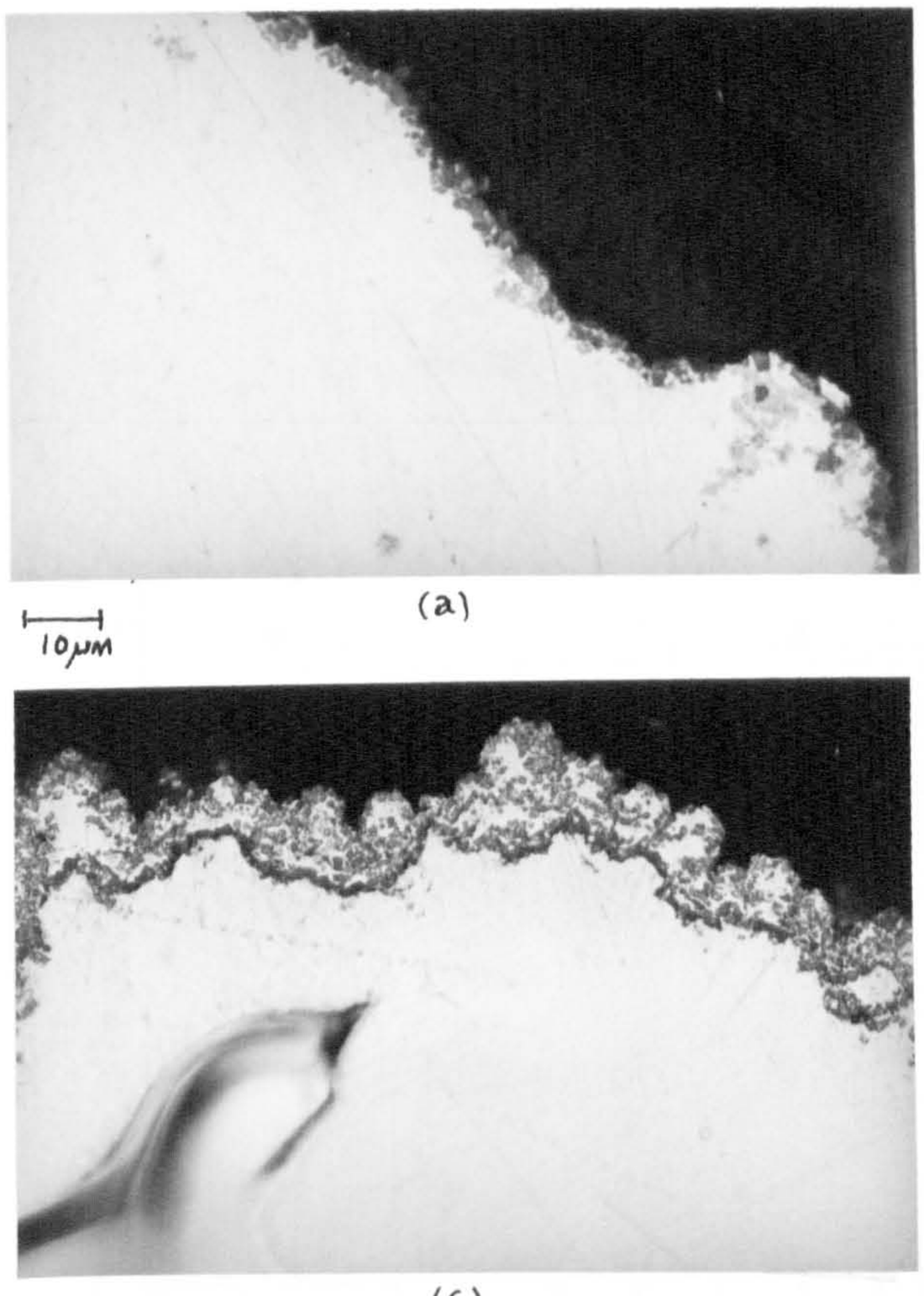

Figure 7.8 Sections through oxide-melt interface showing development of nodular growths, illustrated in (e) after 20h in humid air covering surface and (f) after 5h in gettered argon at isolated area

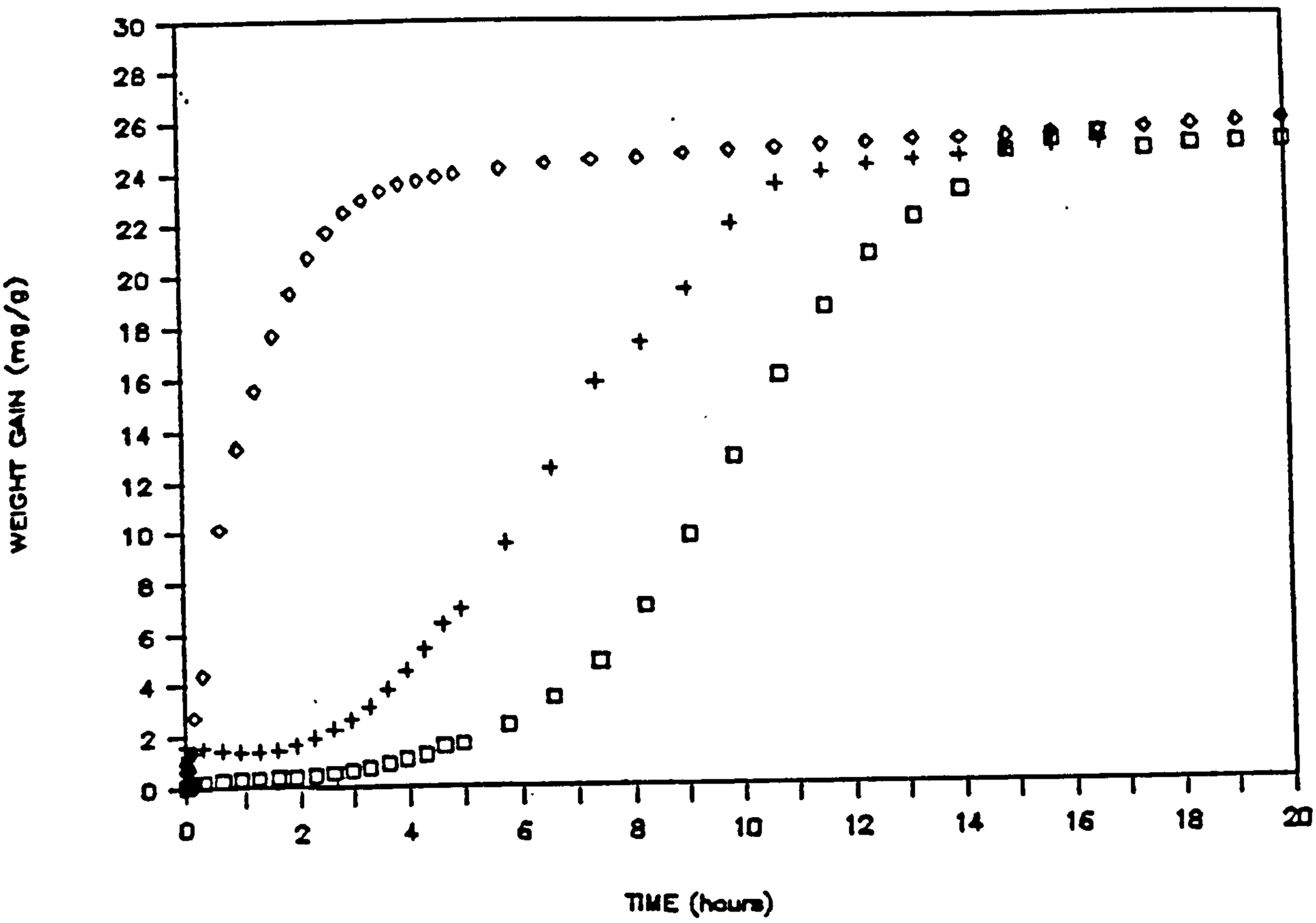

Figure 7.9 Oxidation of machined 5005 NGR alloy in air and argon at 750°C

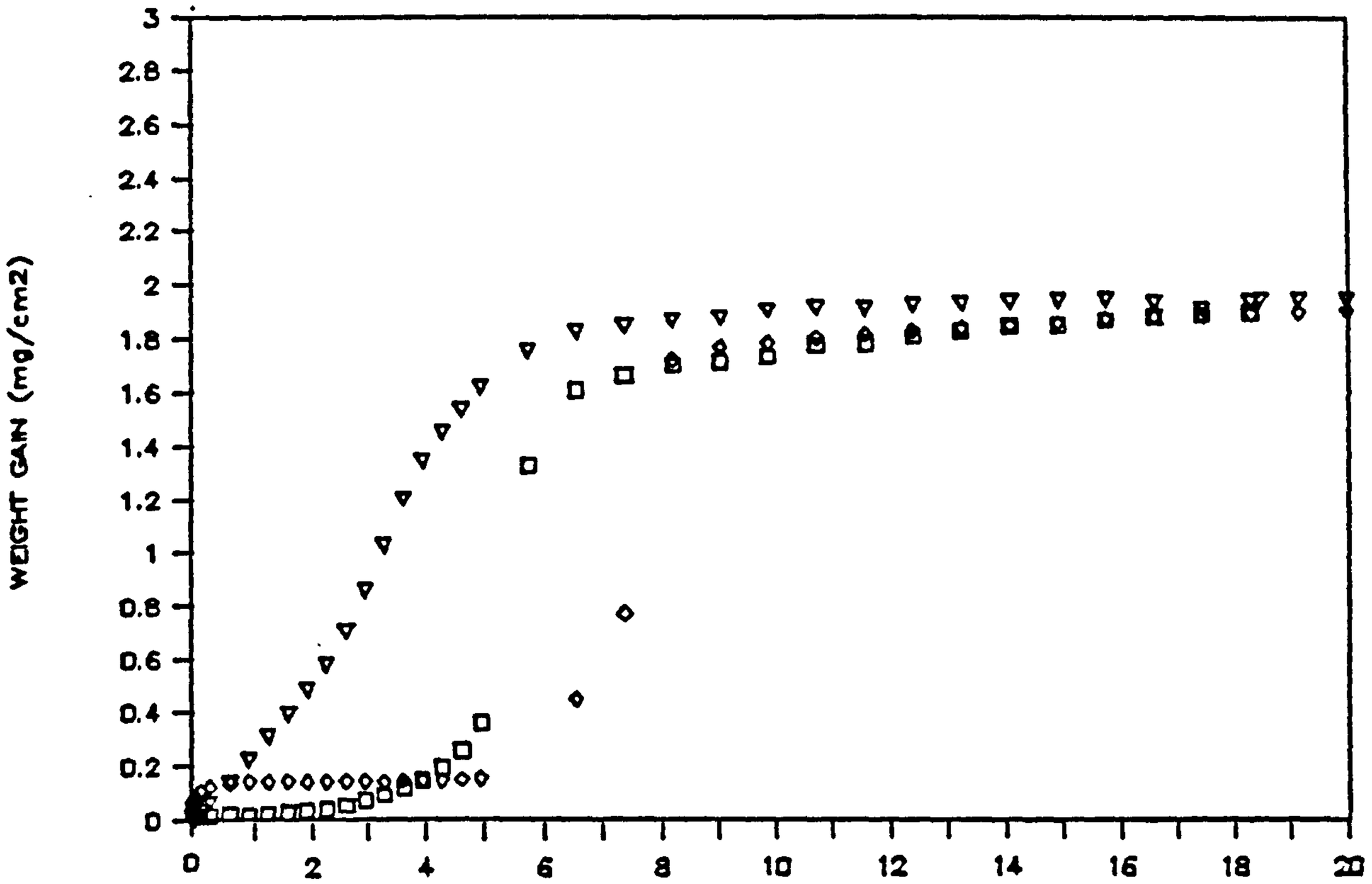

◇ *gas flow at specimen surface*

□ *small separation between gas and specimen surface*

▽ *increased separation between gas and specimen surface*

Figure 7.10 Influence of specimen position to gas flow on the oxidation of polished (1μm) 5005 GR alloy in gettered argon at 750°C.

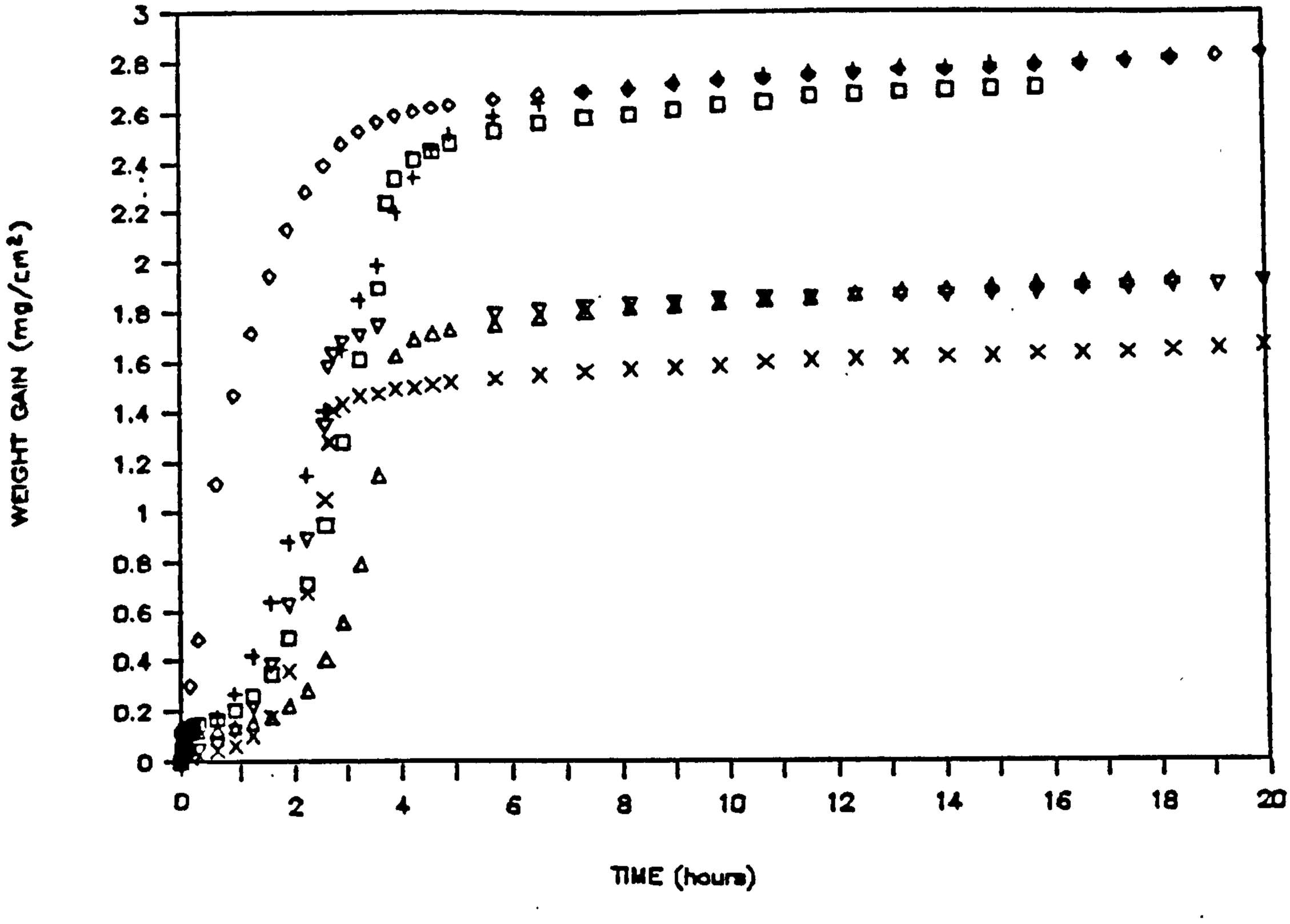

□,+ *machined surface of 5005GR*
◇ *machined surface of 5005NGR*

△,× *polished (1μm) surface of 5005GR*
▽ *polished (1μm) surface of 5005NGR*

Figure 7.11 Oxidation of machined and polished 5005GR and NGR alloy at 750°C in gettered argon (plotted per unit surface area).

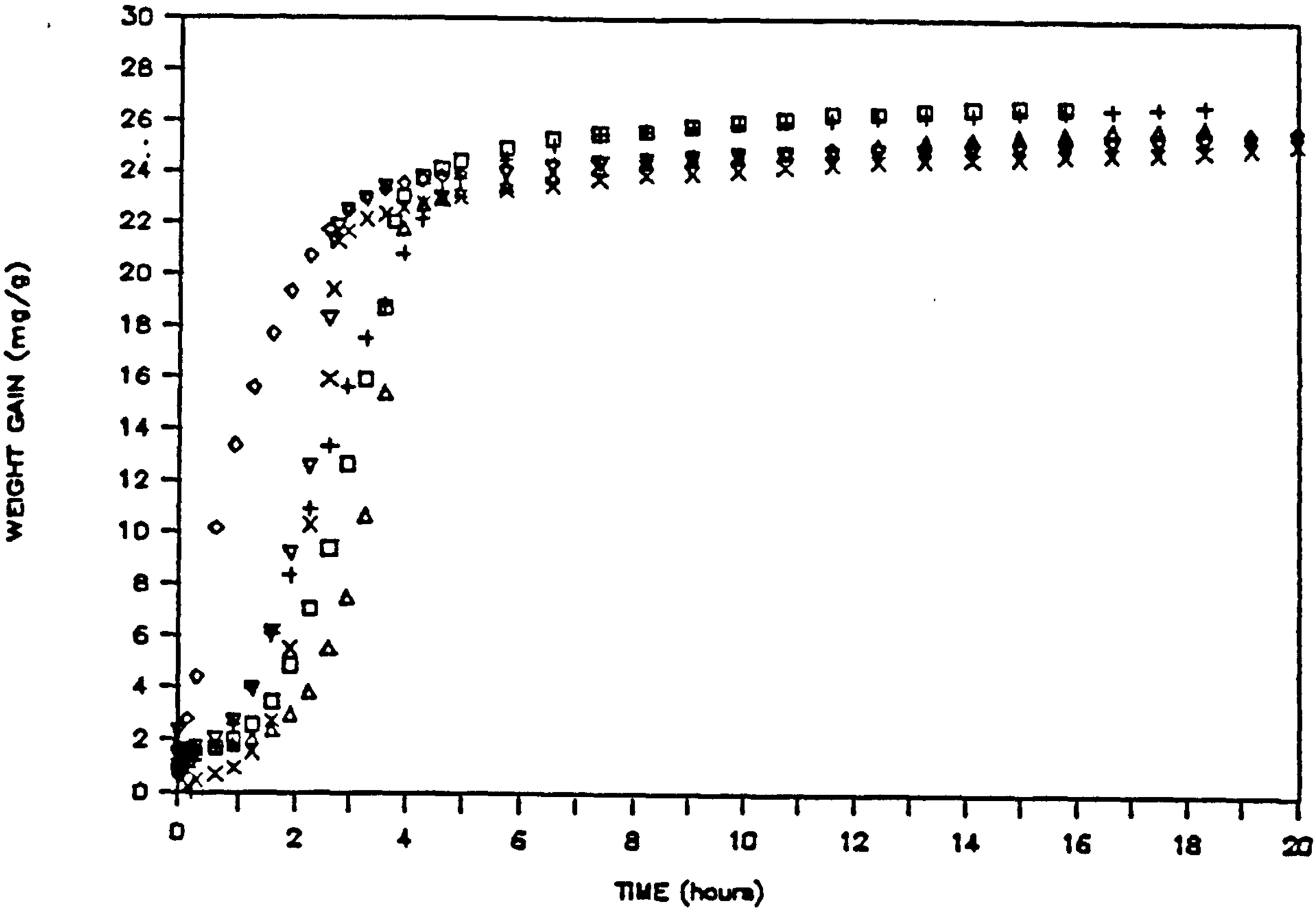

□ , + *machined surface of 5005GR*

◇ *machined surface of 5005NGR*

Δ , × *polished (1μm) surface of 5005GR*

▽ *polished (1μm) surface of 5005NGR*

Figure 7.12 Oxidation of machined and polished 5005GR and NGR alloy at 750°C in gettered argon (plooted per unit weight)

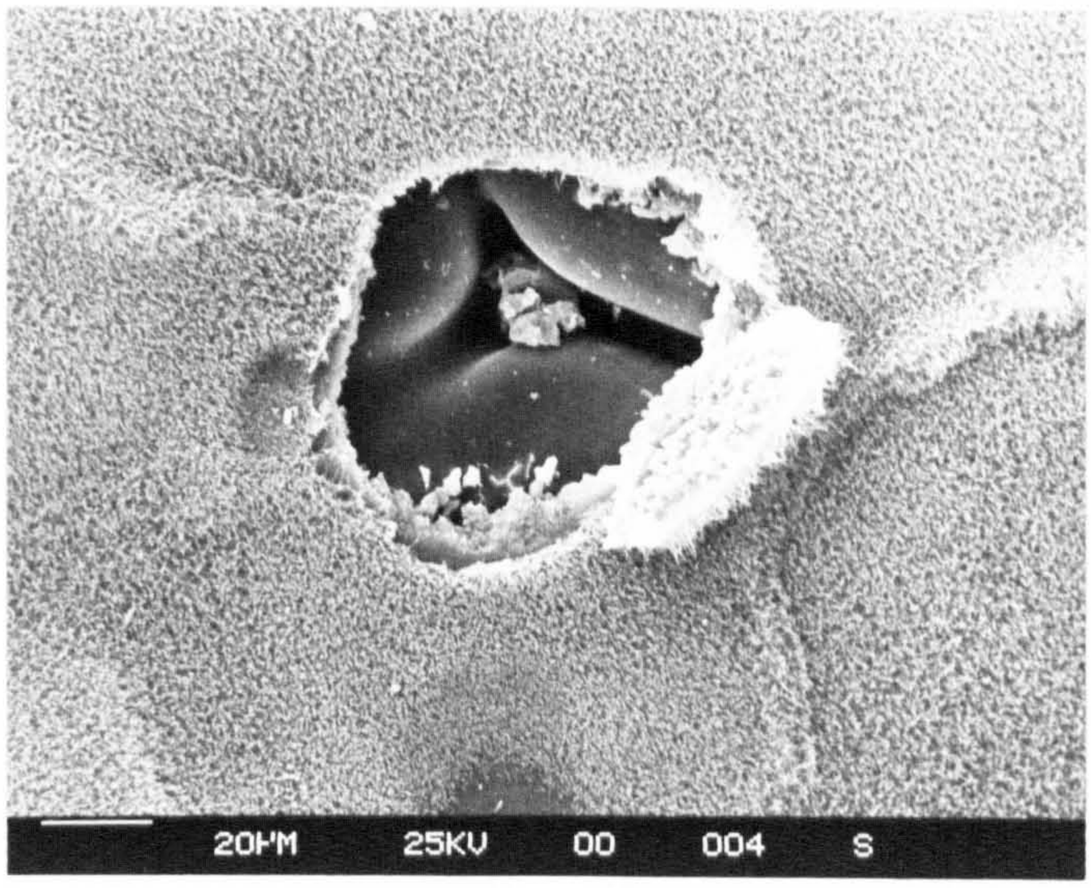

(a)

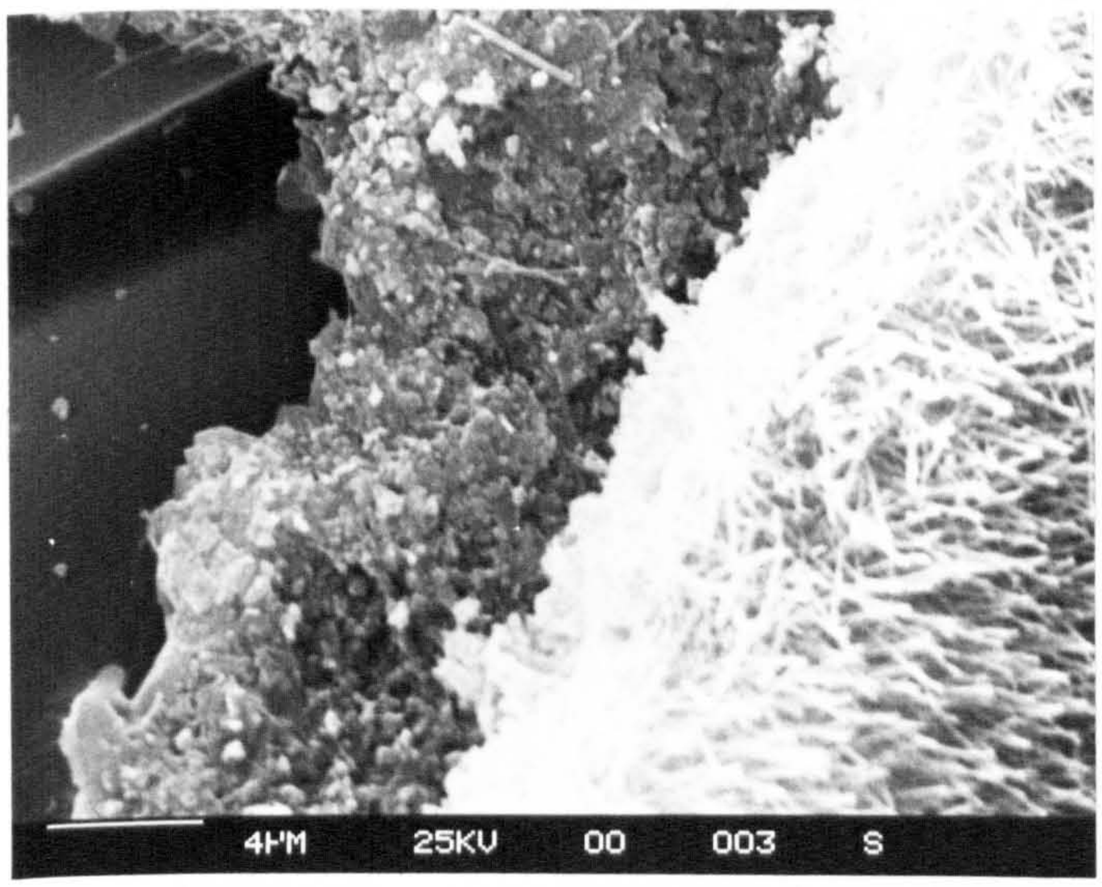

(b)

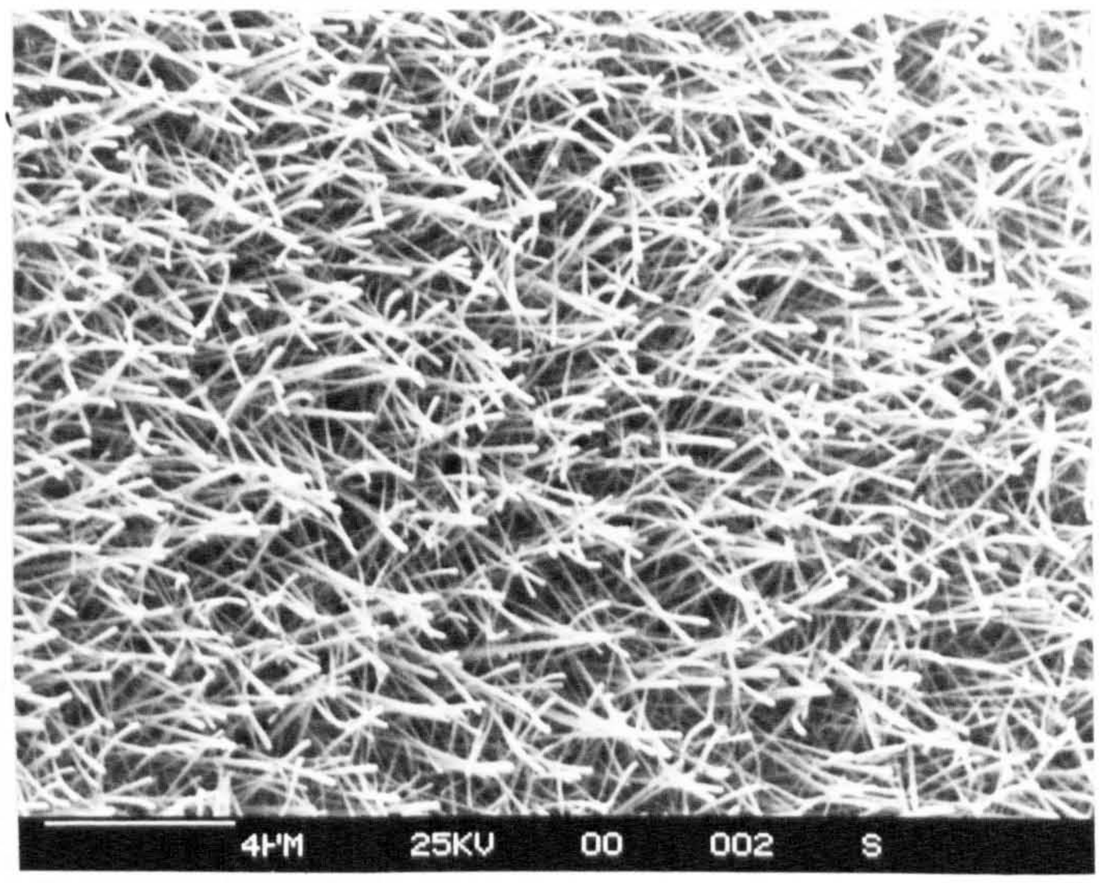

(c)

Figure 7.13 Hole in oxide on Al-1%Mg (a) low and (b,c) high magnification of surface layers and melt after 5h in fluoride at 750°C

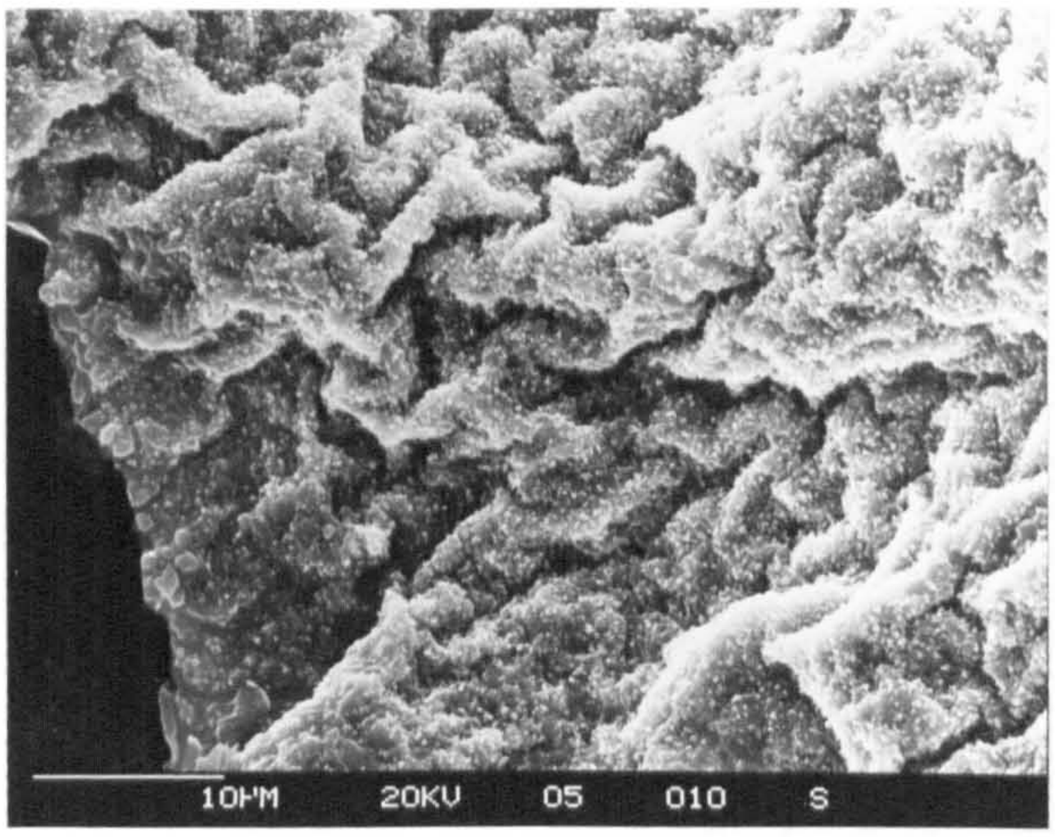

(a) unskimmed

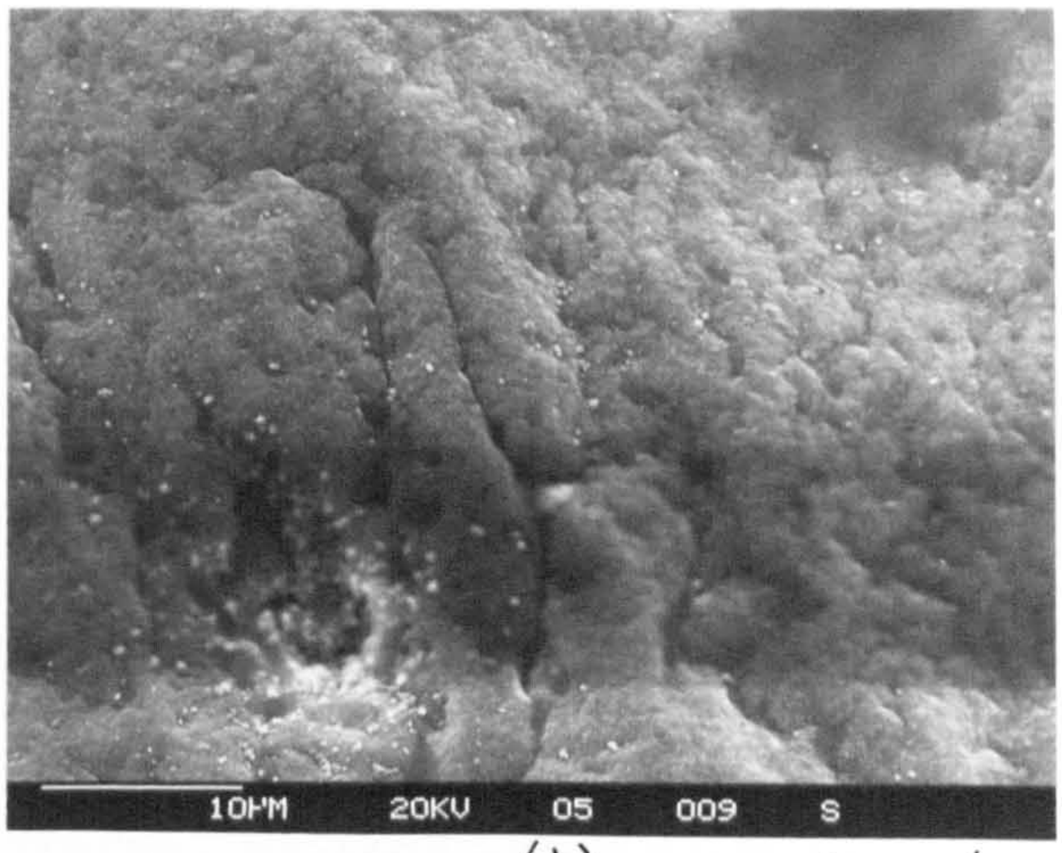

(b) skimmed

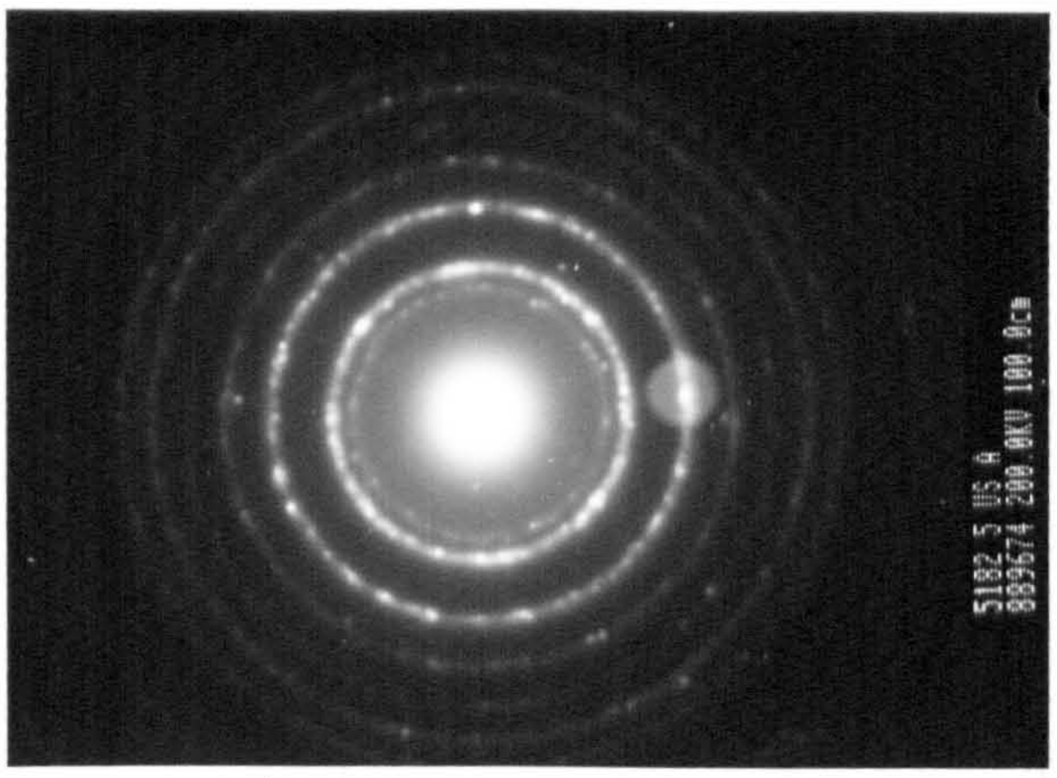

(e) diffraction pattern of (a)

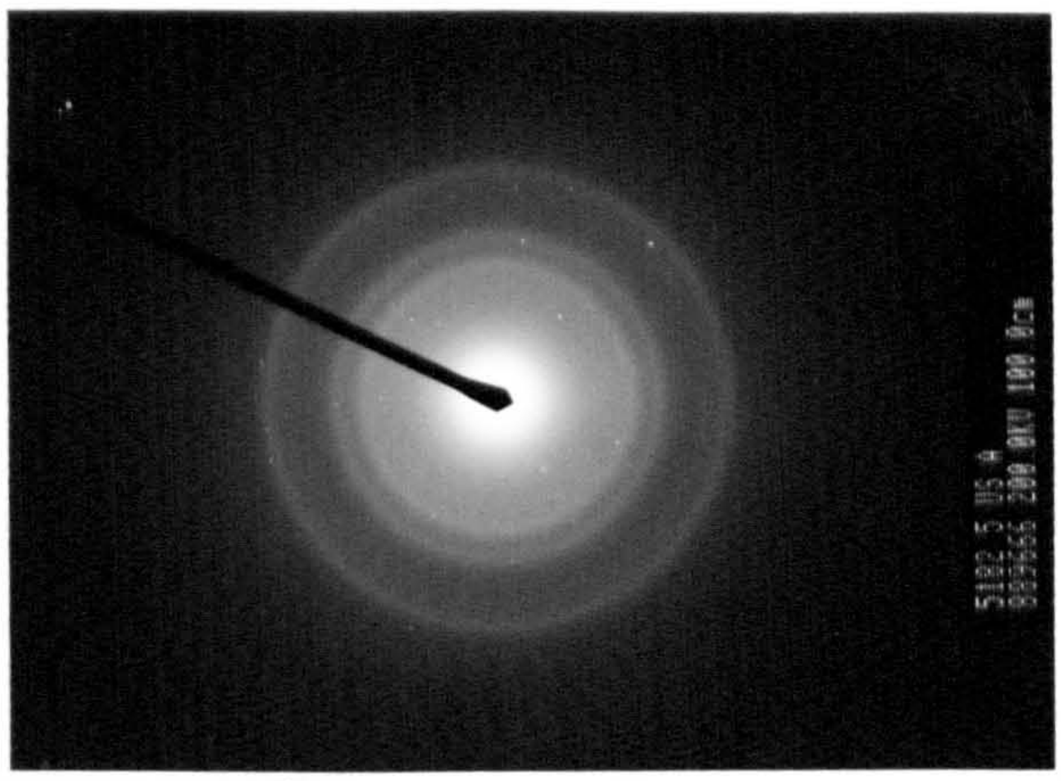

(f) diffraction pattern of (b)

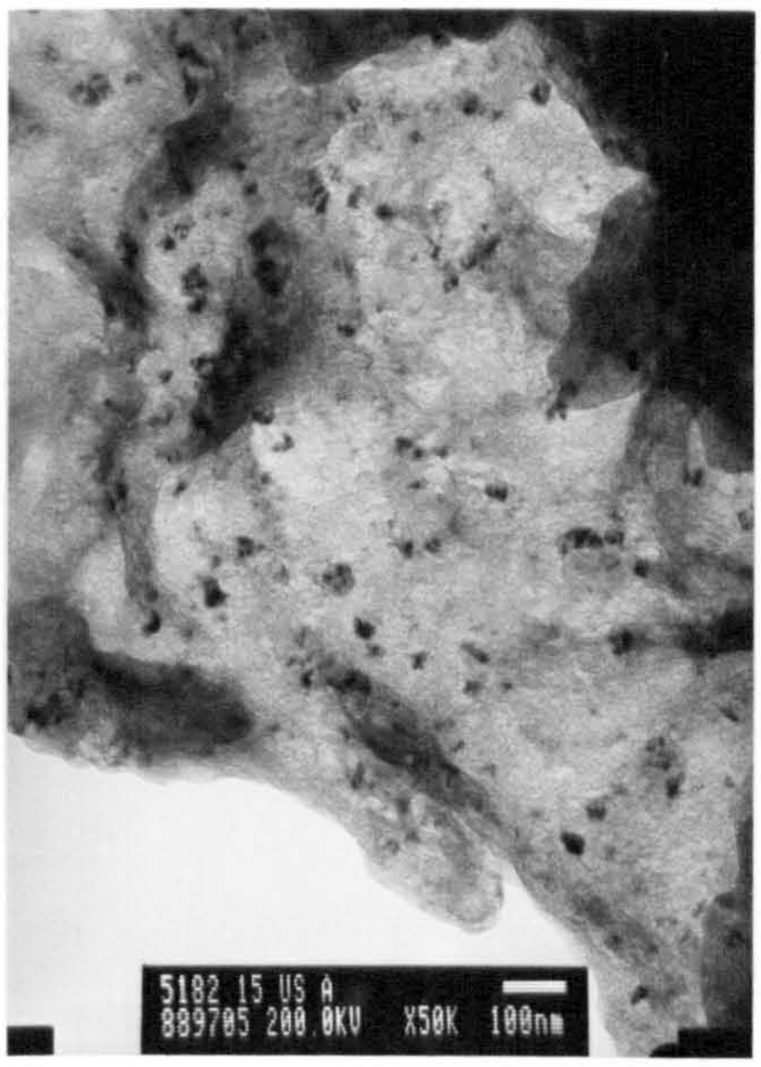

(c)

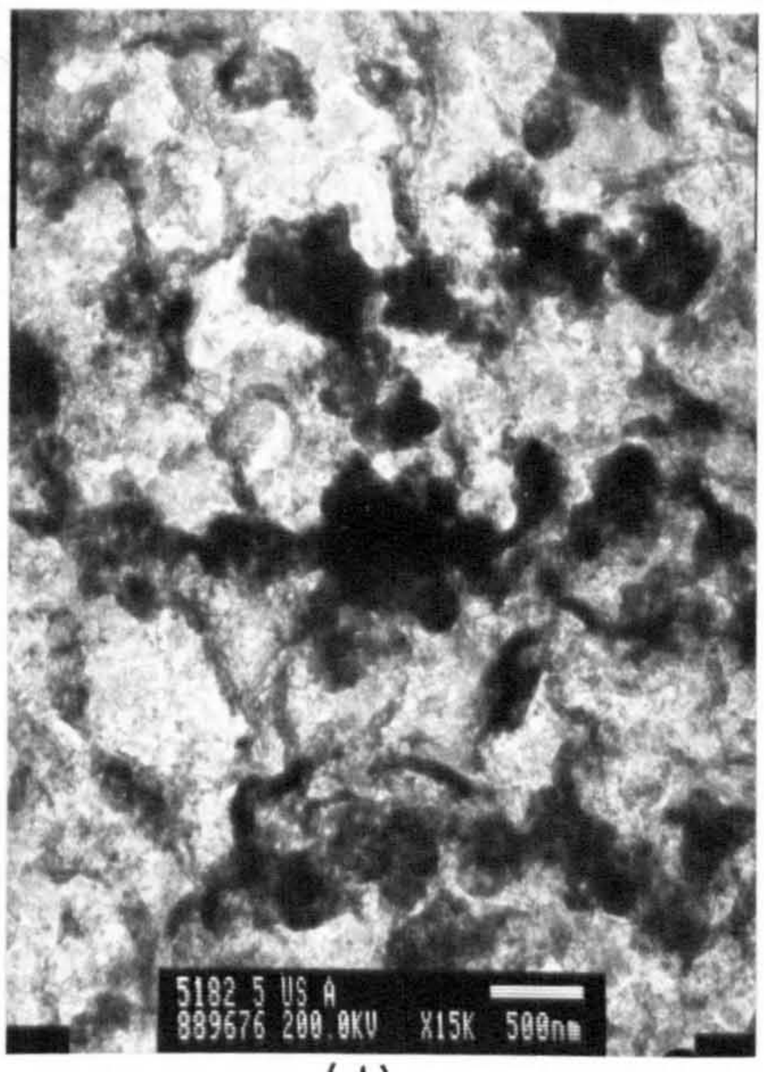

(d)

Figure 7.14 Micrographs of (b,f) skimmed 'amorphous' oxide and (a,e) unskimmed magnesia on 5182 melts after 5min in humid air at the oxide gas surface and (c,d) in transverse section

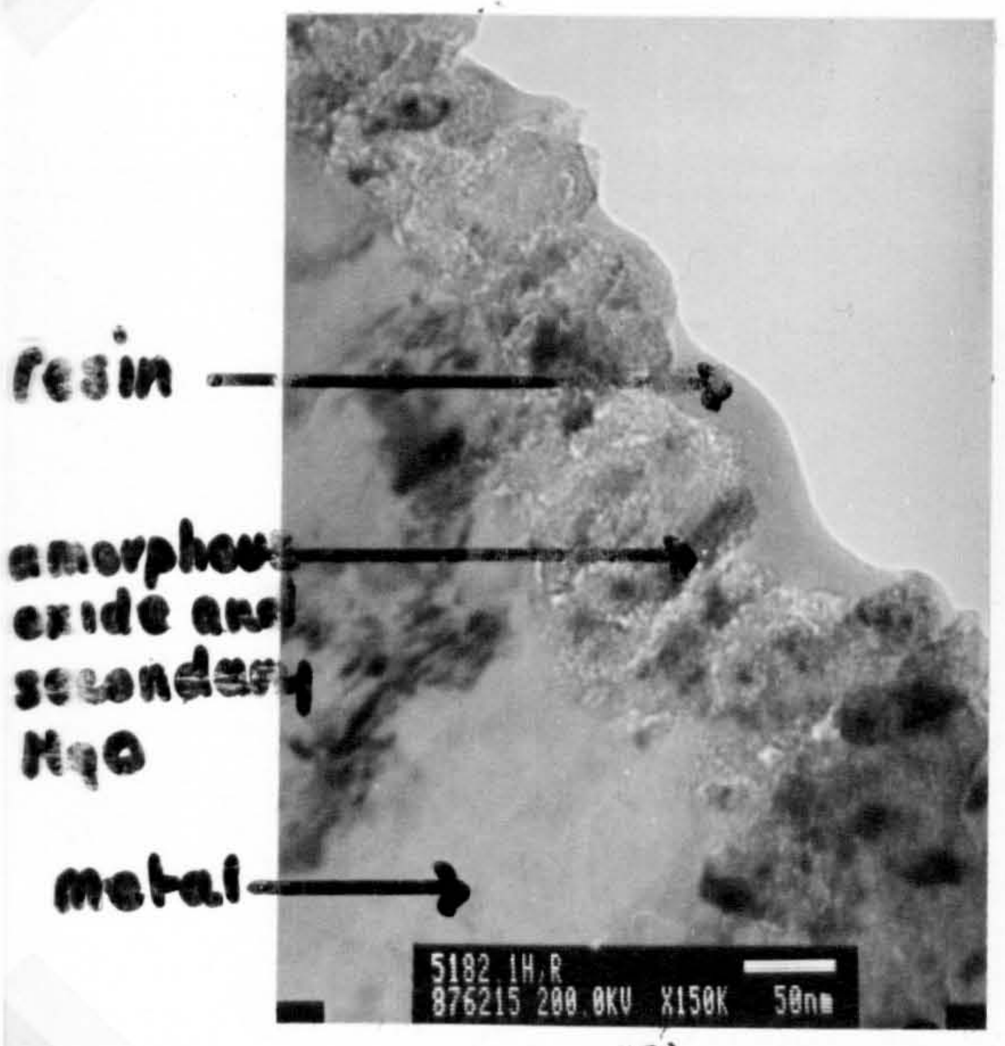

(a)

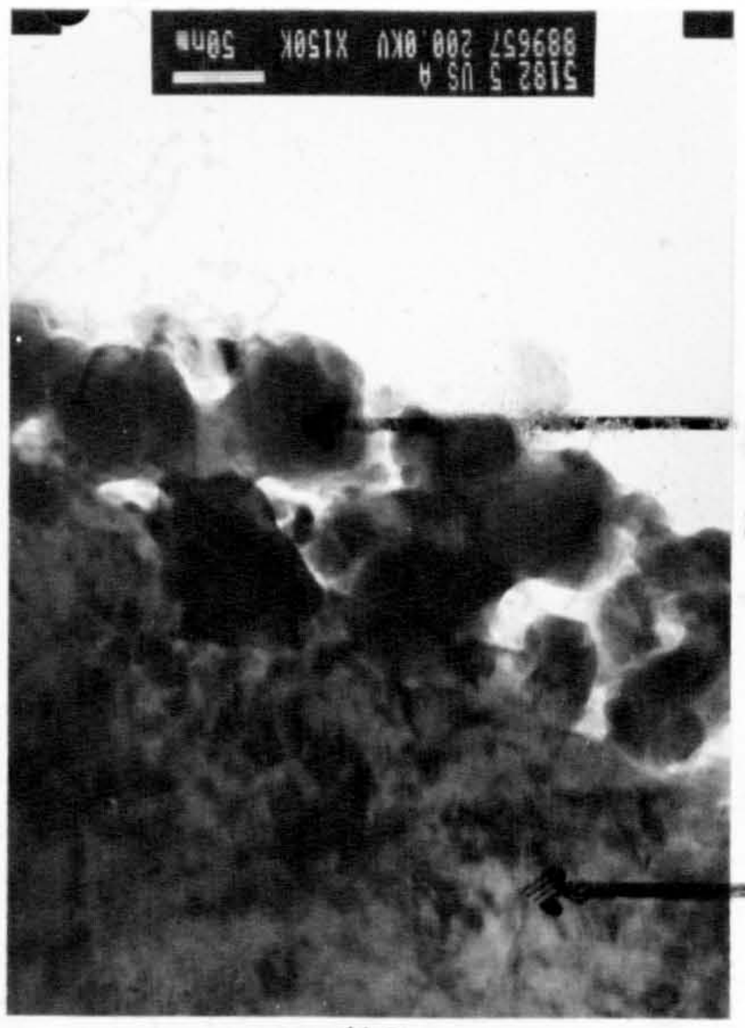

(b)

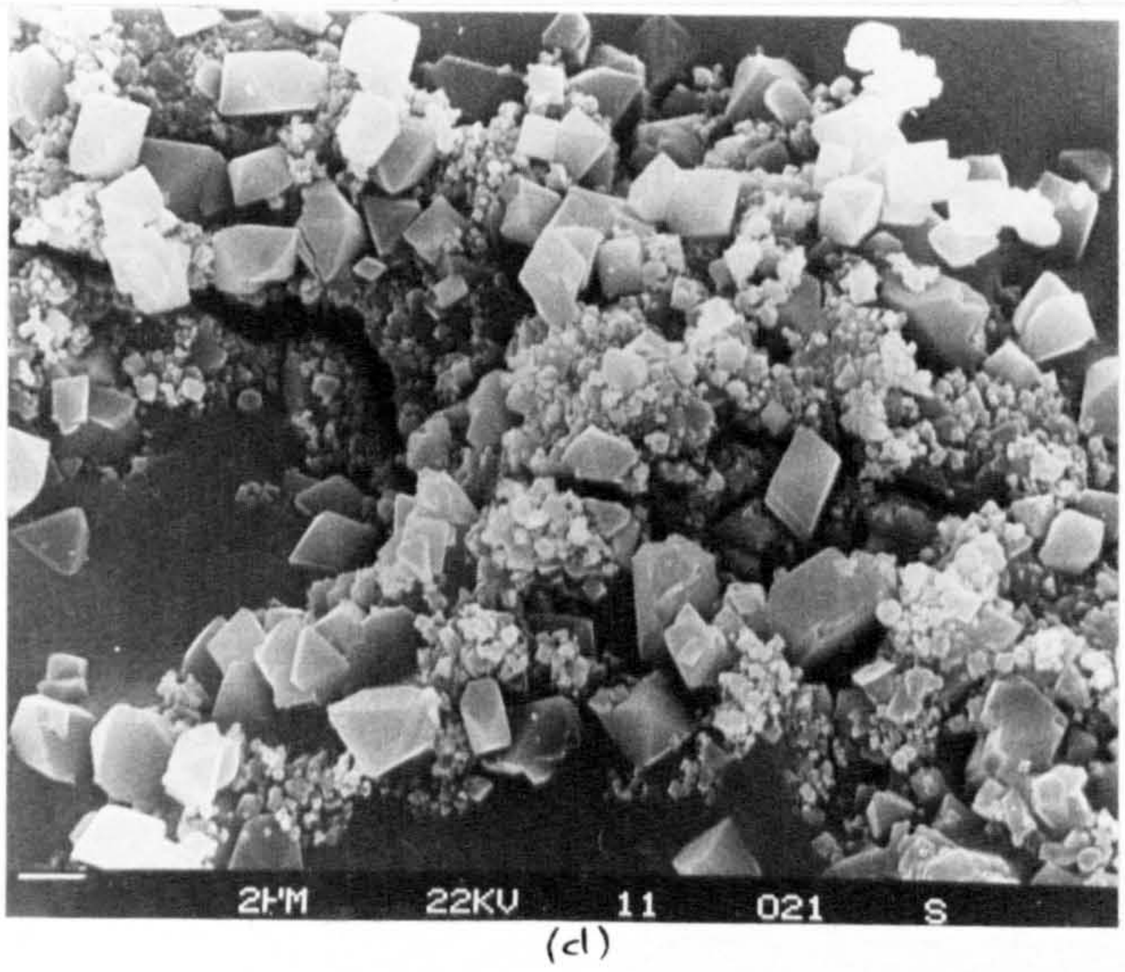

(d)

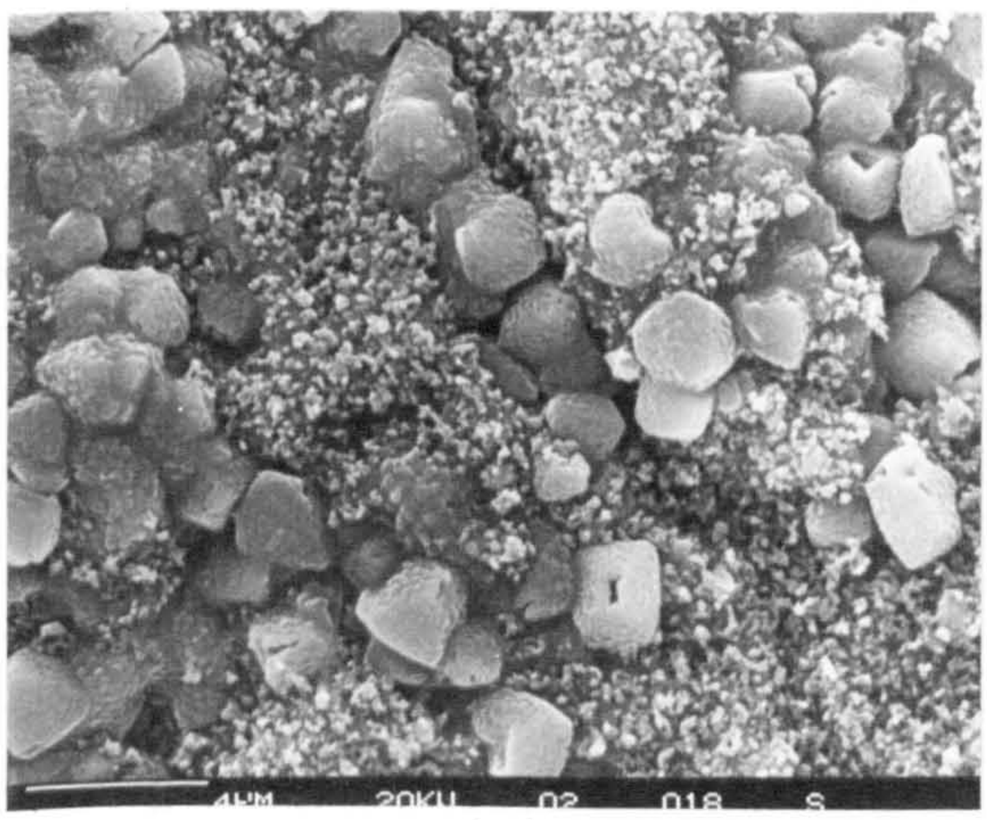

(c)

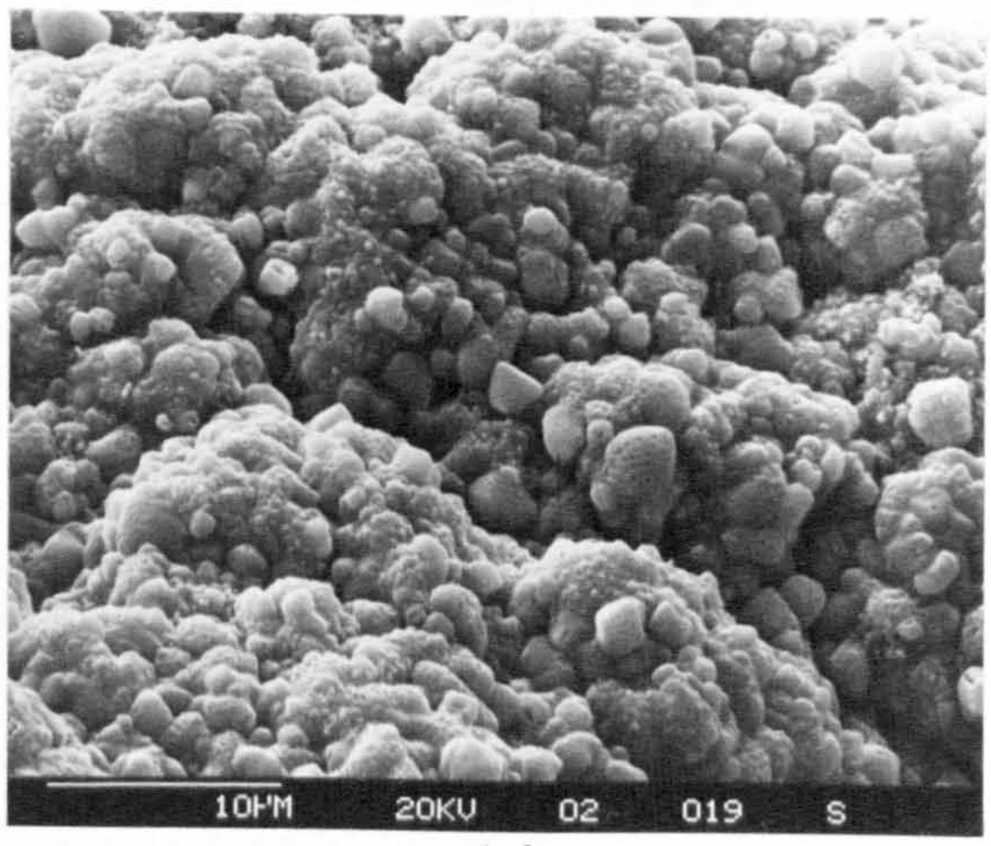

(e)

Figure 7.15 Sections through oxide-melt interface on 5182 oxidised at 750°C (a) showing primary MgO crystals after 5min and (b) smaller secondary MgO crystallites after 1h. Oxide crystal dispersion (d) at the oxide-melt interface and (c) the thickening oxide surface (e) after 80min

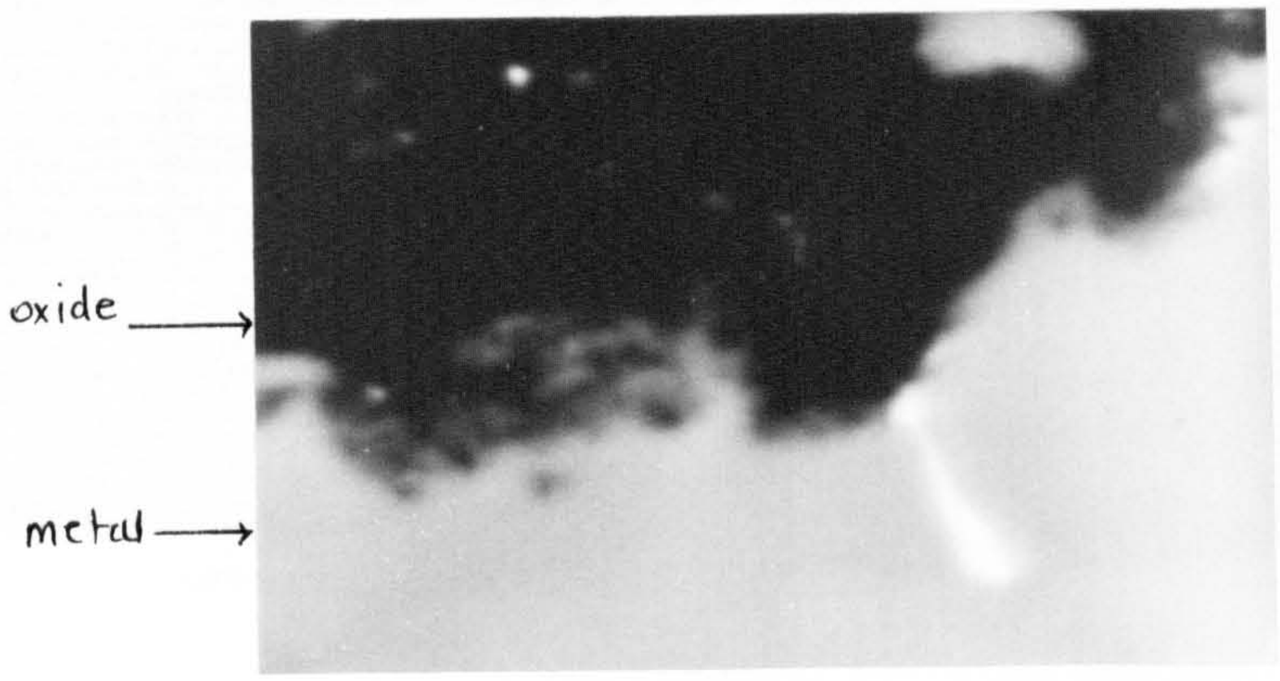

(d)

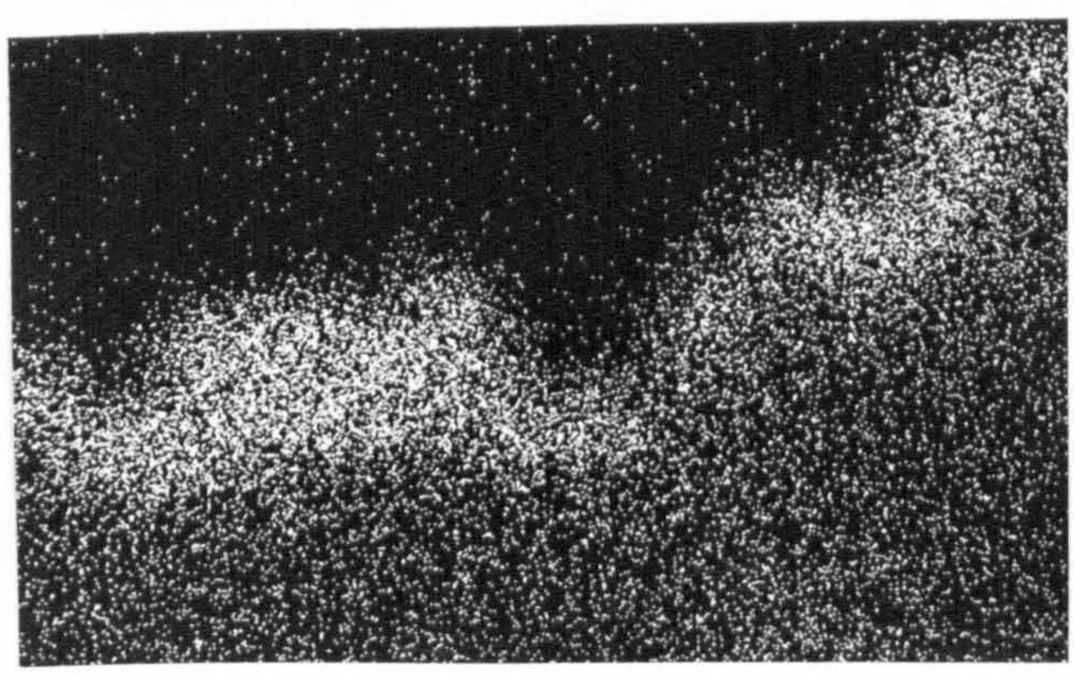

(b)

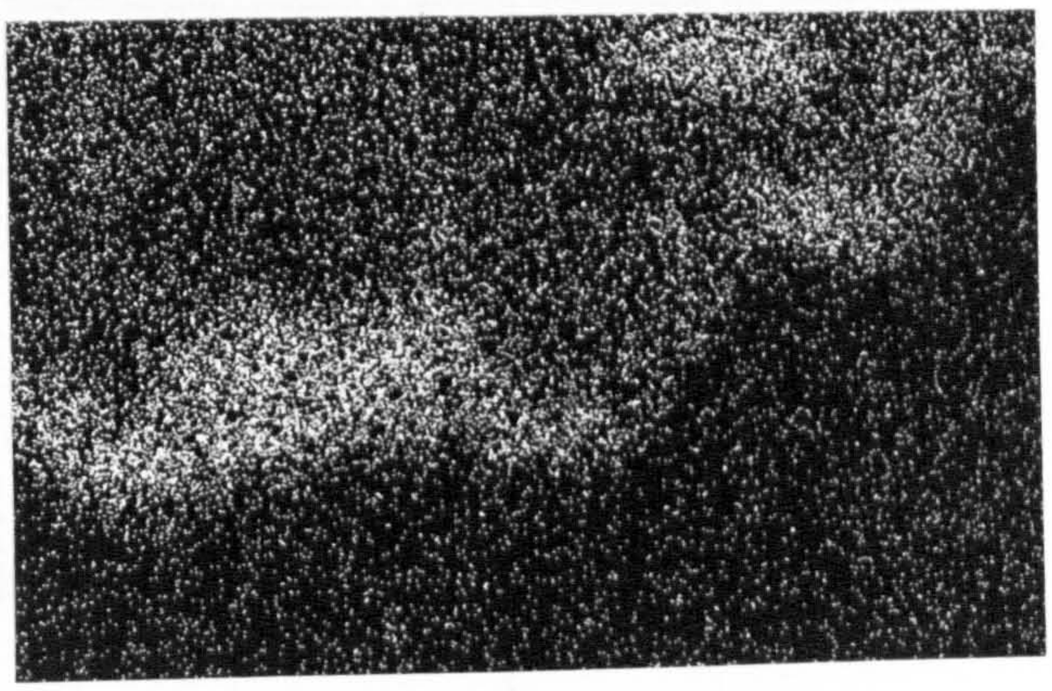

(c)

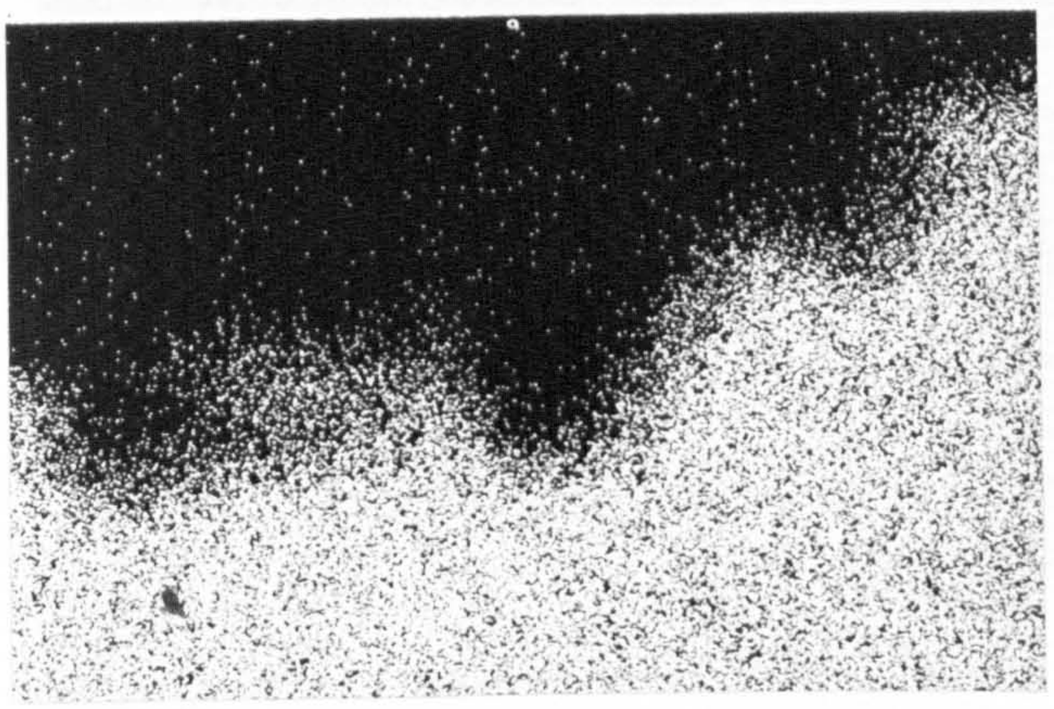

30μm

(d)

Figure 7.16 Element distribution (by electron microprobe) on a 5182 alloy section oxidised for 1h. Showing (b) magnesium (c) oxygen enrichment of the oxide and (d) remaining aluminium metal

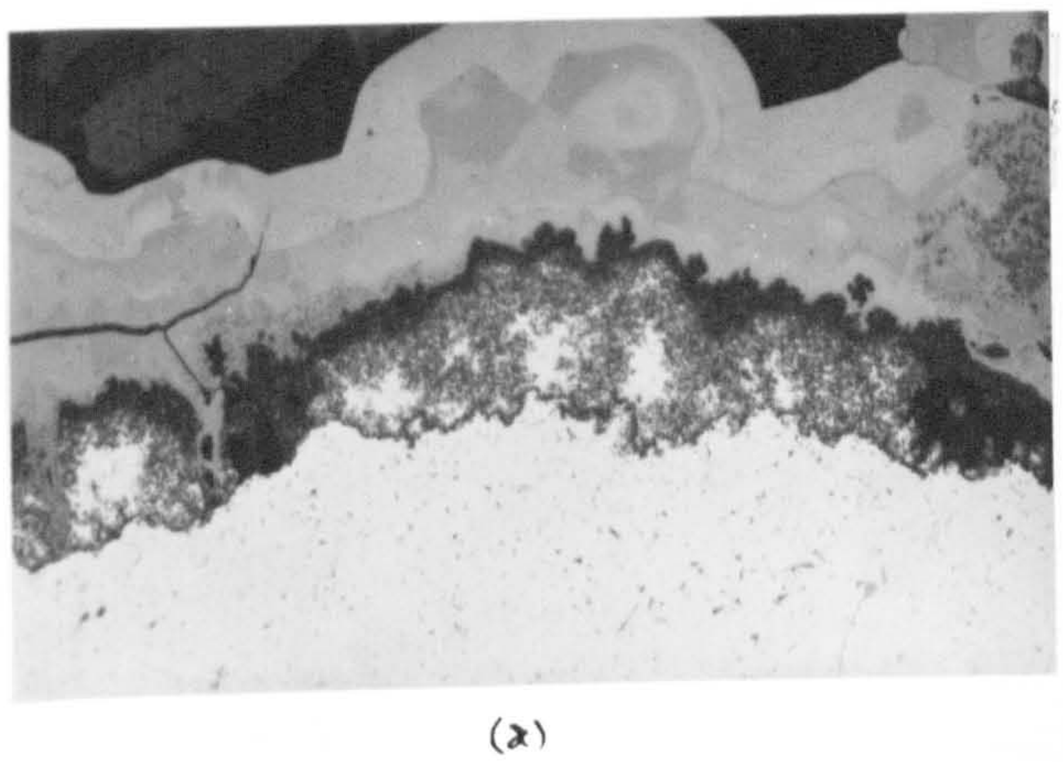

(a)

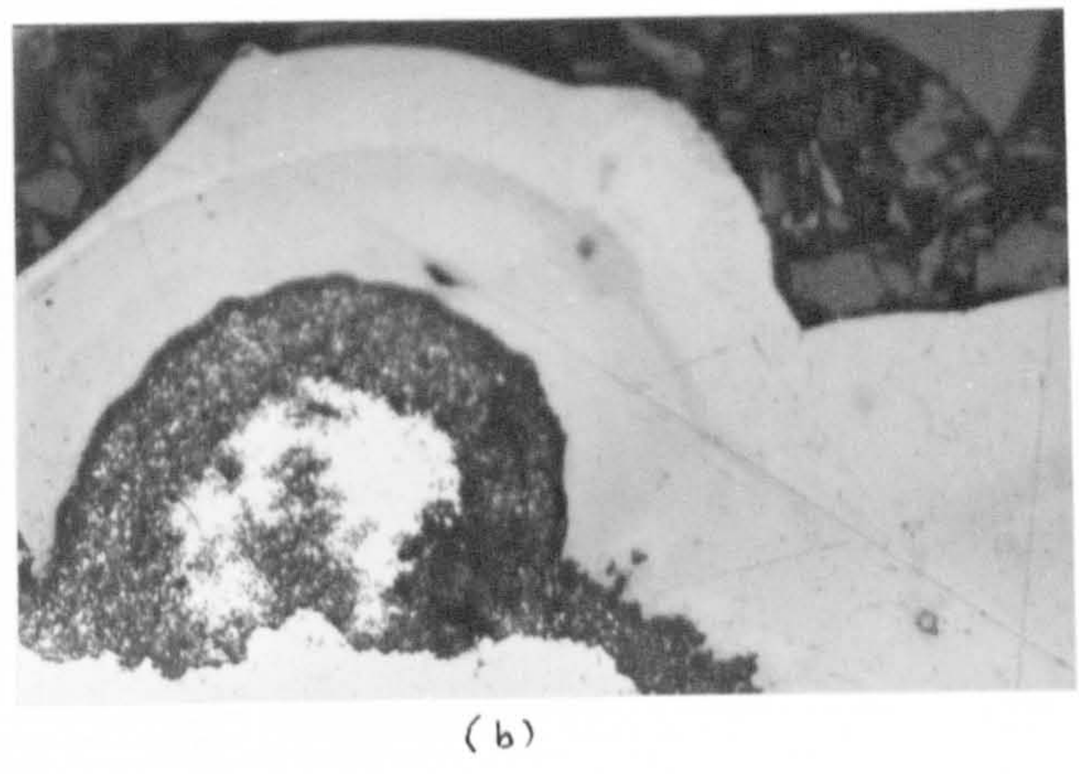

(b)

40 μm

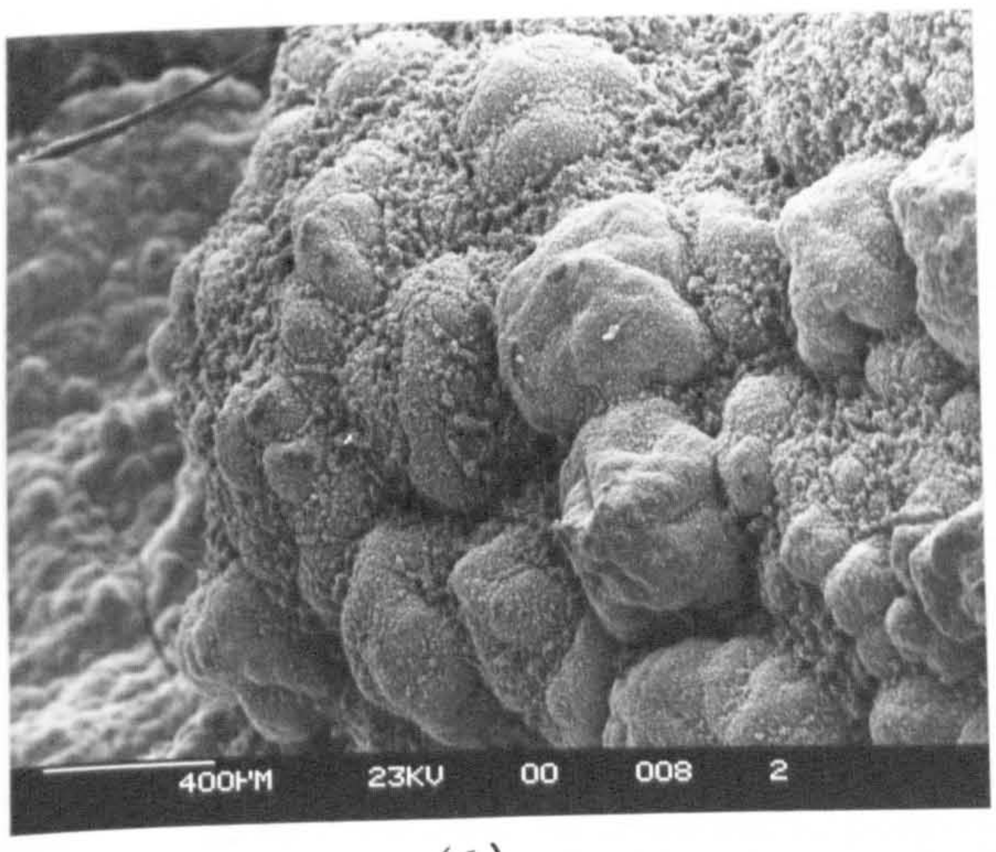

(c)

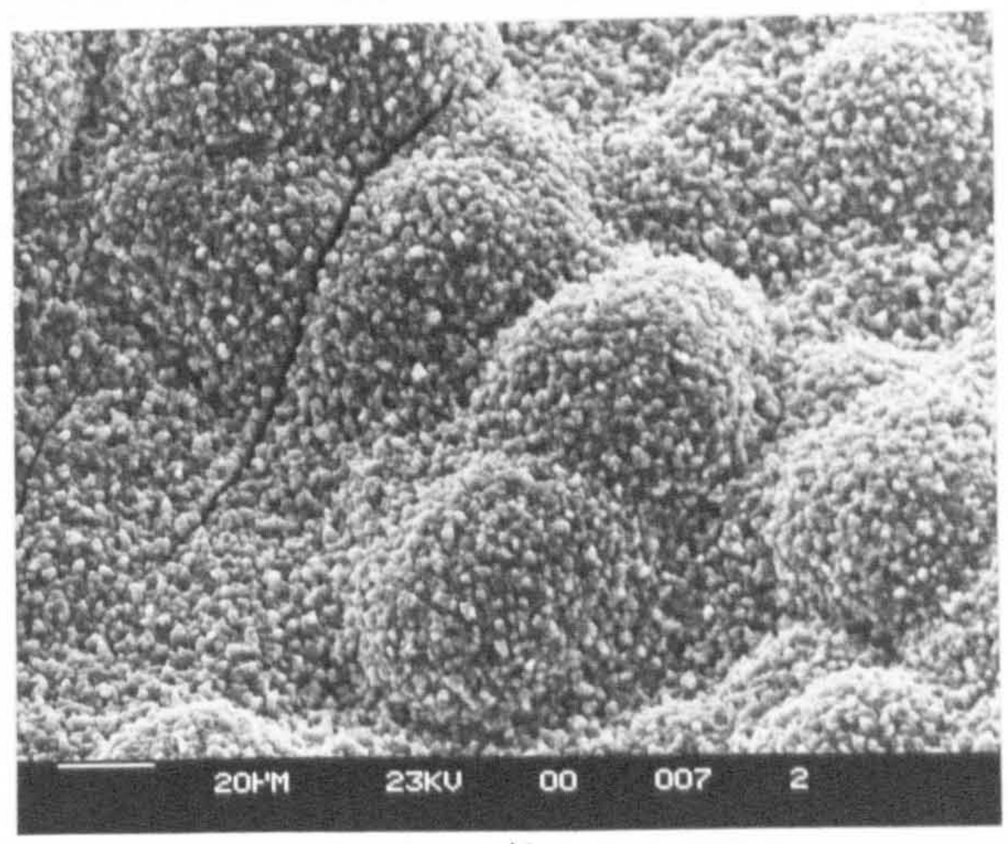

(d)

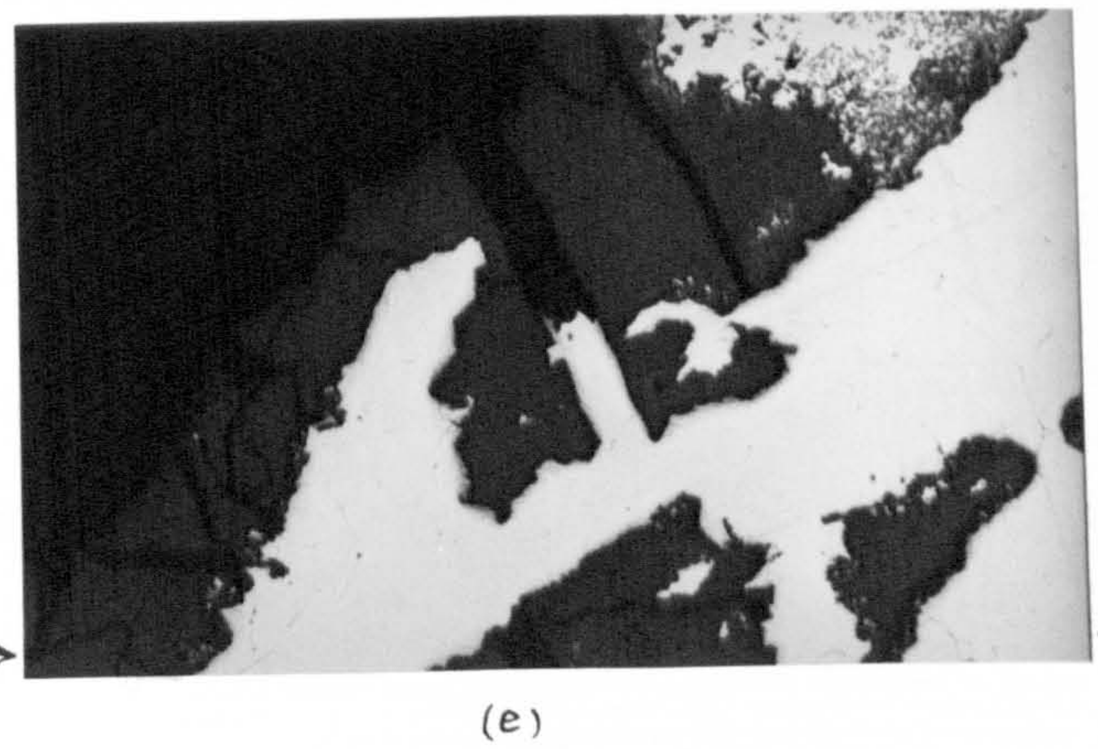

oxide → ← metal

(e)

100 μm

Figure 7.17 (a, b, e) sections through growths on heavily oxidised 5182 alloy 20h at 750°C in gettered argon on the (c, d) oxide surface

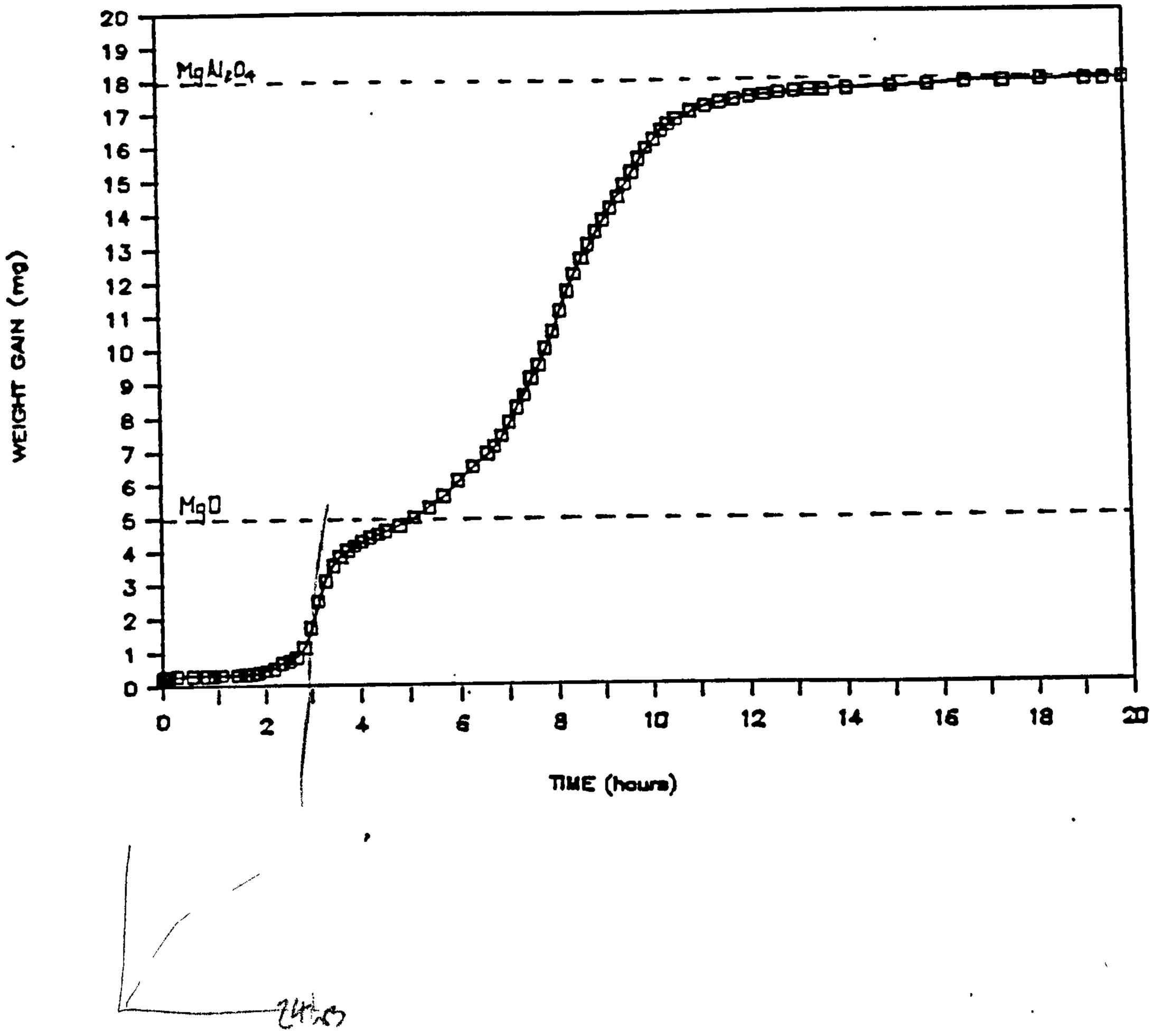

Figure 7.18 Oxidation of machined 5182 alloy in dry air at 750°C.

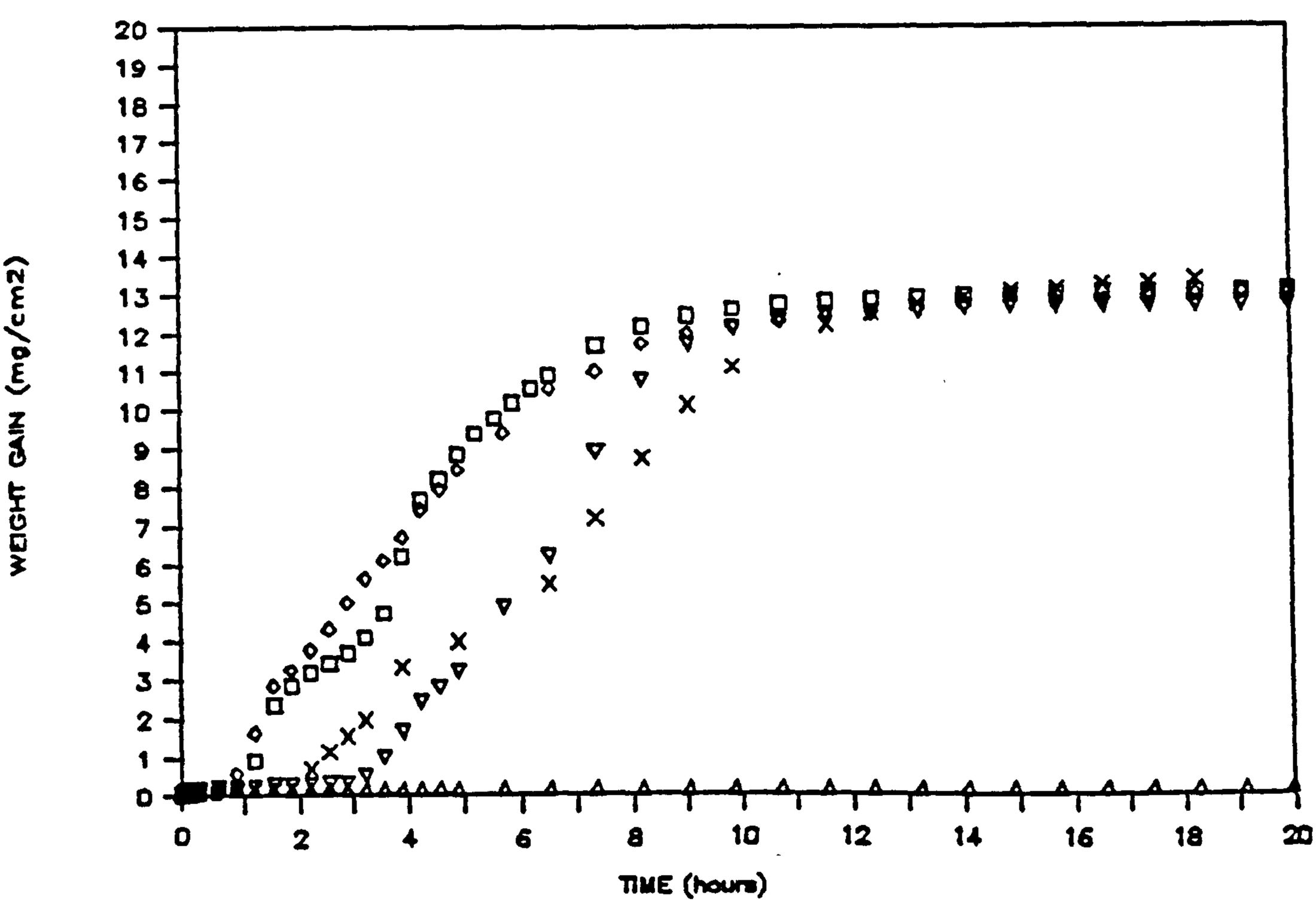

□ *still dry air*

× *flowing dry air*

△ *flowing humid air*

◇ *still humid argon*

▽ *flowing humid argon*

Figure 7.19 Oxidation of machined 5182 in air and argon atmospheres at 750°C.

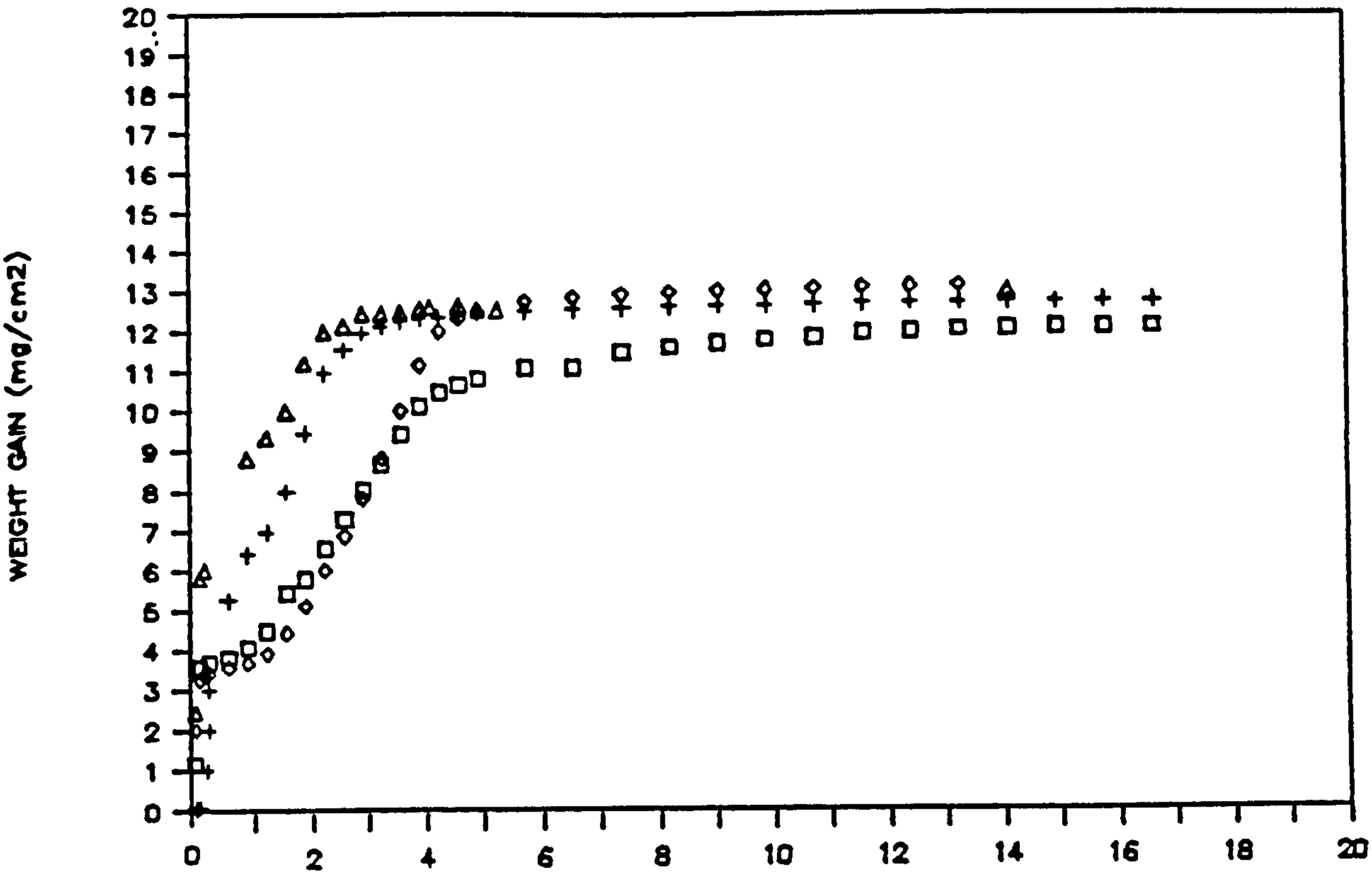

Δ , + *still gettered argon*

□ , ◇ *flowing gettered argon*

Figure 7.20 Oxidation of polished (600μm) 5182 in still and flowing gettered argon at 750°C.

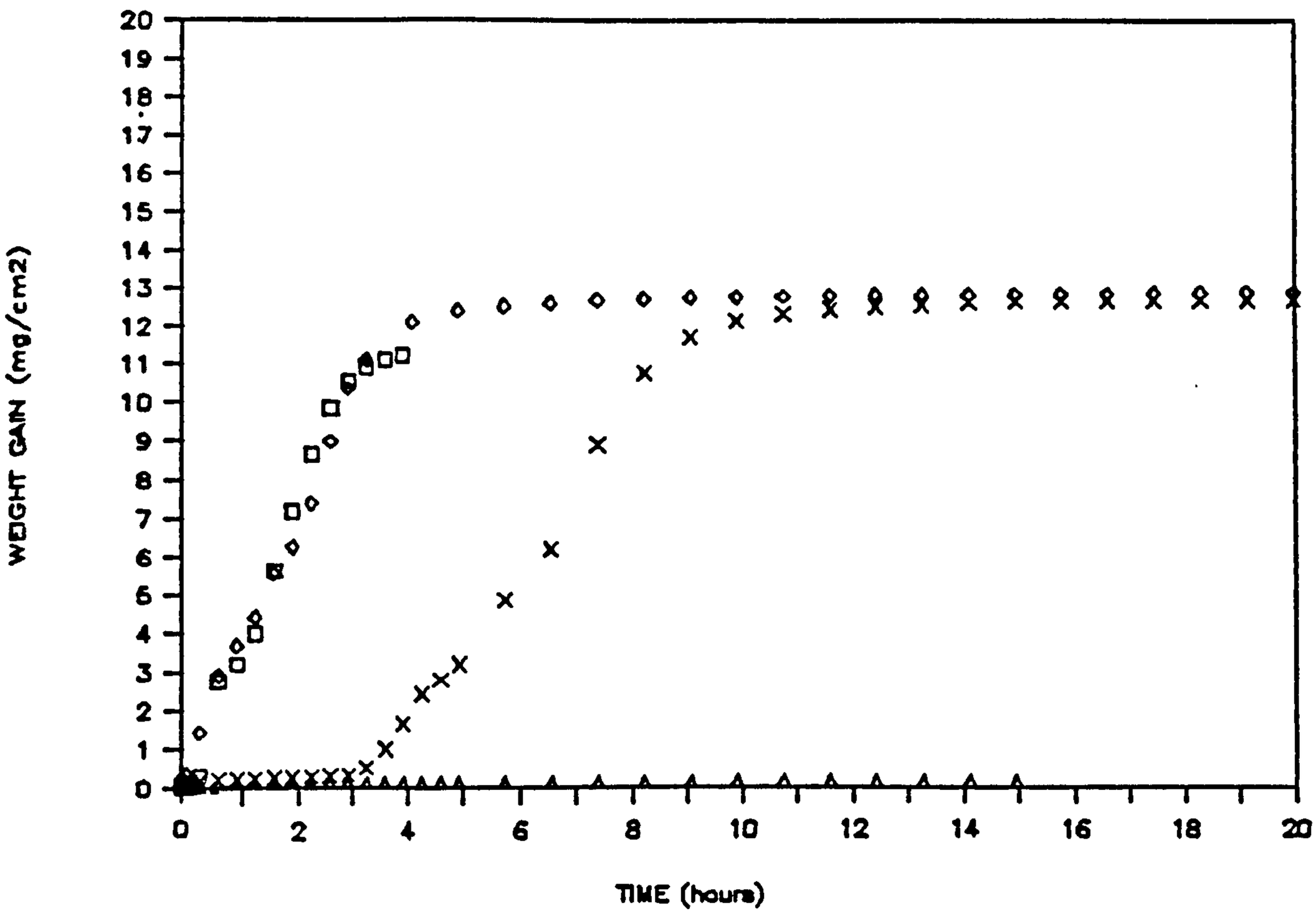

◇ *gettered argon* × *dry air*

□ *humid argon* Δ *humid air*

Figure 7.21 Oxidation of polished (1μm) 5182 in still air and argon at 750°C.

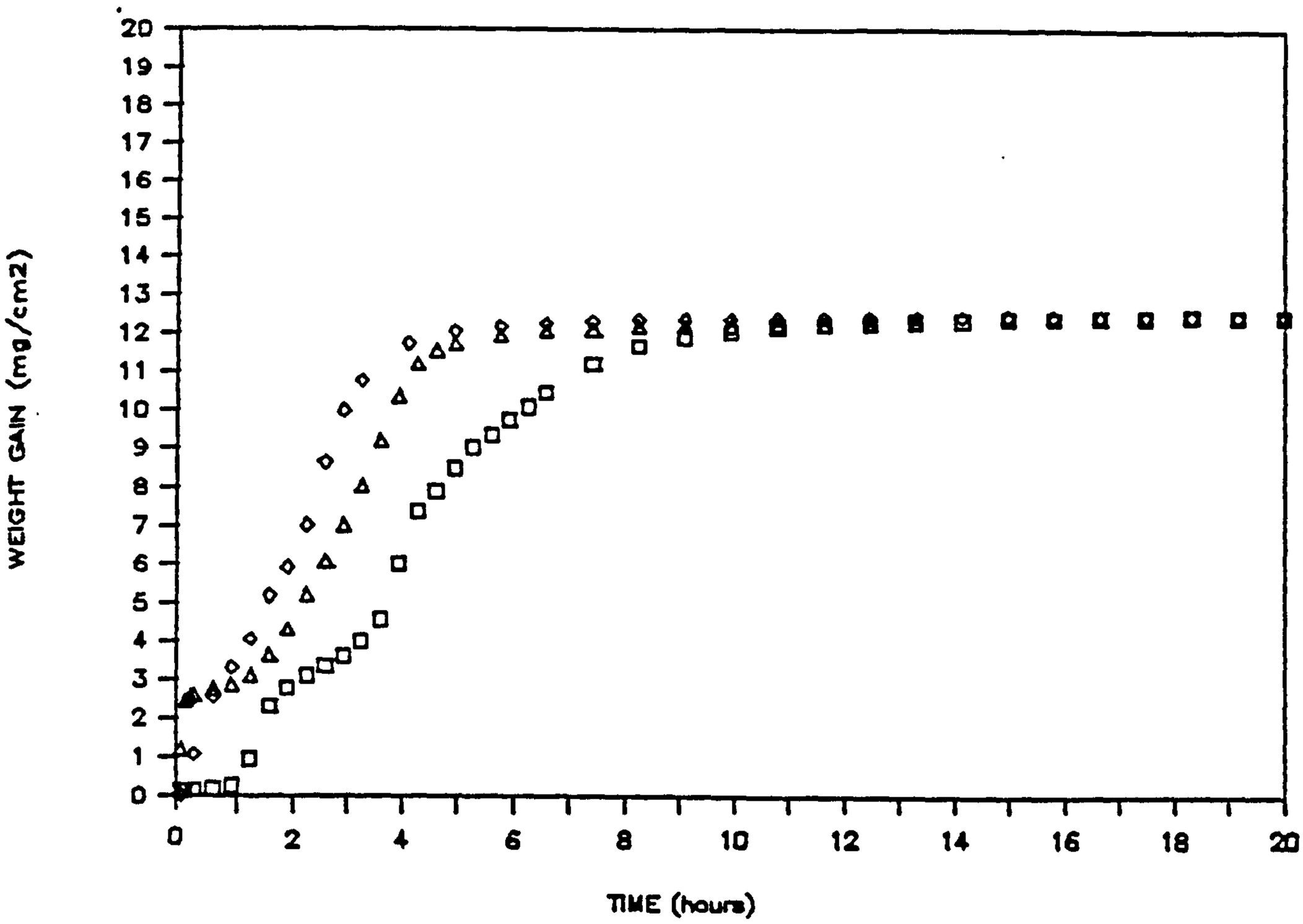

◇ *polished (1μm) surface*

△ *polished (600μm) surface*

□ *machined surface*

Figure 7.22 The influence of surface finish on the oxidation of 5182 in gettered argon at 750°C.

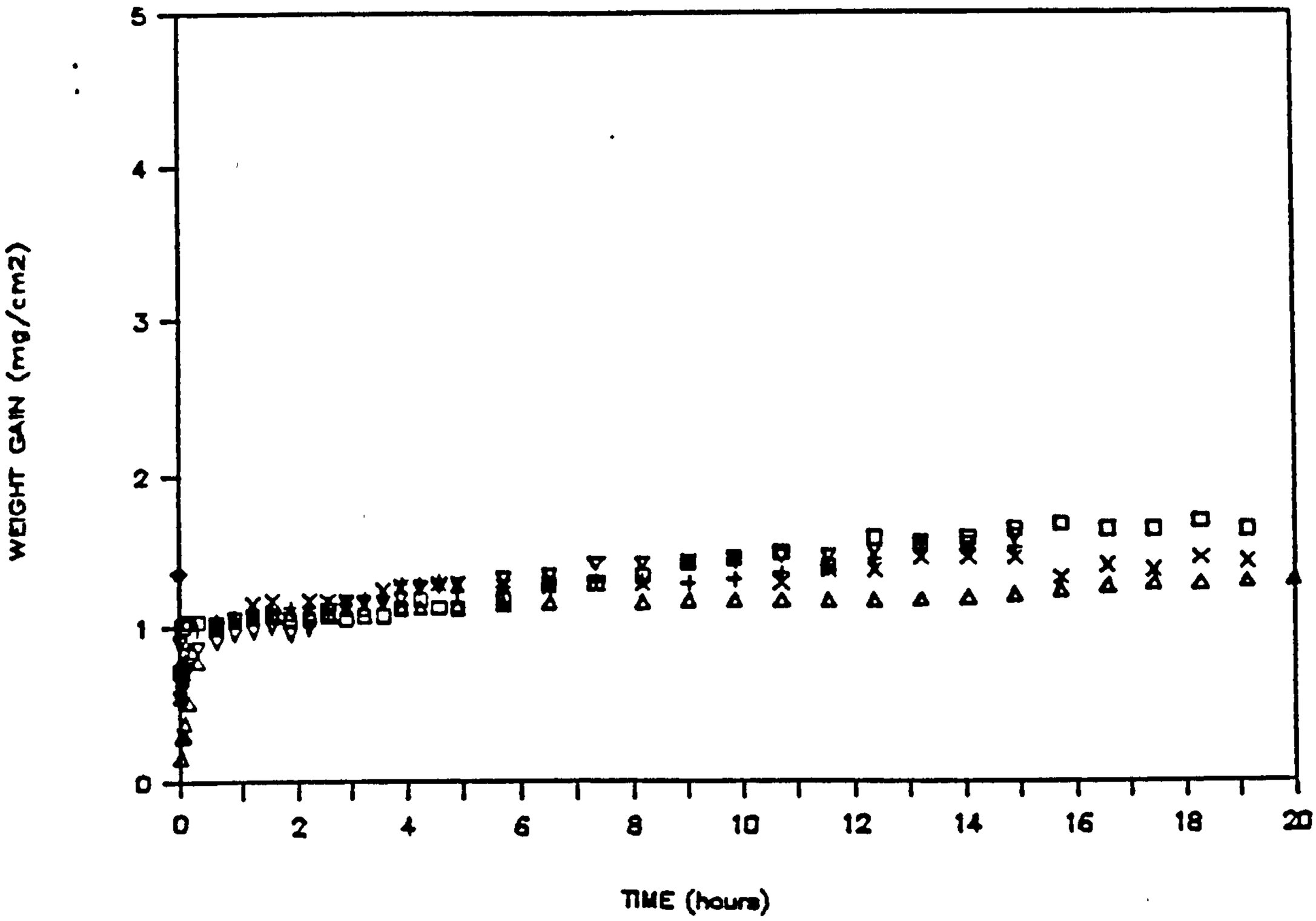

+, ∇, Δ *static humid air*

□, × *flowing humid air*

Figure 7.23 Oxidation of machined and polished 5182 in humid air at 750°C.

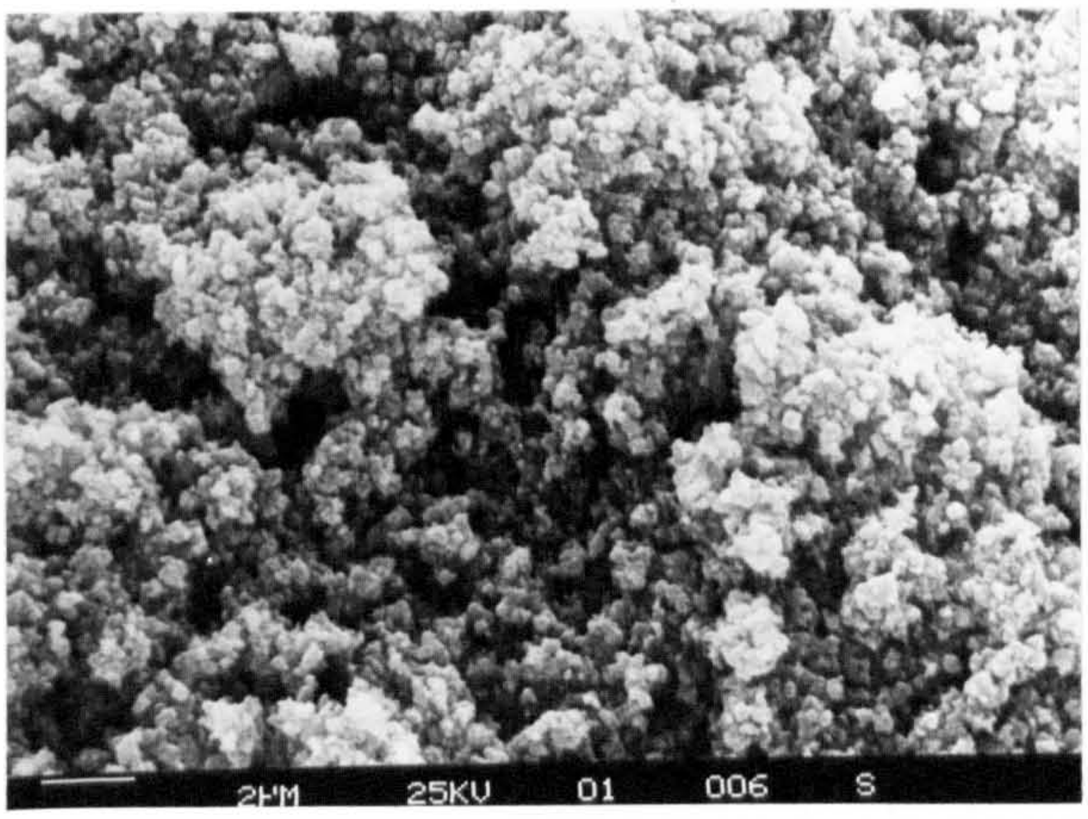

(a)

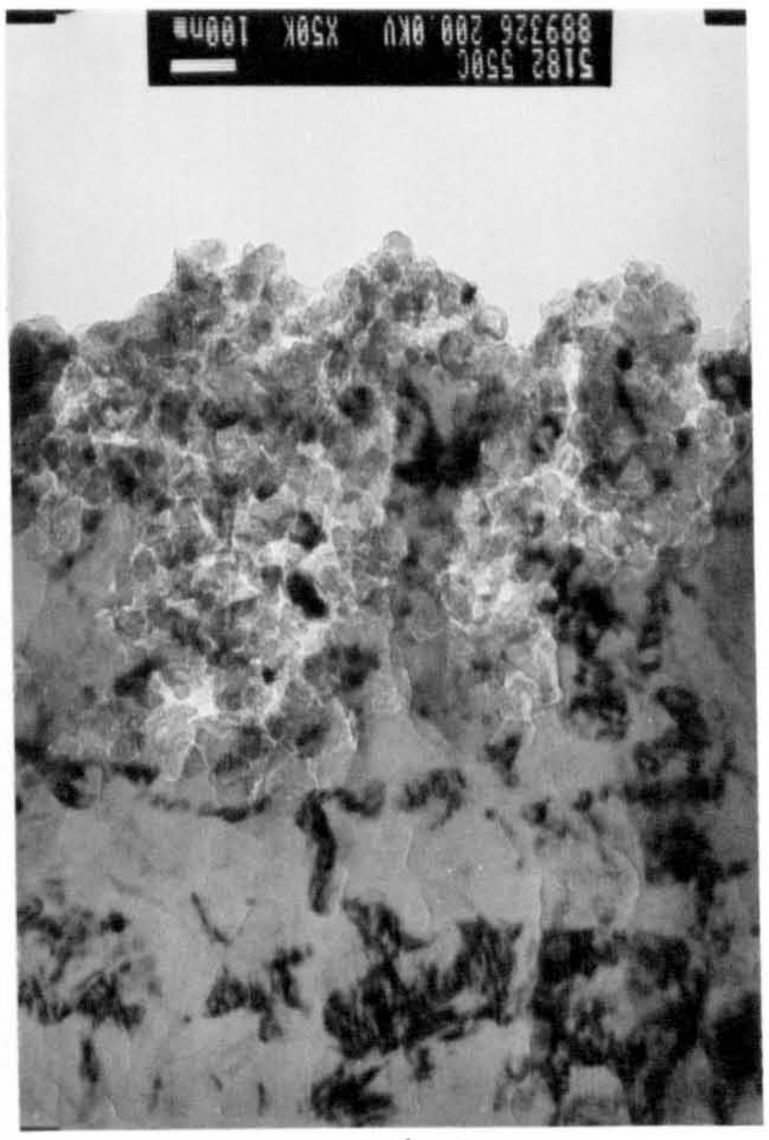

section of (a)

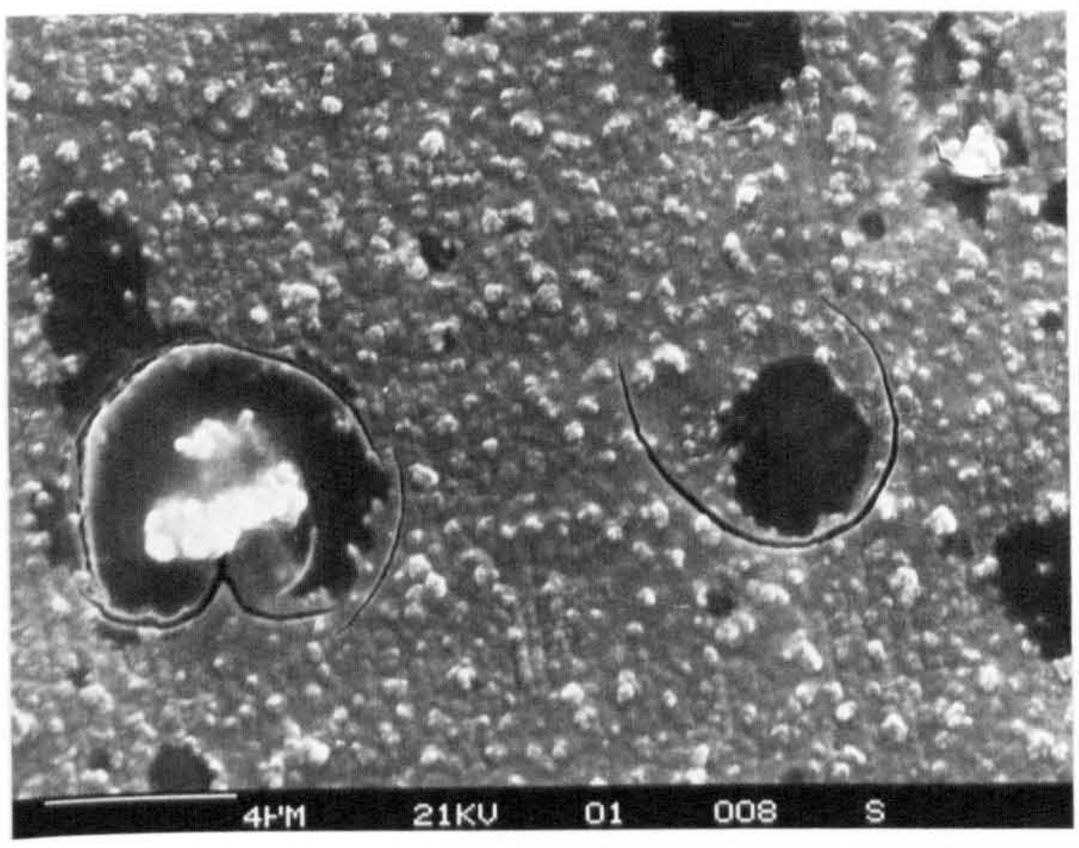

(b)

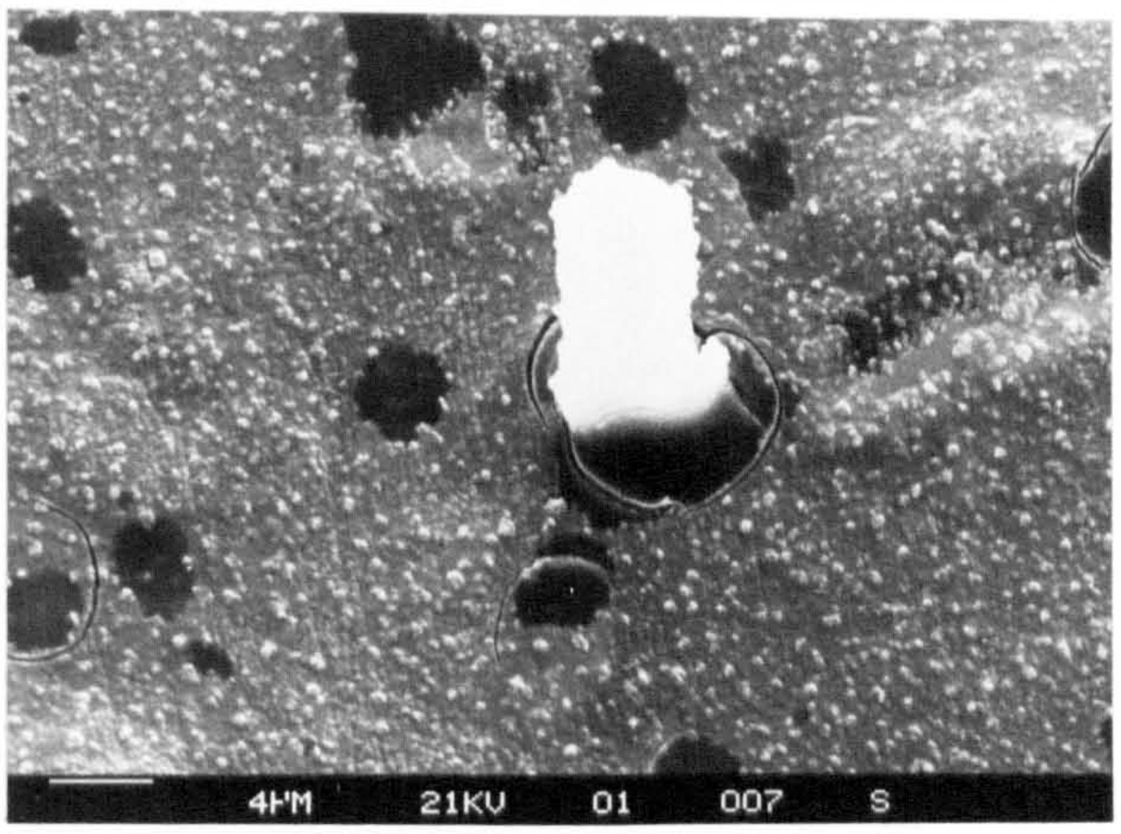

(c)

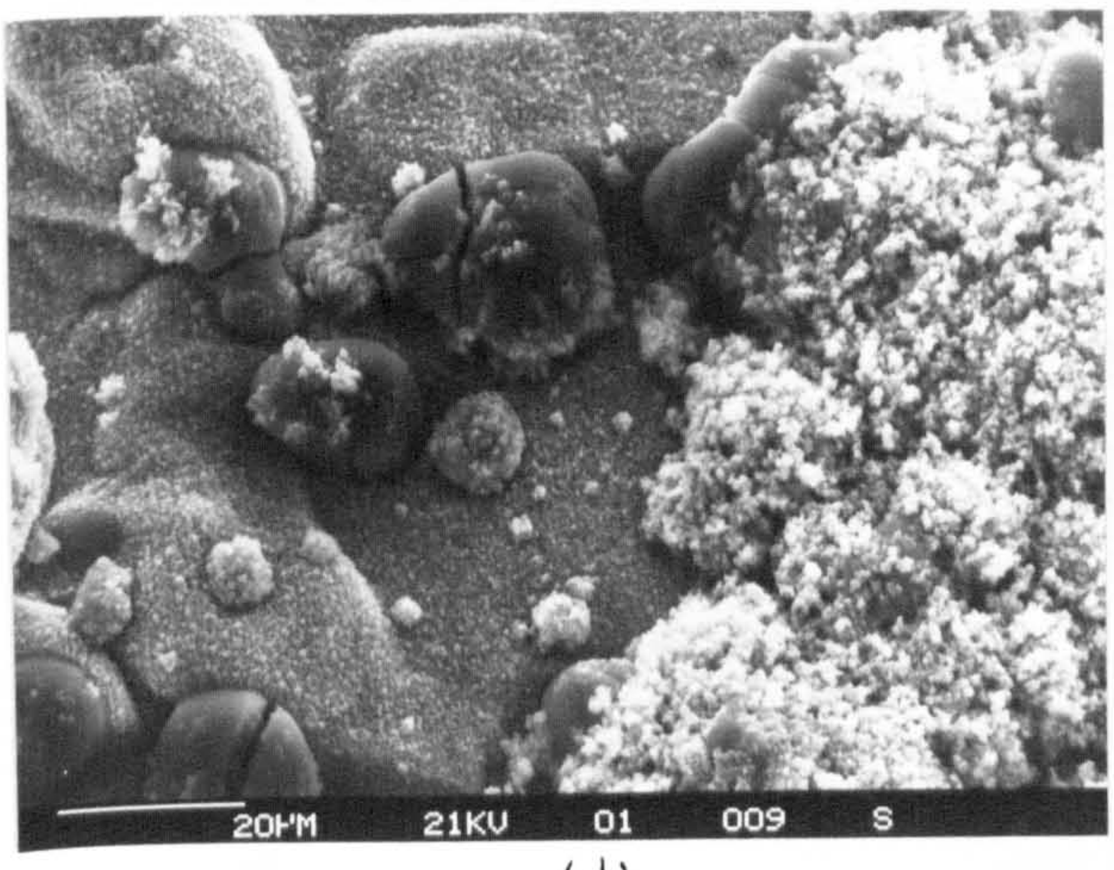

(d)

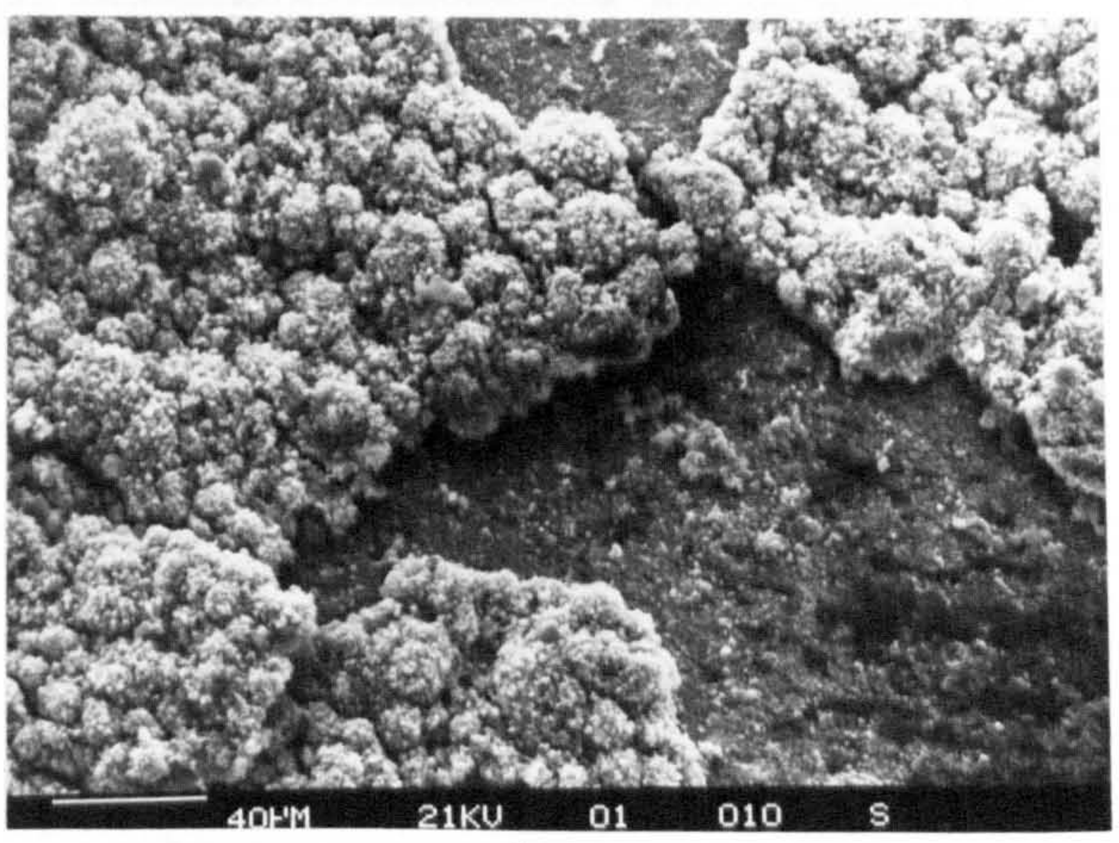

(e)

Figure 7.24 Vertical section through magnesia of 5182 oxidised at 550°C in gettered argon. (b-e) shows the development of growths on (a) oxide surface

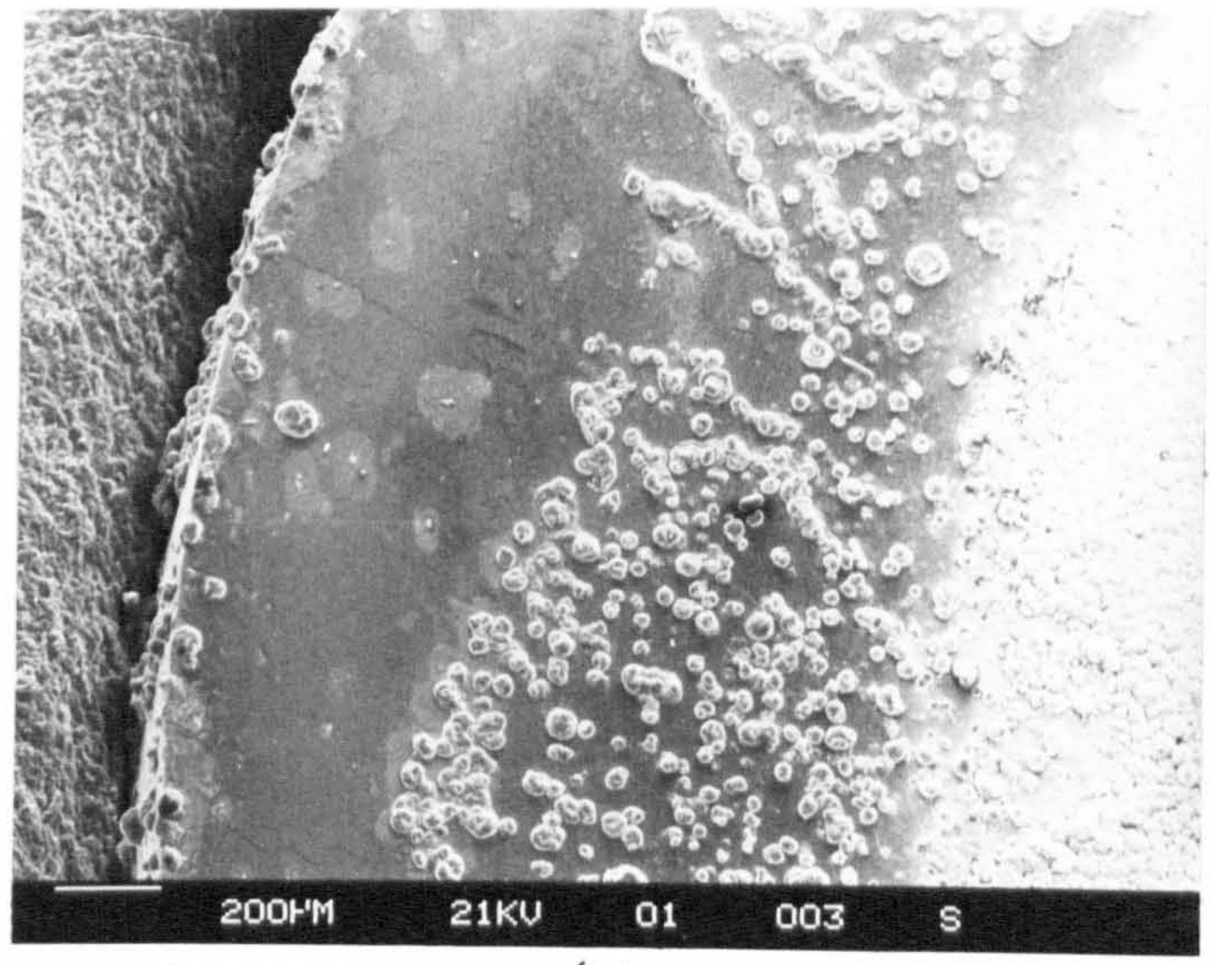

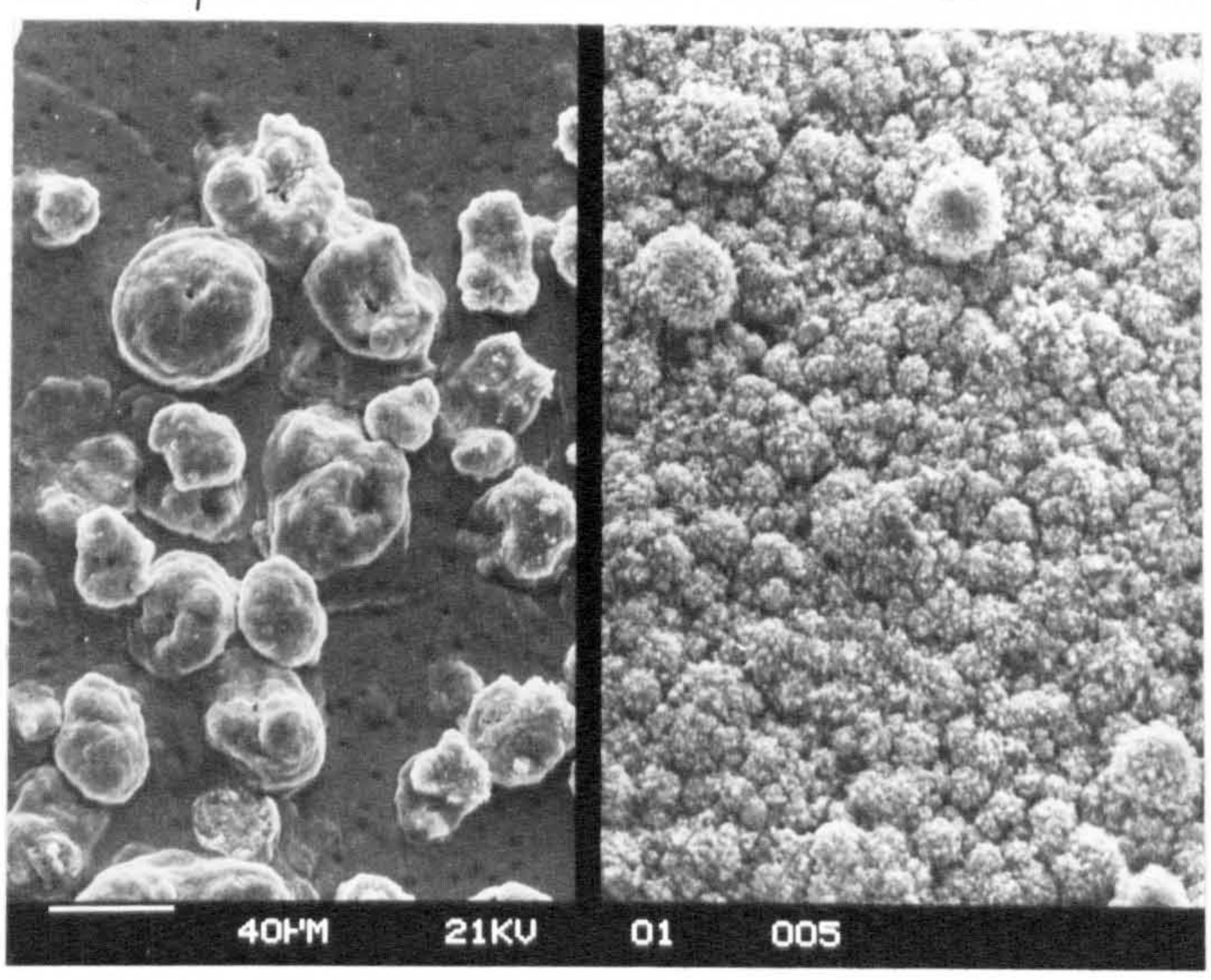

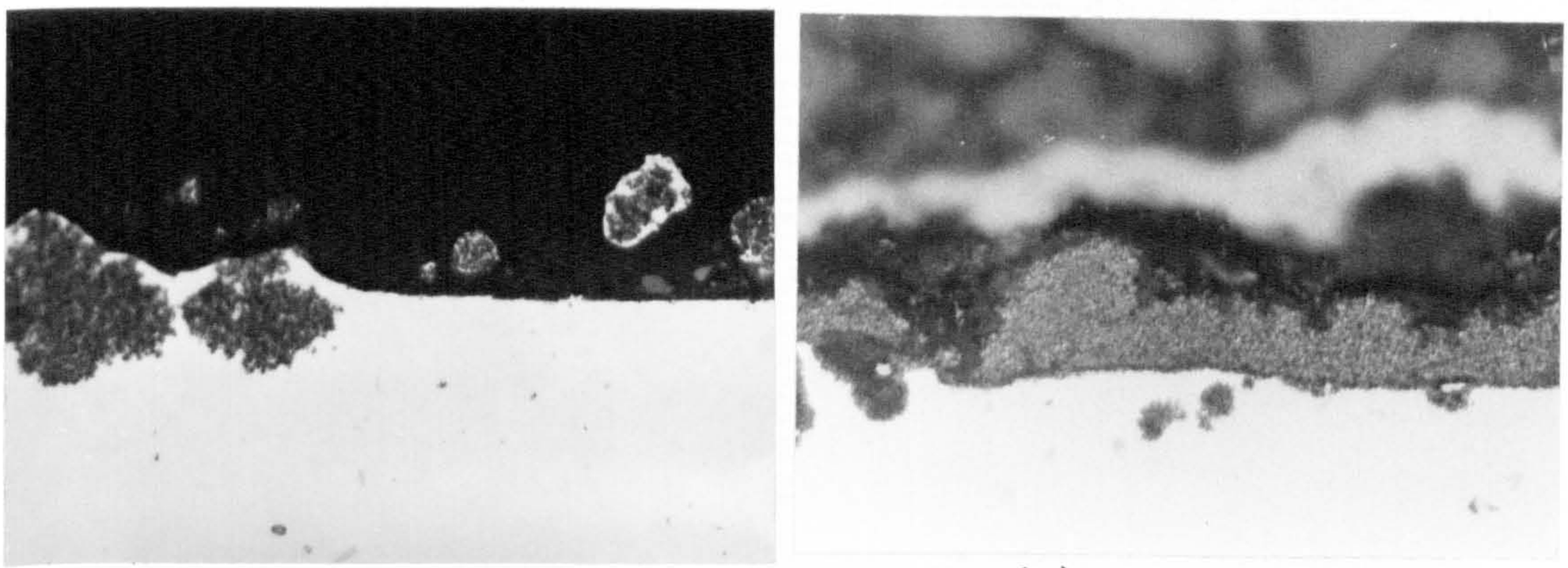

Figure 7.25 (a) Section of the reverse surface of 5182 oxidised in gettered argon at 550°C showing increased growth at (c,e) the centre to (b,d) the outer edge

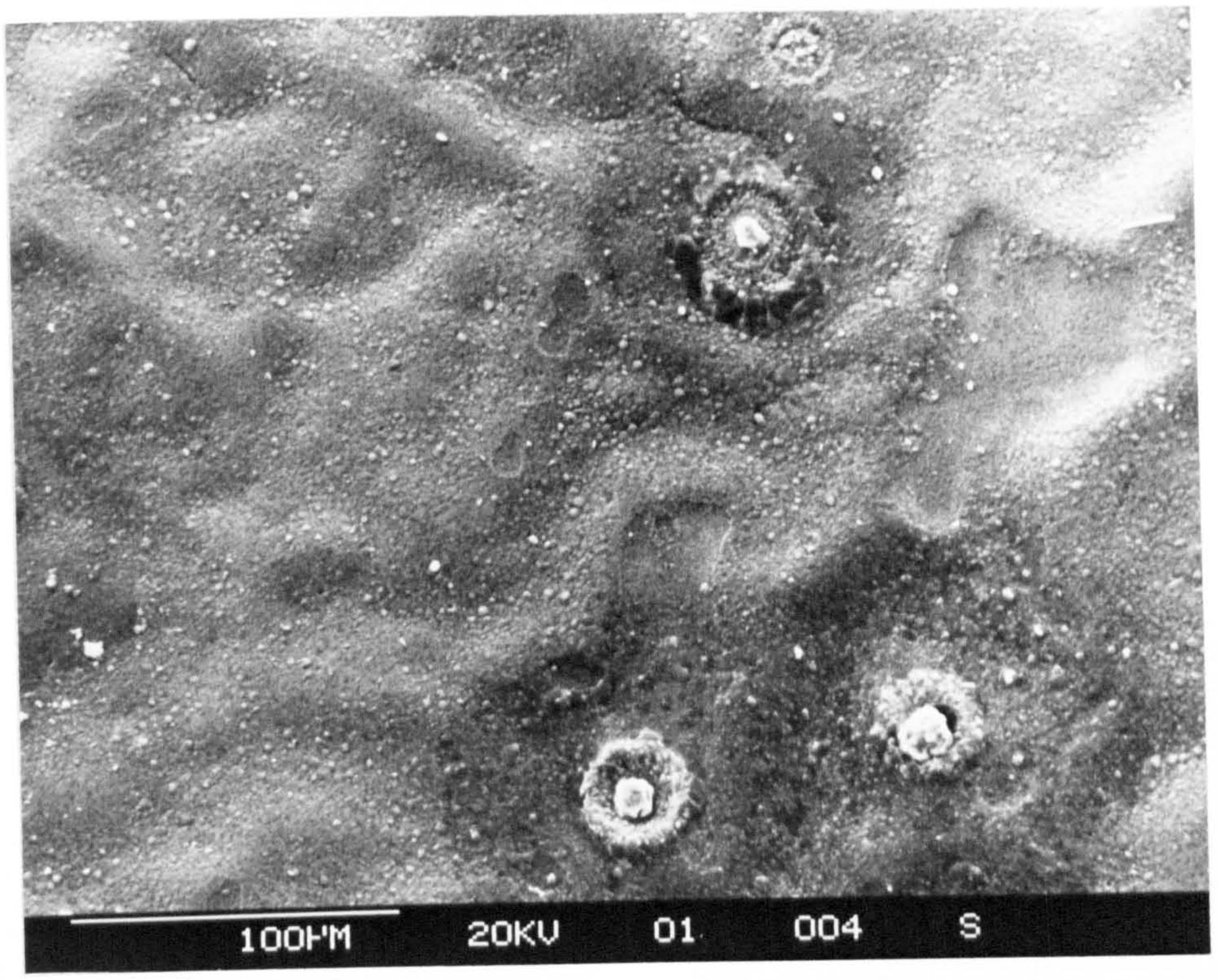

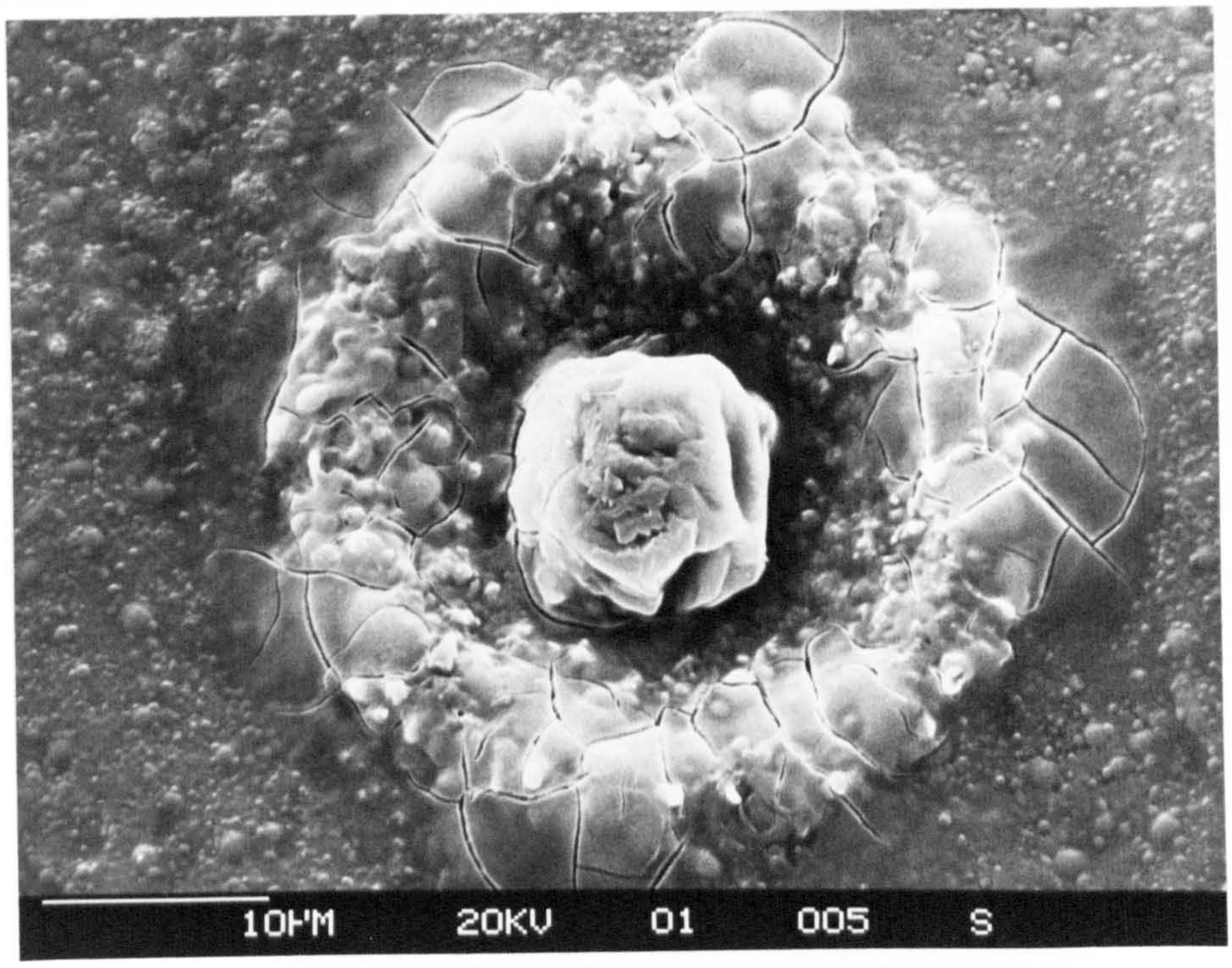

Figure 7.26 Oxide growths protruding through glass coat on a 5182 alloy after 15h oxidation at 550°C in gettered argon

(a)

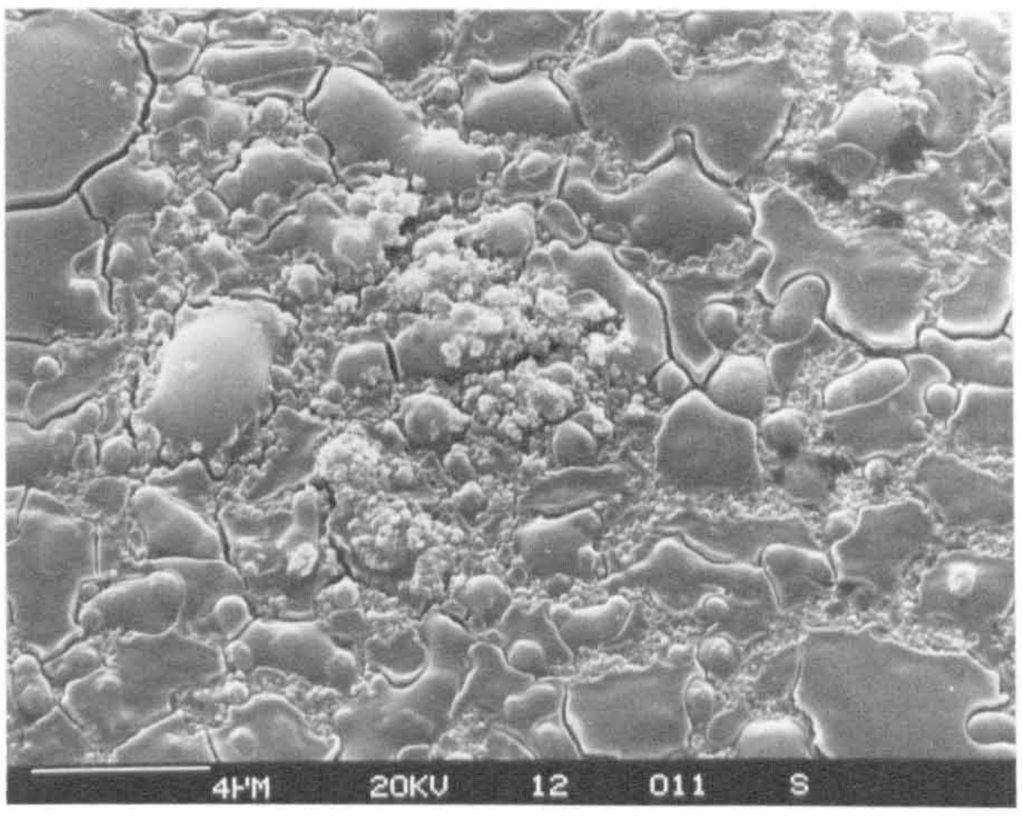

(b)

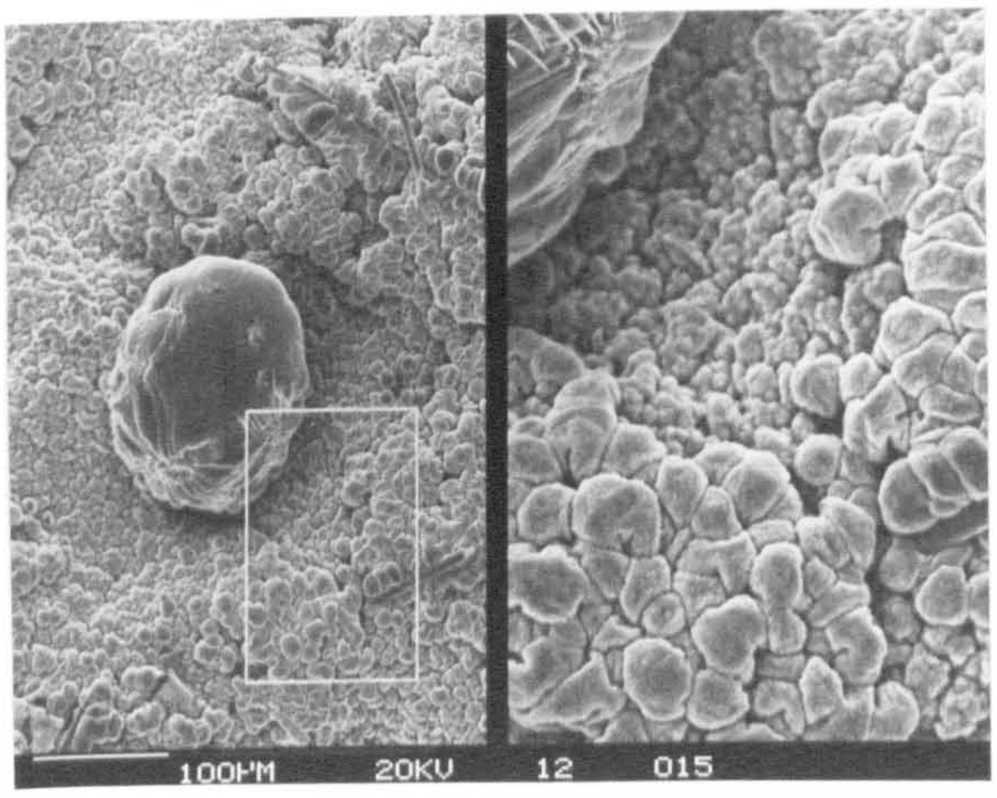

(d)

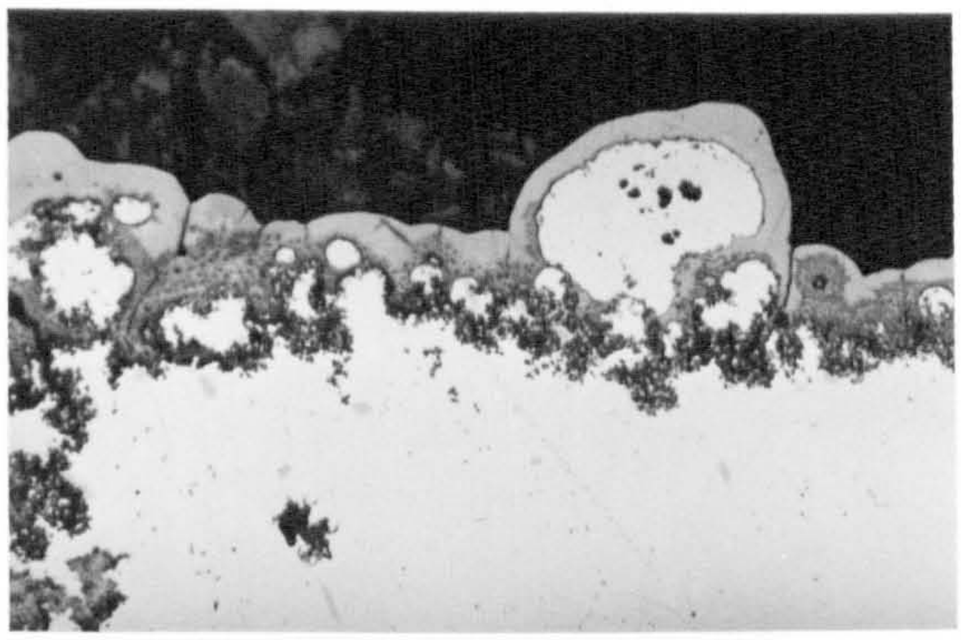

20μm

(e)

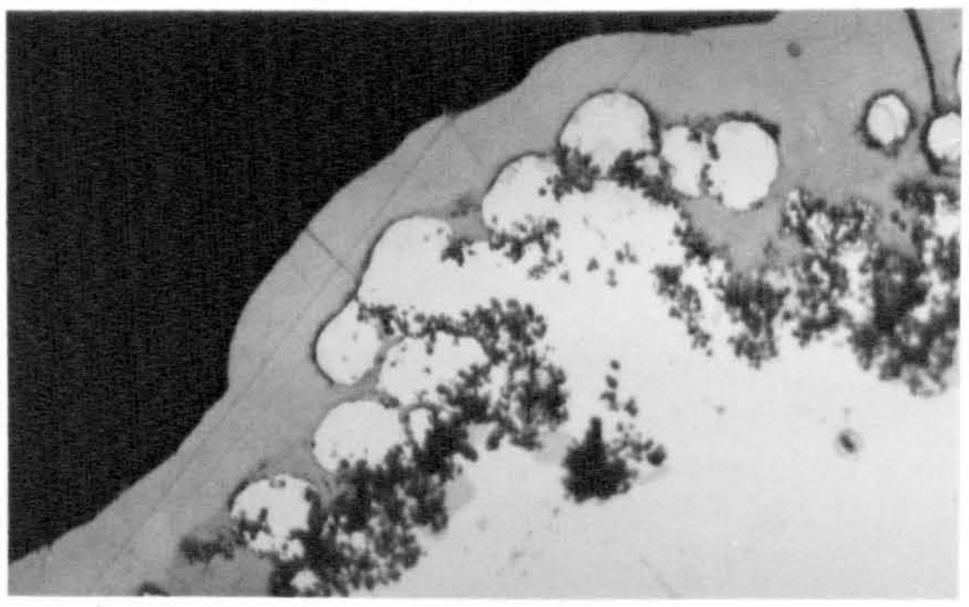

20μm

(f)

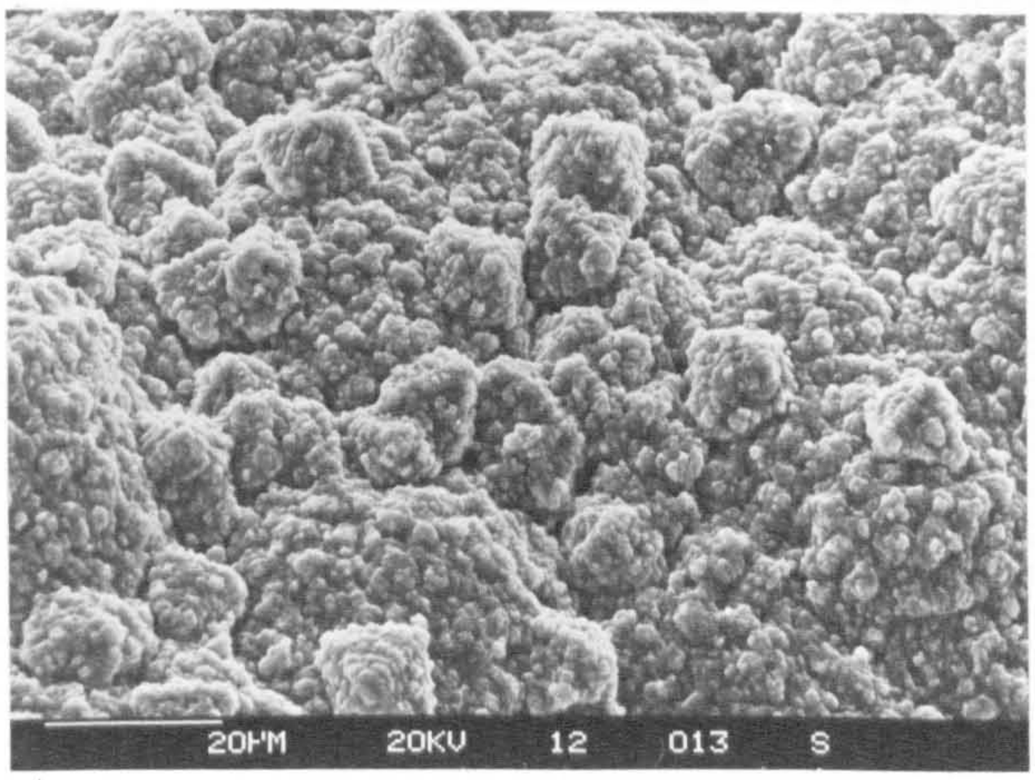

Figure 7.27 Micrographs of oxide surface after 5182 oxidation in gettered argon at (a) 450°C (b) 650°C and (d,e) in section (f) 850°C

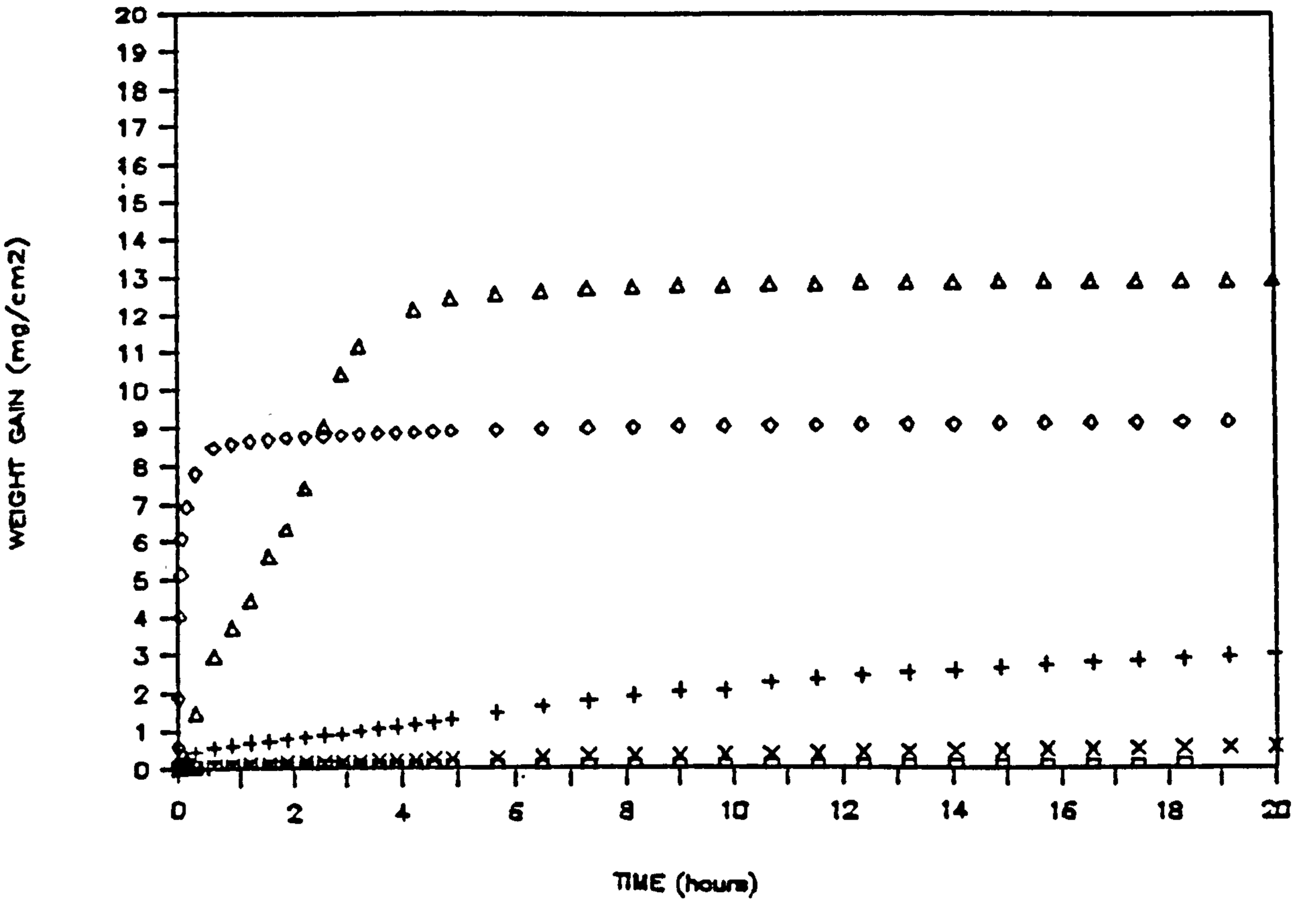

□ *450°C*

× *550°C*

\+ *650°C*

Δ *750°C*

◇ *850°C*

Figure 7.28 The effect of temperature from 450-850°C on the oxidation of polished 5182 alloy in gettered argon.

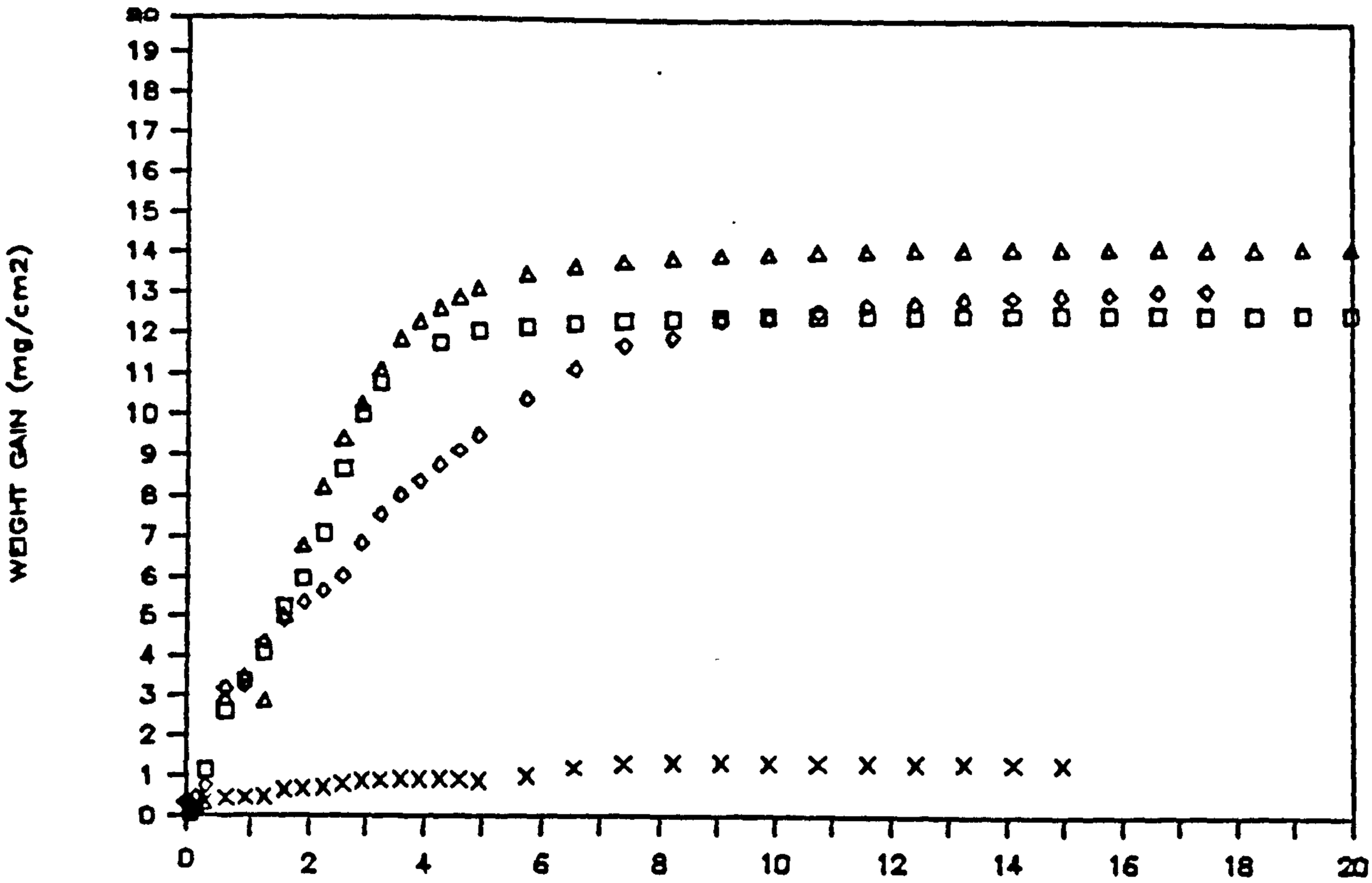

□ *with no preconditioning*

Δ , ◇ *after 5h preconditioning*

× *after 15h preconditioning*

Figure 7.29 Effect of preconditioning in humid air at 550°C over 0-15h on the subsequent oxidation of 5182 in gettered argon at 750°C.

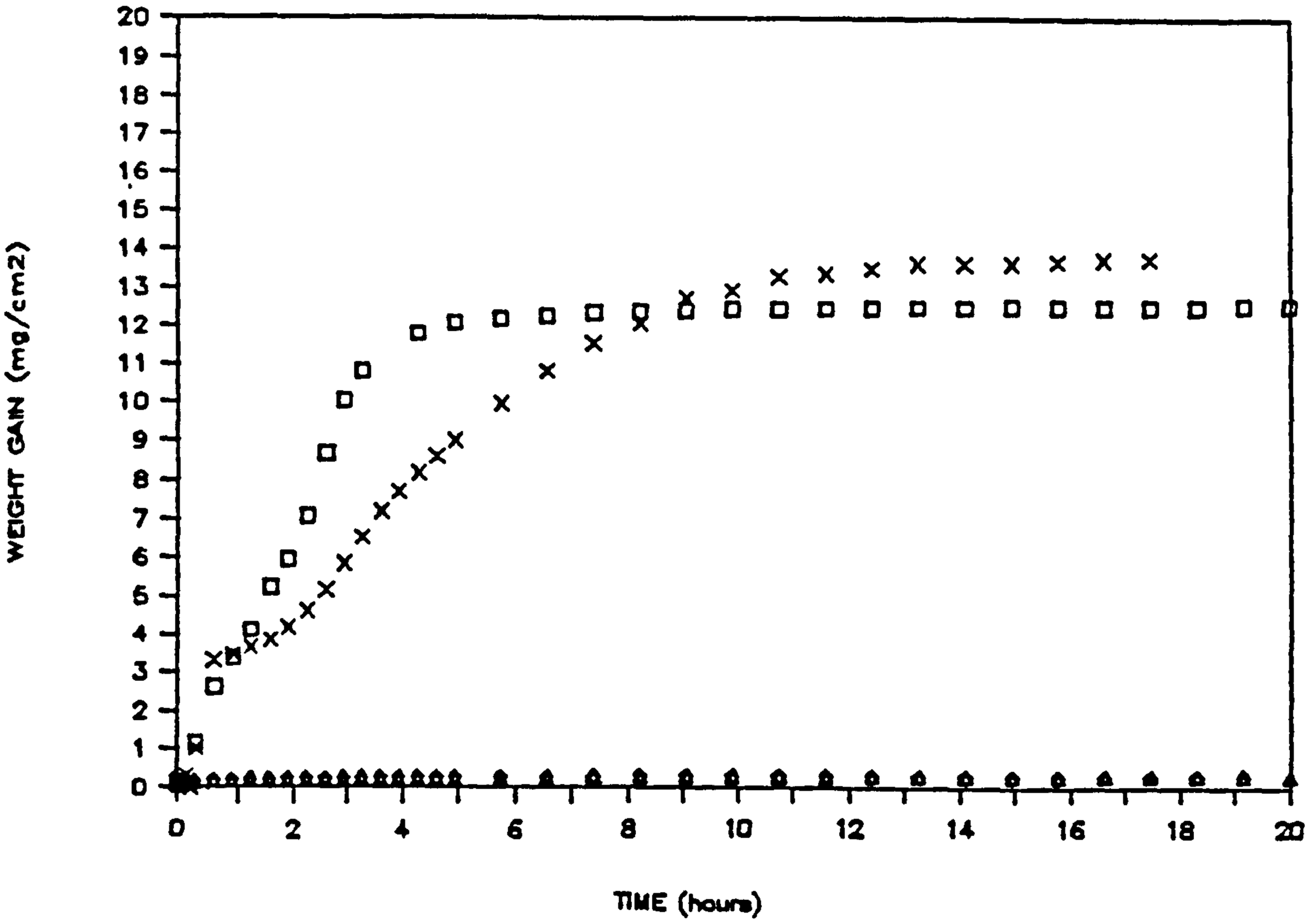

□ *with no preconditioning*

◇ *after 5h preconditioning*

△ *after 15h preconditioning*

× *after 15 preconditioning, but cooled prior to further exposure*

Figure 7.30 Effect of preconditioning in humid air at 750°C over 0-15h on the subsequent oxidtion of 5182 in gettered argon at 750°C.

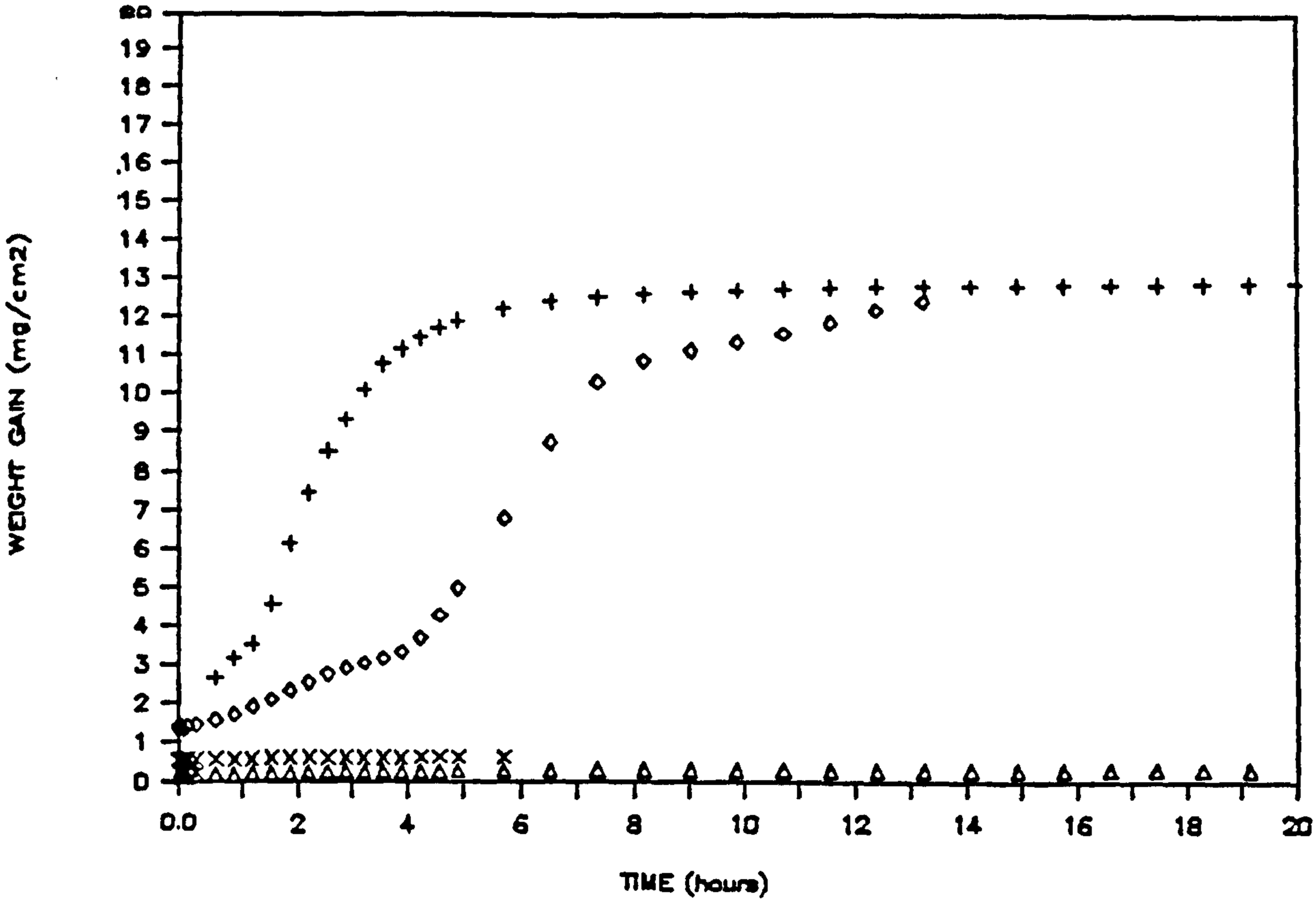

+ *550°C* Δ *750°C*

◇ *650°C* × *850°C*

Figure 7.31 Effect of preconditioning in humid air at 550-850°C for 5h on the subsequent oxidation of 5182 in gettered argon at 750°C.

(a)

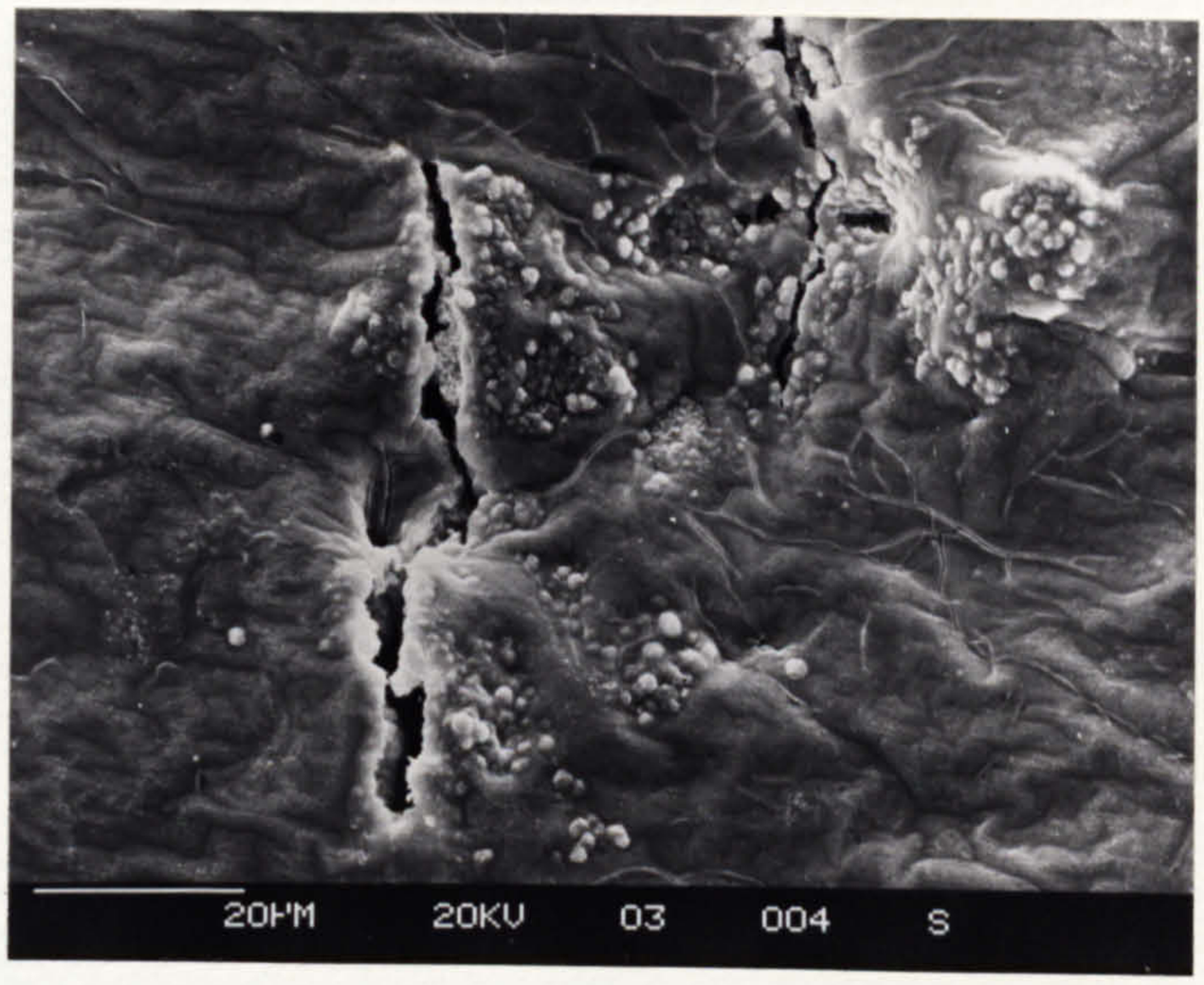

(b)

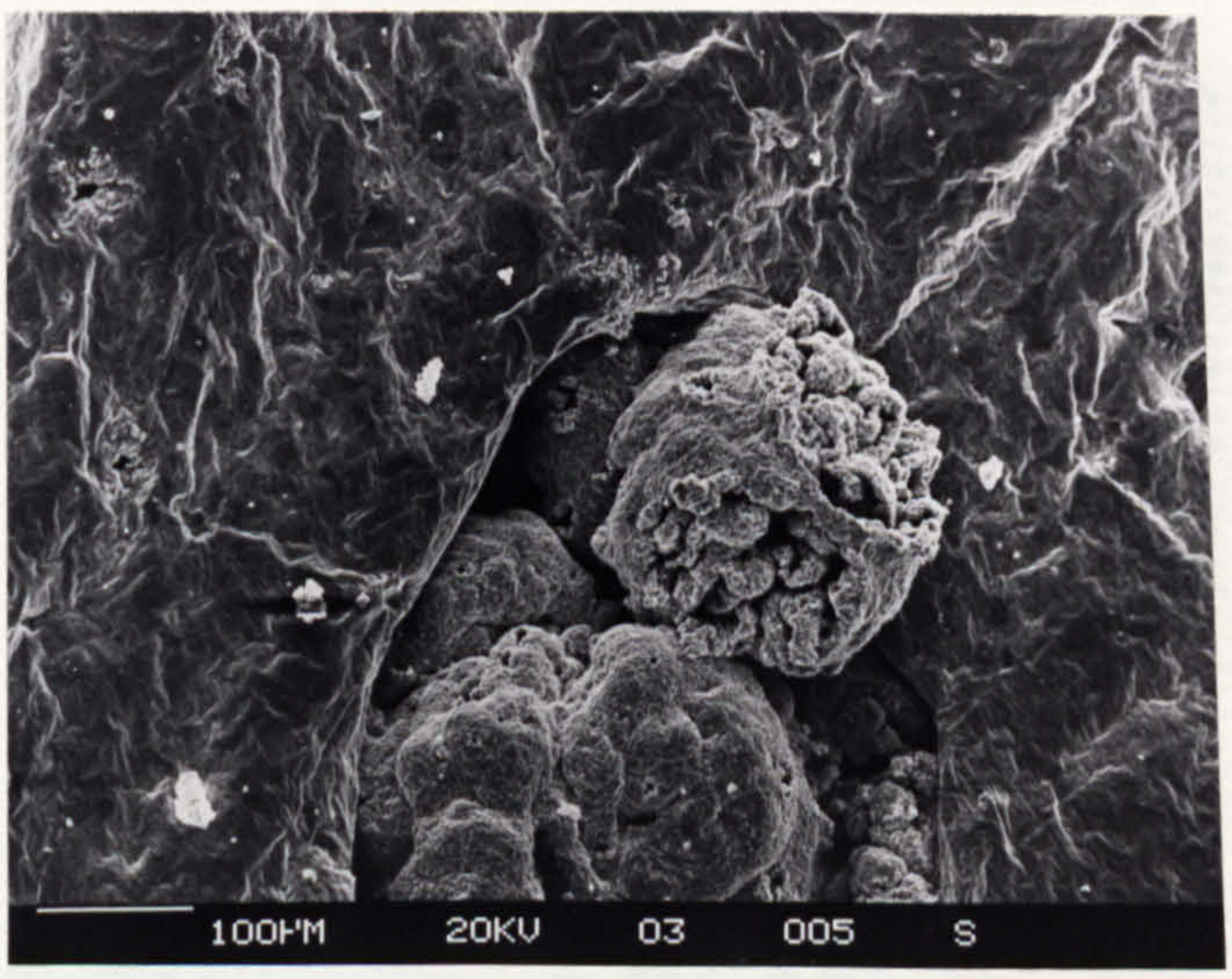

(c)

(d)

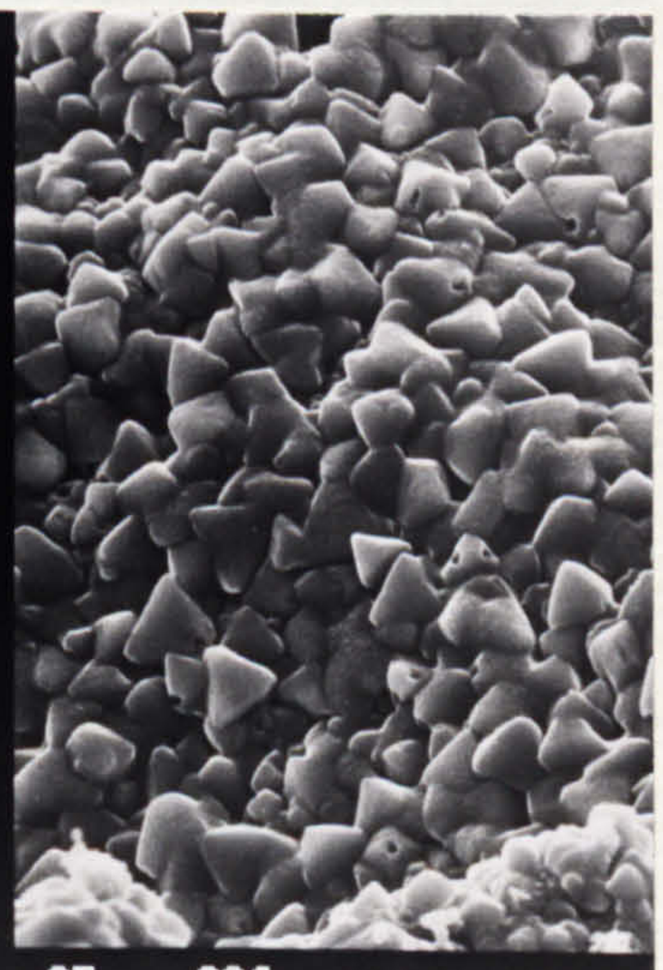

Figure 7.32 The oxide surface on 5182 after preconditioning in humid air for 15h showing cracking on exposure to gettered argon after (a) 2h and (b) 5h. With magnification (c) the surface and (d) the growth

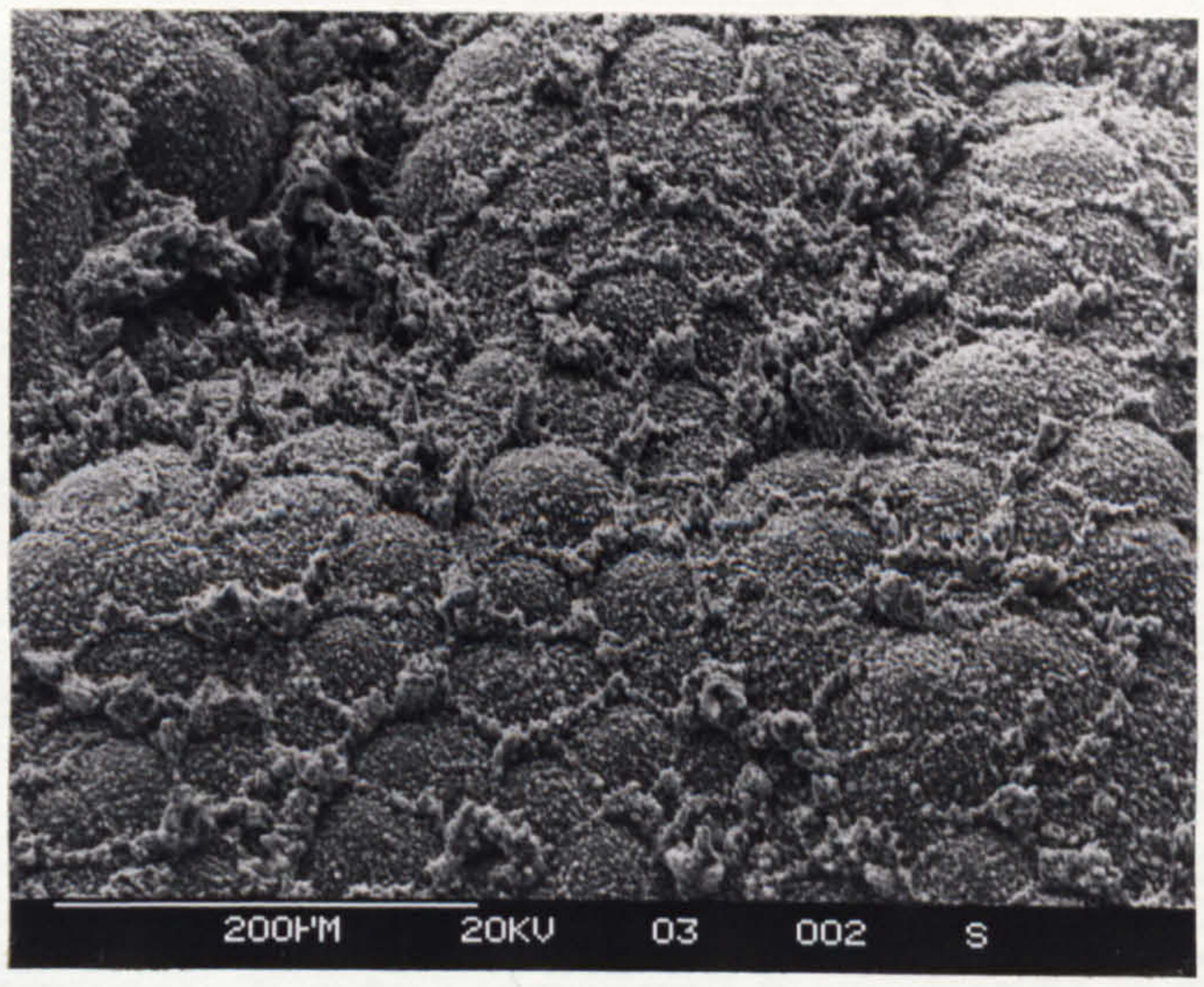

(a)

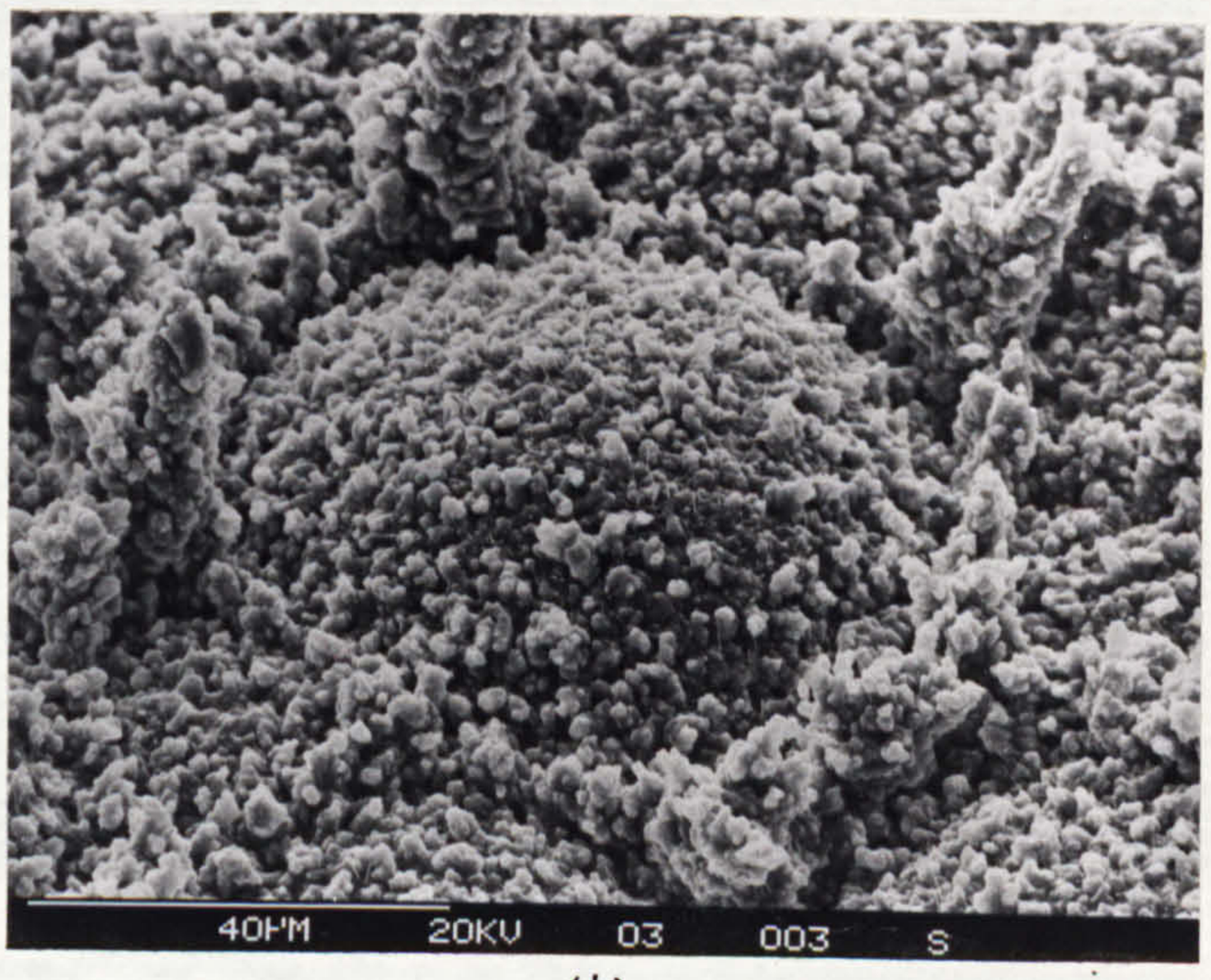

(b)

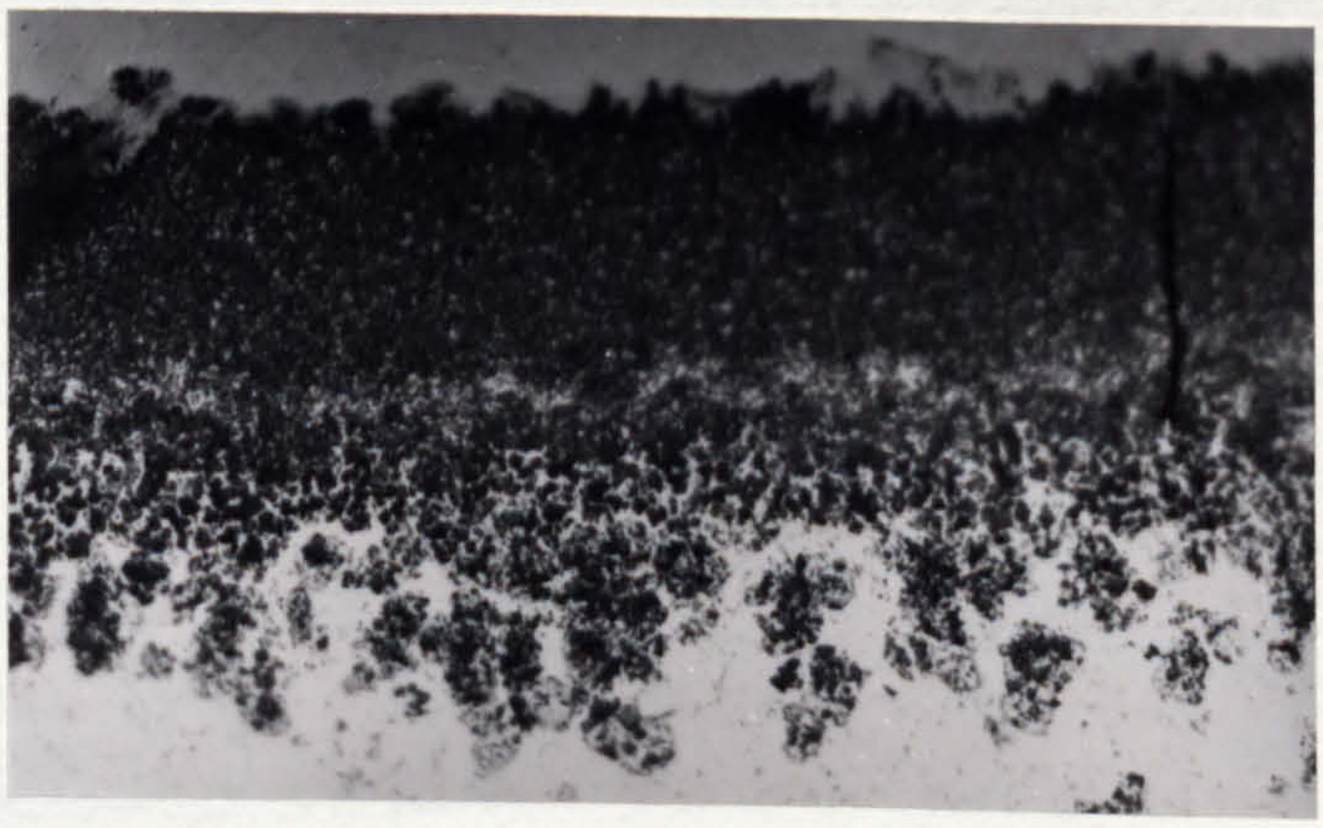

(c)

Figure 7.33 The (a,b) oxide surface and (c) oxide section of 5182 after 5h at 550°C and 15h at 750°C

(a)

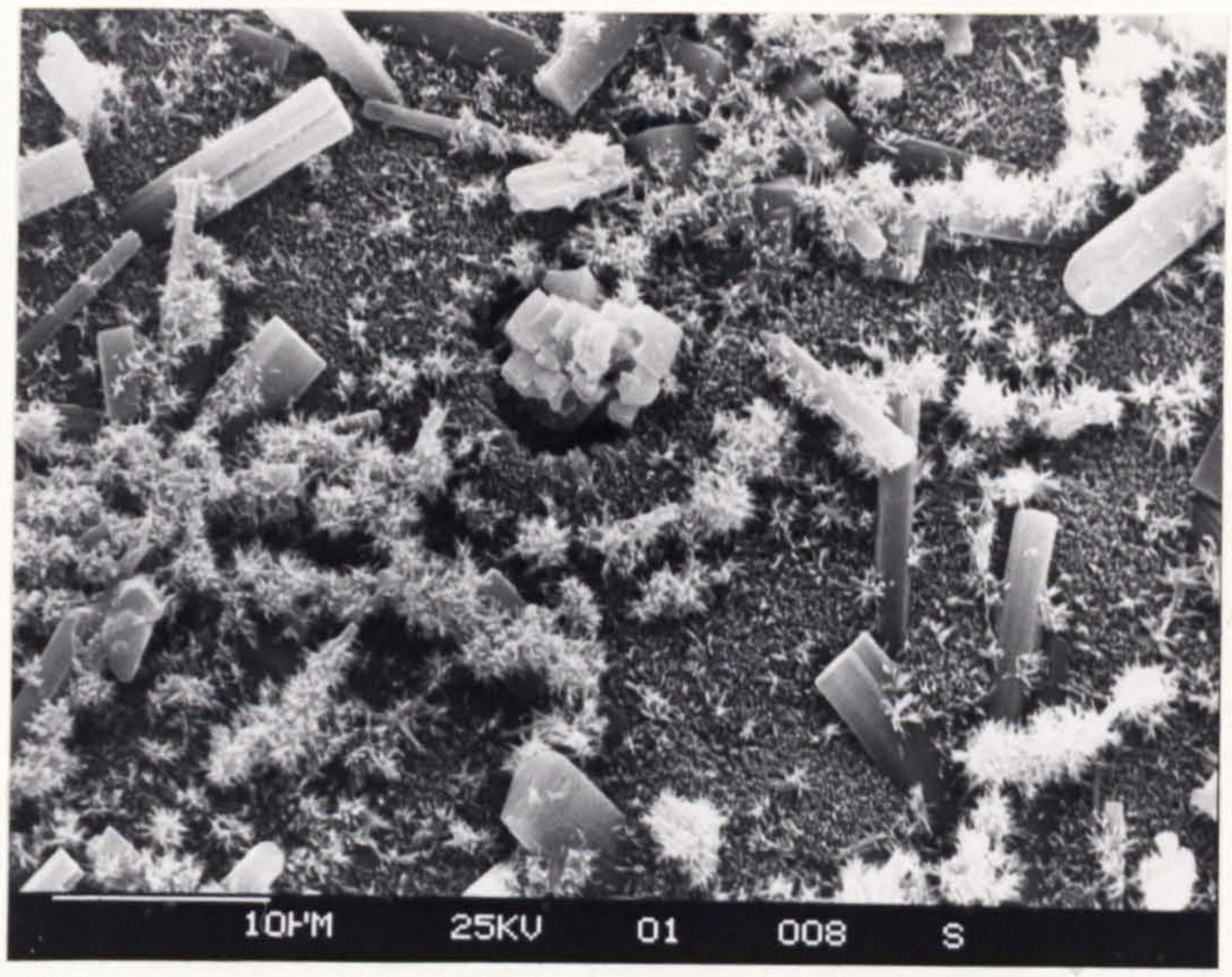

(b)

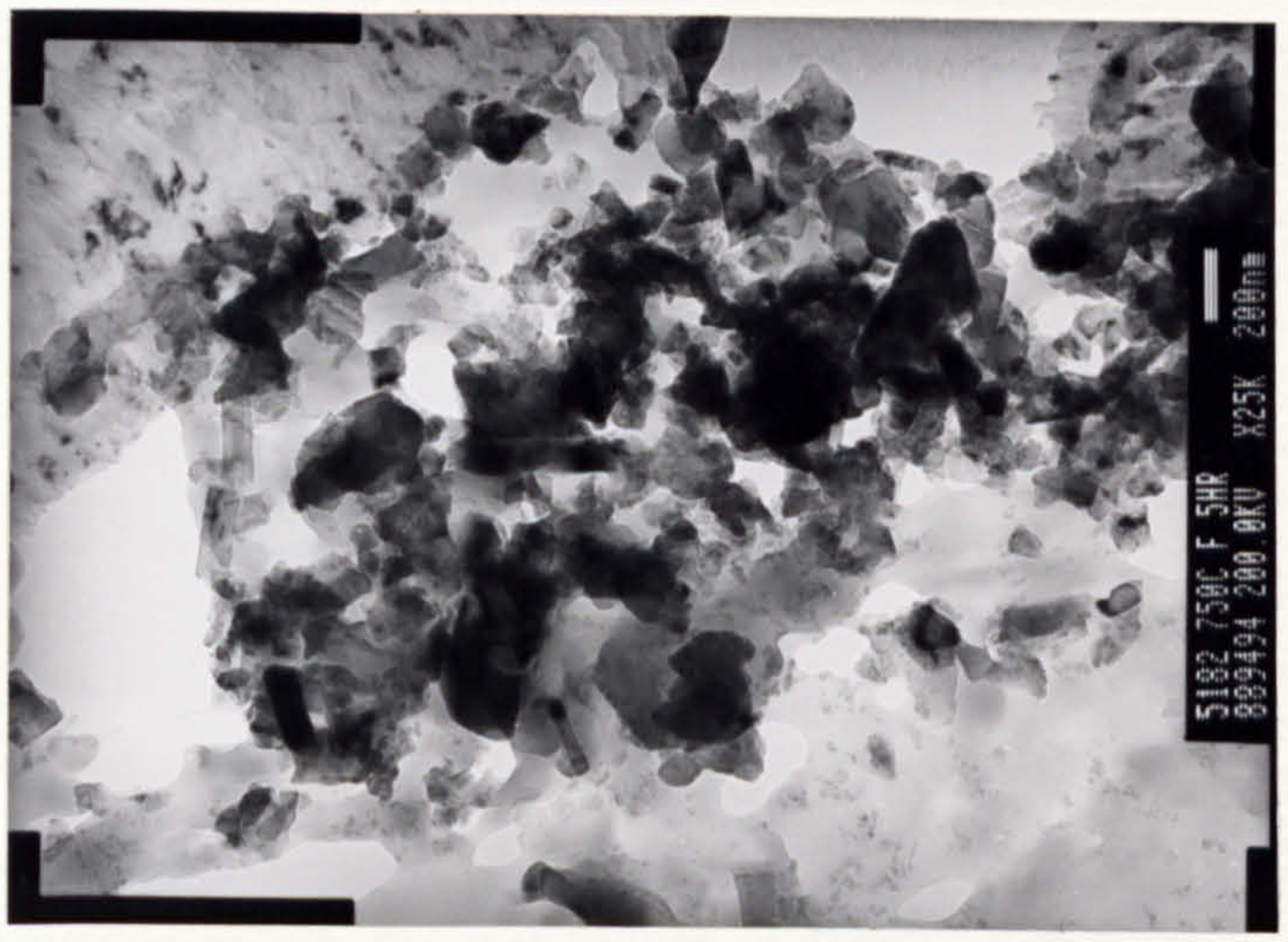

(d)

(c)

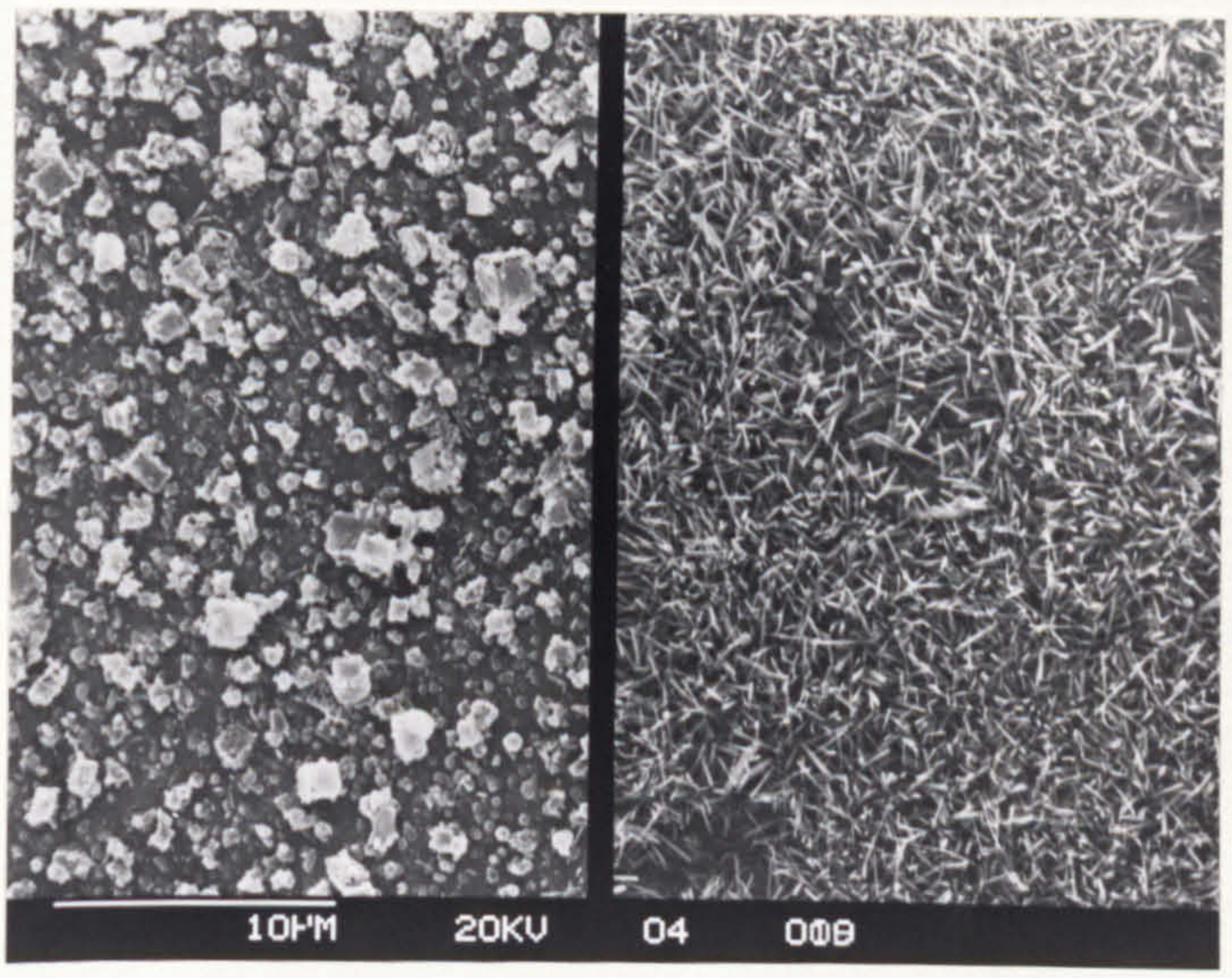

Figure 7.34 Oxide growth on 5182 in fluoride for 5h at (a) 550°C and (b) 750°C with (c) in section and (d) chloride (5h at 750°C)

(a)

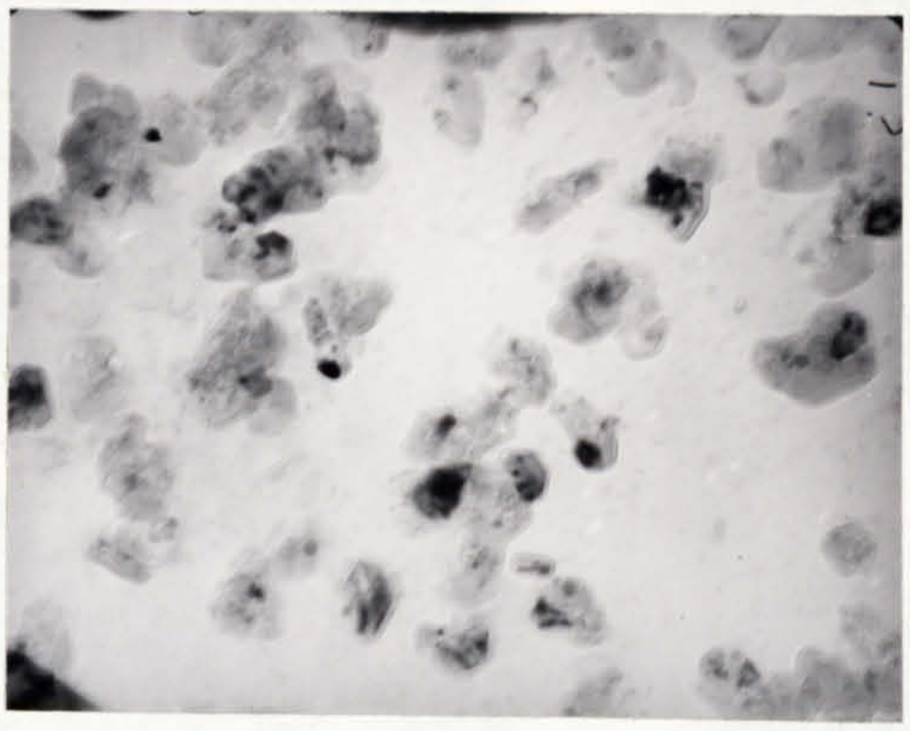

200nm

(b)

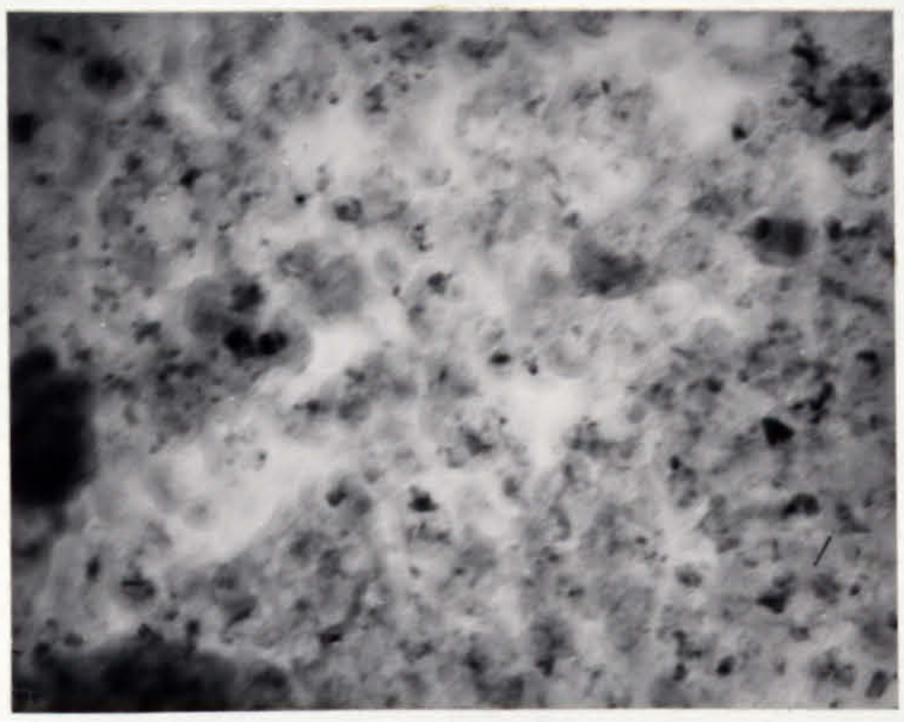

(c)

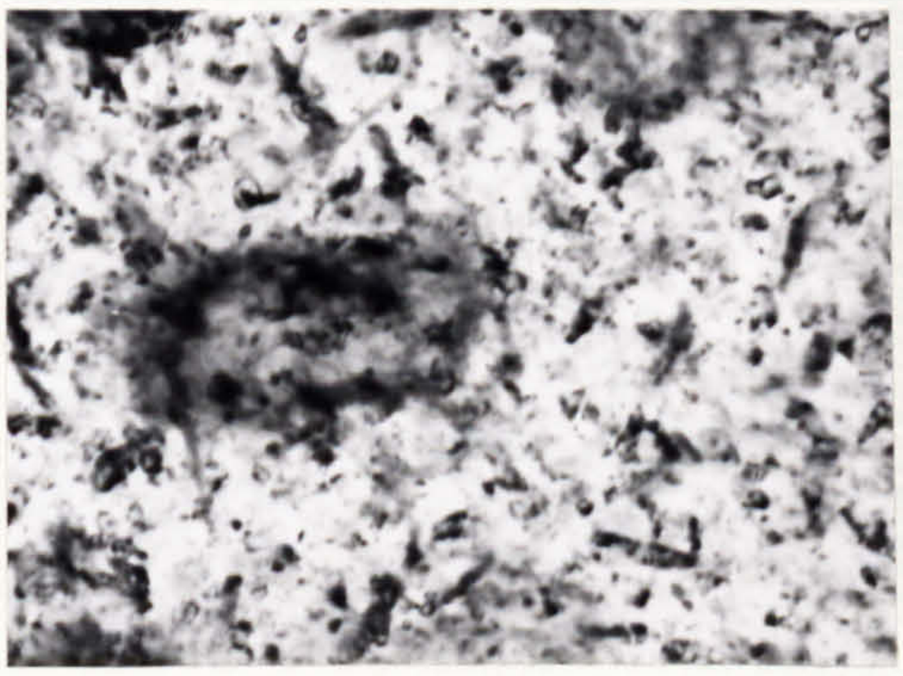

Figure 7.35 BeO crystallites on skimmed 5182 melts containing 50ppm Be after 5min oxidation in air at 750°C with (c) MgO and BeO surface film, after 15h in gettered argon

(b)

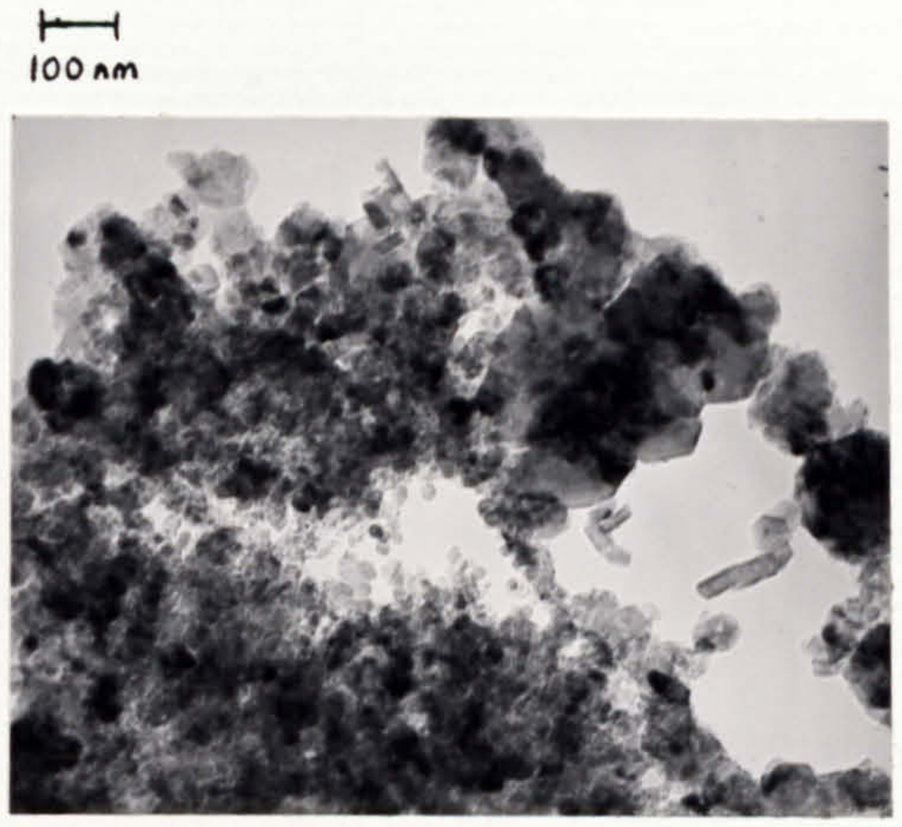

(a)

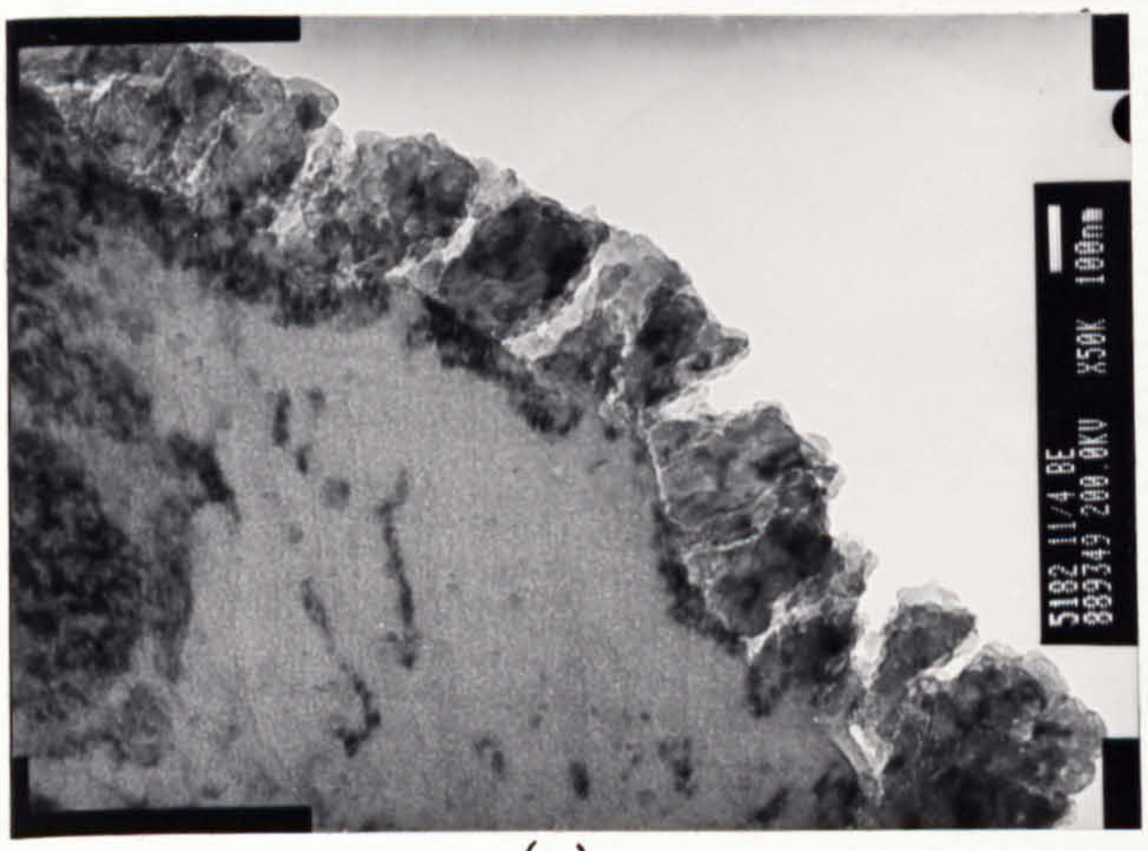

(c)

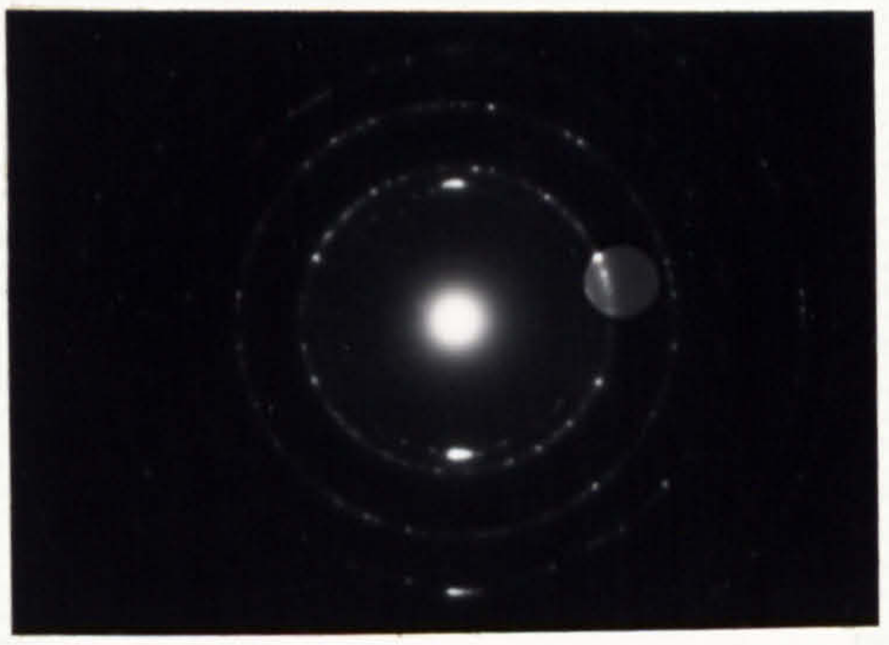

diffraction pattern of (a)

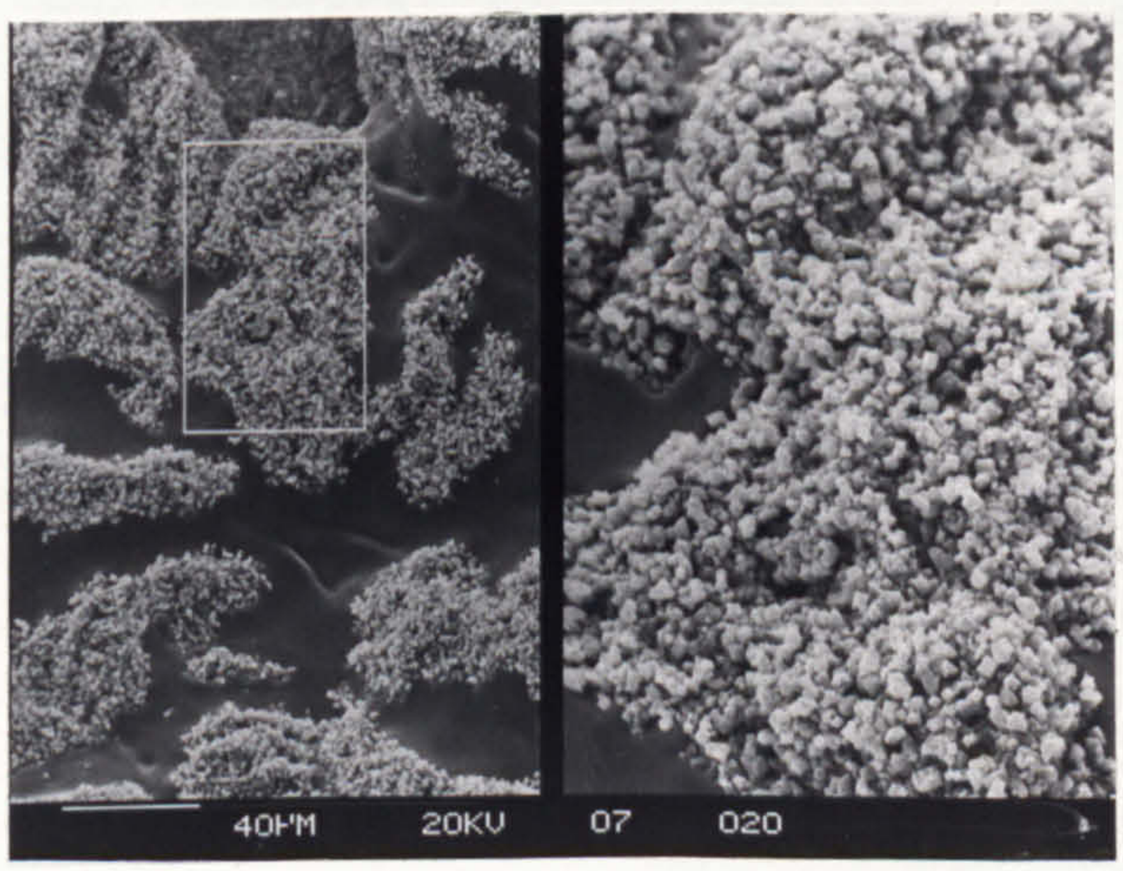

(d)

Figure 7.36 Mixture of MgO and BeO formed on 5182 alloy with 50ppm Be in gettered argon at 750°C (a) 5min and (b,c) in section after 15h (d) MgO crystals at base of a hole

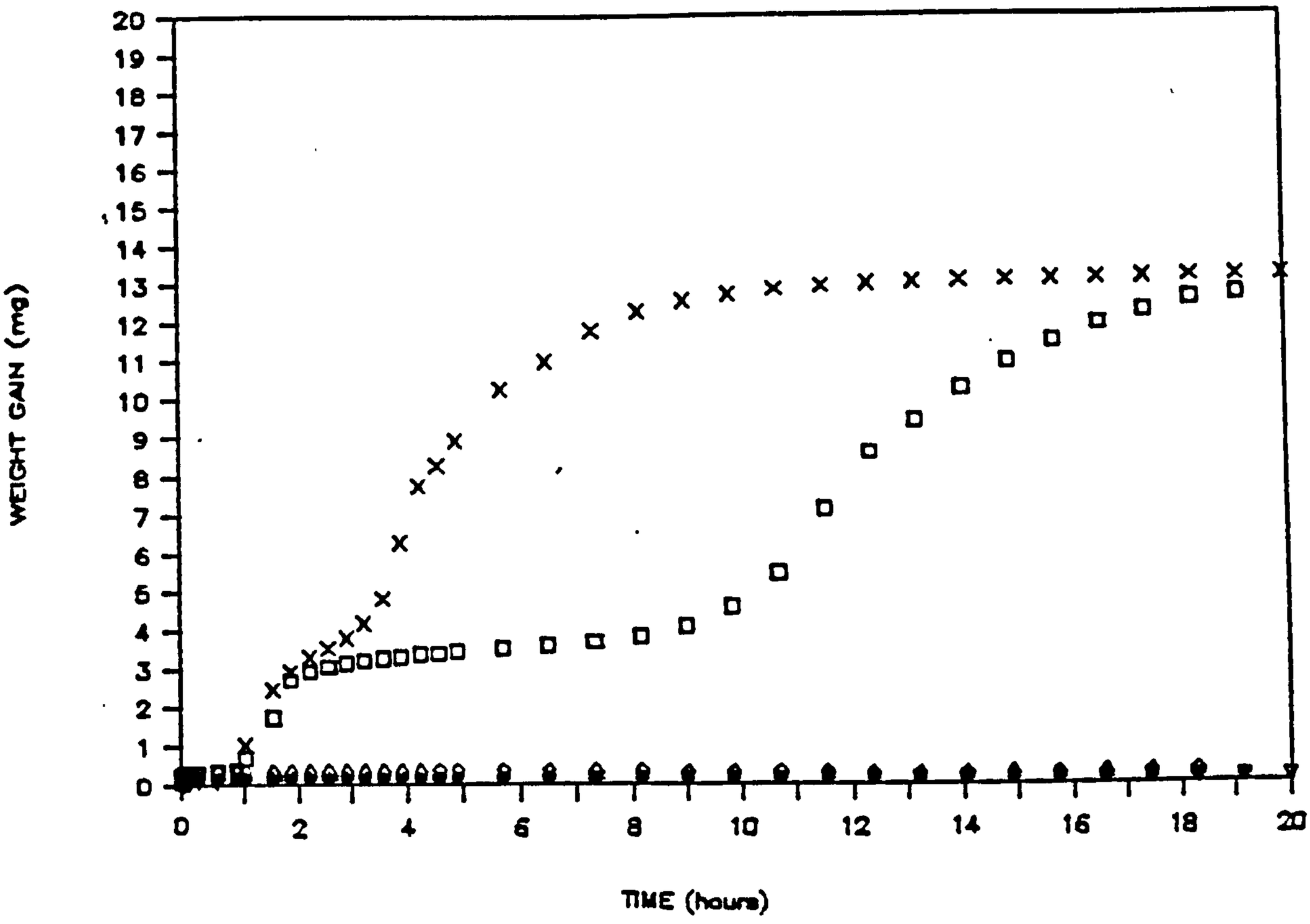

× *5182 with no Be in gettered argon*

□ *5182 with 10ppm Be in gettered argon*

\+ *5182 with 10ppm in humid argon*

▽ *5182 with 50ppm Be in gettered argon*

Figure 7.37 Oxidation rates of 5182 GR alloy with 10ppm and 50ppm beryllium additions at 750°C in air and argon.

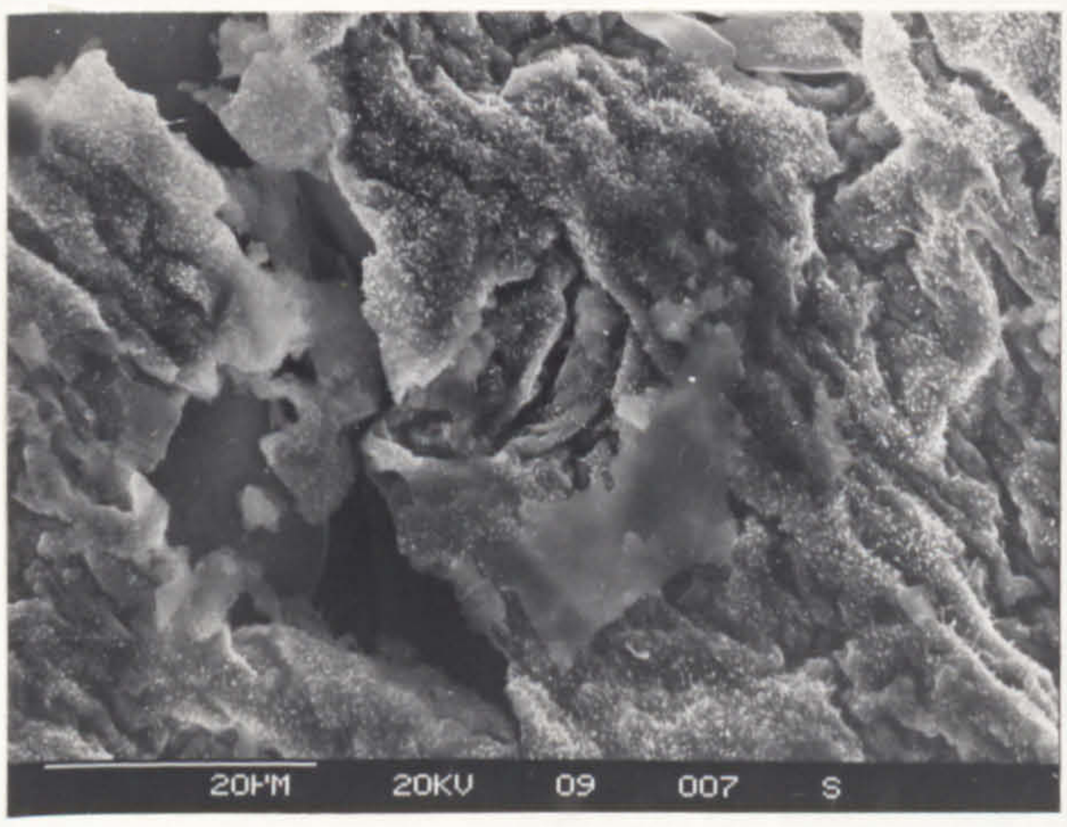

(a)

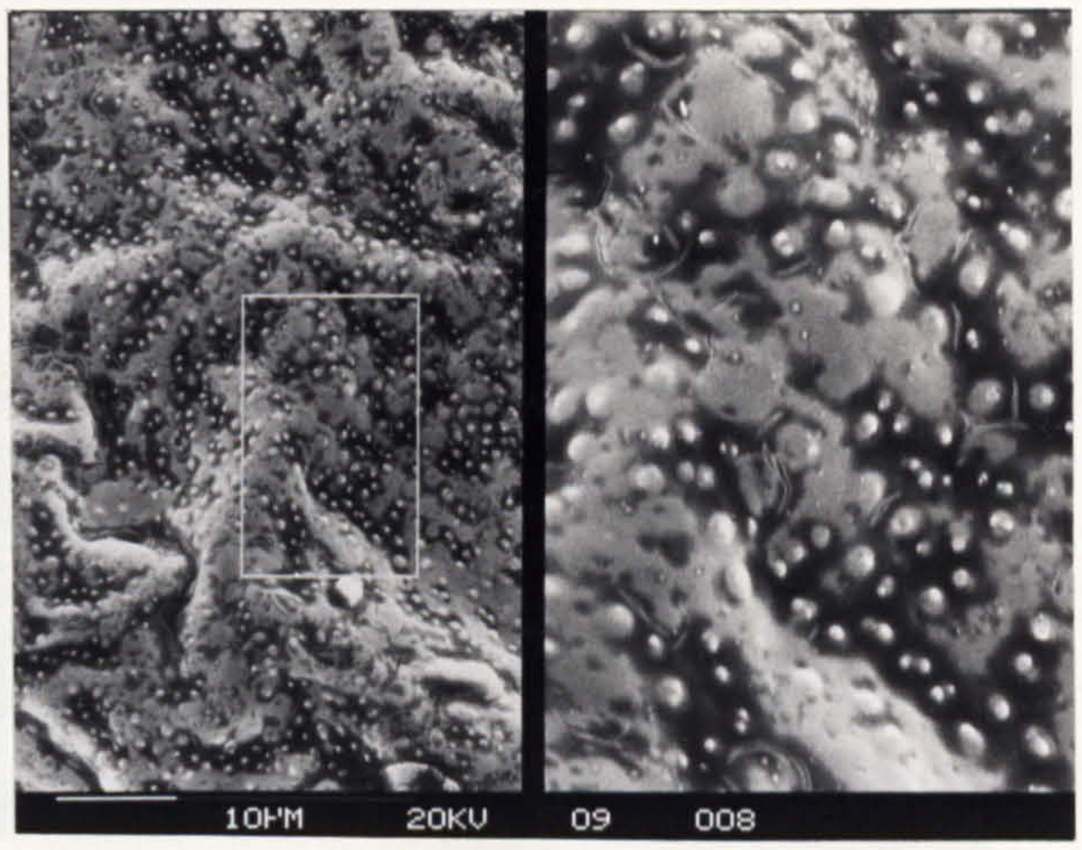

(b)

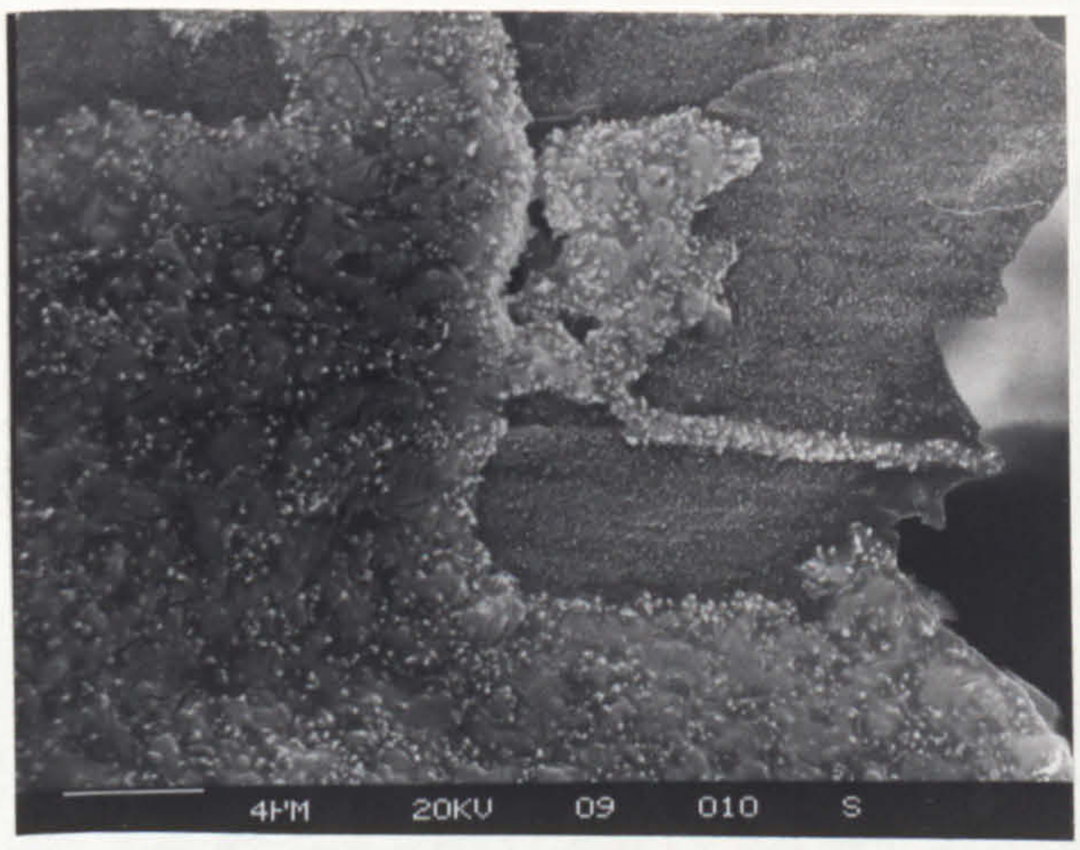

(d)

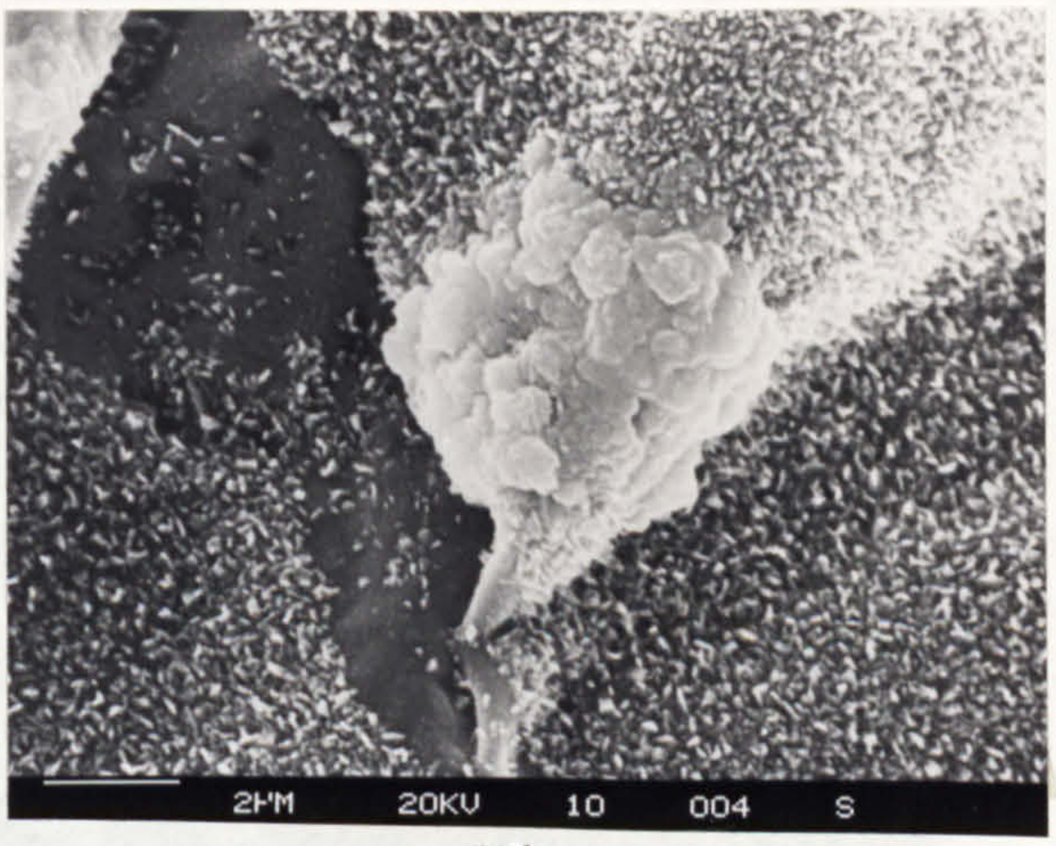

(c)

Figure 7.38 Oxide surfaces of 5182 GR alloy after 15h in humid air at 750°C (a,b) with 10ppm Be and (c,d) 50ppm Be

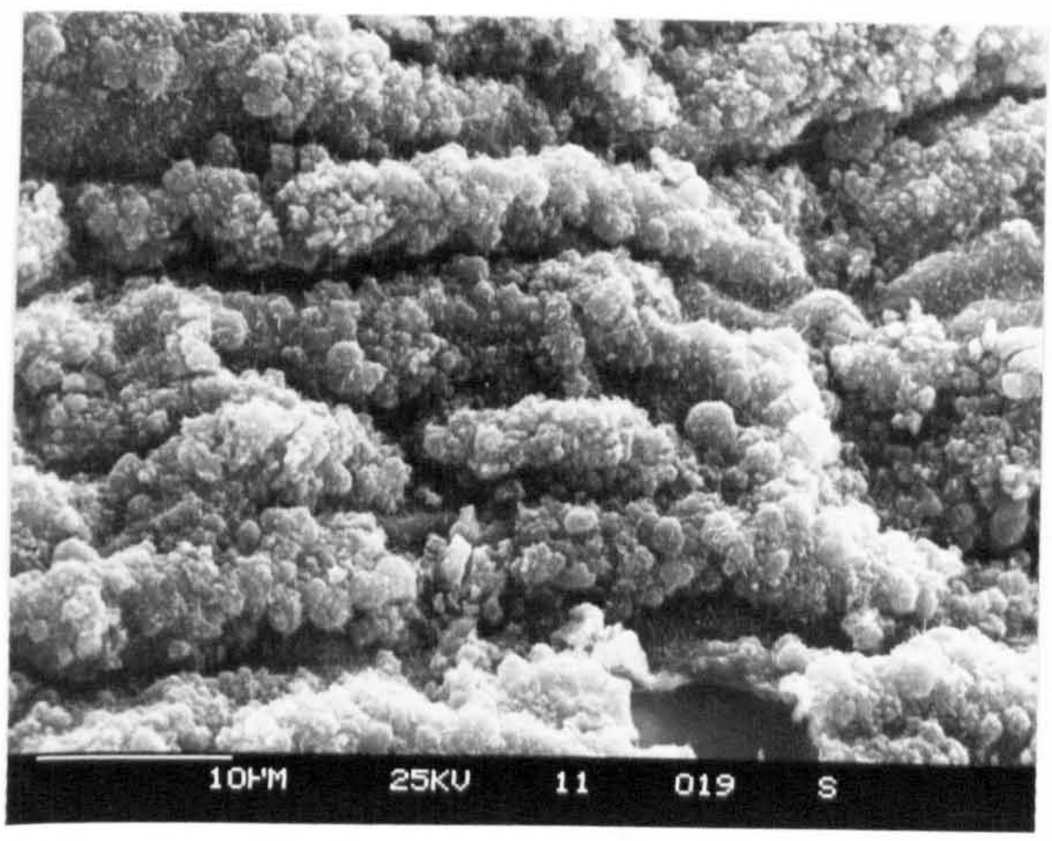

(a)

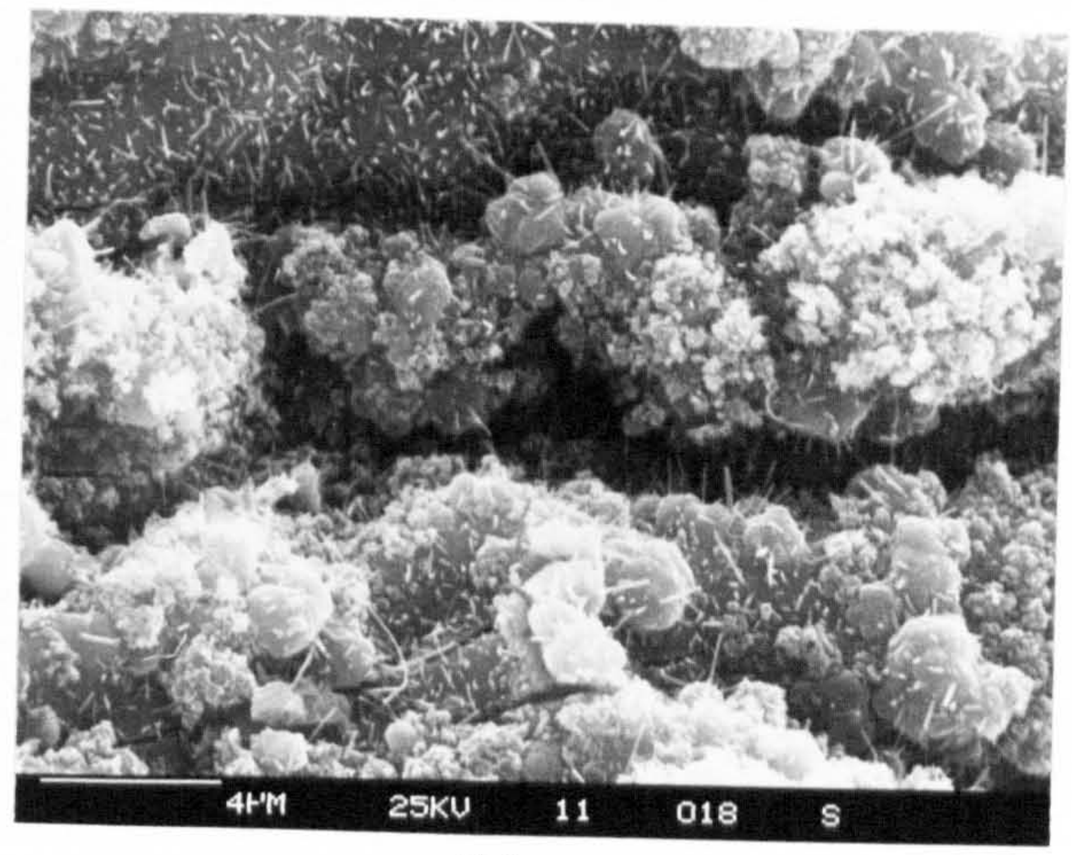

(b)

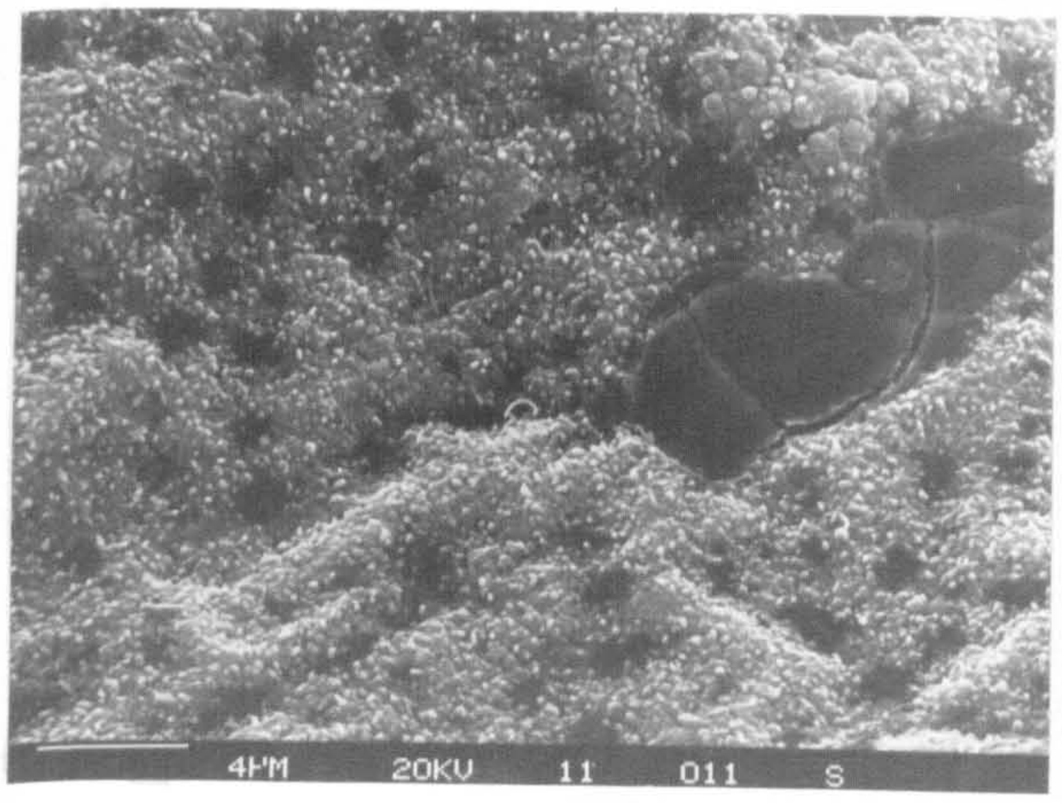

(c)

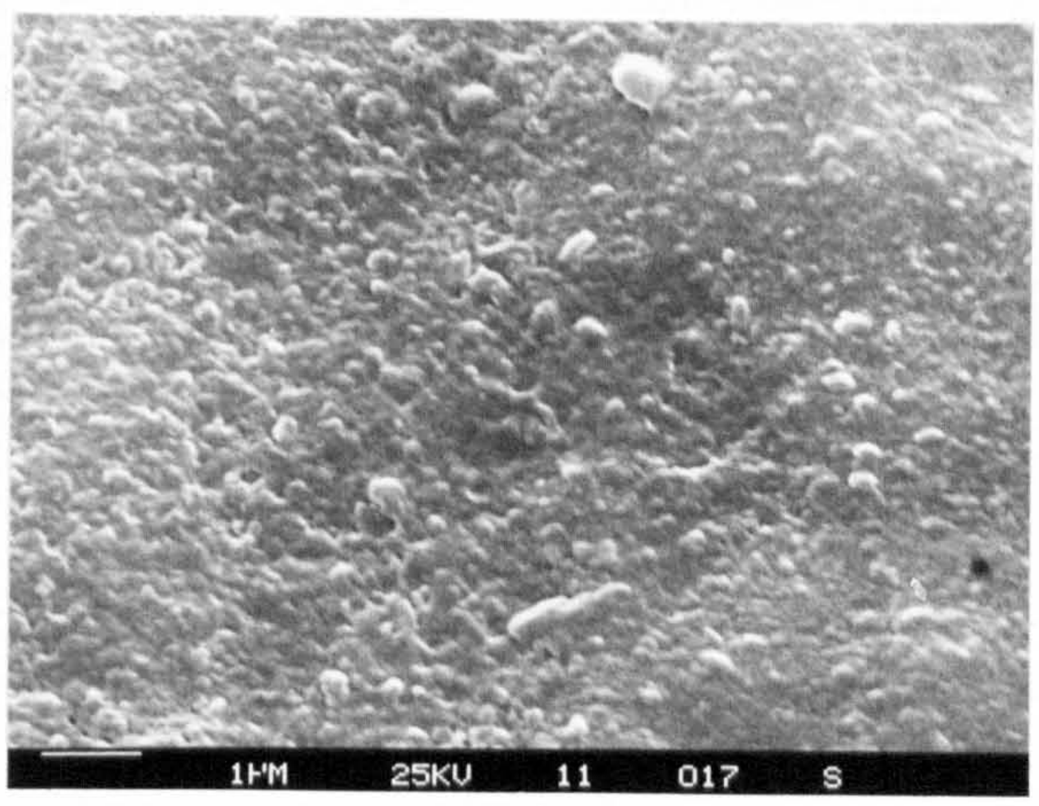

(d)

Figure 7.39 Oxide surfaces of 5182 NGR alloy after 15h exposure to gettered argon at 750°C (a,b) with 10ppm showing breakdown of protective oxide surface and (c,d) with 50ppm Be

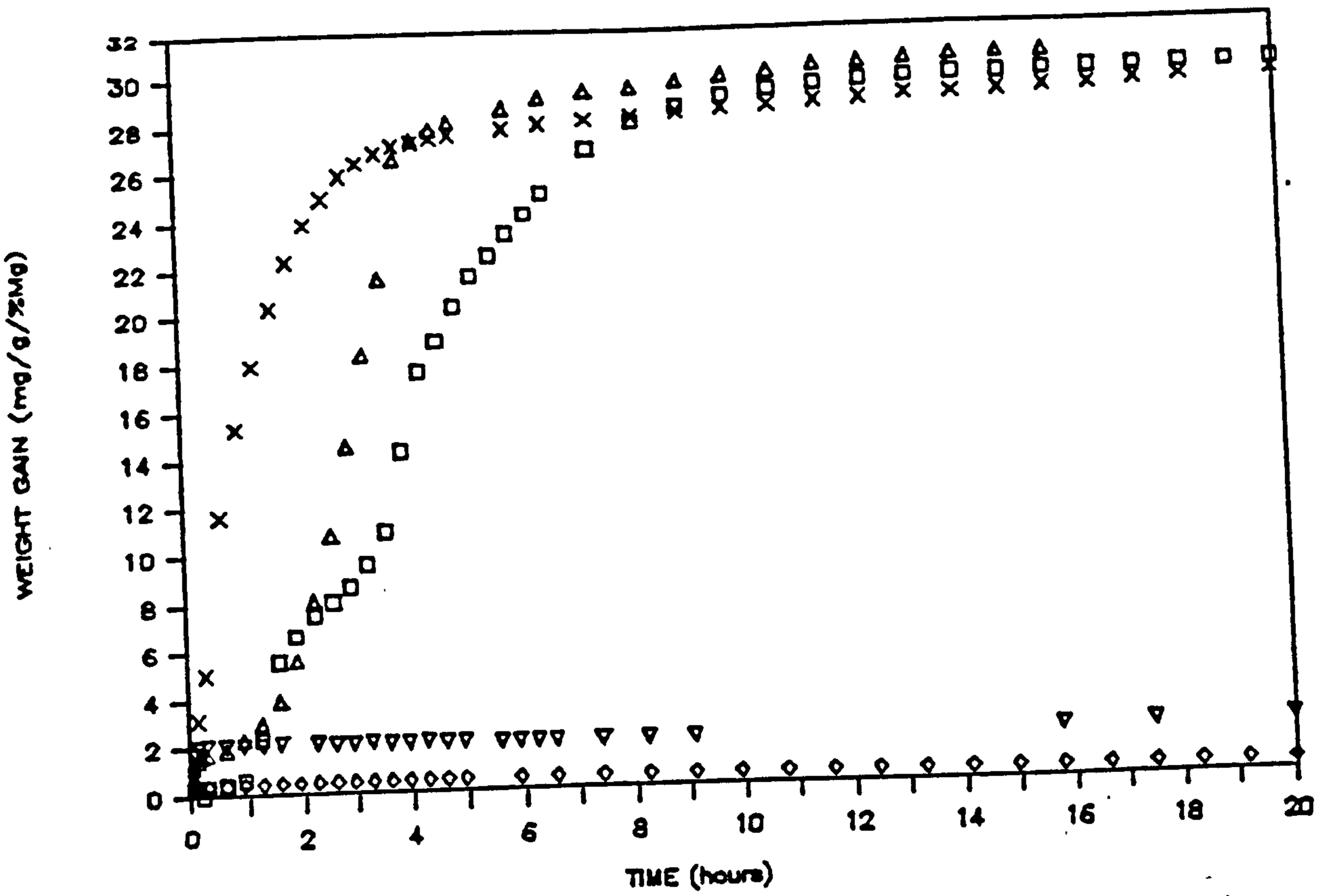

▽ *pure aluminium*

△ *Al-1%Mg GR*

× *Al-1%Mg NGR*

◇ *Al-5%Mg-Be*

□ *Al-5%Mg*

Figure 7.40 Summary of oxidation rates at 750° in gettered argon on machined aluminium and Al-Mg alloys plotted as weight gain per unit of magnesium against time.

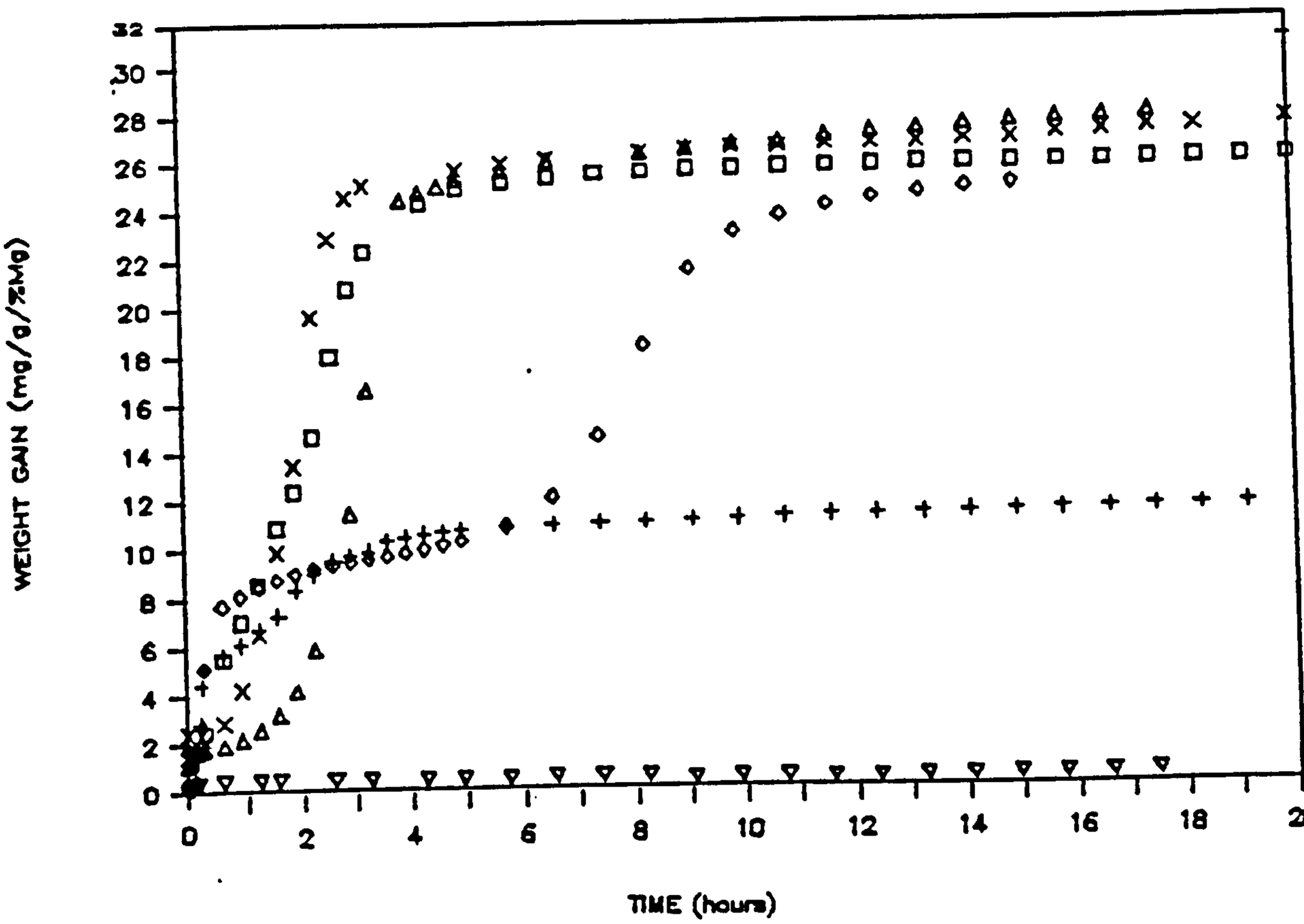

▽ *pure aluminium*

△ *Al-1%Mg GR*

× *Al-1%Mg NGR*

\+ *Al-4.5%Mg GR*

◇ *Al-4.5%Mg NGR*

□ *Al-5%Mg*

Figure 7.41 Summary of oxidation rates at 750°C in gettered argon on polished (1μm) aluminium and Al-Mg alloys plotted as weight gain per unit of magnesium against time.

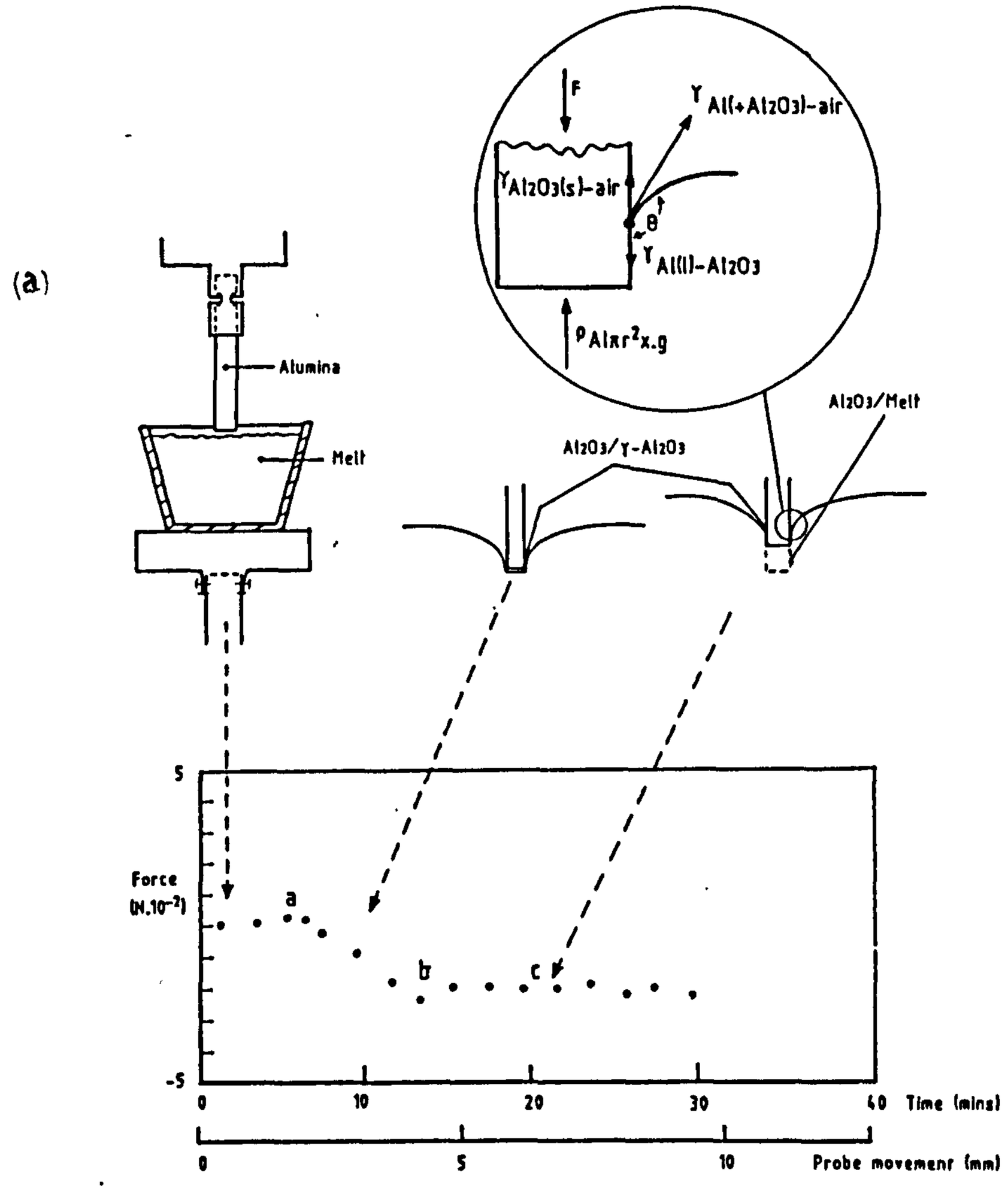

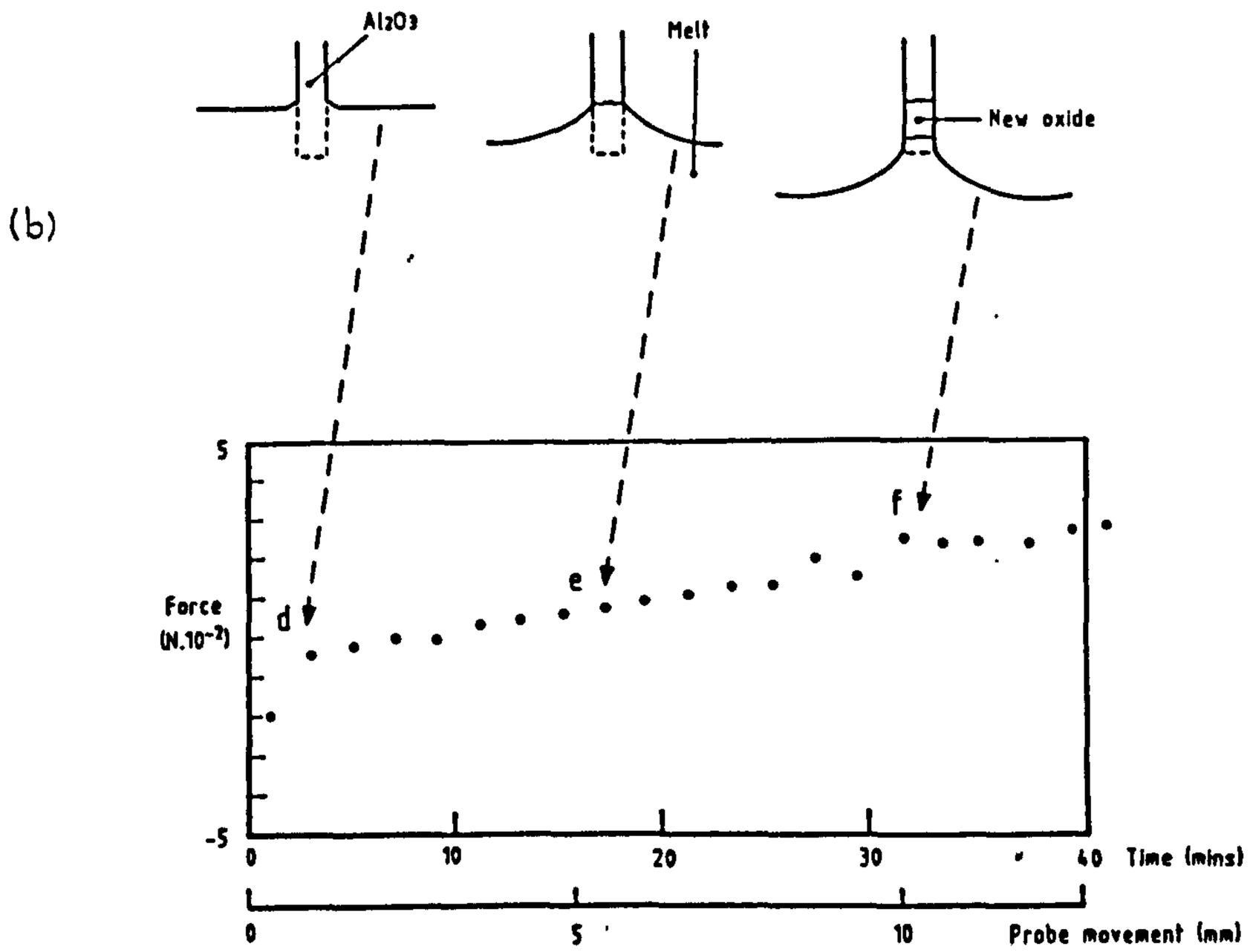

Figure 8.1 Change in force during oxide probe (a) immersion into molten aluminium and (b) removal of probe.

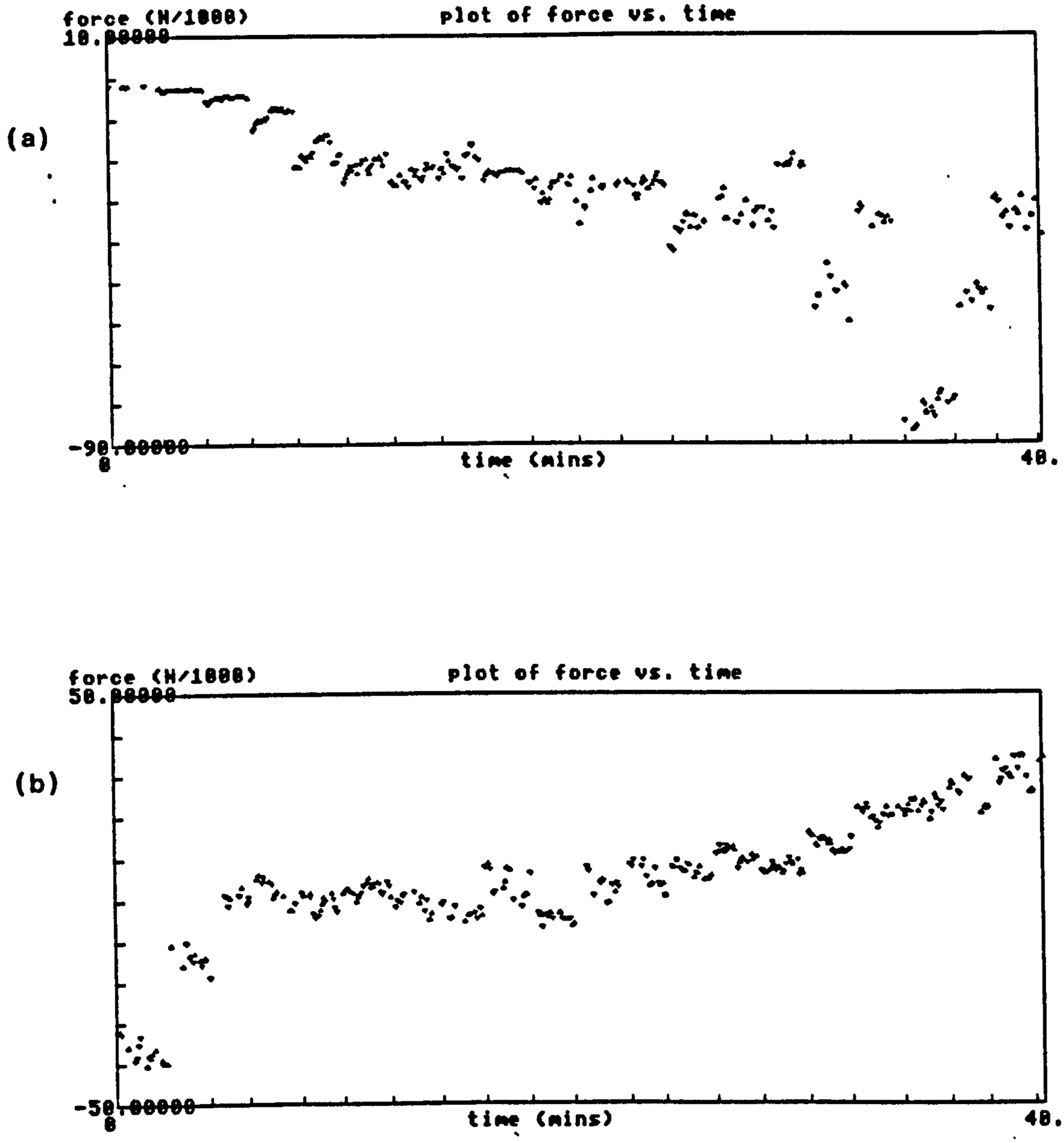

Figure 8.2 Change in force during
(a) immersion by oxide probe into skimmed molten Al-5%Mg alloy
(b) removal of oxide probe.

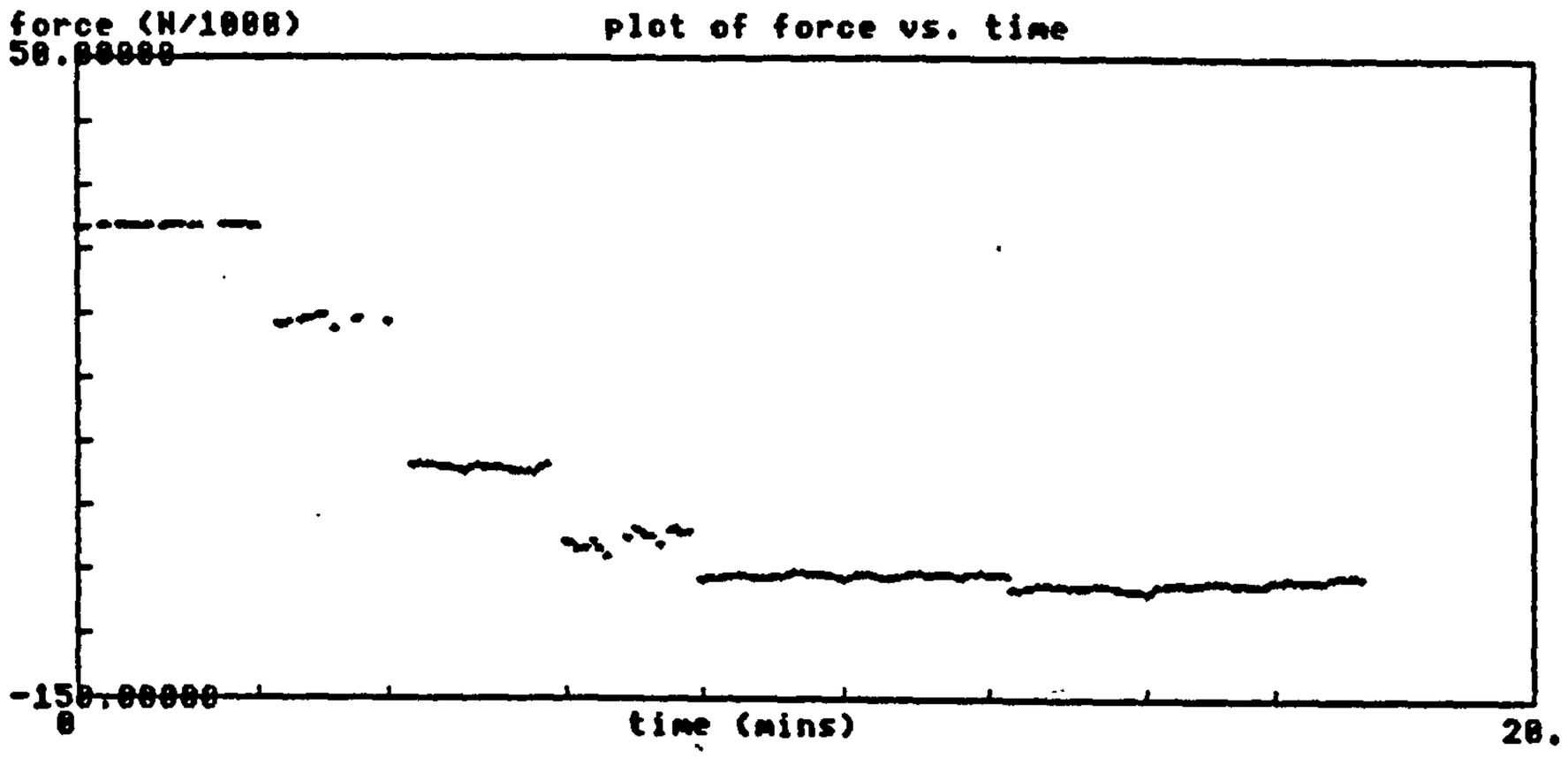

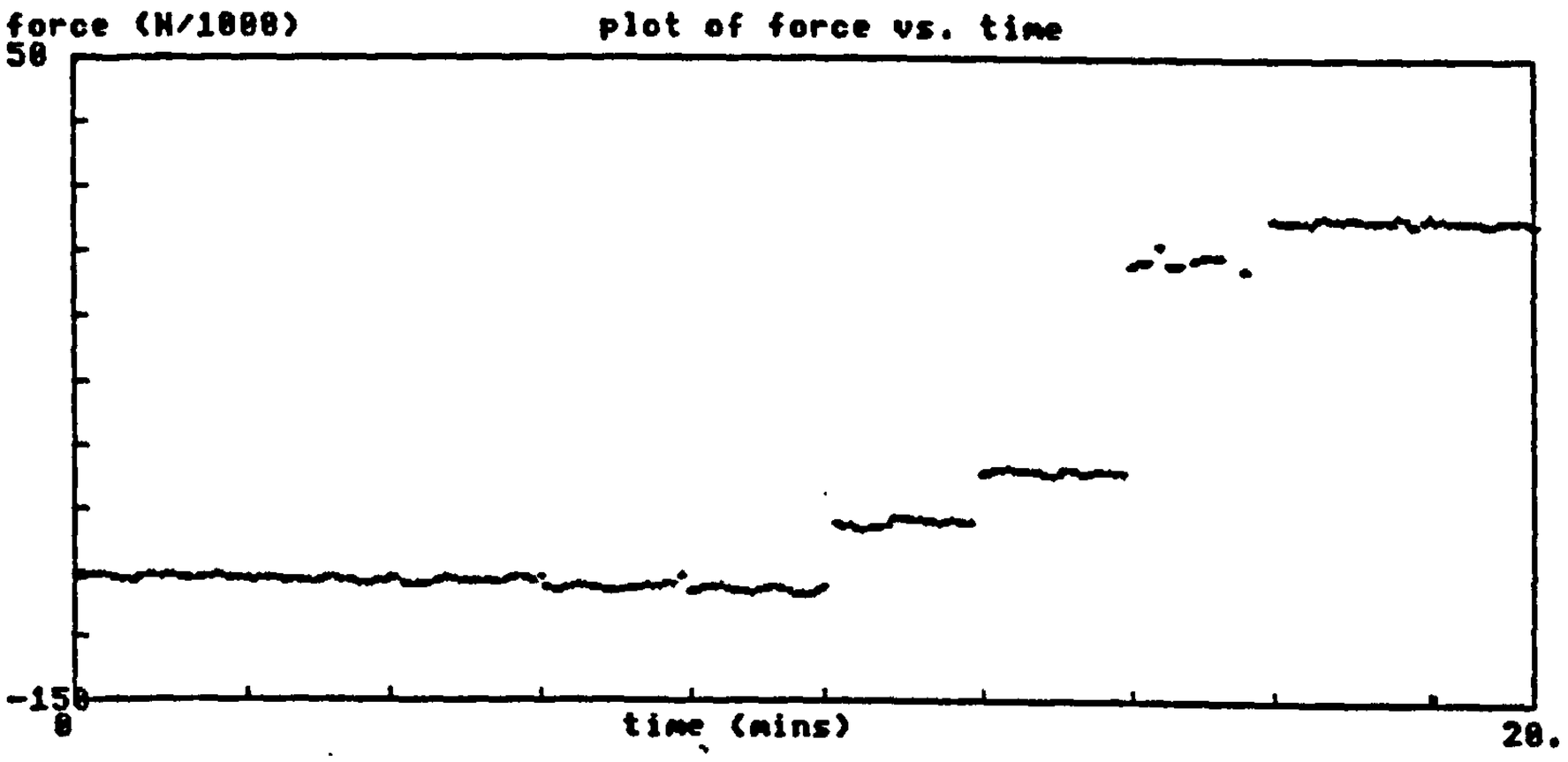

Figure 8.3 Change in force during
(a) immersion of oxide probe into unskimmed molten Al-5%Mg alloy.
(b) removal of oxide probe.

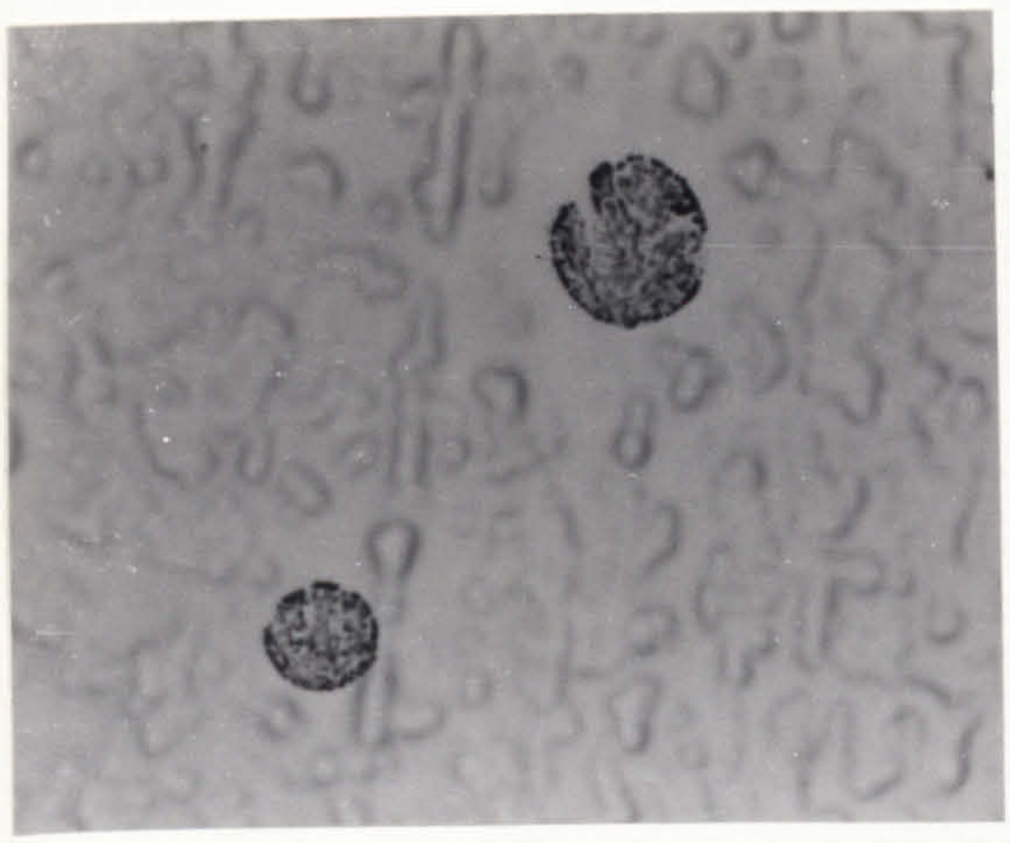

(a)

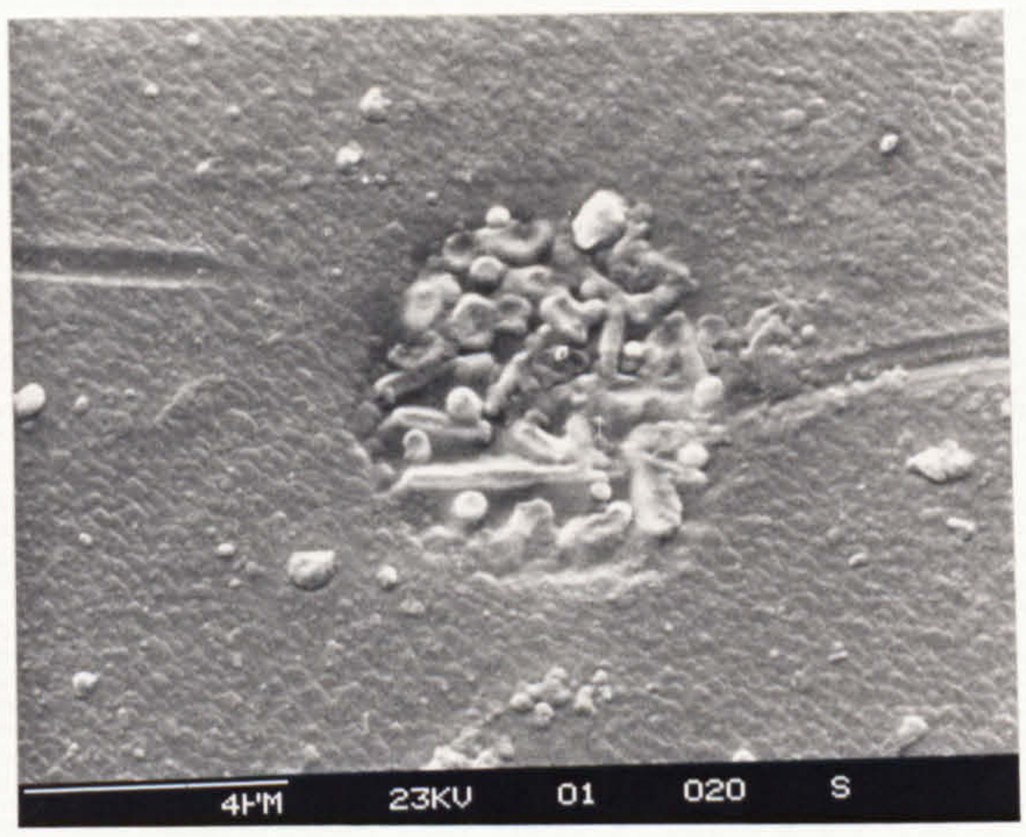

(b)

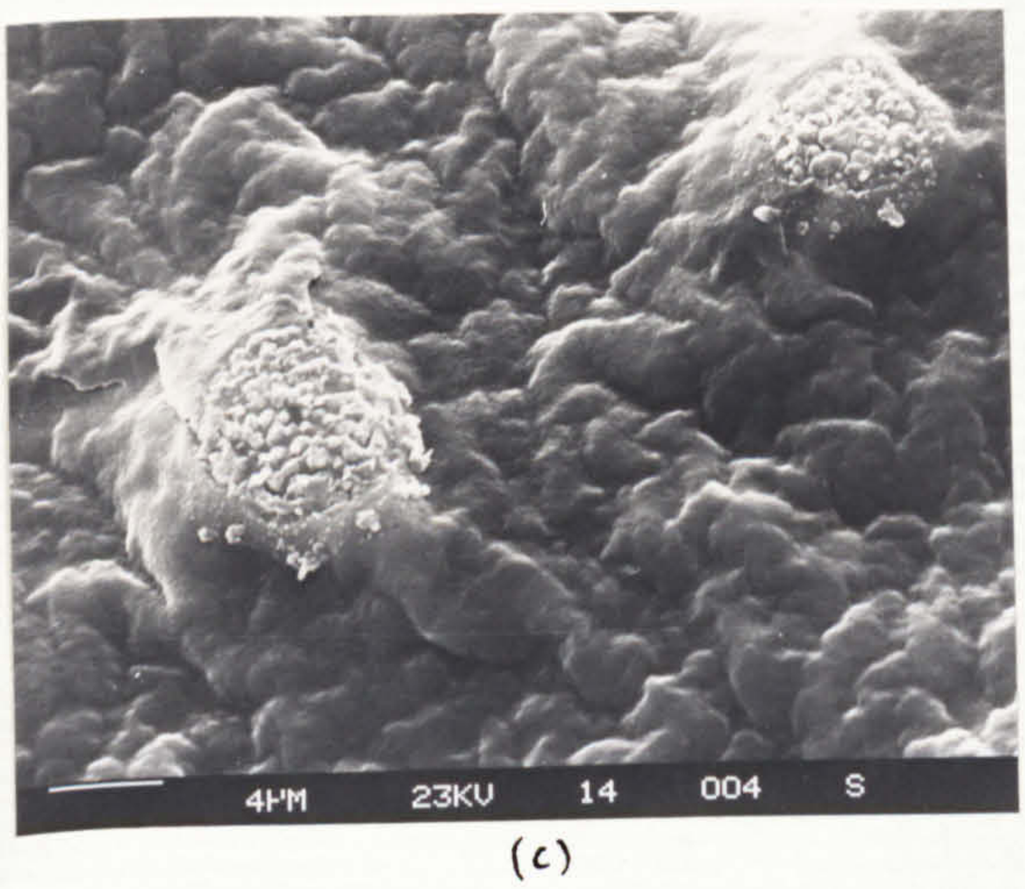

(c)

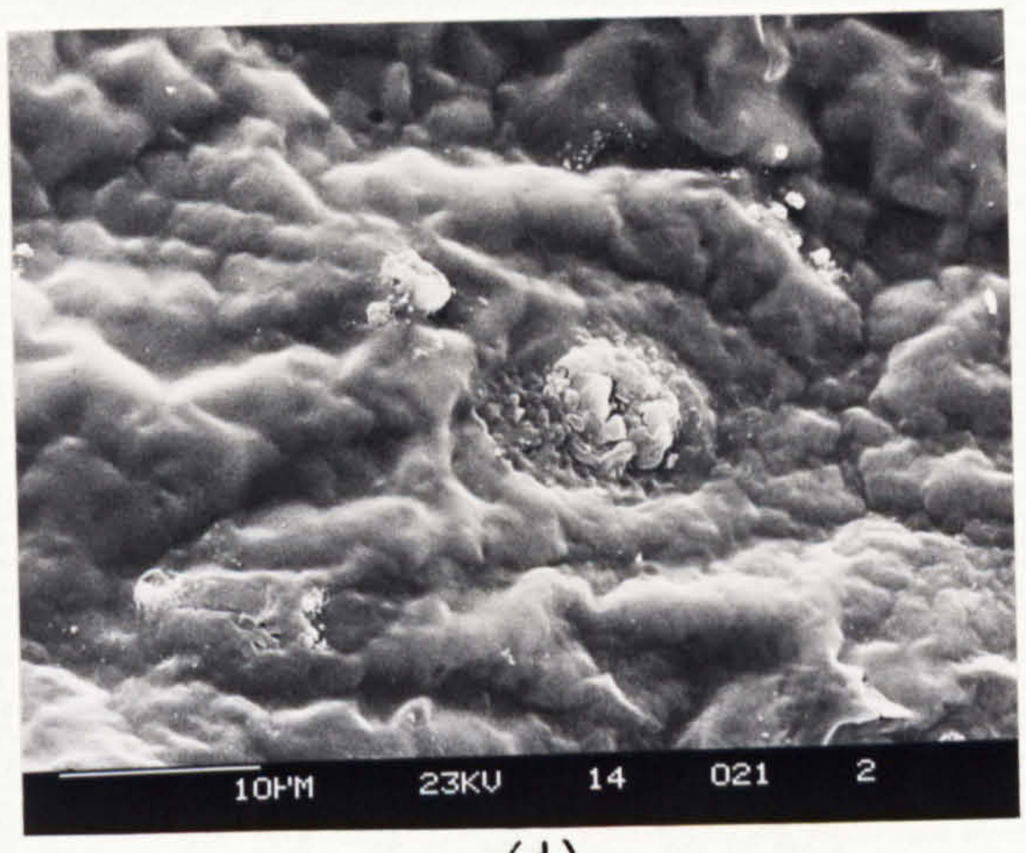

(d)

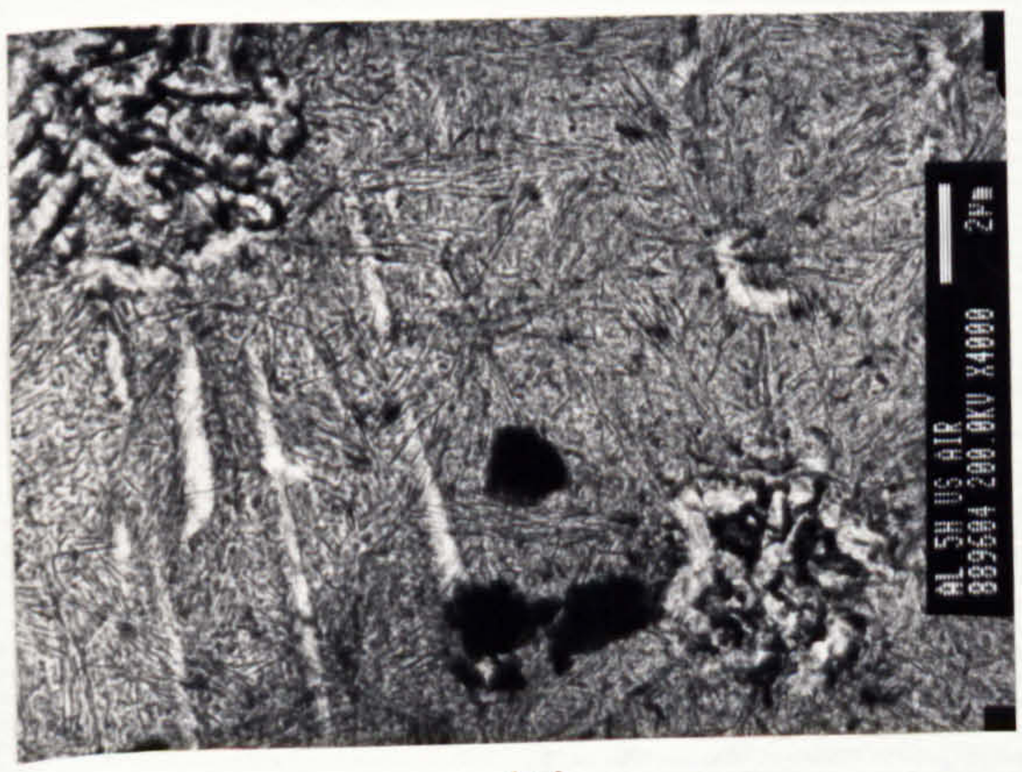

(e)

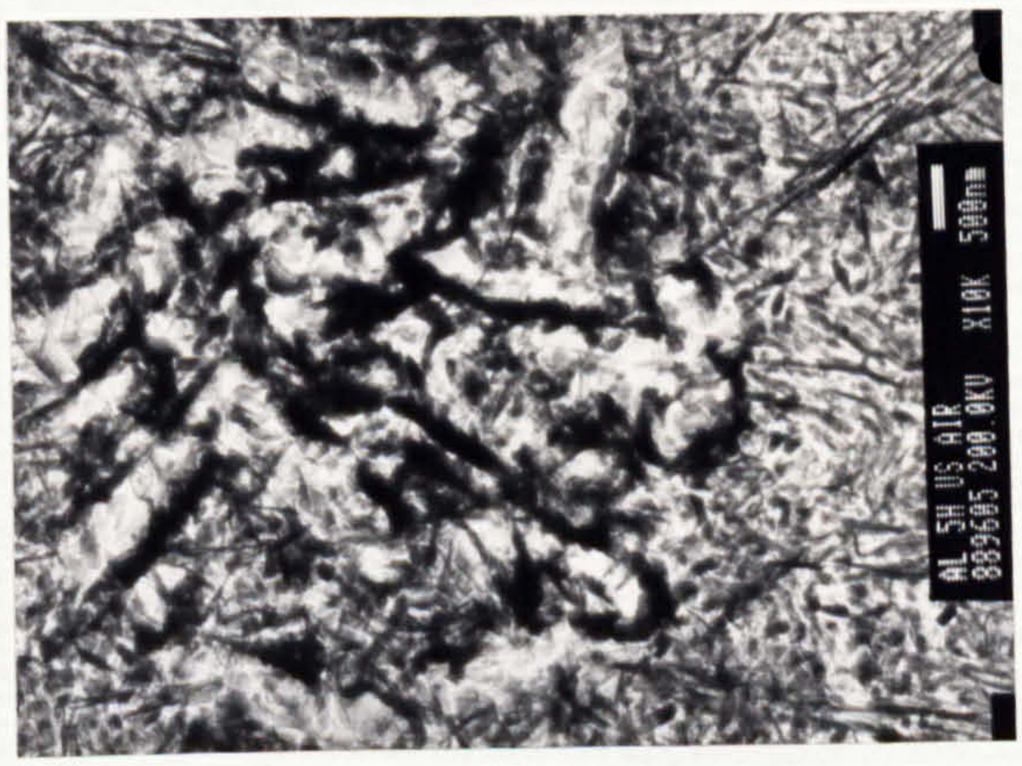

(f)

Figure 9.1 Electropolished aluminium showing iron rich structures (a,b) before oxidation and (c,d) after 20h at 750°C (e,f) section after 5h oxidation in air

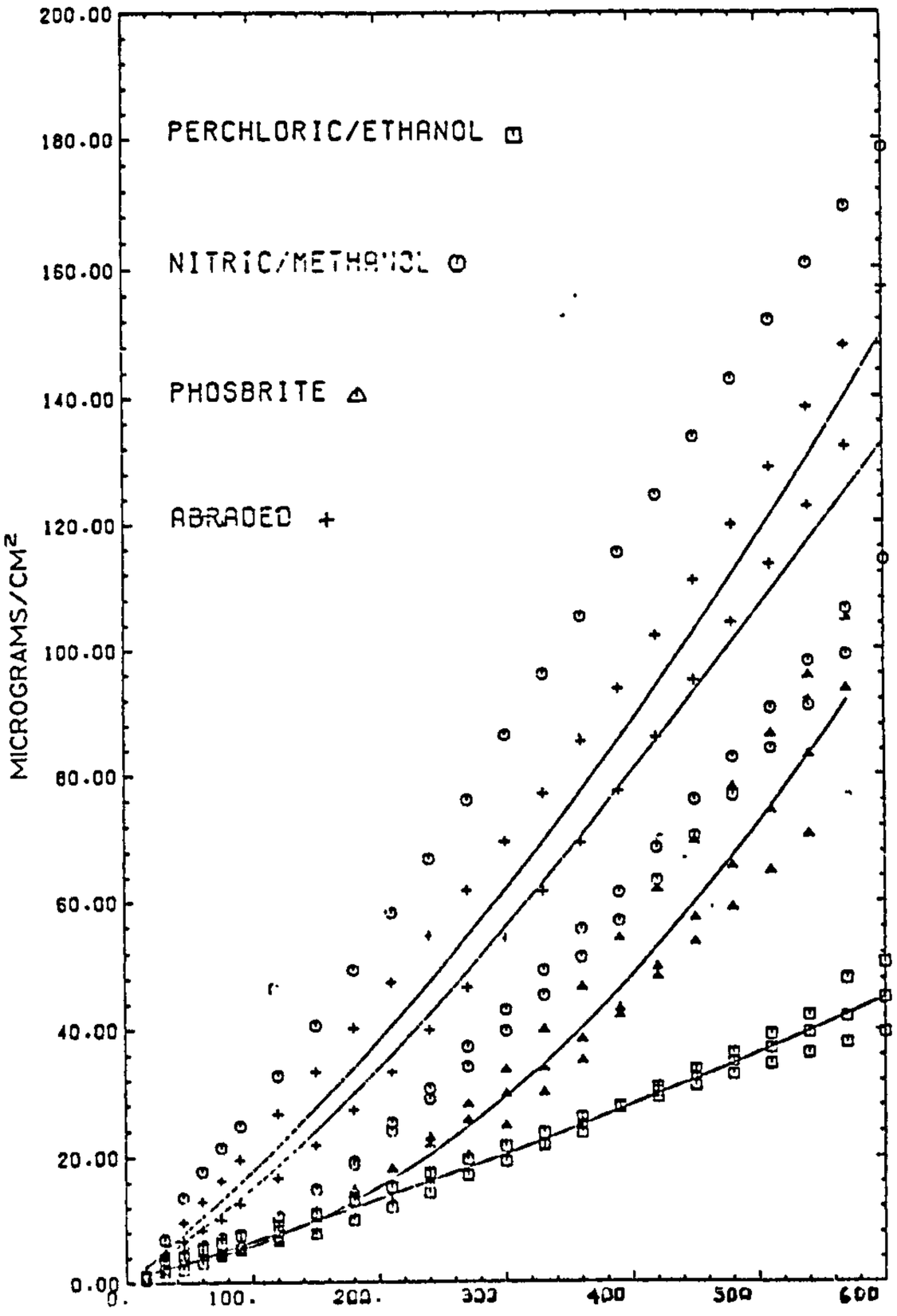

Figure 9.2 Effect of surface finish on the oxidation rates of Al-4.2%Mg in dry O_2/Ar at 480°C as found by Field [102]

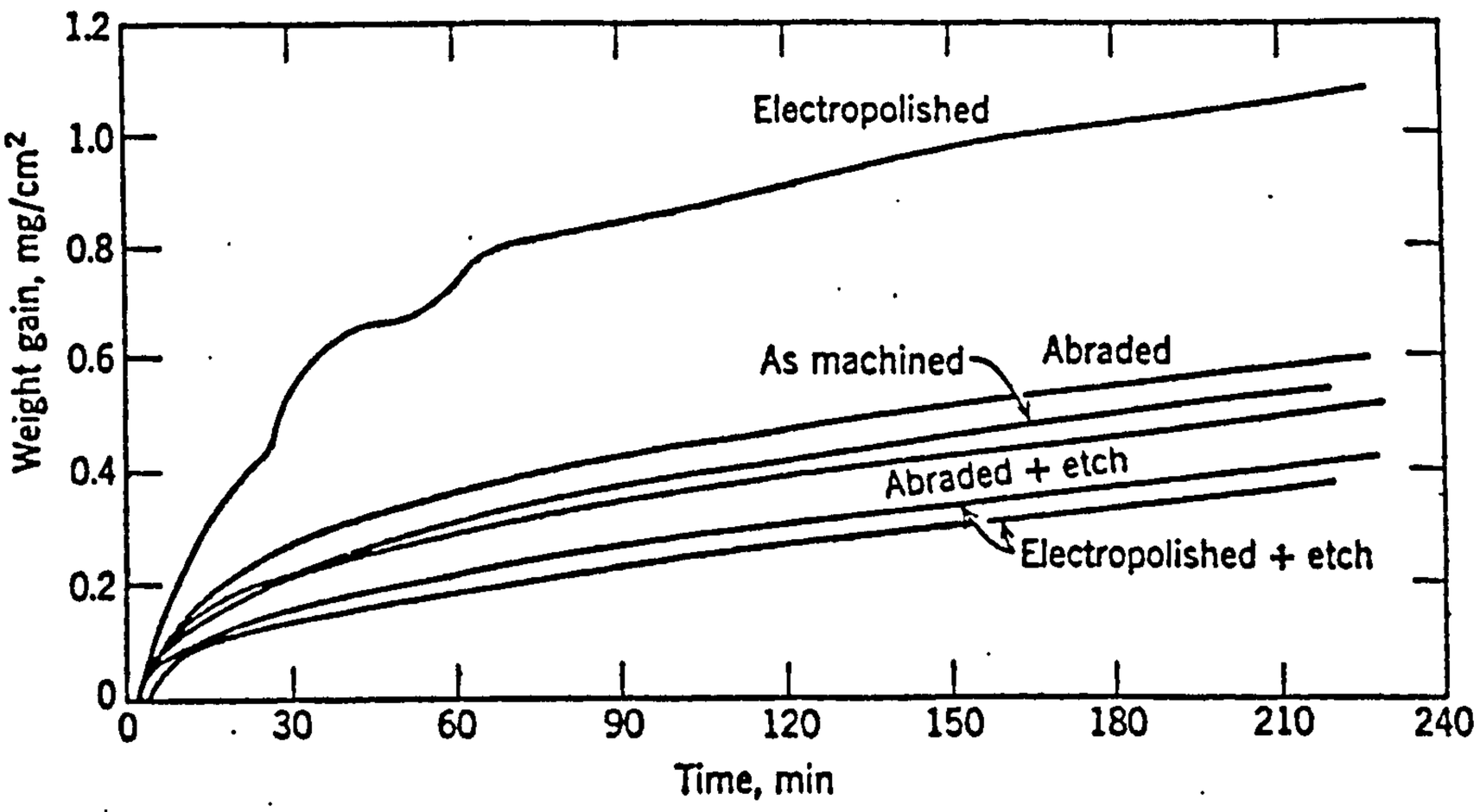

Figure 9.3 Effect of surface pretreatment on Fe-26%Cr-0.5%Si alloy in flowing dry oxygen at 1100°C after [230]

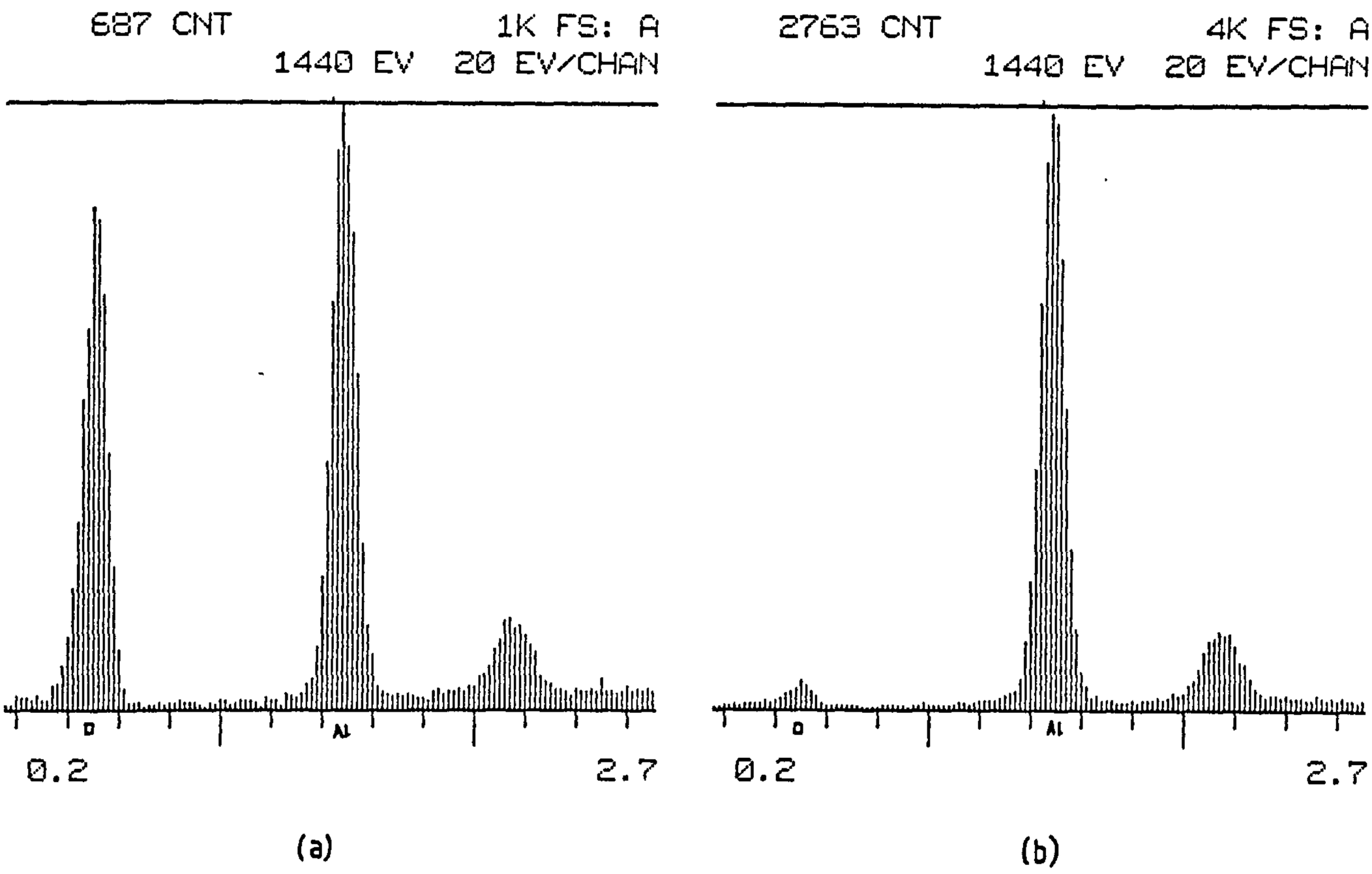

Figure 9.5 Analysis of (a) the surface of an oxide growth and (b) the surrounding area

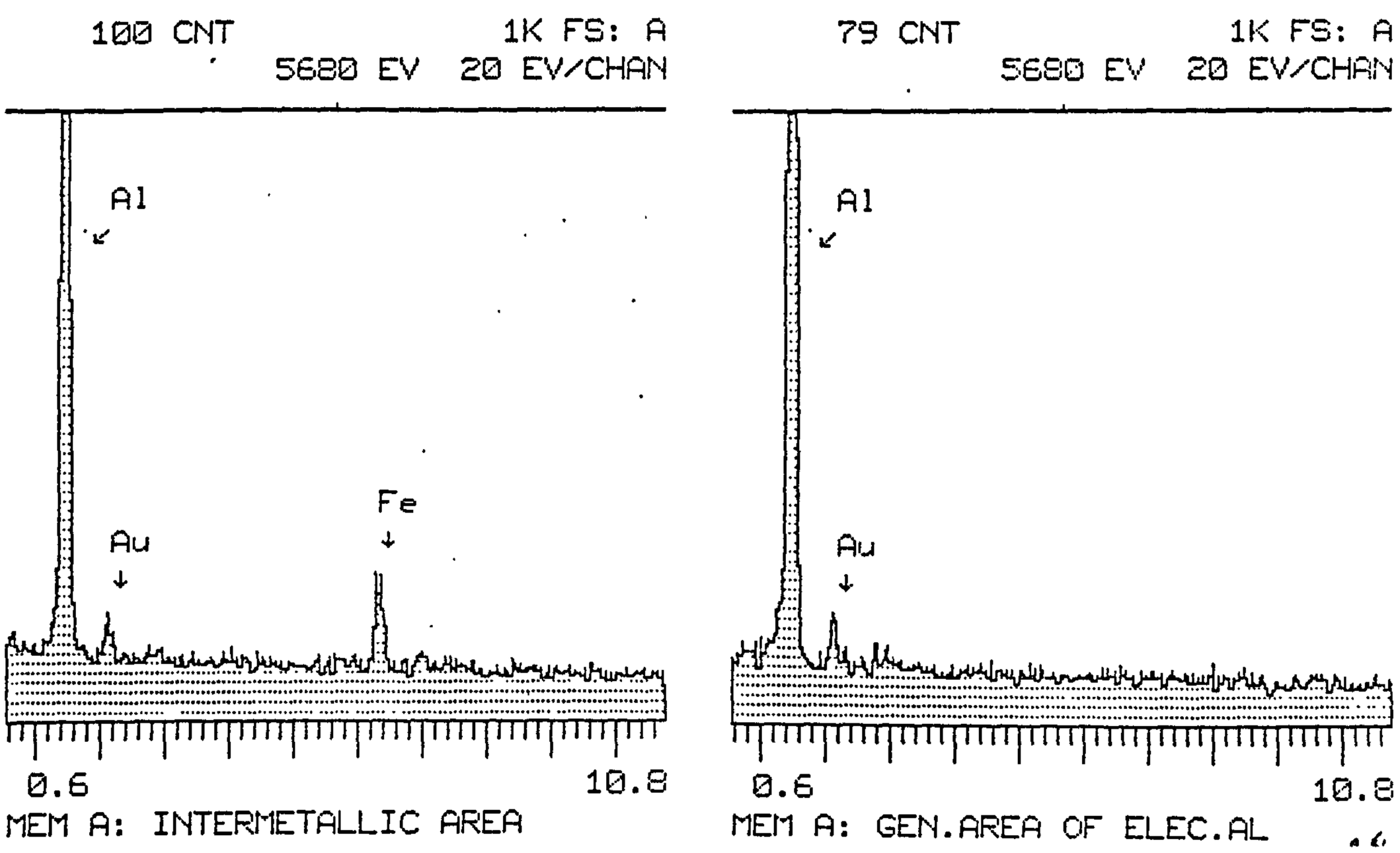

Figure 9.6 Analysis of (a) circular feature on electropolished aluminium and (b) the surrounding area

(a)

(b)

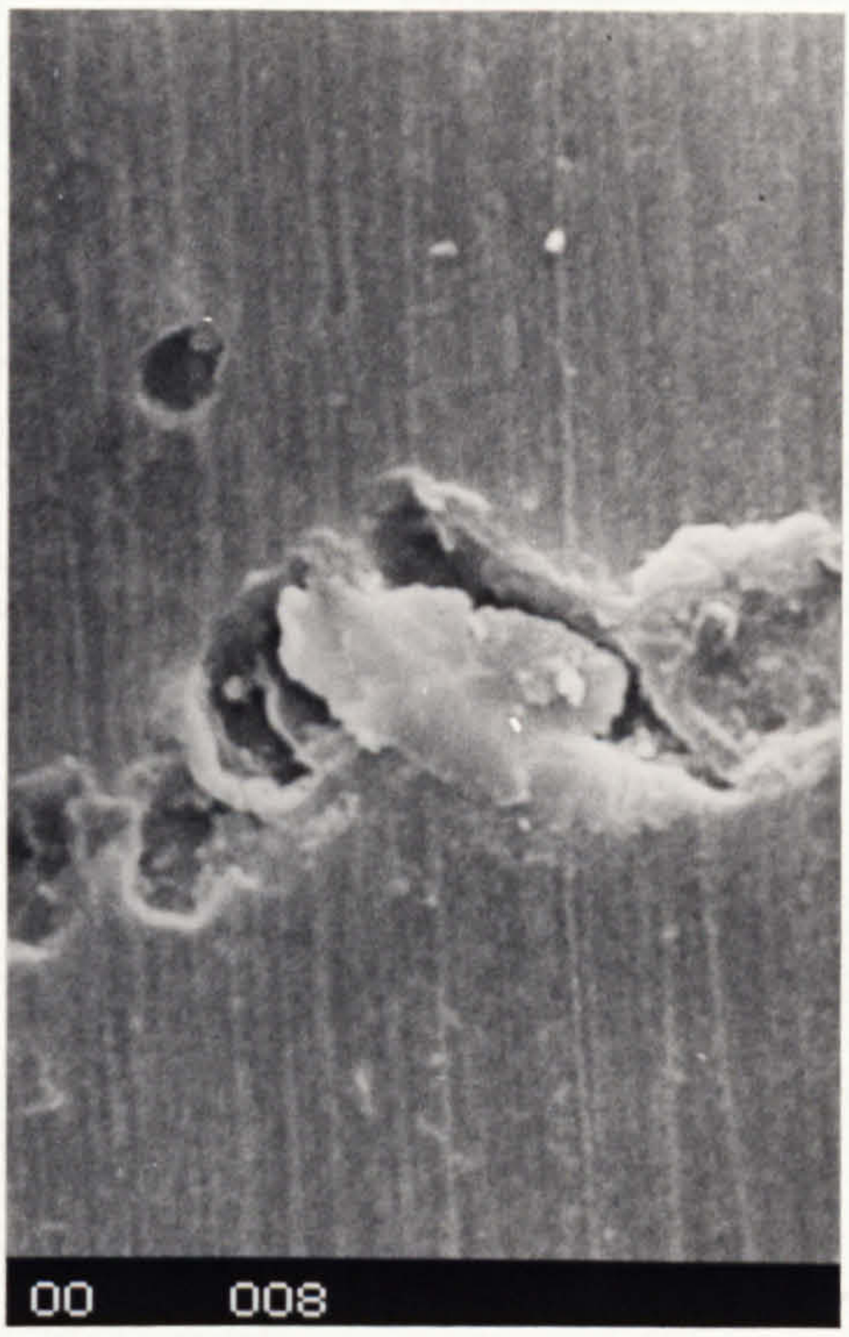

(c)

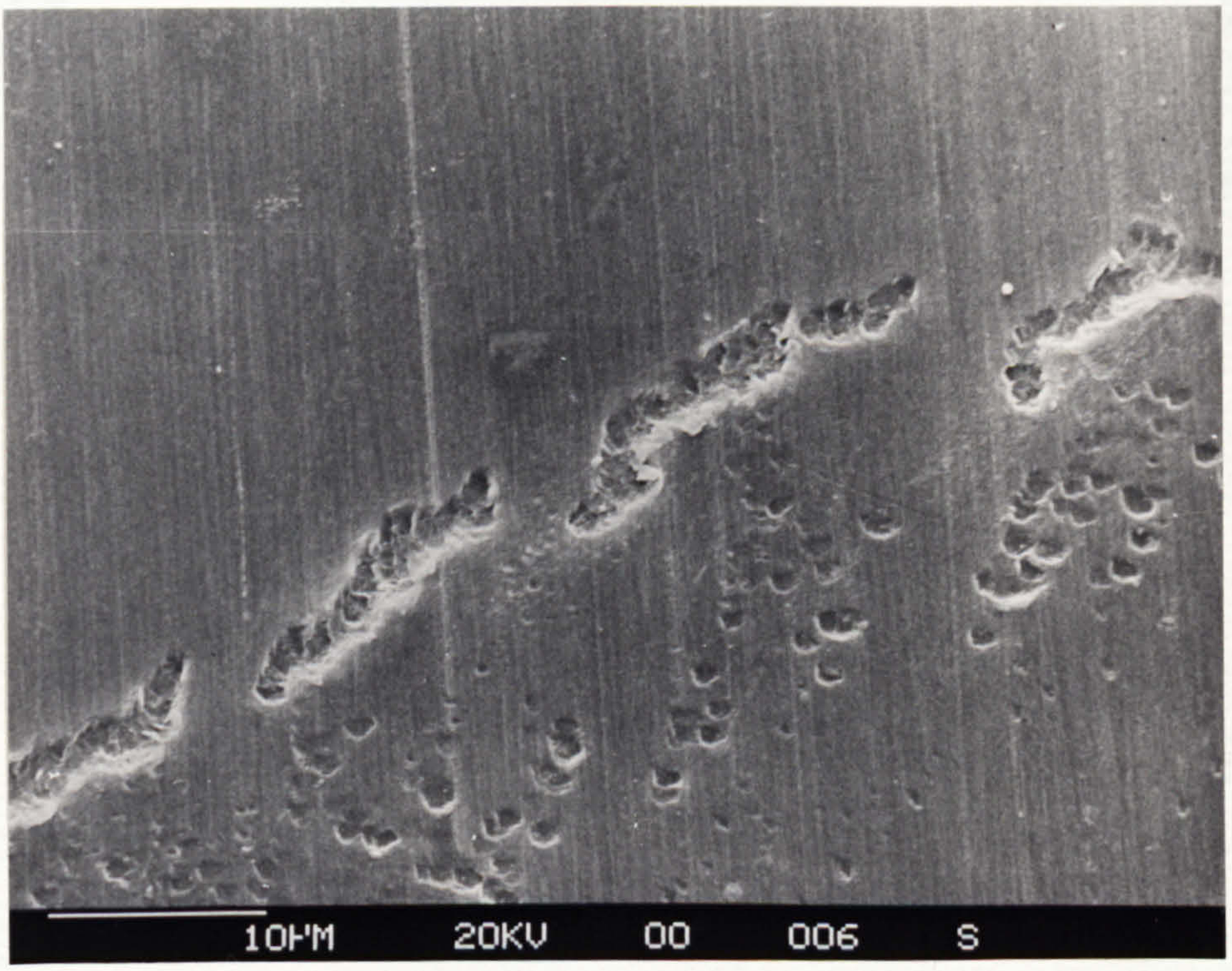

Figure 9.7 The surface of polished aluminium after ultrasonic cleaning for (a) 30 s and (b,c) 5 mins

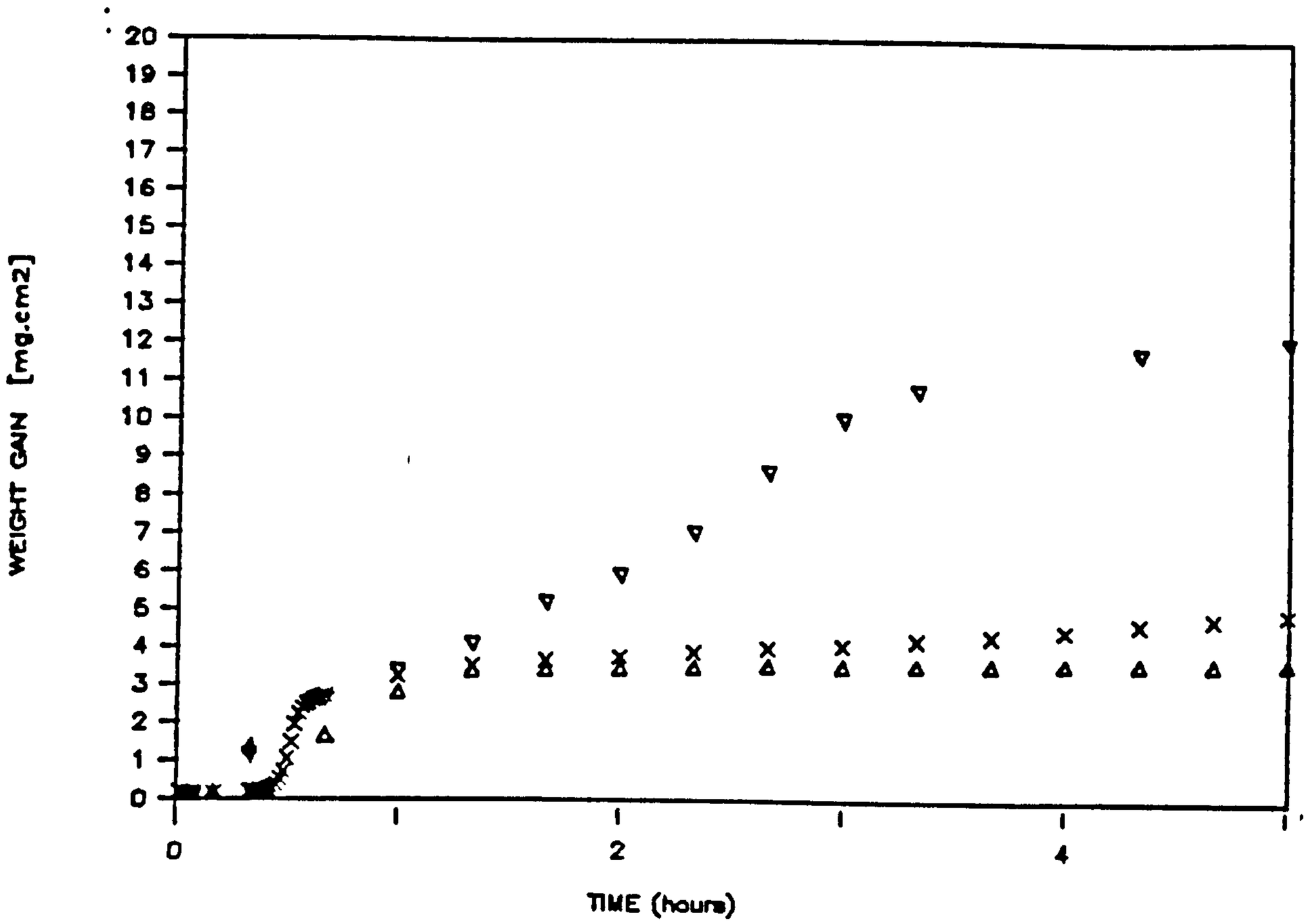

× , ▽ *with ultrasonic treatment*

△ *without ultrasonic treatment*

Figure 9.8 The effect of ultrasonic cleaning on the oxidation of Al-5%Mg GR alloy in gettered argon at 750°C.

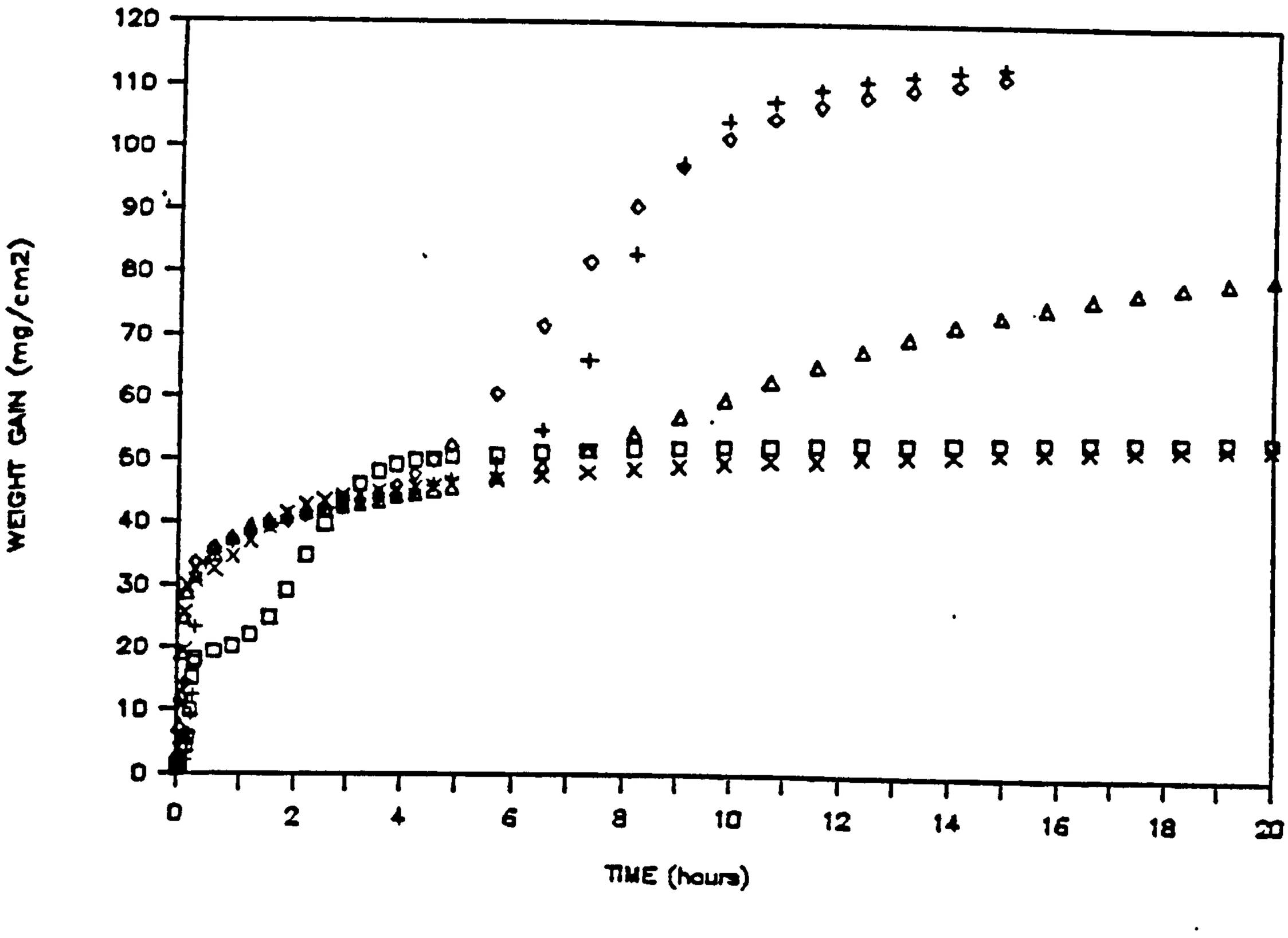

◇ *diamond (1μm) polished surface with ultrasonic treatment*

+, Δ *diamond (1μm) polished surface*

□ *diamond (1μm) polished Al-4.5%Mg GR alloy surface*

× *alumina (0.3μm) polished surface*

Figure 9.9 The influence of surface preparation on the oxidation of Al-4.5%Mg NGR alloy at 750°C in gettered argon.

Solidification structures
on cooling

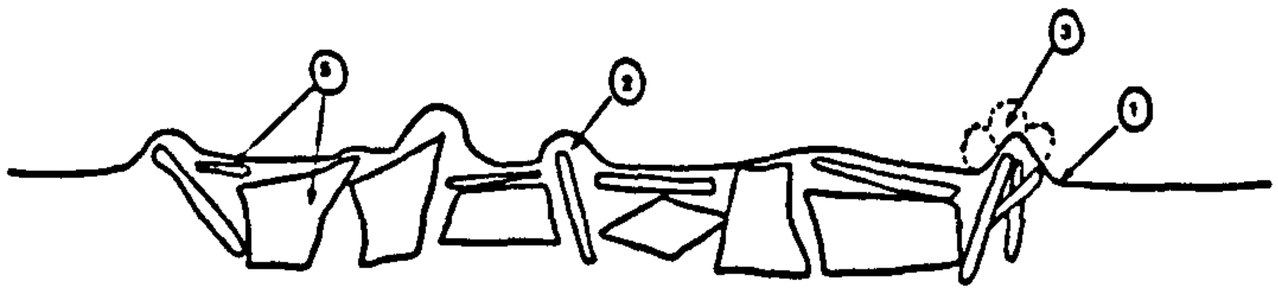

Oxide beneath
surface film spherodizing

Breakaway oxidation

Oxide growths

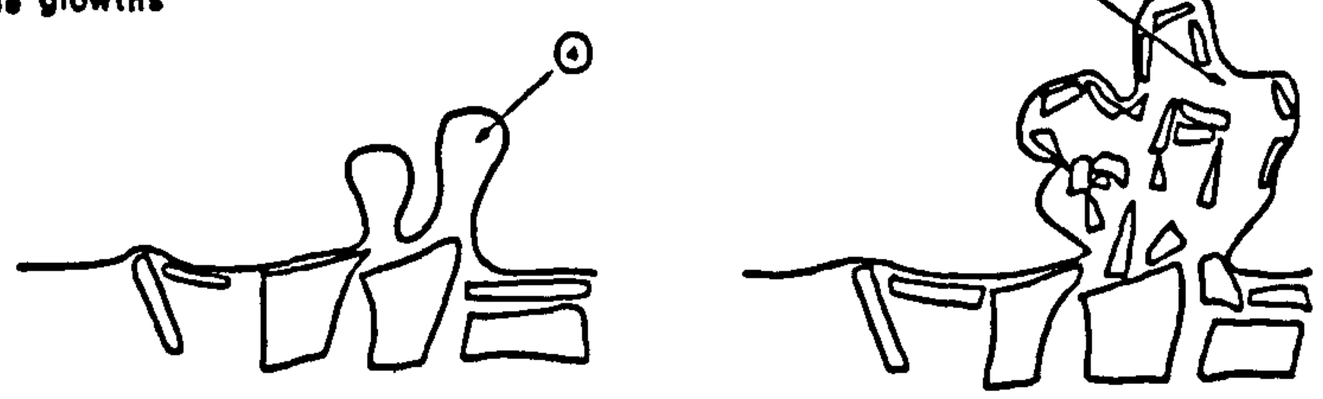

Classification	Description	Schematic label	Illustration on micrographs
surface film	thin oxide covering of amorphous γ-Al_2O_3	1	6.22a,b
nodule	single crystal covered by surface film	2	6.15a, 6.22b
crowns	circular ring of nodules		6.15b, 6.19c
cluster	collection of nodules	3	6.15a
oxide growth	large cluster of nodules, molten metal and crystals	3	6.15c, 6.18 6.24a
spheroids	smooth projections of molten metal	4	6.24b
oxide crystals	angular or rod-like crystals of γ and α-alumina	5	6.12-6.14, 6.17
granules	spheroidised oxide crystals beneath the surface film	6	6.22, 6.21

Figure 9.10 Schematic of oxide morphologies formed on aluminium melts.

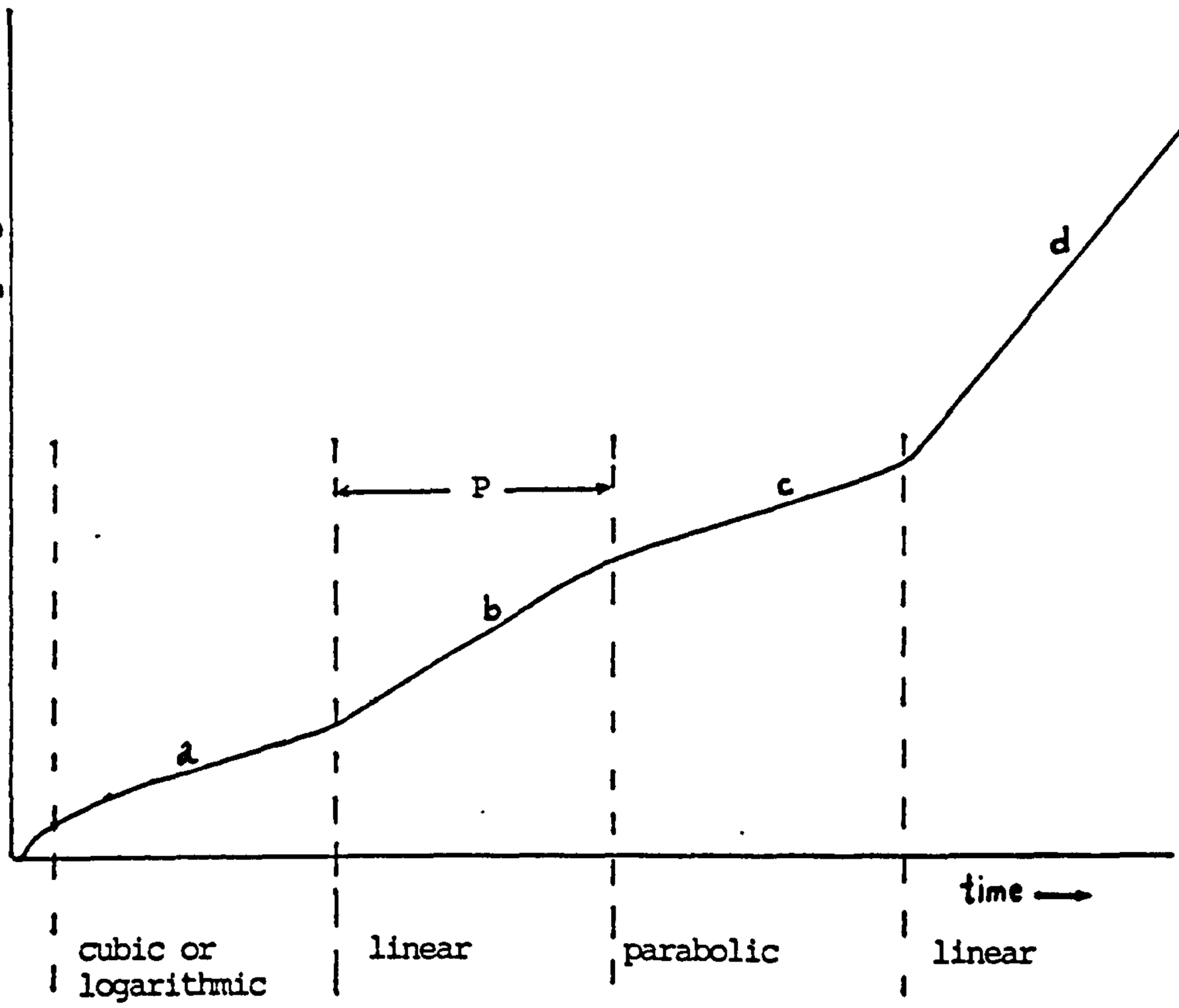

kinetics	cubic or logarithmic	linear	parabolic	linear
oxide morphology	thickening of 'amorphous' film	nucleation of γ-Al_2O_3 and/ or α-Al_2O_3 crystals	thickening of crystals nucleation of α-Al_2O_3	formation of oxide growths
rate determining step	combination of O^{2-} and Al^{3+} ions at surface for 'amorphous' film formation	adsorption of H_2O at oxide-gas interface or H^+ adsorption at the oxide-melt interface	diffusion of O^{2-} or Al^{3+} ions to the growing crystals at the oxide-melt interface	melt exposed by ruptured oxide. Surface or interfacial reactions dominate
Period of extension P		decreased in the absence of water vapour, and with increasing temperature		

Figure 9.11 Schematic of oxidation kinetics of molten aluminium.

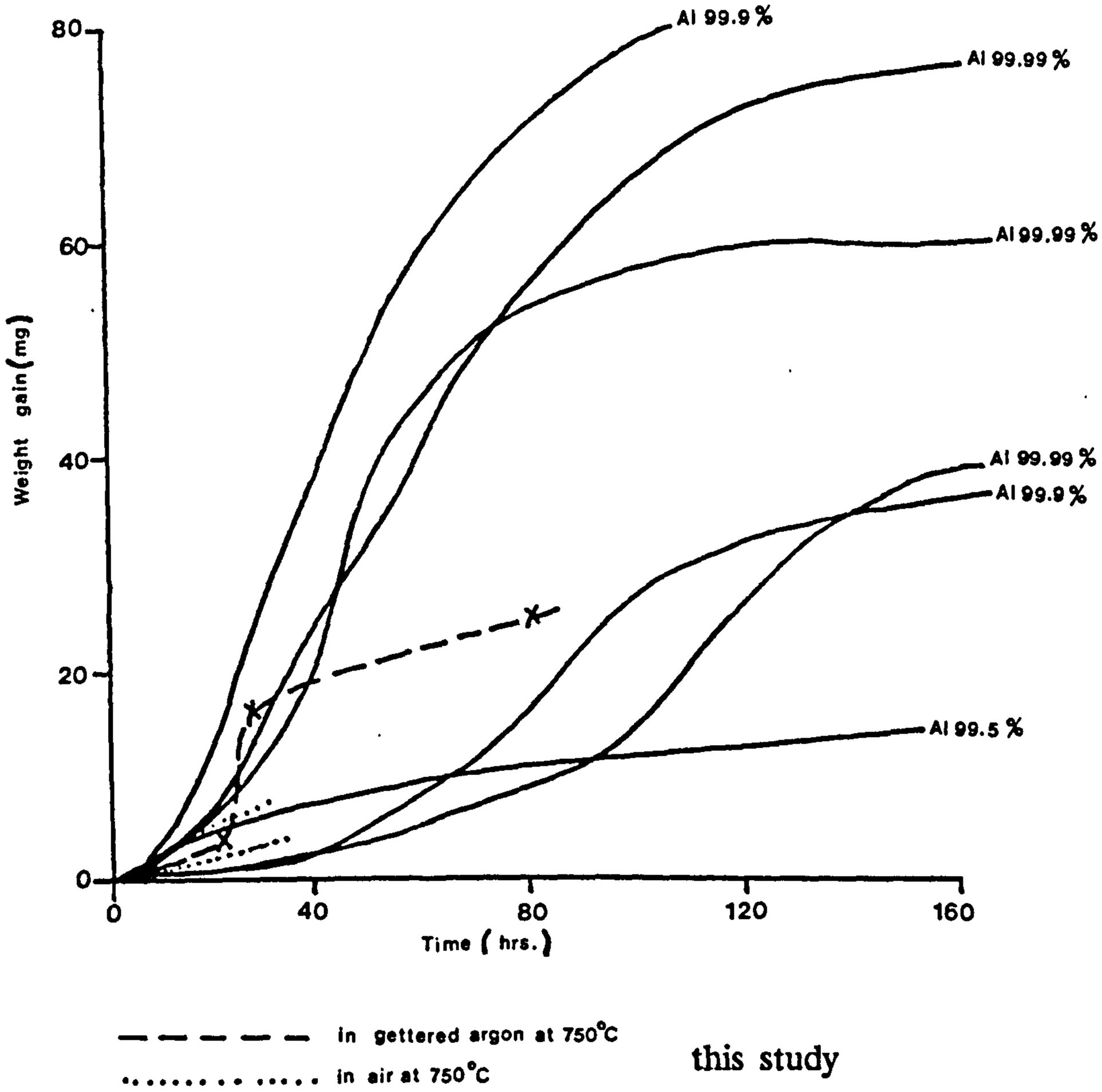

Figure 9.12 Oxidation of pure aluminium at 800°C as found by Thiele [111] and at 750°C in this study.

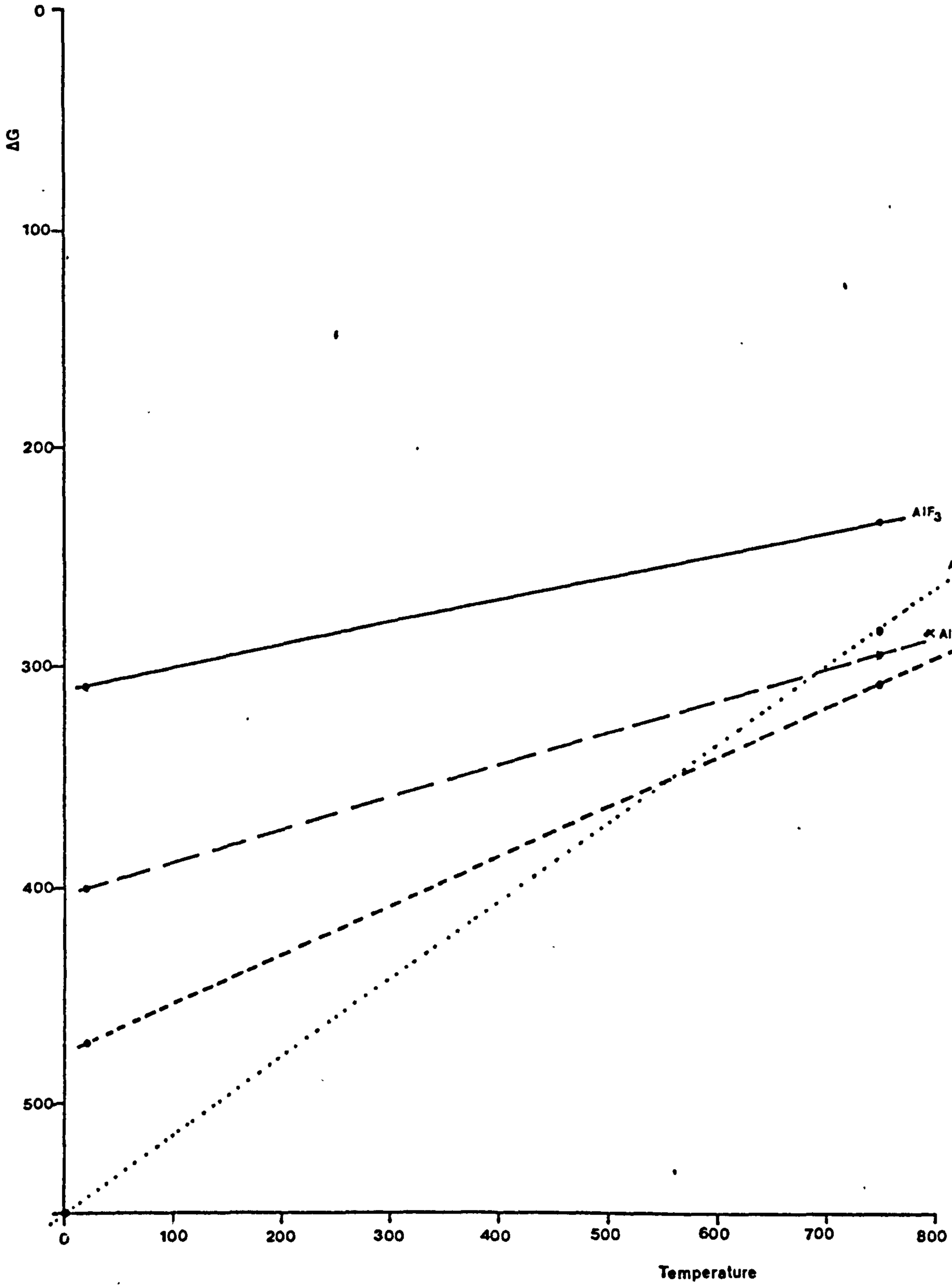

Figure 9.13 Plot of Gibbs energy with temperature for aluminium oxide and fluoride.

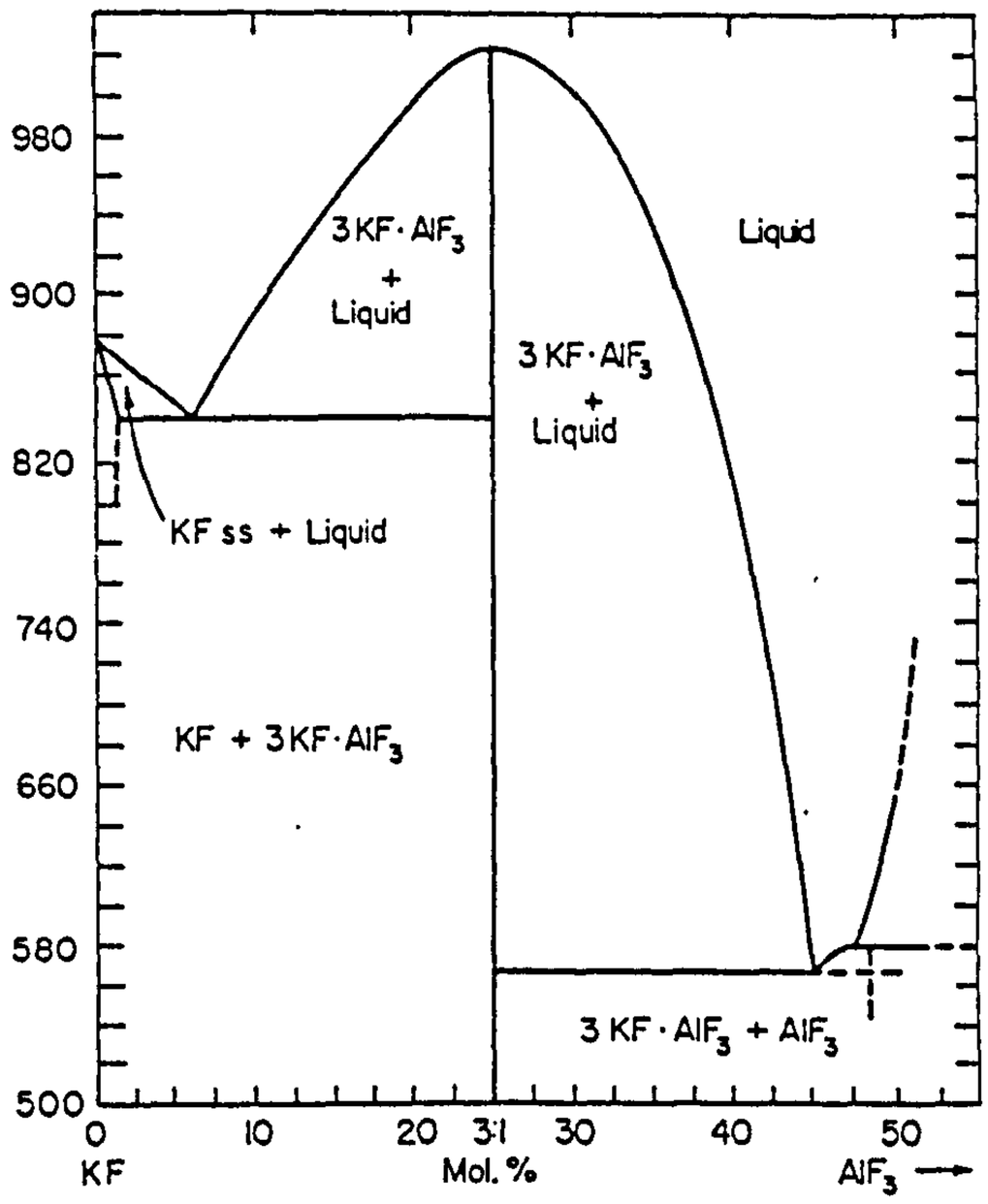

Figure 9.14 Phase diagram of KF–ALF_3 [238]

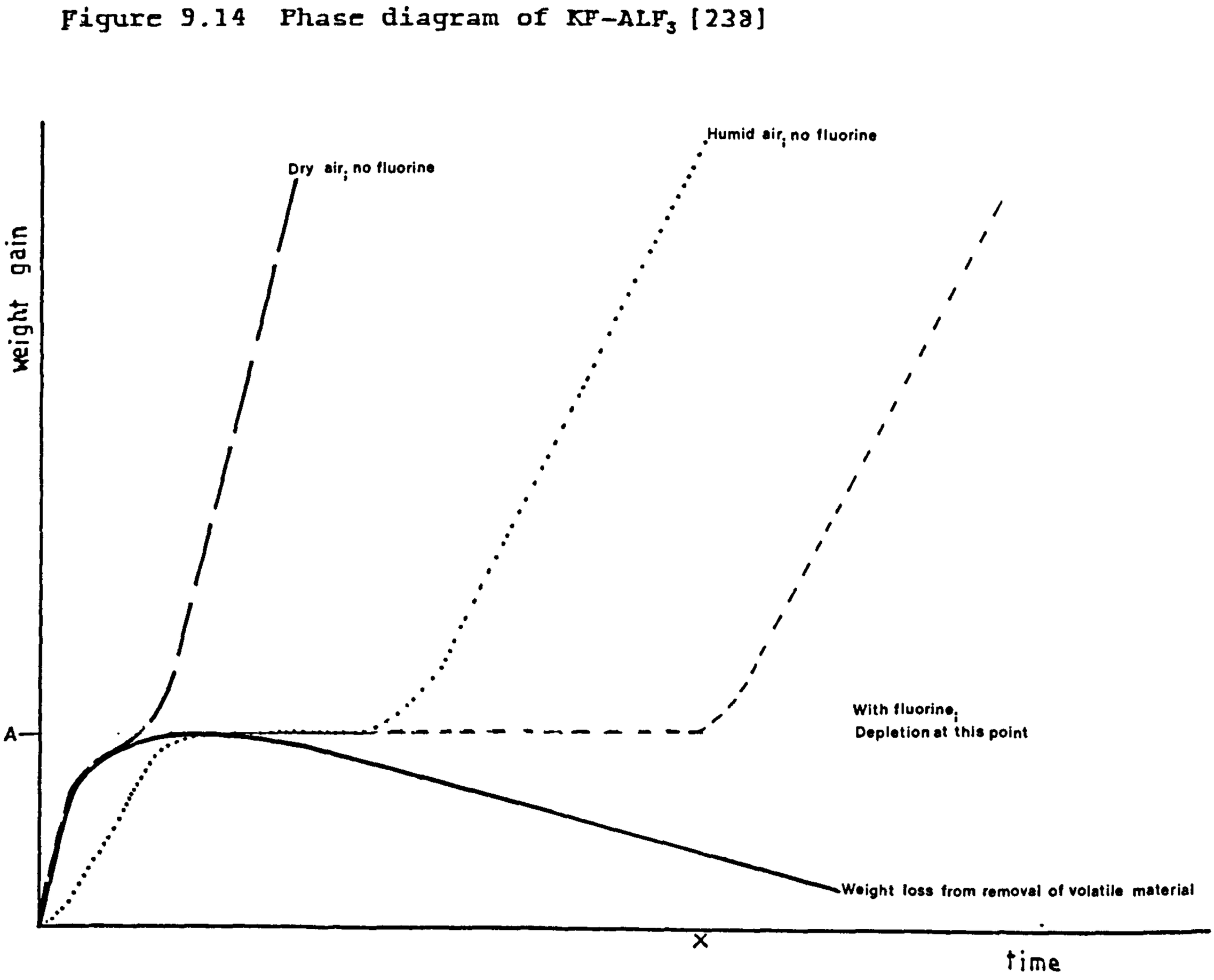

Figure 9.15 Schematic of the oxidation of molten aluminium at 750°C in the presence of fluoride

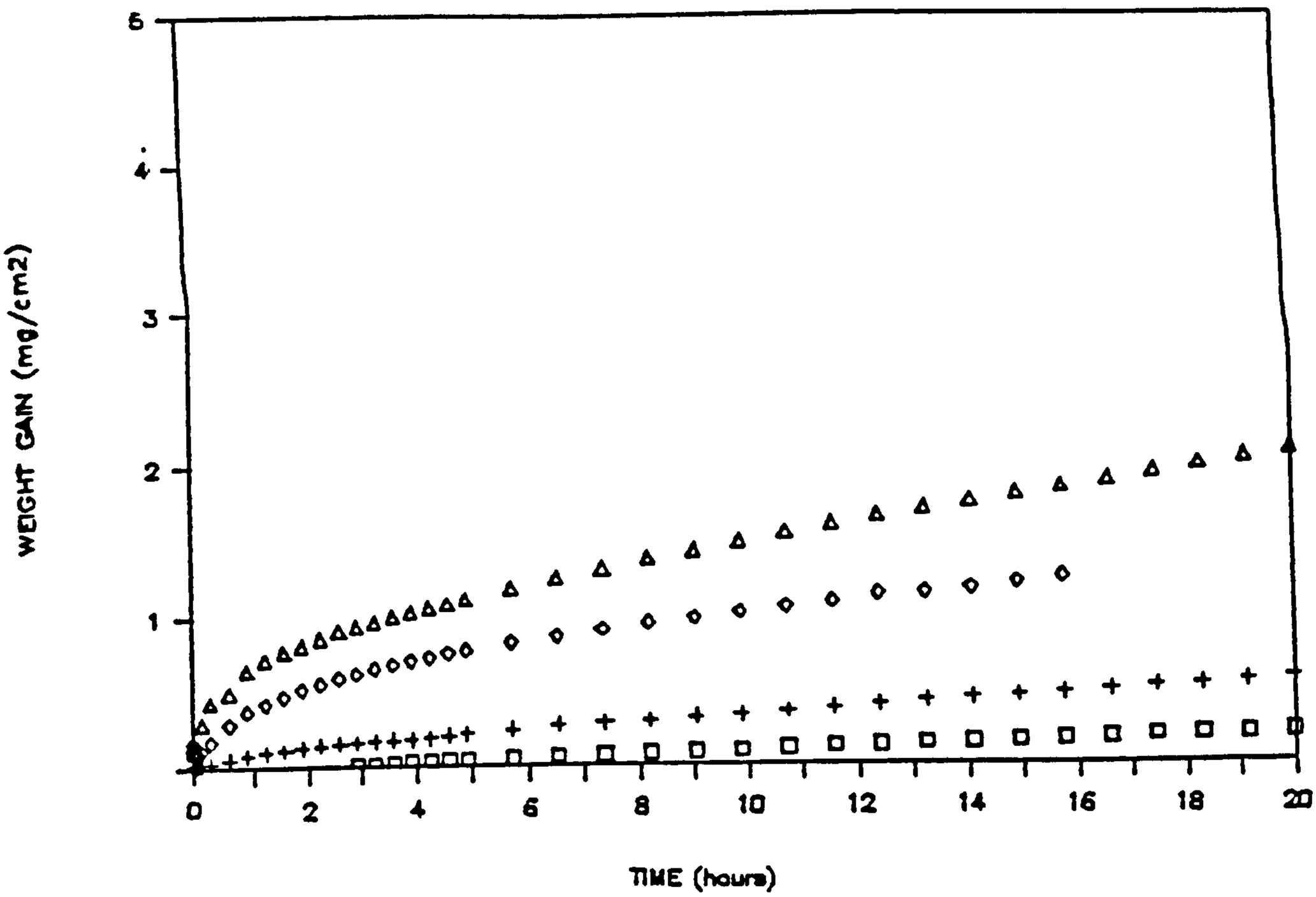

Figure 9.16 Oxidation of 5182 at 550 °C in gettered argon with increased specimen length (0.5-3mm) plotted per unit surface area

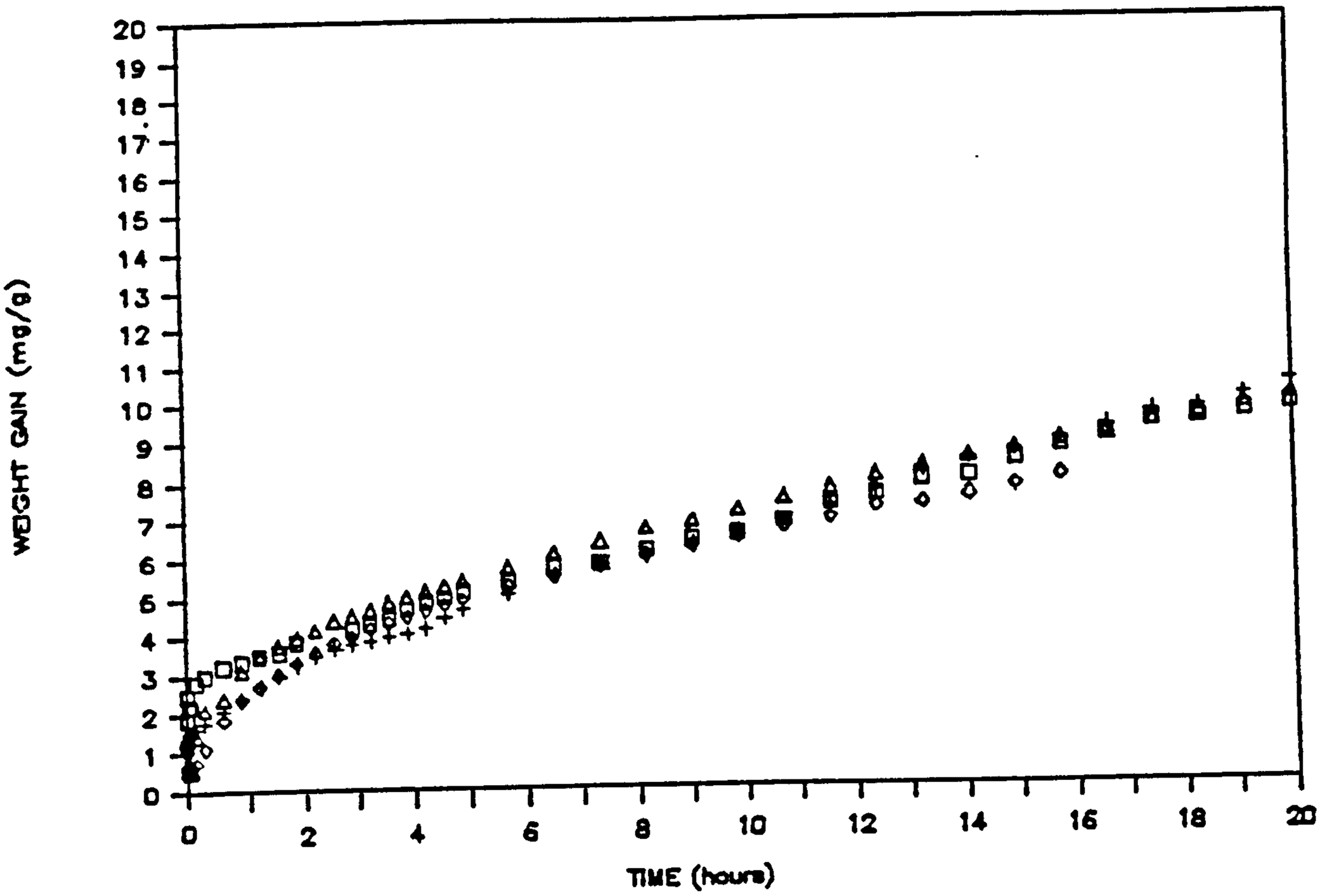

Figure 9.17 Oxidation of 5182 at 550°C in gettered argon with increased specimen length (0.5-3mm) plotted per unit weight of specimen.

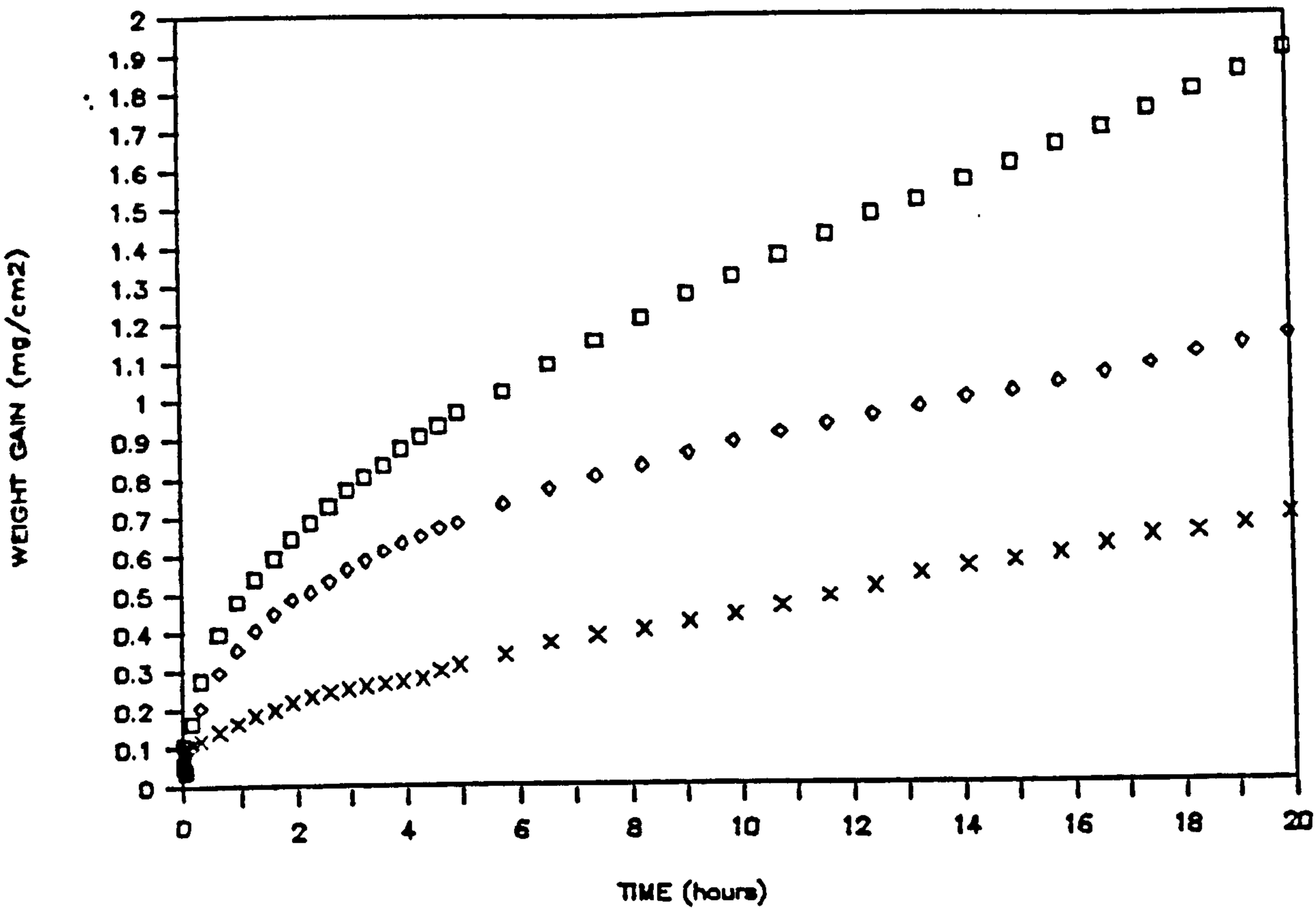

× *No plates*

◇ *One plate*

□ *Two plates*

Figure 9.18 Oxidation of 5182 at 550°C in gettered argon with surfaces covered with alumina plates, plotted per unit surface area.

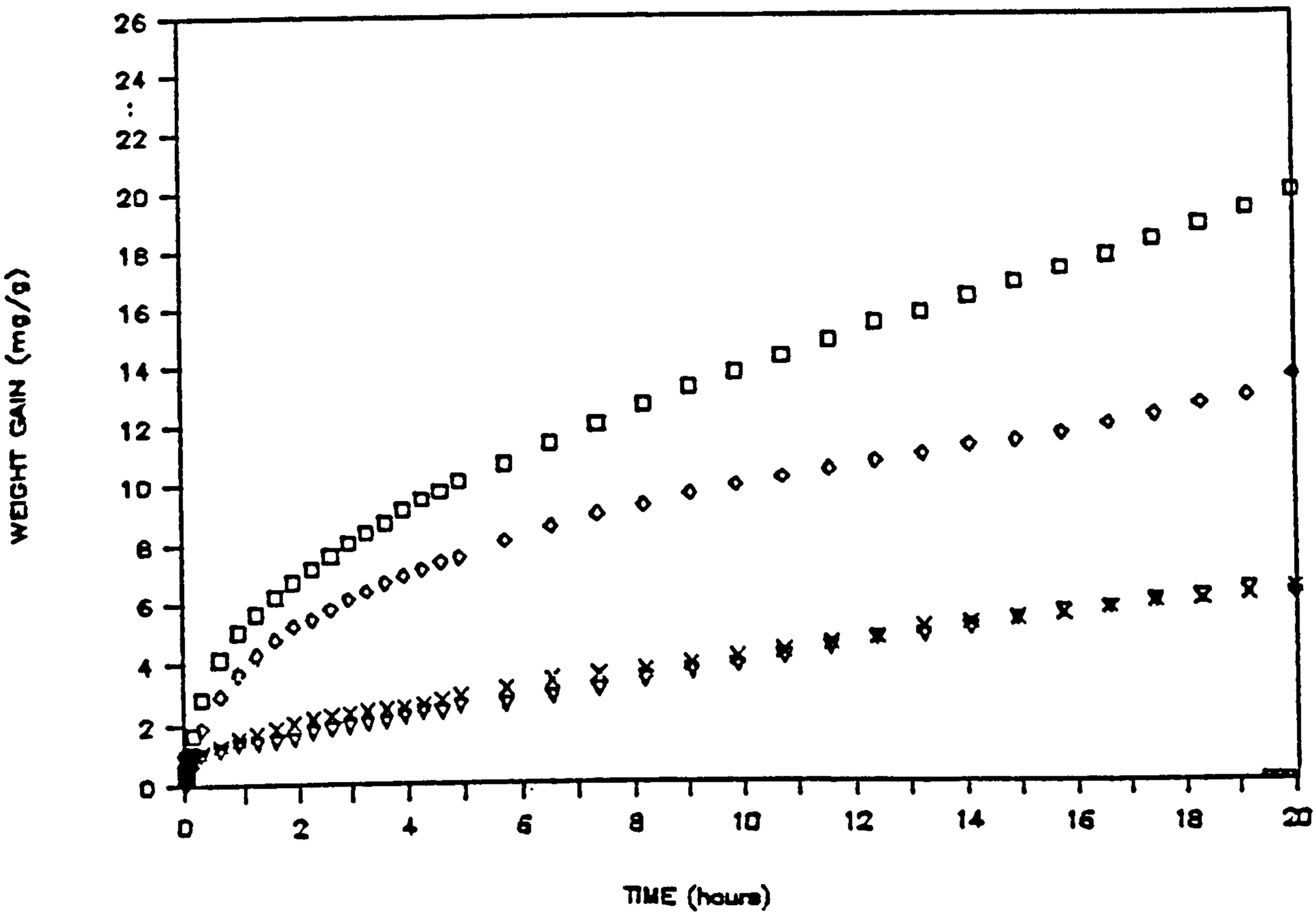

Figure 9.19 Oxidation of 5182 at 550°C in gettered argon with surfaces covered with alumina plates, plotted per unit weight of specimen.

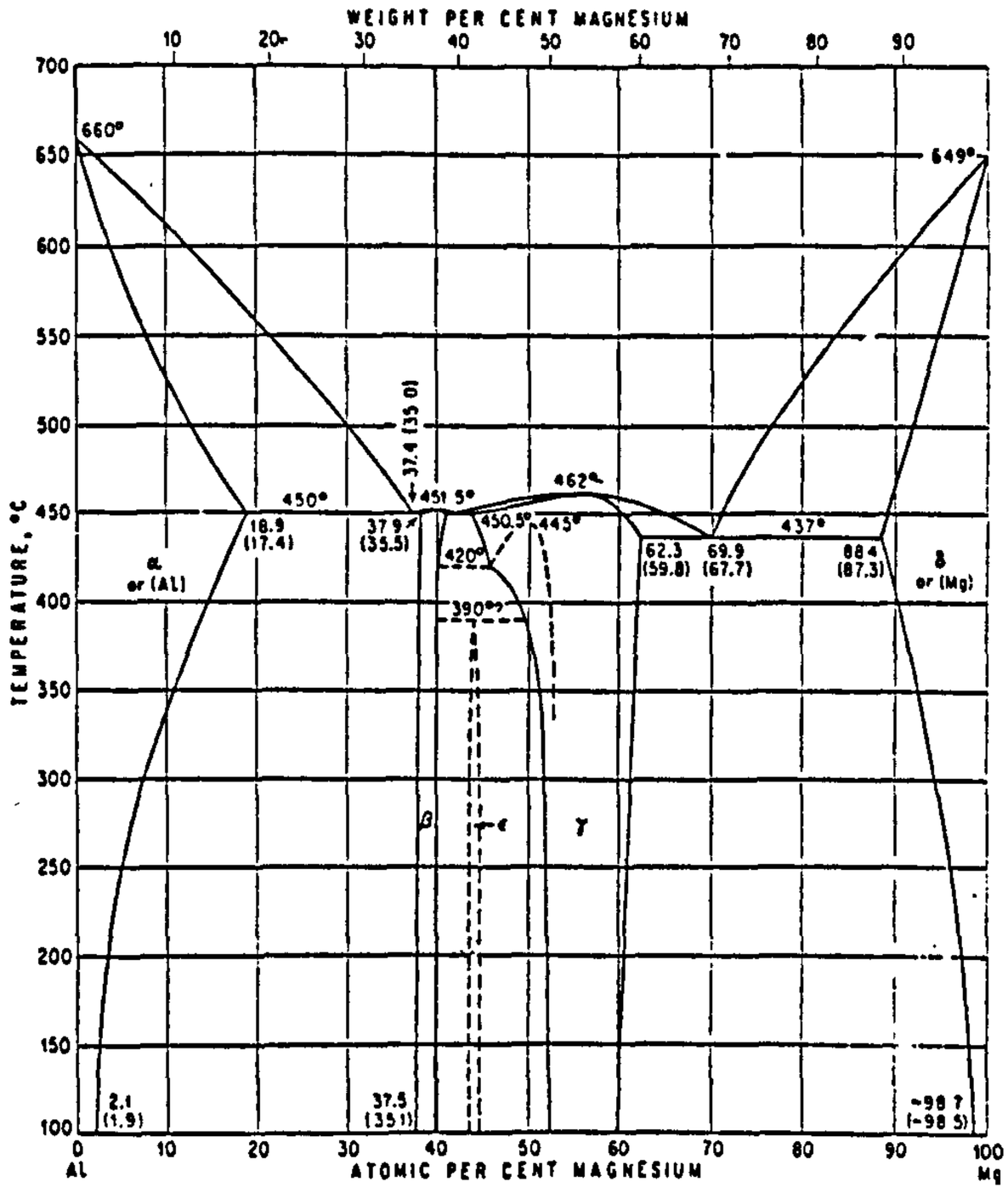

Figure 9.20 Phase diagram of aluminium – magnesium [240]

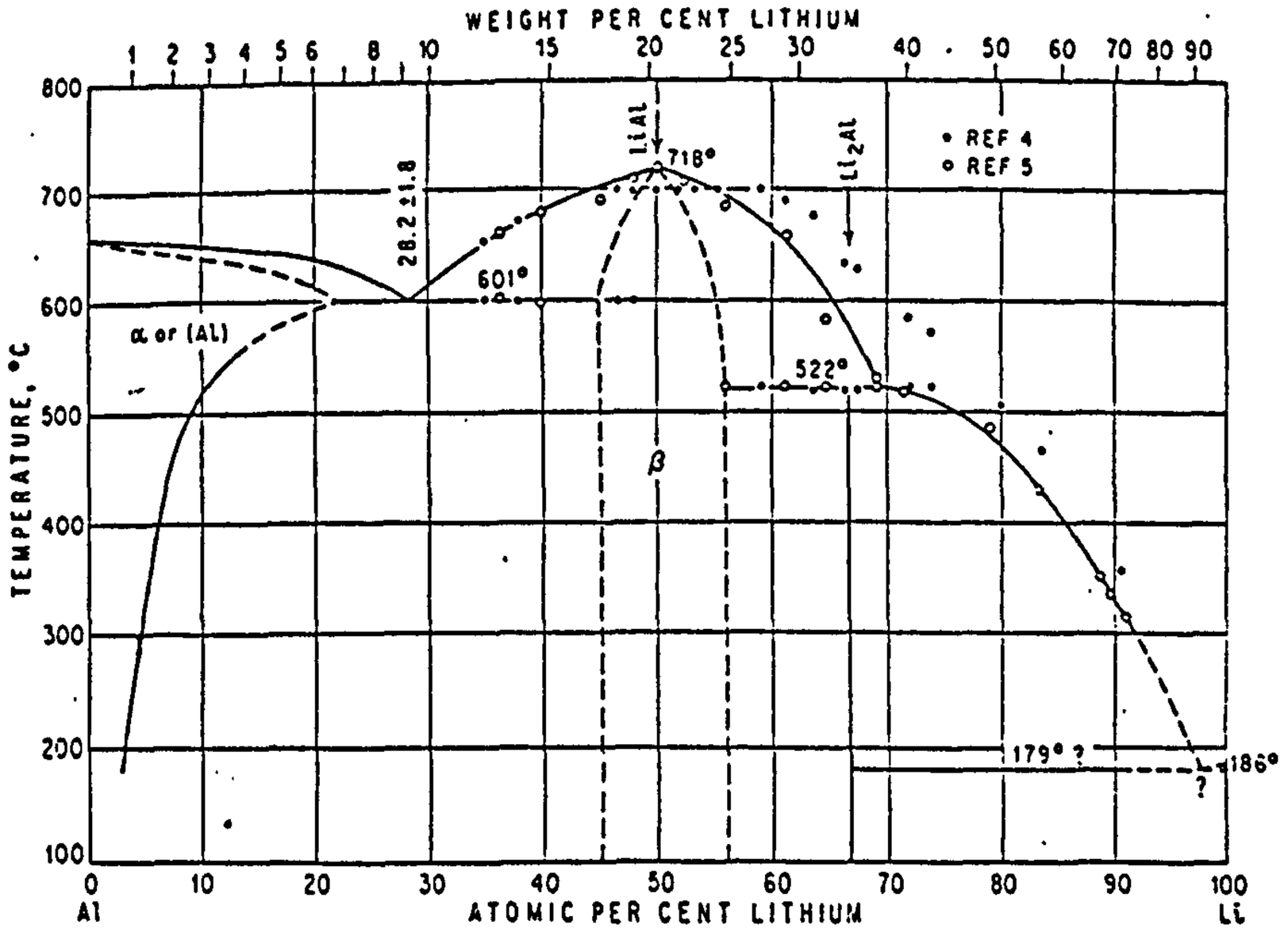

Figure 9.21 Phase diagram of aluminium – lithium [240]

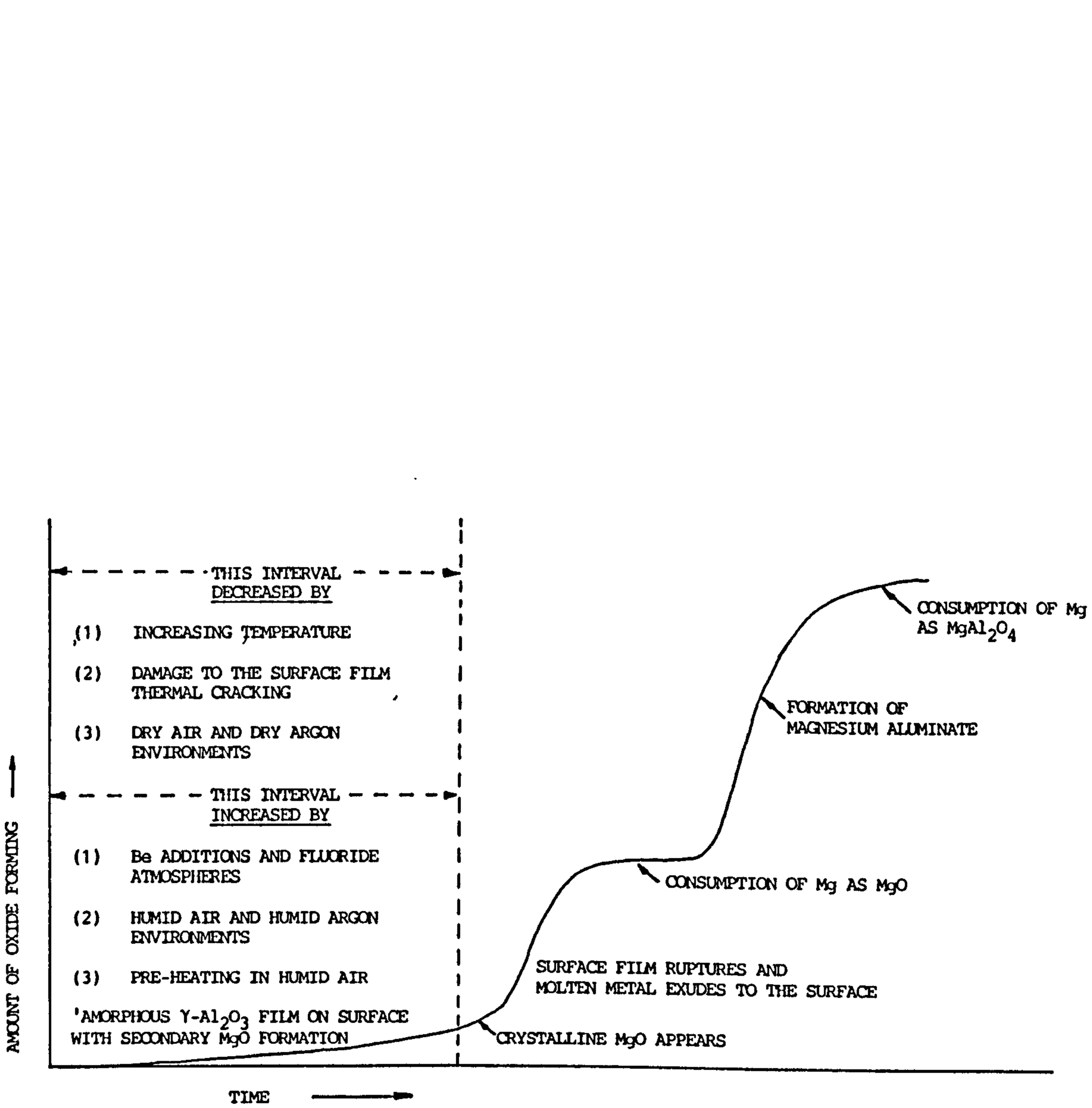

Figure 9.22 Summary of the oxidation behaviour of Al-Mg melts after Cochran et al [124]

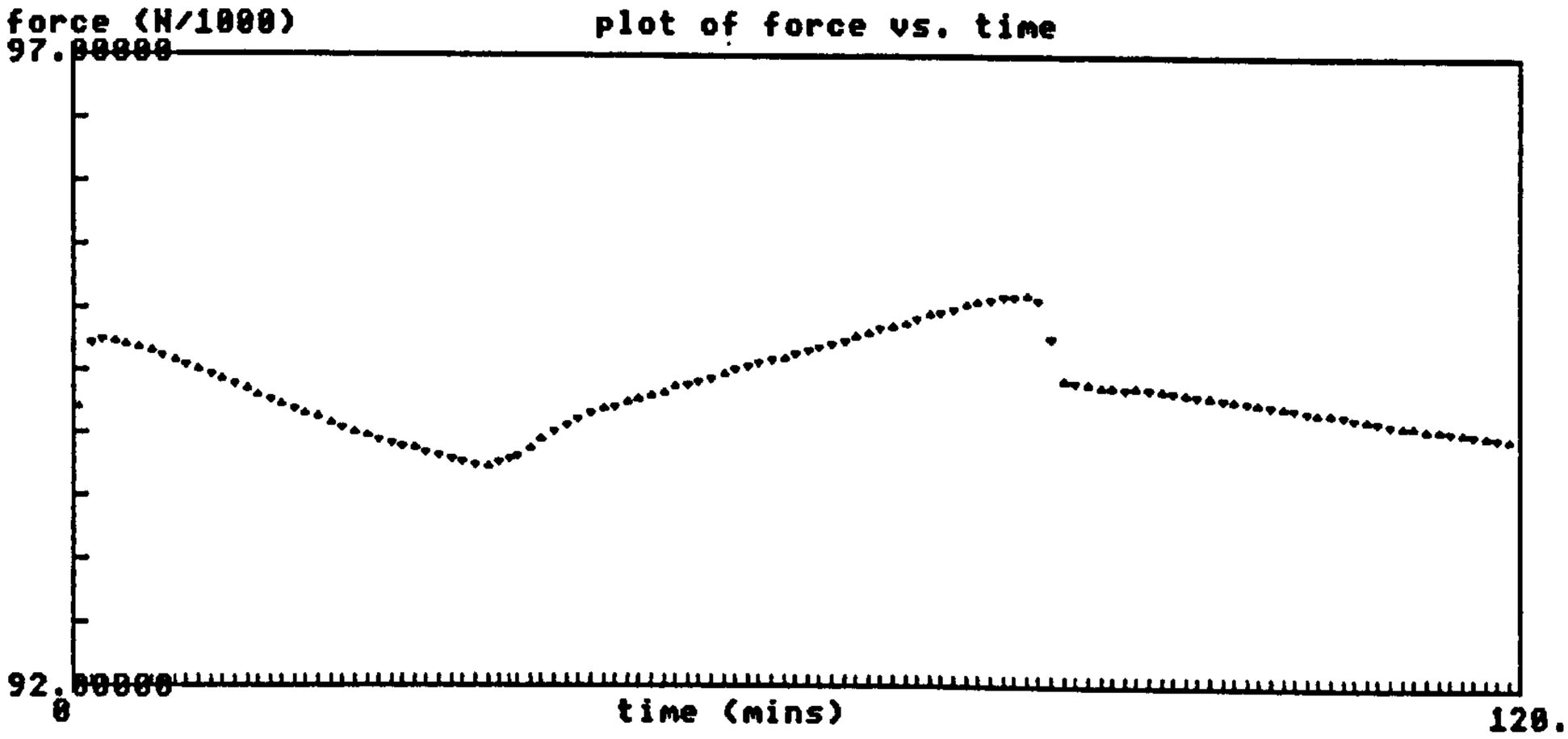

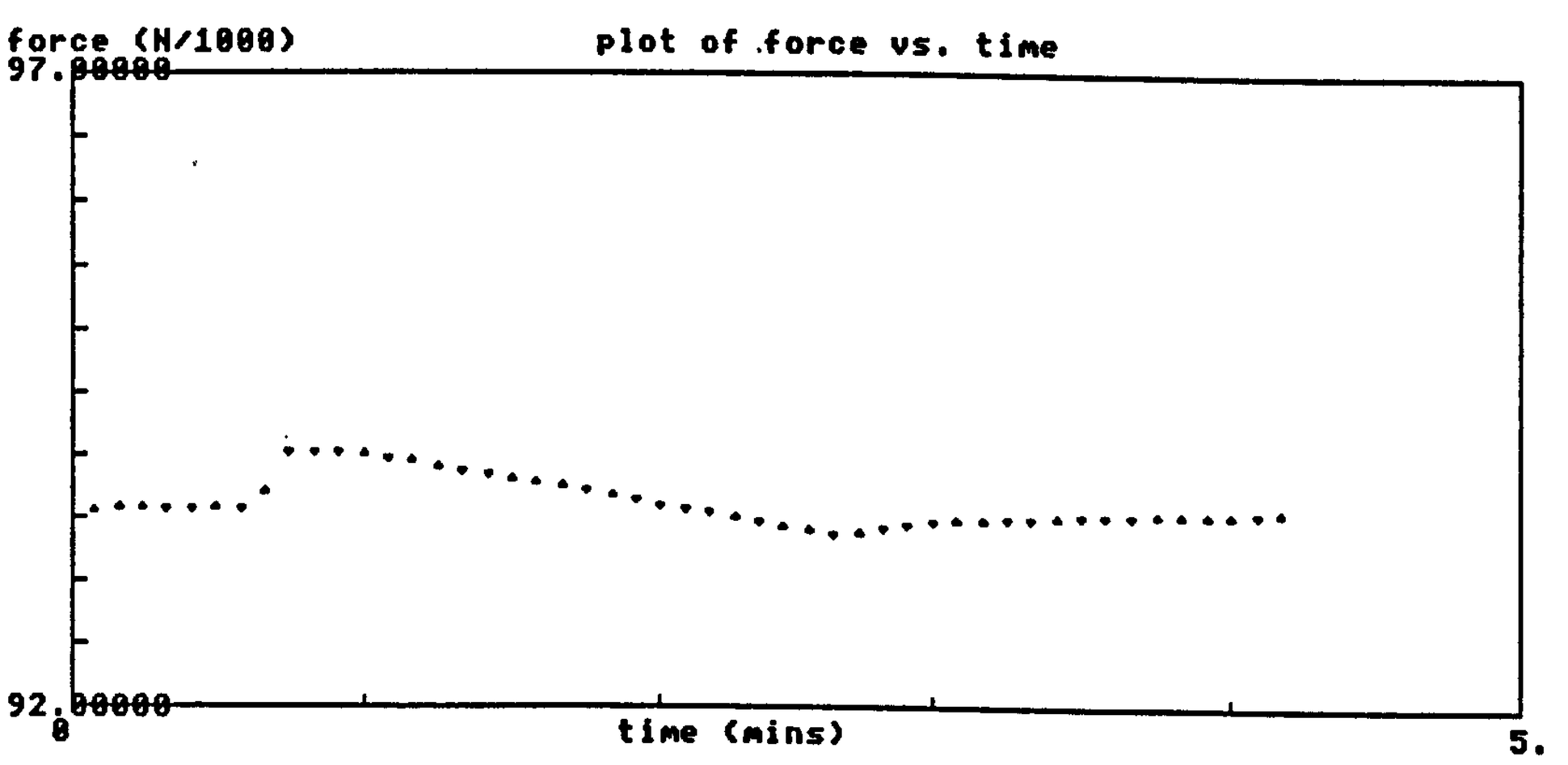

Figure 9.24 Plot of force with time for the immersion and removal of an alumina probe from water

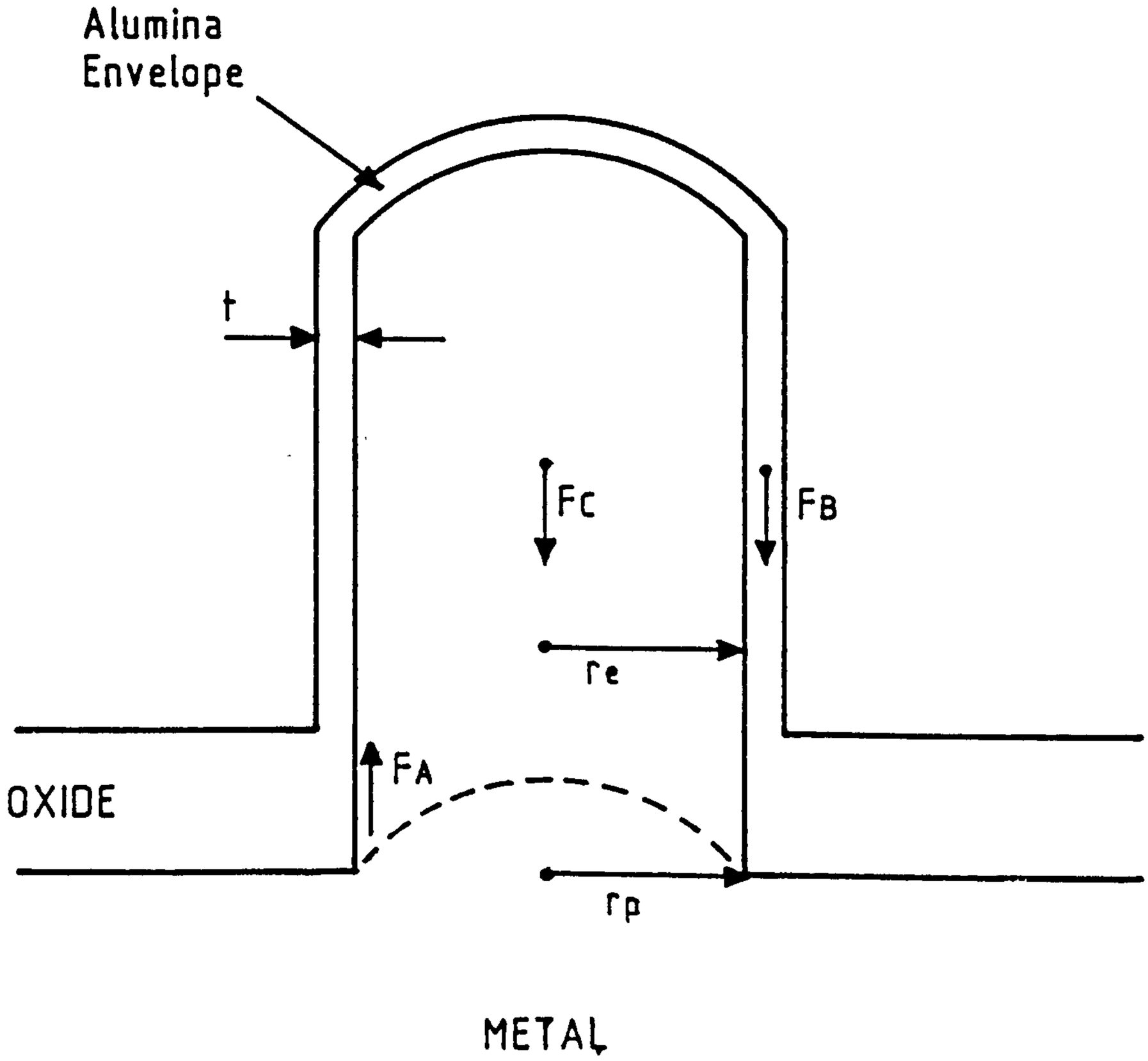

$$F_A = 2\pi\gamma . r_p$$

$$F_B = 2\pi r_e . t . \sigma_{oxide}$$

$$F_C = \rho_{AL} . \pi r_e^2 . g h_e$$

Figure 9.25 Balance of forces on an exudation at the oxide surface

Fig 3.6

Figure 9.26 Schematic of molten metal oxidation

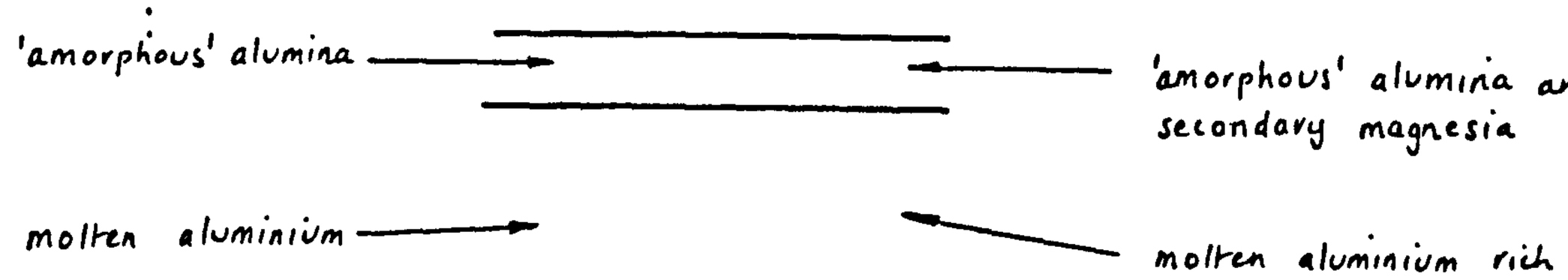

1. Thickening of the 'amorphous' film

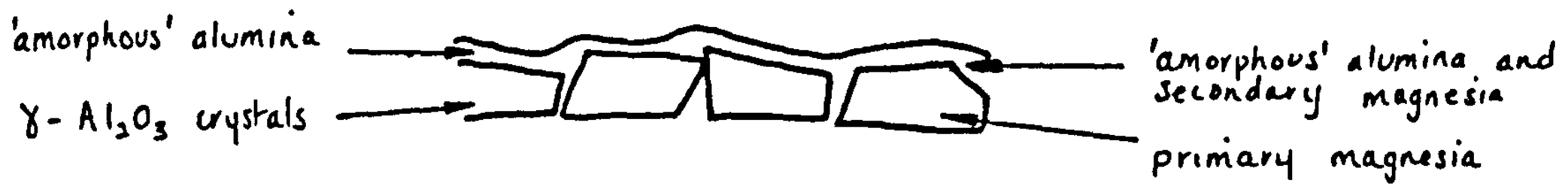

2. Growth of crystallites

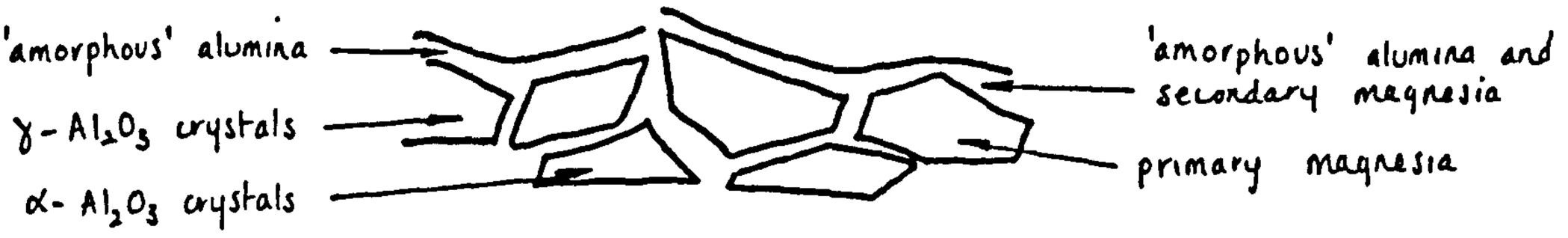

3. Oxide overlayer ruptures

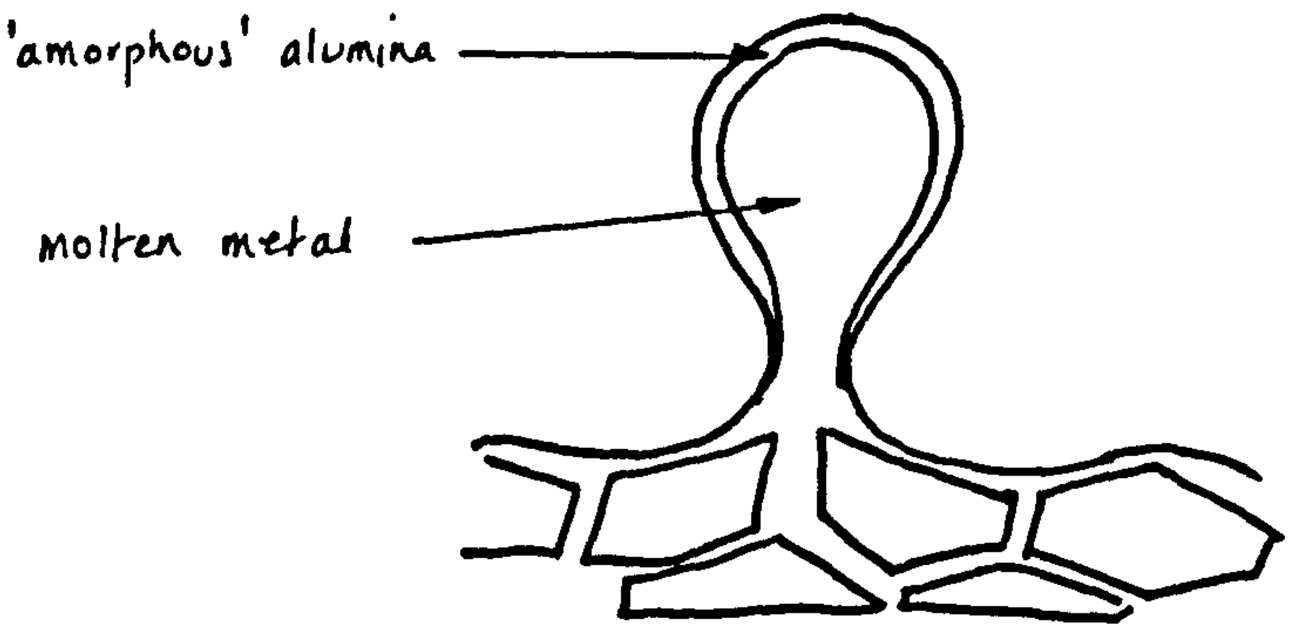

4. Exudation of molten metal

CONTINUED

Fig 3 3.6

Figure 9.26 Schematic of molten metal oxidation (cont.)

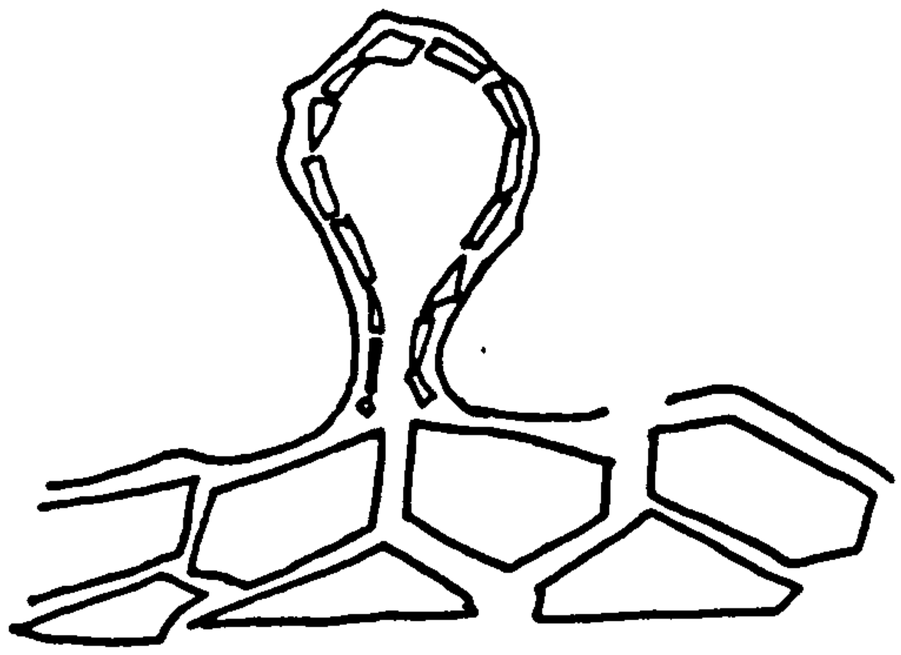

5. Growth of oxide on exudation

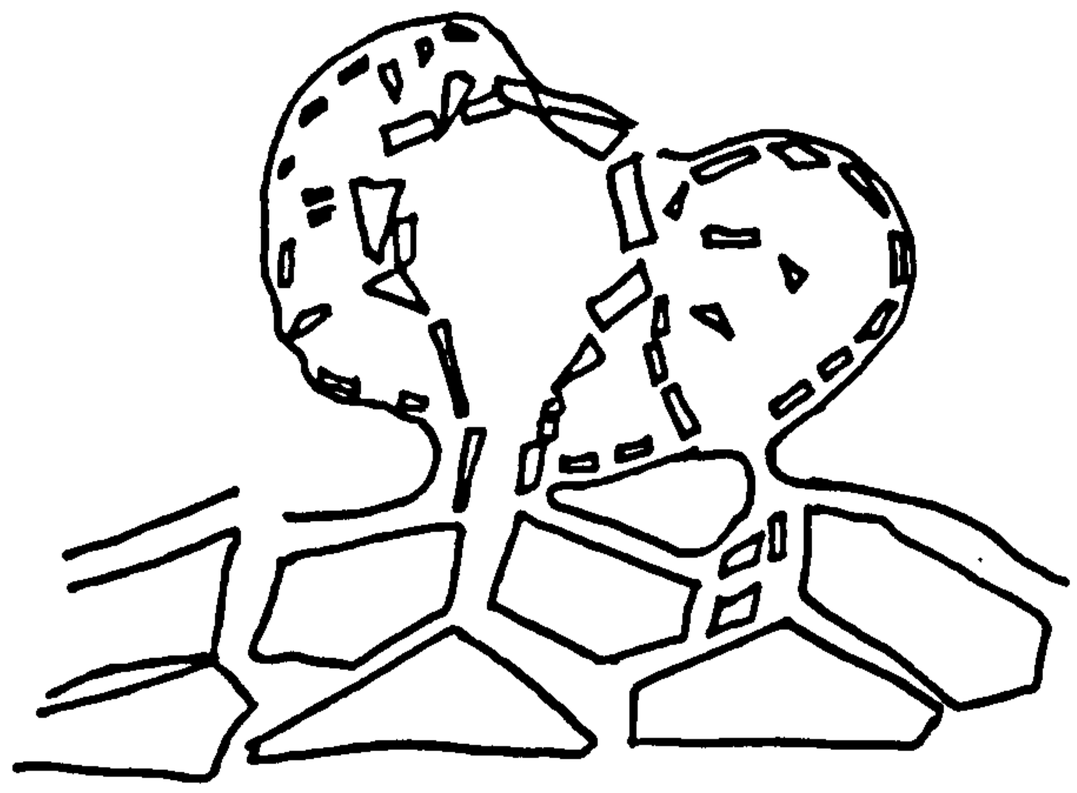

6. Secondary exudations of molten metal

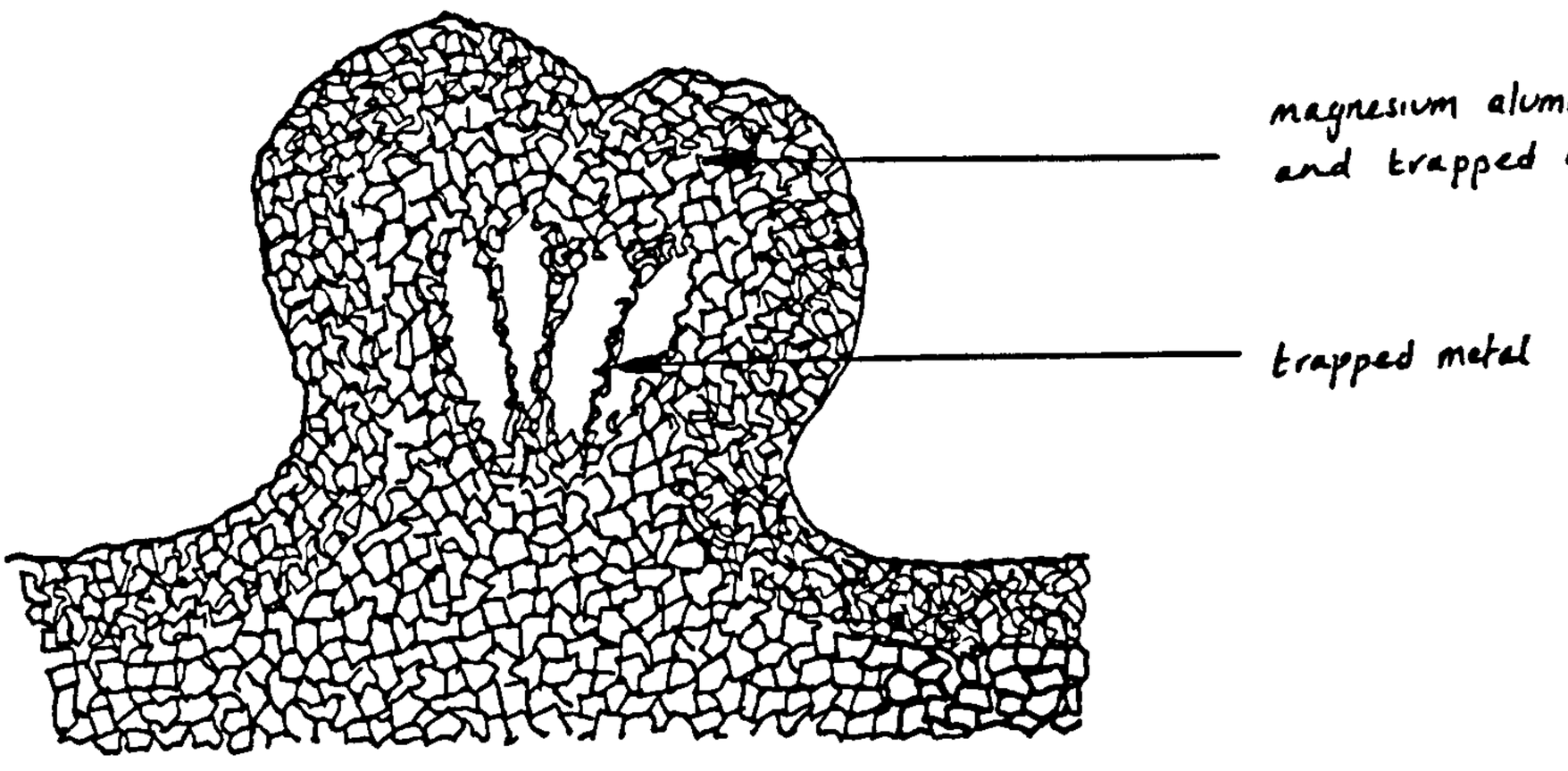

7. Consumption of trapped metal as oxide

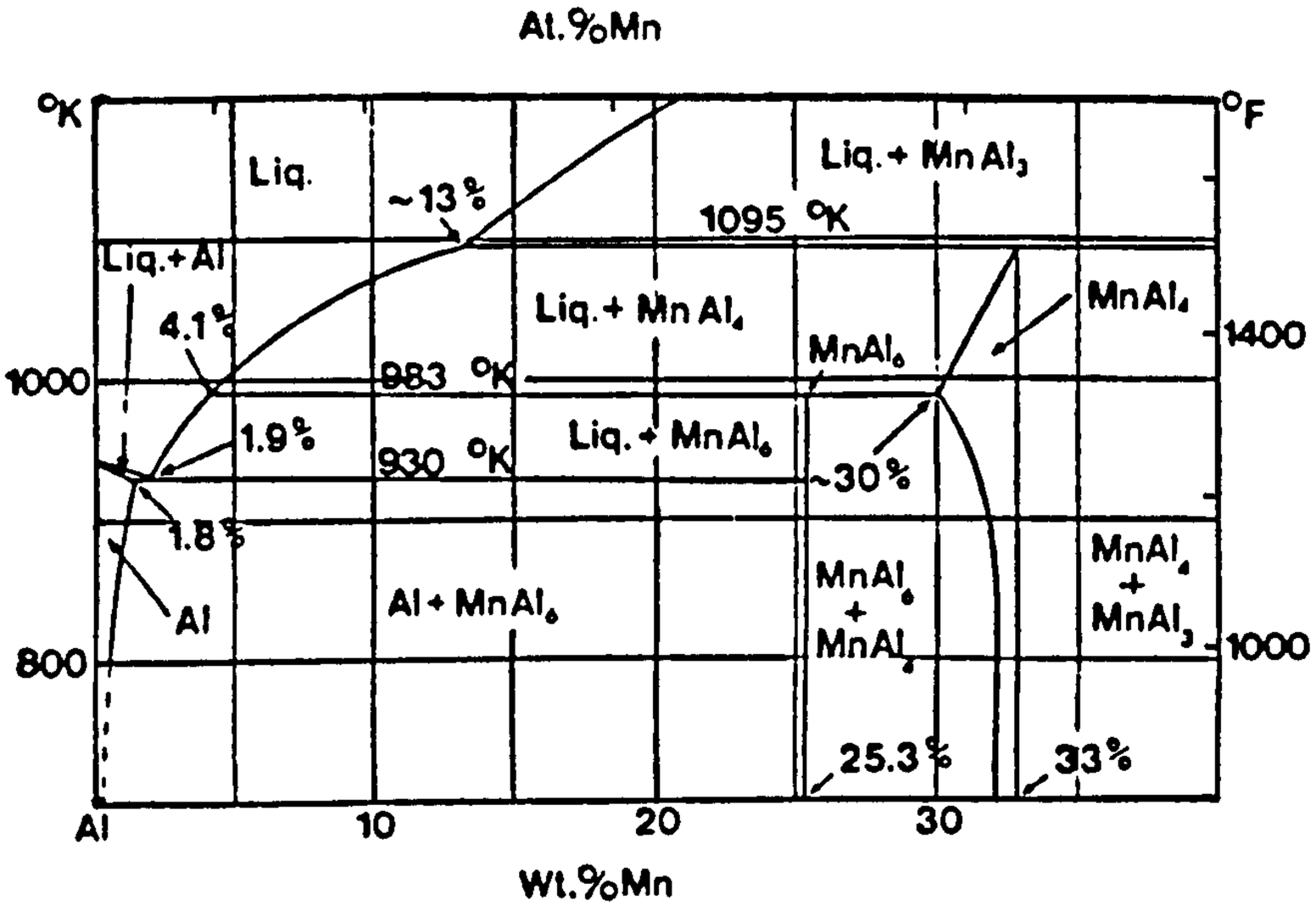

Figure 9.27 Phase diagram of aluminim-manganese [240].

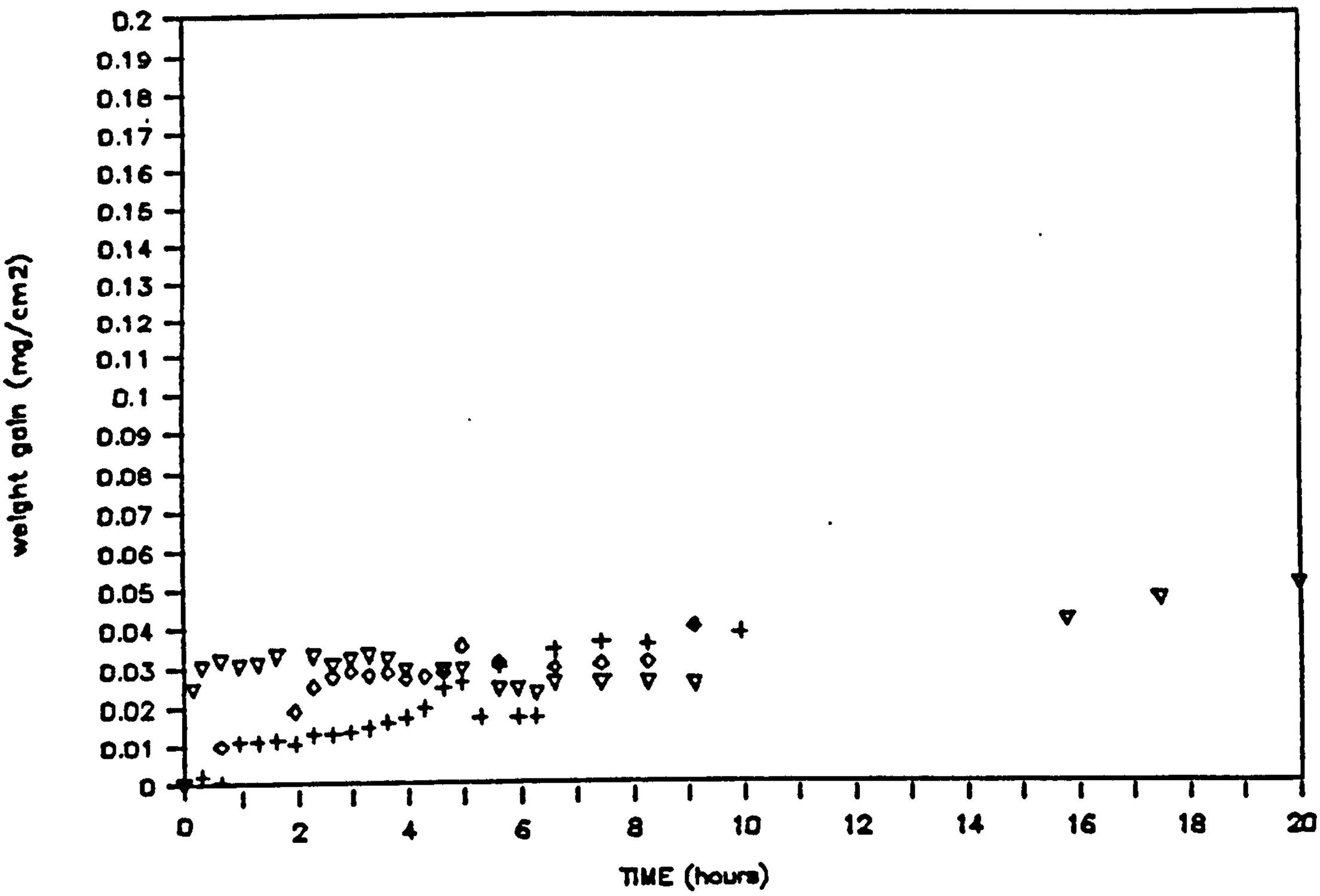

▽ *pure aluminium*

\+ *Al-1%Mn in flowing gettered argon*

◇ *Al-1%Mn in still gettered argon*

Figure 9.28 Oxidation of Al-1%Mn (3003) alloy at 750°C in gettered argon.

(a)

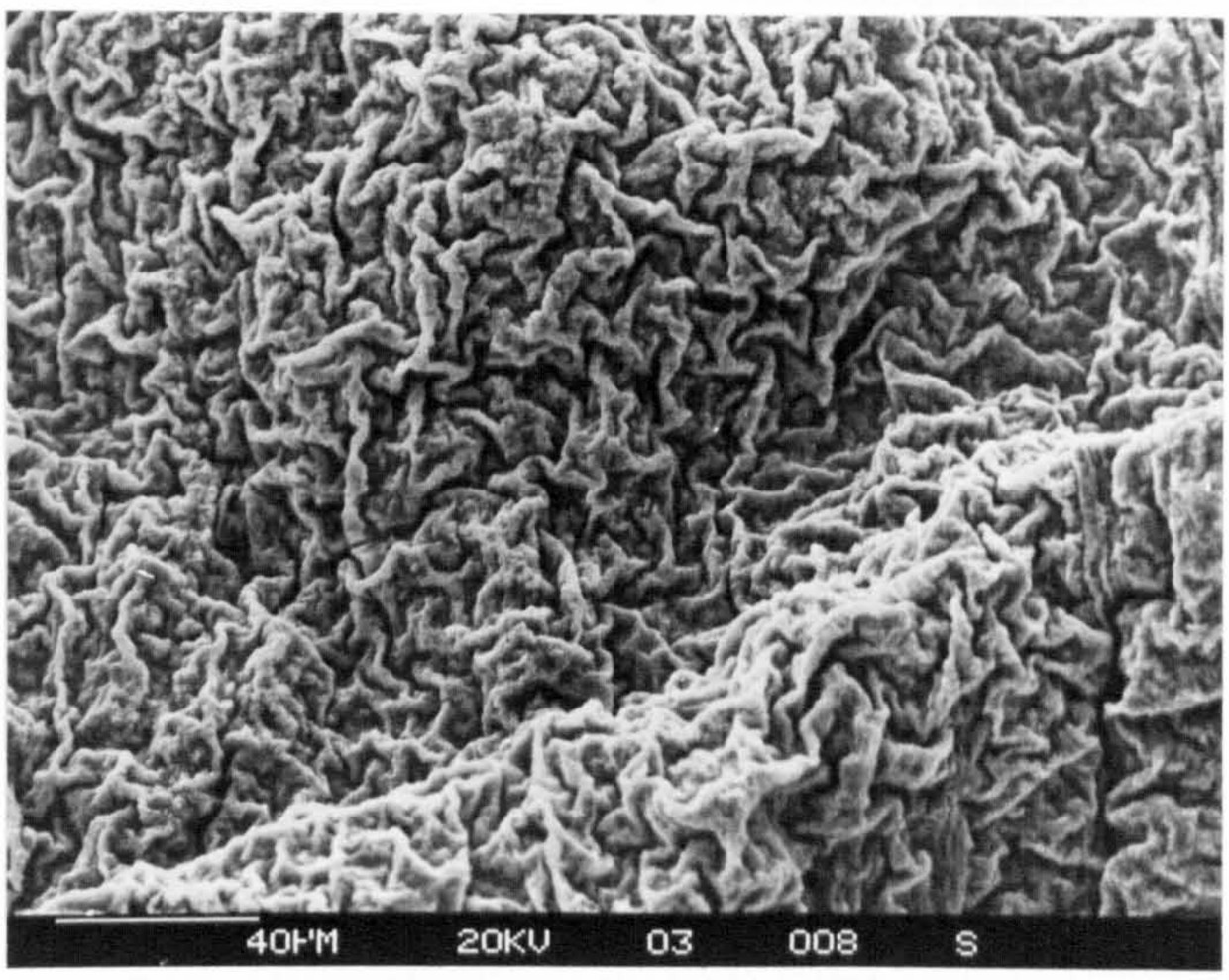

(b)

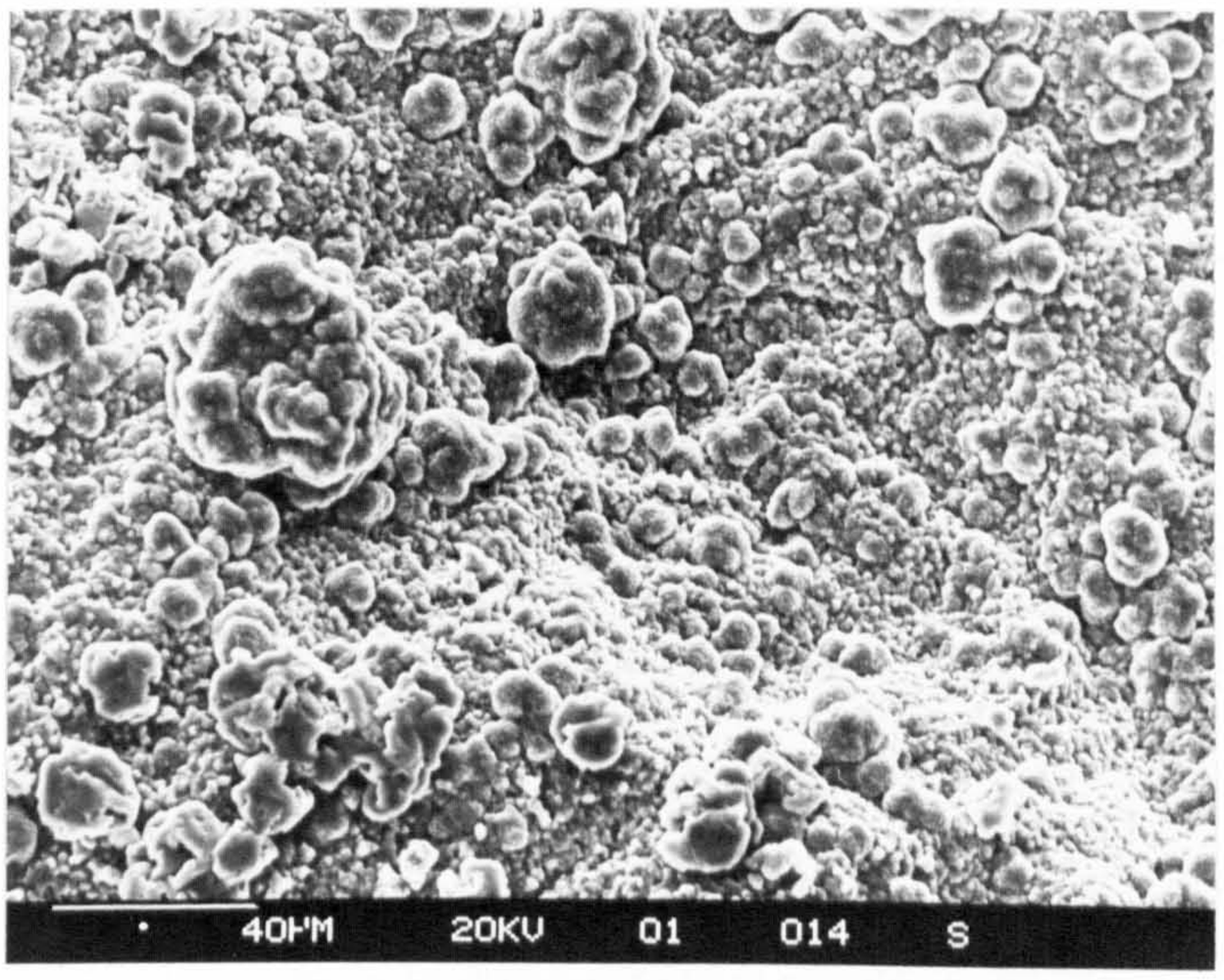

(c)

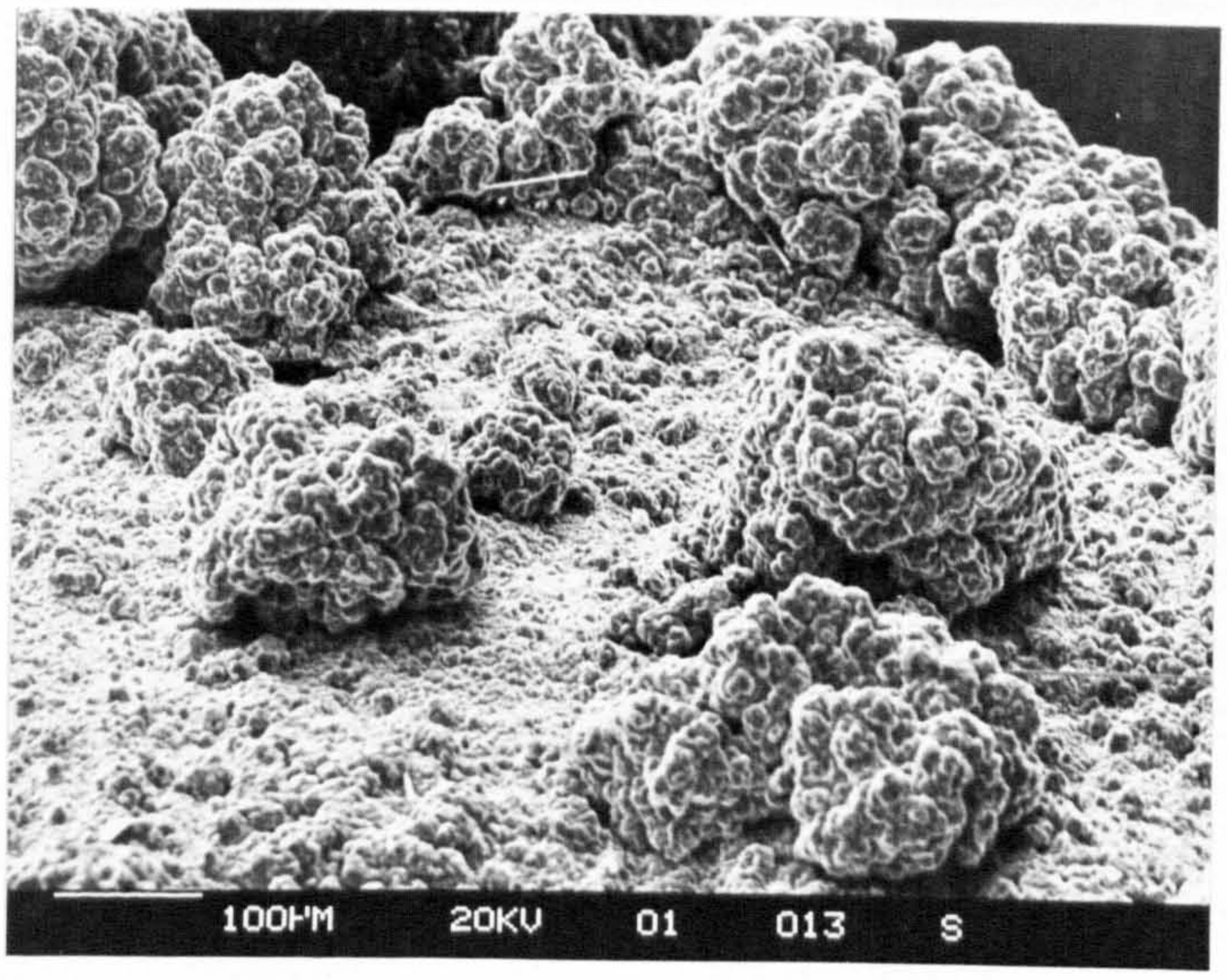

Figure 10.1 Micrographs of the surface of beverage cans after 5h oxidation in air at (a) 550°C and (b,c) 750°C

TABLE 1.1 WORLD PRODUCTION OF ALUMINIUM [2,3,4,13,17]
(thousand tonnes)

			1960	1974	1979	1981	1983	1985	1987
PRIMARY ALUMINIUM	USA		1827	4448	4557	4489	3353	3500	3343
	EUROPE		849	1981	3597	3721	3581	3598	3701
	UK		29	300	420	339	253	275	294
	TOTAL		4400	13460	14562	15108	13890	15365	16189
SECONDARY RECOVERY	USA	old scrap	240	557	758	820	850	852	
		new scrap	886	1055	1031	953	912	1134	
		cans	-	160	460	919	902	-	
		total	1126	1621	1789	1773	1762	1986	
	EUROPE		1029	1231	1327	1490	1517	1665	
	UK	secondary	189	160	141	123	122	111	
		direct use	23	27	31	33	28	33	
		total	200	187	172	156	150	144	
	TOTAL		3137	4126	4477	4685	4794	5411	
TOTAL PRODUCTION			16597	18688	19585	18575	20159	21600	

TABLE 1.2 WORLD CONSUMPTION OF ALUMINIUM [2,3,4,8,13]
(thousand tonnes)

		1974	1979	1981	1983	1985	1987
PRIMARY	USA	5128	5018	4140	4218	4324	4536
	EUROPE	3391	3837	3513	3793	3959	4238
	UK	494	418	331	323	350	384
	TOTAL	14062	15994	14497	15373	16138	-
		81	79	76	76	75	-
SECONDARY	TOTAL	3391	4359	4614	4914	5432	-
		19	21	24	24	25	-
TOTAL CONSUMPTION		17453	20353	19171	20259	21588	-

TABLE 1.3 FORECAST FOR TOTAL WORLD CONSUMPTION OF ALUMINIUM

	consumption in 1990		consumption in 1995		consumption in 2000	
	thousand tonnes	percentage	thousand tonnes	percentage	thousand tonnes	percentage
PRIMARY	18000	73	20000	70	22100	69
SECONDARY	6800	27	8700	30	11100	33
TOTAL	24800		28700		33200	

TABLE 2.1 COMPOSITIONS OF WROUGHT ALUMINIUM ALLOYS IN CURRENT USE [21,27]

ALLOY	Mg	Mn	Si	Fe	Cu	Zn	Cr	Melting Range(oC)
CARS								
Type 1	1.0	0.2	5.0	1.0	1.0	0.5	0.15	538-636
Type 2	2.5	0.2	1.0	1.0	1.0	2.5	0.15	565-642
CANS								
3004(body)	1.0	1.0	0.3	0.7	0.25	0.25	-	
5182(end)	4.5	0.4	0.2	0.35	0.15	0.25	0.1	579-641
SHEET								
auto 6003	1.2	0.15	0.5	0.7	0.25	0.25	0.2	
5252	2.5	0.1	0.08	0.1	0.1	0.05	-	
aero 2024	1.5	0.5	0.5	0.5	4.0	0.25	0.1	549-646
7010	2.4	0.1	0.12	0.15	1.7	6.2	0.05	
7178	2.8	0.1	0.15	0.20	2.0	6.8	0.3	
PLANT (General purpose)								
3003	1.0	1.2	0.6	0.7	0.1	0.1	-	
5005	1.0	0.2	0.3	0.7	0.2	0.25	0.1	
5251	2.4	0.3	0.4	0.5	0.15	0.15	0.2	
5083	4.5	0.7	0.4	0.4	0.1	0.25	0.2	
6061	1.0	0.15	0.6	0.7	0.25	0.25	0.2	
6063	0.65	0.1	0.4	0.3	0.1	0.1	0.1	
6351	0.6	0.6	1.0					

TABLE 2.2 COMPOSITIONS OF SOME COMMON FOUNDRY CASTING ALLOYS [13,26]

	Mg	Mn	Si	Fe	Cu	Zn
LM 2	0.3	0.5	9.0-11.5	1.0	0.7-2.5	2.0
LM 24	0.1	0.5	7.5- 9.5	1.3	3.0-4.0	3.0
LM 4	0.15	0.2-0.6	4.0- 6.0	0.8	2.0-4.0	0.5
LM 21	0.1-0.3	0.2-0.6	5.0- 7.0	1.0	3.0-5.0	2.0
LM 27	0.3	0.2-0.6	6.0- 8.0	0.8	1.5-2.5	1.0
LM 6	0.1	0.5	10.0-13.0	0.6	0.1	0.1
LM 20	0.2-0.6	0.5	10.0-13.0	1.0	0.4	0.2
Type 380	0.1	0,5	7.5-9.5	1.0	3.0-4.0	1.0
(with	Sn 0.1-0.2;	Pb 0.1-0.3;	Ni 0.1-0.5;	Ti 0.2)		

	Fuel Fired Reverberatory [9,37,43]		Electric Reverberatory [37]	Fuel Fired Crucibles	Electric Crucibles [38,39,40]	Electric Induction Medium Frequency Channel	Coreless	High Frequency [24]
Capacity-(tonnes)	large	20-90	0.5-8	0.02-0.9	1-15	0.3-1.5	0.15-3	0.1-0.5 tilt
	small	1-10			0.5			0.02-0.05 lift
Efficiency-(%)	fuel	18-30	10-15	25		90-95	65-75	
	thermal	37		15-30	45-55	70-75	90-95	
						60-75	50-70	55-65
Melting-Speed (t/hr)	large	5-9	11-13				6	
	small	0.5-2.5		0.05-0.7	0.15	0.05-0.5	0.12-1.6	
		0.05*		0.1*	0.1*			
Metal Losses (%)		3-15	0.5-3		1-2.5	2-6	0.5-5.9	

* from cold

TABLE 2.3 Comparison of Furnace Characteristics [36]

TABLE 2.5 COMPOSITION OF GAS AND OIL FURNACE FUELS [27,36]

Gas

(%)	N_2	O_2	Ar	CO_2	CH_4	C_2H_6	C_3H_8	C_4H_9
Air	78.9	20.95	0.93	0.03				
Natural Gas	1.5			0.2	94.5	3.0	0.5	0.2
Dutch N. Gas	14.2			0.9	81.3	2.9	0.4	0.1
Propane						1.5	91.0	2.5
Butane					0.1	0.5	7.2	87.0

Typical Light Fuel Composition [27,36]

(%)	C	H	S	O + N	*
Gas Oil	85.7	13.4	0.3-0.9		14.80
Light Fuel Oil	85.5	11.5	1.1-3.0	0.7	13.88
Medium Fuel Oil	85.3	11.2	1.4-3.5	0.8	13.78
Heavy Fuel Oil	85.1	10.9	1.9-4.0	0.9	13.68

* Dry air required for stoichiometric combustion
(unit mass of fuel Kg:Kg)

TABLE 3.1 Structural properties of oxides and hydroxides of aluminium [57]

	Phase	Formula	Crystal System	Space Group	Molecules Per Unit Cell	Unit Axis Length, nm a	b	c	Angle	Density g/cm^3
Aluminium Trihydroxides	Gibbsite	$Al(OH)_3$	Monoclinic	C_{2h}^5	4	0.8684	0.5078	0.9136	94° 34'	2.42
	Gibbsite	$Al(OH)_3$	Triclinic	-	16	1.733	1.008	0.973	94° 10' 92° 08' 90° 0'	-
	Bayerite	$Al(OH)_3$	Monoclinic	C_{2h}^5	2	0.5062	0.8671	0.4713	90° 27'	2.53
	Nordstrandite	$Al(OH)_3$	Triclinic	C	2	0.5114	0.5082	0.5127	70° 16' 74° 0' 58° 28'	-
Aluminium Oxide Hydroxide	Boehmite	A100H	Orthohombic	D_{2h}^{17}	2	0.2868	0.1223	0.3692	-	3.01
	Diaspore	A100H	Orthorhombic	D_{2h}^{16}	2	0.4396	0.9426	0.2844	-	3.44
	Tchdite $5Al_2O_3-H_2O$		Hexagonal	C_{6V}^4	1	0.5576	-	0.8768	-	3.72
Aluminium Oxide	Gamma γ	Al_2O_3	Tetragonal	-	-	.562	.780	-	-	3.2
	Delta δ	Al_2O_3	Orthorhombic	-	12	.425	1.275	1.021	-	3.2
	Eta η	Al_2O_3	Cubic spinel	O_h^7	10	.790	-	-	-	2.5-
	Theta θ	Al_2O_3	Monoclinic	C_{2h}^3	4	1.124	.572	1.174	103° 20'	3.56
	Chi χ	Al_2O_3	Cubic Hexagonal Hexagonal	- - -	10 - -	.795 .556 .557	- - -	- 1.344 8.64	- -	3.0 - -
	Kappa κ	Al_2O_3	Hexagonal Hexagonal Hexagonal	- - -	28 - -	9.71 9.70 1.678	- - -	.1786 .1786 .1786	- - -	3.1-3.3 - -
	Iota ι	Al_2O_3	Orthorhombic Orthorhombic	- D_{2h}^9 or C_{2V}^8	4 3	.773 .759	.778 .767	.292 .287	-- -	3.17 3.0
	Corundum α	Al_2O_3	Hexagonal (Rhombohedral)	D_{3d}^6 ($R\bar{3}C$)	2	0.4759	-	1.2992	-	3.98

TABLE 5.1 Analysis of materials used in this work

Material	Nominal Composition	Composition (wt%)								
		Si	Fe	Cu	Mn	Mg	Cr	Zn	Ti	B
Al	Al	<.001	.32	-	<.001	<.001	-	.015	.004	-
3003	Al-1Mn	.60	.70	.10	1.20					
3004	Al-1Mn-1Mg	.10	.24	.008	1.21	.94	<0.01	.01	.006	<.001
3004GR	Al-1Mn-1Mg	.10	.22	.008	1.20	.95	<0.01	.01	.014	.002
5005	Al-1Mg	.02	.16	<.001	.002	.87	<.01	<.01	.003	<.001
5005GR	Al-1Mg	.02	.15	<.001	.002	.87	<.01	<.01	.003	.005
5182GR	Al-5Mg	.10	.25	.004	.30	5.0	.08	.02	.016	.002
5182	Al-5Mg	.10	.14	-	.36	4.55	-	.016	.001	<.001
5182GR	Al-5Mg	.08	.19	-	.34	4.54	-	.017	.013	.003
5182	Al-5Mg+Be (10ppm)	.08	.14	-	.35	4.69	-	.015	.001	<.001
5182GR	Al-5Mg+Be (10ppm)	.09	.14	-	.35	4.70	-	.015	.013	.002
5182	Al-5Mg+Be (50ppm)	.08	.14	-	.35	4.60	-	.015	.013	<.001
5182GR	Al-5Mg+Be (50ppm)	.09	.14	-	.35	4.60	-	.015	.013	.002

TABLE 6.1 Summary of kinetic data - Principal reaction during rates exhibited and duration in each regime for molten aluminium specimens at 750°C

Environment	surface finish	Time in hours from melt a logarithmic/cubic n=2.72-3	b linear n=1	c parabolic n=2	d linear n=1
Humid Argon	machined polished electropolished	0 — 15	15 — 20	not achieved during test	not achieved during test
Dry Air	machined polished electropolished	c. during heat up	0 — 20	not achieved	not achieved
		s. during heat up	0 — 5	5 — 20	not achieved
		c. during heat up	0 — 5	5 — 20	not achieved
		s. during heat up	0 — 2	2 — 15	15 — 20
Gettered Argon	machined polished electropolished	c. during heat up	0 — 5	5 — 20	not achieved
		s. during heat up	0 — 1	1 — 10	10 — 20
		c. during heat up	during heat up	0 — 5	5 — 20
		s. during heat up	during heat up	0 — 1	1 — 20

KEY

c. Circulating environment
s. Static environment

TABLE 9.4 Reported and calculated values of the fracture stress of aluminium and magnesium oxides

Oxide	Oxide Fracture Stress σ_f (MPa)	Calculated Oxide Fracture Stress σ_f (MPa)	Reference
Thin film Al_2O_3	206-700	154-162	265
	200-310		251
	300-500		257
Thin Film MgO	140	150-158	257
	138		265
Bulk oxide MgO		798	

TABLE 9.5 The surface energy of aluminium and magnesium oxides

Oxide	Temperature °C	$\gamma_{oxide-air}$ Nm^{-1}	Reference
Al_2O_3	750	1.510	253
Al_2O_3	800	1.716	259
Al_2O_3(s)	750	0.93	267
MgO (s)	750	1.365-2.113	267
MgO	20	1.63	271
MgO	20	0.75-5.0	257
MgO	-196	1.2	272
$MgAl_2O_4$	750	1.878-2.41	267

TABLE 9.6 Surface tension values of molten metal

Material	Year	Technique	Atmosphere	γNm^{-1}	Reference
99.99%Al	1970	sessile drop	vacuum	0.760	175
99.997%Al	1974	sessile drop	vacuum	0.788	266
99.99%Al	1974	sessile drop	vacuum	0.860	263
99.999%Al	1979	sessile drop	vacuum	0.865	268
99.999%Al	1982	sessile drop	vacuum	1.050	200
99.999%Al	1986	max bubble	Argon	1.100	186
Al-0.8%Mg	1986	max bubble	Argon	0.856	186
Al-5.0%Mg	1986	max bubble	Argon	0.798	186

TABLE 9.7 Contact angles of pure aluminium and Al-Mg alloy on single crystal α-alumina

Substrate	Temperature (°C)	Atmosphere	Contact Angle θ	Reference
Al	870	Vacuum	139	269
Al-0.85Mg	870	Vacuum	118	269
Al-1.07Mg	870	Vacuum	137	269
Al	970	Vacuum	148	270
Al	950	Vacuum	105	196
Al	800	Argon	93	194
Al-3%Mg	800	Argon	83-93	259
Al	700	Argon	90	198
Al	700	Vacuum	88	195

REFERENCES

1. Cowdell, R. L. (Ed) : Metals and Materials, March 1986, p123.

2. Brondyke, K. J. : J. Metals, 1983 35 (4) p63-7.

3. World Bureau of Metal Statistics, 1986.

4. Roskill : The Economics of Aluminium, July 1988, Roskill Information Services Ltd.

5. Jacobi, J. S. : Proc. 4th BNF Conf., 1975, (6).

6. Hawkins, J. E. : Metallurgist and Materials Technologist, 1984 16 (8) p407-413.

7. Energy Audit Series : The Aluminium Industry, June 1979, (6) Dept. Energy and Dept. Industry.

8. Harris, D. : Suppl. to Sheet Met. Ind. Foundry Trade J, etc., March 1986, p4-6.

9. Roscrow, W. J. : Metallurgist and Materials Technologist 1982 14 (12) p553-557.

10. La Verne, L. (Ed) : Mat. Eng., Sept 1985, p47.

11. Goddard, C. B, : Proc. 4th BNF Int. Conf., Nov 1974, (9).

12. Atkins, P. R. : Engineering and Mining J., 1973, p69-71.

13. Johnston, R. D. et al : The Met. Soc. Nutting, J. (Ed) p19-22.

14. Arnot, D. S., and Willson, R. T. : Int. Iron and Steel Inst., 21st Session, June 1983, Brussels.

15. Kenahan, C. B. and Flint, E. P. : Information circular 8595, 1973, US Bureau of Mines.

16. Garst, O. C. et al : Report Investigation No.3874, 1946, p1-43, US Bureau of Mines.

17. Parkes, L. R. : Metallurgist and Materials Technologist, Oct. 1977, p547-548

18. Peterson, W. S. : Light Metals, 1986, 1 p154-161.

19. Quist, W. E. et al : Aluminium-lithium alloys II, 1984, p313-334 Warrendale Pa, The Metallurgical Soc. of the American Inst. of Mining, Metallurgy and Petroleum Engineers.

20. Quist, W. E. and Lewis, R. E. : Rapidly Solidified Powder Aluminium Alloys, 1986, p7-38 Philadelphia, American Soc. for Testing Materials.

21. Gruhl, W. and Lossack, E. : Proc. Conf. Recycling of Metals, 1980.

22. "UBC Separation Process" : Proc. Conf. Recycling and secondary recovery of metals, p429-444, Dec 1-4 1984, Florida.

23. Van Linden, J. H. L. and Hannula R. E. : Proc. Conf. Recycling of Metals, 1980.

24. Goddard, C. B. : Elec. Council Research Centre Report R549 Oct. 1972, No.488.

25. Waldman, J. : Rapidly Solidified Powder Aluminium Alloys, 1986 Philadephia, American Society for Testing and Materials.

26. Harrison, D. A. et al: Aluminium Metals and Materials, Jan, 1974, p59-68.

27. Private Communication : Alcan International, Banbury Laboratories, Oxon.

28. Cochran, C. N., et al : Society of Automotive engineers, Tech. Paper Series 830099, Int. Congress and Exposition, Feb-March 1983, Michigan Aluminium Company of America.

29. Smith, L. : Proc. Conf. Aluminium Technology March 1986, London, The Institute of Metals.

30. Private Communication : British Aluminium Alloys, Warrington, Cheshire.

31. Hatch, J. E. (Ed) : Aluminium-properties and physical metallurgy, 1984, American Soc. for Metals.

32. Woodward, A. R. : Metallurgist and Materials Technologist, Jan 1984, 16 (1) p20-23.

33. Stewart, A. L., et al : Light Metal Age, 1977, 35 (11,12) p13-15.

34. Barber, J. B. : Metals and Materials, 1986 2 (11).

35. Grimes, R., et al : Metals and Materials, 1985, 1 (6) p357.

36. Source book on selection and fabrication of aluminium alloys, 1978, American Society for Metals.

37. Davies, I. : Metals and Materials, 1986, 2 (11) p701-5.

38. Elec. Council Information brochure and Technical Information Elec. Furnaces, 4923/9-86.

39. Elec. Council Information brochure and Technical Information Electric Furnaces, 4139/6-86.

40. Elec. Council Information brochure and Technical Information on Electric furnaces 4102R/3-85.

41. Robertson, J. L., : Proc. 4th BNF Conf. 1975 paper 7.

41a. Emley, E. F. and Subramanian V. : Light Metals 1974 8. AIME

42. Energy Efficiency Office Final Report ED/62/94, Sept. 1985 Prepared by BNF Metals Technology Centre for the Technology Support Unit, AERE Harwell.

43. Meier, R. : Proc. 6th BNF Conf. Sept 1986. paper 18, Birmingham.

44. Banji, P. J. : Proc. Conf. Recycling and secondary recovery of metals, Dec 1984, p121-139, Florida. The Metallurgical Soc of AIME.

45. "Efficient Melting of Low Density Scrap" : Proc. Conf 'Recycle and Secondary Recovery of metals' Dec. 1984 p51-64 Florida. The Metallurgical Soc of AIME.

46. Devereux, W. C. : Proc. Inst. Brit. Found. 1938 32 p167-170.

47. Friend, E. W. et al. : Proc. Conf 'Recycle and Secondary Recovery of Metals', Dec. 1984, p457-464, Florida. The Metallurgical Soc. of AIME.

48. Stephenson, D. J. : PhD Thesis, Brunel University 1978.

49. Bowers, J. E. : Proc 6th BNF Conf. Sept 1986, paper 21, Birmingham.

50. Groteke, D. E. : Modern Castings, April 1983, p25-27.

51. Mollard, R. F. and Davidson N. : AFS Transactions 1978 86 (78-115) p479-486.

52. Simmons, W. and Sibley S. : 6th BNF Int. Conf. Sept.1986, Paper 20, Birmingham.

53. Foseco Minsep Communication at Int. Exhibition of Metals, Sept 1986, Birmingham.

54. Harris, R. J. : Proc. 6th BNF Int. Conf. Sept. 1986, paper 23, Birmingham.

55. Hart, R. K. and Maurin, J. K. : Surface Sci. 1970 20 p285-303.

56. Cocke, D. L. et al : Catal. Rev. - Sci. Eng., 1984, 26, p163-231.

57. Wefers, K. and Misra, C. : Alcoa Technical Paper No.19 (Revised) 1987, Alcoa Laboratories.

58. El-Mashri, S. M. and Forty A. J. : Inst. Phys. Conf. Series No.61, Sept 1981, p395-398, Cambridge.

59. de Brouckere, L. : J. Inst. Metals, 1945, 71, p131-147.

60. Pryor, M. J. : Oxidation of Metals, 1971, 3 (6), p523.

61. Scamans, G. M. and Butler, E. P. : Metall. Trans A., Nov. 1975 6 p2055.

62. Brock. A. J. and Heine, M. A. : J. Electrochem. Soc., 1972, 119 (8) p1124.

63. Batra, I. P. and Kleinman, L., : J. Electr. Spectr. 1984, 33, p175-241.

64. Crowell, J. E. et al : Surface Science (1986), 165.

65. Henry, R. M. et al : Solid State Communications, 1982, 42, (1) p23-26.

66. Dignam, M. J. et al : J. Electrochem. Soc. 1966 113, (7) p656-662.

67. Olefjord, I. and Karlsson A. : Proc. Conf. Aluminium Technology, March 1986, p383-391, The Institute of Metals, London.

68. Greenberg, L. and Wright, K. R. N. : Proc. Royal Soc. A., 1955, 232, p403-406.

69. Heine, M. A. and Sperry, P. R. : J. Electrochem. Soc., 1965, 112, p359-363.

70. Miller, A. C. : Cited Wefers [57].

71. Van Beek, H. J. and Mittemeijer, E. J. : Thin Solid films, 1984, 122, p131-151.

72. Maciver, D. S. et al : J. Catal., 1963, 2, p485-497.

73. Soled, S. : J. Catal, 1983, 81, p252-257.

74. Csanady, A et al : Oxidation of Metals, 1979, 13, (3) p245-254.

75. Grauer, R. and Schmoker, P. : Werkstoffe and Korrosion, 1976, 27, p769.

76. Beck, A. F. et al : Corrosion Science, 1967 7, p1.

77. Cochran, C. N. and Sleppy, W. C. : J. Electrochem. Soc. 1961, 108, (4), p322-327.

78. Aylmore, D. W. et al : J. Inst. Metals, 1960, 86, p205.

79. Hunter, M. S. and Fowle, P. : J. Electochem. Soc., 1956, 103 p482-485.

80. John, C. S. et al : Appl. Catal., 1983, 6 p341-346.

81. Lippens, B. C. : Thesis, Tech. Univ. Delft, 1961.

82. Newhaus, A. and Heide, H., Ber. Deut. Keram. Ges, 1965, 42 p167-184.

83. Kennedy, G. C. : Amer. J. Sci., 1959, 257, p563-573.

84. Wefers, K. : K., Metall., 1967, 21, p423-431.

85. Ginsberg, H. et al : Z. Anorg. Allg. Chem., 1962, 318, p238-256

86. An Atlas of Alumina; British Aluminium Chemical Company Ltd.

87. Alwitt, R. S. : Oxides and oxide films, 1976 4.

88. Noda, T., and Isihara, Y. : J. Soc. Chem. Ind. Japan 1940, 43 (6) p166.

89. Hoch, M. and Johnston, H. L. : J. Amer. Chem. Soc. 1954, 76a p2560-2561.

90. Brewer, L. and Stearcy, A. W. : J. Amer. Chem. Soc., 1951, 73 (11) p5408-5414.

91. Smeltzer, W. W. : J. Electrochem. Soc., 1956 106, (4) p209-214.

92. Cabrera, N. and Mott, N. F. : Rep. Progr. Phys, 1948, 12 p163-184.

93. Kirk, C. T. and Huber, E. E. Jr: Surf. Science, (1968) 9 p217-245.

94. Fehlner, F. P. and Mott, N. F. : Oxidation of Metals, 1971, 3 (3) p275.

95. Gulbransen, E. A. and Wysong, W. S. : Phys. Coll. Chem. 1947, 51, p1087.

96. Blackburn, P. E. and Gulbransen, A. E., : J. Electrochem. Soc. 1960, 107, (12) p944-950.

97. Plewa, J. and Kolny, A. : Metal. Odelew, 1985 11, (2) p155-169.

98. Bianconi, A. et al : Phys. Rev. B. 1979, 19 p2837-2850.

99. Doherty, P. E. and Davis, R. S. : J. Appl. Phys., 1963, 34 p619-623.

100. Timsit, R. S. et al : Ultramicroscopy, 1985 18, p387-394.

101. Czanderna, K. K. : PhD Thesis, Cornell Univ. 1984.

102. Field, D. J. : PhD Thesis, Univ. of London, 1982.

103. Shinohara, K. et al : Z Metallkde, 1982, 73, (12) p774-780.

104. Dignam, M. J. and Fawcett, W. R. : J. Electrochem. Soc., 1966, 113, p663-671.

105. Aziz, P. M. and Godard, H. P. : J. Electrochem, Soc., 1957, 104 (12), p738.

106. Lewis, J. E. and Plumb, R. C. : Internat. J. Appl. Radiation and Isotopes, 1956, 1, p33.

107. Brock, A. J. and Pryor, M. J. : Corr. Sci., 1973, 13, p199.

108. Stroup, P.: US Patent to Alcoa, 29th May 1945. 2,377,281.

109. Draley, J. E. and Ruther, W. E. : J. Electrochem Soc. 1957, 104, No.6 p329

110. Winter, F. amd Gruhl, W. : D. G. N. Symposium on Heat Treatment. Oct. 1973, Bad Nauheim

111. Thiele, W. : Aluminium, 1962, 38, p707-715.

112. Cochran, C. N. and Sleppy, W. C. : J. Electrochem. Soc. 1961, 108, p1097-1102.

113. Trilliat, J. J. et al : Revue de l'aluminium 1960, (280) p1115-1123.

114. Malt'sev, M. V. et al : Bull Acad. Sci. USSR., Phys. Sci. 1956 p747.

115. Richards, L. E. and Meussner, R. A. : Report of NRL progress, March 1964, p25-27.

116. Sturm, E. and Winterhager, H. : Aluminiuim (Ger). 1978, 54 (6) p441-444.

117. Wightman, G. and Fray, D. J. : Metall. Trans. 1983, 14, p625-631.

118. Derbyshire, J. A. and Cooper, E. R. : Trans Faraday Soc. 1934 30, p1038-1048.

119. Sharova, M. V. : Trudy, Moskov, Aviation Tekhnol. Inst. 1961, (49) p97-119.

120. Ginsberg, H. and Datta, P. K. : Aluminium 1966, 42, (11) p681-687.

121. Talbot, D. J. and Stephenson, D. J. : Not yet published.

122. Talbot, D. E. J. : The Oxidation of Liquid Aluminium, August 1979, lecture given at ALCOA Tech. Centre, Pennsylvania.

123. Hine, R. A. and Guminiski, R. D. : J. Inst. Metal. 1961, 89, p417-422.

124. Cochran, C. N. et al : Light Metals, 1976, 2, p203-227.

125. Smeltzer, W. W. : J. Electrochem. Soc. 1958, 105 (2) p67-71.

126. Kofstad, P. : High Temperature Oxidation of Metals, 1966 John Wiley and Son Inc., New York,

127. Leighly, H. P. and Alam, A : J. Phys. F; Met. Phys., 1984 14 p1573-1583.

128. Lee, S. T., et al : Aluminium, 1985, (7) 61, p504-509.

129. Grauer, R. and Schmoker, P : Werkstoffe und Korrosion, 1976 27, (11) p769-774.

130. Ritchie, I. M. et al : Oxidation of Metals, 1971 3 p91.

131. Drouzy, M. and Richard, M : Fonderie 1974, 29 (332) p121-128.

132. Davies, O. N. C. and Treverton, J. A., Japanese Institute of Light Metals. May 1982, Osaka.

133. Scamans, G. M. and Butler E. P. : 4th Int. Cong. on HVEM, 1975, p341-344, Toulouse.

134. Wefers, K. : Aluminium, 1981 57 (11) p722-726.

135. Baliki, S. : Prace Inst. Huta, 1958, 10, (4) p208-213.

136. Haginoya, I. and Fukusako, T. : Trans. Japan Inst. of Metals, 1983, 24, (9) p613-619.

137. Belitskus, D. L. : Oxidation of Metals, 1971, 3, (4) p313-317.

138. Haginoya, I : J. Japan Inst. Light Metals, 1976, 26 (3) p131-138.

139. Wenz, D. A. : Light Metals 1979, p771-780.

140. Terrill, J. R., et al : Welding J., Dec. 1971, p833-9.

141. McGurran, B. and Nicholas, M. G. : Welding Research Supplement. Oct. 1984, p295-5.

142. Singleton, O. R., and McNamara, P. : Aluminium, 1974, 50 p407-409.

143. Winterbottom, W. L., and Gilmour, G. A. : J. Vac. Sci. Technol, 1976, 13 (2) p634-643.

144. Anderson, W. A. : Welding J., 1977, 56 (10) p3145-3185.

145. Whitaker, M, and Heath A. R. : J. Inst. Metals. 1953-4 82, p107.

146. Houska, C. : Metals and Materials, Feb. 1988 p100.

147. Heath, A. R. : J. Inst. Metals, 1953-4 82, p114-116.

148. Christiakov, Y, D. and Malt'sev, M. V. : Vsesoyuz. Konf. 1955, p289-297, Moscow.

149. Muromachi, S. : Metall. Abstracts on Light Metals and Alloys 1956-60, 1, p42-3.

150. Calvet, J. and Potemkine, V. : La Recherche Aeronautigue, 1952, (29) p21-28.

151. Castle, J. E. et al : J. Electrochem. Soc. 1962 10, (11) p1018-1023.

152. Kogan, M., Reed, G. : Proc. Int. Symp. 1-4 Dec 1984, Florida. The Metals Soc. of AIME.

153. Ford, W. R., and Christ, N. : Light Metal, 1974, VII p639-648.

154. Johnson, T. J., and Peterson, R. D. : Proc. Int. Symposium 1-4 Dec 1984, Florida. The Metals Soc. of AIME.

155. US Patent 4540163, Mechanical press for obtaining molten metal from dross.

156. Pietsch, W. B. : Proc. Int. Symp. 1-4 Dec 1985, p683-699, Florida, The met. Soc of AIME.

157. McDonald, J. E., and Eberhart, J. G. : Trans Met. Soc of AIME, 1965 233, p512-517

158. Woodruff, D. P. : The Solid-liquid Interface, 1973, Cambridge Univ. Press.

159. Young, T., : Trans R. Soc., 1805, 94, p65, London.

160. Dupre, A. : Theorie Mechanique de la Chaleur, 1869, p369.

161. Johnson, R. E. : J. Phys. Chem 1959, 68, p1655.

162. Elliot, G. E. P. and Riddiford, A. C. : Recent Prog. in Surface Sci. 1964, p111-128 Academic Press.

163. Adam, N. K. and Livingston, H. K. : Nature, 1958, 18 p128.

164. Zisman, W. A. : U.S. Naval Res. Lab. Report, 1961, No.5699.

165. Gibbs, J. W. : The collected works of J. W. Gibbs, 1928, Yale Univ. Press. New Haven.

166. Johnson, R. E. and Dettre, R. H. : Surface and Colloid Science Vol. 2, 1969, Wily Interscience.

167. Burtell, F. E., and Bjorklund, C. W. : J. Phys. Chem, 1952, 56 p453.

168. Zisman, W. A. : Advances in Chem., 1964 43 (1).

169. Langmuir, I : Chem. Rev. 1929 6 p451.

170. Wade : Advances in Chem. 1964, 43, (15).

171. Johnson, R. E. and Dettre, R. H. : Advances in Chem 1964, 43 (7) p112-135.

172. Faber, T. E. : Theory of liquid metals, 1972, Cambridge Monographs on Physics, Cambridge Univ. Press.

173. Fowkes, F. M. : Treatise on Adhesion and Adhesives, Ed. Patrick, R. L, 1966, 5, p379-401.

174. Good, R. J. : Advances Chem. Ser., 1964, 43, p74.

175. Rhee, S. K. : J. Amer. Ceram. Soc, 1971, 54, (7) p332-334.

176. Eustathopoulos, N. : Int. Metal Reviews, 1983, 28, (34) p189-210.

177. Shimoji, M. : Liquid Metals 1977, Academic Press, London.

178. Lang, N. D. and Kohn, W. : Phys. Rev. B. 1973, 8, p6010.

179. Evans, R. and Sluckin, T. J. : J. Phys. C. 1981, 14, p3137.

180. Iakubov, I. T. et al : Solid State Comm, 1985, 56, (8) p709-712.

181. Wood, D. M. and Stroud, D. : Phys Rev. B, 1983, 28 (8) p4374-4386.

182. Kozakevitch, P. and Urbain C., Mem. Sci. Rev. Met. 1961, 58, p517.

183. Bozack, M. J. : PhD thesis, 1985, Oregan Graduate Centre, NBE 85 03865.

184. Korol'kov, A. M. : Otdelenie Teknicheskik Nauk, 1956 2 p35-42.

185. Camel, D. et al : Acta Metall 28, p239-247.

186. Garcia-Cordovilla C. et al : J. Mat. Sci., 1986, 21 p2787-2792.

187. Ray, B. R. et al : J. Phys. Chem. 1958, 62 p1220.

188. Good, R. J. : Advances Chem. Serv., 1964 (4), Amer. Chem. Soc.

189. Miedema, A. R., and den Broeder, F. J. A. : Z Metallkde, 1979, (70) p14.

190. Kingery, W. D. : J. Amer. Ceram. Soc, 1955, 36, (11) p362.

191. Naidich, J. V. : Progress in Surface and Membrane Science, 1981, 14, p353, Academic Press.

192. Juhovizki, A. A. et al : DAN USSR, 1964, 45, (7), p392.

193. Stoneham, A. M., and Tasker, P. W. : J. Phys. C : Solid State Phys, 1985, 18 p543-548.

194. Wierauch, D. : Conf. Proc. Ceramic Microstructure '86'. 1987 Plenum Press, New York.

195. Naidich, J. V. et al : Poroshk Metall, 1983, 6 p481-483.

196. Champion, J. A. et al : J. Mat. Sci, 1969, 4 p39-49.

197. Coudurier, L : Rev. Int. Haute Temper. Refrac. Fr. 1984, 21 p81-93.

198. John, H. and Hausner, H. : J. Mat. Sci letters, 1986 (5) p549-551.

199. Naka, M. et al : Trans JWRI, 1984, 13 (2)

200. Goumiri, L., and Joud, J. C. : Acta Metall., 1982, 30, p1397-1405.

201. Brennan, J. J., and Pask, J. A. : J. Amer. Ceram. Soc. 1968. 51, (10), p569.

202. Barsoum M. W. and Ownby, P. D. : in 'Surfaces and Interfaces in Ceramic-Metals Systems. 1981, Plenum Press, New York.

203. Robinson, S. W. et al : Metal, Tech, 1979 p152-169.

204. Kozakevitch, P. and Lucas, L. D. : Rev. Met., 1968 65 (9) p589-598.

205. Rao, S. and Dawson, P. R. : Warren Spring Laboratory LR 369, 1980.

206. Wall, A. J. and Milner, D. R. : J. Inst. Metals, 1962, 90, p394-402.

207. Impey, S : MSc Thesis, 1985, Cranfield Institute of Technology.

208. Mikhail, R. S. and Roubens, E. : Microstructure and Thermal analysis of Solid Surfaces, 1983 Wiley-Heyden, Chichester.

209. Ransley, C. E. and Talbot, D. E. J. : Z Metallkunde, 1955, 46, p238.

210. Preston, G. D. and Bircumshaw, L. L. : Philos, Mag., 1936, 22 (7) p654-665.

211. Ball, M. D. and Furneaux, R. C. : Inst. Phys. Conf. Serv. 1981 No. 61, 4 p179, EMAE, Cambridge.

212. Index to the Powder Diffraction File. 1983, American Society for Testing and Materials.

213. Laplace, P. S. : Phil. Mag. 1859, 17 p61.

214. Padday, J. F. : in Surface and Colloid Science, Vol. I, 1969 p101, Wiley Interscience.

215. Partington, J. R. : An Advanced Treatise on Physical Chemistry 2, The property of liquids, 1951, p174 Longmans.

216. Dorsey, N. E. : J. Washington Acad. Sci., 1928, 18 (19) p505-509.

217. Smolders, C. A. and Duyvis, E. M. : Recueil, 1961, 80, p635-649.

218. Bashforth, F. and Adams, J. C. : At Attempt to test the theory of Capillary Action, 1892. Cambridge University Press and Deighton Bell & Co.

219. Padday, J. F. : Proc. Royal Soc. London A., 1972, 330 p561-572.

220. Maze, C. and Burnet, G. : Surf. Sci., 1971, 24, p335-342.

221. Butler, J. N. and Bloom, B. H. : Surf. Sci, 1966, 4, p1-17.

222. Clark, A. J. and Metcalfe, S. : Interlabmate 1987, Vol. XII (5)

223. Babu, S. R. : Bull. Mat. Sic. 1986 8 (2) p217-224.

224. Gustalla, J. : Proc. 2nd. Intern. Congr. Surface Activity 1957, 3 p143, London.

225. Wilhelmy, L. : Ann. Physik, 1963, 119, p177.

226. Wallis, D. R. : Brazing, Soldering, 1982, 3, p11-16.

227. Martin Garin, L., Dinet, A. and Hicter, J. M. : Mémoires et Etudes Scientifiques Revue de Metallurgies, 1981 May p269-278.

228. Savitsky, A. and Galay, H. J. E. : Analytical Chemistry, July 1964, p1627.

229. Waterhouse, K. : Private Communication, University of Surrey.

230. Caplan, D., Harvey, A. and Cohen, M. : J. Electrochem Soc. 1961, 108, 134.

231. Tidswell, R. : PhD Thesis 1989, Cranfield Institute of Technology.

232. ✓ Stephenson, D. J. and Nicholls, J. R. : Mat. Sci. and Tech. 1990 Jan. (1).

233. ✓ Cochran, R. C. : Microstructural Characterisation, 1988 Book 443, The Institute of Metals.

234. Kahl, W. and Fromm, E. : Metall. Trans B, 1985, 1613, p47.

235. Talbot, D. E. and Anyalebechi, P. N. : Mat. Sci. and Tech. 1988, Jan 4 p1-4

236. Topchiev, A. V. et al : Boron fluoride, 1959 Vol. 2, Pergammon Press, London.

237. Selivanov, V. G. and Stender, V. V. : Zhur. Neorg. Khim, 1958 3 (2) p448.

238. Fedotieff, P. P. and Timofeeff, K. : Z. Anorg U. Allgem Chem. 1932 206, p265.

239. Noda, T. and Hagesawa, M. : J. Soc. Chem Ind. Japan 1940 43 (3) p72B.

240. Mondolfo, L. F. : Aluminium Alloys, structure and properties 1976, Butterworth and Co.

241. Kubachewski, O and Hopkins, B. E. : Oxidation of metals and alloys, 1953, Butterworths Publications, Acad. Press, N. York.

242. Giggins, C. S. and Pettit, F. S. : Oxidation of metals, 1980 14 p363.

243. Ostberg, G. et al : Trans. Am. Nucl. Soc., 1965, 8, p122.

244. Manning, M. I. : Corrosion Science, 1981, 21 (4) p301-316.

245. Rotenburg, Y., Boruvka, L. and Neumann, A. W. : J. Coll. and Interf. Sci. 1983 93 (1).

246. Thwaites, C. J. : Soft-soldering handbook, 1977, International Tin Research Institute Publication No. 533.

247. Martin-Gavin, L., Dinet, A. and Hicter, J. M. : J. Mat. Sci 1979 14 p2366-2372.

250. Wakeham, H. and Skau, E. L. : J. Am. Chem. Soc. 1946, 67, p268-272.

251. Richerson, D. W. : Modern Ceramic Eng. 1982, Manuf. Eng and Mat. Proc. (8) Marcel Dekker Inc. USA.

252. ✓ Impey, S. A., Stephenson, D. J. and Nicholls, J. R. : Materials Science and Technology 1988, December 4, p1126-1132.

253. Hardie, D. and Petch, N. J. : Proc. Br. Ceram. Soc. 1965, 5, p85.

254. Livey, D. T. and Murray, P. : J. Am. Ceram. Soc. 1956, 39, p363.

255. Parkins, R. N. : Report no ASD-TR-61-628, Armour Research Foundation, 1963, part II

256. Evans, A. G. : Philos. Mag. 1970, 22, p841.

257. Davidge, R. W. : Mechanical Behaviour of Ceramics, 1979, Cambridge University Press.

258. Munitz, A., Metzger, M. and Mehrabian, R. : Metall. Trans. A 1979, 10A, 1491-97.

259. Wierach, D. A. : Proc. Conf. 'Interfacial Science and Engineering', 1987, July 13-16, Lake Placid, New York.

260. McEnvoy, A. J., Williams, R. H. and Higginbotham, I. G. : J. Mat. Sci. 1976, 11, p297-302.

261. Lang, G. : Aluminium 1974, 50 (11) p731-734.

262. Korol'kov, A. M. and Bychkova, A. A. : Akad, Nauk SSR. Inst. Met. Issledovaniye Splavov. Tsvetnykh Metal, 1960, (2) p122-134.

263. Eustalopolous, N., Joud, J. C., Desré, P. and Hicter, M. : J. Mat. Sci. 1974, 9, p1233-42.

264. Utiguard, T., Toguri, J. M. and Nakumura, T. : Metall. Trans. 1986, 17B (2).

265. Kingery, W. D., Bowen, H. K. and Uhlmann, D. R. : Introduction to Ceramics, 1976, 2nd Ed. Wiley Interscience.

266. Dawihl, W. and Federmann, H. : Aluminium 1974, 50 (9), p574.

267. Bruce, R. H. : Aspects of Surface Energy of Ceramics, Sci. Ceram,, 1965, 2, p359-381.

268. Goumiri, L., and Joud, J. C. , Desré, P. : Surface Sci. 1979 83 p471.

269. Wolf, S. M., Levitt, A. P. and Brown, J. : Chem. Eng. Progress 1966, 62 (3) p74-76.

270. Livey, D. T. and Murray, P. : Plansee Proc. 2nd Seminar, 1955, p375-404, Reutte/Tirot.

271. Hanock, P. : MRS Europe, 1985, p163.

272. Gilman, J. J. : J. Appl. Phys. 1960, 31, p2208.

273. Handbook of Chemistry and Physics : 1978-9 Ed. Weast R. C. and Astle, M. J. 59th Ed. CRC Press Ltd.

274. Juenker, D. W., Meussner, R. A. and Birchell, C. E. : Corrosion 1958, 14, p57.

275. Grosskreutz, J. C. : Surf. Sci. 1967, 8, p173.

276. Fruehling, J. W. and Hanawalt, J. D. :. Modern Casting, 1958 56, p159-164.

277. Pownall, S. : Metals and Materials, 1988 4 (1) p35-37.

ACKNOWLEDGEMENTS

The discussions and guidance I have had from my supervisors Dr. D. J. Stephenson and Dr. J. R. Nicholls is most gratefully acknowledged. I also wish to thank the following:

Dr. R. W. Wilson and Dr. D. J. Field of Alcan International. The electron optics group at Banbury Laboratories, Mr. D. Allen for the foundry work and Mr. P. Enright for his encouragement.

The laboratory and workshop staff at Cranfield, in particular Mr. J. Hedge. Mr. T. Pryor, Mr. D. Hardwicke and Mr. D. Timpson for their invaluable help in manufacturing experimental apparatus.

Mr. C. Matthews, for his considerable assistance with electron microscopy.

Dr. J. Strutt, Mr. G. Solt, Mr. J. Reyes and Mr. C. Norton for the loan of computers over this period, also Mr. B. Minehane, Dr. A. Nowosielski and Mr. R. Passmore for their advice with computer software.

Miss. S. Cooper for her excellent typing. Mrs. C. Kimpton and Mr. N. Meyers.

Finally, I am indebted to SERC for the provision of a CASE studentship and to Alcan International for sponsorship of this thesis.

APPENDIX A

THE MICROBALANCE DATA STORAGE AND PROCESSING SYSTEM

This appendix describes the microbalance system used in the present work. The microbalance sensitivity was investigated using several parameters and the system modified accordingly in order to ensure that all data were reproducible and the accuracy known. The results are discussed in terms of noise level and drift (i.e. apparent gain or loss in weight in the absence of a specimen) and compared with other microbalance systems.

The microbalance arrangement is as follows. The specimen is held on an alumina plate or crucible, freely suspended by a platinum wire in the centre of a quartz glass tube (with a gas inlet and outlet) within the hot zone of a vertical furnace. Thermocouples monitor the temperature of the furnace and the sample. Progressive displacements of a balance beam (counter-balanced by a pan of weights) record the weight gain. The beam position relative to a fixed point is monitored by a C.I. electronics system MK2 vacuum balance head linked to a Robal digital control unit which displays readings of ± 1μg on a chart recorder.

Source of error that may arise during microbalance operation, resulting in spurious mass changes or high noise levels and drift, have been listed in section 5.1. Figure A1, trace e, shows a poor microbalance trace with highly irregular mass changes attributable to mechanical disturbances or physical contact with the inside wall of the tube from balance pans or wire. To minimise external disturbances and detrimental air movements the microbalances were installed in a vibration free room and activity in the room was kept to a minimum.

In this work low pressures and vacuum were avoided in order to reduce magnesium loss, consequently air and residual gases were evacuated by flushing the apparatus through with the required

environment. Electrostatic effects were observed particularly in humid environments, the platinum wire became strongly attracted to the wall of the glass chamber. With drier atmospheres these effects became noticeable after several experiments.

It is likely however that water droplets, formed from cooling steam condensing near the water jacket, produced surface tension forces bringing the wire and glass into close proximity thereby causing disturbance. Attempts to reduce static build up by coating glassware with antistatic material and earthing glassware were sufficient for most conditions except humid environments where the noise was greater than ± 60μg.

When the gaseous atmosphere was first introduced to the microbalance chamber a weight gain of approximately 5μg was recorded. As the flow rate was increased no further effect was observed upto 70cm^3/min at which point a substantial drift was recorded. This was attributed to surface adsorption by the alumina plate or crucible and is expected to be removed by heating.

The flow of gas through a hot chamber produces a turbulance which is reflected in the noise level observed. Provided the specimen did not start swinging the background noise level increased from ± 1μg at room temperature to ± 10μg at 750°C, as figure A2 shows. Thus the major part of the high background noise was generated after the gaseous atmosphere was introduced. Even in still air however the high temperature gradient between the specimen and the balance head will produce convection as a result of thermal density changes of gas. This results in spurious mass changes. Mikhail and Roubens [208] observe large fluctations in weight occurring with a balance pan temperature of -196°C and beam at 27°C. Figure A3 shows that the noise level and fluctuations increase as the pressure of nitrogen gas increases. A thin glass tube suspended over the wire in the centre of the quartz glass tube was found to reduce disturbances from turbulence.

A distinction can be made between weight fluctuations from convection as a result of thermal density changes of gas (shown in figure A3) and from Knudsen forces arising from direct impulse exchange of striking gas molecules of different temperatures. This latter effect occurs mainly at pressures below 10^3Pa but is at a maximum at 1Pa, depending on gas type and geometry [208].

The force acting on a body in a flowing atmosphere can be estimated using the expression below:

$$\text{force} = \frac{\rho . V^2 . A}{2}$$

If V is the linear velocity of a gas with density ρ of ($1.2 Kg.m^{-3}$) flowing at $20 cm^3/min$ a force of 0.95mg is exerted by the flowing gas. If 10% of this figure is subject to small fluctuations or oscillations in the flow rate, an error of 100µg or less will be observed. Indeed, the gas flow was controlled using flow meters regulated by a small sphere in a calibrated capillary tube, which tends to generate fluctuations in intensity in the regulated gas entering the microbalance chamber.

To reduce electronic drift microbalance runs were conducted with a horizontal balance beam, the suspension wire shortened and the suspended weight reduced as far as possible. Despite these measures to achieve a stable base line at 750°C, the microbalance trace exhibited cycles of rapidly alternating gains and losses in mass superimposed on a trace drifting over a very wide range. Such a record is shown in figure A4a.

Following lengthy investigations the cause of wide drift was attributed to the Robal control units, varying as much as 10µg/°C (now specified by the manufacturers). The associated cyclic variation, similar to that of trace figure A1, is found to be due to the thermostatically controlled air conditioning system, maintaining the ambient temperature to within ± 1°C. This cyclic oscillation is observed in figures A2, A4 and A7. Generally as the temperature decreases (from chiller operation) the weight gain on the Robal display increases.

The cycle span was found to be dependent on the size of the temperature change and the rate of temperature change. If the size of the temperature change was large, for example with warm ambient temperatures from an open top furnace and low thermostat setting, the cyclic variation was considerably large as shown in figure A4a. Figure A4b and A4c show a gradual reduction in the cycle span as the temperature change decreases, corresponding to an ambient temperature closer to the thermostat setting.

The extent of the drift corresponds to the average or overall temperature change. With no thermostatically controlled air conditioner the room temperature became extremely hot. Condensation on water pipes and around water jackets in the tube became a problem generating static build up. Further, the drift associated with temperature variations was uncontrolled and non-reproducible. However, when the thermostat was set to generate a rapid response from the conditioning system drift was kept to a minimum. A 3kw heater was placed next to the thermostat to encourage the air conditioning unit to cool the room down as often as possible. The temperature trace of figure A5 shows the rapid rate of temperature change when the heater was switched on. Allowing a little time for the Robal control unit to adjust to the increased room temperature, overall drift in Robal response decreases. When the temperature changes are slower the Robal responds by drifting widely.

The air conditioning system and 3kw heater were placed on a separate electricity phases to ensure the unstable base line was not due to the response of the air conditioning system. Large amounts of current may be drawn when the system is switched on thereby inducing voltage changes directly reflected in the Robal unit. However, the temperature effect of the heater dominated.

Most thermogravimetric determinations have been conducted in vacuum or at low temperatures. However, since magnesium vapourises in vacuum this work necessitated high temperature experimentation in gaseous environments. Thus a way of overcoming the high noise level and drift was required particularly to investigate low weight gains obtained during high temperature oxidation of pure aluminium.

A data logger was programmed to store values obtained over one 13 minute cycle and to subtract this from subsequent data averaged over two consecutive one minute intervals with a 13 point digital smooth [207]. The program is listed in Figure A6, and a typical trace illustrated in Figure A7.

Kinetic results from smoothed data (group B) and from randomly selected previous runs [207] (group A) using identical pure aluminium specimens oxidised in humid air at 750°C are illustrated in Figure A8. The results of group A show poor correlation between each other, and between weight gains recorded by the microbalance and weight gains determined after oxidation using an electronic analytical balance.

The second set of points (group B) plotted with smoothed data, are contained within the experimental band shown in Figure A8. Correlations between the measured weight gains are more representative giving confidence in the accuracy of the data. Furthermore, the specimen weight gains recorded with the pan balance before and after oxidation of the previous experimental runs (group A) fit well into this band. The estimated error in the results with data smoothing now becomes ± 5μg, in humid air at 750°C.

Difficulty with microbalance sensitivity has been reported in the literature although the cause has not been identified. Grauer and Schmoker [129] report that the background oscillation of a Mettler recording balance in a oyxgen stream was ten times the reproducibility given by the manufacturer.

The performance of the Cranfield microbalance systems was compared with proven facilities. A Sartorius microbalance system used by Alcan International at their Banbury Laboratories was tested with platinum samples in humid air at 750°C, the conditions used at Cranfield. As Figure A9 shows, the resulting trace is extremely unstable with a noise amplitude estimated around 95μg. In comparison with figure A7, a trace obtained from the Cranfield

microbalances under the same conditions, the noise amplitude of 25μg can be reduced with data smoothing to almost one tenth of the Alcan system. Later modifications of temperature control brought the noise amplitude of the Cranfield system, without data smoothing to 2μg, as Figure A4 and A5 illustrate.

Perhaps due to the poor performance of the microbalance under the conditions used above, Alcan International usually use their system under vacuum. Figure A10a illustrates that in vacuum (3.4 x 10^{-7}KPa) a noise amplitude of 5μg was obtained at 750°C in air. Interestingly a cyclic variation is exhibited on the traces generated at Alcan (figures A9 and A10a). The author identified that the variation was an effect of room temperature and is removed by switching off the thermostatically controlled air conditioning unit installed in the microbalance room.Figure A10b shows the 'apparent' weight loss as the room heated up. Thus comparison of the system at Alcan, which works well in vacuum, gives confidence in the experimental results generated by this author. It is anticipated that other microbalance systems used by researchers behave in a similar manner.

Three modifications to the Cranfield system are suggested:

1. If the temperature fluctations from areas of circulating air in a thermostatically controlled room are found to be too coarse, the temperature of the Robal control unit may be maintained more effectively by using a water jacket or an insulated light box. Alternatively, improvements may be obtained with temperature compensated analogue to digital converters.

2. The base of the microbalance environmental chamber can be modified to incorporate a surge tank to reduce gas turbulence. Gas oscillations set up at the flow meter will be nullifed on reaching the surge tank. Cool gas entering the base rises towards the heated tapered chamber, the flow increases and gas

travels past the specimen at the specified temperature towards the exit at the top. This controlled gas flow in a tapered chamber greatly reduces gas turbulence [229].

3. A reflecting metal disc fastened on the suspension wire just above the sample can reduce heat radiation as the shield assumes the temperature of the near environment [208].

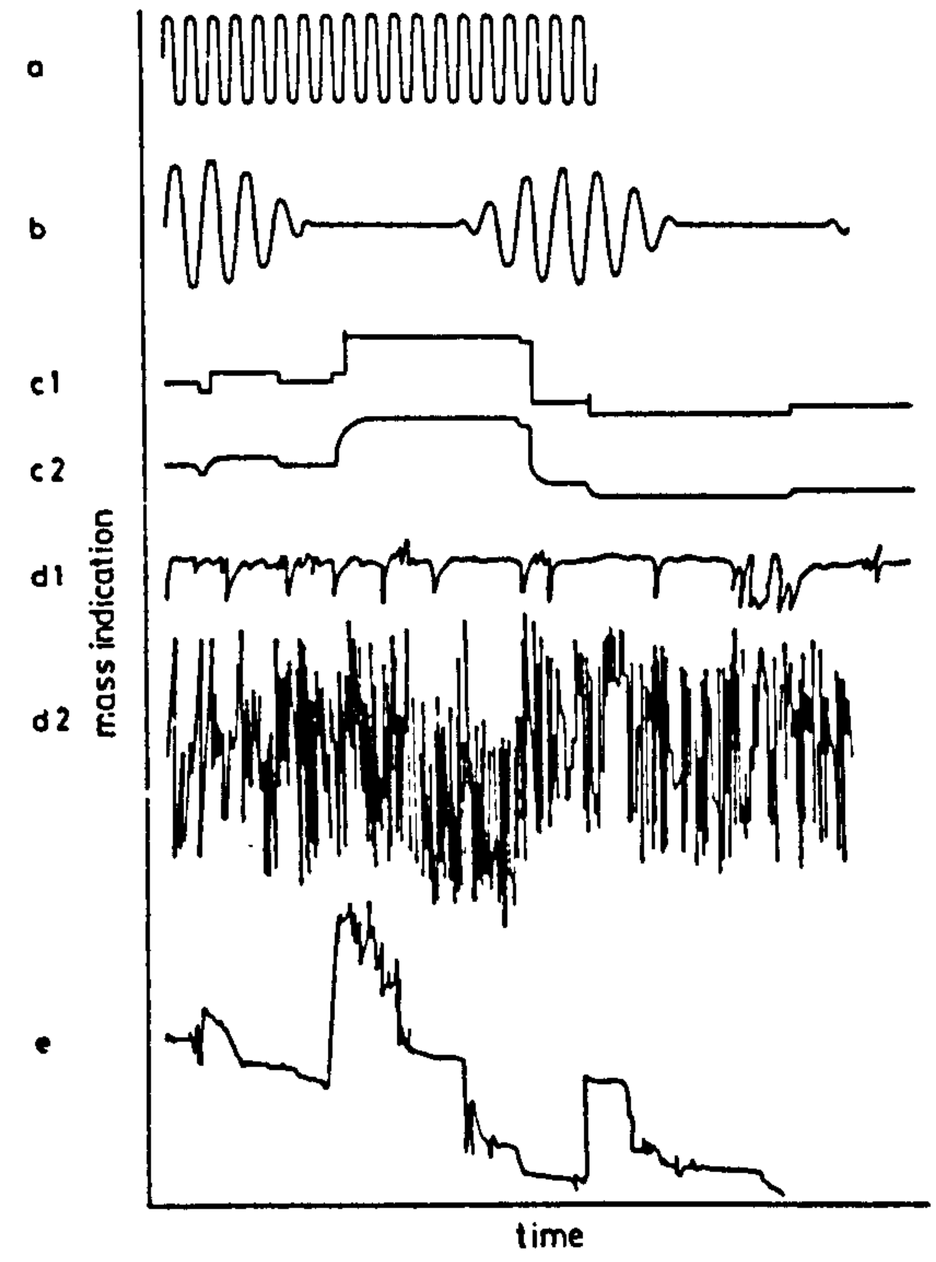

a, vibration of balance beam due to resonant oscillations of the control unit, b, pendular motion of balance pans, scarcely damped in vacuum, c1, shifting point of support caused by damaged or contaminated knife edges (diamonds), c2, the above signals electrically attenuated, d, convection in nitrogen sample 77 K, balance 300 K, d1, 2×10^4 Pa, d2, 5×10^4 Pa, e, contact between pans and tube or other mechanical disturbances

Figure A1 Typical fluctuations of microbalance readings

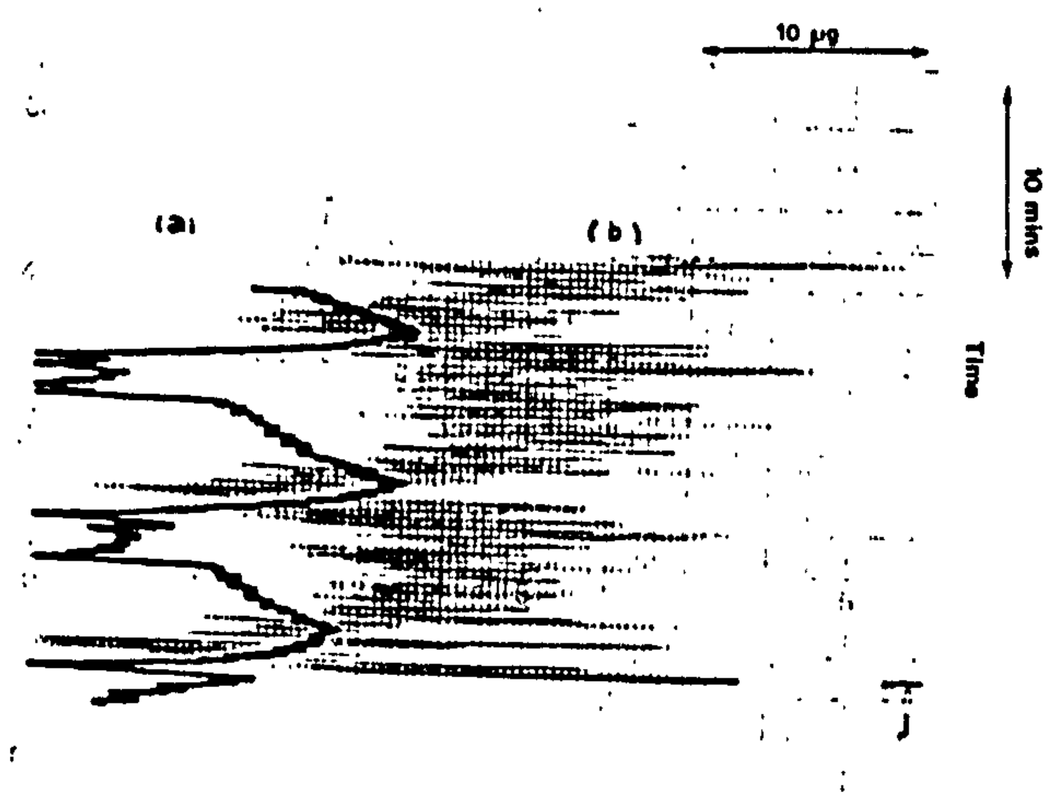

Figure A2 Gain in background noise level with (a) room temp. (b) 750°C

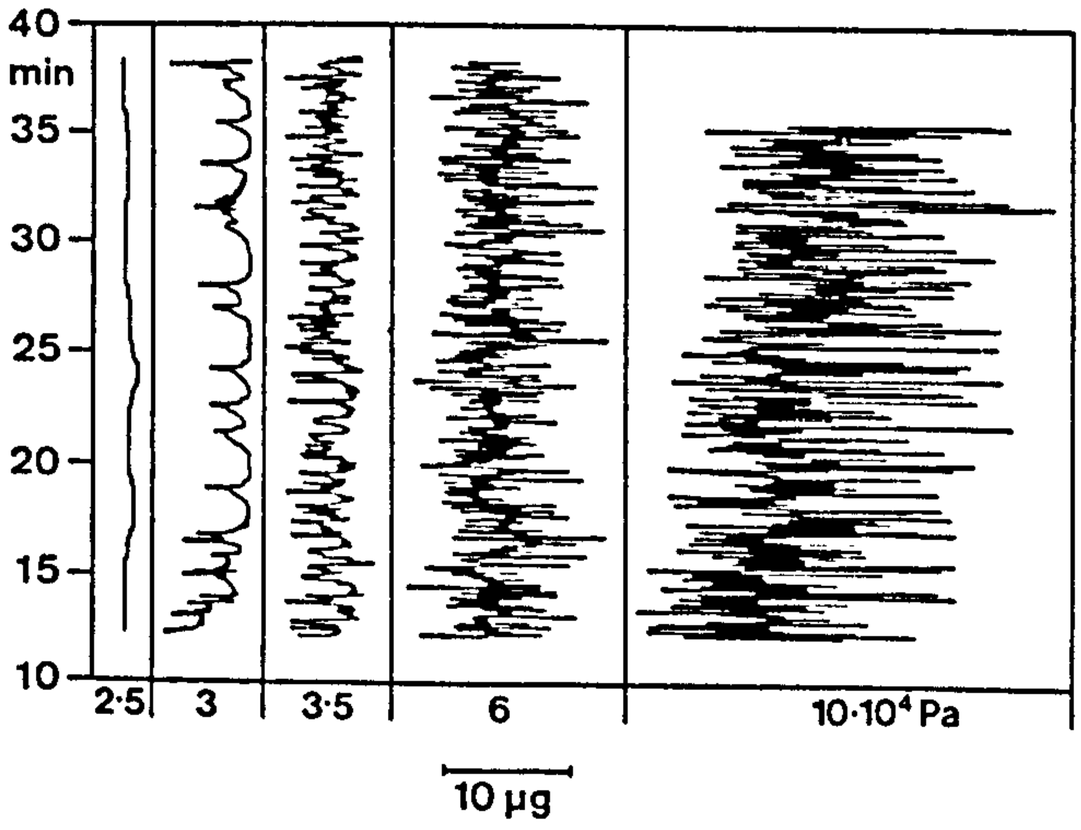

Figure A3 Variations in microbalance readings with nitrogen pressure

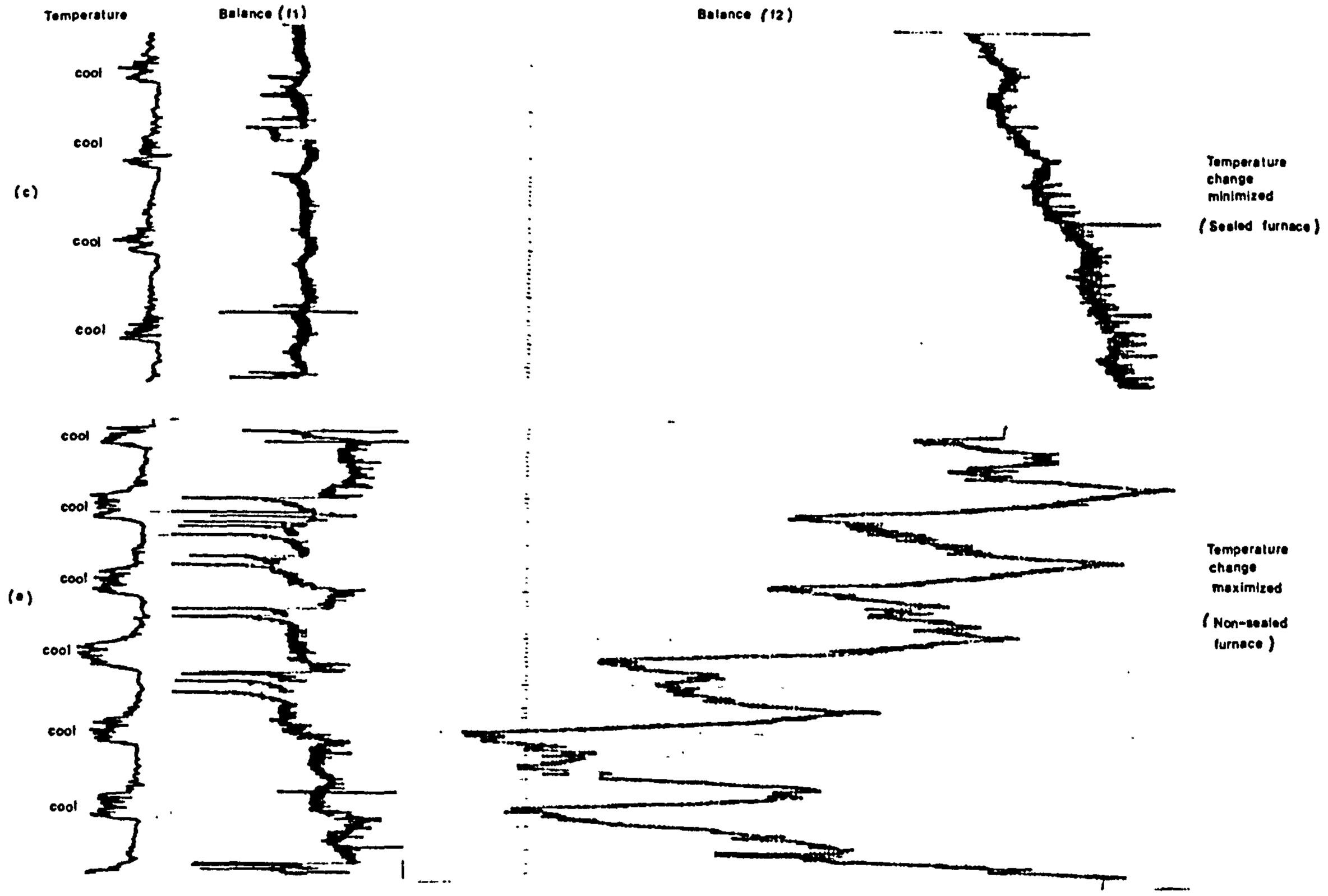

Figure A4 Influence of the temperature change on microbalance readings when (a) maximised and (c) minimised

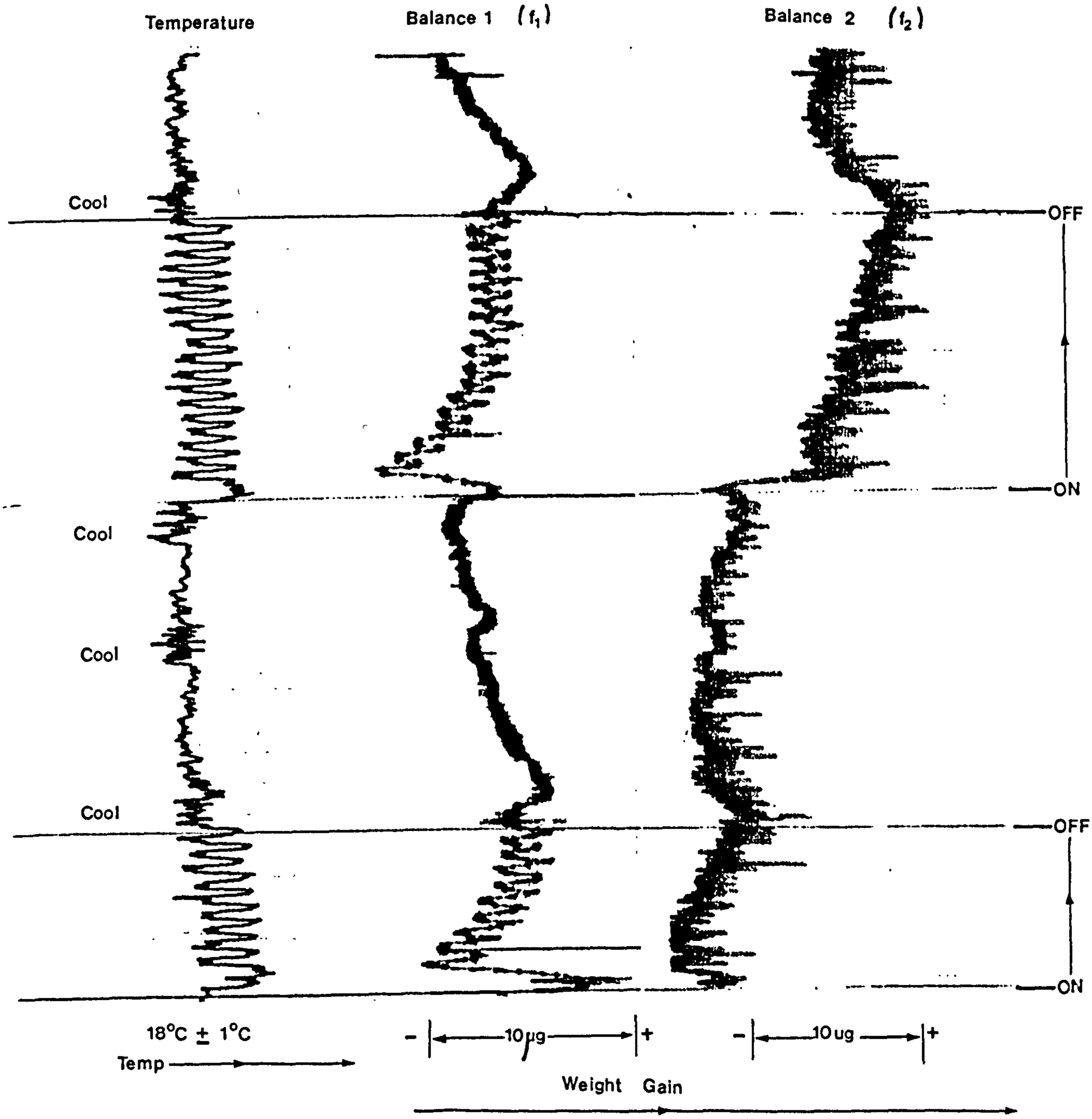

Figure A5 Influence of an external heat source on microbalance readings

```
 10 G (1) = 3
 20 G (2) = 3
 30 K = 1
 40 L = 51

100 TI = 0000.00
110  A = 0
115  C = 0

120 FOR J = 1 to 12
130 IF TI >= 000.05 THEN 150
140 GOTO 130
150 TI = 0000.00

160 A = A + I(1)                    I(1) = Robal 1
170 C = C + I(2)                    I(2) = Robal 2

180 NEXT J
190 B = A/120
200 D = C/120
210 GOSUB 300
220 GOTO 110

300 D(K) = B
310 D(L) = D
315 PRINT K, D(K)
320 K = K + 1
330 L = L + 1
340 IF K  <27 THEN 500

350 W = (25 x D(13) + 24 x (D(11) + D(15)) + 21 x (D(9) + D(17)) +
        16 x (D(7) + D(19)) + 9 x (D(5) + D(21)) - 11 x (D(1) +
        D(25)))/143

360 X = (25 x D(14) + 24 x (D(12) + D(16)) + 21 x (D(10) + D(18)) +
        16 x (D(8) + D(20) + 9 x (D(6) + D(22)) - 11 x (D(2) +
        D(26)))/143

370 Y = (25 x D(63) + 24 x (D(61) + D(65)) + 21 x (D(59) + D(67)) +
        16 x (D(57) + D(69)) + 9 x (D(55) + D(71)) - 11 x (D(53) +
        D(73)))/143

380 Z = (25 x D(64) + 24 x (D(62) + D(66)) + 21 x (D(60) = D(68)) +
        16 x (D(58) + D(70)) + 9 x (D(56) + D(72)) - 11 x (D(54) +
        D (74)))/143


385 PRINT W, X
390 01 = (W + X)/2
400 02 = (Y + Z)/2
410 FOR M = 2 to 26
420 N = M - 1
430 P = M + 50
440 Q = N + 50
450 D(N) = D(M)
460 D(Q) = D(P)
470 NEXT M
480 K = K-1
490 L = L-1
500 RETURN
```

Figure A6 Program for smoothing microbalance data

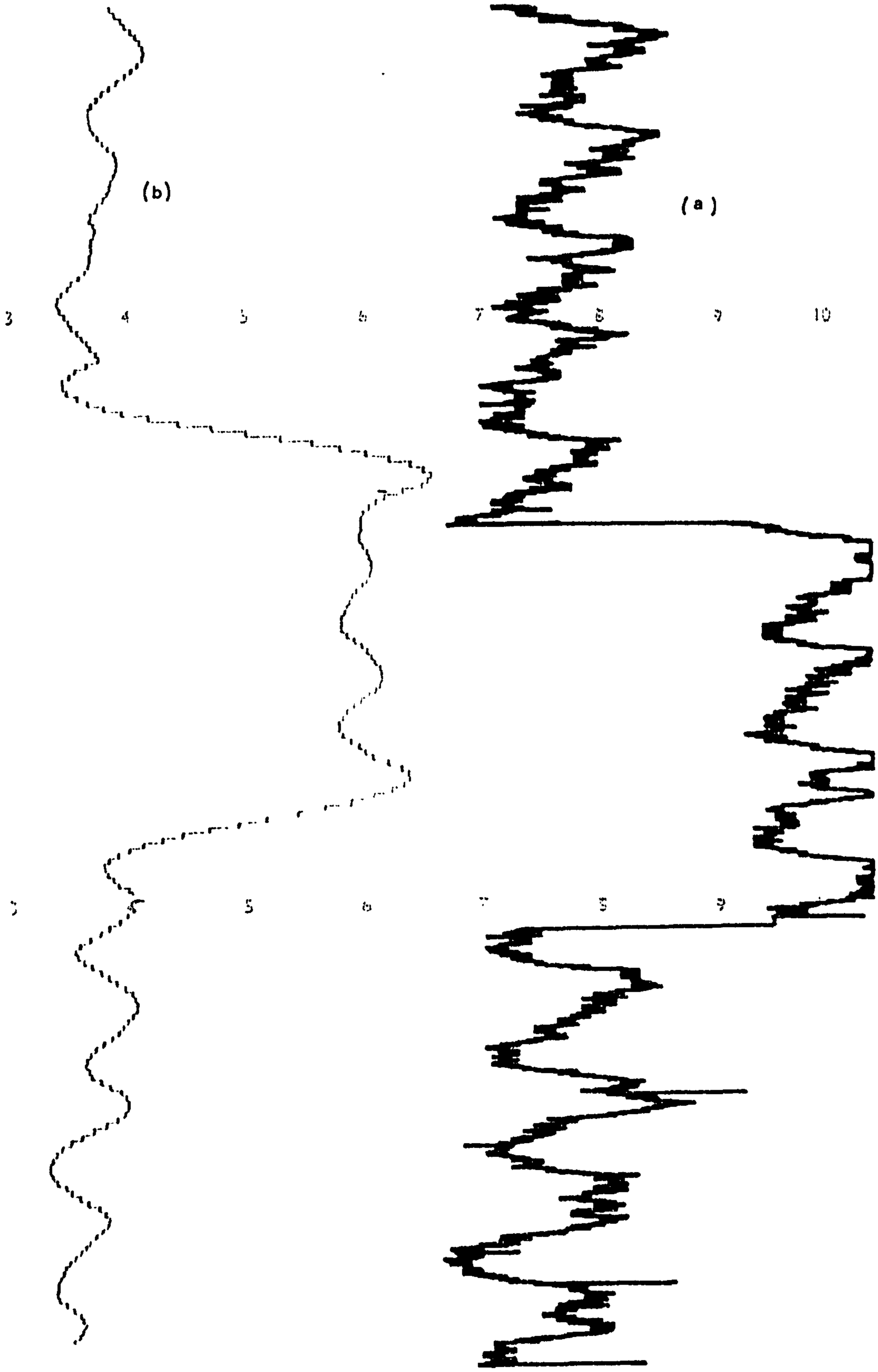

Figure A7 Example of data acquired during the oxidation of pure aluminium in humid air at 750°C with (b) smoothed data (Cranfield system)

Oxidation of C.P. Al in Humid Air at 750°C over 15-17 hrs.

Specimen		Weight Gain ($mg.cm^{-2}$) microbalance	Weight Gain ($mg.cm^{-2}$) pan balance	Deviation (%)
A	41a	0.400	0.020	95
	16b	0.150	0.020	87
	40a	0.120	0.030	75
B	A102	0.025	0.020	20
	A601	0.040	0.040	0
	A501	0.033	0.030	3

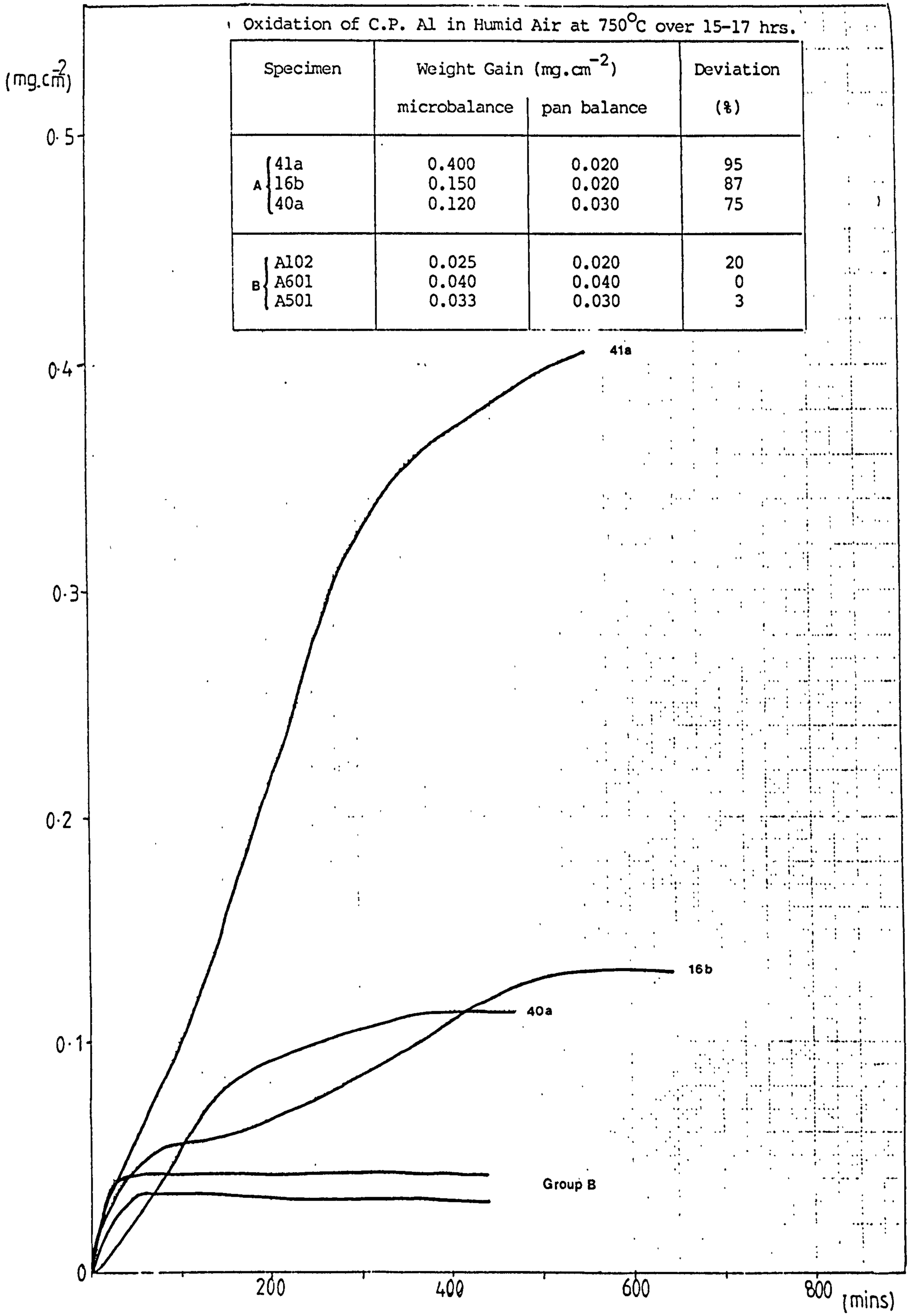

Figure A8 Oxidation of pure aluminium in humid air at 750°C

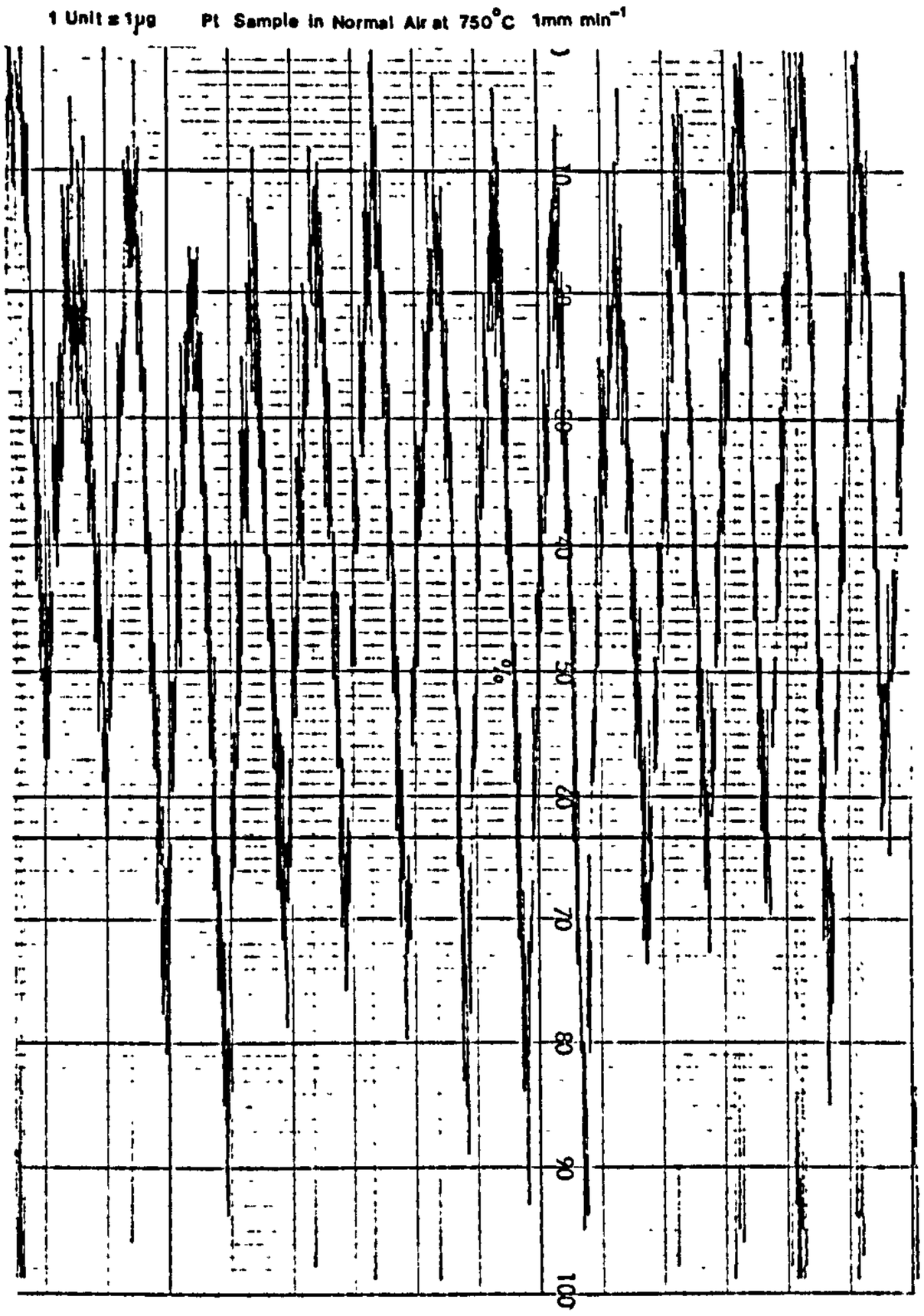

Figure A9 Oxidation of platinum in humid air at 750°C (Alcan system)

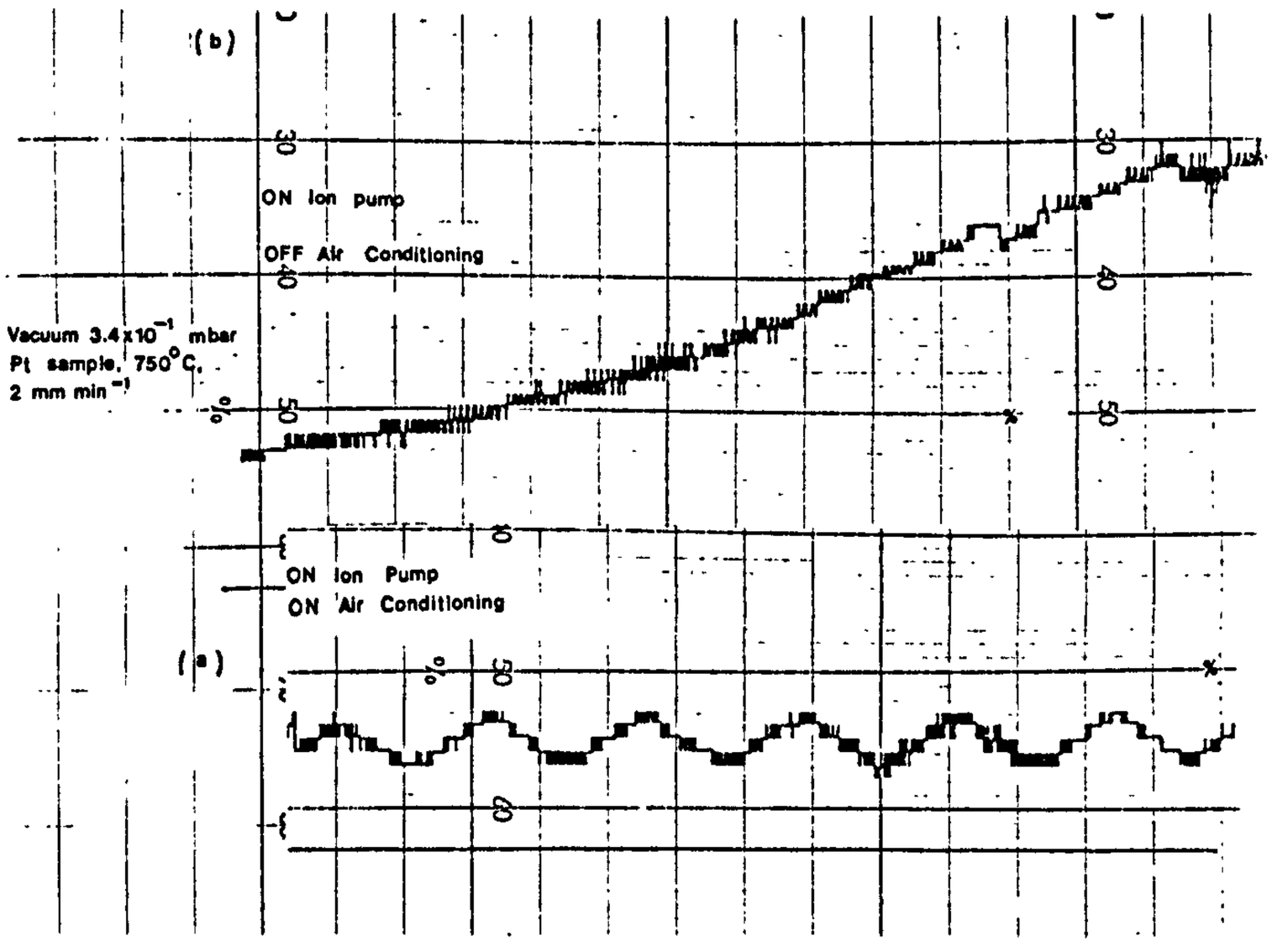

Figure A10 Oxidation of platinum in vacuum at 750°C with thermostatic control (a) on (b) off (Alcan system)

APPENDIX B

THE SURFACE TENSION BALANCE DATA REQUEST AND PROCESSING SYSTEM

This appendix describes the data storage and processing system developed for use with electronic balances used in the measurement of surface tensions. A Sartorius or Mettler electronic analytical balance with weighing ranges 0-30g and 0-160g respectively and readabilities of 0.01mg and 0.1mg, were linked via an RS232 data output to a BBC B microcomputer.

The BBC software generates an external print command which requests data through the RS232 port. Figure B.1 lists the programmes used to request data from a) the Sartorius balance and b) the Mettler electronic balance by the microcomputer.

The collected data are stored on disc and can be listed or plotted graphically with time. Three programmes are listed for use with the Mettler electronic balance:

Menu - this short programme provides easy access to the two main programmes.

Balance programme - this programme requests, collects, stores and plots data graphically throughout the experimental procedure.

Data recall programme - Stored data can be recalled for printing or further processing via this programme.

(a) L.1870,2050

```
1870REM: this is where the balance needs to interface
1875
1880*FX7,7
1890*FX8,7
1895PROCweight
1900data(1)=mass
1910data(0)=TIME/6000
1920
1930DEFPROCweight
1935
1940LOCAL CHAR$,APRAY$
1950*FX3,7
1960*FX2,1
1970*FX21,1
1980ARRAY$=""
1990PRINT CHR$(27);"P";CHR$(13),;CHR$(10)
2000 REPEAT CHAR$=GET$
20101F CHAR$="" THEN GOTO 2014
2012APRAY$=ARRAY$+CHAR$
2014UNTIL CHAR$=CHR$(10)
2016*FX2,0
2018*FX3,4
2020mass=VAL(LEFT$(ARRAY$,10))
2022*FX2,0
2030ENDPROC
2040
2050
```

(b) 1870 REM: this is where the balance needs to interface

```
1880 *FX7,4
1890 *FX8,4
1895 PROCweight
1900 data(1)=mass
1910 data(0)=TIME/6000
1920
1930 DEFPROCweight
1940 LOCAL CHAR$,ARRAY$
1945
1950 *FX3,7
1960 *FX2,1
1970 *FX21,1
1975 *FX15,0
1980 ARRAY$=""
1990 PRINT CHR$(27);"P";CHR$(13),;CHR$(10)
2000 REPEAT CHAR$=GET$
2010 IF CHAR$=" " THEN GOTO 2014
2012 ARRAY$=ARRAY$+CHAR$
2014 UNTIL CHAR$=CHR$(10)
2016 *FX2,0
2018 *FX3,4
2019
2020 mass=VAL(MID$(ARRAY$,2,10))
2022 *FX2,0
2030 ENDPROC
2050
```

Figure B1 Data requests from (a) Sartorius and (b) Mettler electronic balances

L.

```
 10 REM: MENU PROGRAM
 20
 30 MODE 7
 40 VDU23,1,0;0;0;0;
 50 PRINT TAB(5,8);"BALANCE MENU FOR METTLER"
 60 PRINT TAB(5,9);"--------------------------"
 70 PRINT TAB(7,13);"DATA-LOG BALANCE   1."
 80 PRINT TAB(7,15);"RECALL DATA        2."
 90 REPEAT
100 I%=INKEY(1)
110 UNTIL I%=49 OR I%=50
120 IF I%=49 THEN CHAIN"MSUE1"
130 IF I%=50 THEN CHAIN"MREC1"
150 END
```

Menu Program

Balance Program

```
 10 REM: BALANCE PROGRAM
 20 REM:      C.I.T. 1987
 30 REM:     TECHNOLOGY CENTRE
 50MODE 7
 60 VDU23,1,0;0;0;0;
 70DIM data(2)
 75 data(2)=0
 80PROCsetup
 90PROCdisc
100PROCstart
110MODE 0
120PROCrun
130PROCend
135PROCins
140CHAIN"M.MENU"
150END
160
170DEFPROCsetup
180
190REM: sets up variables and limits
200
210 CLS
220PROCexplong
230PROCexpmax
240PROCexpmin
250ENDPROC
260
270DEFPROCexplong
280
290REM: sets experiment length in mins.
300
310PRINT TAB(7,5);"EXPERIMENT LENGTH";TAB(7,6);"-----------------"
320PRINT TAB(0,10);"ENTER TIME FOR EXPERIMENT TO RUN (mins)"
330REPEAT
340REPEAT
350 PRINT TAB(10,12);"            "
360PRINT TAB(3,14);"                                    "
370INPUT TAB(10,12) rtime%
380UNTIL rtime%>0
390PRINT TAB(3,14);"RUN TIME OF ";rtime%;" MINS, Y/N ?"
400REPEAT
410I%=INKEY(1)
420UNTIL I%=89 OR I%=78
430UNTIL I%=89
440rtime%=rtime%*6000
450ENDPROC
460
470DEFPROCexpmax
480
490REM: inputs the high balance reading for the graph
500
510CLS
520PRINT TAB(7,5);"HIGH GRAPH READING";TAB(7,6);"-----------------"
530PRINT TAB(0,10);"ENTER THE MAX BALANCE READING (grams)"
540REPEAT
550PRINT TAB(10,12);"            "
560PRINT TAB(3,14);"                                    "
570INPUT TAB(10,12) high
580PRINT TAB(3,14);"MAX VALUE OF ";high;" GRAMS, Y/N ?"
590REPEAT
600I%=INKEY(1)
610UNTIL I%=89 OR I%=78
620UNTIL I%=89
630ENDPROC
640
```

```
650DEFPROCexpmin
660
670REM: inputs the low balance reading for the graph
680
690CLS
700PRINT TAB(7,5);"LOW GRAPH READING";TAB(7,6);"-----------------"
710PRINT TAB(0,10);"ENTER THE MIN BALANCE READING (grams)"
720REPEAT
730REPEAT
740PRINT TAB(10,12);"            "
750PRINT TAB(3,14);"                                    "
760INPUT TAB(10,12) low
770UNTIL low<high
780PRINT TAB(3,14);"MIN VALUE OF ";low;" GRAMS, Y/N ?"
790REPEAT
800I%=INKEY(1)
810UNTIL I%=89 OR I%=78
820UNTIL I%=89
830ENDPROC
840
850DEFPROCdisc
860
870REM: sets up the disc file
880
890CLS
900PRINT TAB(7,5);"DISC FILES ON DRIVE 0";TAB(7,6);"--------------------"
910PRINT TAB(5,10);"PLACE DISC FOR DATA IN DRIVE 0"
920PRINT TAB(7,12);"PRESS SPACE-BAR WHEN READY"
930REPEAT
940I%=INKEY(1)
950UNTIL I%=32
960REPEAT
970REPEAT
980CLS
990PRINT  TAB(7,2);"FILES ON THE DISC";TAB(7,3);"----------------"
1000*.
1010PRINT  TAB(2,20);"FILE NAME FOR RUN? (7 LETTERS MAX)"
1020INPUT TAB(7,21) file$
1030L%=LEN(file$)
1040UNTIL L%<8 AND L%>0
1050PRINT  TAB(7,22);"FILE NAME ";file$;", Y/N?"
1060REPEAT
1070I%=INKEY(1)
1080UNTIL I%=89 OR I%=78
1090UNTIL I%=89
1100ENDPROC
1110
1120DEFPROCstart
1130
1140REM: lock clock to run time
1150
1160CLS
1170PRINT TAB(1,14);CHR$(141);"AS SOON AS YOU WISH TO START PRESS <S>"
1180PRINT TAB(1,15);CHR$(141);"AS SOON AS YOU WISH TO START PRESS <S>"
1190REPEAT
1200I%=INKEY(1)
1210UNTIL I%=83
1220TIME=0
1230N%=0
1240time%=0
1245 S%=0
1250ENDPROC
1260
1270DEFPROCrun
1280
1290REM: main program section
1300
```

```
1310PROCsetplot
1320PROCopen
1330PROCmain
1340ENDPROC
1350
1360DEFPROCsetplot
1370
1380REM: sets up the graphics screen
1390
1400CLS
1410VDU 24,50;100;1254;1000;
1420VDU 28,0,31,79,30
1430MOVE 1204,150
1440DRAW 100,150
1450MOVE 1204,950
1460DRAW 1204,150
1470MOVE 100,950
1480DRAW 1204,950
1490MOVE 100,150
1500DRAW 100,950
1510VDU5
1520 @%=&20003
1530MOVE 500,980:PRINT"plot of balance weight vs. time"
1540MOVE 500,130:PRINT " time (mins)"
1550MOVE 200,980:PRINT "weight (grams)"
1560MOVE 1180,130:PRINT rtime%/6000
1570MOVE 85,130:PRINT "0"
1575 @%=&20508
1580MOVE 50,160:PRINT low
1590MOVE 50,965:PRINT high
1600VDU4
1610@%=10
1620FOR I%=150 TO 950 STEP 80
1630MOVE 100,I%
1640DRAW 110,I%
1650NEXT I%
1660VDU 29,100;150;
1670VDU23,1,0;0;0;0;
1680PRINT "            <N> NEW SETTING      <Q> QUIT RUN "
1690ENDPROC
1700
1710DEFPROCopen
1720file=OPENOUT file$
1730ENDPROC
1740
1750DEFPROCmain
1760REPEAT
1770PROCread
1780nutime%=TIME
1790IF nutime%-time%>=500 THEN PROCplot:time%=nutime%
1800I%=INKEY(1)
1805IF S%>69 THEN PROCmark:data(2)=data(2)+1
1810IF I%=78 THEN PROCmark:data(2)=data(2)+1
1815 S%=S%+1
1820UNTIL I%=81  OR TIME>=rtime%
1830ENDPROC
1840
1850DEFPROCread
1870REM: this is where the balance needs to interface
1875
1880*FX7,4
1890*FX8,4
1895PROCweight
1900data(1)=mass
1910data(0)=TIME/6000
1920
1930DEFPROCweight
```

```
1940LOCAL CHAR$,ARRAY$,FLAG
1945FLAG=1
1950*FX3,7
1960*FX2,1
1970*FX21,1
1975*FX15,0
1980ARRAY$=""
1990PRINT CHR$(27);"P";CHR$(13),;CHR$(10)
2000 REPEAT CHAR$=GET$
2010IF CHAR$=" " THEN GOTO 2014
2012ARRAY$=ARRAY$+CHAR$
2014UNTIL CHAR$=CHR$(10)
2016*FX2,0
2018*FX3,4
2019IF FLAG=0 THEN PRINT ARRAY$
2020mass=VAL(MID$(ARRAY$,2,10))
2022*FX2,0
2030ENDPROC
2040
2050
2060DEFPROCplot
2070X%=data(0)*1104*6000/rtime%
2080Y%=(data(1)-low)*800/(high-low)
2090MOVE X%+2,Y%
2100DRAW X%-2,Y%
2110MOVE X%,Y%+2
2120DRAW X%,Y%-2
2130PROCdump
2140ENDPROC
2160DEFPROCdump
2170FOR I%=0 TO 2
2180PRINT#file,data(I%)
2190NEXT I%
2200ENDPROC
2210
2220DEFPROCclose
2230CLOSE#file
2240ENDPROC
2250
2260DEFPROCmark
2270MOVE X%,10
2280DRAW X%,0
2285 S%=0
2290ENDPROC
2300
2310DEFPROCend
2320
2330REM: SHUTS DOWN THE SYSTEM
2340PROCclose
2350ENDPROC
2360
2370DEFPROCins
2380
2390PRINT " INSERT PROGRAM DISC IN DRIVE 0 AND PRESS <SPACE-BAR> TO CONT."
2400REPEAT
 2410I%=INKEY(1)
 2420UNTIL I%=32
 2430ENDPROC
>
```

Data Recall Program

```
 10 MODE 3
 30 REM: DATA RECALL PROGRAM
 40 REM: PROGRAM "MREC1"
 60
 70 MODE 7
 80 VDU23,1,0;0;0;0;
 90 DIM data(2)
100 PROCdiscright
110 PROCrecdata
120 PROCplot
130 MODE 0
140 IF D%=65 THEN PROCdiff ELSE PROCgo
150 PROCprinter
160 CHAIN"MMENU"
170 END
180
190 DEFPROCdiscright
210 REM: get the right data disc and the right file
230 CLS
240 PRINT TAB(7,5);"DISC FILES ON DRIVE 0";TAB(7,6);"--------------------"
250 PRINT TAB(5,10);"PLACE DISC WITH DATA IN DRIVE 0"
260 PRINT TAB(7,12);"PRESS SPACE-BAR WHEN READY"
270 REPEAT
280 I%=INKEY(1)
290 UNTIL I%=32
300 REPEAT
310 CLS
320 PRINT  TAB(7,1);"FILES ON THE DISC";TAB(7,2);"----------------"
330 *.
340 PRINT  TAB(2,28);"IS THIS THE DISC YOU WANT Y/N"
350 REPEAT
360 I%=INKEY(1)
370 UNTIL I%=89 OR I%=78
380 UNTIL I%=89
390 REPEAT
400 REPEAT
410 Z$=INKEY$(50)
420 PRINT  TAB(2,28);"                                  "
430 PRINT  TAB(6,28);"WHAT FILE DO YOU WANT"
440 INPUT TAB(11,29) file$
450 L%=LEN(file$)
460 UNTIL L%<8 AND L%>0
470 PRINT  TAB(6,28);"                                  "
480 PRINT  TAB(6,28);"FILE NAME ";file$;", Y/N"
490 REPEAT
500 I%=INKEY(1)
510 UNTIL I%=89 OR I%=78
520 UNTIL I%=89
530 ENDPROC
540
550 DEFPROCrecdata
570 REM: access the data on the file selected
590 CLS
600 PRINT TAB(1,11);"DO YOU WANT A PRINT-OUT OF THE DATA Y/N"
610 REPEAT
620 I%=INKEY(1)
630 UNTIL I%=89 OR I%=78
640 IF I%=89 THEN PROCdump
650 ENDPROC
660
670 DEFPROCopenfile
680 file=OPENIN  file$
690 ENDPROC
700
710 DEFPROCdump
```

```
730 REM: dumps the raw data to printer
750 PROCopenfile
760 VDU2
770 VDU1,27
780 VDU1,77
790 VDU21
800 PRINT TAB(9);"TIME (mins)";TAB(30);"BALANCE (grams)";TAB(50);"DATA SET"
810 PRINT TAB(9);"-----------";TAB(30);"---------------";TAB(50);"--------"
820 PRINT:PRINT
830 @%=&20508
840 REPEAT
850 FOR I%=0 TO 2
860 INPUT#file,data(I%)
870 NEXT I%
880 PRINT TAB(13);data(0);TAB(34);data(1);TAB(52);data(2)
 890 UNTIL EOF#file
 900 CLOSE#file
 910 @%=10
 920 VDU6
 930 VDU3
 940 ENDPROC
 950
 960 DEFPROCplot
 980 REM: shows the data graphically
1000 CLS
1010 PRINT TAB(3,11);"PLOTTING RAW OR AVERAGED DATA"
1020 PRINT TAB(2,13);" <R>  RAW PLOT    <A>  AVERAGE"
1030 REPEAT
1040 D%=INKEY(1)
1050 UNTIL D%=82 OR D%=65
1060 PROClong
1070 PROCexpmax
1080 PROCexpmin
1090 ENDPROC
1095
1100 DEFPROCexpmax
1120 REM: inputs the high balance reading for the graph
1140 CLS
1150 PRINT TAB(7,5);"HIGH GRAPH READING";TAB(7,6);"------------------"
1160 PRINT TAB(0,10);"ENTER THE MAX BALANCE READING"
1162 PRINT TAB(2,12);"(in mNEWTONS, ie.10*grams)"
1170 REPEAT
1180 PRINT TAB(10,14);"            "
1190 PRINT TAB(3,16);"                                    "
1200 INPUT TAB(10,14) high
1210 PRINT TAB(3,16);"MAX VALUE OF ";high;" mNEWTONS, Y/N ?"
1220 REPEAT
1230 I%=INKEY(1)
1240 UNTIL I%=89 OR I%=78
1250 UNTIL I%=89
1255 ghigh = high * 0.1
1260 ENDPROC
1270
1280 DEFPROCexpmin
1300 REM: inputs the low balance reading for the graph
1320 CLS
1330 PRINT TAB(7,5);"LOW GRAPH READING";TAB(7,6);"-----------------"
1340 PRINT TAB(0,10);"ENTER THE MIN BALANCE READING"
1342 PRINT TAB(2,12);" (in mNEWTONS, ie.10*grams)"
1350 REPEAT
1360 REPEAT
1370 PRINT TAB(10,14);"            "
1380 PRINT TAB(3,16);"                                    "
1390 INPUT TAB(10,14) low
1400 UNTIL low<high
1410 PRINT TAB(3,16);"MIN VALUE OF ";low;" mNEWTONS, Y/N ?"
1420 REPEAT
```

```
1430 I%=INKEY(1)
1440 UNTIL I%=89 OR I%=78
1450 UNTIL I%=89
1455 glow = low * 0.1
1460 ENDPROC
1470
1480 DEFPROCgo
1500 PROCscreen
1510 PROCread
1520 ENDPROC
1530
1540 DEFPROCscreen
1560REM: sets up the graphics screen
1580 CLS
1590 VDU 24,50;100;1254;1000;
1600 VDU 28,0,31,79,30
1610 MOVE 1204,150
1620 DRAW 100,150
1630 MOVE 1204,950
1640 DRAW 1204,150
1650 MOVE 100,950
1660 DRAW 1204,950
1670 MOVE 100,150
1680DRAW 100,950
1690 VDU5
1710 MOVE 500,1000:PRINT"plot of force vs. time"
1720 MOVE 500,130:PRINT " time (mins)"
1730 MOVE 50,1000:PRINT "force (N/1000)"
1735 @%=&20003
1740 MOVE 1180,130:PRINT rtime%
1750 MOVE 85,130:PRINT "0"
1755@%=&20508
1760 MOVE 50,160:PRINT low
1770 MOVE 50,965:PRINT high
1780 VDU4
1790 @%=10
1800 FOR I%=150 TO 950 STEP 80
1810 MOVE 100,I%
1820 DRAW 110,I%
1830 NEXT I%
1840 VDU 29,100;150;
1850 VDU23,1,0;0;0;0;
1860 ENDPROC
1870
1880 DEFPROCread
1900 PROCopenfile
1910 M%=0
1920 REPEAT
1930 FOR I%=0 TO 2
1940 INPUT#file,data(I%)
1950 NEXT I%
1955 IF data(1)=0 THEN 1980
1960 IF data(2)>M% THEN PROCmark:M%=M%+1
1970 IF data(1)>glow AND data(1)<ghigh THEN PROCcross
1980 UNTIL EOF#file OR data(0)>=rtime%
1990 CLOSE#file
2000 ENDPROC
2010
2020 DEFPROCcross
2040 X%=data(0)*1104/rtime%
2050 Y%=(data(1)-glow)*784.8/(ghigh-glow)
2060 MOVE X%+2,Y%
2070 DRAW X%-2,Y%
2080 MOVE X%,Y%+2
2090 DRAW X%,Y%-2
2100 ENDPROC
2110
2120 DEFPROCmark
2150 MOVE X%,10
2160 DRAW X%,0
2170 ENDPROC
2180
```

```
 2190 DEFPROCdiff
 2210 PROCscreen
 2220 PROCopenfile
 2225 data(2)=0
 2230 M%=0
 2240 C%=0
 2250 sum=0:otime=0
 2260 REPEAT
 2270 FORI%=0 TO 2
 2280  INPUT#file,data(I%)
 2290 NEXT
 2292 IF data(1)=0 THEN 2320
 2300 C%=C%+1
 2310 IF data(2)>M% AND C%>1 THEN PROCcalc ELSE IF data(2)>M% AND C%=1 THEN PROCskip ELSE PROC
next
 2320 UNTIL EOF#file
 2330 CLOSE#file
 2340 PROCcalc
 2350 ENDPROC
 2360
 2370 DEFPROCnext
 2390 tim=data(0)
 2420 sum=sum+data(1)
 2430 ENDPROC
 2440
 2450 DEFPROCskip
 2470 M%=M%+1
 2480 C%=1
 2490 PROCmark
 2520 sum=data(1)
 2530 otime=data(0)
 2540 ENDPROC
 2550
 2560 DEFPROCcalc
 2580 hold=data(0)
 2590 data(0)=(tim+otime)/2
 2600 hold2=data(1)
 2610 IF C%=1 THEN data(1)=sum/(C%) ELSE data(1)=sum/(C%-1)
 2620 IF data(1)>glow AND data(1)<ghigh THEN PROCcross
 2630 data(0)=hold
 2640 data(1)=hold2
 2650 PROCskip
 2660 ENDPROC
 2670
 2680 DEFPROCprinter
 2700 PRINT "        HAVE YOU GOT A PRINTMASTER CHIP"
 2710 A$=INKEY$(200)
 2720 PRINT "IF SO <P> TO PRINT,<S> TO SCREEN DUMP <PROG.DISC IN DRIVE 0>, ELSE <SPACE-BAR>"
 2730 REPEAT
 2740 I%=INKEY(1)
 2750 UNTIL I%=80 OR I%=83 OR I%=32
 2758 IF I%=80 THEN *GDUMP 1 1 3 1 50
 2760 IF I%=83 THEN GOTO 2995
 2770 PROCcd
 2780 ENDPROC
 2790
 2800 DEFPROCcd
 2810
 2820 PRINT "       INSERT PROGRAM DISC IN DRIVE 0 AND PRESS <SPACE-BAR> TO CONT."
 2830 REPEAT
 2840 I%=INKEY(1)
 2850 UNTIL I%=32
 2860 ENDPROC
 2870
 2880 DEFPROClong.
 2900 REPEAT
 2910 CLS
 2920 PRINT TAB(5,8);"MAXIMUM TIME ON THE GRAPH (mins)?"
 2930 INPUT TAB(14,10);rtime%
 2940 PRINT TAB(14,12);rtime%;" mins Y/N"
 2950 REPEAT
 2960 I%=INKEY(1)
 2970 UNTIL I%=89 OR I%=78
 2980 UNTIL I%=89
 2990 ENDPROC
 2992 GOTO 160
 2996 *SDUMP
>
```